School of Aerospace, Mechanical & Manufacturing Engineering

RMIT University, Melbourne

Bio-Inspired Design of Aerospace Composite Joints

A thesis submitted in fulfilment of requirements for the degree of

DOCTOR OF PHILOSOPHY

Lauren Anne Burns

B. Eng (Aero) Hons

30 July 2012

DECLARATION

I certify that except where due acknowledgement has been made, the work is that of the author alone; the work has not been submitted previously, in whole or in part, to qualify for any other academic award; the content of the thesis is the result of work which has been carried out since the official commencement date of the approved research program; and, any editorial work, paid or unpaid, carried out by a third party is acknowledged.

Lauren Anne Burns

30 July 2012

ACKNOWLEDGEMENTS

Firstly, I would like to give my deepest thanks to my academic supervisors Dr Stefanie Feih and Professor Adrian Mouritz. I was extremely fortunate to have supervisors who are both world class researchers and highly approachable and personable people and I value you as mentors and friends. I acknowledge your prompt and thoughtful feedback as immeasurably increasing the quality of this thesis and the journal papers based on this research.

I would also like to thank my industry supervisor Mr David Pook for the time he generously donated to our regular meetings, as well as colleagues Andrew Glynn, Chris Howe and Steve Georgiadis from Boeing Research & Technology Australia who all contributed to my understanding of this research from an industry perspective. This PhD would not have happened without the financial support provided by the Australian Postgraduate Award and Boeing Research & Technology Australia.

I would like to acknowledge and thank the tireless efforts of RMIT technical staff Peter Tkatchyk, Bob Ryan and Ian Overend. In particular, Ian for his woodworking skills and machining tooling for my composite samples, Bob for overcoming numerous composite manufacturing crises and Peter for always helping me with such patience through my experimental testing.

I thank the support of industry: David Smith from Hancock Victoria Plantations for narrowly avoiding knocking down a Wombat's verandah in pursuit of my tree samples and Angela Borella who was open minded enough to lend the CT scanner at Central Melbourne Medical Imaging for my tree samples. I also acknowledge the facilities and technical assistance of the Australian Microscopy and Microanalysis Research Facility, in particular Phil Francis at RMIT University and Alan Jones at the University of Sydney.

I thank the composites research team for their regular feedback and fellow PhD candidates Asintha Nanayakkara, Tze Min Koh and Adam Shrimpton for their friendship and support. I thank my family, in particular my mother Barbara who is always there for me and supports me in everything I do.

Special thanks to my favourite person Gerard Drew (Gerry) for your love, patience and support and showing up to the award ceremonies. Without our endless conversations, back massages when I was suffering from computer back, spontaneous holidays, your cultivation of my relentless quest for knowledge and encouraging my killer instinct prior to important presentations my life would be much the poorer. I love you.

In memory of Ashish Miranda, without whom this PhD might not have happened

25 October 1984 – 8 January 2009

PUBLICATIONS

The work presented in this thesis has been published in the papers or presented in the conferences listed below:

JOURNAL PAPERS

i. Burns, LA, Mouritz, AP, Pook, D & Feih, S 2012, *Strength improvement to composite T-joints under bending through bio-inspired design*, Composites Part A, vol. 43(11), pp. 1971-1980.

ii. Burns, LA, Mouritz, AP, Pook, D & Feih, S 2012, *Bio-inspired design of aerospace composite joints for improved damage tolerance*, Composite Structures, vol. 94(3), pp. 995-1004.

CONFERENCE PAPERS

i. Burns, LA, Mouritz, AP & Feih, S 2011, 'Application of a bio-inspired design strategy to delay damage initiation in a FRP T-joint under bending', in *Proceedings of the 18th International Conference on Composite Materials (ICCM18) 24 August, Jeju*, Korea.

ii. Burns, LA, Mouritz, AP & Feih, S 2011, 'Biomimetics for Aerospace Composite T-Joints', in *International Graduate Summer School in Aeronautics and Astronautics Beihang University*, Beijing, China.

iii. Burns, LA, Mouritz, AP, Pook, D & Feih, S 2011, 'Bio-inspired design of aerospace composite joints', in *Proceedings of the Asia-Pacific International Symposium on Aerospace Technology (APISAT) 1 March*, Melbourne, Australia.

iv. Burns, LA 2010, 'Tree Joints: Biomimetic insights for aerospace composite joints', in *Proceedings of the 27th International Congress of the Aeronautical Sciences (ICAS) 21 September,* Nice, France.

AWARDS

The work presented in this thesis has won the following awards:

John McCarthy Student Award 2010

27th International Congress of the Aeronautical Sciences (ICAS)

Awarded for the conference paper "Tree Joints: Biomimetic insights for aerospace composite joints" which was judged by content and presentation to be the best presented in the student sessions of the International Congress of the Aeronautical Sciences (ICAS)

Amelia Earhart Fellowship 2010

This US$10,000 fellowship is awarded annually by Zonta International to 35 women around the world who are pursuing PhD degrees in the aerospace sciences

RMIT Postgraduate Research Award 2012

School of Aerospace, Mechanical and Manufacturing Engineering

TABLE OF CONTENTS

LIST OF FIGURES

LIST OF TABLES

SUMMARY

'*As a general principle natural selection is continually trying to economise every part of the organisation'*, Charles Darwin, On the Origin of Species, 1859

This PhD thesis utilises the design principles of structural joints found in nature, focusing on tree branch joints, in order to create novel prototype designs for carbon fibre reinforced polymer (CFRP) T-joints resulting in improved structural performance. The aim of biomimetic engineering is to understand the connection between the organisation of biological materials and their extraordinary mechanical properties. Conversely, a major risk of biomimetic engineering is synergistic effects of complex hierarchical structures found in nature cannot be replicated using production-scale manufacturing processes.

The primary objectives of this thesis are; the development of an understanding of the relationship between the architecture and the mechanical properties and failure modes of tree branch-trunk joints; the development of a validated optimisation methodology based on the principle of uniform strain to improve the failure strength of composite T-joints by adapting the orthotropic material properties to the prevailing loading conditions; improve the damage tolerance of composite T-joints by introducing bio-inspired structural design changes that promote extrinsic toughening; and quantify the effects of bio-inspired material optimisation and structural design changes on the internal stress distribution in the T-joint radius bend and delta-fillet regions through finite element analysis.

A review of the scientific literature pertaining to biological materials and biomimetics, the material properties of wood, the structural properties of the branch-trunk connection and the parametric design and performance of fibre reinforced polymer angled joints is presented in chapter two. From this evaluation, gaps were identified in the understanding of how to best utilise the anisotropy of fibre reinforced composites, as well as an overall lack of research pertaining to the biomimetic approach to improve the design of aerospace composite joints, which is the focus of this thesis.

Chapter three provides a comprehensive review of the architecture of the branch-trunk joint of *Pinus radiata*, a representative softwood species. The structure from the micro- to the macro-length scale was investigated via mechanical testing and the imaging techniques of micro x-ray computed tomography (micro-CT), scanning electron microscopy (SEM), and computed tomography (CT). It was found that the tree joint deforms via inelastic, non-brittle fracture processes despite the intrinsic brittleness of the constituents and exhibit micro-damage modes of fibre pull-out, fibre bridging and crack deflection.

Chapter four focuses on improving the failure load of CFRP T-joints under bending load by utilising the biological principle of uniform strain under the critical load case. This is achieved via the methodology of tailoring orthotropic material properties to the prevailing loading conditions. An optimisation program was created to automate the optimisation of the laminate ply stacking sequence based on the objective of minimising the peak interlaminar tensile stress in the T-joint radius bend while maintaining similar global laminate stiffness properties to a baseline design. The FE model predicted significant reductions in the interlaminar tensile and shear stresses which were experimentally validated to improve the bending strength by an average of 40%. The optimised T-joint also exhibited an experimental improvement in tensile strength. As an extension of this work a design of experiments (DoE) program was conducted to investigate the effect of tailoring various quasi-isotropic and anti-symmetric hygrothermally stable ply orientations. It was experimentally validated that similar improvements could be made to the bending and tensile strengths of the T-joint using less computationally intensive solutions.

Chapter five focuses on adapting the high levels of integration observed in the macro-structure of the tree joint in chapter three into a composite T-joint design. The flange plies were embedded to 25%, 50% and 75% of the depth of the skin and compared to a geometrically similar baseline T-joint. Experimental testing revealed that the embedded T-joints exhibited increased extrinsic toughening under tensile and bending loading, resulting in increased absorbed inelastic strain energy (defined as pseudo ductility), increased absorbed strain energy to failure (toughness), and higher load-carrying capacity following damage initiation (damage tolerance). However these improvements were achieved at the expense of earlier onset damage initiation. A non-linear FE model revealed early onset damage initiation was due to the increased skin flexibility in the embedded T-joints. 50% embedment was found to represent a balance between the increased toughness of the T-joint and reduced damage initiation load.

In chapter six a prototype T-joint was tested which incorporates the bio-inspired principle of hierarchical design by combining embedded design implemented at the structural length scale with optimised ply orientation implemented at the material (ply) length scale to counteract the deficiencies in each individual bio-inspired design. The hierarchical T-joint exhibited bending and tensile strength equal to or better than the baseline design, and improved damage tolerance under both tensile and bending loading conditions.

Chapter seven presents a preliminary study into the dynamic response of the bio-inspired optimised and embedded T-joints under low energy (2 – 14 J) impact testing. The results showed that fabric 50% embedded T-joint had approximately twice the impact damage resistance of the conventional design. The optimised laminate stacking sequence did not affect impact damage resistance because the global laminate properties of the bio-inspired and quasi-isotropic baseline designs were similar. After impact testing the residual strength of the bio-inspired T-joint prototypes was measured using quasi-static tensile pull-off testing. The results showed that the bio-inspired T-joints had roughly equal impact damage tolerance compared to baseline conventional quasi-isotropic control samples.

Chapter eight briefly discusses certification and manufacturing issues for bio-inspired composite T-joints. Chapter nine concludes that based on the findings of the FEM, optimisation and experimental results, this PhD research proves that biomimetics and specifically the bio-inspired design principles of uniform strain and hierarchical design are a useful approach in creating novel prototype composite T-joints resulting in improved structural performance. Recommendations for future research are provided as advanced manufacturing techniques expand the possibilities of incorporating greater hierarchy into bio-inspired designs.

As a final challenge, looking into the future the new frontier lies in the synthesis of bio-inspired materials through manufacturing processes that are characteristic of biological systems. This involves nano-scale self-assembly of the components featuring a number of toughening and strengthening mechanisms at each of the nano-, micro-, meso- and macro-length scales. Although this approach presents enormous challenges, mastering control over the fundamental mechanisms of self-assembly exemplified by the growth of biological structures will eventually lead to new materials with extraordinary properties.

CHAPTER 1:

1 INTRODUCTION

1.1 AIRCRAFT COMPOSITE JOINTS

The rising cost of fuel is driving commercial airline manufacturers to focus on light-weight structural materials as a means of reducing aircraft operating costs in order to make their products more attractive to their airline customers. The performance gains made possible by light-weight composite materials are driving the ever-increasing use of composites in the primary structure of civil aircraft. In turn this has generated a need for composite joints that are both strong and damage tolerant.

Joints and interfaces are one of the key aspects of the design and production of aircraft composite structures. Aircraft structures are assembled using many thousands of connections, which are usually the weakest links within the structure. Aerospace designers have long realised the advantages of orthotropic composite materials in which the design can be tailored to align the fibres with the primary load direction, resulting in significant weight savings in parts such as aircraft skins. The development of new fibre reinforcements and toughened resins has created an opportunity to transition to polymer matrix composites for load-bearing joints that will reduce structural weight and subsequently also reduce the environmental and economic costs of aircraft. However, the mindset of the designer is influenced by the traditional use of metals, potentially inhibiting the development of improved joint designs that become possible through the use of composites. Paradoxically, when it comes to designing joints, many engineers persist in joining composite parts like ‘black aluminium’, using traditional methods originally developed for isotropic metallic structures.

Composite parts are frequently joined by rows of fasteners. Bolts and rivets destroy the load-bearing fibres and introduce high local stresses into regions already weakened from severed fibres. Conventionally designed bonded composite joints often suffer from poor resistance to through-thickness stresses, which can cause rapid, brittle and potentially catastrophic failure known as ‘unzipping’. The threat of ‘unzipping’ to fail-safe design has resulted in conservative certification requirements for composite airframe commercial airliners, partly negating the weight-saving potential of composites.

Over the last few decades many approaches have been investigated to improve the strength of aerospace joints through both design modification and material selection, for example splicing metal joints and composite skins (refer Figure 1-1). Other attemps to improve the structural efficiency and damage tolerance of bonded composite joints include the use of toughened adhesives, thermoplastic interleaving, and through-thickness reinforcement by z-pinning, stitching or tufting [1, 2]. All of these approaches have gone some way to achieving their aim, however a promising approach that has not yet been assessed is the design of aircraft composite joints based on biomimetic engineering. Designs based on biomimetics represent a novel approach for breaking out of the traditional mindset and improving the performance of aerospace composite joints.

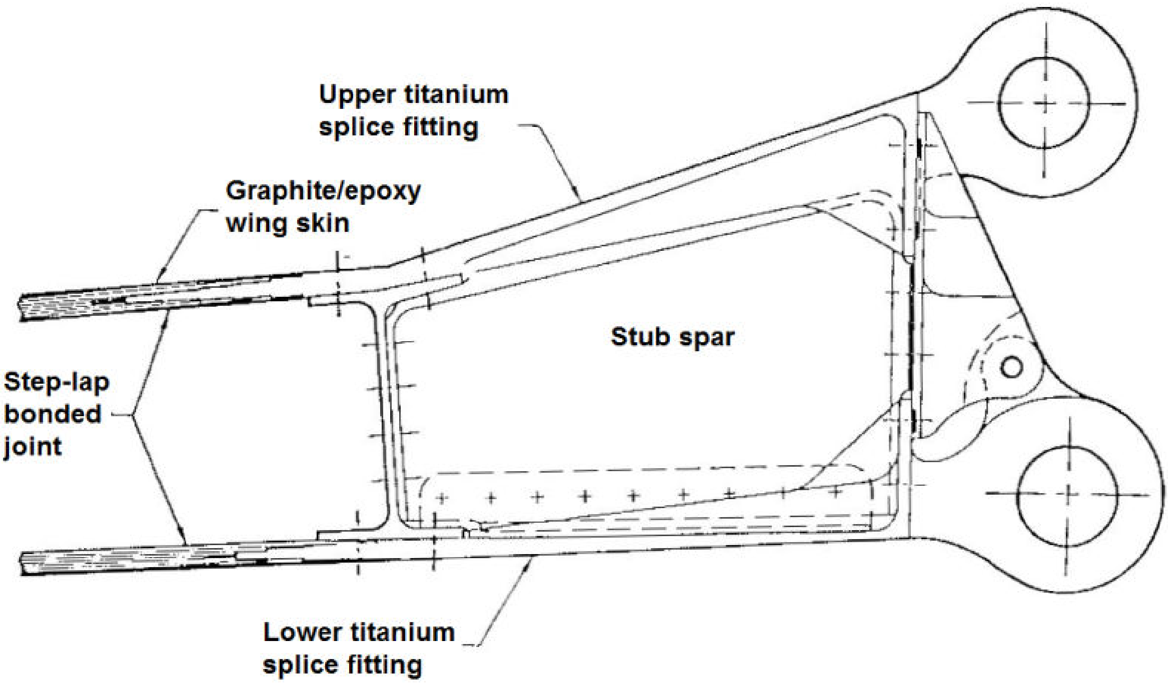

Figure 1-1 Stepped-lap wing root joint on the F/A-18 [3] pp. 315

In this PhD project research will be focused on composite T-joints. T-joints have many applications in aircraft design. They are used in the wing-box and empennage to join orthogonal panels together, for example connecting spars or ribs to the skin. They are also used in control surfaces, wing skins and the fuselage to connect stiffeners of various design (e.g. blade, I-beam or hat-shaped) to stabilise the thin-gauge skin against buckling.

A typical T-joint consisting of a blade stiffener connected to the skin is shown in Figure 1-2. The stiffener is made-up of a vertical stiffener web that is connected to the horizontal skin via two flanges. The stiffener contains details of two radius bends and a delta-fillet region beneath the radii. The radius bends and delta-fillet region are considered the critical region controlling T-joint strength. In this zone the vertical loads are transferred 90° into the horizontal skin which generates significant geometric stress concentrations and out-of-plane loading on the composite.

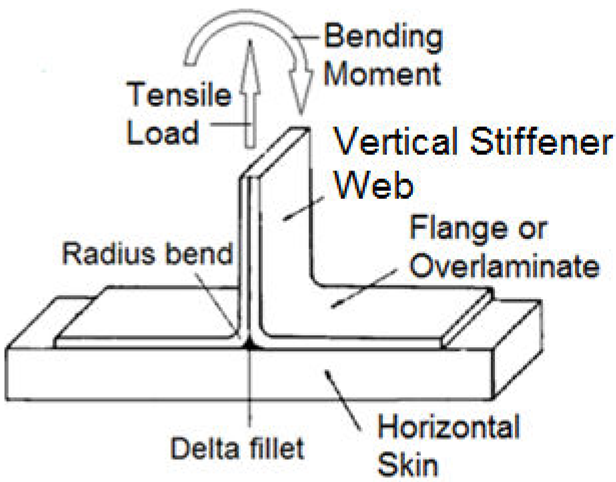

Figure 1-2 Typical T-joint

1.2 BIOMIMETIC DESIGN

Biomimetic design is a potential shortcut to innovation. The simple essence of biomimetics is learning from nature and applying this knowledge to improve engineering performance. It is a multi-disciplinary science lying at the intersection of engineering, materials science and biology. Biological materials comprising trees, bones, shells and sea sponges must withstand bending, shear and compression loading from such things as wind, water, self-weight and dynamic impacts as a matter of survival [4]. Natural load-bearing structures have undergone millions of years of natural selection and are evolutionarily optimised to be fit-for-purpose, inclusive of structural integrity to ensure survival. Charles Darwin surmised, '*as a general principle natural selection is continually trying to economise every part of the organisation*' [5]. Therefore natural load-bearing structures provide a good model for engineering design because they have been evolutionarily optimised to fulfil their function of structural integrity using the minimum of scarce material and energy resources.

Biomimetics can be based on aesthetics, structure or function, or a combination of all three. The Eden project located in Cornwall, UK, displays plants from around the globe in the world's largest greenhouse. Figure 1-3 shows the design of the roof of the education centre is derived from a mathematical basis found in nature called phyllotaxis which describes the opposing spirals found on biological structures such as pinecones, pineapples and sunflower heads. However in this case a functional design has been appropriated purely for aesthetic purposes.

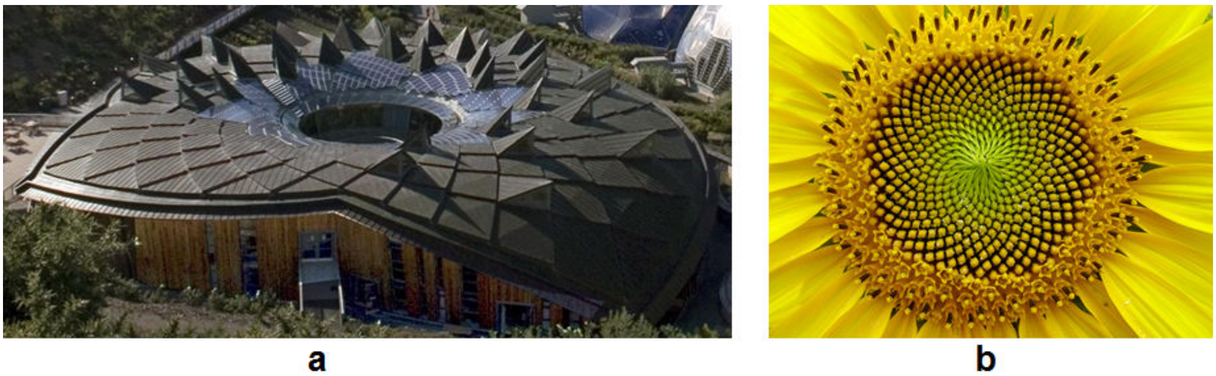

Figure 1-3 Bio-inspired aesthetics: (a) Eden project, Cornwall, UK [6] inspired by; (b) sunflowers [7]

In central London 30 St Mary Axe, also known as 'the gherkin', is an example of a bio-inspired structure. The diagonal steel grid structure, known as a diagrid, reinforces the building with sufficient stiffness not to require internal reinforcement [8]. A similar diagrid forms the main structure of the deep sea sponge *Euplectella aspergillum* (refer Figure 1-4).

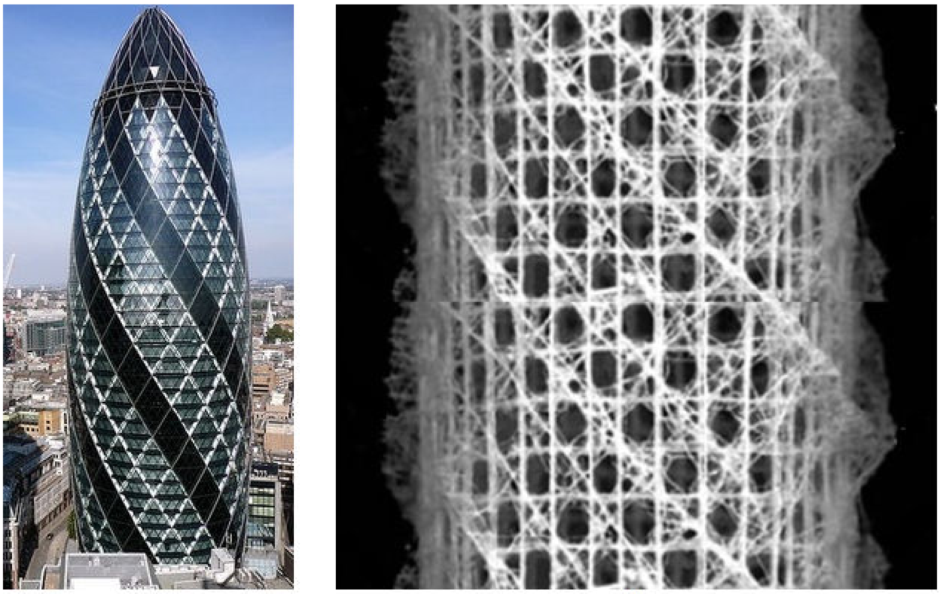

a b

Figure 1-4 Bio-inspired structure: (a) 30 St Mary Axe aka “the gherkin”, London, UK [8], structurally inspired by the diagrid also found in; (b) *Euplectella aspergillum* deep sea sponge; provides structural stiffness [9]

The Chinese National Aquatics Centre, also known as the ‘water cube’, built for the Beijing Olympics is based on both aesthetics and function. While the design based on the natural formation of soap bubbles (refer Figure 1-5) no doubt contributes to the aesthetics of the building, it also serves the function of allowing natural light to permeate the building, reducing lighting energy requirements by 55% [10].

An example of biomimetics being utilised in the aeronautical sciences is the aerodynamic improvement gained from the ‘shark skin effect’ (refer Figure 1-6). At the micro-level shark skin has grooved scales directed almost parallel to the body axis of the shark. These riblets reduce drag by affecting the viscous boundary layer as the shark swims through water. An A-340 fitted with a plastic film with a similar ribbed coating experienced a drag reduction of up to 8%, corresponding to a 1.5% reduction in fuel burn [11]. Similar technology had been utilised for high performance racing swimsuits, banned in competition by the world swimming body FINA since 2010.

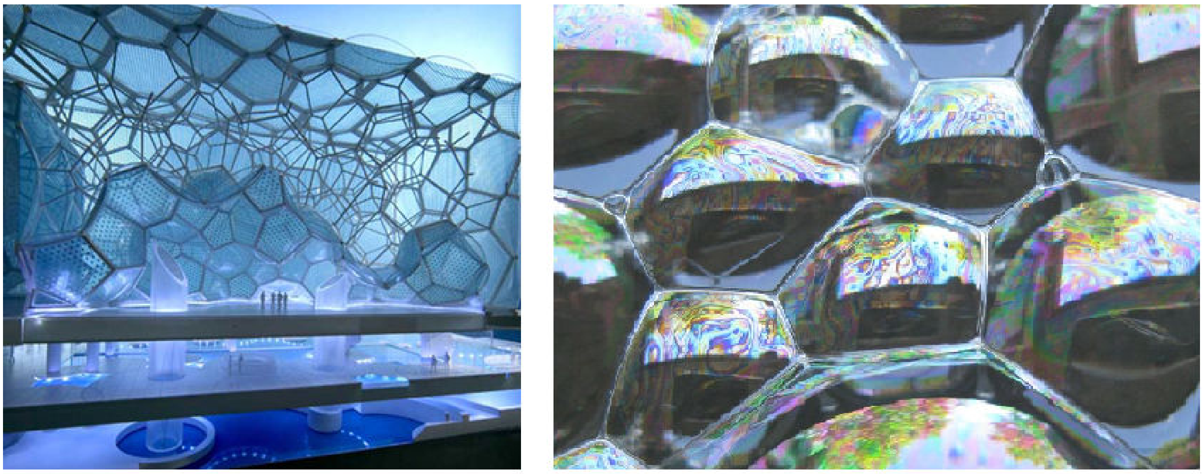

a b

Figure 1-5 Bio-inspired aesthetics and function: (a) The ‘water cube’ swim centre built for the Beijing Olympics, China [10], inspired by; (b) soap bubbles; allows natural light to reduce building energy consumption [12]

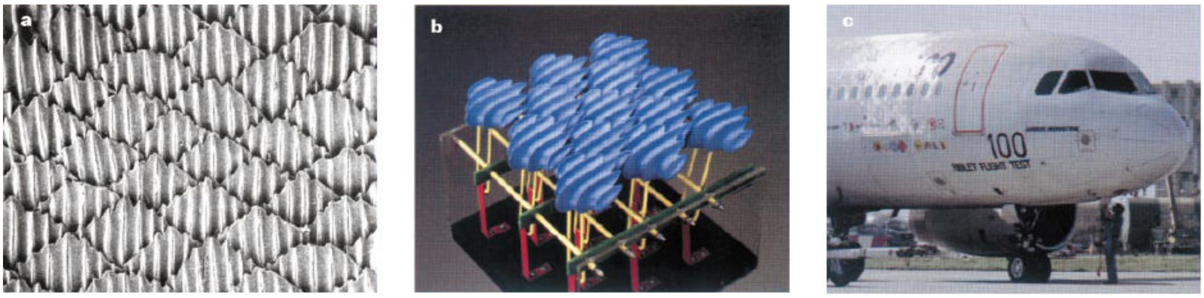

Figure 1-6 (a) The riblets on shark skin provided the inspiration for; (b) modelling studies of the drag reduction they confer leading to (c) trials of aircraft coated with this same microscopic texture [11]

In the context of structural design, biomimetics is based on the idea of elucidating principles of biological growth using the language of mathematics to relate the form of biological creatures to their function. This idea was raised in 1893 by the German forester Metzger [13] who hypothesised that the structure of tree trunks experiencing wind loads was based on the mathematical principles of uniform bending stress. It was further expanded in Darcy Wentworth Thompson’s seminal 1917 book “On Growth and Form” [14]. The literature on biological structures and bio-inspired design will be reviewed in chapter two.

1.3 AIMS AND SCOPE OF THE PHD THESIS

Developing new materials as a means to achieve performance gains is both time-consuming and extremely costly for aircraft manufacturers. It makes better business sense to target research funds towards getting more out of existing materials that are already certified. Biomimetic engineering, which emphasises hierarchical design incorporating both materials and structure, has the potential to drive next-generation improvements in structural performance analogous to the development of a new material class, with less commercial risk compared to the 20+ years of development required to define the processing parameters and develop design practises for a new material.

A bio-inspired design methodology has been used to optimise an adhesive butt-joint of dissimilar materials subject to tension loading [15] and optimise fibre lay-ups in fibre-reinforced polymers such as fibreglass [16-18]. However, to date bio-inspired engineering has not been applied to the problem of optimising aerospace composite T-joints. Research is required in order to assess the feasibility of applying the biomimetic approach to aircraft structures. Concepts, prototypes and testing are required to broadly assess the potential benefits of biomimicking and assess produceability. The major risk of the biomimetic approach is that it will simply be too difficult to replicate the complex hierarchical structures found in nature in composite airframes due to the limitations of production-scale manufacturing processes.

The central scope of the PhD is to determine how architecture and organisational principles observed in tree branch-trunk joints can be transferred to carbon/epoxy composite T-joints through bio-inspired engineering for improved structural performance.

The aims of the PhD thesis can be summarised as:

⇒ Develop an understanding of the interaction between the hierarchical macro- and micro-level architecture and the damage mechanisms, failure modes and mechanical performance of a representative tree branch-trunk joint under bending load.

⇒ Develop an experimentally validated bio-inspired optimisation methodology to improve the failure strength of CFRP T-joints by adapting the material properties to the prevailing loading conditions.

⇒ Improve the static and impact damage tolerance of CFRP T-joints by introducing bio-inspired structural design changes that introduce extrinsic toughening mechanisms into the structure of the T-joint.

⇒ Develop a hierarchical design by combining bio-inspired material optimisation with bio-inspired structural design changes to generate a composite T-joint that is both strong and tough under the prevailing loading conditions.

⇒ Quantify the effects of bio-inspired material optimisation and structural design changes on the internal stress distribution in the T-joint radius bend and delta-fillet regions through finite element analysis.

1.4 STRUCTURE OF THE PHD THESIS

Chapter two provides a comprehensive review of the scientific literature pertaining to biological materials and biomimetics, the material properties of wood, the structural properties of the branch-trunk joint and the parametric design and performance of fibre-reinforced composite T-joints under quasi-static and dynamic loading. Reference is made to the available analytical and experimental models relating the strength and toughness of composite T-joints to their design parameters including flange thickness, flange radius, skin thickness, delta-fillet area, ply stacking sequence and material selection. From this evaluation gaps were identified in the research concerning how to exploit the anisotropy of fibre reinforced composites by utilising the full spectrum of ply orientations as a variable in joint design, the effect of integrating adherends through embedded design, as well as an overall lack of research pertaining to the biomimetic approach to improve the design of aerospace composite joints, which is the focus of this thesis.

In chapter three the macro- and micro-level architecture of the tree branch-trunk joint is investigated and related to the mechanical properties and failure modes of the representative softwood species *Pinus radiata*. The structure of the tree branch-trunk joint from the micro- to the macro-length scale was investigated using the imaging techniques of micro x-ray computed tomography (micro-CT), scanning electron microscopy (SEM), and computed tomography (CT). Micro-CT was performed on samples where loading was stopped at the onset of damage initiation and SEM was used to image the branch-trunk fracture surfaces after final failure. Mechanical bending tests were performed on freshly cut (green wood) branch-trunk connections of *Pinus radiata* in the gravity direction of the self-weight of the branch on both intact and vertically bisected specimens, and in the reverse gravity direction. Coupon tests were performed to determine the transverse tensile strength and modulus of wood samples taken across the branch-trunk joint in comparison to the tangential-radial and radial-longitudinal planes in the trunk wood.

Chapter four presents finite element ananlysis, optimisation and experimental findings concerning improvement in the damage initiation strength of composite T-joints through the development of a bio-inspired optimisation methodology. The optimisation program considers the orientation of each ply within the stiffener radius bend laminate as a design parameter and was developed as an extension of a linear-elastic finite element model. The optimisation program alters the laminate stacking sequence with the objective of minimising the interlaminar tensile stress concentration across the radius bend while keeping the global stiffness properties of the laminate within ±10% of the baseline quasi-isotropic lay-up. The optimisation objective is based on the principle of uniform strain observed within tree branch-trunk joints [19]. The bending load case was considered because of the consistently observed failure mode of delamination in the radius bend which is controlled primarily by interlaminar tensile and shear stresses. Finite element analysis (FEA) provides details of the internal stress distribution across the radius bend and delta-fillet regions of the baseline and optimised T-joint under bending load.

As an extension of the work on bio-inspired optimisation, two design of experiments (DoE) programs were conducted to investigate improvements in the quasi-isotropic laminate stacking sequence to maximise the T-joint damage initiation load under bending and a hygrothermally stable laminate stacking sequences with a reduced number of ply angle variables. These designs were also experimentally validated to improve the bending damage initiation load.

Chapter five presents experimental and finite element results on the effect of integrating plies from the stiffener flange into the skin through embedded design (as observed in the macro-structure of the tree branch-trunk joint) on the damage tolerance of composite T-joints under quasi-static loading. Both bio-inspired (embedded) samples with the flange embedded to 25%, 50% and 75% of the depth of the skin and geometrically similar conventionally designed T-joints were subjected to experimental bending, tension and compression loads. A non-linear FE model is used to investigate the effect of progressively embedded design on the interlaminar stresses in the radius bend/delta-fillet region. A strength-based delamination criterion is used to predict the failure initiation load based on the interlaminar tensile and shear stresses extracted from the FEA, which is then compared with experimental results.

In chapter six the findings of an investigation into hierarchical design are presented. The hierarchically designed composite T-joint combines the structural modification of embedded design with the material modification of optimised laminate stacking sequence. The strength and toughness of a unidirectional prepreg T-joint with an optimised flange stacking sequence that is embedded to 50% of the depth of the skin is experimentally evaluated under tensile and bending loading.

Chapter seven presents the experimental and finite element results from a preliminary study into the impact damage tolerance of the two bio-inspired concepts of optimised laminate stacking sequence and embedded design, in comparison to conventional composite T-joints under low energy (2 – 14 J) impact loading. A dynamic explicit element FE model is used to investigate the elastic stresses within the radius bend and delta-fillet regions of the T-joints.

Selected manufacturing and certification issues are discussed in chapter eight along with a summary of key research findings and concluding remarks. Based on the key research findings recommendations are made for future research into biomimetic design to further improve the design of aerospace composite T-joints.

CHAPTER 2:

2 LITERATURE REVIEW

2.1 INTRODUCTION

In the context of light-weight structural design, the objective of biomimetics is to understand the connection between the complex organisation of biological materials and their extraordinary mechanical properties. The properties of biological materials - including strength, flexibility and toughness - regularly surpass by an order of magnitude the properties of their constituent materials [20-22]. Elucidating how nature extracts maximum efficiency from relatively weak and brittle constituents by transforming them through hierarchical design into strong and tough composite materials provides engineers with an enormous opportunity to apply these concepts to a much wider range of materials and manufacturing conditions, driving next-generation improvements in mechanical properties.

This chapter presents a wide-ranging review of published research concerning structural biological materials; the application of biomimetics to engineered materials and structures; the relationship between the architecture and material properties of wood; the relationship between the architecture and the structural properties of the tree branch-trunk connection; and a review of parametric design and the fracture mechanics of fibre-reinforced composite T-joints. The review is diverse (and consequently extensive and long) due to the multi-disciplinary nature of biomimetic design of composite structures, such as T-shaped joints, which is the focus of this PhD. It is necessary to review the state-of-the-art research on a variety of topics to understand the fundamental principles of biomimetic design. In particular there is a significant focus on wood in section 2.4 because wood is the biological material that is the primary focus of the subsequent biomimetic engineering of the composite T-joint.

The literature review of biological materials will cover the defining characteristics of biological materials, generalities of strengthening and toughening strategies, and case studies of the design of four biological materials: nacre, bone, sea sponge and wood. The review of biomimetics will then examine how biological materials have been used as the basis for bio-inspired materials and structures. The scope of the literature review of wood will cover the structure of the wood cell wall, including the relative importance of the S1, S2 and S3 layers to mechanical performance, the in-plane and transverse properties of wood, wood grain patterns, growth rings, radial reinforcements and the fracture mechanics of the wood cell in and beyond the linear-elastic range. The review of the tree branch-trunk joint will include how tree branches are attached to the trunk, the axiom of uniform strain, adaptive growth around branches and mechanical testing and failure modes of the tree branch-trunk joint. The literature review of fibre-reinforced composite T-joints will include a review of the main parameters governing the strength and failure modes of T-joints under tensile, 45° pull-off and bending loads applied to the stiffener web, strength-based delamination failure criteria, fracture mechanics, damage tolerance under static and impact loading, strength, influence of the delta-fillet on T-joint strength and process and hygrothermal stability.

2.2 BIOLOGICAL MATERIALS

2.2.1 Defining characteristics of biological materials

Virtually all biological entities such as tooth, bone, muscle, shells, antlers, sea sponge, wood, birds beaks and claws are made from composite materials [4, 23]. Natural composites generally contain a strong/stiff phase made from a bio-mineral or polysaccharide and a compliant/flaw resistant phase formed from a bio-polymer.

Wegst and Ashby [23] classified natural materials into four classes;

1) Natural ceramics and ceramic composites: Examples such as bone, antler, tooth enamel, nacre in abalone shell and coral are all made from ceramic particles such as hydroxyapatite (with chemical structure $Ca_{10}(PO_4)_6(OH)_2$ found in bone and teeth) or aragonite (a polymorph of $CaCO_3$ found in abalone nacre [22]) in a collagen matrix with densities between 1.8 – 3 kg/m^3. Their moduli are typically lower than engineered ceramics, tensile strength is roughly the same ,and toughness is generally greater by a factor of ten [23].

2) Natural polymers and polymer composites: Examples such as cellulose which is found in the microfibrils of wood [24]) and chitin, found in arthropods e.g. crab exoskeletons [4] are both polysaccharides. The structural proteins collagen (present in blood vessels, tendons, bone and muscle) and keratin (α-keratin is found in skin, wool, hoof and whale baleen and β-keratin is found in claw, scales, feathers and beaks [4]) have densities of ~ 1.2 kg/m^3. Structural proteins are themselves comprised of amino acids. The moduli and tensile strengths of natural polymers are superior in comparison to engineered polymers [23].

3) Natural elastomers: Examples include elastin - present in skin, the walls of veins and arteries and lung tissue [4] - and resilin, which is found in insects have densities of about 1.15 kg/m^3. Moduli and densities are similar in comparison to engineered elastomers [23].

4) Natural cellular materials: Examples include wood and plant materials, coral and cancellous bone (refer Figure 2-1) with low densities of 0.1 – 1.2 kg/m^3 due to the high volume fraction of voids. These materials are anisotropic because of the shape and orientation of the fibres along the cell axis [23]. Classifying cellular materials together is more a distinction of structure rather than material, since wood is comprised from natural polymers which are a distinctly different material compared to cancellous bone which is made from a natural ceramic composite.

To this list of classes Meyers and co-workers added a fifth category [4];

5) Functional biological materials: These are materials that exhibit a structure developed for a specific function such as optical properties (e.g. cornea) or adhesion (e.g. gecko feet) [4]. However it could be argued that all natural materials are also functional biological materials since in general the form of living things will not exist without a function [14].

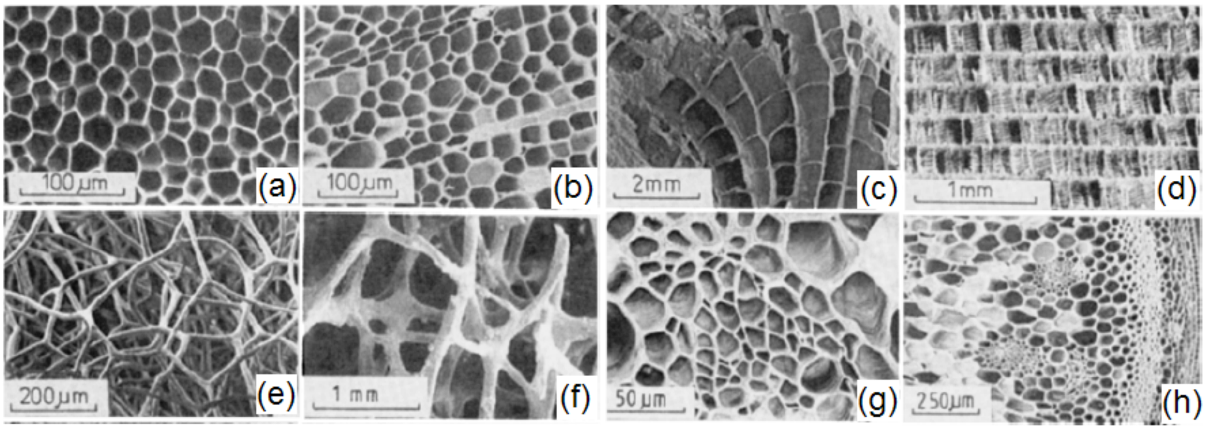

Figure 2-1 Natural cellular materials: (a) cork; (b) balsa; (c) coral; (d) cuttlefish bone; (e) sponge; (f) cancellous bone; (g) iris leaf; (h) stalk of a plant [25]

A summary of the defining characteristics of biological materials is listed below; [4]

- Constructed from a "*limited library*" [21] of chemical elements (Carbon, Oxygen, Hydrogen, Phosphorous, Nitrogen, Sulphur, Calcium, and Silica)
    - Synergic effects mean nature has no respect for the law of mixtures. The relative percentage of each constituent element gives no indication to the overall mechanical properties of the biological composite.
- Strongly hierarchical with an organised structure at the nano-, micro-, meso- and macro-scales interacting in synergy across the various length scales:
    - Nano-crystalline particle or fibrous strong/stiff phase reinforced by an amorphous polymer matrix.
    - Density gradients as a result of load-controlled adaptive growth avoid over-loading or under-utilising material by generating a uniform strain field. Natural materials often feature periodically varying density gradients for improved damage tolerance [26].
    - Many biological materials (e.g. bone, horn, tooth and wood) have a characteristic microstructure consisting of concentric fibre-directional lamellae surrounding long hollow anisotropic tubules.
    - Multiple extrinsic toughening mechanisms such as fibre pull-out, fibre bridging and micro-cracking from weak interfaces resulting in rising R-curve behaviour.
- Self-assembled at ambient temperature and pressure from the nano-scale upwards.

- Multi-functional, for example the tracheids (wood cells) of softwoods provide both mechanical strength and vascular flow of water and other nutrients for the tree.
- Self-healing capability through cellular metabolic function.

2.2.2 Strength and stiffness

The material property chart of specific modulus v specific strength is shown in Figure 2-2. It can be seen that natural ceramic composites and natural polymer composites exhibit the best combination of modulus and strength (specific to density) with natural polymers generally more refined towards higher strength compared to natural ceramics.

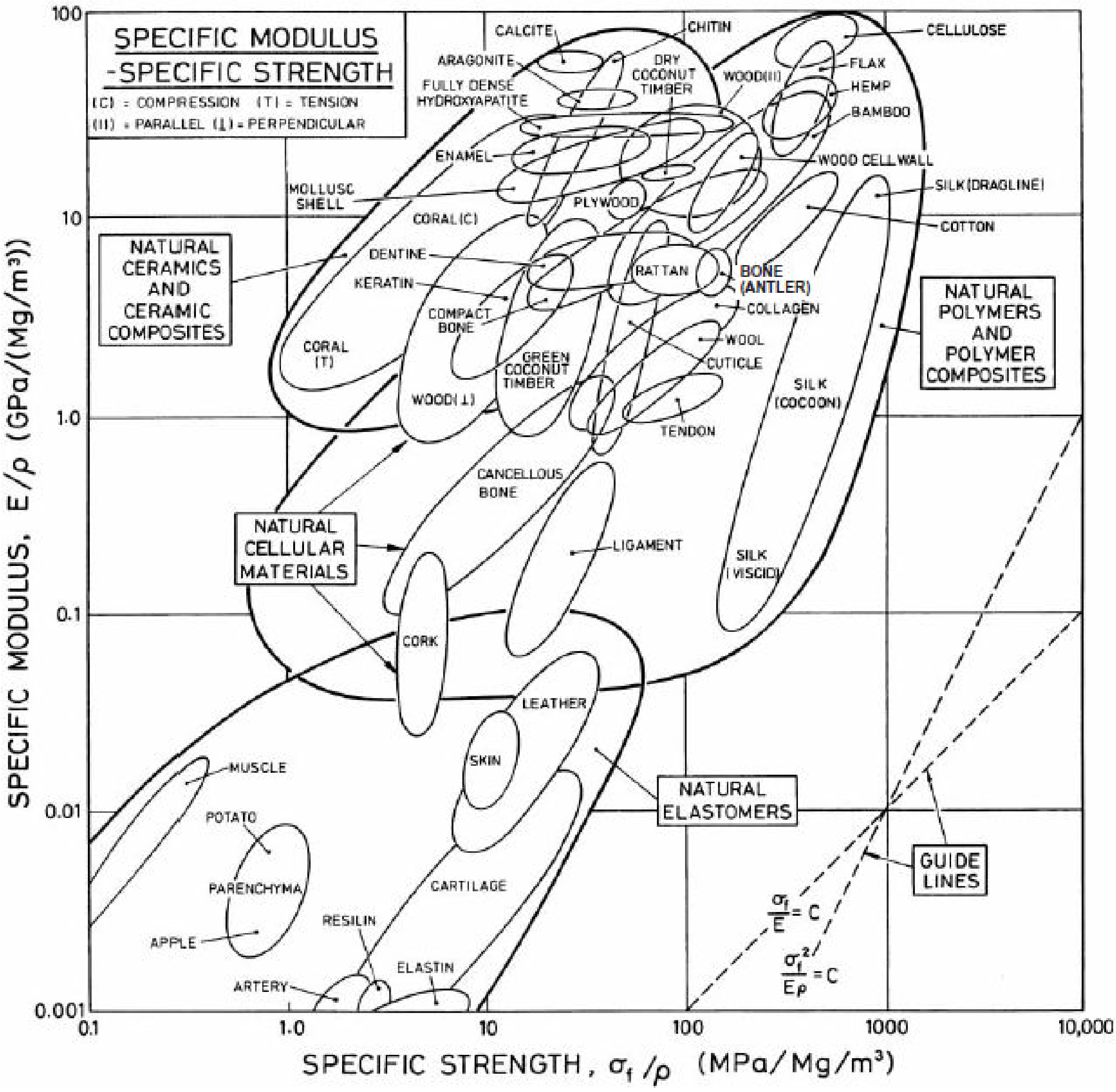

Figure 2-2 A material property chart for natural materials, plotting specific Young's modulus against specific strength [23]

High strength is linked to atomic structures containing strong directional bonding (such as covalent bonds) and high Peierls-Nabarro forces (the force required to move a dislocation in the plane of atoms of a representative unit cell) associated with limited dislocation mobility in crystalline solids [27]. Typically this type of atomic structure also produces brittle fracture.

The importance of microstructural defects to the strength of brittle materials was first demonstrated by Leonardo da Vinci who found that unlike yield strength, the fracture strength of brittle iron wires varied inversely with wire length [28]. Da Vinci deduced that a longer wire had a higher probability of containing a significant flaw and therefore strength was controlled by microstructural flaws in the material, which is the basis of fracture mechanics.

Natural materials overcome this strength dependency difficulty by 'hiding' flaws at the nano-length scale within the nano-crystalline particle or fibrous strong/stiff reinforcement in the composite [20, 26, 27, 29].

Ji and Gao [29] showed that because the stress concentration around a flaw is proportional to its size nano-sized crystalline structures become insensitive to flaws and failure is then governed by the theoretical strength of the material. As noted, self-assembly at the nano-scale is a defining characteristic of the growth processes of biological materials. In addition, the robustness associated with 'hiding' flaws in the nano-structure is very favourable to survival.

Considering the Griffith criterion for brittle fracture which relates the stress required to fracture a brittle material containing a flaw size of $2a$ as given in Equation 2-1;

$$\sigma = \frac{K_c}{\sqrt{\pi a}} \qquad \text{Equation 2-1}$$

Where σ = stress, K_c = toughness of the material and a = flaw size.

The fracture strength of a brittle material increases with decreasing flaw size. At a critical flaw size the fracture strength of a brittle material reaches the theoretical strength of a material free from defects [26]. Experimental observation shows that in certain biological composites such as tooth dentin, tooth enamel, bone and wood the mineral particles follow this criterion [21]. But in other natural materials made from brittle constituents such as nacre or silica sea sponges, the length scale of the ceramic phase is close to the micrometre range, which is higher than the requirement of the criterion [26]. For example, in nacre from abalone the fracture toughness of aragonite ($CaCO_3$) is ~ 1 MPa$\sqrt{m}$ and the Young's modulus is ~ 100 GPa [4]. The theoretical strength of the material is ~ E/10, which is reached for particles ~ 25 nm, however in nacre the ceramic bricks scale at lengths of about 5 – 20 μm length [22].

2.2.3 Intrinsic and extrinsic toughening

Intrinsic toughening involves plastic flow and strain hardening within the plastic zone ahead of the crack tip, which is how ductile materials such as metals derive toughness. Intrinsic toughening is an inherent property of the material influencing both crack initiation and crack propagation and is not affected by crack size or specimen geometry [27]. However, most biological materials contain brittle ceramic composites with poor intrinsic toughening and therefore rely on extensive extrinsic toughening. In contrast to intrinsic toughening that occurs ahead of the crack tip, extrinsic toughening utilises 'crack tip shielding' in which microstructural mechanisms such as fibre bridging act mainly behind the crack front to reduce the crack driving force at the crack tip. Because extrinsic toughening acts in the crack wake it is dependent on the size of the crack and can only improve material resistance to crack propagation (it does not affect crack initiation) [27]. Extrinsic toughening mechanisms result in non-constant crack-resistance curve, which is known as rising R-curve behaviour. The concepts of extrinsic and intrinsic toughening mechanisms are illustrated in Figure 2-3.

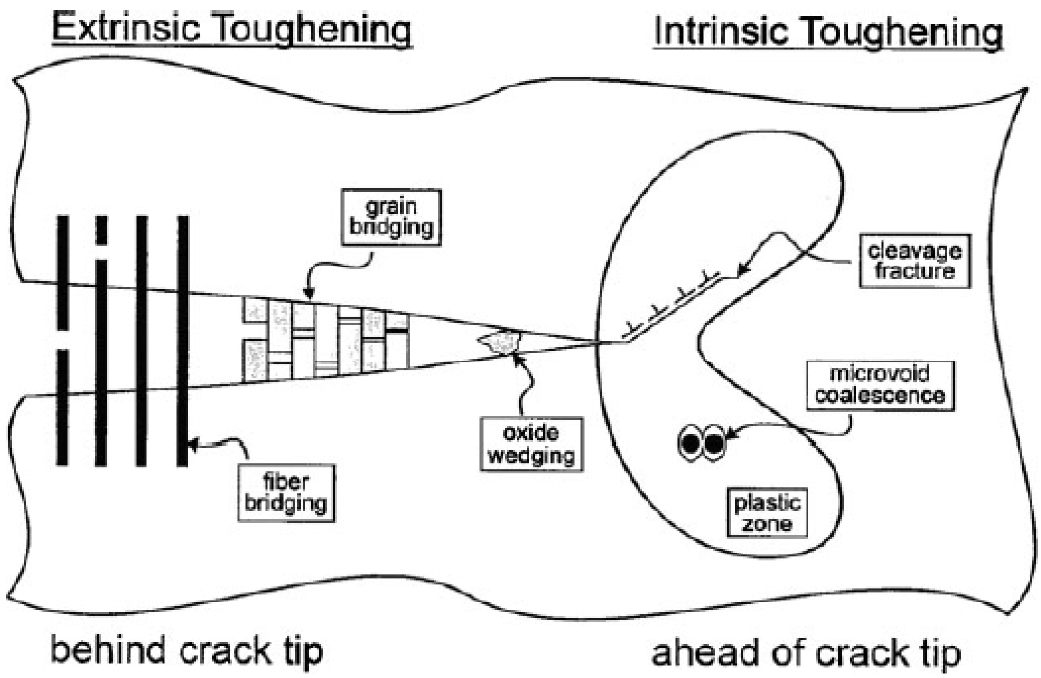

Figure 2-3 Extrinsic versus intrinsic toughening mechanisms. Intrinsic toughening acts ahead of the crack tip while extrinsic toughening mechanisms act mainly behind the crack tip to impede crack advance [27]

Crack-growth resistance R-curves are used to characterise how toughness changes with crack extension. A material with a flat R-curve has a single value of toughness (K_c) that unambiguously characterises the material and there is no stable crack extension because the initial crack size is the same as the critical crack size (refer Figure 2-4a). Traditionally these single value parameters have been used to quantify toughness. However a major weakness of K_c is it is based on crack initiation and cannot capture the hierarchical extrinsic toughening mechanisms found in biological composites whereby fracture resistance increases with crack extension (refer Figure 2-4b). When a material has increased crack growth resistance with increasing crack extension (rising R-curve behaviour) there is no single value of toughness that characterises the material toughness because the driving force for crack propagation is dependent on the crack length. Measurements are required to quantify how the resistance to fracture changes with crack extension. In materials with rising R-curve behaviour stable crack growth can occur because the critical crack size will be larger than the initial crack size. Increased crack growth resistance is characteristic of biological materials [27].

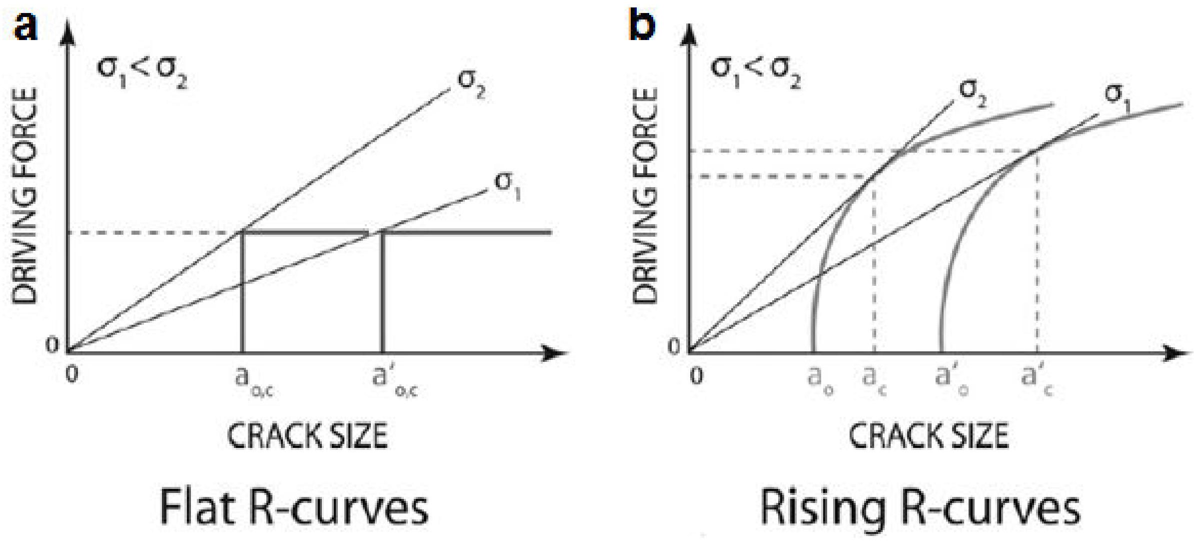

Figure 2-4 Schematic illustrations of (a) flat; and (b) rising crack-growth resistance curves (R-curves) [27]

Extrinsic toughness is influenced by the architecture of a material, including hierarchical structure. Nano-scale size effects and the effect of hierarchical arrangements on different combinations of strength and robustness (flaw tolerance) of H-bonds were examined in a study of combinations of 16,384 sub-elements in an alpha-helical protein filament [22]. The results showed that > 98% of combinations fell on the 'banana curve' where robustness and strength were mutually exclusive (refer Figure 2-5). However < 2% of hierarchical arrangements retained both strength and robustness. Natural materials are formed from the rare hierarchical arrangements that retain both strength and toughness through the mechanism of natural selection preferencing these arrangements as favourable to survival.

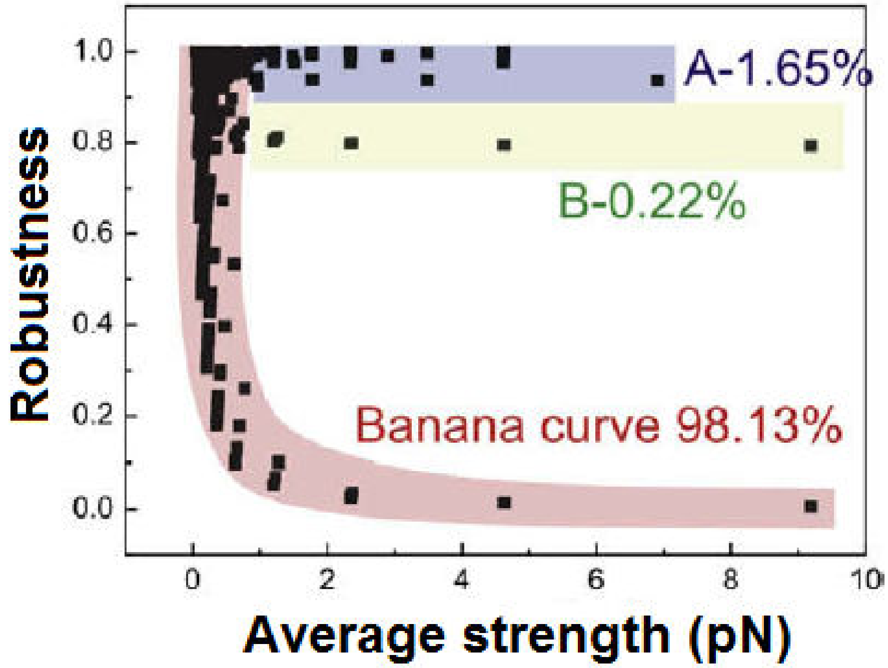

Figure 2-5 Hierarchical strength-robustness relation for alpha-helical protein filaments composed out of clusters of H-bonds [30] [22]

2.2.4 Extrinsic toughening mechanisms in biological materials

Common extrinsic toughening mechanisms observed in biological materials are: fibre/particle pull-out; fibre/particle bridging; micro-cracking; weak interfaces creating tortuous crack paths (increasing the strain energy release rate per volume of material); non-elastic deformation of the compliant bio-polymer phase; sacrificial ionic bonds; mechanical interlocking and periodically varying Young's modulus [4, 22, 26, 27, 31].

Periodically varying Young's modulus is an interesting toughening mechanism observed in brittle biological composites such as the silica spicules (refer Figure 2-7) which anchor the sea sponge to the ocean floor. This feature is characterised as a composite in which soft or compliant layers are embedded in between the stiff/strong material.

Kolednik et al. [26] used finite element analysis to show that spatial variation of material properties has a significant effect on the fracture toughness of composites. The study assumed perfect interfaces so the crack propagates perpendicular to the soft layers and crack deflection does not occur (if the crack is deflected parallel to the soft interface the material toughness is significantly degraded). They compared the driving force of a crack in a homogeneous material (J_{tip}^{hom}) with Young's modulus E = 42 GPa to the driving force of a crack in a composite material (J_{tip}^{comp}) with a Young's modulus periodically varying between 42 and 1 GPa with a wavelength of 5.1 microns. In the composite material as the crack enters the soft layer, at first J_{tip}^{comp} increases, which could trigger early crack initiation for a flaw located close to the soft layer. However this does not matter because the crack is quickly arrested as J_{tip}^{comp} reduces sharply when the crack tip attempts to cross the interface back into the stiffer material since the crack tip field requires more strain energy in the stiffer material [26]. The crack can be safely arrested in a very thin soft layer, meaning the effect of the soft/compliant layers on the global moduli is negligible. This effect is replicated if the Young's modulus is constant but the material contains a periodically varying yield strength (σ_y) [26].

A flaw located in a material will begin to grow if the crack driving force J_{tip} is equal to or greater than the crack growth resistance (R) of the material (refer Figure 2-6). In a homogenous material (with flat R-curve behaviour) J_{tip} increases linearly with increasing crack length and therefore is always larger than crack growth resistance, meaning crack growth will not be arrested. In the composite with periodically varying Young's modulus J_{tip} drops to a minimum value five times less than the isotropic material after the crack tip enters the soft layer. The crack stops since J_{tip} < R (crack growth resistance) as shown in Figure 2-7. As discussed, biological composites frequently contain multiple extrinsic toughening mechanisms resulting in rising R-curve behaviour [26, 27].

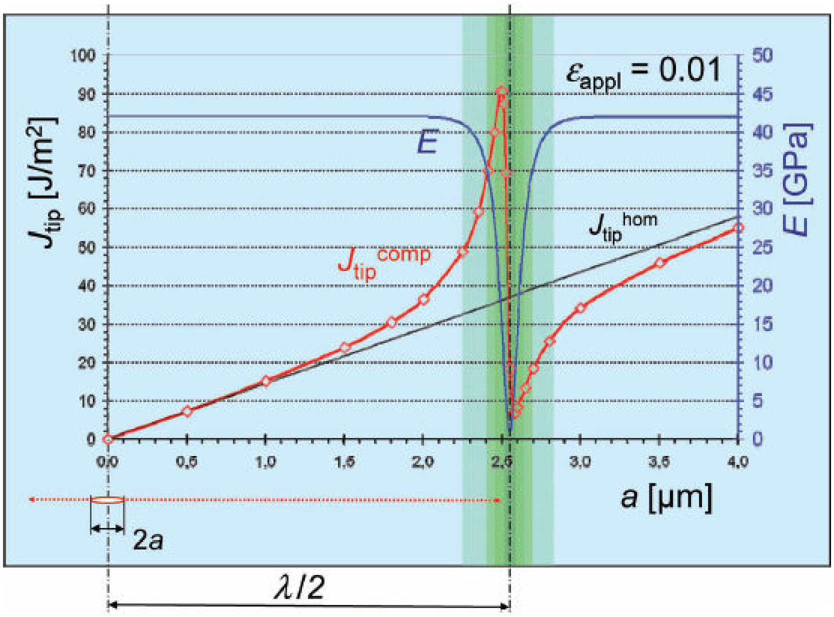

Figure 2-6 Comparing the crack driving force in a homogeneous material J_{tip}^{hom} (black line) with E = 42 GPa to the crack driving force in a composite with periodically varying Young's modulus J_{tip}^{comp} (red line) [26].

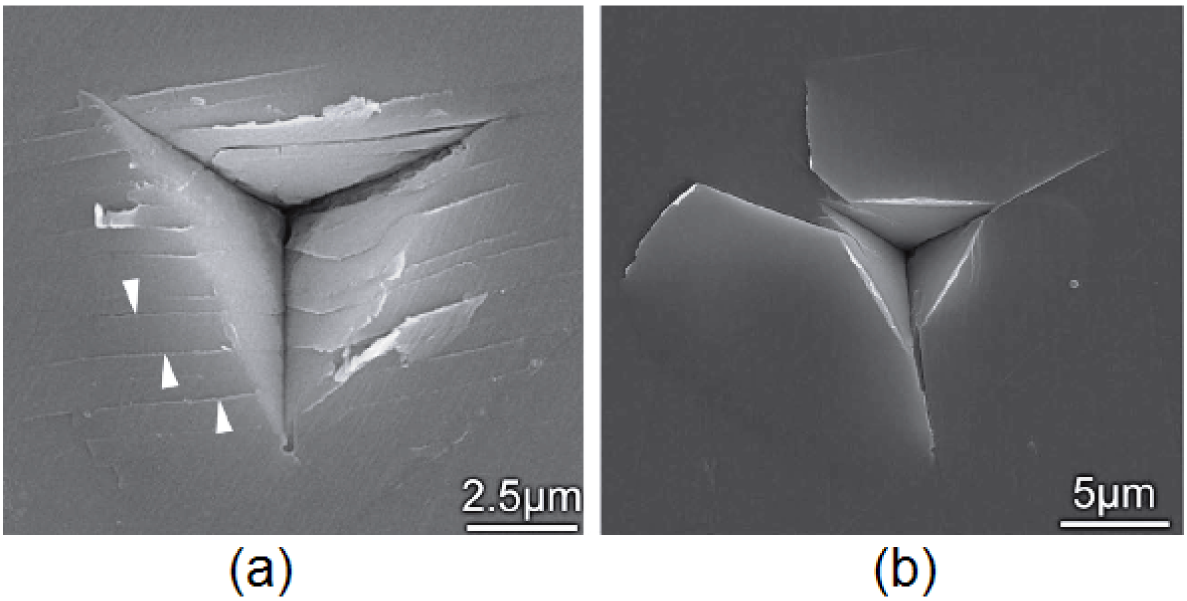

Figure 2-7 Crack propagation from 100 mN indents in a spicule of the deep-sea sponge *Monorhaphis chuni* (a) with lamination resulting in periodically varying Young's modulus; compared to (b) a region of the same spicule where the biosilica is monolithic [26]

2.2.5 Case studies of biological materials

2.2.5.1 Nacre – case study in extrinsic toughening

Nacre is a biological material comprising part of abalone shell (refer Figure 2-8) and is a good case study in extrinsic toughening mechanisms. Nacre is composed of ~ 95 vol.% ceramic aragonite and only 5 vol.% bio-polymer, but the stress-strain response of nacre is very different to the main constituent of aragonite as shown in Figure 2-9a and Figure 2-9d. Failure modes under tensile, compressive, shear and interlaminar tensile stresses are shown in Figure 2-10.

Nacre is 3000 times tougher than monolithic aragonite as measured by the non-linear elastic strain energy release rate J_c [32] due to the high degree of chemical and mechanical interlocking between the bio-mineral and bio-polymer phases. Nacre has a remarkably uniform structure with hexagonal aragonite 'bricks' of about 5 – 20 µm long and 0.3 – 1.5 µm thick [33] forming a three dimensional ceramic brick wall joined by thin 20 – 30 nm layers of bio-polymer 'mortar' (refer Figure 2-8c) [22]. Nacre exhibits highly anisotropic mechanical properties with the tensile strength parallel to the brick surfaces ~ 540 MPa compared to just 5 MPa perpendicular to the brick surface [20].

Brick particle pull-out (refer Figure 2-9b and Figure 2-9c), brick sliding, mechanical interlocking from brick waviness (refer Figure 2-9e), mineral bridging (refer Figure 2-9f), micro-cracking and non-elastic deformation of the bio-polymer are key toughening mechanisms of nacre controlled by the flaw resistant bio-polymer interface between the bricks. Although the ceramic bricks appear flat, there is actually a degree of waviness which generates progressive locking, hardening and spreading of non-linear deformation around cracks and defects as shown in Figure 2-9e. The ceramic bricks also contain nano-asperities on the surface which interact as the interfaces shear as shown in Figure 2-10c. As a consequence the mineral aragonite bricks become progressively harder to pull-out (rising R-curve behaviour) so micro-cracking and pull-out preferentially occur at unbroken brick interfaces. This allows pull-out to occur over a large volume, enabling the large increase in strain to failure observed in nacre compared to aragonite (refer Figure 2-9a).

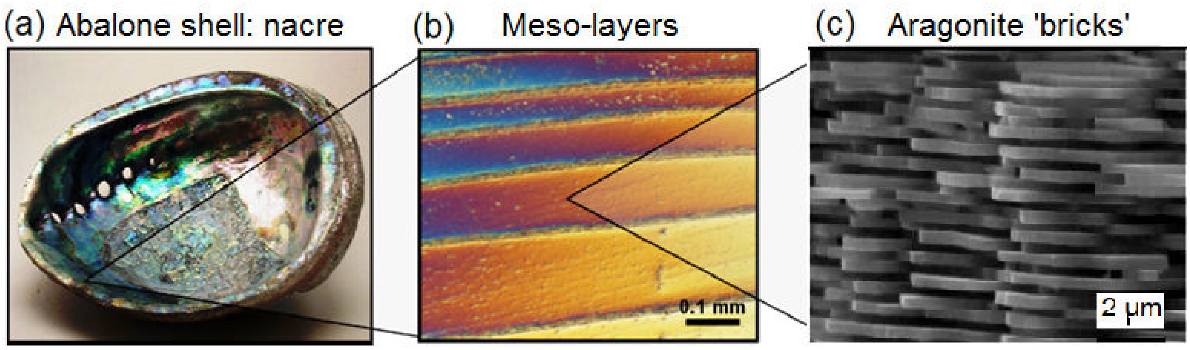

Figure 2-8 Hierarchical structure of nacre in abalone shell: (a) Macro-; (b) meso-layers; and (c) Hexagonal bricks at micro-length scale [20]

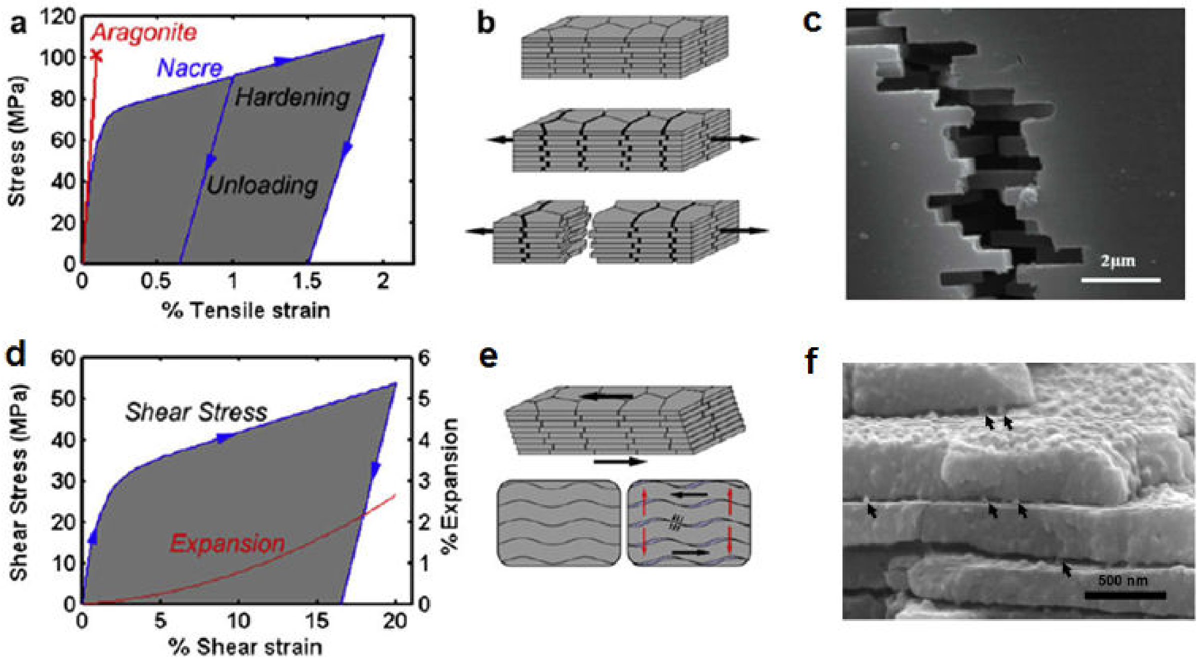

Figure 2-9 (a) Experimental tensile stress-strain curve for aragonite and nacre; (b) tensile deformation mechanism; (c) tensile fracture by brick pull-out [34]; (d) experimental shear stress-strain curve for nacre; (e) shear deformation with brick waviness; and (f) SEM showing mineral bridges (black arrows) between bricks after de-proteination [4]. Adapted from [4, 22, 34]

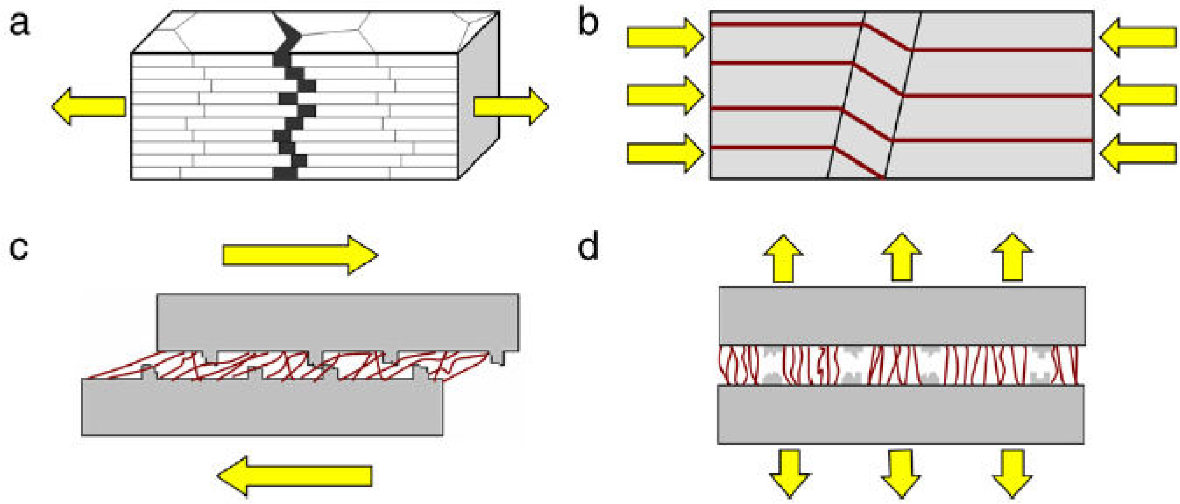

Figure 2-10 Failure mechanisms of nacre under different loading conditions: (a) Tension parallel to shell surface; (b) compression parallel to shell surface; (c) shear parallel to shell surface showing nano-asperities; and (d) tension perpendicular to shell surface [20]

2.2.5.2 Bone – strong and tough with high impact resistance

Bone is an example of a mineral particle (hydroxyapatite $Ca_{10}(PO_4)_6(OH)_2$) reinforced composite. The hierarchical structure of bone is illustrated in Figure 2-11. Other hydroxyapatite based materials include antler, horn and tooth (with an internal region called dentin and a hard external coating called enamel) [4]. The main function of bone is to provide protection and mechanical support for the body. Antlers are an extension of bone used for aggression and defence and therefore sustain high impact loads [21]. The antlers of deer weighing 320 kg with speeds of 11 m/s can sustain impact loads of up to 19 kJ and rarely break [21].

There are two types of bone. The first type is compact bone, which has a density of ~ 2 g/cm^3 and the characteristic microstructural feature that is called the osteon. Osteons are long tubules with a diameter of ~ 30 µm composed of concentric lamellae surrounding a cavity containing a blood vessel. The lamellae are comprised of mineralised collagen fibrils formed from triple helix tropocollagen and mineral crystallites of hydroxyapatite. The mineral constituent (hydroxyapatite) in the collagen fibrils stiffens the micro-structure [22, 35].

Significant (15 – 25 vol.%) amounts of water occur within and between the fibrils [21], and greater hydration means higher toughness and lower Young's modulus. Cross-linking across Ca^{2+} creates sacrificial bonds that increase shear strength in the bio-polymer and along the bio-polymer/bio-mineral interface, effectively converting the elastic behaviour of bio-polymers into a resemblance of metal plasticity. This allows collagen deformation and interface slipping to occur simultaneously under similar stress levels, making it possible to engineer a long range of deformation under significant stress in order to maximize energy absorption.

The mechanical properties of compact bone and its constituents are given in Table 2-1. The tensile strength of bone is significantly higher than the main constituents. The fracture toughness of bone is more than 20 times higher than hydroxyapatite, excluding the effect of rising R-curve behaviour. In fact, the toughness of bone in the transverse direction (across the grain) is an order of magnitude higher again, exceeding 20 $MPa.m^{1/2}$ [36] when rising R-curve behaviour is considered.

The second type of bone is cancellous bone, which has a spongy structure of interconnected rods and platelets with a diameter of ~ 200 μm [37] with high porosity and a density of ~ 0.4 g/cm^3 [21]. Cancellous bone fulfils the role of foam in a sandwich construction and occurs in areas of the body which require high impact resistance (e.g. skull, ribs, vertebrae, head of the femur, and antlers [21]).

SEM micrographs taken from cross-sections of hydroxyapatite-based natural materials, including bone (bovine femur), ram horn, elk antler and dentin (human tooth) (refer Figure 2-12) show all materials have strong similarities with circular or elliptically shaped hollow tubules aligned in the growth direction. Tubules are an important microstructural feature of energy absorbent design because of the high amount of energy required to collapse the tubules. Toughness is also generated from crack deflection. Weak interfaces along the anisotropic tubules in bone create tortuous crack paths that make it very difficult to generate a tensile fracture across the grain, with cracks deflecting in the longitudinal direction [27].

An important design variable is the percentage of the mineral phase in the bio-composite, and its effect is shown in Figure 2-13. As the percentage of the bio-mineral hydroxyapatite increases, bending strength, Young's modulus and hardness increase but the work-of-fracture decreases. If the main function of the bone is to resist impact loading the mineral content is kept low because under dynamic loading hydroxyapatite acts like a brittle solid [21]. Antlers and horn both need to be very tough and impact resistant. However, antlers are shed yearly whereas horns are kept for life, and therefore horn contains less brittle hydroxyapatite because it is more critical that they do not break. Bone is a compromise of strength and toughness. Tooth enamel does not contain collagen because it needs to be extremely hard so it does not wear away from grinding and chewing food. Instead it is formed from hydroxyapatite rods with a very small diameter of ~ 5 µm which are woven into a fabric-like composite. Any cracks that develop in the enamel are generally arrested at the dentin-enamel junction [4].

Table 2-1 Mechanical properties of compact bone and its constituents [4, 38, 39]

	Volume fraction V_f (%)	**Young's Modulus E**	**Tensile strength σ_t (MPa)**	**Fracture toughness K_{Ic} (MPa.$^{m1/2}$)**
Collagen	55 - 60	50 – 100 MPa	20	-
Hydroxyapatite	40 - 45	50 – 100 GPa	30	<<1
Bone	-	10 – 20 GPa	100	2 - 7

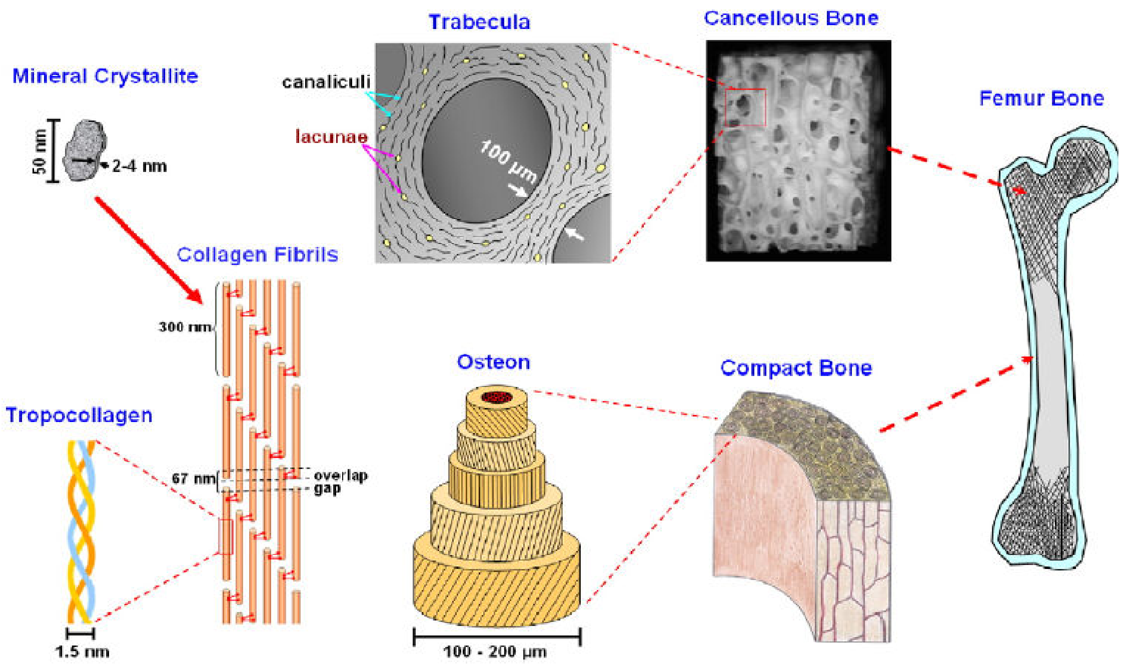

Figure 2-11 Hierarchical structure of bone [21]

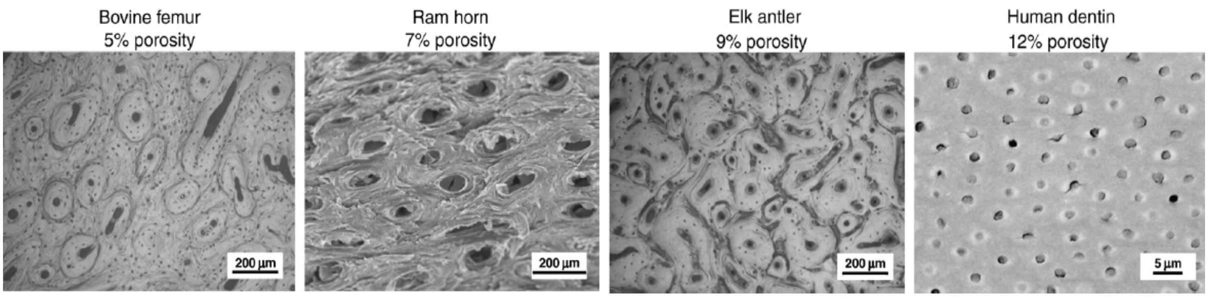

Figure 2-12 Similarities between the transverse microstructures of bovine femur, ram horn, elk antler and dentin from human tooth [21]

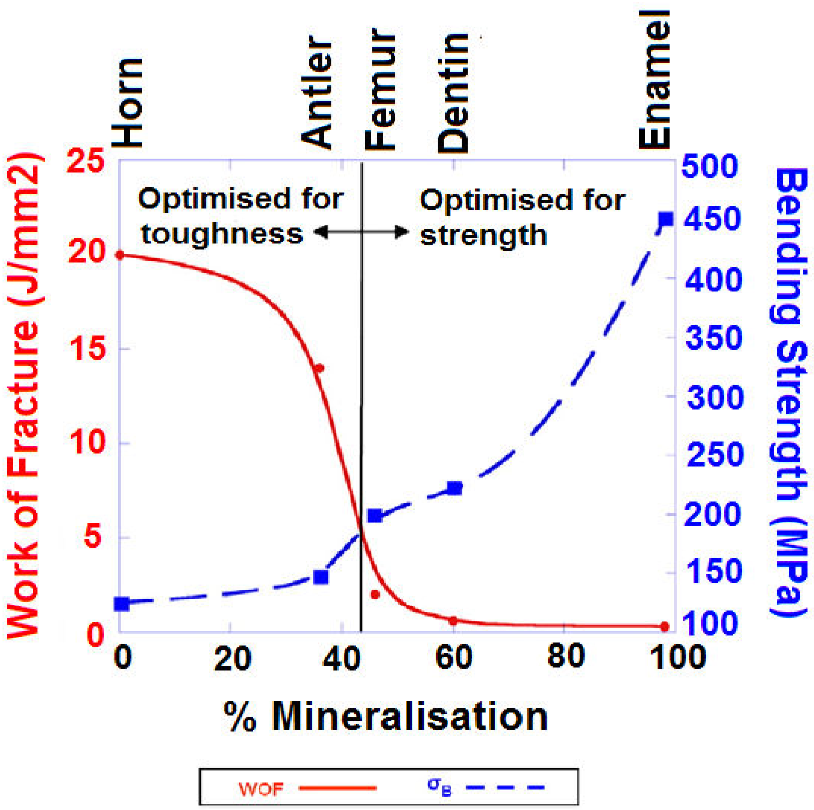

Figure 2-13 Effect of mineralisation on the work-of-fracture and bending strength of hydroxyapatite based biological materials [21]

2.2.5.3 Sea sponge – flexible glass

Sea sponge is comprised of a rigid silica basket and multi-functional flexible silica spicules (refer Figure 2-14a) that anchor the basket to the ocean floor and also carry light (resembling fibre optics) [4]. The hierarchical structure of sea sponge is shown in Figure 2-14. The sea sponge is comprised of a rigid silica basket and flexible silica anchoring spicules, The basket exhibits many common design strategies utilised in engineering: composite materials; beams formed from bundled spicules; longitudinal, horizontal and diagonal stiffeners; and out-of-plane transverse diaphragms to prevent ovalisation (refer Figure 2-14b) [40]. The novelty is that all of these strategies are implemented into the one structure. The sea sponge spicules are made from onion-like circumferential layers of silica (refer Figure 2-14g) with thin layers of soft bio-polymer protein embedded between the glass (refer Figure 2-14h) which stabilise small cracks by strongly reduce the crack driving force (refer Figure 2-7). The thickness of the concentric layers varies from 2 – 15 microns. The total number of layers across the thickness of the spicule is about 50 – 200 [41].

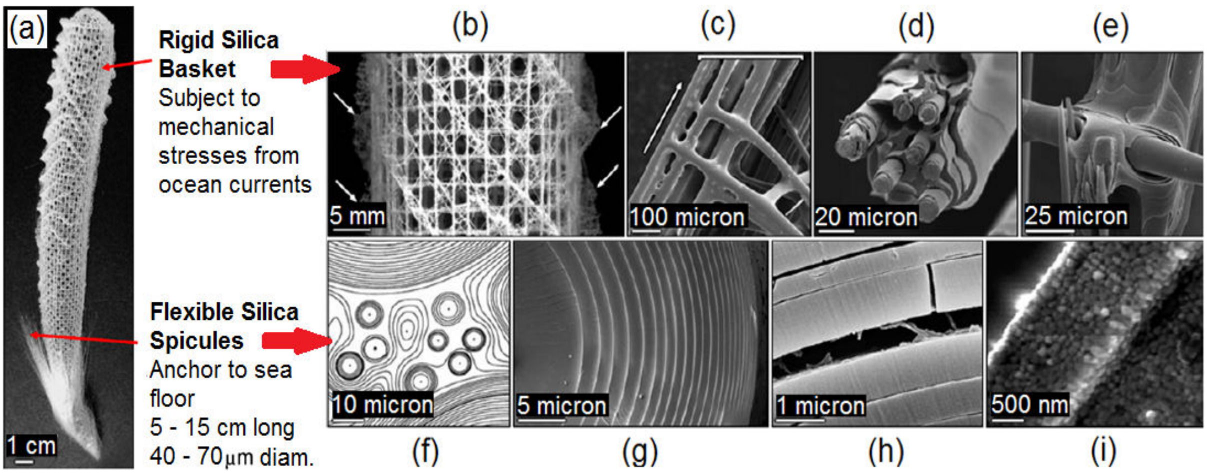

Figure 2-14 Structural analysis of the deep sea sponge *Euplectella aspergillum* [9]

The bending strength of the spicules is more relevant than the tensile strength because they undergo bending and possibly torsional stress in their natural marine environment [41]. Bend tests performed on silica sponge spicules from the species *Euplectella aspergillum* (refer

Figure 2-15a) revealed the fracture stress is more than four times the fracture stress of monolithic silica fibres with similar diameters. In addition, the fracture of the spicule is more controlled compared to the brittle failure of the silica rod (Figure 2-15b).

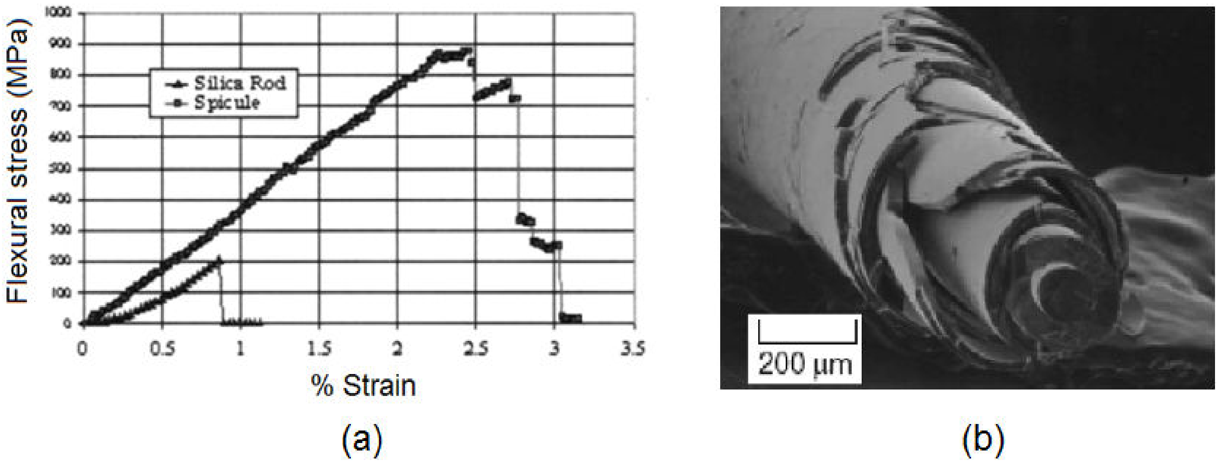

Figure 2-15 (a) Three-point bend test of a silica rod (500 µm diameter) and a sea sponge spicule (~ 120 µm diameter) tested in 3-point bending [41]; (b) Fractured sea sponge spicule [4] (courtesy of G. Mayer, U. Washington [42])

The mechanical properties of silica, bio-protein and the sea sponge spicule are compared in Table 2-2. The Young's modulus of silica sea sponge spicules is only about 1.3% lower than hydrated homogenous silica [41]. Defying the law-of-mixtures through hierarchical design, the fracture strain of the spicule is 3.5 times higher and the fracture toughness is up to 20 times higher than the main constituent, silica.

Table 2-2 Mechanical properties of sea sponge spicule and its constituents [41]

	Volume fraction V_f (%)	Young's Modulus E	Bending strength σ_b (MPa)	Fracture strain ε	Fracture toughness K_{Ic} (MPa.$^{m1/2}$)
Protein	~ 5	50 – 100 MPa	~ 20	-	-
Silica rod	~ 95	~ 38 GPa	200 ± 15	1.0 ± 0.1	0.78 ± 0.05
Sea Sponge Spicule	-	38 ± 3 GPa	880 ± 15	3.5 ± 0.1	2.26 – 5.60 ± 0.10

2.2.5.4 Wood

Wood is a very important biological material that has been utilised by humans for thousands of years as a building material. The specific Young's modulus and tensile strength of wood along the grain is comparable with steel [27]. The hierarchical structure of wood versus the length scale is shown in Figure 2-16.

Wood is a cellular material. The hollow wood cell wall is a composite-like structure composed of 40 – 55% cellulose, 15 – 35% lignin and 25 – 40% hemi-cellulose [4]. Cellulose forms crystalline and amorphous regions known as microfibrils which are the stiff/strong phase. Hemi-celluloses and lignin form the matrix. Hemi-celluloses are not forms of cellulose but a group of polysaccharides that remain associated with cellulose after lignin has been removed [4]. As shown in Figure 2-16, wood contains five layers of hierarchy: 1) the molecular nano-crystallines of cellulose in the microfibrils; 2) the composite microfibrils comprised of cellulose, hemi-cellulose and lignin; 3) the concentric lamellae of aligned microfibrils surrounding the hollow wood cell; 4) aligned wood cells comprising the grain of wood; and 5) the macrostructure of the growth rings with seasonally varying density which occurs as a result of periodic changes to the diameter and wall thickness of the wood cells.

Characteristic of biological materials, wood exhibits extrinsic toughening mechanisms. A good example is fibre pull-out. Under tension, as more fibres are torn out of the wood cell wall more friction has to be overcome to further tear out the fibres, resulting in rising R-curve behaviour [43]. Fibre bridging also contributes to the high toughness of wood [44] (analogous to stitching or z-pinning in synthetic fibre/polymer composites).

In this PhD study, the tree branch-trunk joint was chosen as the primary biological structural joint for biomimicking of aerospace composite T-joints because tree branch-trunk joints undergo similar loading conditions, including static bending and shear loads caused by self-weight and wind, and fatigue loading caused by cyclic wind loading. Consequently they have many structural properties which are desirable in composite joints, including: strength, toughness, fatigue resistance and damage tolerance [45-49]. In addition, wood is an orthotropic composite (ratio of E_1/E_2 of ~ 20 [50]) fibrous structure with a similar fibre volume fraction (~ 0.4 – 0.55 [4]) compared to a fibre reinforced polymer material [51-53]. Trees respond to the prevailing loading conditions caused by wind and self-weight by tailoring both the material properties of the nano-sized wood cell wall [54], micro-sized wood cell [53], meso-sized grain pattern [55-57] and the macro-sized structural details [19, 46, 47].

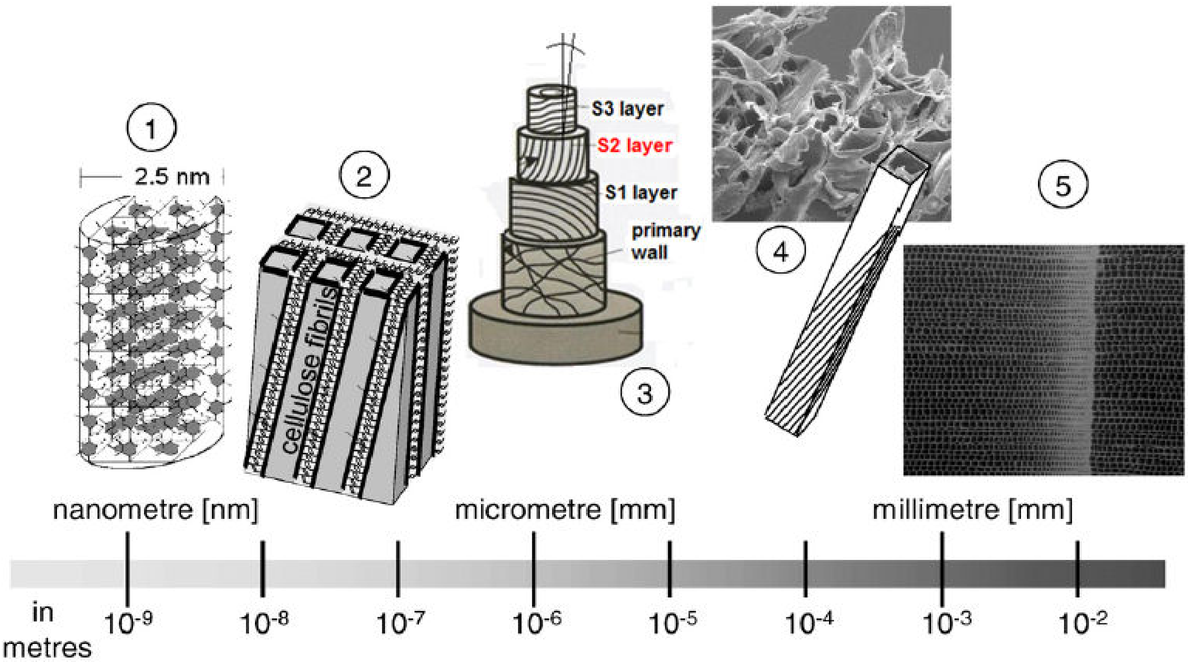

Figure 2-16 Hierarchical structure of wood: (1) the nano-crystalline structure of a cellulose microfibril; (2) model of the arrangement of the cellulose fibrils in a matrix of hemicelluloses reinforced by lignin within the S2-layer; (3) structure of the wood cell wall of softwood tracheids with the S1, S2 and S3 layers; (4) broken tracheids within a fracture surface of spruce wood, the schematically drawn wood cell and the cellulose fibrils spiralling around with an inclination against the long cell axis known as the microfibril angle; and (5) cross-section through the stem showing the sequence of earlywood (cellulose structure of low density, darker grey) and latewood (light grey) within an annual ring [24]

2.3 BIOMIMETICS

Biomimetics is based on the idea of learning from nature and utilising this knowledge to improve engineering design. As discussed in section 2.2.1, the defining characteristics of natural materials provide ample principles and ideas to apply to engineered structures. However to date research into biomimetics has generated relatively few advances in materials science and structures technology. The main problem is the enormous challenge of replicating the synergistic effects of complex hierarchical structures using production-scale manufacturing processes. This is compounded by a disconnect in manufacturing philosophy with engineers tending to tackle manufacturing from a ‘top down’ approach e.g. machining, whereas natural materials are grown from the ‘bottom up’ beginning with nano-scale self-assembly. Some aspects of natural materials can be implemented using current manufacturing techniques e.g. through-thickness reinforcements such as z-pins which are analogous to fibre bridging. However the challenges of replicating the full structural hierarchy ranging from the nano- to the macro-length scales using a ‘top down’ manufacturing approach are probably insurmountable using contemporary design and manufacturing technologies. Therefore, in the future, the new frontier lies in the synthesis of bio-inspired materials through manufacturing processes that are characteristic of biological systems. Although this approach presents enormous challenges, mastering control over the fundamental mechanisms of nano-scale self-assembly, exemplified by the growth of biological structures, will eventually lead to new materials with extraordinary properties. A review of bio-inspired materials and bio-inspired structures with application for aerospace composite joint design is presented.

2.3.1 Bio-inspired materials

Research into bio-inspired materials has focused mainly on creating a material analogous to the nacre found in abalone shells [31, 36, 58-60]. The ordered nano-scale ‘brick-and-mortar’ arrangement of ceramic and organic layers is one of the key features responsible for producing outstanding strength and toughness (refer Figure 2-8). The challenge of reproducing this nano-scale structure has been approached in several different ways resulting in different platelet volume contents (V_p) as shown in Figure 2-17.

Tang and co-workers [31] produced a nano-scale layered organic-inorganic composite made from montmorillonite clay platelets (C) and polyelectrolytes (P) using the technique of layer-by-layer adsorption of organic and inorganic dispersions resulting in $(P/C)_n$ multilayers where n = 50, 100 and 200 layers with thicknesses of 1.2 – 5 µm. Bonderer et al. [58] constructed their nacre-inspired nano-composite from high tensile strength ceramic alumina platelets (Al_2O_3) and a ductile polymer matrix (chitosan polymer). For platelet volume fractions (V_p)

higher than 20% swelling of the thin chitosan layers during dip coating led to platelet misalignment and voids within the film [58]. Munch and co-workers [36] created synthetic nacre using Al_2O_3 as the ceramic and PMMA (polymethyl methacrylate) as the polymer phase. Lamella architecture was fabricated using the novel technique of freeze casting. Controlled directional freezing of ceramic-based suspensions in water promotes lamellar ice crystals, creating a large porous ceramic scaffold which acts as the 'negative'. This is infused with the polymer phase. The characteristic 'brick-and mortar' structure was fabricated by pressing to collapse the scaffold and sintering to promote cross-linking resulting in ceramic contents of up to 80 vol. % [36]. The ceramic 'bricks' are 20 - 100 µm long and 5 - 10 µm wide with polymer layers ~ 1 - 2 µm thick.

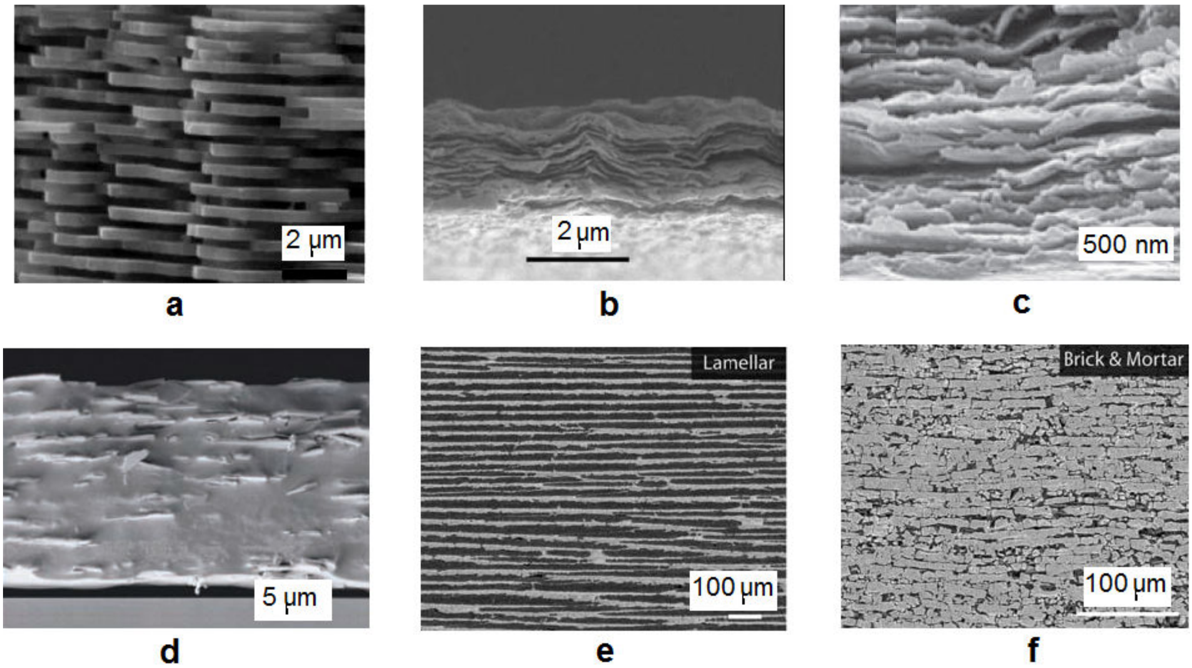

Figure 2-17 Natural and synthetic nacre with varying platelet volume content (V_p): (a) natural nacre with V_p = 0.95 [34]; (b) montmorillonite clay/PDDA film with V_p = 0.30 [31]; (c) montmorillonite clay/cross-linked PVA with V_p = 0.50 [60]; (d) Al_2O_3 platelet/chitosan with V_p = 0.11 [58]; (e) Al_2O_3 platelet/PMMA lamellar composite with V_p ~ 0.4 [36]; and (f) same Al_2O_3 platelet/PMMA composite after pressing and sintering with V_p = 0.80 [36]

The reported mechanical properties of synthetic nacre are compared to natural nacre in Table 2-3. Tang et al. found that independent of the number of layers the bio-inspired material had strength = 100 ± 10 MPa and E = 11 ± 2 GPa, compared to nacre with strength = 130 MPa and E = 64 GPa.

Table 2-3 Comparison of the mechanical properties of natural and synthetic nacre nano-platelet composites

Natural and Synthetic Nacre (ceramic/polymer)	**Volume of ceramic particles V_p**	**Tensile strength σ_t (MPa)**	**Young's Modulus E (GPa)**	**Strain at rupture $\varepsilon_{rupture}$ (%)**	**Fracture Toughness K_{Ic} ($MPa.m^{1/2}$)**
Nacre aragonite/ bio-polymer [29]	95 – 99	130	64	~ 2	3 – 7
Montmorillonite clay/PDDA [31]	~ 0.30	100 ± 10	11 ± 2	10 ± 2*	Not tested
Montmorillonite clay/cross-linked PVA [60]	0.50	400 ± 40	106 ± 11	0.33 ± 0.04	Not tested
Al_2O_3 platelet/ chitosan [58]	0.15	315 ± 95	9.6 ± 2	21 ± 5	Not tested
Al_2O_3 platelet/ PMMA (brick-and-mortar) [36]	0.80	~ 200	~ 36	~ 6	4.4 (up to 30 with crack extension)

*samples only bear considerable load for strain values higher than 9%

The toughness was not tested but clay-based nano-composites do not usually mimic the high ductility and flaw tolerance of natural ceramic composites [58]. The lower Young's modulus was attributed to the high organic content in the $(P/C)_n$ composite compared to the 5 vol.% in nacre. Another major difference was the bio-inspired clay platelets are flat in comparison to nacre where the $CaCO_3$ 'bricks' have 30 - 50 nm asperities to provide additional friction to resist pull-out (refer Figure 2-9f) [31]. Representative results from Bonderer et al. showing high ductility in the stress v strain curves for $V_p = 0.10$ and $V_p = 0.15$, compared favourably to nacre and other natural mineralised composites as shown in Figure 2-18a. Munch et al. were able to recreate the extrinsic toughening mechanisms of delamination, ligament bridging and 'brick-and-mortar' pull-out, resulting in rising R-curve behaviour. As shown in Figure 2-18b the Al_2O_3/PMMA 'lamellar' and 'brick-and-mortar' structures reached a steady-state fracture toughness K_{JC} of 15 $MPa.m^{1/2}$ and 30 $MPa.m^{1/2}$ which are outstanding compared to the Al_2O_3 constituent (~ 2 $MPa.m^{1/2}$).

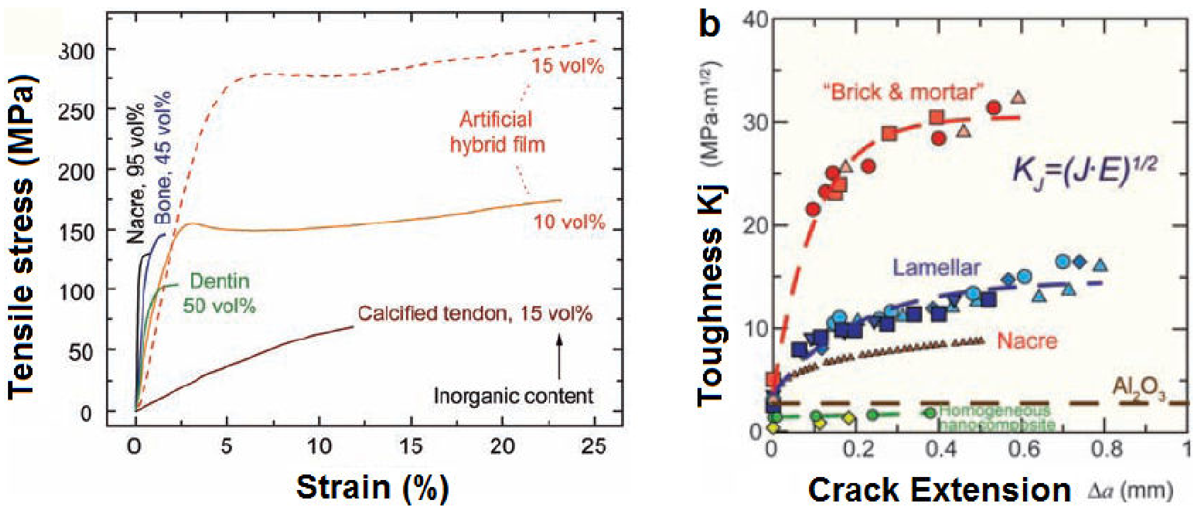

Figure 2-18 (a) Tensile stress v strain curves for nacre (red abalone *Haliotis refuscens*), bone, dentin and calcified tendon [58]; and (b) lamellar and 'brick-and-mortar' synthetic nacre showing rising R-curve behaviour similar to natural composites [36]

Research into bio-inspired materials highlights the importance of not only replicating the nacre structure, but also the interfacial bonding between the ceramic platelets and the polymer which plays a crucial role in controlling the load transfer efficiency from the ductile polymer to the strong ceramic phase.

In general, the synthetic nacres were unable to replicate the remarkably uniform structure of natural nacre which results in a very low (<5 vol.%) binder content and therefore had lower Young's modulus than natural nacre. Thus far only thin films of synthetic nacre have been produced (< 5 μm thick), once again highlighting the challenge of manufacturing production scale quantities of bio-inspired materials.

2.3.2 Bio-inspired structures

Research into the application of bio-inspired design can broadly be divided into two categories: shape optimisation and material optimisation.

2.3.2.1 Shape optimisation

Shape optimisation occurs at the macro-level and involves changes to the shape of the joint to reduce or eliminate high stress concentrations. Smoothing sharp notches is standard practice to reduce the geometric stress concentration factor in engineered structures, which has been widely verified to increase the failure load of joints.

A novel bio-inspired shape optimisation method uses Computer Aided Optimisation (CAO), which mimics the adaptive growth of biological structures by translating the stress distribution calculated by finite element analysis (FEA) into a temperature field. If the surface region exceeds a reference temperature (i.e. over-loaded) it is allowed to grow through a defined thermal expansion coefficient, which effectively adds material to highly loaded areas to reduce the stress and produces an optimised topology [15, 16, 18, 61-64]. Computer Aided Adhesive and Assembly Optimisation (CA^3O) uses similar principles [15], but if the surface region is below the reference temperature (i.e. under-loaded) the surface shrinks. Using CAO, Mattheck analysed the problem of a tree growing into a steel railing interface as shown in Figure 2-19a [62]. The intrusion of the railing creates a high stress concentration on the tree trunk. The tree responds through adaptive growth and produces extra wood in a convex shape to relieve the stress. The loading condition was idealised as shown in Figure 2-19b and optimisation based on CAO generated a similar convex shape as observed in the tree (refer Figure 2-19c).

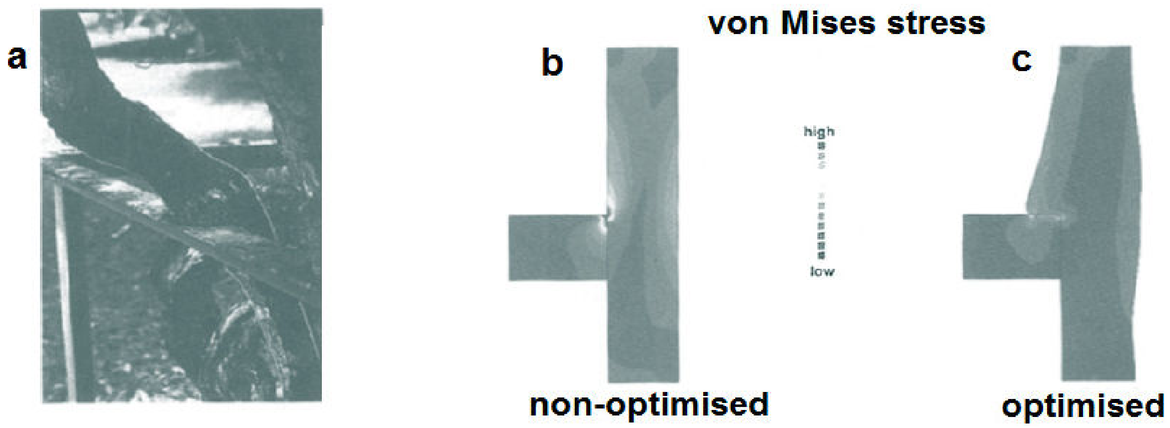

Figure 2-19 (a) Tree-steel railing interface; (b) FE stress analysis showing stress concentration at notch; and (c) optimised joint with convex addition of material eliminating stress concentrations [62]

Xu et al. [63] used the CAO technique to optimise the design of butt-joints made using dissimilar materials: aluminium/polymethyl methacrylate (Al/PMMA) and aluminium/ polycarbonate (Al/PC). Building on [62] the baseline butt-joint design with straight edges (Figure 2-20a) was altered to create a convex bond-line at the free edges of the butt to eliminate the bond-line stress singularity. The taper angles of the convex bond-line were θ_1 = 45˚ (Al) and θ_2 = 65˚ (polymer) with a taper length of 3 mm (refer Figure 2-20b-c). Coherent gradient sensing (CGS) was used to detect stress concentrations and stress singularities at the free edges of the bi-material corners of the bio-inspired shaped joint (refer Figure 2-20d) and baseline straight edged joint (refer Figure 2-20e). The joints were tested under tensile loading, and the convex shaped Al/PC joint had an increase in the average ultimate tensile load from 2.6 to 4.7 MPa (+81%), however the high standard deviation (2.0 MPa) indicated large scatter in the results (refer Figure 2-20f).

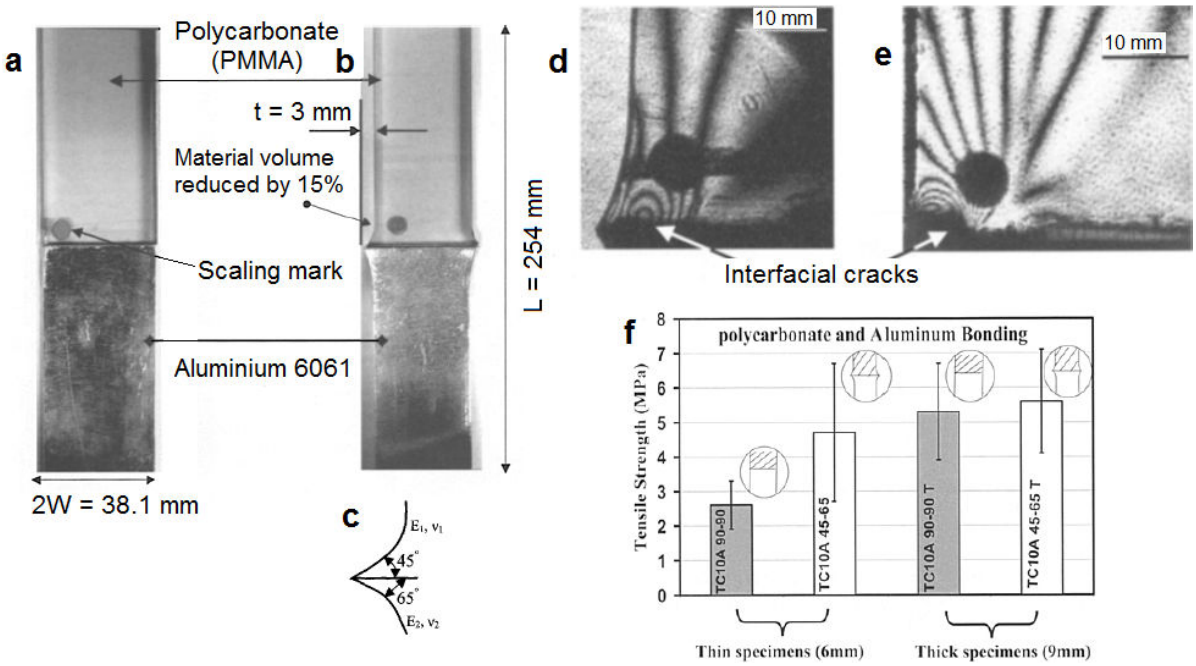

Figure 2-20 (a) Baseline Al/PC butt-joint with straight edges; (b) bio-inspired butt-joint; (c) schematic of taper angles at butt-joint of dissimilar materials; (d) coherent gradient sensing (CGS) (with scaling mark) showing stress singularity eliminated in the bio-inspired butt-joint with shaped edges; (e) CGS showing stress singularity in the baseline butt-joint with straight edges; and (f) tensile test results for baseline and bio-inspired shaped Al/PC joints considering thin and thick specimens, Reproduced from [63].

There was more success for Munzinger et al. [15] who used a bio-inspired design methodology based on wood rays to optimise adhesive butt-joints of dissimilar materials subject to tension loading. Trees contain radial reinforcements known as rays that reinforce abrupt changes in the Young's modulus of wood at the interface between the seasonal earlywood (low density) and latewood (high density) growth rings (refer Figure 2-21a). The modulus ratio of $E_{latewood}/E_{earlywood}$ is typically ~ 5.6 [15]. Each year the ray grows by the width of the annual growth ring. The interface of the new ray growth can be idealised as an adhesive joint subject to radial tension (refer Figure 2-21a). Computer Aided Adhesive and Assembly Optimisation (CA^3O) was used to optimise the geometry of a butt-joint made from aluminium and steel (refer Figure 2-21b). A finite element model calculated the stress distribution in the adhesive and adherends and the rules of the optimisation were set: i) if an element stress exceeds the reference stress (optimal stress in adhesive) the element shall grow according to the overload; ii) if an element stress is smaller than the reference stress the element shall shrink according to the underload; and iii) growth processes take place more rapidly than shrinkages [15]. For the purpose of the optimisation the element stresses and reference stress (optimum stress in the adhesive) were converted into a temperature field and a reference temperature and a bi-linear thermal expansion coefficient was set.

Only one side of the butt-joint was actively optimised (black adherend shown in Figure 2-21b). The other adherend was passively fitted to the contours of the optimised adherend. In the non-optimised butt-joint the stresses in the adhesive are non-uniform across the load-bearing section with high stresses located at the edges of the adhesive which causes the joint to fail prematurely. As the optimisation progresses the overloaded edges grow and the lightly loaded region in the centre of the adhesive shrinks, resulting in the cone-shaped morphology of the optimised joint shown in Figure 2-21b. This shape optimisation means the stress field is no longer in one plane and it also significantly increases the load transfer area of the adhesive, thereby lowering the stress on the joint. The similarly of the optimised joint with the natural model of the ray is obvious. It is also somewhat similar to the concept of Pi pre-form bonded joints [65]. It will be shown in chapter three that this two-dimensional cone-shaped optimised joint design is analogous to the three-dimensional cone-shaped architecture of the tree branch-trunk connection. The FE stress predictions for the butt-joint and optimised joint are shown in Figure 2-22a. These results were validated experimentally for both static tension and fatigue loading (refer Figure 2-22b). The ratio of the fracture force of the optimised and non-optimised butt-joints was 3.6 under static tensile loading and 5.4 under fatigue loading [15].

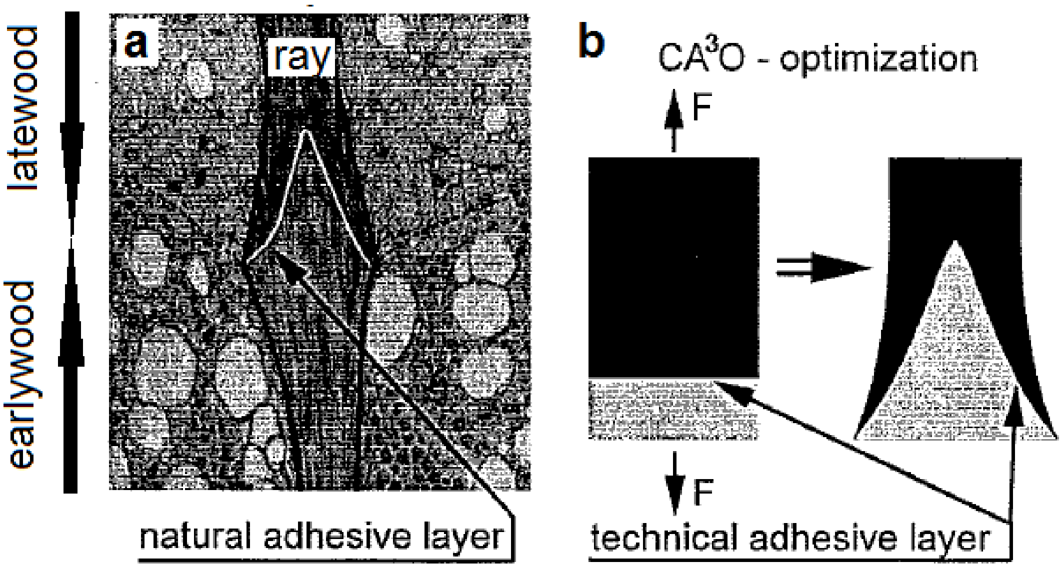

Figure 2-21 Comparison of the geometries of the (a) wood ray; and (b) perpendicular butt-joint and the optimised model [15]

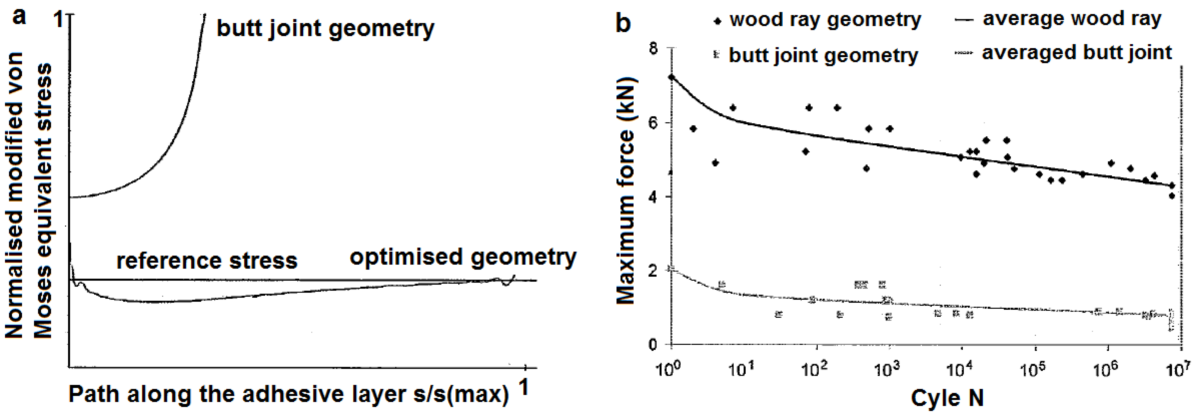

Figure 2-22 (a) Modified von Mises equivalent stresses in the centre of the adhesive layer of the initial butt joint geometry and the optimised geometry, normalised to the maximum stress in the butt joint; and (b) Woehler diagram for the two joint designs [15]

2.3.2.2 Material optimisation

Material optimisation is especially well suited to anisotropic composite materials and has been performed at the fibre level using Computer Aided Internal Optimisation (CAIO) by Mattheck et al. [16-18]. CAIO was developed in response to a lack of research into optimising the fibre arrangement within a composite structure for given load and boundary conditions [16-18]. The mechanism of CAIO has been adapted from fibrous biological materials. Mattheck and co-workers assume biological materials such as bone and wood align the longitudinal cell axis with the direction of principal stress (force flow). The objective of the optimisation is to eliminate shear stresses within each element by aligning the fibre direction to the force flow, thus suppressing failure mode by fibre/matrix interface splitting. Firstly, the force flow is calculated using FEA and then the CAIO routine alters the orientation of the orthotropic axes of each element into the directions of force flow through an automated iterative process [16-18].

The shear stresses in a unidirectional laminate are maximised when the force flow is misaligned to the fibre direction by 45° (refer Figure 2-23a). Under general shear stresses the force flow is misaligned by less than 45° (refer Figure 2-23b). Under no shear stresses the force flow misalignment = 0° (refer Figure 2-23c), which is the objective of the optimisation.

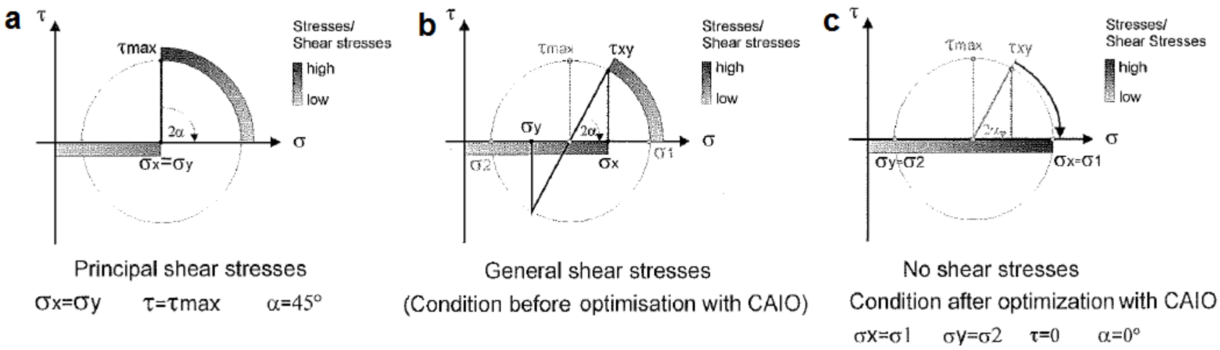

Figure 2-23 Mohr's circle diagrams for stress states: (a) stress state of a non-optimised element with maximum shear stresses; (b) stress state of a random element in the structure before the use of CAIO; and (c) stress state in the random element after optimisation to eliminates shear stresses [16]

Eliminating shear stresses eliminates the failure mode of splitting along the fibre/matrix interface and therefore fibres must fracture, which absorbs more strain energy. The strength of fibrous composite materials under axial loading is reduced by every layer of fibres which is not aligned with the force flow. Quasi-isotropic stacking sequences of $[0_i/\pm45_j/90_k]$ lead to quasi-isotropic in-plane properties requiring more material under axial loading. Improved versions of CAIO are capable of calculating the optimum fibre arrangement in three-dimensional shell and solid structures [16, 18]. As an example, the results of CAIO on a 3D cantilever tube loaded in bending are shown in Figure 2-24.

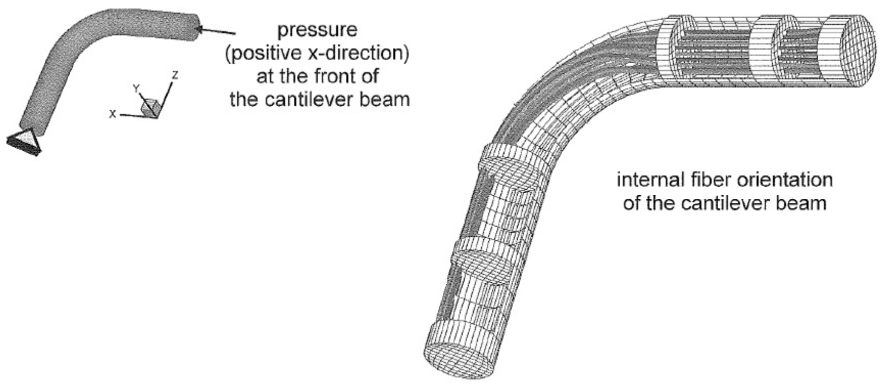

Figure 2-24 Boundary conditions and fibre arrangement of a cantilever beam under axial pressure optimised by CAIO [16]

Tensile plates containing a circular notch were produced from glass fibre reinforced polymer (GFRP) [17]. One set was unidirectional (non-optimised) and another was laid up according to the two-dimensional CAIO optimal fibre arrangement using a fibre laying machine. The fracture strength of the optimised tensile plates increased on average 36% compared to the non-optimised tensile plates. However the lay-up of the optimum samples was inhibited by the inaccuracy of the fibre laying machine. In order to simplify the manufacturing process the critical zone near the hole edge in a unidirectional tension plate was reinforced by sticking on three discrete patches of unidirectional fibre on each side of the hole (12 in total on the front and back of the plate) (refer Figure 2-25). FEA predicted the optimum reinforcement angle for strength improvement to be 13° for GFRP and 20° for CFRP. The variance is due to the difference between the elastic moduli ratio E_1/E_2 for the different reinforcing materials. The optimum angle for GFRP was confirmed by experiment, however the strength improvement was far higher than predicted using FEA (refer Figure 2-25). This was attributed mainly to the conservative assumption of the Tsai-Hill failure criterion which equates first ply failure with total failure. In real life the fracture load for a laminate far exceeds this conservative estimate due to progressive failure modes [17].

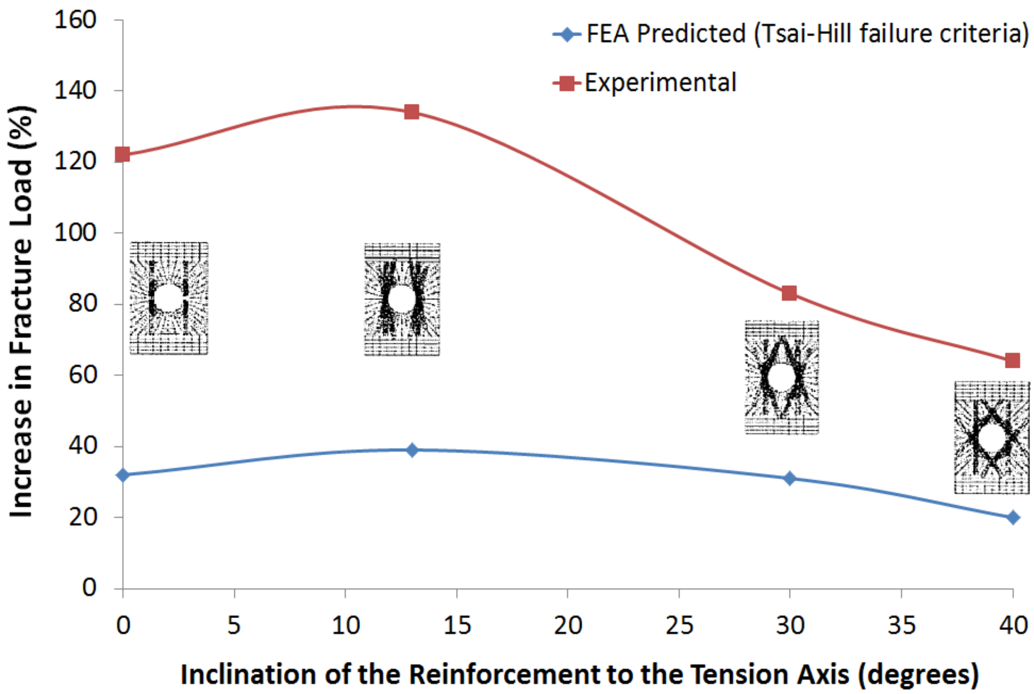

Figure 2-25 FEA predicted and experimental increase in the tensile fracture load of a glass fibre reinforced notched plate as a function of the inclination of the reinforcement structure to the tension axis [17]

Apichattrabrut and Ravi-Chandar [66] examined the effect of a helicoidal laminate stacking sequences bio-inspired from bone on the static and impact strength of composite samples with a $[180/170/160/150/140/130/120/110/100/90/80/70/60/50/40/30/20/10/(0)2]_S$ lay-up. Tensile testing revealed the helicoidal laminate had the highest energy absorption in comparison to unidirectional and ±45 samples. The drawn arrows in Figure 2-26 show that the tensile fracture propagated along different planes and directions in successive plies, increasing energy absorption. In a circular plate bend test the helicoidal samples had the highest failure load and absorbed strain energy compared to unidirectional and ±45 samples (refer Figure 2-27). In addition the laminate showed superior penetration resistance under high energy impact loading [66]. However the disadvantage of helicoidal laminate stacking sequences is they create isotropic laminate properties, leading us back to 'black Aluminium'. The challenge is to find a bio-inspired laminate stacking sequence with improved mechanical properties that retains the advantages of anisotropic materials that can be tailored to the main load paths.

Figure 2-26 The failure pattern of a helicoidal composite specimen under uniaxial tension [66]

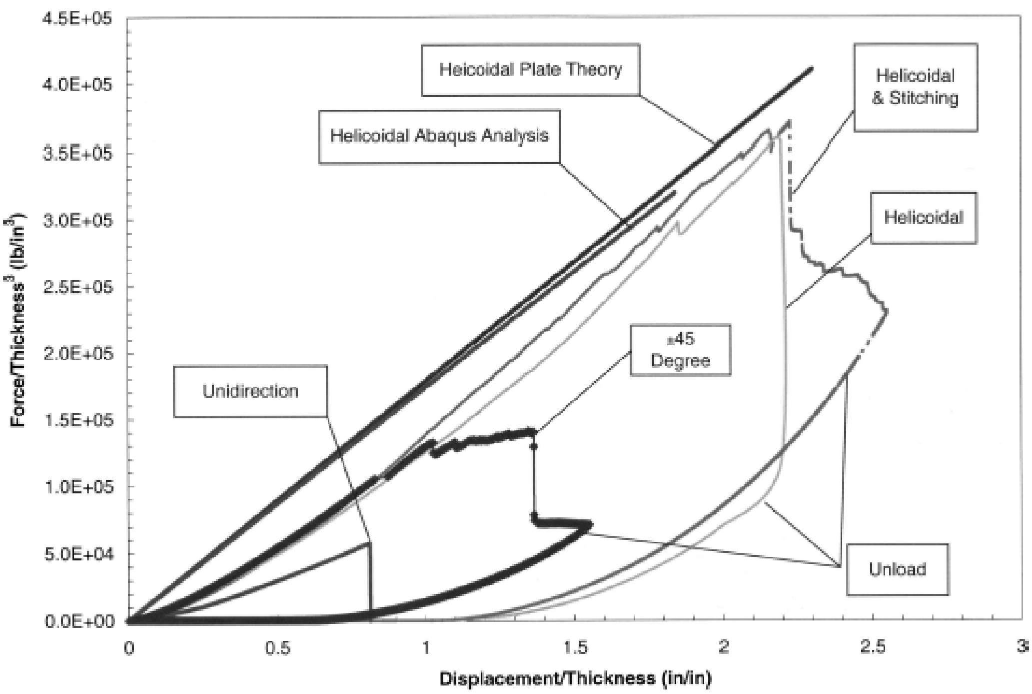

Figure 2-27 Load-displacement relationship for helicoidal, [±45] and unidirectional circular plate laminates under bending test [66]

Another bio-inspired methodology based on material optimisation is known as the Soft Kill Option (SKO) [16]. This was developed based on the principle of tailoring the elastic properties of the material to suit the external loading conditions. The calculated stress distribution is used as the parameter to determine the optimum variation of Young's modulus through the material. Highly-loaded regions are stiffened with high modulus material and lightly-loaded areas are softened with more compliant material or material is removed. The method of altering the modulus for manufacture is not specified by the SKO, although in composite materials this could potentially be achieved through changes to the fibre volume fraction, orientation of the fibres, or hybrid composites with materials selected according to desired stiffness properties. This work was developed using the ABAQUS finite element analysis program and was not validated through experiment [16].

2.4 MATERIAL PROPERTIES OF WOOD

Characteristic of all biological materials, wood contains a strongly hierarchical structure. As a consequence the material properties of wood very much depend on the length scale that is being considered. Table 2-4 lists the mechanical properties of wood at different length scales.

Table 2-4 Mechanical properties of wood at various length scales

		Long. Young's modulus E_1 (GPa)	**Long. Tensile strength σ_t (MPa)**
Cellulose (nano-scale) [67]		167.5	
Hemi-cellulose (nano-scale) [68]		7	
Lignin (nano-scale) [69]		2	
Wood cell wall* (micro-scale) [53]	Earlywood	15	400
	Latewood	22	850
Wood cell* (single tracheid) (micro-scale) [53]	Earlywood	1.5	30
	Latewood	15	550
Wood** (macro-scale) [70]	Earlywood	1 - 5	15 - 45
	Latewood	5 - 10	~ 250
	Overall	~ 5	~ 150

* Norway spruce (*Picea abies*), ** Radiata pine (*Pinus radiata*)

Analogous to carbon fibre reinforced polymers (CFRPs) the fibre phase, cellulose, has a Young's modulus almost two orders of magnitude higher than the lignin and hemi-cellulose matrix phase. Micro-tensile tests have been performed on single wood cells extracted from a growth ring of a softwood Norway Spruce (*Picea abies*) [53]. Tensile tests have also been performed on clear earlywood samples from the species Radiata pine (*Pinus radiata*) to determine the macro-scale properties of wood [70].

2.4.1 Structure of the wood cell

Wood is classified as either hardwood or softwood. Hardwoods such as oak, ash and balsa contain three cell types: i) tracheids that provide longitudinal mechanical support; ii) rays that provide radial support; and iii) large porous longitudinal cells called vessels that provide vascular flow. Softwoods such as pine, spruce and fir contain only tracheids and rays. Softwood has a simpler structure because the tracheids are adapted to be multi-functional to provide both mechanical support and vascular flow and the softwood tracheid will be the characteristic wood cell considered in this review.

The structure of the softwood tracheid cell wall is shown schematically in Figure 2-28a. The tracheids of Radiata pine (*Pinus radiata*) (which is the species considered in this PhD study) are typically 2 – 4 mm long with diameters ranging from 20 – 60 μm [71]. The thickness of the cell wall is about 2 – 4 μm in less dense earlywood and 3 – 7 μm in denser latewood (refer Figure 2-28b) [71]. The tracheid tips are turned over at an angle of about 90˚ to the cell axis to reduce fracture forces between cells that could cause the wood to split [72].

The wood cell wall consists of concentric lamellae surrounding the hollow centre, known as the lumen, which gives wood its cellular structure. The lamellae are formed from a fibrous composite containing cellulose, lignin and hemi-cellulose [4, 72]. The cellulose forms crystalline regions known as microfibrils that are embedded in a hemi-cellulose and lignin matrix. The microfibril angle is defined as the angle between the helically wound cellulose microfibrils and the vertical cell axis (refer Figure 2-28).

The lamellae are divided into primary wall (P), secondary wall (S) and middle lamellae (M). The middle lamella does not contain cellulose. It is made from hemi-cellulose and lignin, analogous to adhesive 'glue' that bonds the wood cell to adjacent cells. The primary wall contains a randomly oriented network of microfibrils. The secondary wall contains helically wound microfibrils and is further divided into the S1, S2 and S3 layers. These three layers differ in thickness, microfibril angle and chemical composition [73]. An estimate of these differences is given in Table 2-5 [71]. The microfibril angle of the S1 layer is crossed whereas the S2 and S3 layers contain mono-rotational microfibrils. The S2 layer is the main layer by volume and the microfibril angle has primary influence on the mechanical properties of the wood. Two adjacent tracheids form a double cell wall that can be modelled as a seven ply laminate [S3/S2/S1/P+M/S1/S2/S3] (refer Figure 2-28c).

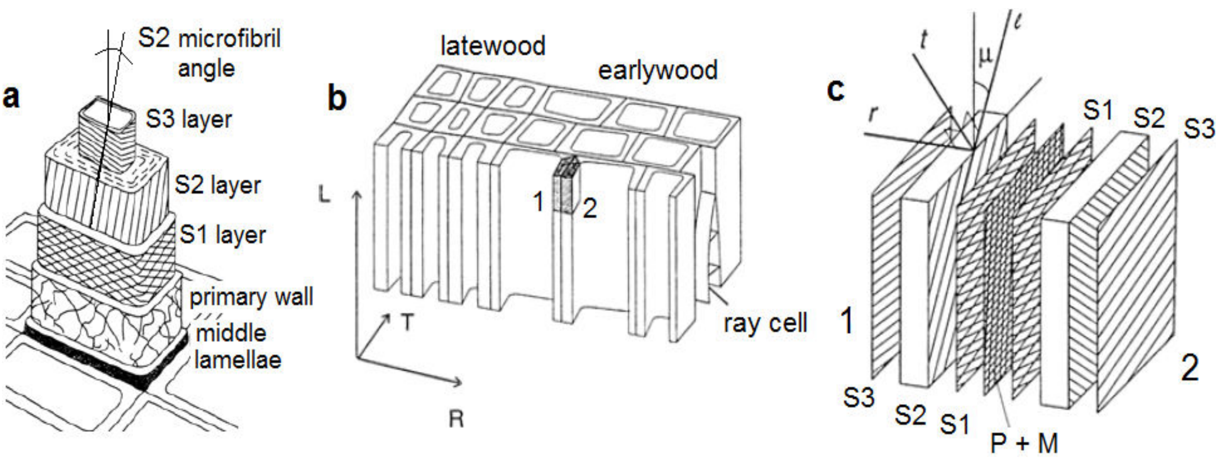

Figure 2-28 (a) Structure of the softwood tracheid cell wall [24]; (b) schematic of the double cell wall; and (c) the double cell wall forms a seven ply laminate [71]

Table 2-5 The structural and chemical properties of the tracheid cell wall layers of an earlywood fibre [74]

Layer	Thickness (μm)	Cell wall volume (%)	Typical microfibril angle (°)	Cellulose volume (%)	Hemi-cellulose volume (%)	Lignin volume (%)
Middle	0.30	14	-	0	44	56
Primary	0.10	5	Unordered	15	33	52
S1	0.15	7	±70	28	31	41
S2	1.6	73	10 – 40	50	31	19
S3	0.03	2	70	48	36	16
Total	2.18	100		40	33	27

A summary of the functions of each cell wall layer in the living tree is given in Table 2-6.

Table 2-6 Functions of the cell wall layers in the living tree [72]

Cell wall layers	Functions of the cell wall layers in the living tree
S3 layer	Strengthens the cell against collapse such as implosion caused by water tension. Resists trans-wall fracture in the transverse direction: A crack propagating in the transverse direction first has to penetrate the S3 layer in which most of the reinforcing microfibrils lie almost perpendicular to the direction of the crack.
S2 layer	Carries the axial tension and compression forces generated by wind and self-weight. Strongly resists trans-wall crack propagation in the axial direction.
S1 layer	The cellulose reinforcement in the S1 layer prevents excessive radial expansion of the S2 layer under compression. As radial expansion and rotation of the S2 layer are coupled, this also limits the maximum rotation of the secondary wall that can occur, which in turn limits the maximum shear stress in the middle lamella. Prevents intra-wall cracks from developing into trans-wall cracks.
Combined S3, S2 and S1 layers	The laminate construction with microfibril-reinforced radial ribs creates extra resistance against buckling and collapse.
Primary wall and middle lamella	Resists inter-cell failure between the double cell wall. Dissipates vibration energy. Under axial load each half of the double wood cell wall twists slightly in opposite directions because the S2 layers have opposite microfibril angles. This places the strongly lignified middle lamella in shear which dissipates vibration energy through 3D chain molecules moving against each other (analogous to rubber).

2.4.2 In-plane properties of wood

In softwoods such as *Pinus radiata* the S2 layer typically occupies a large fraction of 60 – 80 vol.% of the wood cell wall. It also contains the highest cellulose fibre volume fraction of 0.5 in the form of ordered microfibrils oriented towards the direction of the cell axis. Analogous to carbon fibre in carbon fibre reinforced polymer composites the material properties of the cellulose fibre phase and the orientation of the S2 microfibril angle dominate the longitudinal mechanical properties of wood to such a degree that some models of the wood cell wall consider it to consist of the S2 layer only [73].

The S2 microfibril angle and the wood cell density (measured by cell diameter and cell wall thickness) are the key variables that determine the bulk longitudinal mechanical properties of wood including Young's modulus, tensile strength, fracture toughness and non-linear behaviour [44, 53, 54, 72, 75-79]. Figure 2-29 shows the effect of the S2 microfibril angle on the longitudinal Young's modulus and strain-to-failure of wood. Under axial loading longitudinal stiffness is optimised at a microfibril angle of 0° and strain-to-failure is minimised. As the microfibril angle increases, the helical winding of the microfibrils means the wood cell resembles a spring with decreasing stiffness. Consequently the Young's modulus reduces and the strain-to-failure increases.

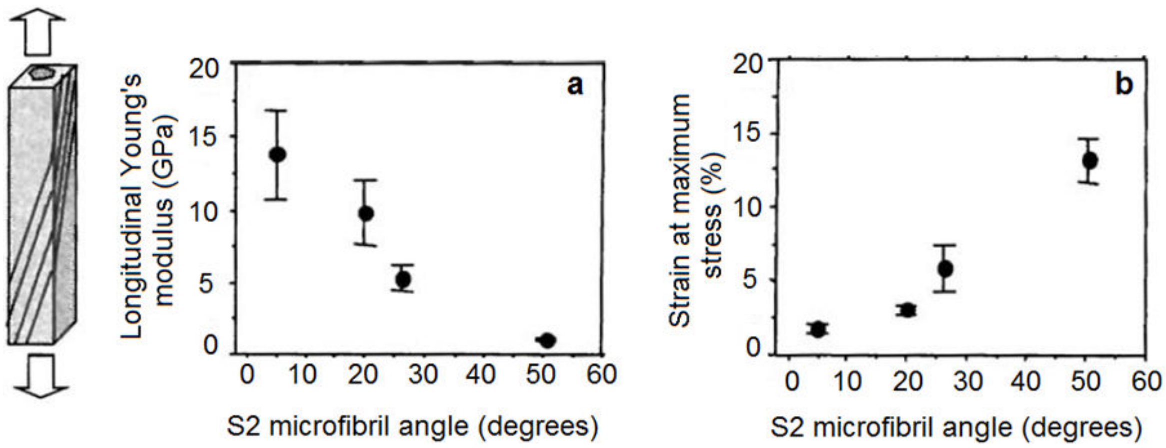

Figure 2-29 Influence of S2 microfibril angle on the mechanical properties of wood: (a) longitudinal Young's modulus v microfibril angle; and (b) strain at maximum stress v microfibril angle [78]

Figure 2-30a shows the variation of longitudinal tensile strength of Norway spruce versus S2 microfibril angle and compares it to the longitudinal tensile strength of CFRP versus carbon fibre angle in the laminate (refer Figure 2-30b). In both cases the tensile strength decreases to about 10% of the original value at reinforcement angles of ~50° (the highest microfibril angle typically found in the S2 layer). Figure 2-29 and Figure 2-30 show that the mechanical properties of both wood and fibre-reinforced composite materials are highly dependent on fibre orientation.

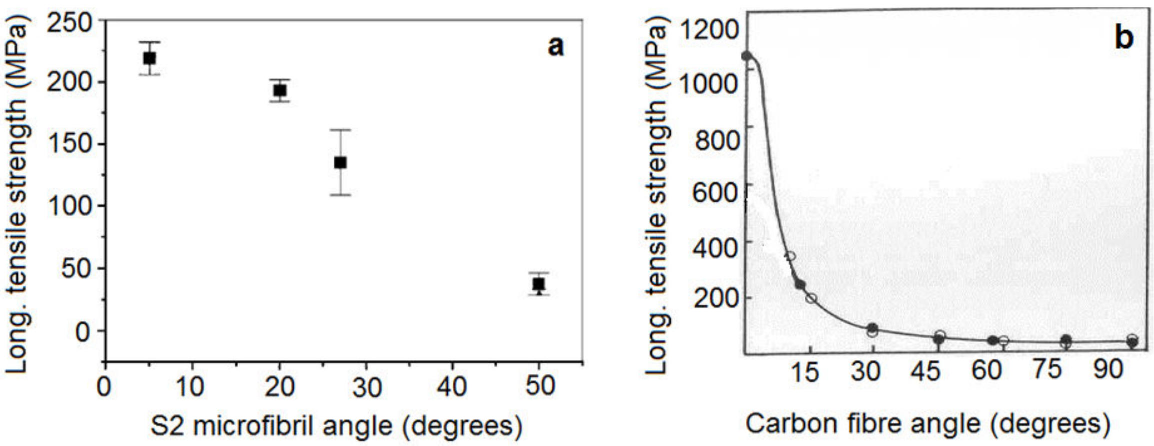

Figure 2-30 Influence of fibre angle on the longitudinal tensile strength of fibre-reinforced composites: (a) Norway spruce (*Picea abies*) [80]; and (b) carbon fibre reinforced polymer laminate [81]

It has been shown that an S2 microfibril angle of 0° (aligned with the cell axis in the direction of growth of the tree trunk) provides maximum axial modulus and tensile strength. However an axially aligned microfibril would make the wood cells very vulnerable to axial crack propagation and trans-wall fracture [72, 80] (this is discussed further in section 2.4.7). Therefore trees select the optimum microfibril angle depending on the loading condition of the wood. This varies depending on the age of the tree as shown in Figure 2-31. The microfibril angle decreases from a maximum of 45° for earlywood and 38° for latewood in the first annual rings near the pith to 20° for earlywood and 0° for latewood in the last annual rings near the bark [82]. The microfibril angle is higher in earlywood than in latewood.

The change in S2 microfibril angle over time is explained as follows: when trees are young saplings their biggest peril is fracture caused by high wind loads. Therefore wood in young trees forms higher S2 microfibril angles for optimum flexibility. As the tree grows the self-weight increases such that axial stiffness is required to prevent the tree trunk from buckling under its own weight and the S2 microfibril angle correspondingly decreases. The microfibril angle also varies according to structural features such as tree branches. This will be discussed further in section 2.5.

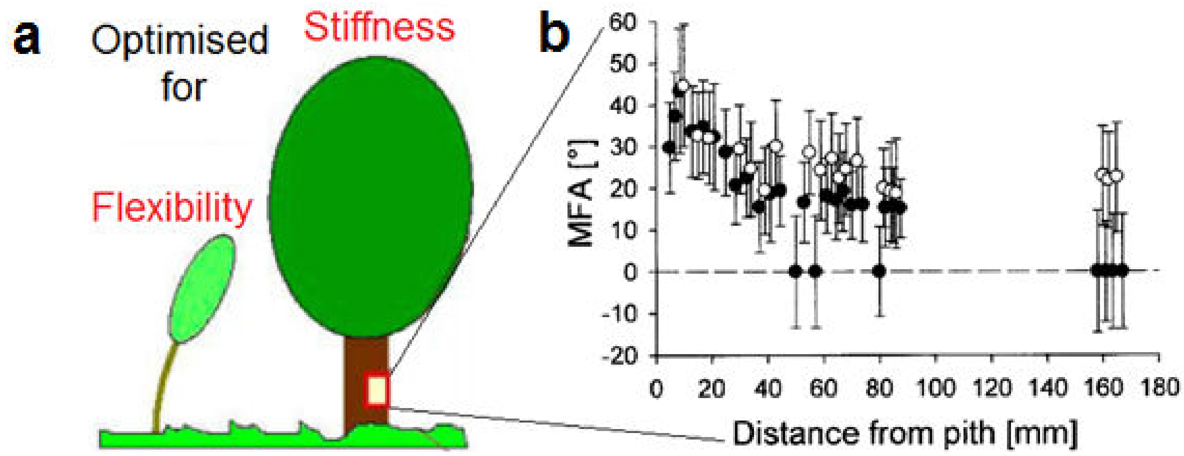

Figure 2-31 (a) Different survival priorities of young and mature trees [37]; and (b) microfibril angle in a softwood decreasing from pith to bark [82]

Wood has a lower yield strength under compressive loading due to micro-buckling of the tracheids [83]. Softwoods respond to high compressive loads by developing compression wood. Compression wood is characterised by a higher volume fraction of lignin, the absence of the S3 layer and higher microfibril angles in the S2 layer. The S1 layer, which normally forms about 10% of the secondary cell wall in normal tracheids forms about 25 – 30% of the secondary cell wall in compression wood [84]. The microfibril angle of the S1 layer was measured to be 90.0˚ ± 2.7˚ and 88.9˚ ± 2.4˚ in two growth rings of compression wood [84]. The effect of these adaptions is compression wood has a lower modulus but a higher compressive strength and strain-to-failure (refer Figure 2-32a). Compression failure modes include micro-kinking and buckling of wood cell walls, which have similarities to kink bands in composite materials loaded in axial compression (refer Figure 2-32b-c) [77].

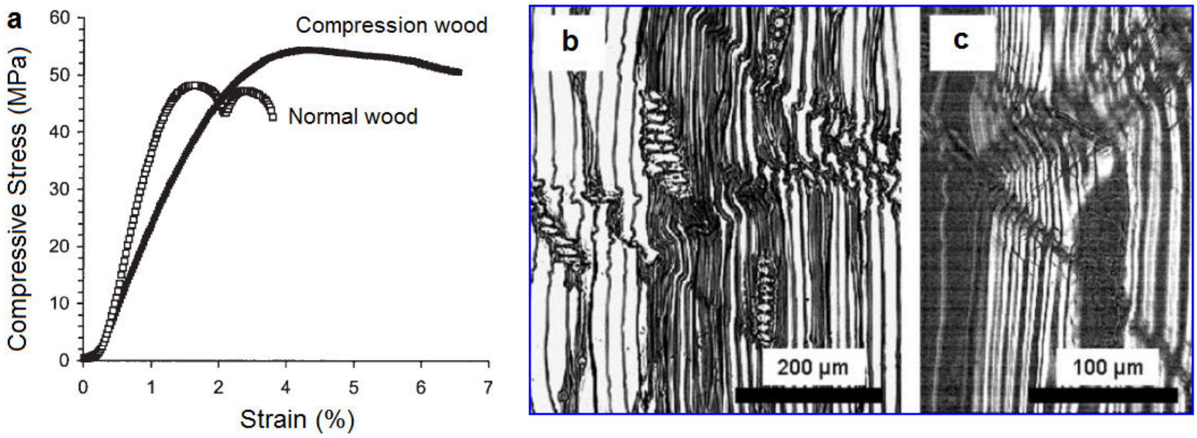

Figure 2-32 (a) Typical load deformation curves for normal and compression wood; (b) buckling of cell wall; and (c) micro-kinking becomes visible in polarised light [77]

2.4.3 Transverse properties of wood

The transverse properties of wood are controlled primarily by the S1 and S3 layers and dominated by the material properties of the hemi-cellulose and lignin matrix phase [74, 84]. The S1 and S3 layers have helically wound microfibrils almost perpendicular to the cell axis at microfibril angles of about 70 - 90° [71, 84].

Directional properties of Norway spruce are given in Table 2-7. The ratio of longitudinal to transverse Young's moduli of wood $E_{longituidnal}/E_{transverse}$ ~ 20, which is similar to quasi-isotropic CFRP composites. However wood is not transversely isotropic. It is stiffer, stronger and tougher in the radial-longitudinal plane, compared to the tangential-longitudinal plane due to the presence of rays (refer section 2.4.6).

The microfibril angle and wall thickness of the S2 layer has little influence on the transverse properties of wood. The transverse elastic modulus of wood is mostly dependent on the properties of the S1 and S3 layers and increases with increasing microfibril angle and wall thickness in these layers [74]. The transverse properties of the hemi-cellulose and lignin matrix are important and it has been found to be impossible to model the transverse properties of wood without accurate values of this data [71, 73, 74, 85].

Table 2-7 Longitudinal, radial and tangential Young's modulus of Norway spruce (*Picea abies*) [86]

	$E_{Longituidnal}$ (GPa)	E_{Radial} (GPa)	$E_{Tangential}$ (GPa)
Norway spruce	10.7	0.71 GPa	0.43 GPa

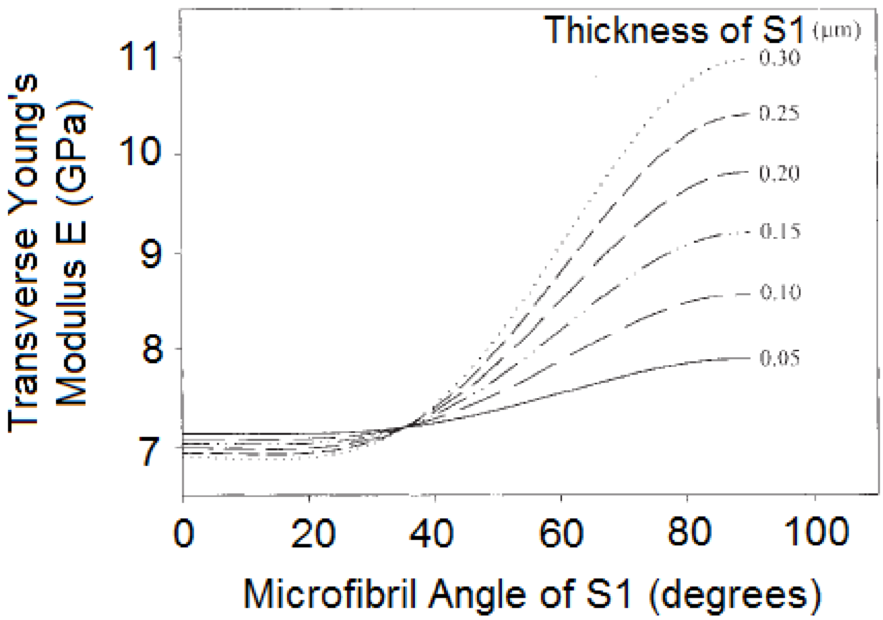

Figure 2-33 Influence of the thickness and the microfibril angle of the S1 layer on the transverse elastic modulus (E_t) of the double radial fibre wall with S2 = 10° and S3 = 70° [74]

2.4.4 Grain patterns

The wood cell tracheids of a tree are arranged in a larger system known as the grain pattern, which forms the mechanical and hydraulic architecture of the tree. The details of the grain orientation are determined in an area just underneath the bark known as the vascular cambium. This is the only part of the tree that contains living cells, which is why it is possible to kill a tree by ring barking. The vascular cambium contains stem cells that differentiate into either long fusiform initials, which form tracheids, or short square ray initials, which form rays (refer Figure 2-34a) [57]. The vascular cambium controls the orientation of the fusiform initials to generate the grain pattern in response to structural details such as branches or external stimuli such as wounds or constricting vines (refer Figure 2-34b – e). Once a grain pattern has been laid down it is not possible for the tree to remodel it [57].

The mechanism by which the vascular cambium determines the grain pattern is not well understood. Mattheck and co-workers [16-18] believe the vascular cambium senses the mechanical strains acting on the tree and differentiates the fusiform initials so that the grain is aligned with the direction of principal stress (force flow). This would have the advantage of eliminating shear stresses that can cause fibre/matrix rupture and is the basis of the bio-inspired methodology known as computer aided internal optimisation (CAIO) (refer section 2.3.2). However this approach ignores the importance of grain patterns in delivering water to different parts of the tree. The phenomenon of dead branches being excluded from grain flow (refer Figure 2-34c) suggests that the sensing of mechanical forces is not solely responsible for the formation of grain patterns. Kramer et al. [57, 87] created a computer model that considers the plant hormone auxin as the major co-ordinating signal, with fusiform initials rotating in the presence of the auxin axial polar gradient to point their apex towards zones of high auxin content and their bottom away. Model simulations qualitatively reproduced wood grain features and this approach also explains why when a branch dies the auxin is cut off and the new grain reorients to bypass the dead branch.

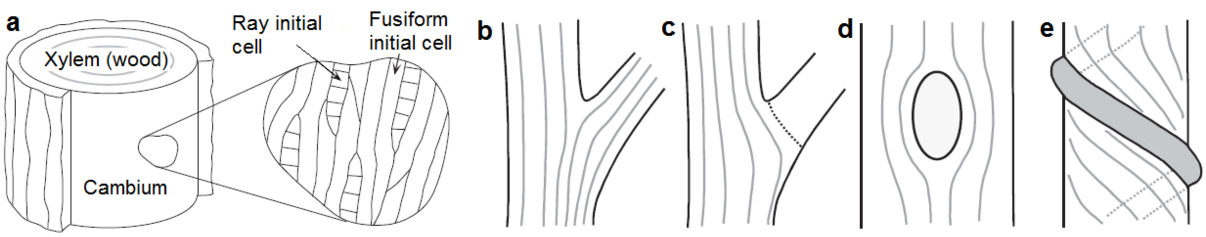

Figure 2-34 (a) Sketch of the tree trunk anatomy showing the vascular cambium beneath the bark which controls grain orientation in response to; (b) a lateral branch; (c) death of a lateral branch; (d) an elliptical wound; and (e) constriction by a vine [57]

Most trees contain straight wood grains aligned with the growth of the trunk. In some cases the wood grain in the tree trunk grows at an angle to the trunk and this is known as spiral wood grain. Eklund and Saell [88] looked at the influence of wind on spiral wood grain formation in conifers and found a significant correlation between the spiral angle and an off-axis tree crown as a result of prevailing wind loads. Another interesting phenomenon of grain patterns is whirled grain, which often occurs at branch junctions with some examples shown in Figure 2-35. The purpose of whirled grain is not well understood and is either a different form of order compared to straight wood fulfilling a particular biological function, or the result of a breakdown in the orienting signal in the cambium [57, 87, 89, 90].

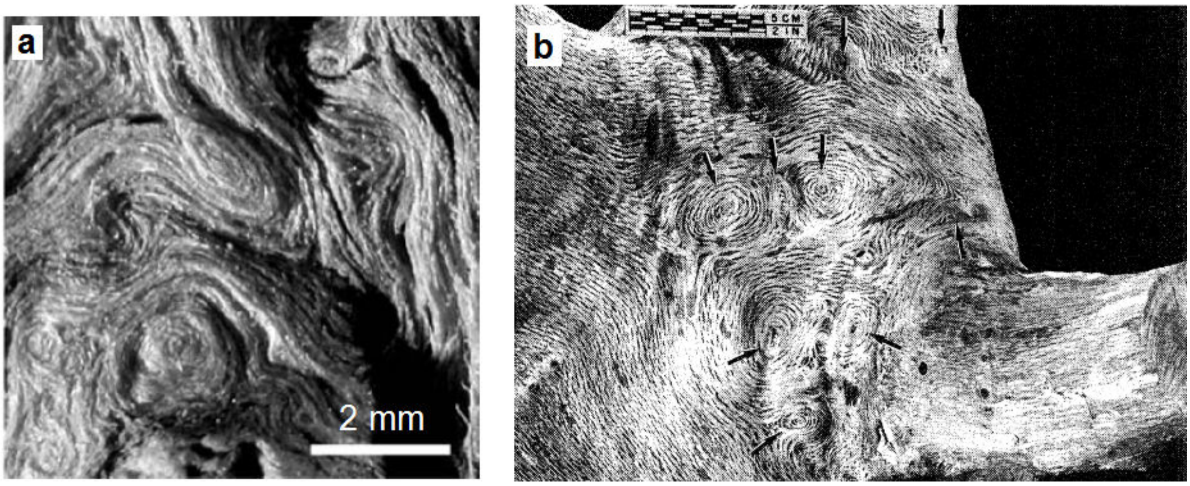

Figure 2-35 (a) Whirled grain on the de-barked surface of a Quaking aspen (*Populus tremuloides*) above a dead lateral branch [57]; and (b) whirled grain between a trunk and two lateral branches of Tabor oak (*Quercus ithaburensis*) [90]

2.4.5 Growth rings

Growth rings provide a record as to the age and the growth history of the tree (refer Figure 2-36a). A new growth ring forms every year and is divided into two sections: i) less dense earlywood; and ii) dense latewood. The density of the material in the cell wall remains constant between earlywood and latewood. The macro change in density is due to seasonal fluctuations in growing conditions influencing the void content of the wood. Earlywood is a less dense wood that forms early in the growing season during spring rains when trees undergo rapid growth. It is characterised by large tracheid diameters and relatively thin cell wall thicknesses. Latewood is a much denser wood that is a mechanical consolidation of the rapid spring growth that forms during the drier summer months. It is characterised by reduced tracheid diameters and increased cell wall thickness (refer Figure 2-36b). Figure 2-36c shows the area of the hollow lumen and the ratio of the cell wall area to the total cell area (cell wall + lumen) highlighting the effective increase in density in latewood caused by a reduction in cell porosity.

As wall thickness increases work by Booker et al. [72] showed that trans-wall fracture will become less probable unless the microfibril angle also decreases. Therefore the microfibril angle decreases in latewood (refer Figure 2-31). The alternating earlywood/latewood bands create a periodically varying density across the radius of the tree, resulting in a macro-level periodically varying Young's modulus. The Young's modulus ratio $E_{latewood}/E_{earlywood}$ is about 3 – 4 across a growth rings (refer Table 2-4).

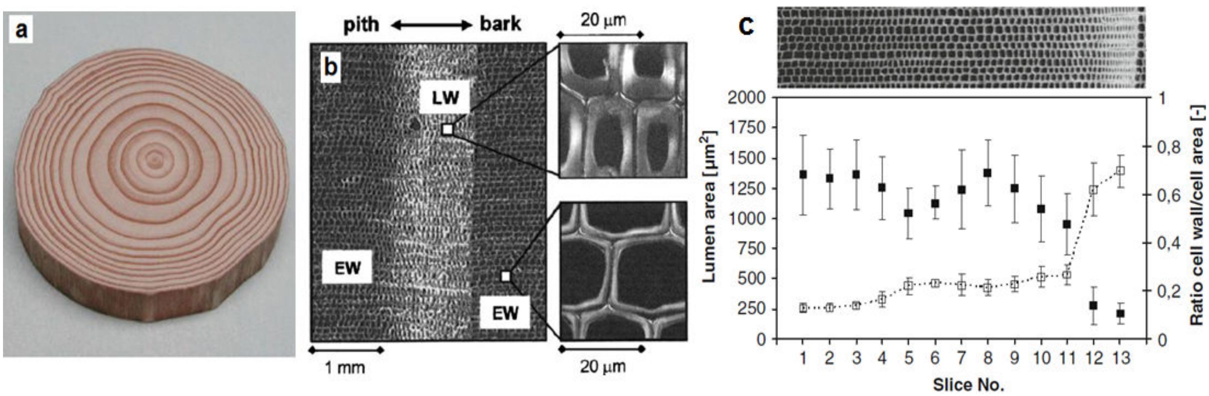

Figure 2-36 (a) Growth rings; (b) polarisation microscopic image of earlywood and latewood tracheids across a growth ring of mature wood Norway spruce (*Picea* abies) [82]; and (c) lumen area (black rectangles) and ratio of the cell wall/cell cross-section (white rectangles) across a growth ring of *Picea abies* [53]

2.4.6 Rays

As described in section 2.4.1 the primary wood cell of softwoods is the tracheid which provides mechanical strength and vascular flow in the longitudinal direction along the trunk. Radial cells form a secondary feature of wood known as rays (refer Figure 2-37). Rays have the biological function of transmitting sap radially across the tree and they also play a role in the mechanical properties, reinforcing and strengthening wood in the radial direction [74, 91].

The seasonal variation of wood density resulting in the earlywood/latewood growth rings leads to a discontinuity in the Young's modulus in the radial direction (refer Table 2-4). When trees undergo bending (e.g. during wind loading) this periodical variance in the radial Young's modulus means wood can crack under the shear forces that develop between the earlywood and latewood bands. The rays act as stiff pins preventing the layers from slipping off each other as shown in Figure 2-38a [91]. Rays are spindle shaped, but interestingly it has been shown that if they are subjected to bending loads they reinforce the top and bottom of the spindle by developing more lignin in these regions to resist bending, which is equivalent to the engineering I-beam (refer Figure 2-38b) [92].

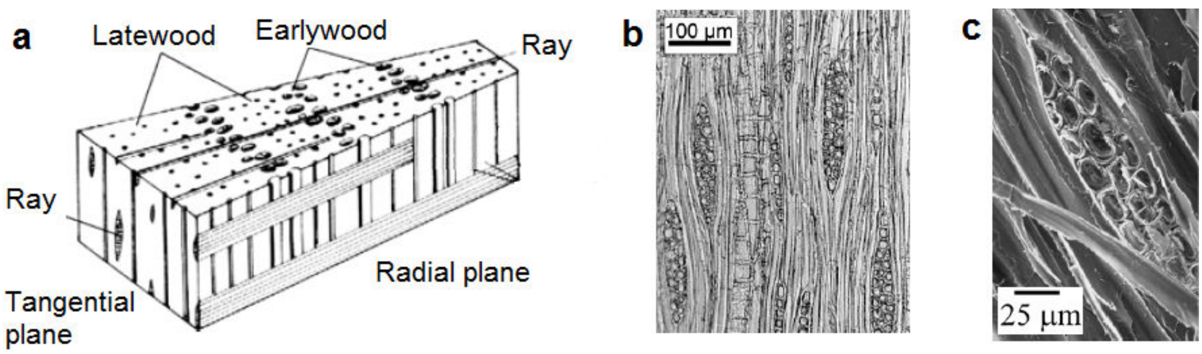

Figure 2-37 (a) Schematic drawing of typical features of the anatomy of wood; (b) SEM of the ray structure of Oak; and (c) SEM of the fracture surface of Ash in the R-L plane showing a ray cell [91]

Reiterer et al. [91] experimentally compared the mechanical properties of wood specimens cut from the radial and tangential planes of Ash and Oak. The wood was characterised by the volume fraction, number, shape and size of rays as measured from image analysis. Radial tensile strengths of 11 – 18 MPa were measured, which were about 50 – 100% higher than tangential tensile strengths. The stiffness (Young's modulus) and fracture toughness (K_{IC}) in the radial plane were both about twice that measured in the tangential plane [78, 91]. It is possible that rays build fibre bridges behind the crack tip, creating an extrinsic toughening mechanism that consumes fracture energy [91].

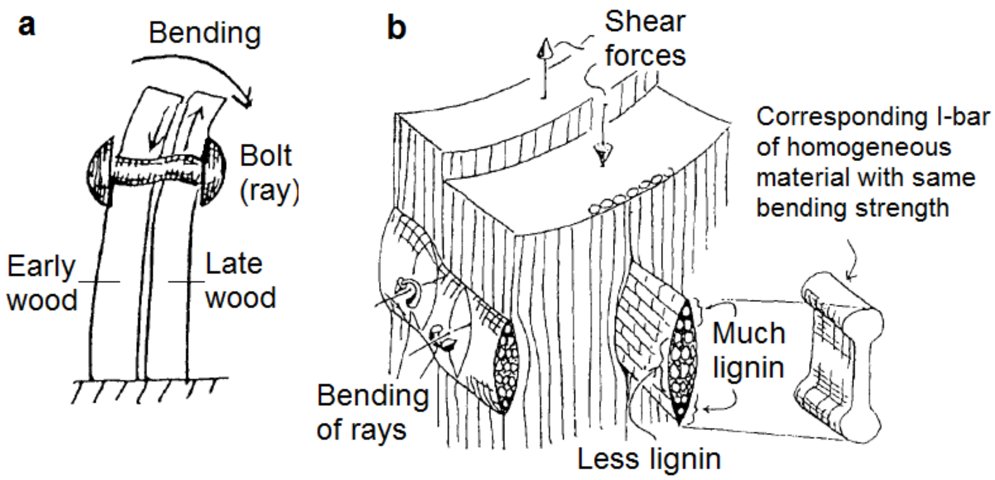

Figure 2-38 (a) Rays interlocking the annuals rings; and (b) rays subject to bending loads have more lignin at the upper and lower ends of the spindle, equivalent to an equivalent I-beam [92]

2.4.7 Fracture mechanics of wood

The specific work-of-fracture of wood is superior to glass fibre composites and comparable with mild steel (refer Table 2-8). The fracture energy of wood is several orders of magnitude higher than its free surface energy, indicating energy is dissipated in regions away from the crack plane (i.e. intrinsic and/or extrinsic toughening) [79]. At the micro-length scale there are three types of wood cell failure under tensile load: inter-cellular, intra-wall and trans-wall (refer Figure 2-39). Inter-cellular failure involves the separation of cells fracturing at the middle lamella, and is less commonly observed [72]. Intra-wall failure occurs within the cell wall layers (usually at the S2/S1 interface) and trans-wall failure involves the crack cutting across the double cell wall exposing the interior of the cell (refer Figure 2-39) [93]. Cell wall thickness has a strong influence on the fracture toughness of individual cells. The dominant fracture in low density earlywood is typically trans-wall whereas thick-walled latewood typically exhibits intercellular or intra-cell fracture [78, 93].

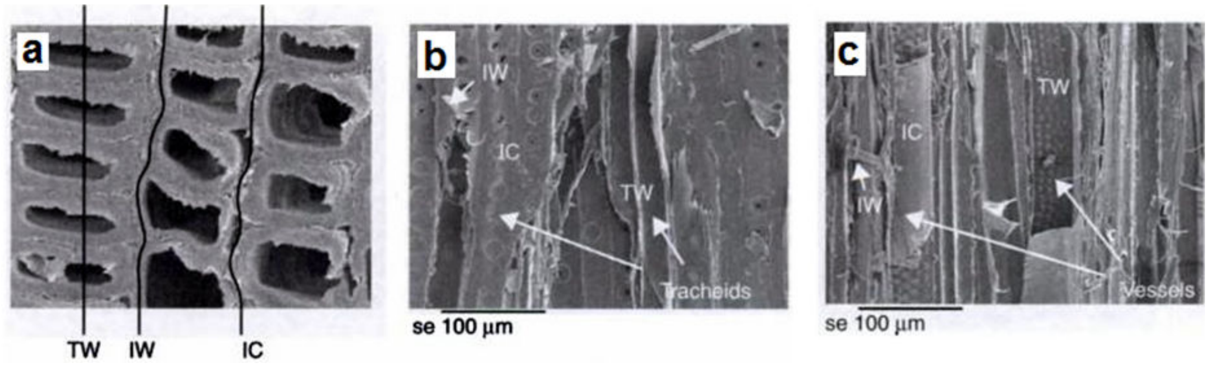

Figure 2-39 Basic fracture paths in wood are inter-cellular (IC), trans-wall (TW) and intra-wall (IW): (a) SEM of fracture paths; (b) fracture in spruce; and (c) fracture in maple [93]

Table 2-8 The absolute and specific work-of-fracture of various materials [79]

Material	**Work-of-fracture γ_t (kJ/m^2)**	**Relative density ρ**	**Specific work-of-fracture γ_t/ρ (kJ/m^2)**
Wood across grain	10	0.4 - 0.8	12.5 - 25
Wood along grain	0.1	0.4 - 0.8	0.125 – 0.25
Mild steel	100 – 1000	7.8	12.8 - 128
Aluminium	100 - 1000	2.7	3.7 - 37
Glass	0.01	2.4	0.004
Glass fibre reinforced plastics	10	2.0	5

Considering the double cell wall (refer Figure 2-28c), during trans-wall fracture the crack can either propagate in the axial direction alternatively cutting through microfibrils and matrix (for non-zero values of the microfibril angle) or follow the microfibril direction in the S2 layer. The structure of the double cell wall is non-symmetrical which means that when the crack follows the (non-zero) microfibril angle the crack front must branch into separate cracks in each S2 layer. The crack will take the path that requires the least strain fracture energy, whether that be penetrating the interface or propagating along the interface, with the main S2 layer microfibril angle key to determining the fracture mode [72].

It was described in section 2.4.2 that wood has the highest axial modulus and strength (translating to lowest weight design) when the S2 microfibrils are axially aligned with the cell growth direction. However at a microfibril angle of 0° wood cells are very susceptible to trans-wall fracture because the crack does not need to penetrate fibres in order to propagate. The solution is to find the best compromise between axial stiffness, strength and work-of-fracture. Reiterer et al. [80] plotted E x ε_0^2 (E = longitudinal Young's modulus; ε_0 = strain at maximum stress) and determined the optimum microfibril angle for the highest work-of-fracture is about 27° (refer Figure 2-40a). This is very similar to the average microfibril angles measured in a mature Scots pine shown in Figure 2-31. The increase in work-of-fracture with increasing S2 microfibril angle can be interpreted visually. At a microfibril angle of 5° (refer Figure 2-41a) there is a much smoother fracture surface compared to wood with a microfibril angle of 50° (refer Figure 2-41b), which shows a deformed fracture surface with strong evidence of the S2 layer pulling out of the tracheids [80]. Thus the ideal microfibril angle represents a moderate sacrifice in axial stiffness and strength in order to increase the fracture toughness of wood. In many structural applications that undergo bending or compression loading the modulus is less crucial since the stresses are proportional to $E^{1/2}$ or $E^{1/3}$ [94].

Gordon and Jeronimidis [94] applied the concept of helical winding to an engineered composite at a higher length scale, constructing macro glass fibre composites consisting of hollow cylindrical tubes with a diameter of about 1.5 mm and a length of 80 mm. The synthetic composites had a smaller fibre volume fraction than wood due to the large proportion of resin infiltrating the gaps between the packing of the macro-fibres. These bio-inspired composites were tested under axial tension and three-point-bending at winding angles of 10°, 15°, 25° and 35° with a maximum energy absorption of ~ 5.1 J/m^2 [94]. The synthetic composite exhibited fibre pull-out as a failure mode, which contributed to the high work-of-fracture (refer Figure 2-41c). Plotting the experimental results of work-of-fracture versus fibre winding angle produced a very similar shaped curve to the results for wood (refer Figure 2-40b). The optimal fibre winding angle compromising between axial stiffness and strength and work-of-fracture was 15° compared to 27° for spruce because of the difference in elastic moduli between wood and glass composites. Single wood cells can reach breaking strains of up to 20% by means of 'pseudo tension buckling' [79]. This is attributed to the architecture of the helically wound pattern of cellulose microfibrils in the S2 layer to the fracture behaviour of wood which is analogous to ductile metals, including a 'yield point' signifying the onset of inelastic deformation (refer Figure 2-42a).

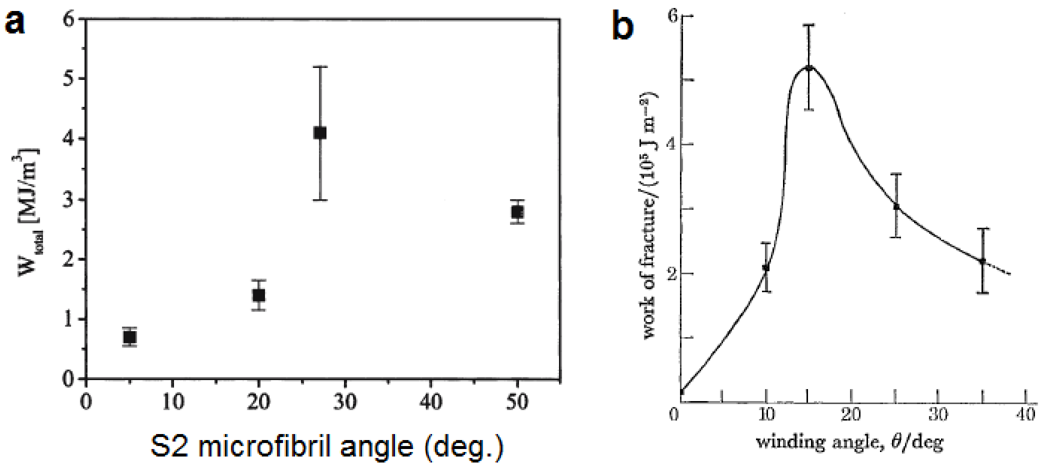

Figure 2-40 Comparison of optimal fibre winding angles for total work-of-fracture of; (a) thin foil samples of Norway spruce [80]; and (b) a bio-inspired glass fibre composite

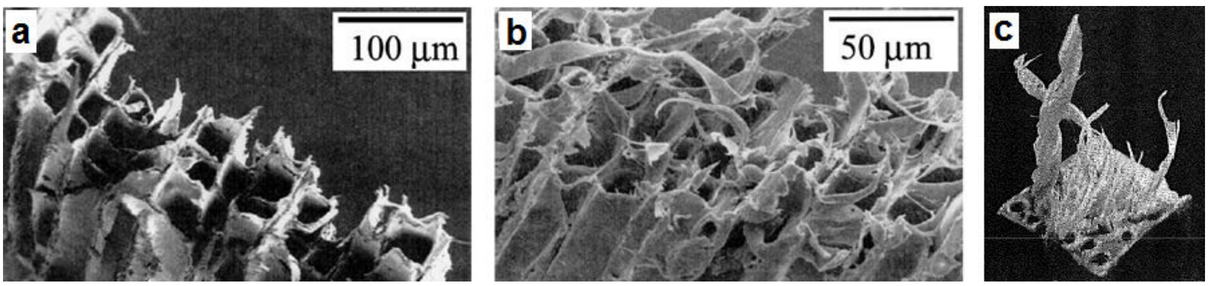

Figure 2-41 Fracture morphology of: (a) Norway Spruce (*Picea abies*) with a microfibril angle of ~ 5° showing smooth fracture surface; and (b) microfibril angle of ~ 50° with S2 layer spiralling out of the tracheids [80]; and (c) composite reinforced with glass macro-fibres at a winding angle of 25° under bending [94]

As the wood cell is loaded in tension the more or less axially aligned microfibrils of the main S2 layer takes up the load. In the initial linear-elastic load phase both the fibres and matrix undergo the same strain, inducing shear stresses at the interfaces between the cellulose microfibrils and hemi-cellulose/lignin matrix due to their differing elastic moduli. The wood cell wall will tend towards collapsing inward towards the hollow centre ('pseudo tension buckling') [79].

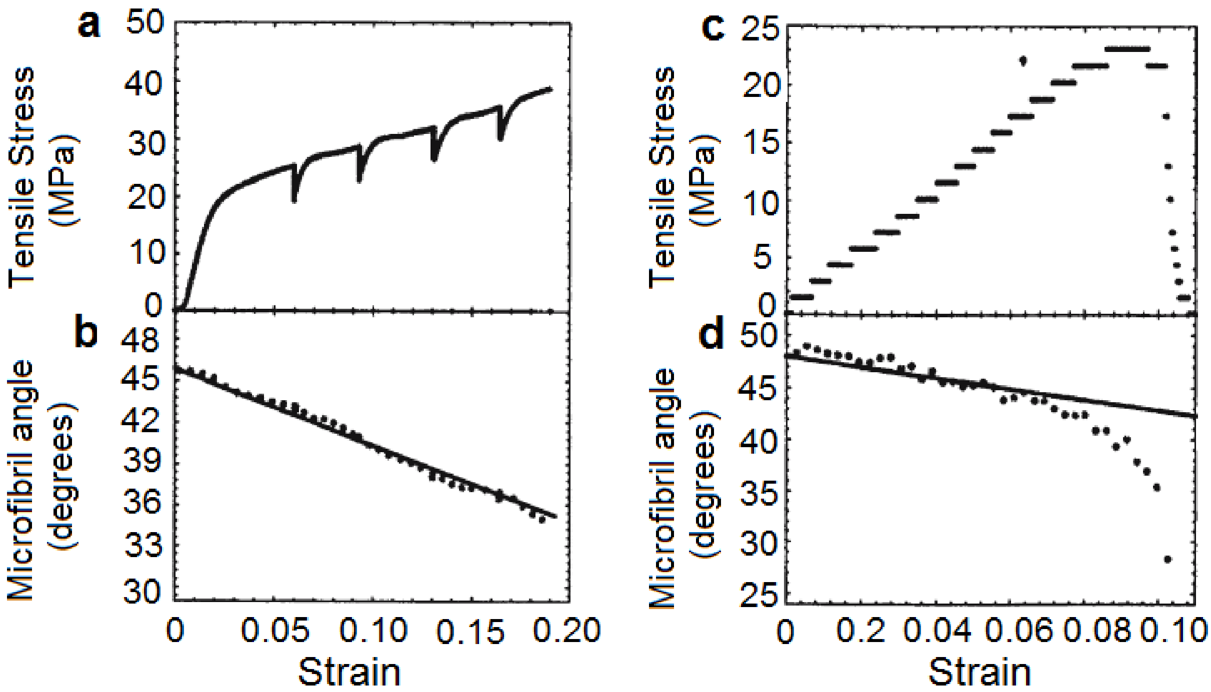

Figure 2-42 (a) Stress-strain curve with four interruptions of loading for a thin foil of Norway spruce; (b) decrease of microfibril angle with increasing strain. Solid line = theoretical prediction; (c, d) analogous results for single wood cell [78]

Beyond the linear-elastic range the mechanical behaviour of the wood composite is determined by two processes: microfibrillar re-orientation and slippage due to plastic deformation of the matrix [95]. Above the 'yield point' the matrix experiences plastic deformation and the microfibrils can slide with respect to each. Under tension load this causes the microfibril angle to decrease [51, 78, 95]. Before fracture the microfibril angle decreases significantly (refer Figure 2-42b and Figure 2-42d). After unloading the plastic deformation remains, compressing the matrix with the fibres under tension. These pre-stresses mean the matrix yield stress increases, leading to larger pre-stresses, generating larger and larger shear forces within the microstructure that cause helical cracks to develop between the cellulose fibre/matrix interface (refer Figure 2-43a) [51]. This failure mode was also observed in the bio-inspired glass composite with macro-fibres (refer Figure 2-43a). At a maximum tensile stress the fibres detach from the matrix, creating fracture surfaces characterised by fibre pull-out (refer Figure 2-41).

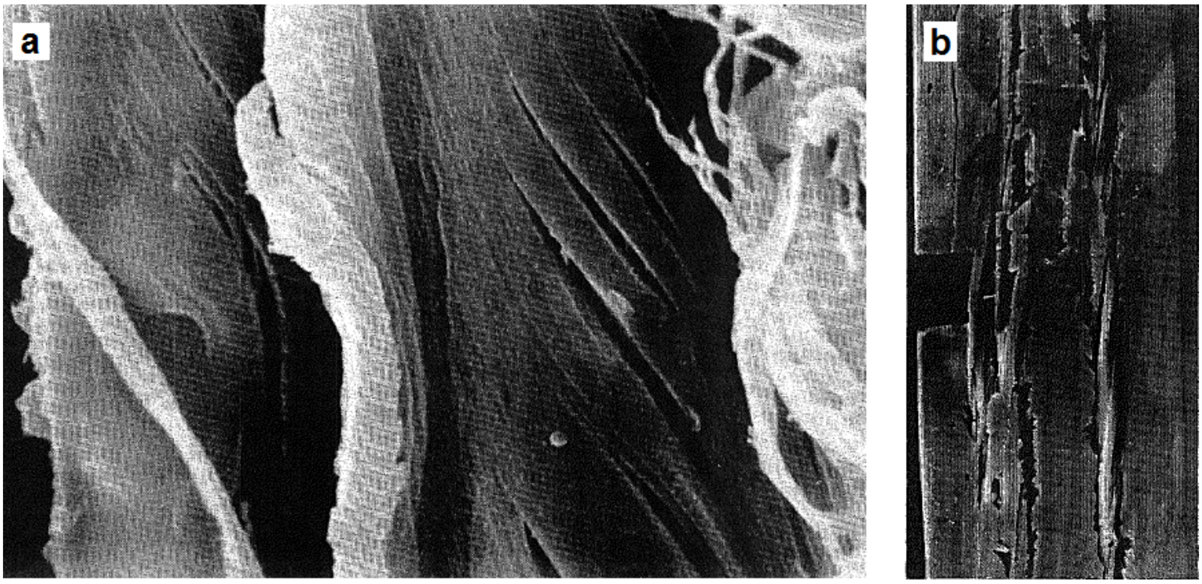

Figure 2-43 Tensile failure of: (a) Sitka spruce (*Picea sitchensis*) wood cell showing helical shear cracks in the S2 wall [79] analogous to; (b) single-edge notched glass composite with winding angle of 15° [94]

2.5 STRUCTURAL PROPERTIES OF THE TREE BRANCH-TRUNK JOINT

2.5.1 How tree branches are attached to the trunk

The branch is a part of the tree that protrudes laterally from the trunk with the function of supporting leaves, allowing the ‘solar powered’ tree to capture more light for photosynthesis. Shigo [96] dissected over 12,000 large and small hardwoods and softwoods over a 25 year period including maple, oak, birth, beech, ash, elm, pine, fir and spruce. This experience, together with pruning experiments and dye experiments designed to determine the vascular flow through the grain identified the architecture of the tree branch-trunk connection. The branch structure is incorporated from the first growth rings of the trunk and consequently each branch has an internal architecture that penetrates to the centre of the trunk. A magnified view of the growth rings of the branch-trunk joint shows the architecture forms a ‘ball-and-socket’ type connection (refer Figure 2-44a). During each year of seasonal growth the branch tissue ('ball') firstly forms to thicken the existing branch. Trunk tissue ('socket') then forms a collar encircling the branch tissue, stabilising the branch. Figure 2-44b presents a computed tomography (CT) image showing the alternating pattern of branch and trunk tissue in the tree branch-trunk joint. The dense latewood layers appear bright.

Dissection showed that the branch and trunk wood are not continuous except for the strip of wood below the branch where the branch wood flows into the trunk (refer Figure 2-45a). Dye experiments indicate there is no conduction directly from the trunk tissues above the branch into the branch, indicating the trunk wood above the branch does not grow into the branch at all [96]. Instead the trunk wood above the branch diverges to deviate around the branch (refer Figure 2-45b).

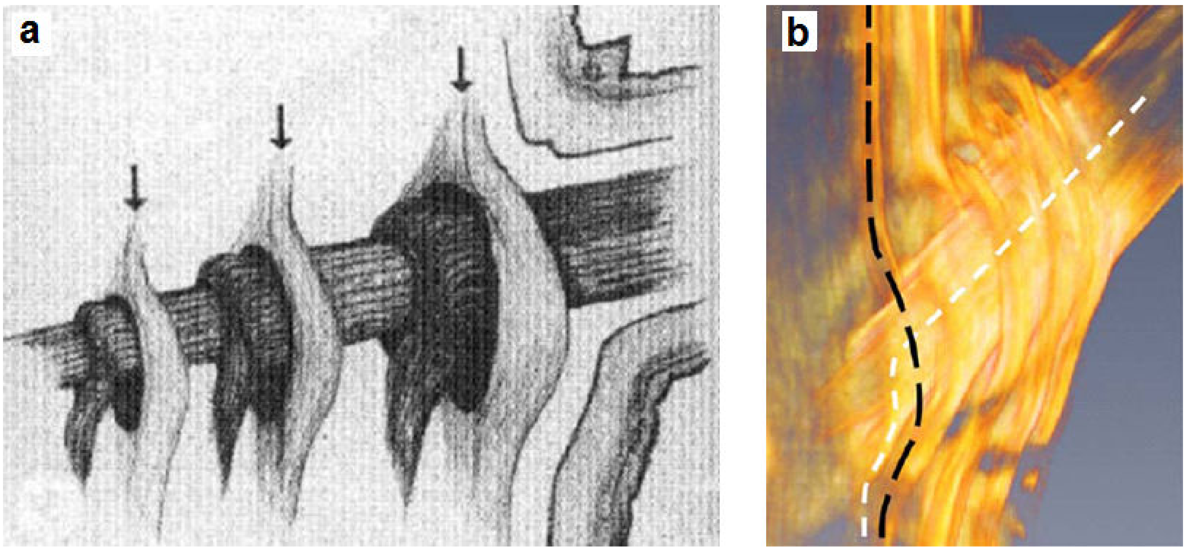

Figure 2-44 (b) Growth rings of the branch-trunk joint showing 'ball and socket' arrangement. Dark wood = branch wood. Light wood = trunk wood[96]; and (b) CT image of the tree branch-trunk joint showing the alternating pattern of trunk (black line) and branch (white) tissue [46]

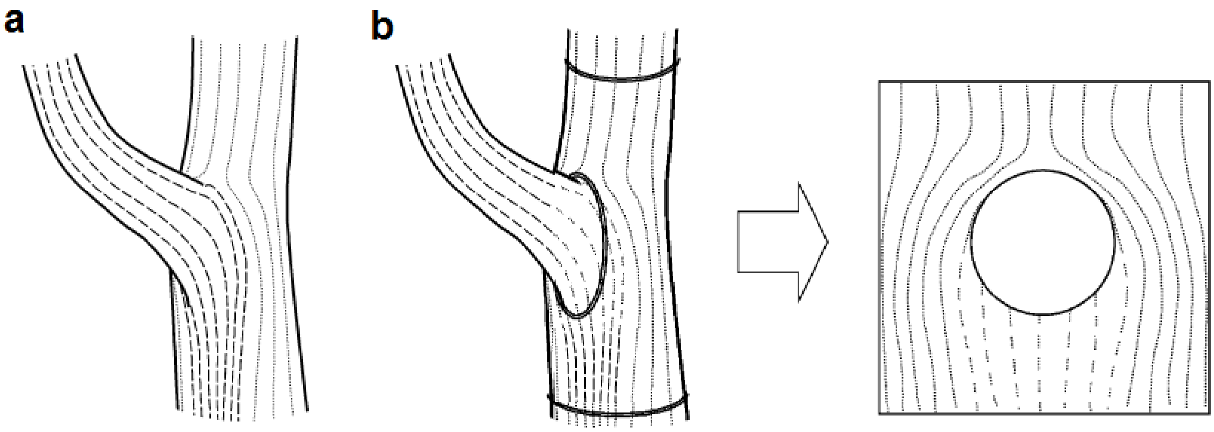

Figure 2-45 Idealised branch junction with dashed lines representing the branch grain and solid lines representing the trunk grain [87]

As a result fluids conduct between the trunk and the lower side of the branch. The amount of trunk wood integrated into the lower side of the branch generally indicates the water supply and hence the vigour of the branch [57, 87]. In the area beneath the branch there is a gradual transition between the branch wood and the trunk wood [55].

Phillips et al. [55] applied the equations of fluid mechanics to model the grain divergence around an elliptical branch as an inviscid two-dimensional laminar flow using streamlines. The resulting streamlines, representing the wood grain, are dependent on the semi-major (*a*) and the semi-minor (*b*) axes of the cross-section of the elliptical branch (refer Figure 2-46a). Inputting measured branch dimensions produced a pattern of wood grain where the divergence of the trunk wood around the branch was mathematically represented as a stagnation point (refer Figure 2-46b). This approach was validated by taking two-dimensional grain angle measurements from the longitudinal-tangential plane and three-dimensional grain angle measurements from Douglas fir and Lodgepole pine specimens with branch diameters from 0.3 – 2.1 inches (7.6 – 53 mm). The overall error between the streamline predictions was 4 - 7° for the two-dimensional and 5 – 11° for the three-dimensional measurements [55].

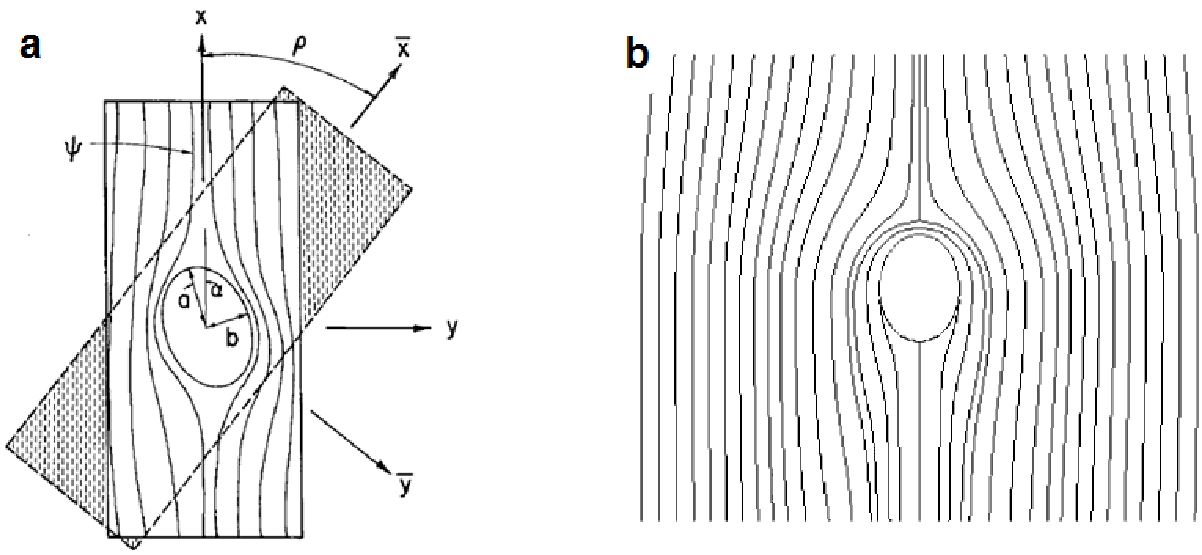

Figure 2-46 (a) Laminar flow streamlines (ψ) around an elliptical body [55]; and (b) streamlines representing the pattern of the fibre flow chain components parallel to the longitudinal-tangential plane [56]

2.5.2 The axiom of uniform strain

In 1893 the German forester Metzer [13] was the first to hypothesise that biological structure can be described by underlying biological principles. He proposed the axiom of uniform stress as a governing principle in which a system of load-controlled adaptive growth shapes the form and structure of natural load-bearing materials such as bone and wood to avoid over-loading or under-utilising material by generating a uniform stress field. Over the past century researchers have investigated field evidence to support this proposal in the context of measuring tree trunk diameters and calculating whether they maintain uniform bending stress along the height of the trunk in the presence of lateral wind forces [13, 62, 97, 98].

Dean and Long [98] derived a model based on the flexure formula for cantilever beams that predicts trunk diameter (D_h) at height (h) using a simple power function fit to the bending moment acting on the trunk at that height (M_h) as given in Equation 2-2:

$$D_h = \phi \times \left(M_h\right)^{\delta}$$ Equation 2-2

Where ϕ and δ are fitted coefficients.

It is assumed the tree is a vertically oriented, tapering beam with a constant elastic modulus rigidly fixed at the base. It is also assumed that the wind forces acting on the trunk only cause small deflections, rendering bending effects caused by gravity negligible. The bending moment (M_h) is calculated as the moment produced by wind pressure acting on the measured leaf area, with the moment arm calculated as the distance to the centre of the leaf area. The leaf area was determined directly by stripping and weighing foliage or indirectly by relating foliage mass to individual branch diameters. Under the assumptions detailed above, uniform bending stress along the stem and across trees is indicated by a fitted value of $\delta = 0.333$.

The model of the uniform stress hypothesis was tested by measuring the trunk diameter at a number a locations of nine commercially important coniferous softwoods (refer Table 2-9) [97]. Fitted values less than $\delta = 0.333$ correspond to more cylindrical trunks and fitted values greater than $\delta = 0.333$ correspond to more rapidly tapering trunks. Results from Table 2-9 show the uniform stress hypothesis is a good approximation of trunk taper for most of the tree species. All but one of the δ values are within 15% of the theoretical value of 0.333 predicted by the model. This supports previous findings by Dean and Long [98] who calculated a fitted value of $\delta = 0.313$ for multiple diameter measurements taken along the trunk and West [99] who concluded that tree trunk morphology can be predicted by the uniform stress hypothesis if wind velocity is small and constant with height.

A limitation of the models used to test the uniform stress hypothesis is the validity of the assumptions. The models assume that the material properties of wood are radially and longitudinally constant across the entire tree. However research discussed in section 2.4.2 has shown that the material properties (including Young's modulus, strength and strain to failure) vary according to changes in the S2 microfibril angle (refer Figure 2-29 and Figure 2-30). S2 microfibril angle varies both radially and longitudinally in the tree trunk in response to the structural requirements of the tree over its growth history (refer Figure 2-31) and therefore the material properties in the trunk are usually to some degree both radially and longitudinally heterogeneous. In addition, most trees are not vertically aligned, rendering gravity bending effects significant.

Table 2-9 Summary statistics for uniform strain hypothesis [97]

Species	**δ fitted coefficient Hypothesis: δ = 0.333**		**P-value**
	Mean	**Standard deviation**	
Balsum fir (*Abies balsamea*)	0.334	0.017	0.95
Rocky Mountain fir (*Abies lasiocarpa*)	0.288	0.008	<0.001
Red spruce (*Picea rubens*)	0.309	0.022	0.330
Lodgepole pine (*Pinus contorta*)[a]	0.283	0.016	0.008
Loblolly pine (*Pinus taeda*) (summer)	0.285	0.051	0.390
Loblolly pine (*Pinus taeda*) (winter)	0.349	0.025	0.540
Douglas fir (*Pseudotsuga menziesii*)	0.254	0.017	<0.001
Slash pine (*Pinus elliottii*)	0.317	0.017	0.349
Longleaf pine (*Pinus palustris*)	0.366	0.016	0.052
Ponderosa pine (*Pinus ponderosa)*	0.303	0.008	<0.001

[a] Data from [98]

The results from Table 2-9 align with other observational evidence to support the hypothesis that natural structures do not quite fit the axiom of uniform stress, but more closely assume the related axiom of uniform strain in which the structure and material properties are tailored to the prevailing loading conditions in order to achieve a uniform strain field [19, 45, 97]. Wilson and Archer [45] hypothesised that maintaining uniform bending strain may be a more general principle governing the variation of the trunk diameter than maintenance of uniform bending stress. If the Young's modulus of wood is fairly uniform the observations of trunk taper will also conform to the axiom of uniform stress hypothesis, but if there is significant variation then it will deviate.

Further observational evidence indicates the axiom of uniform strain extends to the tree branch-trunk connection. Müller et al. [19] used electronic speckle pattern interferometry (ESPI) to directly measure the strains of a vertically bisected branch-trunk junction from the softwood Norway spruce (*Picea abies*) with the branch mechanically loaded in bending (refer Figure 2-47a). These strain patterns were compared to the strain patterns measured from a shape-identical polyester cast made from the isotropic material polyester in order to ascertain the influence of material heterogeneity on the strain field. In addition the strain patterns of a simplified polyester model made from two cylinders were measured to ascertain the effect of shape optimisation.

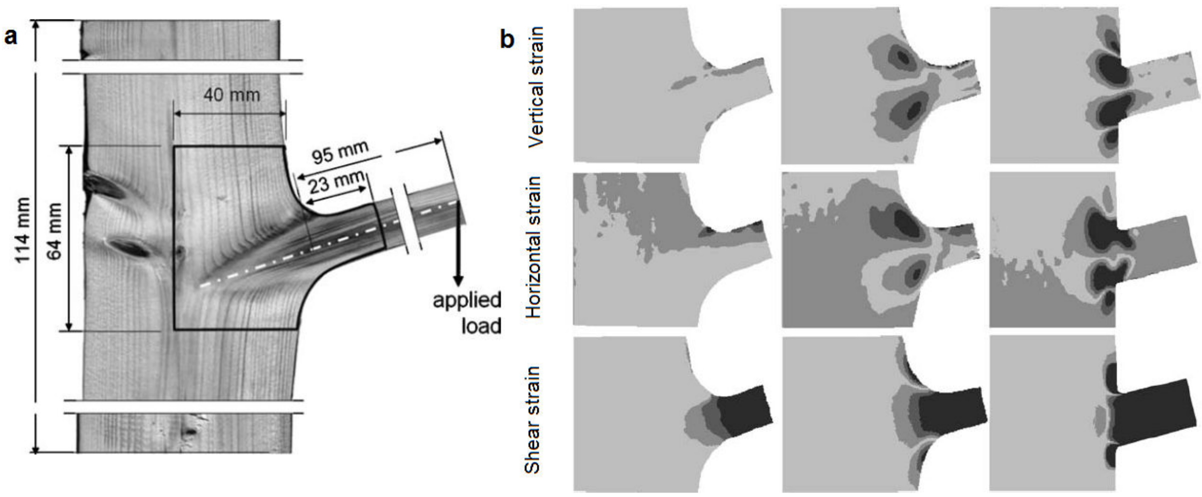

Figure 2-47 (a) Branch-trunk junction as observed in the electronic speckle pattern interferometry experiment; (b) simplified maps of in-plane vertical, horizontal and shear strain intensity. From left to right: tree joint, shape-identical polyester cast joint, simplified polyester joint made using two cylinder [19]

The results of the ESPI strain measurements are shown as in-plane strain maps in Figure 2-47b. These maps reveal the absence of vertical, horizontal and shear strain concentrations in the tree joint, i.e. uniform strain. Only 3.2% of the wood was at the highest interval of strain intensity (strain > 1.11 x 10^{-3}) compared to 22.2% of the polyester in the shape identical cast. Comparing the wood joint to the shape-identical polyester cast quantifies the effect of 3D fibre placement and material optimisation, which is achieved by tailoring the microfibril angle and density gradients of the wood.

A maximum strain value of 5.58 x 10^{-3} was observed in the upper and lower notches of the simplified polyester interconnected cylinder model, compared to 1.34 x 10^{-3} for the shape-identical polyester cast and just 1.11 x 10^{-3} for the wood joint [19]. The higher strain concentrations at the sharp intersection of the interconnected cylinders of the simplified polyester model compared to the shape-identical polyester cast quantifies the effect of shape optimisation. The polyester cast that is shape-identical to the tree has a smoother notch between the 'branch' and 'trunk', alleviating the geometric strain concentration and relocating the region of maximum strain to beneath the external surface of the joint.

Müller et. al. [19] established that the homogenization of strains within branch joints is owed in significant part to "*the optimisation of tissue (or material) in the branch–stem junction area"* [19]. The authors concluded that despite the reduction in the strain concentration from the self-optimised shape of the branch-trunk connection in trees, under loading the structure will still experience at least some strain concentration due to the geometry. As a result of both the anisotropic properties of the fibre composite wood grain and the heterogeneous tailoring of material properties across the joint the strain maps cannot be directly converted into stresses, i.e. it cannot be assumed that there is a uniform stress field [19]. However, in the area around the branch-trunk joint, the wood takes on different mechanical properties to ensure that even though areas may be "*loaded to [a] different absolute strain [as a result of the geometric stress concentration],"* they will experience loading at a "*homogeneous fraction of their respective strength (critical stress*)" [19], with "*the mechanical properties of the newly formed wood tissue…adapted to [meet] the local mechanical demands*." [46]

The mechanism by which trees achieve uniform strain across the branch-trunk joint will be further investigated in section 2.5.3.

2.5.3 Adaptive growth in and around branches

Adaptive growth is a well-known phenomenon in trees used for modifying their structural properties under changing load conditions. Trees mainly undergo bending and shear stresses as a result of the self-weight and wind loads that create a bending moment profile along the branches and the trunk. Trees grow a distinct type of wood called reaction wood to generate internal strains that counteract high bending strains in the branch or trunk [45, 46, 77, 83, 84]. Reaction wood grows to maintain the orientation of the trunk relative to the light source (e.g. a tree growing on a hillside will grow vertically) and to regulate branch patterns.

Interestingly, softwoods and hardwoods apply opposite but equally valid strategies. Softwoods generate compression reaction wood in the compression zone of the bending stress field, which is tailored to tolerate high compressive stress. Compression wood is characterised by shorter tracheids with a circular cross-section and decreased porosity due to a thicker cell wall compared to normal wood (refer Figure 2-48a – b). In the cell wall structure the S3 layer is absent, the S2 layer has a higher microfibril angle (refer Figure 2-48c - d) and the cell has is higher lignin content. In contrast, hardwoods generate tension wood in the tension zone of the bending stress field, which is tailored to tolerate high tensile stress. The wood that grows opposite to reaction (either compression or tension) wood is known as opposite wood. In softwoods opposite wood that occurs on the tension side of a bending stress field is characterised by tracheids with a lower S2 microfibril angle (refer Figure 2-49d) and an S3 layer that is 2 or 3 times thicker than normal tracheids [19, 47, 77, 84, 96, 100, 101].

The branch tissue of softwoods is characterised by an eccentric neutral axis (refer Figure 2-49a) with a high proportion of compression wood having increased S2 microfibril angle (refer Figure 2-49c), higher density, small or partly missing growth rings, and decreased tracheid length [19, 47, 77, 84, 96, 100, 101]. Directly at the branch-trunk junction wood exhibits a different cell wall composition with higher lignin content. A higher microfibril angle is beneficial in compression wood because under axial compression local plastic deformation in the matrix allows the microfibrils to compress a certain amount without significantly damaging the cell. Lower microfibril angles provide higher stiffness, but beyond a certain compressive load the cellulose microfibrils kink and the cell will undergo catastrophic failure and collapse [83]. In compression wood the S2 microfibril angle decreases along the length of the branch as shown in Figure 2-49 because the compressive stress caused by the self-weight bending moment of the branch decreases from root to tip. Thus trees tailor the material properties along the branch to generate an optimal distribution of structural, mechanical properties and internal strains to maintain optimal growth according to the loading conditions of an increasing bending moment towards the trunk [47, 83].

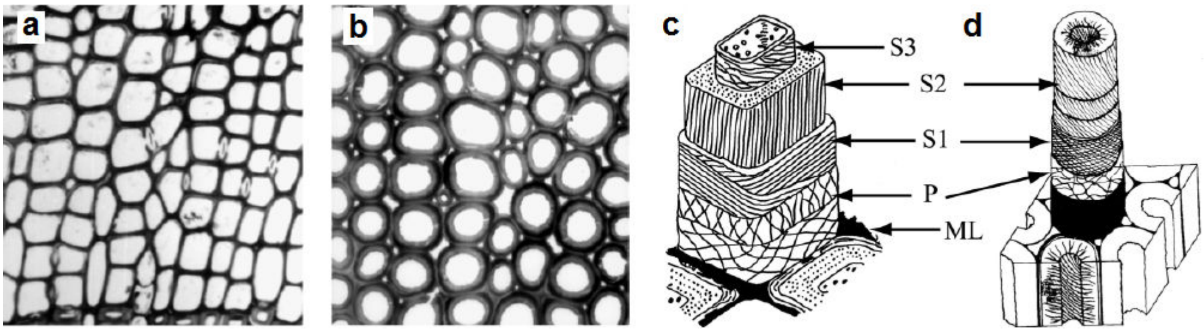

Figure 2-48 Douglas fir seedling stems displaying: (a) normal wood with square tracheid cross-section and thinner cell wall; (b) compression wood with circular tracheid cross-section and thicker cell wall; (c) normal wood tracheid; and (d) compression wood tracheid showing absence of S3 layer [102]

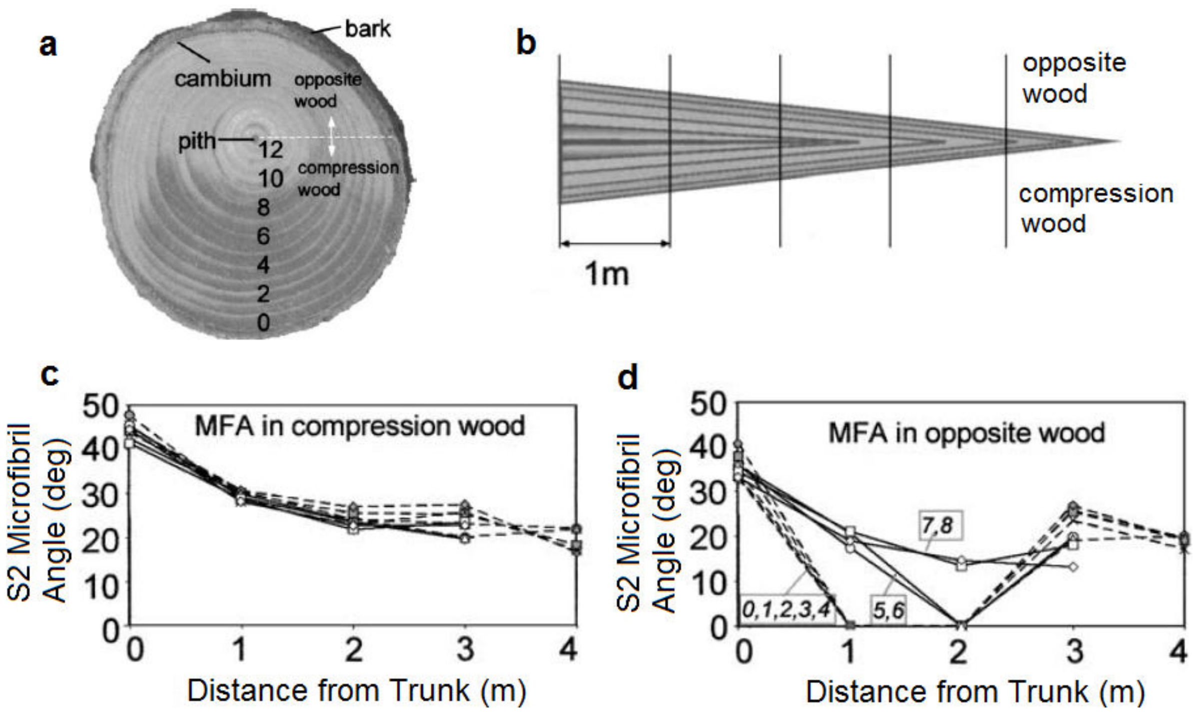

Figure 2-49 (a) Cross-section of the branch at a position close to the trunk; (b) the branch consists of a set of cones as shown schematically; (c) in compression wood the microfibril angle decreases continuously from ~ 45° near the trunk to ~ 20° near the branch tip; and (d) variation of microfibril angles on the tension side [83]

Burgert and Jungnikl [47] examined the S2 microfibril angle (refer Figure 2-50a) and density (refer Figure 2-50b) at three different locations in a spruce and yew branch and examined the resulting influence on the mechanical properties of Young's modulus (refer Figure 2-50c) and tensile strength (refer Figure 2-50d). The top, lateral and underside locations represented compression, normal and opposite branch wood, respectively. It was found that there is a large spatial variation in the mechanical properties of wood in the branch due to the influence of adaptive growth. In both species there was a roughly linear variation of S2 microfibril angle with the smallest microfibril angle occurring in the opposite wood from the top side and the highest in the compression wood taken from the underside. The compression wood and the opposite wood had roughly the same density while the lateral side had lowest density. This is probably because branch wood located at the lateral side does not undergo high bending stresses because it is located near the neutral axis of bending. The Young's modulus decreased linearly from about 3 GPa in the top branch wood to about 1 GPa in the underside compression wood due to the decreasing S2 microfibril angle. The tensile strength followed a similar trend. The stress-strain curves all had a short linear-elastic region followed by a large region of inelastic deformation due to deformation and damage to the matrix allowing the microfibrils to slip past one another and straighten (refer section 2.4.7) [51, 78, 95].

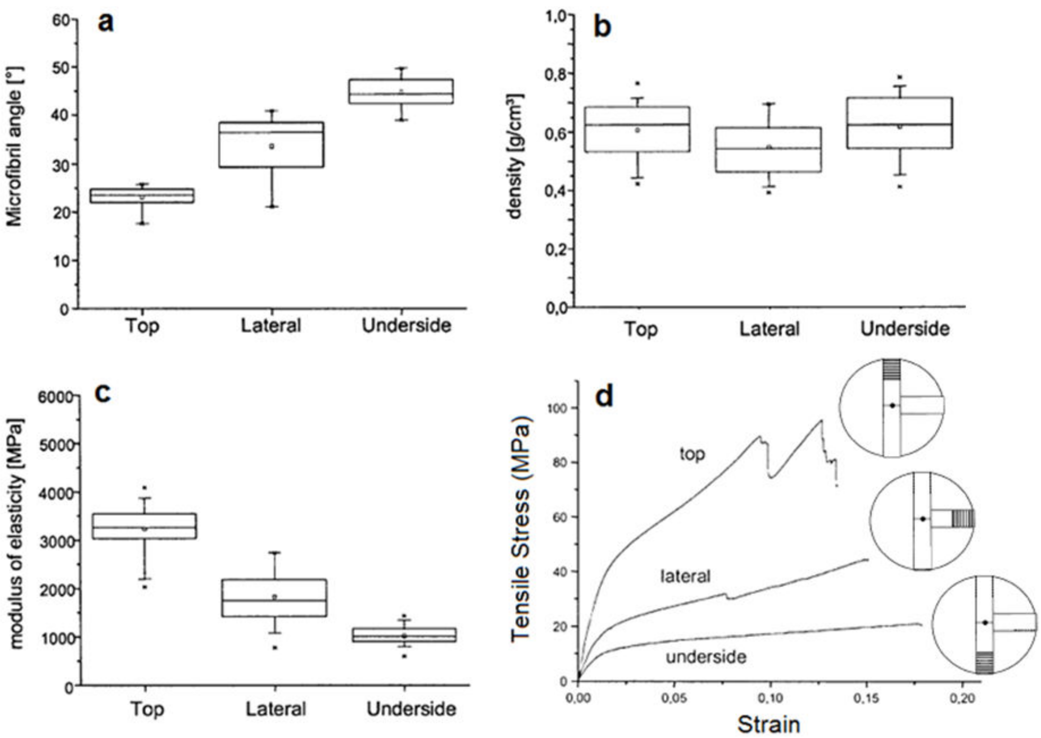

Figure 2-50 Thin tissue foil samples of spruce wood taken from top side, lateral side and underside (compression wood) of the branch: (a) microfibril angle in the S2 layer; (b) tissue density; (c) Young's modulus; and (d) representative tensile stress-strain curves [47]

Contrasting with the finding of a radial variation in the S2 microfibril angle across the tree trunk (refer Figure 2-31), no radial variation of the S2 microfibril angle and hence no variation of the mechanical properties within a single branch section was observed [47]. Similarly Faeber et al. [83] showed that the S2 microfibril angle varies with respect to the branch length but found no definite trend of microfibril variation across the growth rings in the radial direction.

Jungnikl et al. [46] used small angle x-ray scattering (SAXS) to measure the S2 microfibril angle and computed tomography (CT) to investigate the density variation around the branch-trunk joint. Figure 2-51b shows a branch junction from a sheltered part of the plantation that was not subject to prevailing winds and therefore the only significant load was the self-weight of the branch. In the sheltered tree joint the S2 microfibril angle is regular and shows that far from the branch (blue region) the microfibril angle is small and aligned almost in line with the trunk in order to provide high stiffness to prevent buckling collapse. Above and below the branch joint (yellow region) the S2 microfibril angle increases in order to increase the work-of-fracture of the wood in this structurally vulnerable region (refer Figure 2-40a).

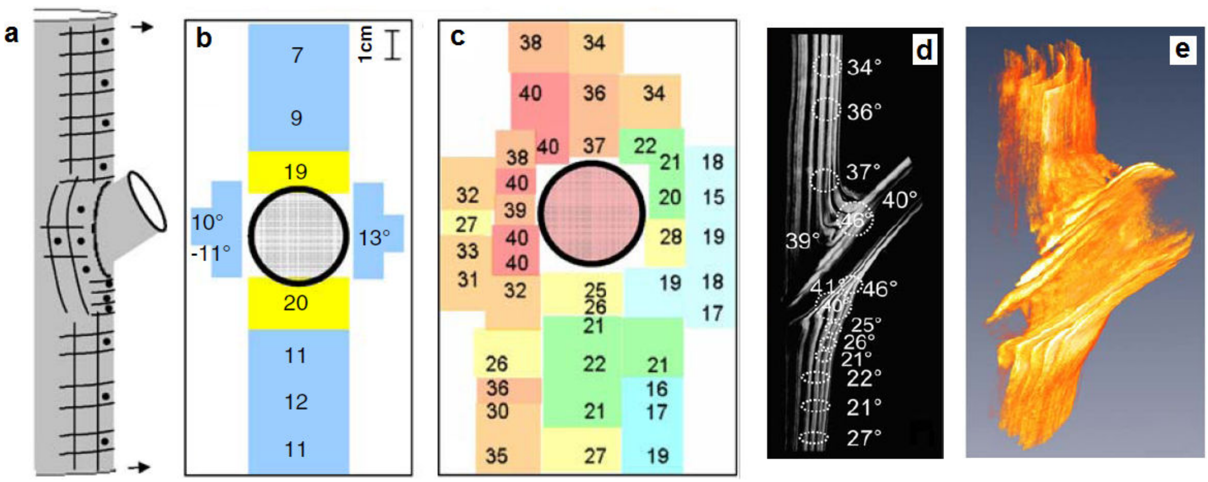

Figure 2-51 Microfibril angle and density variation: (a) S2 microfibril distribution around the branch junction; (b) joint sheltered from wind loads. (c) joint subject to prevailing wind with compression wood in the trunk; (d) CT of joint (c) showing microfibril angles and relative density. Brightness corresponds to higher density; and (e) CT showing detail of density variation at the branch-trunk joint [46]

Figure 2-51c shows the microfibril angle distribution in a branch junction that has been subjected to a wind load prevailing from the right hand side. All microfibril angles are higher compared to the sheltered branch. There is a complex pattern with higher microfibril angles signifying the formation of compression wood on the left hand side of the branch in the region under compression due to wind loads.

Figure 2-51d and Figure 2-51e are computed tomography (CT) scans which qualitatively show the density variation of the earlywood (dark regions) and latewood (bright regions) in the branch-trunk connection. The density variation between earlywood and latewood is not gradual but abrupt. Trunk wood located a few centimetres away from the branch-trunk junction shows decreased density compared to the wood in the joint. The wood located in the notches of the branch joint shows the highest density corresponding to the locations of maximum tensile and compressive stress under the bending moment induced by the self-weight of the branch. The wood in the branch core shows lower density corresponding to the low bending stresses around the neutral axis of the branch.

2.5.4 Mechanical testing and tree failure modes

Published research into the mechanical properties, damage behaviour and final failure modes of tree branch-trunk joints has been presented to assess the impact of the hierarchical optimised structure on the structural properties. For example, Beismann et al. [43] investigated the twig-stem connections from eight Willow species within the genus Salix. The samples were small with the main stem (length ~ 5 cm) clamped over its entire length and the twigs (length 2 – 6 mm) placed in a ring-shaped clamp at a distance about 1 cm from the twig-stem connection and pulled in the direction of the gravity bending load using an Instron machine (refer Figure 2-52a). Equation 2-3 and Equation 2-4 were used to calculate bending stress and Equation 2-5 was used to calculate strain on the tension surface of the bent twig at fracture [43]. Strain at fracture was calculated using the formula for cantilever bending corrected for the angle (α) of the lateral twig before breaking (for the derivation see [103]). The test set-up, geometry and parameters used for stress and strain calculations in the bending experiments are shown in Figure 2-52.

$$\sigma_b = M \times \frac{y}{I}$$ Equation 2-3

Where σ_b = bending stress, M = bending moment, y = distance from the neutral plane to tension surface of the lateral twig, and I = moment of inertia of the lateral twig.

$$M = a \times F_{crit}$$ Equation 2-4

Where a = the effective lever arm just before breakage and F_{crit} = the critical force.

$$\varepsilon = \frac{3 \times \sin\alpha \times f \times r}{l^2}$$ Equation 2-5

Where ε = strain at fracture, α = the twig angle to the stem just before breakage, f = the deflection of the lateral twig at breakage and l = the distance from the twig base to the point where the bending force acts.

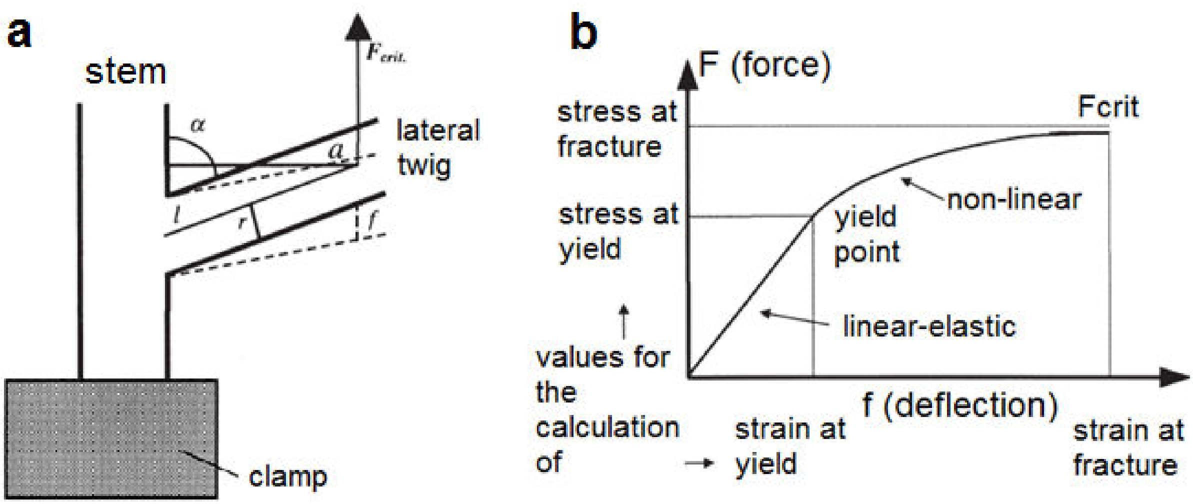

Figure 2-52 (a) Geometry and parameters used for stress and strain calculations in breaking experiments; and (b) schematic load-deflection curve [43]

The bending stress at yield of the eight Willow species varied from 8 to 19 MPa and failure stresses varied from 18 to 55 MPa [43]. The strain at yield varied from 2.3 – 3.7% and the strain at fracture varied from 6 – 11% [43]. The twig failures were classified as either ductile or brittle. The bending loads and displacements were much higher for ductile failure. A representative bending force-displacement curve showing ductile failure is shown in Figure 2-53a. Ductile failure occurred with the twig pulling out of the stem, with the fracture surface frequently running into the main stem and was characterised by a force-displacement curve showing a large inelastic region and high load carrying capacity followed peak load. The stem fracture surface corresponding to ductile failure is shown in Figure 2-53b. In brittle failure the twig snapped near the base of the twig-stem connection. A typical bending force-displacement curve showing brittle failure is presented in Figure 2-54a. It was characterised by a linear-elastic region up until failure and a low load carrying capacity followed peak load. Inspection of the fracture surface of the twigs that exhibited brittle failure showed the tension side was mainly smooth with some evidence of fibre pull-out and the compression side was "*rough and crumbled*" (refer Figure 2-54b) [43].

Some species of Willow grow in forests and others grow along river banks or in avalanche tracks. The ductile twigs had higher strength and were more damage tolerant, however breakage often injured the main part of the stem. The brittle branches were hypothesised to have the biomechanical function of a 'mechanical fuse' to protect the main part of the plant in the event of sudden heavy loads such as during an avalanche [43].

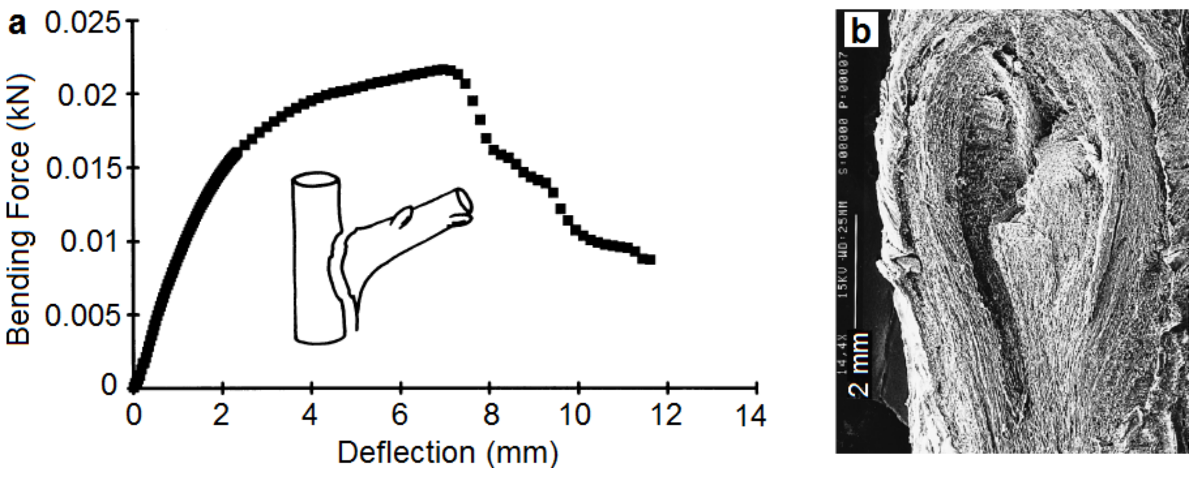

Figure 2-53 (a) Bending load-deflection curve from *Salix appendiculata* showing ductile failure; and (b) damage in the trunk of Purple willow (*Salix purpurea)* where a twig was attached [43]

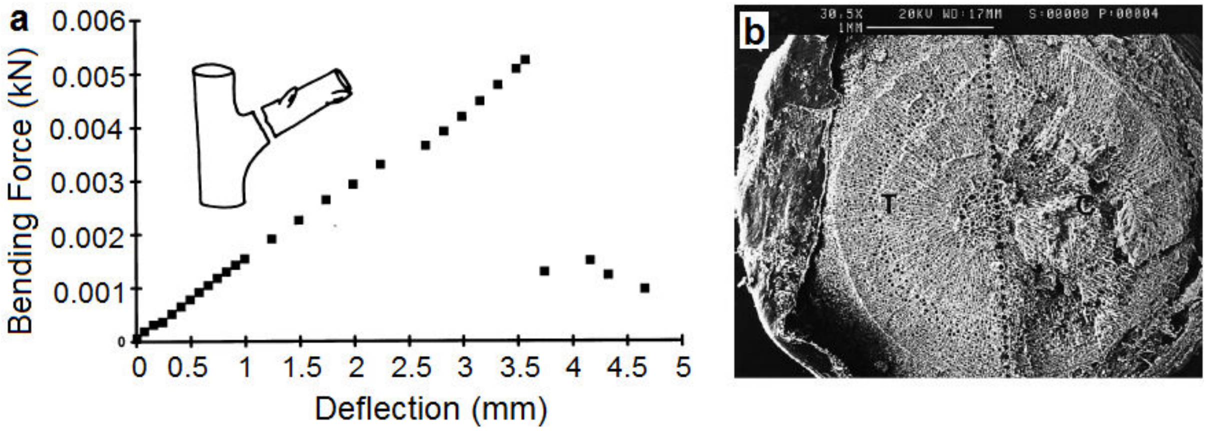

Figure 2-54 Bending load-deflection curve from *Salix fragilis* showing brittle failure; and (b) SEM of the brittle fracture surface of the trunk. Tension side (T) shows a smoother fracture surface compared to the compression side (C) [43]

As well as ascertaining strain maps by ESPI Müller et al. [19] also performed bending tests on the Norway spruce (*Picea abies*) branch-trunk joint, shape-identical polyester cast, and simplified polyester model constructed from two intersecting cylinders (refer Figure 2-55).

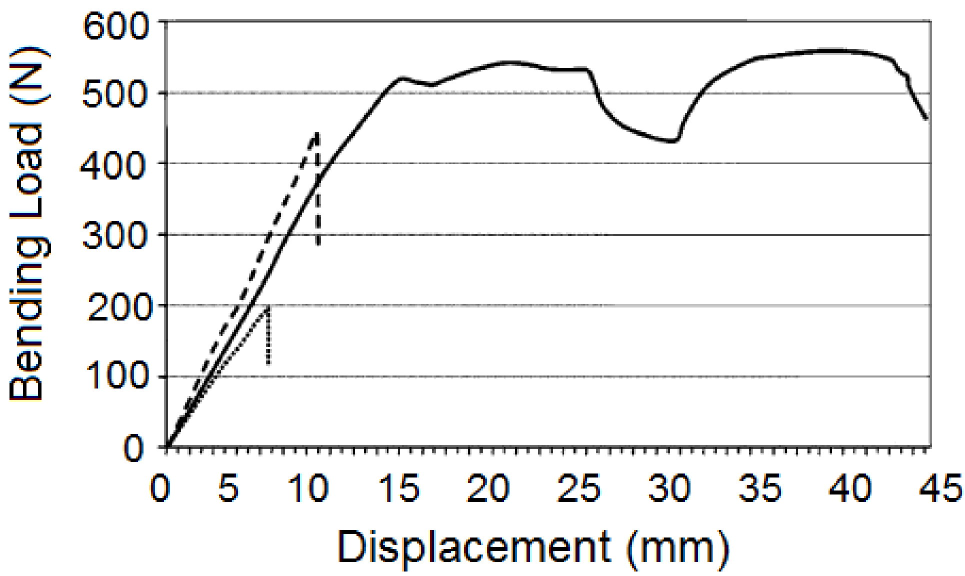

Figure 2-55 Bending load-displacement curve of the branch-trunk joint (bold line), shape-identical polyester cast (dashed line) and simplified polyester model of two interconnected cylinders (dotted line) [19]

The spruce bending load-displacement curve is very similar to the ductile load-displacement curve for the Willow twig-stem joint presented in Figure 2-53a. The failure was ductile with a large region of inelastic damage indicating higher fracture toughness in the tree compared to the polyester models. The failure of the branch-trunk joint was described as occurring due to the annual rings of the branch and trunk delaminating and the branch pulling out on the tensile side about 2 cm distant from the branch collar [19]. In contrast to the tree branch-trunk joint, both polyester models showed an abrupt brittle failure located at the base of the 'branch' in the region of highest strain (refer Figure 2-47b). The simplified model of two cylinders attained a peak load less than 50% of the peak load attained by the polyester cast that was shape-identical to the tree [19].

2.6 FIBRE-REINFORCED COMPOSITE T-JOINTS

T-joints (refer Figure 2-56) join orthogonal structure together and therefore transfer out-of-plane loads. Typical applications of T-joints include connecting structural components such as the spar or rib to the skin, transmitting bending, tensile and shear loads between the two panels [104]. T- or L-joints are also used to join stiffeners to the skin in stiffened panels such as those used in the construction of the aircraft wings and fuselage. Common stiffener designs include Z, top hat and C-shapes (refer Figure 2-57), which undergo pull-off and bending loads as a result of the skin deforming or buckling under aerodynamic loading (refer Figure 2-58).

T-joints joints made from fibre-reinforced composite materials are particularly challenging to design because in-plane loads carried by the strong and stiff fibres in the orthogonal panels must be transferred via the weak through-thickness direction. Load transfer occurs out-of-plane, creating a geometric interlaminar stress concentration that reduces structural efficiency. However T-joints cannot be avoided because orthogonal structures (which include some of the most flight-critical components) need to be connected. Therefore optimum design of fibre-reinforced T-joints is crucial to the overall cost and safety of composite airframe aircraft.

The T-joint considered in this study is made from a carbon fibre reinforced polymer (CFRP) composite with a similar design to Figure 2-56a, constructed from two back-to-back 90° brackets (refer Figure 2-56b) attached to a horizontal skin via a flange, with a delta-fillet ‘noodle’ fabricated from unidirectional prepreg reinforcing the gap between the two radii.

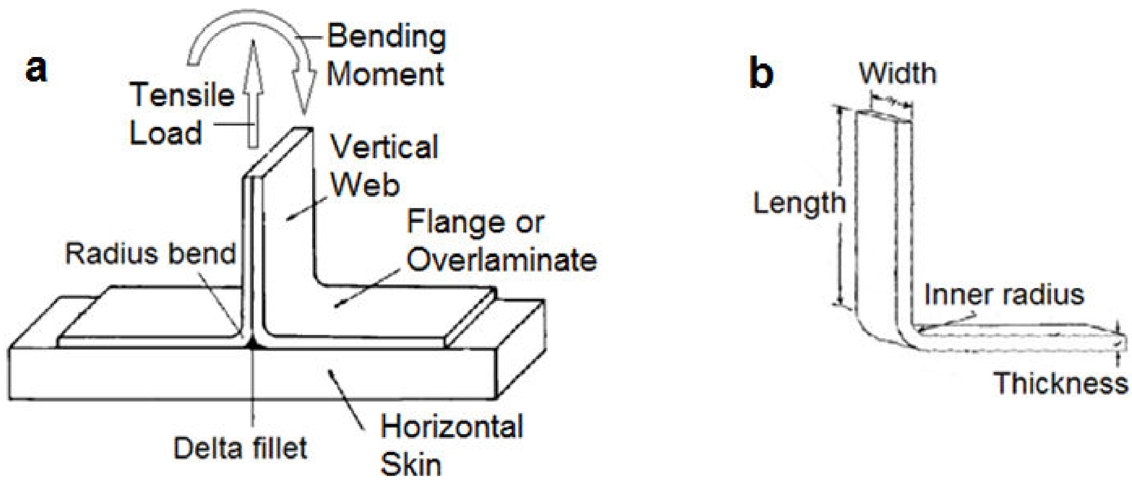

Figure 2-56 (a) Bonded fibre-reinforced T-joint showing tensile and bending loads acting on the vertical stiffener web. [105]; and (b) geometry of a 90° angle bracket [106]

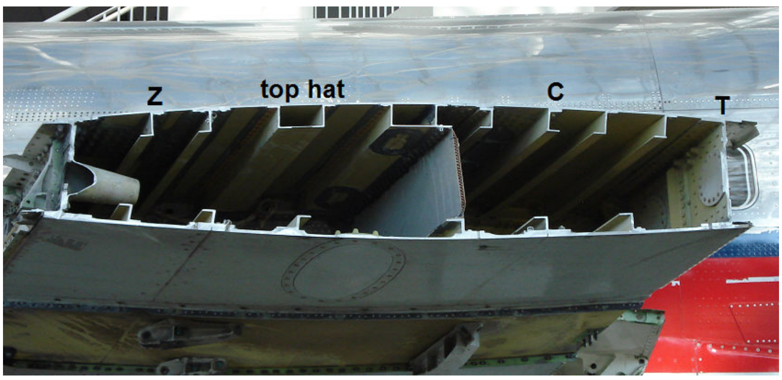

Figure 2-57 Cross section of wing-box from a Boeing 737 showing examples of Z, top hat and C-shaped stiffeners and a T-joint connecting the spar to the wing skin (photographed by author)

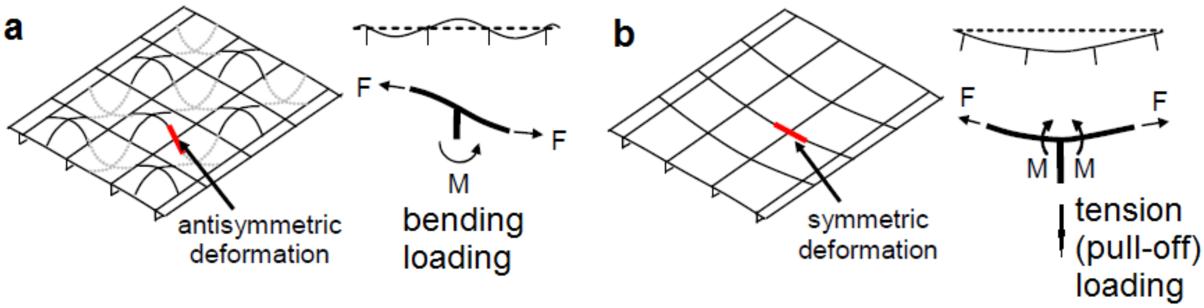

Figure 2-58 Stiffened panel: (a) anti-symmetric deformation leads to a bending moment on the T-joint; and (b) symmetric deformation leads to tension (pull-off) load on the T-joint [107]

2.6.1 Strength and failure modes under tensile, 45° pull-off and bending loading – Experimental, finite element method & parametric studies

The failure modes and fracture mechanics of T-joints cannot be predicted analytically because current methods are incapable of capturing the complexities of the geometric stress concentration in the critical radius bend/delta-fillet region [104]. Therefore analysis into T-joints is done primarily through experimental and finite element method (FEM) studies. Previous research into bonded fibre-reinforced polymer T-joints has considered mainly aerospace and marine applications. Experimental experience has shown T-joints usually fail in the radius bend/delta-fillet region due to high interlaminar tensile and shear stresses induced by the geometric stress concentration as the fibres curve around the radius bend, making this region the critical zone controlling T-joint strength [104, 108-113].

Finite element analysis is capable of computing the interlaminar stress components, allowing more detailed analysis of the critical zone [107, 113-120]. Future improvements in modelling damage growth and failure in composite components might allow virtual certification to significantly reduce the number of experimental tests required to certify new aircraft designs (refer Figure 2-59), which is currently in the order of ~ $40 million for a new design [115].

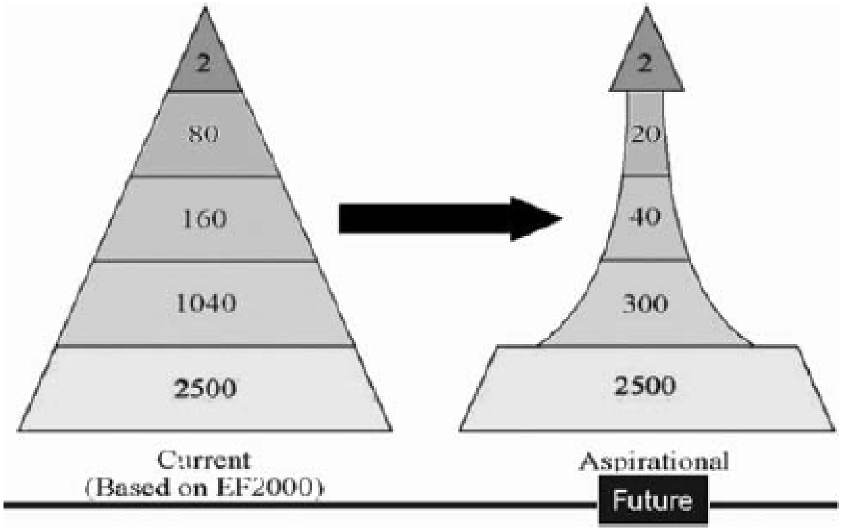

Figure 2-59 Future aspiration to reduce the number of component tests in the 'test pyramid' of a developmental aircraft [115]

Orifici et al. [107, 118-121] considered the case of thin-walled composite T-joints representative of an aerospace stiffener-skin connection. The work was commissioned by the European Commission Project COCOMAT (Improved MATerial Exploitation at Safe Design of Composite Airframe Structures by Accurate Simulation of COllapse) to exploit strength reserves in the post-buckled region through an understanding of how to predict collapse and post-buckling behaviour of stiffened panels [107]. The T-joint specimens were constructed from IM7/8552 unidirectional prepreg with the geometry and lay-up shown in Figure 2-60 (stiffener web thickness of ~ 3 mm and a specimen width of ~ 25 mm). They were subjected to tensile (pull-off), compressive (push) and bending loading on the stiffener web [107].

A 2D FE model of the critical radius bend/delta-fillet region was used to minimise computational time. Each ply was monitored and delamination was predicted using the degenerated Tsai strength-based failure criteria using Equation 2-6. Failure was considered to have occurred when the average of all four values of the integration points of the element satisfied this criteria [107].

$$\left(\frac{\sigma_{11}}{X_t}\right)^2+\left(\frac{\sigma_{33}}{Z_t}\right)+\left(\frac{\tau_{13}}{S_{13}}\right)^2\geq 1$$ Equation 2-6

Where σ_{11} = in-plane stress, σ_{33} = interlaminar tensile stress, τ_{13} = interlaminar shear stress in the longitudinal-transverse plane, X_t = in-plane tensile strength, Z_c = interlaminar tensile strength and S_{13} = interlaminar shear strength in the longitudinal-transverse plane.

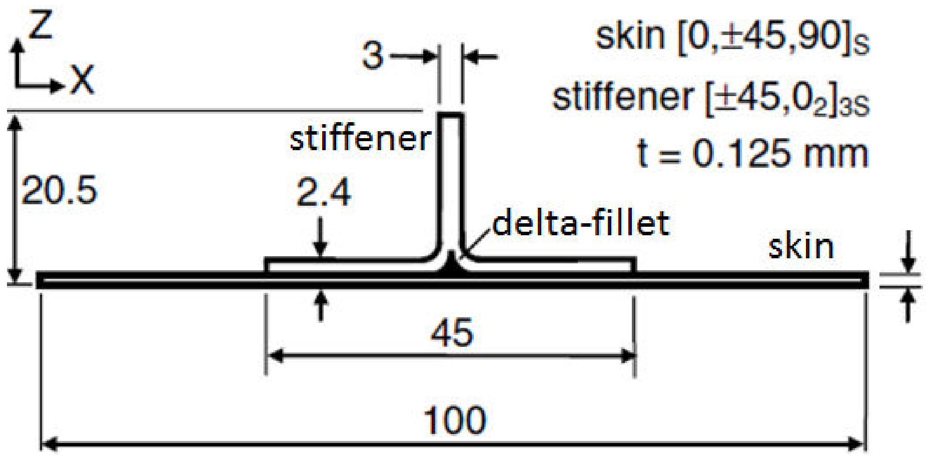

Figure 2-60 T-joint geometry and laminate ply lay-up [107]

The FE results were validated experimentally. Four failure modes were identified (refer Figure 2-61): i) delaminations in the radius bend (bend failure); ii) through-thickness and longitudinal failure of the blade (blade failure); iii) delamination from the stress concentration at the corner of the flange and the skin propagating along the stiffener flange/skin interface (flange failure); and iv) failure across the delta-fillet region 'noodle' (core failure).

In the experimental bending tests 5/8 failures were flange failures and the remaining 3/8 were bend failures. The normalised failure moment ranged from about 1700 – 2300 Nm/m (refer Figure 2-62a). In the tension test flange failure occurred 7/10 times and the remaining 3/10 were bend failure. The normalised energy at failure ranged from about 45 – 80 J/m (refer Figure 2-62b). Blade failure and delta-fillet failure occurred under compression on the stiffener web [107]. The flange failure could be corrected by a less abrupt run-out of the flange, leading to bend failure being the dominant failure mode in both tension and bending loading.

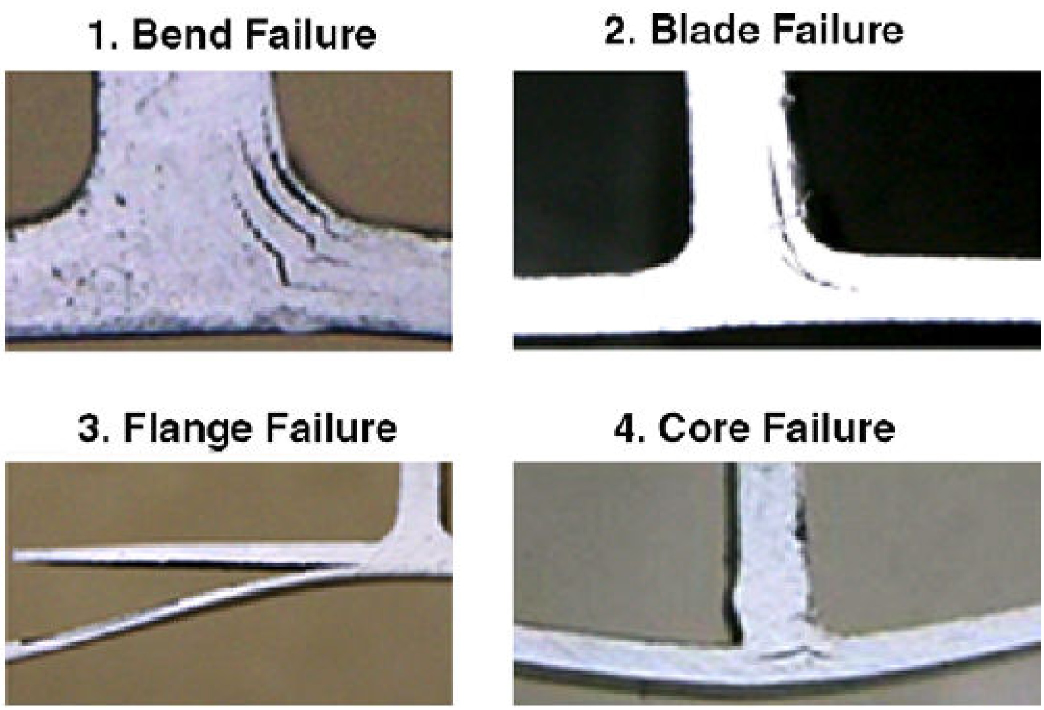

Figure 2-61 Failure mode classification of T-joint [107]

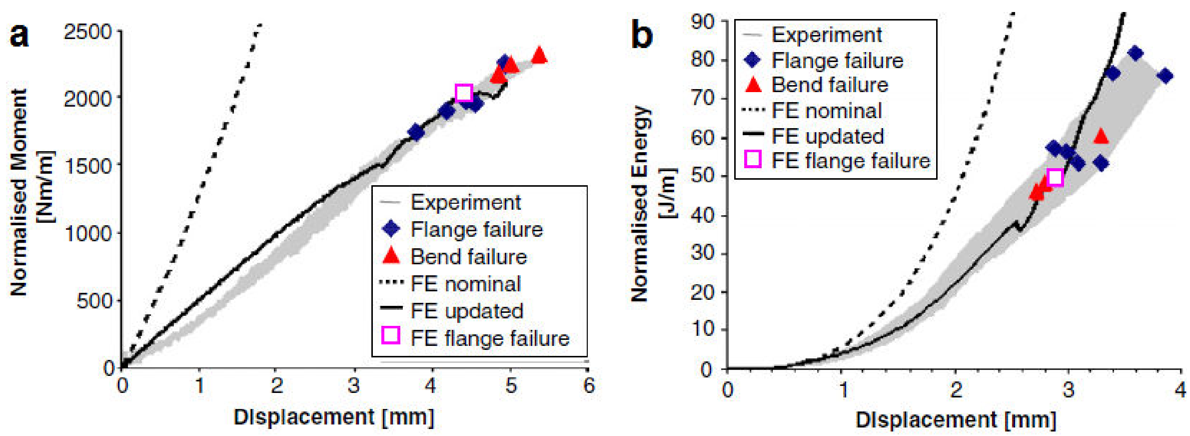

Figure 2-62 Experimental and finite element results: (a) bending moment/flange width versus displacement under bending; and (b) energy/flange width versus displacement under tension [107]

In response to an absence of research validating guidelines on T-joint design Shenoi and co-workers [104, 108-112] undertook extensive experimental and numerical research into the failure modes of a wide range of relatively large geometry E-glass/polyester T-joints designed for the marine application of joining the ship hull to the bulkhead.

Seven T-joint designs incorporating nine design variables were experimentally tested and modelled using FEM in a parametric study. The design variables included: i) presence of an overlaminate; ii) overlaminate material; iii) number of plies (thickness) of overlaminate; iv) length of overlamination on vertical panel; v) length of overlap on horizontal panel; vi) radius; vii) gap between vertical and horizontal panel viii) shape of edge of vertical panel; and ix) type of resin in delta-fillet region (refer Figure 2-63a) [104, 108]. It should be noted that overlaminate ply lay-up was not considered as a design variable. Orthogonal plates consisting of 15 layers of woven glass rovings laminated with polyester resin representing the vertical bulkhead and horizontal hull were joined using seven different configurations that incorporated the aforementioned nine design variables. The T-joints were tested under a 45° pull-off loading that induced both tensile and bending stresses into the critical radius bend/delta-fillet region (refer Figure 2-63b) [104, 108].

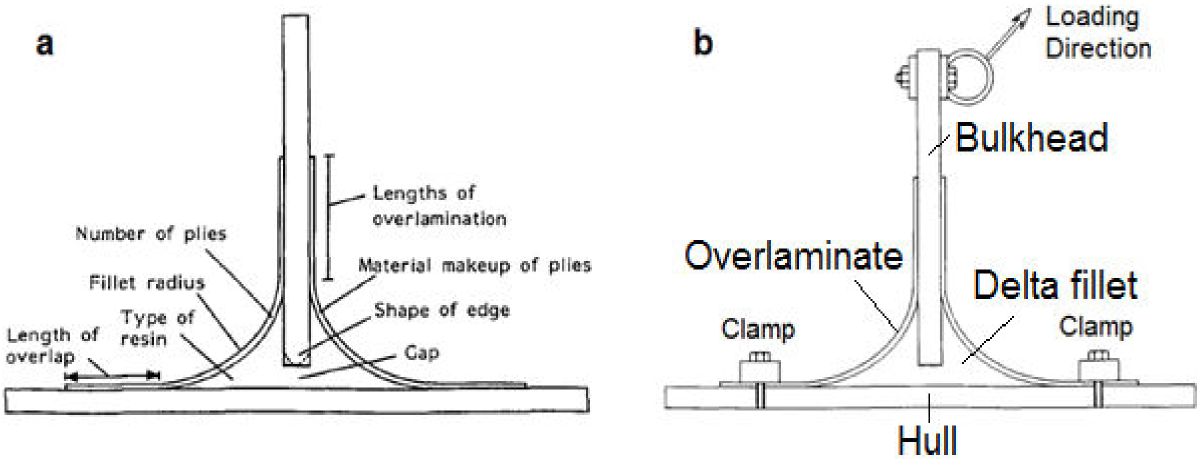

Figure 2-63 (a) Nine variables were considered in the design of the maritime E-glass/polyester T-joints [104]; and (b) the horizontal hull was restrained with clamps and the vertical bulkhead loaded with a 45° pull-off load to induce tension and bending loads on the joint [109]

All seven T-joints failed in the radius bend or delta-fillet due to the geometric stress concentration under the combined tensile/bending loading, confirming this region as the critical zone to focus on for strength and toughness improvement. The results showed that the critical strains causing failure were significantly affected by the joint geometry [104, 108]. Examples of three different T-joint designs and their respective failure modes are shown in

Figure 2-64. Configuration A had a thick overlaminate, configuration C had no overlaminate and configuration F had a thin overlaminate.

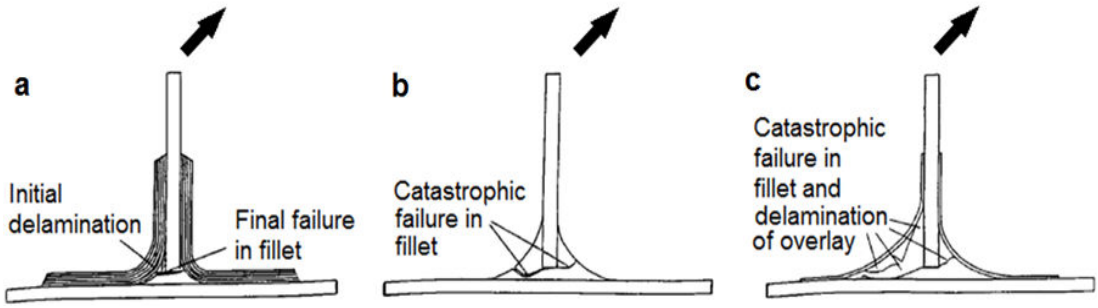

Figure 2-64 Failure modes of bonded E-glass/polyester T-joints tested in pull-off at 45° to the baseplate: (a) baseline configuration A with thick overlaminate; (b) configuration C with no overlaminate; and (c) configuration F with thin overlaminate withstood the highest loads [104]

In configuration A the thick overlaminate took up most of the load and initial damage occurred due to delamination in the radius bend of the overlaminate caused by the high interlaminar tensile and shear stresses in this zone induced by the change in fibre direction caused by the geometry. After a load drop corresponding to the initial delamination, the T-joint was still able to transfer significant load via the remaining overlaminate plies. As the overlaminate plies delaminated more load was transferred to the delta-fillet until final failure occurred in this region (refer Figure 2-64a) [104, 108]. Configuration C did not have an overlaminate, consequently all load was transferred via the urethane-acrylate resin of the delta-fillet and the joint failed catastrophically in this region when the maximum stress exceeded the strength of the resin (refer Figure 2-64b) [104, 108]. Configuration F had a thinner overlaminate so the load was shared more equally between the overlaminate and the delta-fillet region. This joint failed with complete delamination of the overlaminate on the tensile side radius bend and cracking of the delta-fillet (refer Figure 2-64c) [104, 108].

A summary of these results are given in Table 2-10. Configuration F had the highest failure load, followed by configuration A and configuration C had the lowest. The failure load of configuration F (20,345 N) was more than three times the failure load of configuration C (6499 N), highlighting the importance of good joint design to the overall structural integrity of the component. The failure stress values given by FEA indicate how the load was shared between the overlaminate and the delta-fillet region. The results indicate that in configuration F the load was not optimally distributed because the overlaminate had a fairly low interlaminar stress (3.91 MPa) compared to the high stress in the delta-fillet (29.96 MPa), suggesting they did not fail simultaneously, but the failure of the delta-fillet region triggered the unstable failure (delamination) in the overlaminate [104].

Table 2-10 Experimental failure loads and failure modes and FE failure stress values for joints A, C and F

Configuration	Experimental failure load (N)	Failure mode under pull-off loading at 45° to horizontal	FE failure stress values (MPa)
A [104]	9471	Delamination in tensile side radius bend of overlaminate	8.49[1]
C [104]	6499	Catastrophic failure in delta-fillet	17.33[2]
F [104]	20345	Complete delamination in tensile side of overlaminate and catastrophic failure in delta-fillet	3.91[1] , 29.96[2]

[1] Max interlaminar tensile stress in radius bend of overlaminate, [2] Max principal stress in delta-fillet

These results indicate that there is an optimum T-joint design in which the overlaminate reaches the limit of through-thickness strength at the same load as the delta-fillet region reaches its maximum principal stress and they truly fail simultaneously. In this case the through-thickness strength of the glass composite was low (~10 MPa) compared to the strength of the urethane-acrylate delta-fillet (~ 26 MPa), meaning a thin overlaminate that did not generate high through-thickness stress produced a better design [104]. T-joints can be further optimised by choosing a design in which the equivalent peak stresses in the overlaminate and delta-fillet are as small as possible for a nominal T-joint load and deflection [104, 108]. In this context the research showed the most efficient T-joint design has a large radius bend with a flexible delta-fillet resin [104, 108].

Thick T-joints in which the assumption of plane stress was not appropriate were investigated by Zimmermann et al. [113] who considered an ultra-thick CFRP T-joint for the application of a side stay fitting for the main landing gear door with a web thickness of ~ 60 mm (refer Figure 2-65).

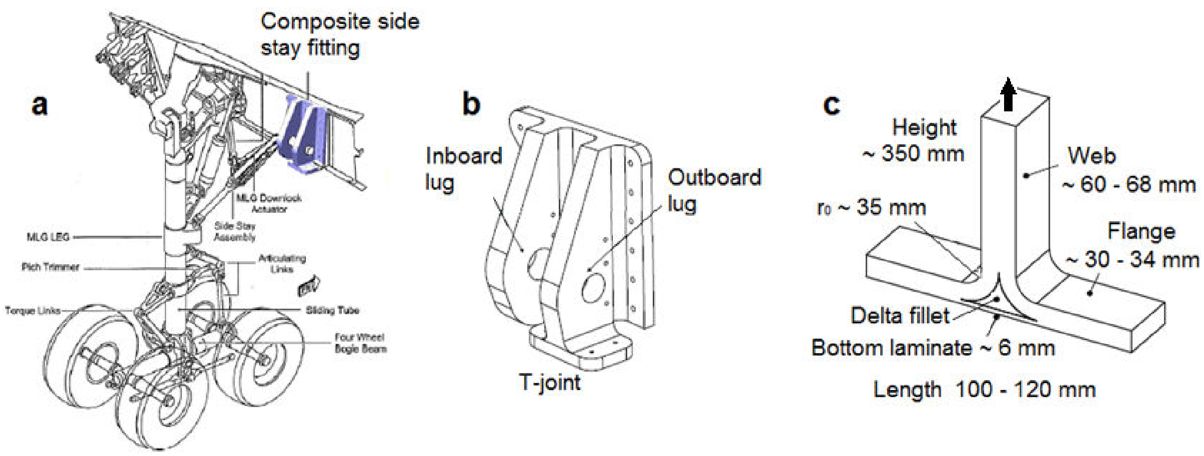

Figure 2-65 (a) Main landing gear with side stay fitting; (b) composite side stay fitting; and (c) geometry and dimensions of T-joint representing part of side stay fitting [113]

The ultra-thick T-joint was fabricated from biaxial non-crimp fabric (Tenax HTS 12K) with a quasi-isotropic lay-up of $[(0/90)/(\pm45)]_n$ [113]. It was subjected to both tensile (pull-off) and bending loading [113]. Due to the thickness of the T-joint and the development of high out-of-plane stresses a 3D finite element model using solid elements was necessary. However it was shown by Kuhlmann and Rolfes [122] that due to the linear shape function of 3D bricks, the transverse shear stress does not disappear at the free surfaces and is therefore discontinuous at ply interfaces. Therefore 3D elements are incapable of accurately calculating shear stresses on the ply level. This was overcome by discretising the geometry and modelling multiple elements through-the-thickness for each ply which satisfactorily modelled the transverse shear stresses [113].

Failure under tensile loading on the web occurred in the delta-fillet corner where the two radii meet due to high interlaminar tensile and shear stresses (refer Figure 2-66a). Under a 150 kN applied tensile load maximum interlaminar tensile stress occurred at the tip of the converging radii (same position as failure initiation) and decreased in the tangential direction. The horizontal laminate under the flange had a big influence on the interlaminar tensile stress in the delta-fillet at the tip of the converging radii and therefore influenced the failure load under tension load. Removing the bottom laminate enabled the radii to move in the lateral direction which decreased the maximum interlaminar tensile stress by about 20% (refer Figure 2-66b) [113].

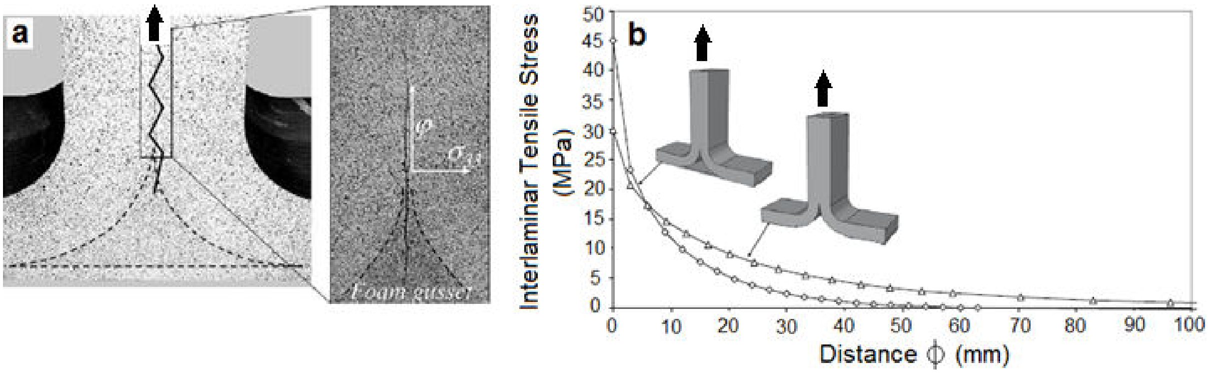

Figure 2-66 (a) Experimental results. Under tensile loading the crack develops in the delta-fillet at the tip of the converging radii dominated by interlaminar tensile stress and propagates up the web; and (b) FE results [113]

However research by Dharmawan et al. [123] on a glass/vinylester marine T-joint under tensile loading (refer Figure 2-67a) showed that increasing the thickness of the horizontal hull significantly decreased the peak interlaminate strain in the overlaminate radius (refer Figure 2-67b). These FE results also showed that increasing the thickness of the horizontal hull substantially reduces the in-plane strain (refer Figure 2-68a) and the addition of a structural delta-fillet decreased all strains in the overlaminate (refer Figure 2-68b-c) [123].

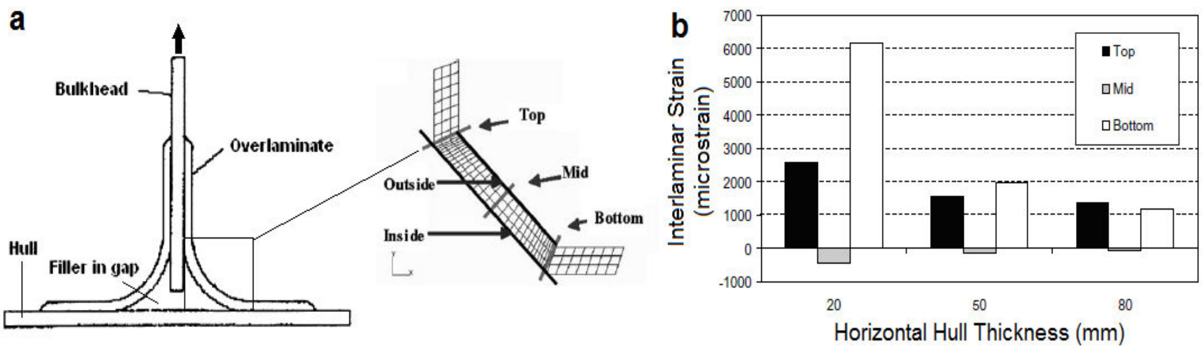

Figure 2-67 (a) Marine glass/vinylester T-joint under tensile loading with overlaminate cross-section considered for strain comparison; and (b) FEA results show peak interlaminar strain in the overlaminate decreases for increasing horizontal hull thickness [123]

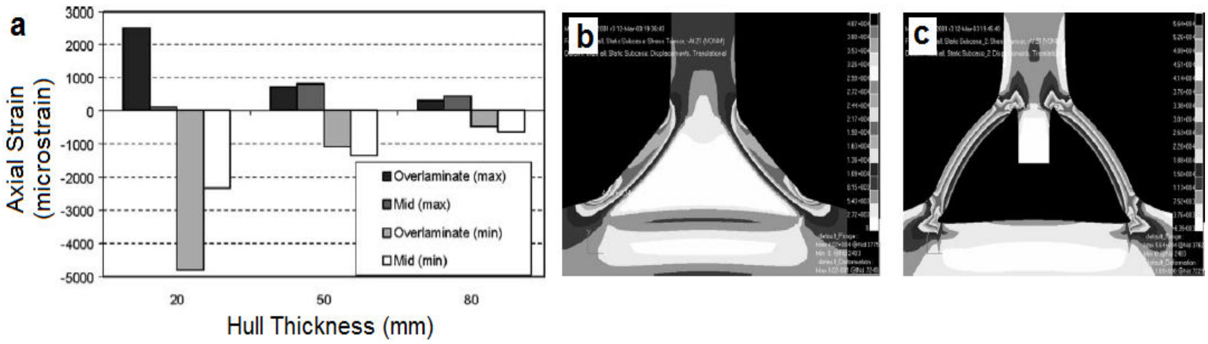

Figure 2-68: (a) FE results showing axial strain in the overlaminate decreases with increasing hull thickness; (b) overlaminate strain with structural delta-fillet is decreased compared to; (c) overlaminate strain in overlaminate without a delta-fillet [123]

Under bending loading (refer Figure 2-69a) the FE results for the ultra-thick T-joint indicated the maximum interlaminar tensile stress of 26 MPa occurs one-third of the way across the laminate thickness (refer Figure 2-69b), which coincided with the position of first failure during the experimental tests (refer Figure 2-70) [113]. In addition to interlaminar tensile stresses, significant interlaminar shear stresses were present which can also induce delamination failure. Figure 2-71 shows the interlaminar stresses along the tangential direction at the delamination interface. Interlaminar shear is at a maximum at the location of minimum interlaminar tensile stress and the failure mode from the experimental test indicate failure is dominated by the interlaminar tensile stresses [113].

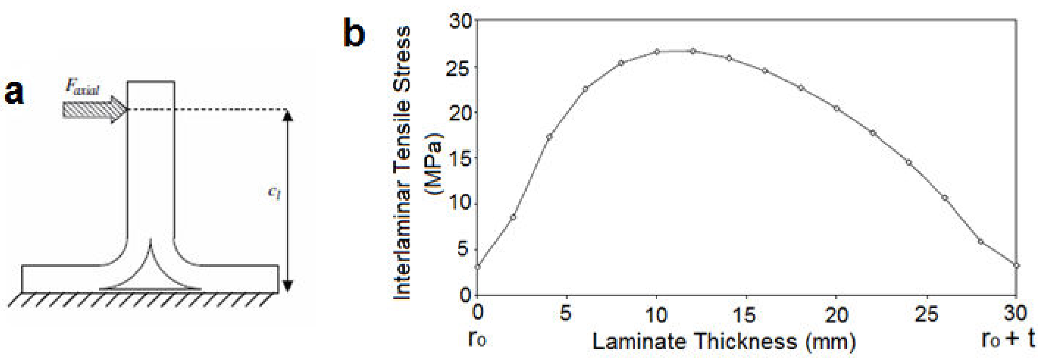

Figure 2-69 (a) Bending loading on the ultra-thick T-joint; and (b) interlaminar tensile stress distribution through the radius bend thickness [113]

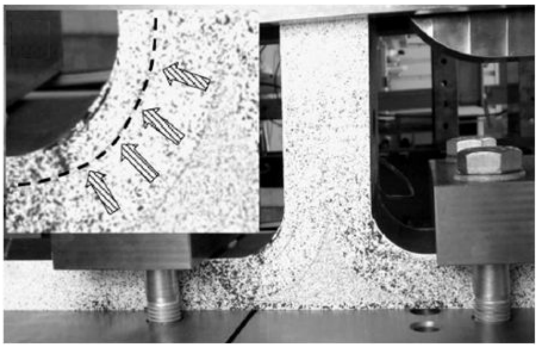

Figure 2-70 Under bending load the first crack initiates one-third of the way through-the-thickness of the radius bend in line with the position of maximum interlaminar tensile stress [113]

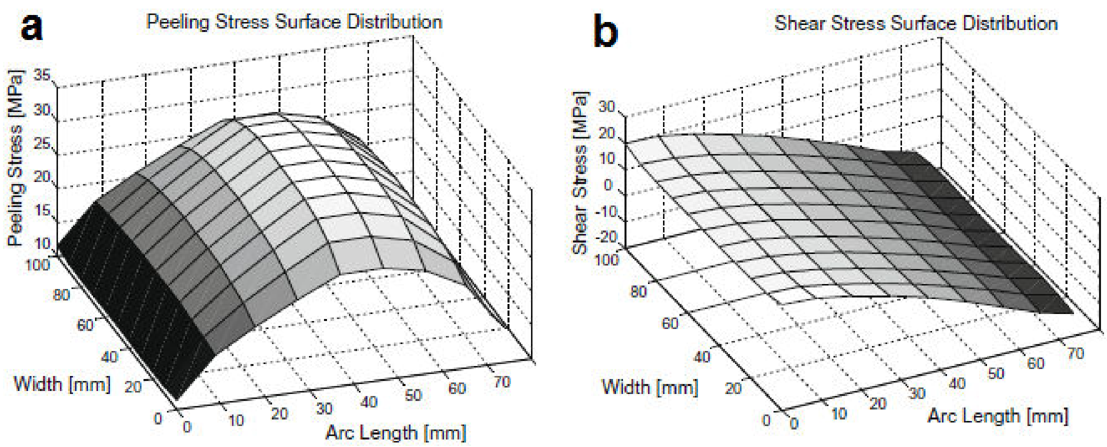

Figure 2-71 Laminate stresses on tension side radius bend on delamination interface: (a) interlaminar tensile stress; and (b) interlaminar shear stress [113]

The simplified Tsai–Hill failure criterion [124] assuming negligible in-plane stress was applied to the radius bend with correction factors as shown in Equation 2-7:

$$\left(\frac{\sigma_{33}k_{33}}{Z_t{}^3}\right)^2+\left(\frac{\tau_{13}k_{13}}{S_{13}{}^2}\right)^2\geq 1$$ Equation 2-7

Where σ_{33} = interlaminar tensile stress, k_{33} = correction factor for interlaminar tensile stress = 2.1, Z_t = interlaminar tensile strength, τ_{13} = interlaminar shear stress in the longitudinal-interlaminar plane, k_{13} = correction factor for interlaminar shear stress = 1.9 and S_{13} = interlaminar shear strength in the longitudinal-interlaminar plane.

It was found there was a strength reduction in the through-thickness direction in the ultra-thick laminates compared to thin coupon data. This was attributed to the volumetric effect of ultra-thick laminates having a higher probability of containing more and larger defects and a reduction in the quality of thicker laminates with higher void content and fibre misalignment. To account for this an empirical correction factor for interlaminar tensile and shear stresses was applied to size the final component. In order to overcome this premature failure, out-of-plane reinforcements such as stitching or z-pins were considered. However this was not implemented due to the inability of z-pins and stitching to prevent initial failure in the form of the onset of delamination in the radius bend [113].

2.6.2 Strength-based delamination criteria

It has been shown that the failure initiation that generates the first significant loss of stiffness in composite T-joints occurs due to delaminations in the critical radius bend and cracking in the delta-fillet region. The delaminations are initiated due to the high interlaminar tensile and shear stresses that occur in this critical radius bend region as a result of the geometric stress concentration coupled with the low strength of CFRP laminates in the through-thickness direction [104, 106, 108-113, 125-127] .

Delamination initiation can be predicted using strength-based failure criteria [128-130]. It should be noted that this is only a prediction for the initiation of delamination damage. Information regarding the fracture mechanics or the toughness of the material and the stability of delamination growth requires a fracture model [131]. Orifici et al. [132] reviewed the methodologies for modelling composite failure including strength-based failure criteria for delamination initiation. The simplest criterion is the maximum stress failure criteria which simply states failure will occur when the stress exceeds the interlaminar strength of the laminate (refer Equation 2-8, Equation 2-9 and Equation 2-10.

Maximum Stress

$$\frac{\sigma_{33}}{Z_t} \geq 1$$ Equation 2-8

$$\frac{\tau_{13}}{S_{13}} \geq 1$$ Equation 2-9

$$\frac{\tau_{23}}{S_{23}} \geq 1$$ Equation 2-10

Where σ_{33} = interlaminar tensile stress, Z_t = interlaminar tensile strength, τ_{13} = interlaminar shear stress in the longitudinal-interlaminar plane, S_{13} = interlaminar shear strength in the longitudinal-interlaminar plane, τ_{23} = interlaminar shear stress in the transverse-interlaminar plane and S_{23} = interlaminar shear strength in the transverse-interlaminar plane.

However most strength-based delamination failure criteria recognise that failure will not be caused solely as a result of one stress, but a superposition of several stresses. Some, such as the Long criterion (refer Equation 2-11) which was developed for adhesively bonded ARALL-1 lap joints consider only two interlaminar stresses.

Long [129]

$$\left(\frac{\sigma_{33}}{Z_t}\right) + \left(\frac{\tau_{13}}{S_{13}}\right)^2 \geq 1$$ Equation 2-11

Others such as the Hashin criterion (refer Equation 2-12) consider all three interlaminar stresses.

Hashin [128]

$$\left(\frac{\sigma_{33}}{Z_t}\right)^2 + \left(\frac{\tau_{23}}{S_{23}}\right)^2 + \left(\frac{\tau_{13}}{S_{13}}\right)^2 \geq 1$$ Equation 2-12

Specific to fibre-reinforced composite L-joints, Feih and Shercliff [130] considered three different strength-based delamination criteria to predict the onset of damage under tensile and bending loading. The Tong-Norris criterion (refer Equation 2-13) - originally developed for the case of adhesively bonded double lap joints - was found to give the closest approximation to the experimental results [130]. This criterion considers delamination initiation to be dependent not only on the interlaminar tensile and shear stresses and strengths, but also weakly dependent on the in-plane stress and in-plane tensile and compressive strength of the material.

Tong-Norris [133]

$$\left(\frac{\sigma_{11} - \sigma_{11}\sigma_{33}}{X_t X_c}\right) + \left(\frac{\sigma_{33}}{Z_t}\right) + \left(\frac{\sigma_{13}}{S_{13}}\right)^2 \geq 1$$ Equation 2-13

Where σ_{11} = in-plane stress, X_t = in-plane tensile strength and X_c = in-plane compressive strength.

The strength-based delamination criteria listed in Equation 2-8 to Equation 2-13 are all limited by the requirement of prior knowledge of the interlaminar strength of the composite laminate. The through-thickness strength properties of fibre-reinforced polymer composites are generally assumed to be isotropic i.e. independent of ply angle and also fairly independent of the fibre properties because interlaminar strength is a resin dominated property. However accurate data for interlaminar strength is not easily obtained by experiment.

Interlaminar tensile strength can be determined experimentally from unidirectional 90° angle bracket specimens using either a tensile test rig (refer Figure 2-72a) or four point bend loading fixture as specified by ASTM D6415 (curved beam strength for a fibre reinforced composite) [106]. Figure 2-72b demonstrates the wide range (~ 18 – 80 MPa) and high standard deviation of experimentally determined interlaminar tensile strength values for CFRPs in the literature. This large range in spread is because interlaminar strength is dependent on the presence of flaws, therefore interlaminar strength decreases in thicker specimens due to the volumetric effect increasing the probability of more numerous and larger defects [106, 125, 134]. Therefore test data is dependent on specimen geometry. Figure 2-72b shows that interlaminar tensile strength decreases as the ply number (specimen thickness) increases from 16 to 32.

There is not yet a consensus on the best strength-based delamination failure criterion. In general the best criterion for each application is determined semi-empirically by fitting to the test data. As a result there are a large number of strength-based failure criteria in the literature. The summary in Table 10 of reference [132] lists 16 different strength-based delamination failure criteria.

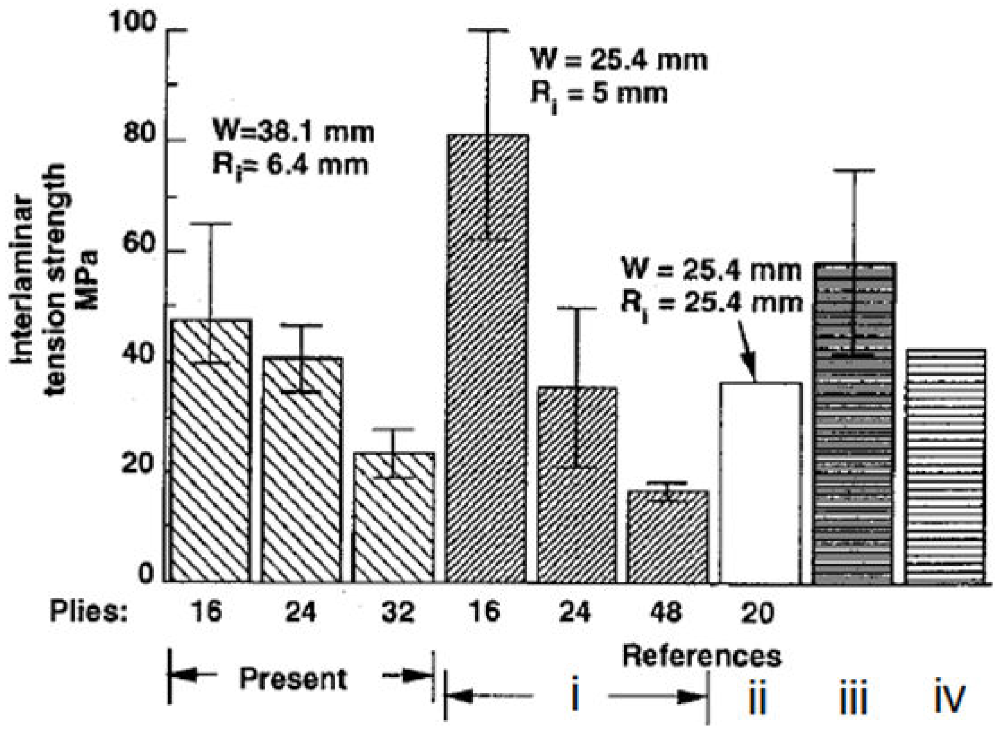

Figure 2-72 Comparison of experimentally evaluated interlaminar tensile strengths of CFRP [125]. References: Present [125]; (i) [134]; (ii) [135]; (iii) [136]; (iv) [137]

2.6.3 Fracture mechanics

Davies and co-workers [115, 116] used the FE modelling technique of virtual crack extension (VCE) to analyse the failure mode progression and stability of a carbon/epoxy T-joint designed for aerospace applications under tensile load during disbonding. This research was performed as part of a parametric T-joint study for British Aerospace (BAe). In VCE the crack is opened and the strain energy release rate is calculated within a 2D slice of the critical radius bend/delta-fillet region. Cohesive interface elements were inserted at interface sites located in the stiffener, radius bend, flange and delta-fillet ('noodle') (refer Figure 2-73a) at the regions of maximum interlaminar stress likely to initiate cracking. This avoided the need for an initial flaw. The strain energy release rate was found for a particular load and used to predict where the crack front would develop [115, 116].

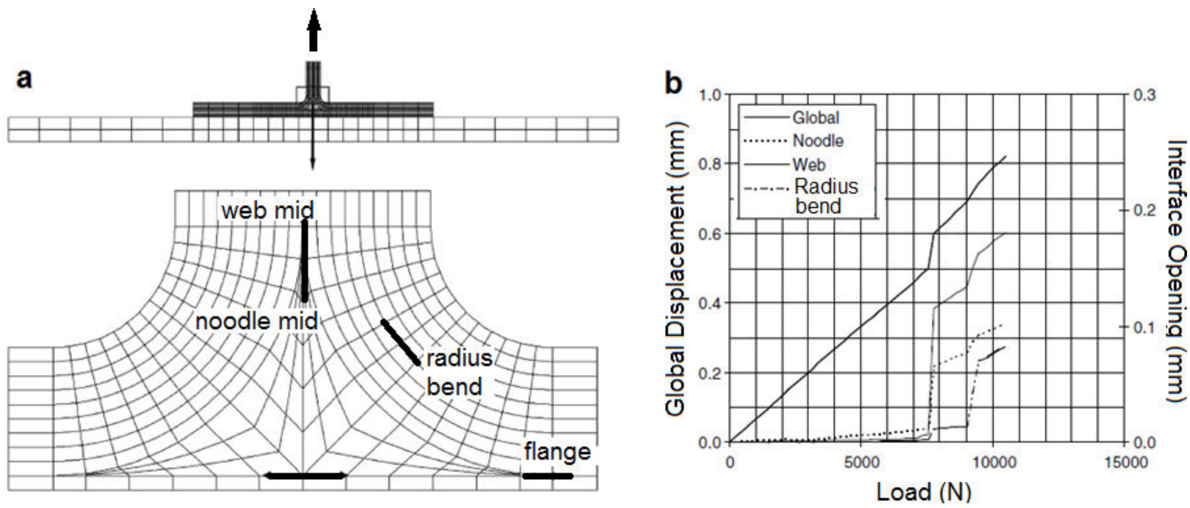

Figure 2-73 (a) Location of interface sites where cracks were inserted to monitor the strain energy release rate under tensile load [116]; and (b) mode I displacement of interfaces in the critical zone [116]

The mode I displacement results are shown in Figure 2-73b. The FE analysis predicted failure to occur in the stiffener, radius bend and delta-fillet (noodle) almost simultaneously under tensile load, indicating an unstable fracture mode. A small amount of damage occurred in the linear-elastic region of global displacement. The first interface to propagate a crack was the central delta-fillet 'noodle', which then hit the radius bend and was arrested. The same interface was then deflected vertically and propagated up the mid-plane of the stiffener and was arrested at the clamped bolts in the test rig. The final failure occurred along the delta-fillet 'noodle'/radius bend interface and propagated along the flange until it was also arrested at the clamping bolts along with some delamination cracking in the radius bend. The failure locations predicted by FEA are shown in Figure 2-74a. The failure locations and prediction of unstable fracture mode were validated experimentally with all three zones delaminating within six frames of a 60,000 frame/second high speed camera (refer Figure 2-74b) [115, 116].

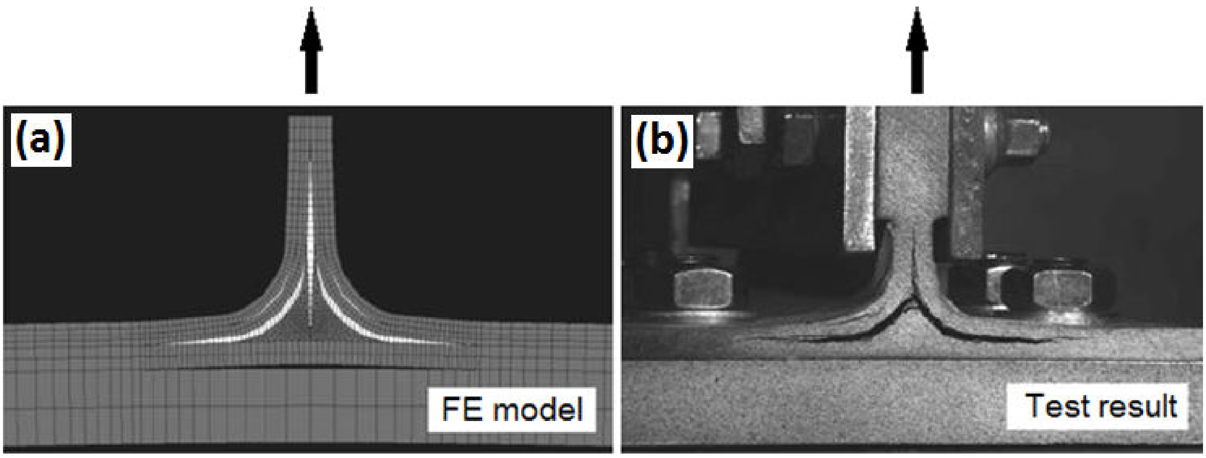

Figure 2-74 Failure modes of bonded T-joints tested in tensile loading: (a) 2D finite element model predictions [115]; and (b) experimental validation [115];

The fracture behaviour of maritime woven E-glass/vinylester T-joints was numerically and experimentally investigated by Li et al [138]. These T-joints were similar in geometry to those studied by Shenoi and co-workers (refer Figure 2-75a) but contained pre-existing disbonds of various sizes located in crucial interfaces between the overlaminate, vertical bulkhead, horizontal hull and delta-fillet (filler) (refer Table 2-11). The T-joints were analysed and tested under pinned boundary conditions with a tensile load applied to the vertical bulkhead [138]. The finite element model used 2D 4-noded shell elements in plane stress. The composite hull (horizontal panel), bulkhead (vertical panel) and overlaminate were modelled using orthotropic properties and the filler material in the delta-fillet region was modelled using isotropic properties. The analysis of the fracture mechanics of the T-joints was performed using the virtual crack closure technique (VCCT) to investigate the propagation of the pre-existing disbond. The strain energy release rate (SERR) at the tips of the disbonds was used to predict crack growth behaviour and the failure loads of the T-joints. The experimental results validated the technique as a tool to assess the criticality of damage occurring in T-joints structures [138].

Figure 2-75b shows the strain energy release rate results for a T-joint with a 30 mm pre-existing delamination between the overlaminate/hull interface. The SERR is dominated by the mode I strain energy release rate at the inner crack tip. The mode I SERR at the outer crack tip is much smaller, and the mode II SERR's at both the inner and outer crack tip are negligible. Therefore only the mode I fracture toughness is required for the failure criteria.

These results indicate that the delamination will propagate towards the delta-fillet region, which was validated experimentally (refer Figure 2-76a-b). Figure 2-76b shows the failure mode for a 30 mm disbond located at the overlaminate/vertical bulkhead interface. In this case the crack propagated vertically down through the delta-fillet and then deflected along the delta-fillet/hull interface [138].

Table 2-11 Damage configurations examined by Li et al. [138]

Designation	Damage Location	Damage Sizes (mm)		
ND	No damage (baseline)	-	-	-
HDS	Horizontal disbond between overlaminate and hull	30	60	90
HDM	Horizontal disbond between filler and hull	Complete disbond (~ 90)		
VD	Vertical disbond between overlaminate and bulkhead	30	60	90
SD	Disbond along slanted overlaminate-filler interface	Complete disbond (~ 53)		

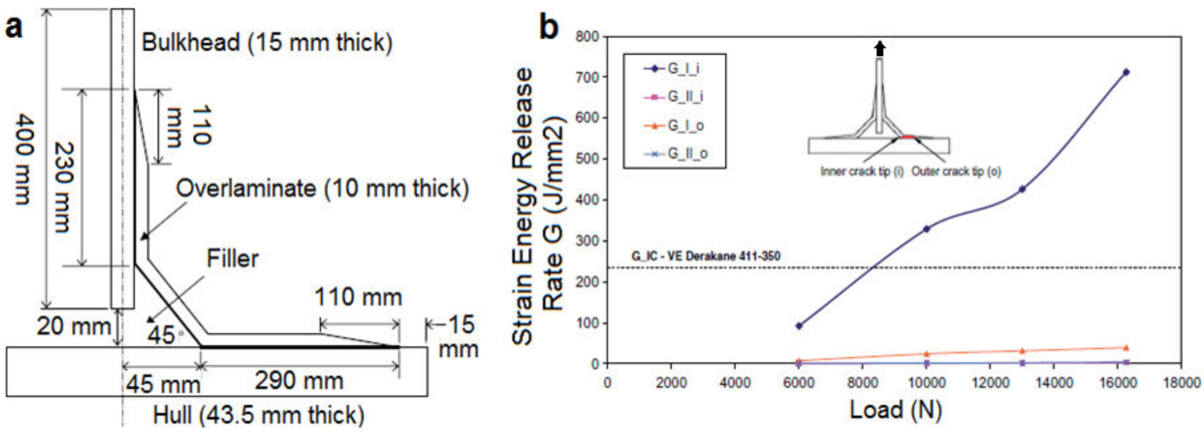

Figure 2-75 (a) Geometry of symmetrical half of the T-joint [138]; and (b) T-joint strain energy release rate with 30 mm initial disband at the overlaminate-hull interface [138]

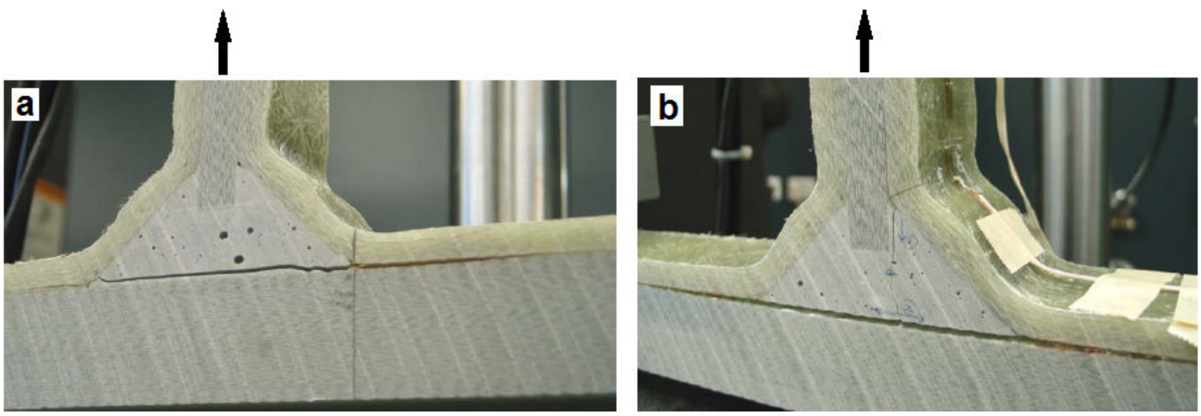

Figure 2-76 Failure modes of E-glass/vinylester T-joints tested under tensile load: (a) the pre-existing 90 mm horizontal disbond between the overlaminate and the hull; and (b) the pre-existing 30 mm vertical disbond between the overlaminate and vertical bulkhead

Dharmawan et al. [123] used a 2D shell element FE model for a parametric investigation into similar marine E-glass/vinylester T-joints loaded in tension, which was validated experimentally. They investigated the effect of disbonds on the strain field in the overlaminate. The results in Figure 2-77 show that in the ideal undamaged T-joint the axial strain is relatively uniform through the thickness of the overlaminate. However the strain distribution is significantly changed with the introduction of disbonds, which change the axial strain distribution to vary linearly through-the-thickness [123].

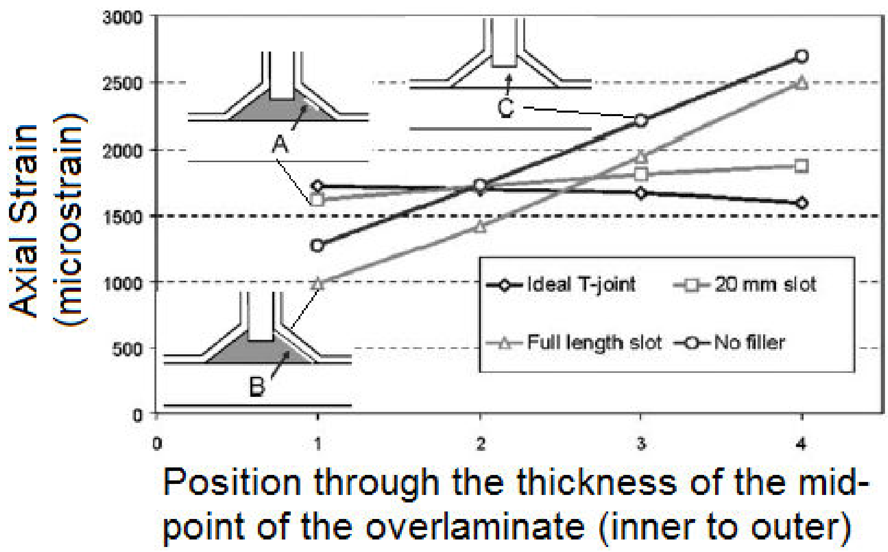

Figure 2-77 Axial strain distribution of ideal and damaged T-joints at the mid-span of the overlaminate [123]

2.6.4 Damage tolerance

Many different strategies have been investigated to improve the toughness and damage tolerance of fibre-reinforced composite laminates under static and impact loading. Laminates can be toughened through careful choice of material selection, laminate stacking sequence, selective interlayers and matrix toughening [139, 140].

The only reference that was found in the literature to the toughening benefits of embedded stiffener design was in a review of novel materials and processes to produce impact tolerant designs for stiffened panels [140], which stated "*Another approach (to toughening T-joints) is embedded stringers which eliminates skin/stringer detachment by incorporating the foot as an integral part of the skin. Although this concept is difficult and time-consuming to manufacture, there is scope to use it in conjunction with other toughening methods*." The schematic illustrating this concept is reproduced in Figure 2-78. The journal paper references this remark to a technical report from the National Aerospace Laboratory of the Netherlands (NLR) examining damage tolerance of stiffened wing panels [141] but on obtaining this report it does not mention the concept of embedded stiffener design.

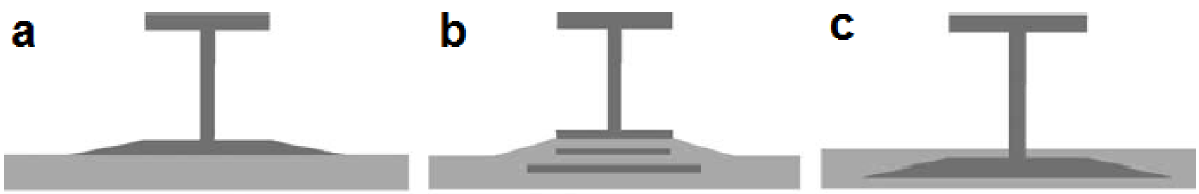

Figure 2-78 (a) tapered stiffener feet; (b) stiffener doublers; and (c) embedded stiffeners [140]

In the absence of published research specifically examining embedded design 3D woven composites that improve extrinsic toughening in the T-joint structure utilising through-thickness reinforcement have been considered in the following section.

2.6.4.1 3D woven composites

Soden et al. [142] assessed the effectiveness of 3D woven composites (refer Figure 2-79b) on the in-plane strength of CFRP T-sections in comparison with similar 2D laminated T-sections (refer Figure 2-79b), with a focus on the resin-rich area at the mid-plane flange interface. The T-section pre-forms were woven on an electronic Jacquard power loom using continuous filament T-300 carbon fibres [142].

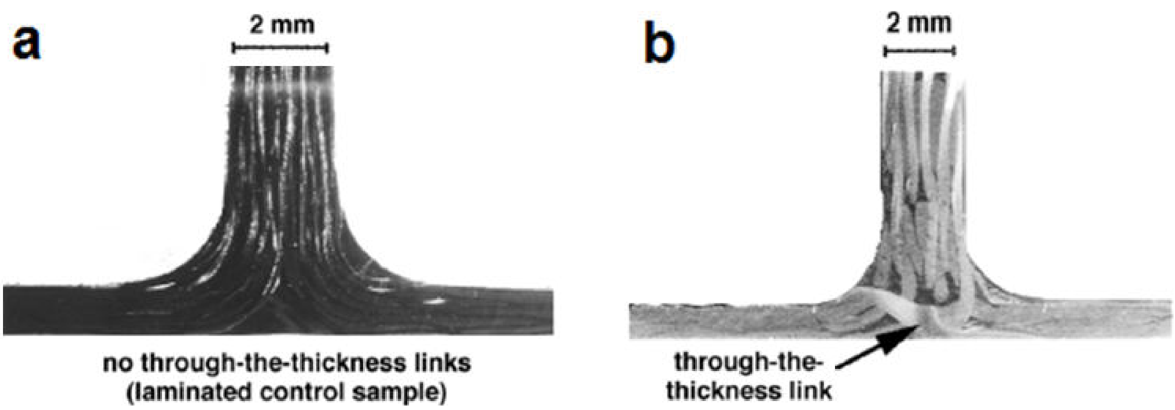

Figure 2-79 Micro-sections showing warp yarn paths at the stiffener-flange interface: (a) baseline sample with no through-thickness links; and (b) through-thickness link across the resin-rich interface [142]

The pre-forms consisted of six warp layers and six weft layers, with the frequency of through-the-thickness interlinks ranging from 1.5 to 5.6 links/cm^2 [142]. A tension force was applied at both ends of the flange (refer Figure 2-80a). The results showed the 3D woven T-sections had higher in-plane strength compared to the 2D laminated samples. Increasing the amount of interlinking in the 3D woven T-sections reduces initial failure load slightly but substantially increases peak load and fracture energy (refer Table 2-12). The architecture and density of 3D cross-links influences the mode of failure but their effect on in-plane strength is complex [142].

Sample 3T was constructed with four 5-end satin weave outer layers and two plain weave layers running along the central axis. Only the surface warp layer was used to form the through-thickness reinforcement. The flanges were folded to form a resin-rich ridge along the central plane (refer Figure 2-80b). Sample 4T was made with four 5-end satin weave outer layers and two plain weave layers running along the central axis. All 6 layers were used to form the through-thickness reinforcement. The flanges were folded out fully to create a high quality interface preventing a resin-rich area forming along the central plane (refer Figure 2-80c). Sample 6T was constructed with an intermediate zone of 3D weave between the stiffener and flange which was designed to increase the number of through-thickness links in the critical zone that undergoes first failure.

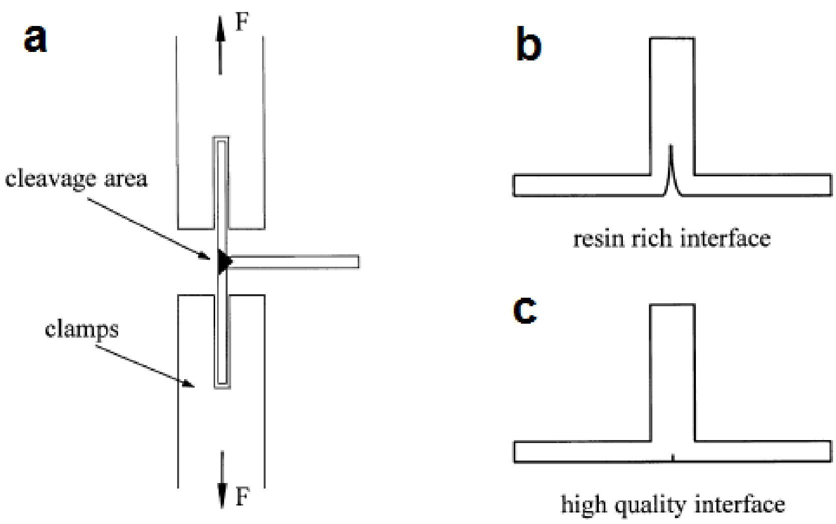

Figure 2-80 (a) Test set-up for in-plane tension tests; (b) resin-rich interface between the flanges; and (c) high quality interface where 3D weave reduces resin-rich interface between the flanges [142]

Table 2-12 shows initial failure occurred at about the same load for the baseline and 3D woven T-joints. This initial failure was resin dominated with initial cracking occurring at the stiffener/flange interface that subsequently propagated through the resin-rich layers between the flange and the stiffener. After initial failure samples without a resin-rich zone could withstand a force higher than the initial failure load, indicating catastrophic failure will not occur. In contrast, specimens with a resin-rich zone could only withstand a subsequent force equal to approximately 50% of the initial load. The baseline 2D laminated T-joint exhibited low work of fracture with a rapid loss of in-plane strength as the crack propagated rapidly up the centre of the stiffener, compared to the 3D samples with increased absorbed fracture energy (refer Table 2-12).

Table 2-12 In-plane tensile test results [142]

Weave structure	Initial failure load (N/mm)	Peak load (N/mm)	Fracture energy (N.m)
Baseline 2D laminate	58.0	13.3	0.181
3T (resin-rich zone)	61.9 (+ 7%)	30.2 (+127%)	0.399 (+120%)
4T	55.6 (- 4%)	73.6 (+453%)	0.732 (+304%)
6T	51.2 (- 11%)	135.1 (+916%)	0.985 (+444%)

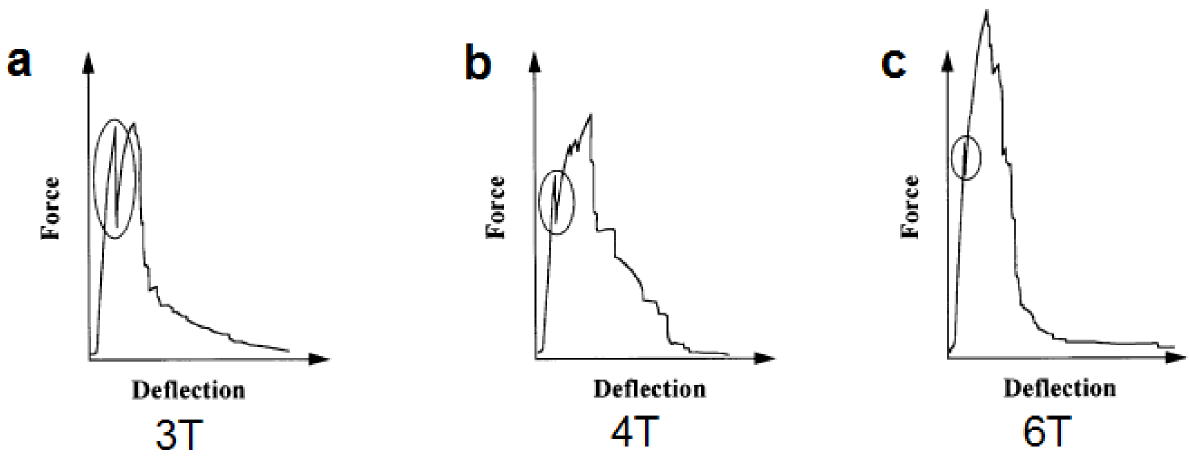

Figure 2-81 Force-deflection curves of 6 ply 3D woven T-shaped laminates with increasing through-the-thickness interlinking: (a) sample 3T; (b) sample 4T; and (c) Sample 6T [142]

2.6.5 Damage tolerance under impact loading

Damage tolerance under impact loading refers to two properties: i) impact resistance, which is the ability to absorb the energy of the impact without sustaining significant damage; and ii) impact damage tolerance, which is the effect of the impact damage on the mechanical performance of the structure [140].

Zhang [131] used a 2D finite element model to investigate impact damage on carbon/epoxy plates and stiffened panels, which was validated by experimental tests. By modelling the in-plane and matrix damage the impact force history can be calculated and the maximum impact force used to predict the initiation of delamination damage using a strength-based criterion. Under impact damage (as under quasi-static loading) it is necessary to create a fracture model to investigate the stability of delamination growth [131].

The main damage modes caused by impact damage are shown in Figure 2-82 and include: contact damage or crushing; internal delamination due to mixed mode shear stresses; failure on impact on the front face due to compressive strains; matrix fracture on the back face due to tensile strains; and delamination due to back-face matrix cracking [131].

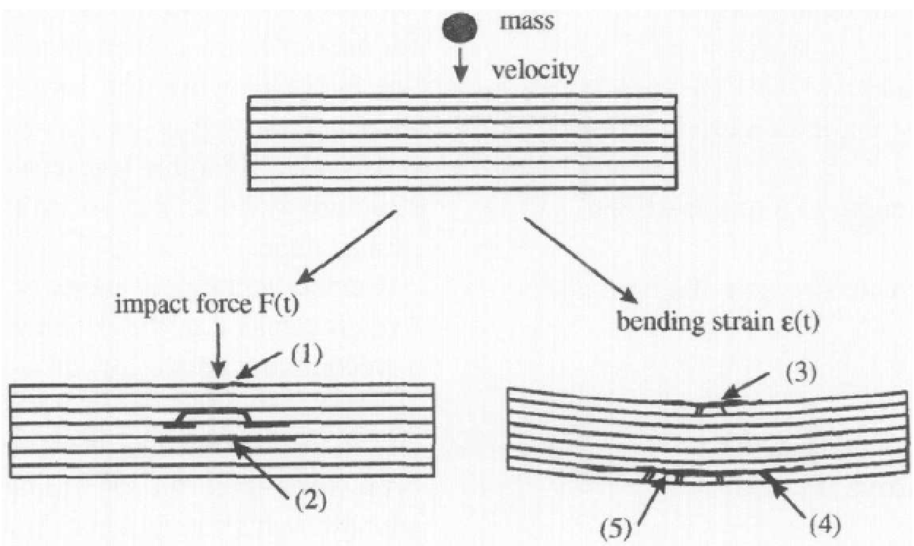

Figure 2-82 Low-velocity impact damage modes in a laminated composite plate. (1) Contact damage; (2) Internal delamination due to transverse shear stresses; (3) Failure on impact due to compressive strains; (4) Matrix fracture on back face due to tensile strains; and (5) Delamination due to back-face matrix cracking [131]

Generally impact damage will cause mixed failure modes. At low velocity impact the dominant failure mode is delamination, which requires energy for initiation and propagation [131]. Under high velocity impact the dominant failure mode is fibre fracture and the impact may sever all the fibres in the laminate (penetration). The proportions of each damage mode are influenced by material properties (fibre stiffness and strength, matrix toughness, fibre surface treatment and moisture content), laminate stacking sequence, structural aspects including laminate geometry and the impactor mass, velocity and shape [131].

When a stiffened panel (refer Figure 2-83a) undergoes low energy impact the initial damage mode is intra-laminar matrix cracking (refer Figure 2-83b) due to the through-thickness shear stresses from the impact force. Delamination initiation is caused by mixed-mode opening forces acting on the matrix cracks. Propagation is caused by interlaminar shear stresses induced by the laminate bending. In general, significant delamination growth only occurs at the interfaces where the driving force is coincident with the ply fibre direction, therefore impact damage tolerance can be controlled by ply stacking sequence. Either the delamination is arrested or ultimate failure occurs by compressive in-plane failure caused by local bending loads (refer Figure 2-83c) [131].

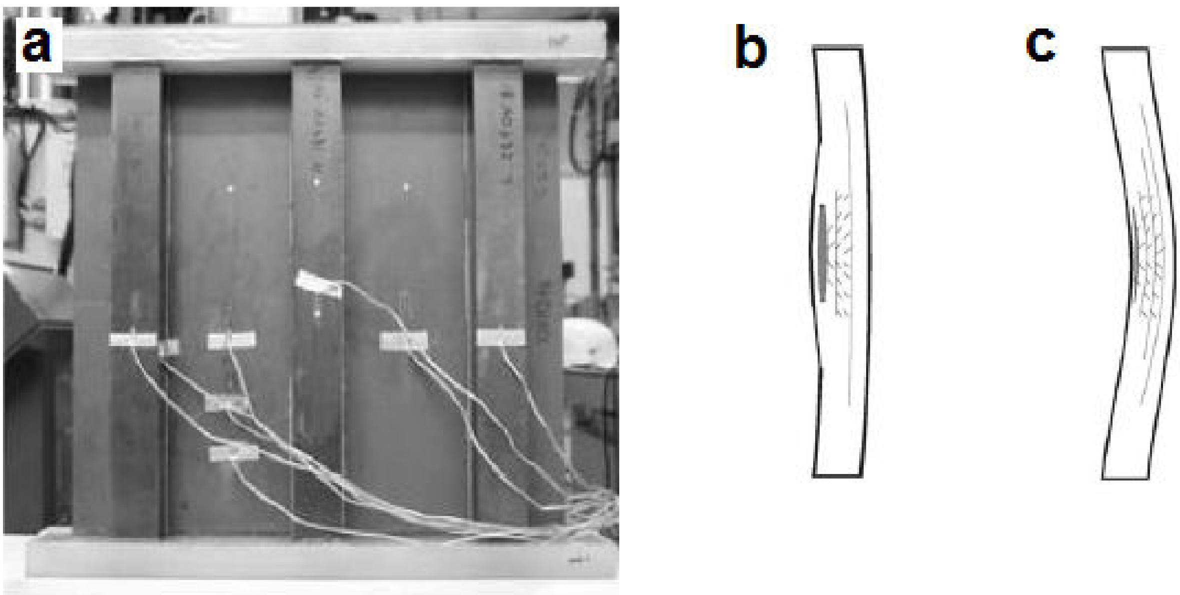

Figure 2-83 (a) Typical stringer stiffened panel; (b) local buckling of the damaged region with intra-laminar cracking; (c) local bending of the delaminated plies and the sub-laminate beneath these plies [131]

Key material parameters and their influence on impact damage tolerance are listed in Table 2-13. The impact damage tolerance of stiffened panels can also be influenced through structural design. The panel deflection can be reduced by changing the stringer geometry to increase the panel moment of inertia. Details such as using tapered feet or stiffener doublers can limit internal forces caused by the external impact load. Laminates in which there are a high number of off-axis plies are generally more impact damage tolerant. However many toughening concepts that have the advantage of increasing the delamination toughness also decrease the undamaged performance of the structure. A toughening concept that reduces material parameters such as compressive and bending strength could potentially degrade the impact tolerance of a composite structure [131].

Table 2-13 Key material parameters and their influence on impact damage tolerance [131]

Key Material Parameter	**Influence on Impact Damage Tolerance**
Mode I toughness	Key driving force for delamination growth induced by local buckling of the delaminated plies
Mode II toughness	Dominant fracture mechanism during impact and skin/stringer detachment
Bending and shear moduli:	During impact bending modulus influences the energy absorption process. Both moduli influence delamination initiation, growth and failure in buckling
Compressive & bending strength	Ultimate failure and impact damage are controlled by these parameters, which are in turn influenced by the fibre/matrix interface strength, fibre waviness, matrix stiffness, fibre stiffness and matrix toughness

2.6.6 Strength and failure modes of 90° angle brackets

The 90° angle bracket is a subcomponent of the T-joint forming the stiffener web and flanges. The interlaminar tensile strength, failure modes and fracture mechanics of 90° brackets were investigated by Avalon and Donaldson [106], Shivakuma et al. [125] and Sun and Kelly [126, 127]. Avalon and Donaldson [106] investigated CFRP composite brackets under four-point-bend loading (refer Figure 2-84a). Shivakuma et al. researched CFRP (AS4/3501-6) with three laminate thicknesses of 16, 24 and 32 plies. The test specimen geometry and the tension/bending test rig used by Shivakuma and colleagues is shown in Figure 2-85. Sun and Kelly investigated CFRP (AS4/3501-6) and glass/epoxy (S-2/CE9000-9) with various $[0_i/90_j]$ stacking sequences, and the geometry of the test samples is given in Figure 2-86a. These samples were subjected to a bending test shown in Figure 2-86b.

Avalon and Donaldson found that the 90° brackets exhibited weakness around the radius due to high through-thickness tensile stresses which lead to delamination. The curved beam strength (or moment/width) was calculated from the failure load using an approximation of Lekhnitskii's exact solution (refer Equation 2-14 to Equation 2-16 [106]).

$$Curved\_Beam\_Strength = \frac{M}{w} = \left(\frac{P}{2w\cos\phi}\right)\left(\frac{d_x}{\cos\phi} + (D+t)\tan\phi\right)$$ Equation 2-14

$$\phi = \sin^{-1}\left(\frac{-d_x(D+t) + d_y\sqrt{d_x^{\ 2} + d_y^{\ 2} - D^2 - 2Dt - t^2}}{d_x^{\ 2} + d_y^{\ 2}}\right)$$ Equation 2-15

$$d_y = d_x \tan\phi_i + \frac{D+t}{\cos\phi_i} - \Delta$$ Equation 2-16

Where M = bending moment on the 90° bracket, w = width of the specimen, d_x = the horizontal distance between the two adjacent top loading bars in the four-point-bend loading fixture, P = the total force at the first load drop (corresponding to the initial delamination), D = the diameter of the loading bars, t = the thickness of the specimen, φ = the angle between horizontal and the specimen legs, and Δ = the relative displacement between the top and bottom halves of the four-point-bend test fixture.

The interlaminar tensile stress was calculated analytically using the exact Lekhnitskii equation for stresses in a curved beam segment with cylindrical anisotropy [106] and approximated from the curved beam strength using Equation 2-17 [106].

$$\sigma_{33}^{\max} = \frac{3 \times CBS}{2t\sqrt{r_i r_o}} \quad \text{Equation 2-17}$$

Where σ_{33}^{max} = maximum interlaminar tensile stress, CBS = curved beam strength, t = the specimen thickness, r_i = inner radius and r_o = outer radius.

The interlaminar tensile stress distribution in the radius bend calculated using the ABAQUS finite element program is shown in Figure 2-84b. The location of maximum interlaminar tensile stress is biased towards the (smaller) inner radius. Ko [143] showed that the location of maximum interlaminar tensile stress moves from the mid-radius surface towards the inner radius of the curved beam as the ratio of the outer radius to the inner radius increases.

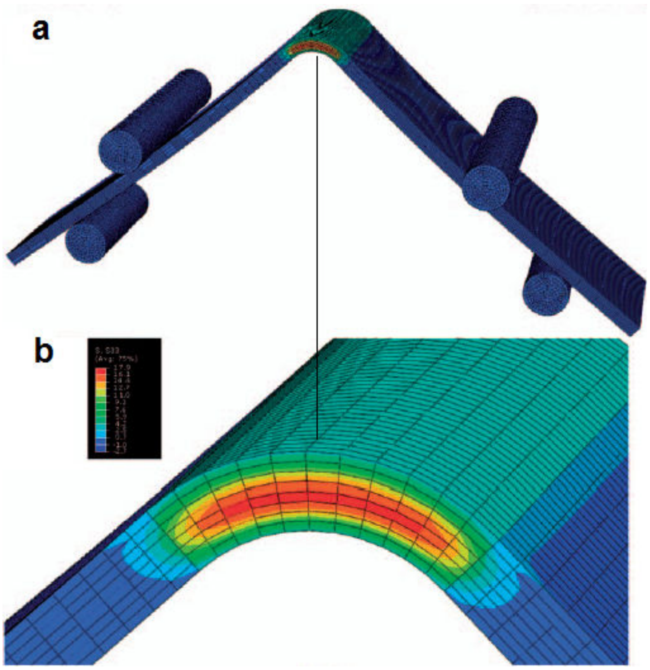

Figure 2-84 (a) 90° bracket with four rollers used in four-point-bend test (ASTM D6415); and (b) ABAQUS FE results for the interlaminar stress for the 90° bracket [106]

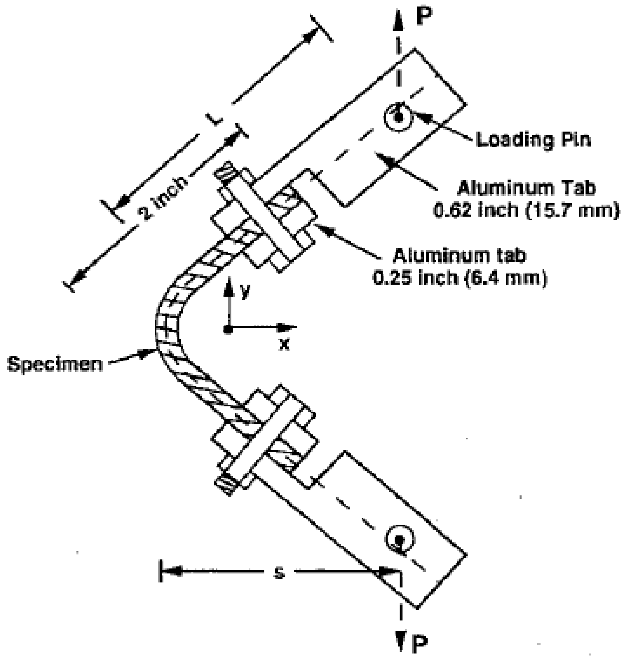

Figure 2-85 Geometry and bend test set-up for 90° bracket [125]

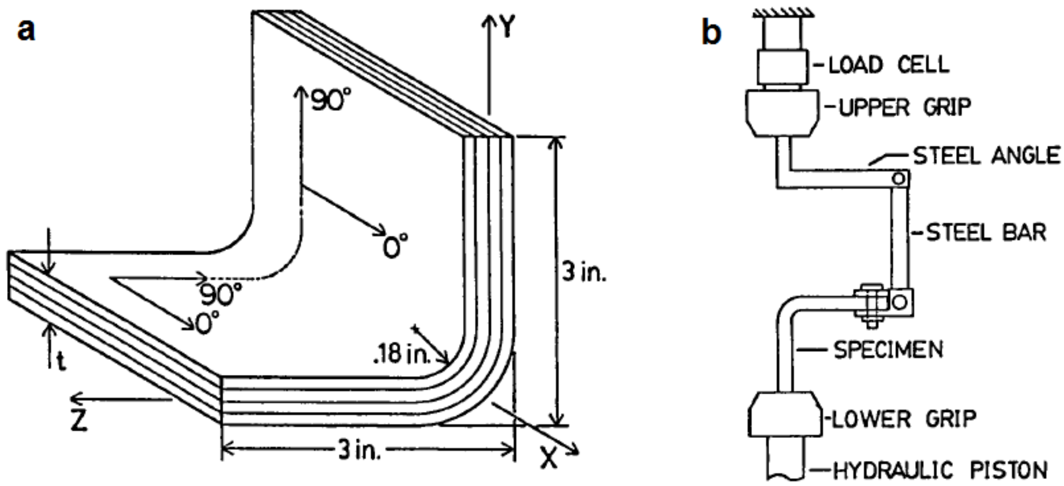

Figure 2-86 (a) Geometry of 90° bracket; and (b) bend test set-up [126]

Despite a large variation in the failure load and curved beam strength of the different samples, the critical value of the interlaminar tensile stress was found to be 30 – 32 MPa for all specimens as calculated using Lekhnitskii's exact solution, the approximation given by

Equation 2-14 to Equation 2-16 and the finite element results. The load-displacement response and optical microscopy showed samples either failed catastrophically, characterised by a large load drop (refer Figure 2-87a) in which plies across the radius thickness delaminated simultaneously (refer Figure 2-87b) or with ‘stick-slip’ behaviour where multiple small load drops (refer Figure 2-87c) corresponded to individual delaminations forming between the radius thickness plies (refer Figure 2-87d) [106].

Shivakuma et al. [125] measured average interlaminar tensile strengths of 47.6, 40.9 and 23.4 MPa for the 16-, 24- and 32-ply laminates, respectively. The values for the 16- and 24- ply specimens agreed well with literature, while the lower interlaminar tensile strength for the 32 ply specimen was attributed to the volumetric effect of a thicker laminate having a greater probably of more and larger defects due to difficulties in consolidation [125].

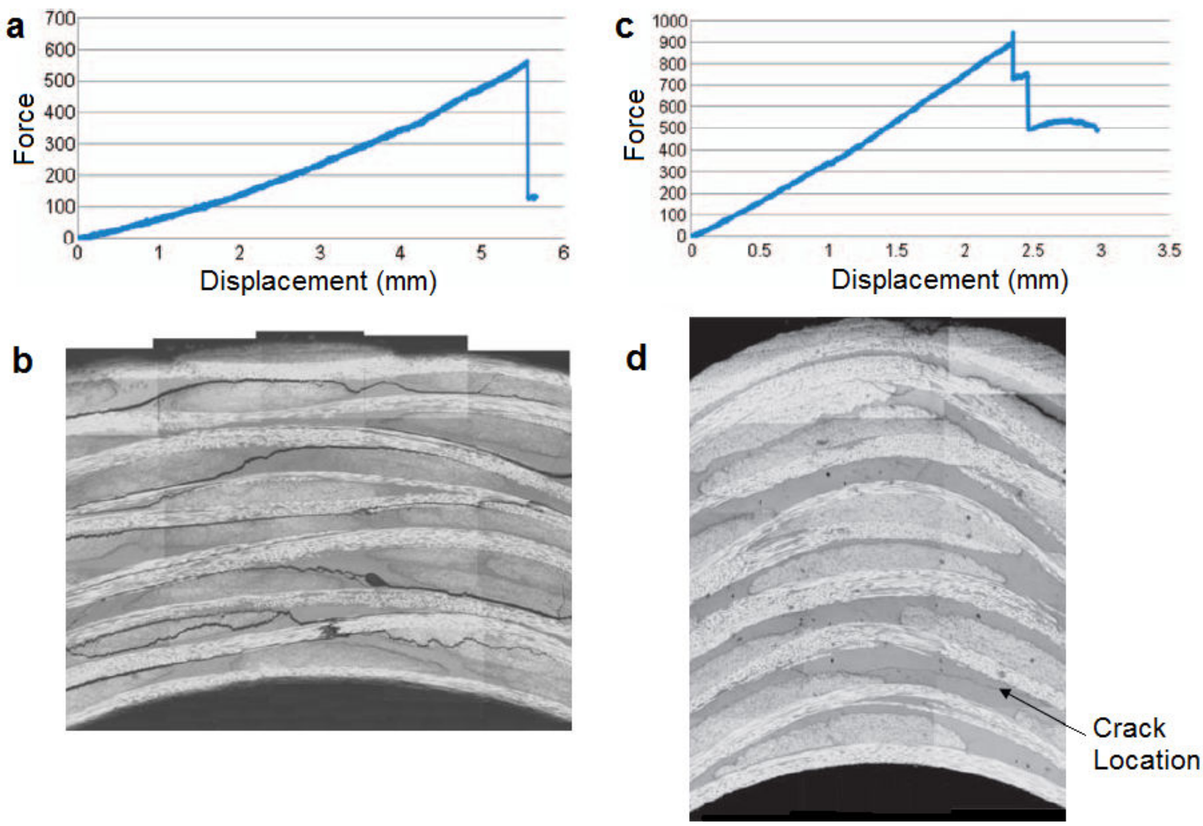

Figure 2-87 (a) Force v displacement curve for 90° brackets that exhibited rapid load drop at failure showed; (b) multiple cracks; and (c) force v displacement curve for 90° brackets that exhibited stick-slip behaviour at failure showed; (d) a single crack [106]

2.6.7 Material selection and laminate stacking sequence

Sun and Kelly [126, 127] found that interlaminar tensile stresses generated in the radius bend of the 90° brackets resulted in a delamination dominated failure mode. In a limited parametric study they considered the effects of changing the material and ply orientation on the in-plane bending stress and interlaminar tensile stress in the 90° bracket radius bend, but only with the limited scope of two $[90_i/0_j]$ stacking sequences. They did not consider ±45° or non-standard ply angles. The specimen material, number of plies and ply orientation (stacking sequence) in the laminates of specimens H, I and J are given in Table 2-14. Changing the stacking sequence of the CFRP 90° brackets had an effect on failure mode. Specimen H had a group of 0° plies close to the surface which attracted a high in-plane bending load of about 450 MPa (refer Figure 2-88a) compared to about 250 MPa in specimen I (refer Figure 2-88b) that led to an initial bending failure with transverse cracks across the radius plies. Final failure occurred in the characteristic delamination dominated mode exhibited by specimen I [126].

Table 2-14 Material, stacking sequence and laminate thickness for each 90° bracket [126]

Specimen	Material	Number of plies	Stacking Sequence	Laminate thickness (mm)	Failure mode
H	Graphite	20	$[90/0_3/90_2/0_3/90]_s$	2.5	Bending cracks
I	Graphite	20	$[90_3/0/90_3/0/90/0]_s$	2.5	Delamination
J	Glass	24	$[90_3/0_3/90_2/0_3/90]_s$	4.6	Bending cracks

The FE results for the interlaminar tensile stress distribution in the radius bend for specimens H and I are given in Figure 2-88d-e. These results show that the interlaminar stress distribution is altered by the stacking sequence, although the maximum interlaminar tensile strength remains virtually unchanged (at about 21 MPa). Sun and Kelly concluded that, *"The analytical results suggest that premature matrix failure due to bending can be controlled merely by varying the stacking sequence. However, the more critical delamination failure mode has been found to occur regardless of stacking sequence. Since the radial stresses depend predominantly on cross-sectional geometry, they cannot be reduced by varying the* *stacking sequence*." This conclusion is based on the results of only two different stacking sequences for CFRP angle brackets containing only 0° and 90° plies without considering the full spectrum of ply angles and therefore seems premature. Figure 2-88c and Figure 2-88f show the effect of material selection. The glass/epoxy sample has a much lower in-plane bending and interlaminar tensile stress compared to the carbon/epoxy sample because of the lower modulus.

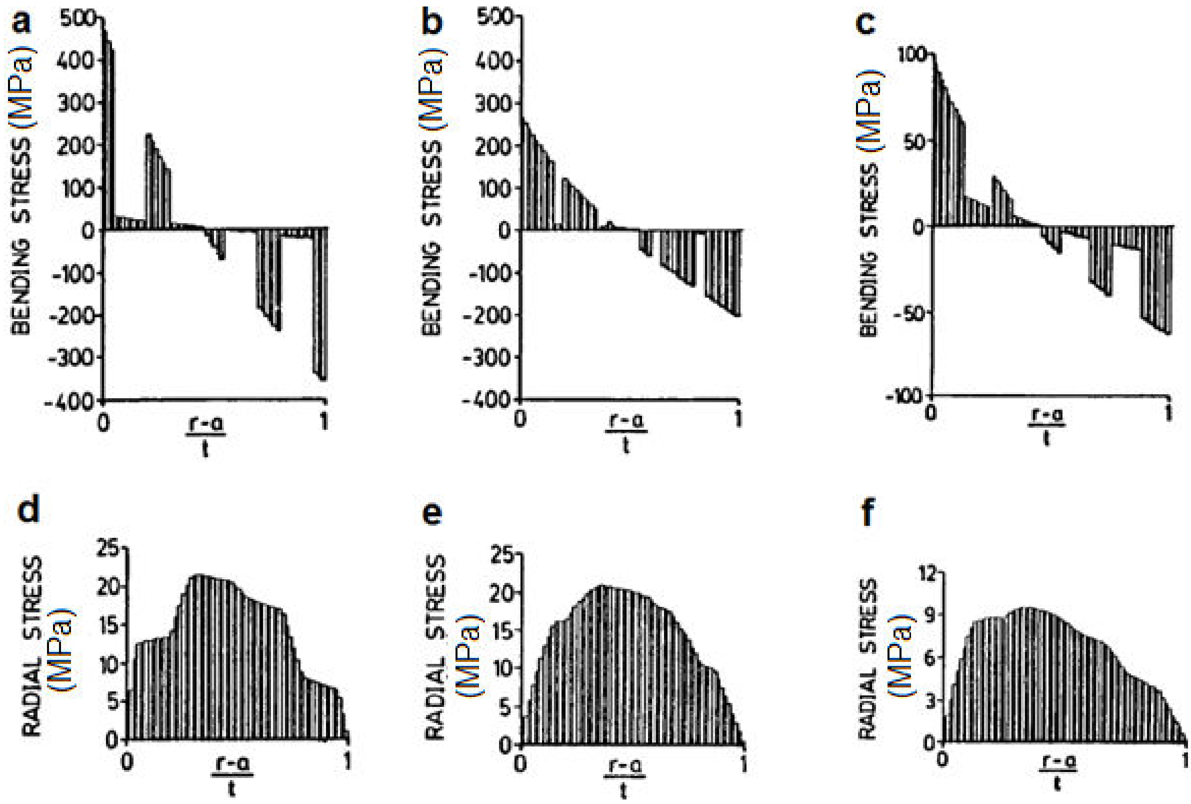

Figure 2-88 FEA stress prediction for angle bracket specimens at a bending load of 100 lb/in: (a) H (Graphite); (b) I (Graphite); (c) J (Glass); Finite element interlaminar radial stress prediction for angle bracket specimens: (d) H (Graphite $[90/0_3/90_2/0_3/90]_s$); (e) I (Graphite $[90_3/0/90_3/0/90/0]_s$); (c) J (Glass $[90_3/0_3/90_2/0_3/90]_s$) [127]

Fracture mechanics was employed to investigate transverse radial cracks (refer Figure 2-89a) and delamination cracks (refer Figure 2-89b) induced by the matrix cracks in the 90° brackets [126, 127]. It was also found that material selection affects the strain energy release rate (SERR), *G*, of the 90° brackets. Figure 2-90 shows the carbon/epoxy brackets had a SERR almost three times higher than the glass/epoxy bracket [126].

Experimental results showed that adhesive layers placed between the plies of laminates increase the failure load of the carbon/epoxy angle joint with lay-up I = $[90_3/0/90_3/0/90/0]_s$ by 55% over the baseline laminate without adhesive layers [126, 127].

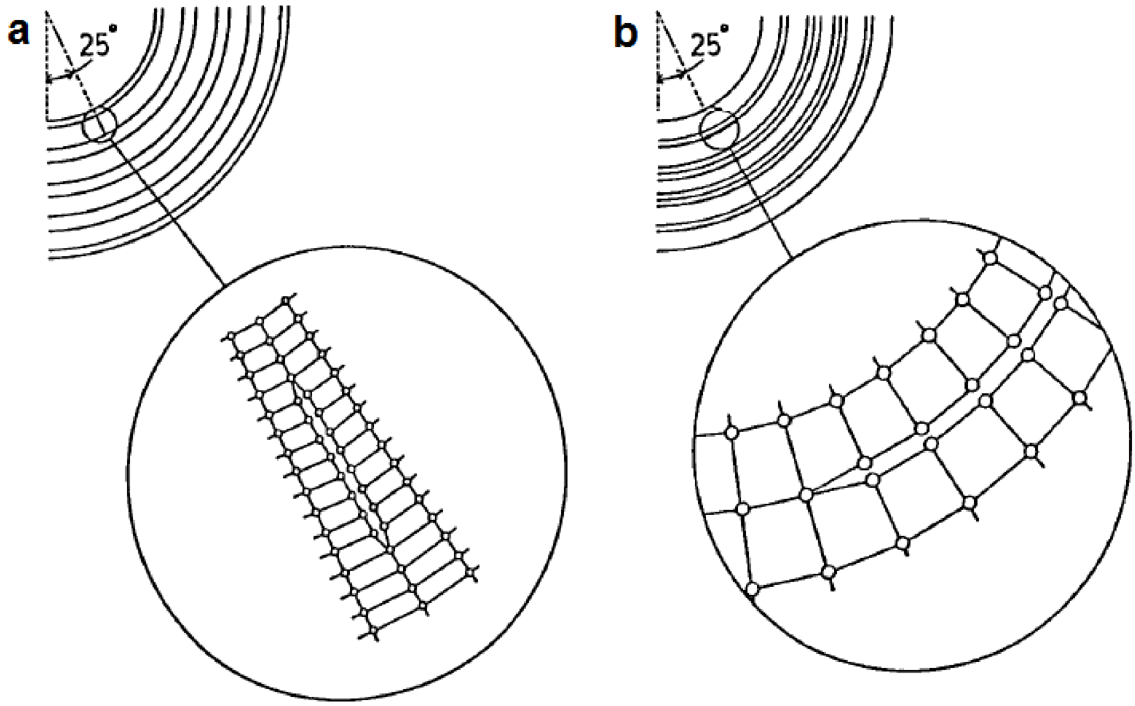

Figure 2-89 (a) FEM for modelling of (a) radial crack; and (b) delamination crack [127]

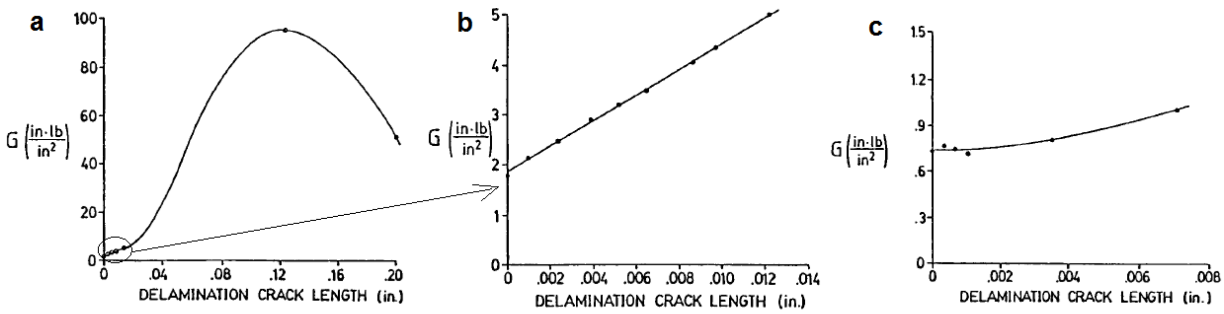

Figure 2-90 Strain energy release rate v delamination crack length calculated at a distributed load = 100 lb/in for: (a) lay-up H (graphite) = $[90/0_3/90_2/0_3/90]_s$; (b) expanded plot for small crack lengths; and (c) lay-up J (glass) = $[90_3/0_3/90_2/0_3/90]_s$ [127]

2.6.8 Influence of the delta-fillet on joint failure

In composite T-joints used in many aerospace and marine structures the vertical stiffener is supported by a delta-fillet, also known as a 'noodle' or deltoid section (refer Figure 2-91). The purpose of the delta-fillet is to fill the gap between the radius bends to ensure the smooth formation of the overlaminate to support load transfer between the orthogonal panels. The delta-fillet is a critical region because it does not contain continuous in-plane fibres. Typically the delta-fillet is filled with either resin, foam or a triangular 'noodle' formed from unidirectional prepreg. The latter helps ameliorate a severe reduction in fibre volume fraction in the delta-fillet that leads to its Young's modulus being much lower than the continuous fibres in the adjacent radius bend ($E_{radius\ bend} >> E_{delta\text{-}fillet}$). Discontinuity in stiffness and strain, combined with the radius bend geometry creates a stress concentration at the interface between the delta-fillet and radius bend.

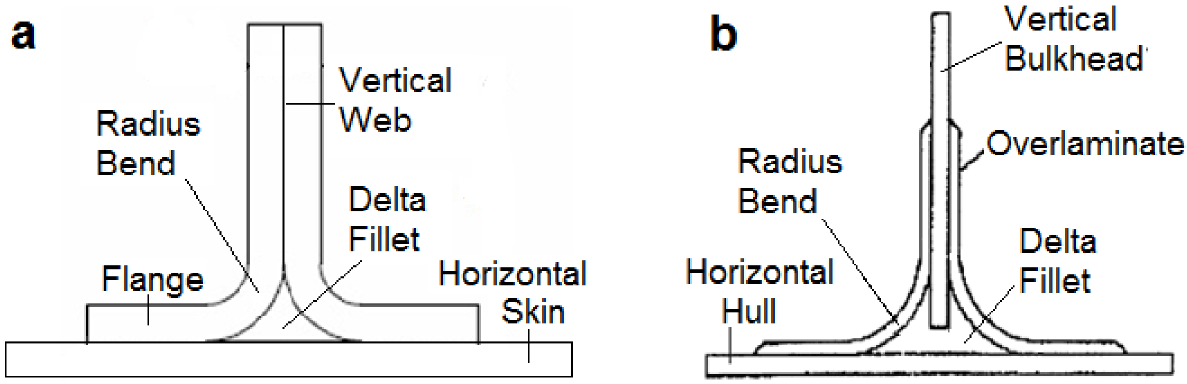

Figure 2-91 The delta-fillet fills the gap between the radius bends in: (a) vertical stiffener connected to horizontal skin via the flange [113]; and (b) vertical bulkhead connected to the horizontal hull via the overlaminate [123]

The Pi pre-form is a T-joint design resembling an upside down π which attempts to eliminate the delta-fillet as shown in Figure 2-92. Pi pre-forms have been shown to increase T-joint strength [65]. However the design of most aircraft airframes continues to use the typical T-joint given in Figure 2-91a that contain a delta-fillet.

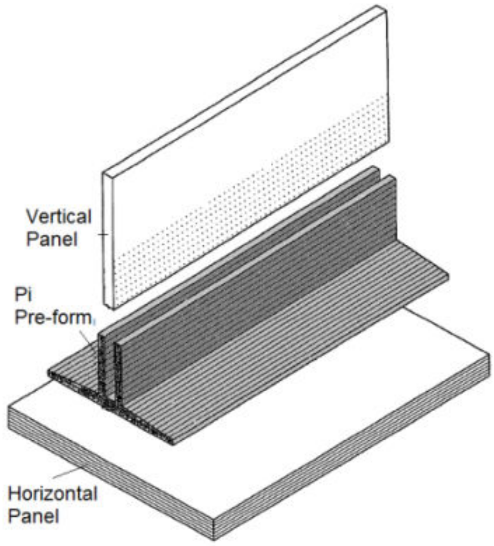

Figure 2-92 Pi pre-form T-joint [65]

The influence of the area and quality of the delta-fillet has been investigated by Kumari et al. [114] and Trask et al. [144]. Kumari et al. developed a 3D FE model of a T-joint using a special thick 8-noded shell element using the material properties of T300/epoxy. Two designs of the delta-fillet were considered. Case 1: The arc length of the radius makes a 90° angle to the centre of its circle at the interface with the stiffener and the skin. This means that increasing radius leads to increasing delta-fillet area as shown in Figure 2-93a. Case 2: The radius of curvature is varied so the end points of the arc length are the same for each radius. This means the arc length of the radius does not make a 90° angle to the centre of its circle and the delta-fillet area is not significantly changed as shown in Figure 2-93b [114]. The Tsai-Wu quadratic interaction criterion was used to predict ply failure. The FE study was not validated experimentally [114].

The results showed that in case 1 the T-joint pull-off strength decreased with increasing radius because the increase in the delta-fillet area offset the reduction in geometric stress concentration. In case 2 the increase in radius between the two fixed end points increased the pull-off strength of the joint because it decreased the geometric stress concentration without increasing the delta-fillet area [114]. The stress at failure was almost identical for variations in radii, although varying the laminate stacking sequence changed the stress components at the failure load [114]. The results showed that decreasing the delta-fillet area is desirable, however below a certain level it is not practical because a very small radius bend or a radius that does not connect smoothly with the vertical and horizontal panels will cause defects such as ply kinking during manufacturing that will prevent smooth load transfer [114].

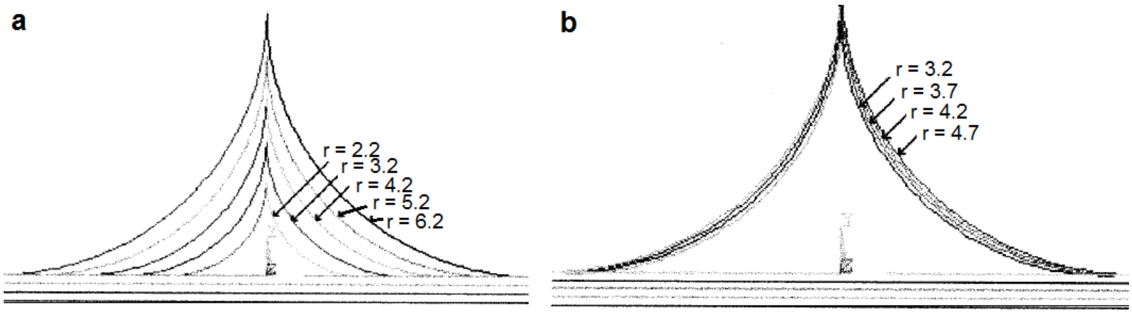

Figure 2-93 Delta-fillet region: (a) case 1: and (b) case 2 [114]

Trask et al. [144] identified a lack of research into the influence of delta-fillet manufacturing defects on the mechanical properties of T-joints. They undertook experimental testing of a baseline T-joint with the lay-up shown in Figure 2-94a and compared them to T-joints where the delta-fillet area was reduced by about 25% and 50% without a change to the external geometry. The T-joints were tested under tensile loading (refer Figure 2-94b.

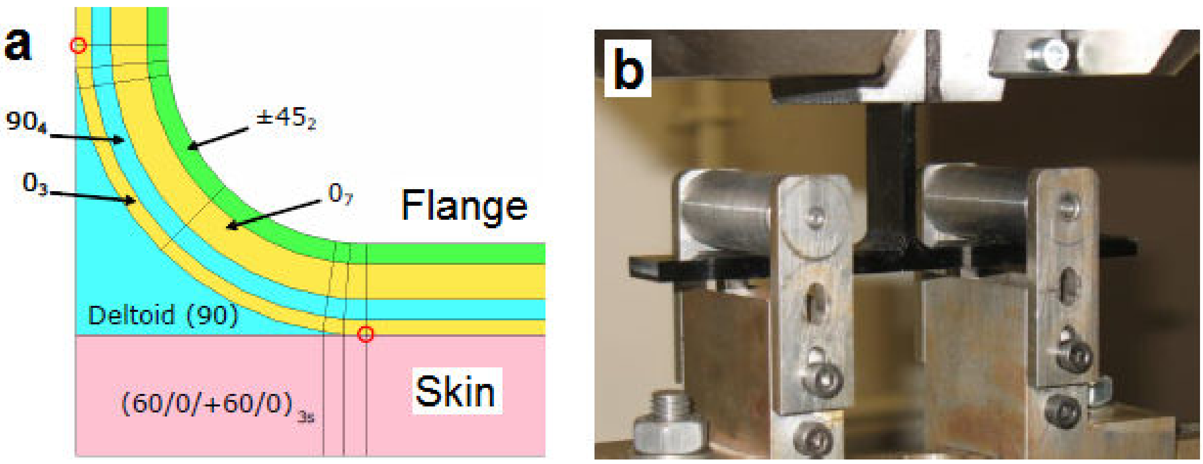

Figure 2-94 (a) Schematic representation of radius bend and delta-fillet region of nominal T-joint specimen; and (b) experimental testing configuration for tensile pull-off testing [144]

Figure 2-95a shows that reducing the delta-fillet area by 25% was tolerated with similar average tensile strength, although increased strength variability compared to the baseline design. Reducing the delta-fillet area by 50% reduced the tensile strength of the joint by 33%. Microscopy results in Figure 2-95b show that reducing the delta-fillet area by 50% produced defects such as voids in the delta-fillet and distortion of the radius bend plies as they were no longer fully supported by the reduced area of the delta-fillet [144].

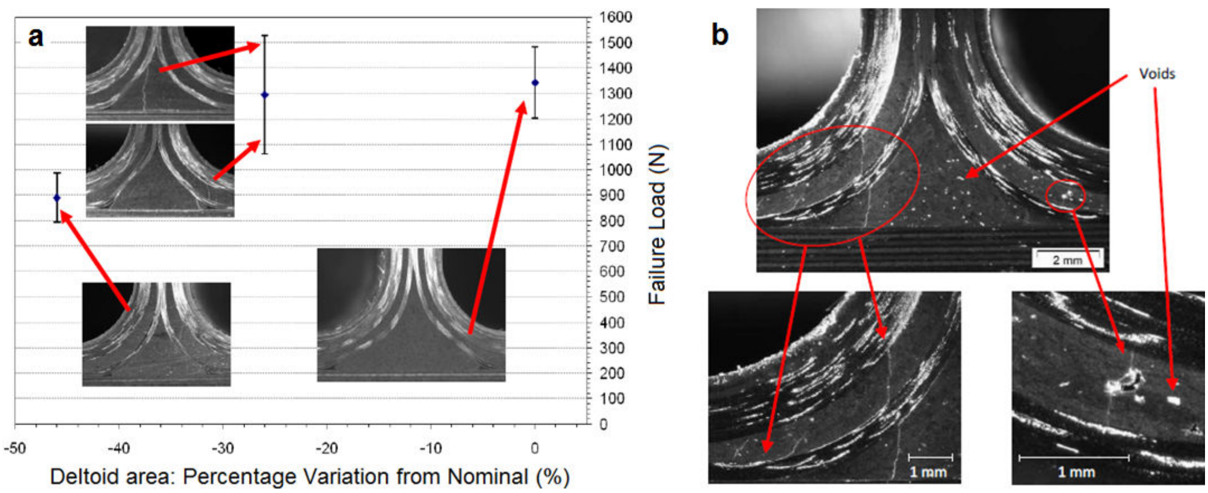

Figure 2-95 (a) Failure load versus percentage reduction in delta-fillet area from baseline T-joint [144]; and (b) T-joint specimens with 46% below nominal delta-fillet area [144]

2.6.9 Shape stability and mechanical coupling

According to Stephen Tsai [145], "*There are two (tarnished) golden rules on composite laminate designers practice: balanced (with matching +/- off-axis plies) and mid-plane symmetric laminates... When the traditional rules for balanced and symmetric laminates are relaxed, many design options emerge. Anisotropic, unsymmetric laminates can make weight and cost benefits possible.*"

Composites such as carbon/epoxy have anisotropic thermal expansion due to differences in the coefficient of thermal expansion (CTE) between the fibres and matrix and the anisotropic variation in the carbon fibre through-thickness coefficient of thermal expansion (CTE_{33}) with ply orientation (refer Figure 2-96). Flat laminates with symmetric lay-ups have shape stability. However, parts with geometric complexity such as 90° brackets often exhibit warpage such as spring-in (< 90°) or spring-back (> 90°) even when the laminate has a symmetric stacking sequence [146].

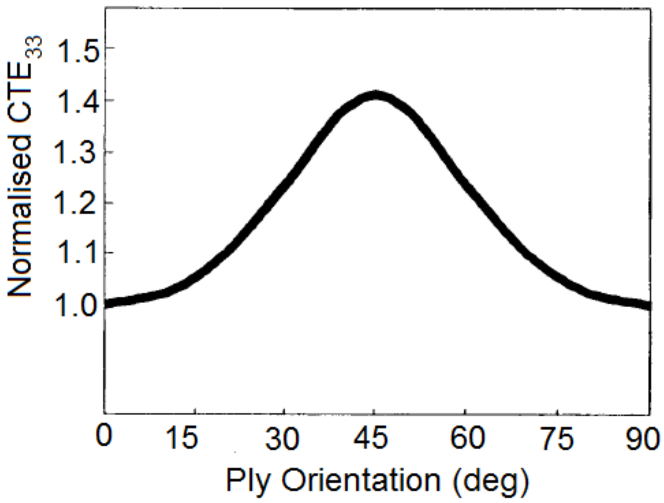

Figure 2-96 Predicted variation of through-thickness coefficient of thermal expansion of carbon fibre with changes in ply orientation [146]

Shape instability can be divided into: i) process-induced warpage; and ii) hygrothermal instability. Process induced warpage is an irreversible shape change caused mainly by resin shrinkage during cure and volatiles outgassing in-service. It can be solved by changing the mould geometry to compensate for spring-in or spring-back or an asymmetric stacking sequence (refer Figure 2-97) which will generate the desired shape at room temperature. Hygrothermal instability is a reversible out-of-plane warpage that occurs with changing temperature and humidity. Hygrothermal instability can be prevented with a stacking sequence fulfilling the conditions necessary to prevent shape instability caused by the operating environment [146].

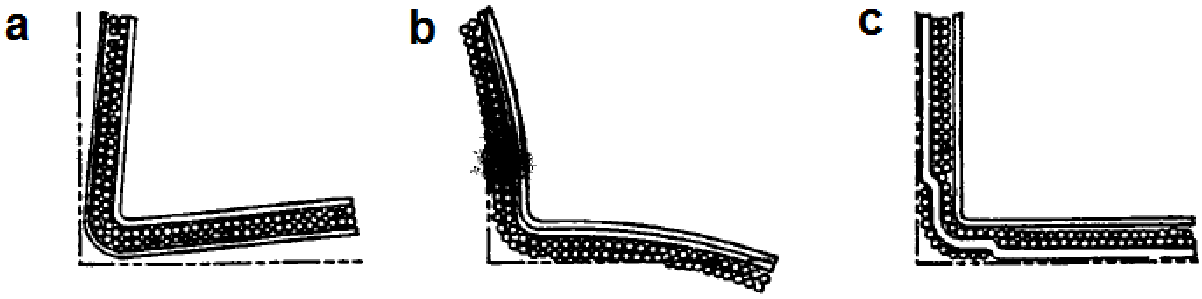

Figure 2-97 Four ply 90° angle bracket: (a) symmetric $[0/90]_{2s}$ with spring-in; (b) fully asymmetric $[0_2/90_2]$ with spring-back; and (c) optimised locally asymmetric laminate with room temperature shape stability [146]

For the case of thin laminates, assuming plane stress and small deformations, classical laminated theory (CLT) can be applied. In the absence of mechanical loading the relationship between the forces and moments due to changes in the temperature and humidity (hygrothermal input) and the mid-plane strains and curvatures of the anisotropic laminate can be expressed by Equation 2-18.

Interestingly hygrothermally stable laminate design depends only on the ply orientation and is independent of the material properties. Therefore it can be implemented early in the design process before material selection has been finalised.

$$\begin{Bmatrix} N_{xx} \\ N_{yy} \\ N_{xy} \\ M_{xx} \\ M_{yy} \\ M_{xy} \end{Bmatrix}^{(T,H)} = \begin{bmatrix} A_{11} & A_{12} & A_{16} & B_{11} & B_{12} & B_{16} \\ A_{12} & A_{22} & A_{26} & B_{12} & B_{22} & B_{26} \\ A_{16} & A_{26} & A_{66} & B_{16} & B_{26} & B_{66} \\ B_{11} & B_{12} & B_{16} & D_{11} & D_{12} & D_{16} \\ B_{12} & B_{22} & B_{26} & D_{12} & D_{22} & D_{26} \\ B_{16} & B_{26} & B_{66} & D_{16} & D_{26} & D_{66} \end{bmatrix} \begin{Bmatrix} \varepsilon_{xx} \\ \varepsilon_{yy} \\ \gamma_{xy} \\ \kappa_{xx} \\ \kappa_{yy} \\ \kappa_{xy} \end{Bmatrix}$$

Equation 2-18

Where *(T,H)* designates forces and moments that are non-mechanical and are caused by changes in temperature and humidity, N_{xx} = force in the longitudinal plane, N_{yy} = force in the transverse plane, N_{xy} = shear force in the longitudinal-transverse plane, M_{xx} = moment in the longitudinal plane, M_{yy} = moment in the transverse plane and M_{xy} = moment in the longitudinal-transverse plane, ε_{xx} = strain in the longitudinal plane, ε_{yy} = strains in the transverse plane, γ_{xy} = shear strain in the longitudinal-transverse plane, κ_{xx} = curvature in the longitudinal-plane, κ_{yy} = curvature in the transverse plane, κ_{xy} = curvature in the longitudinal-transverse plane, A_{ij} = in-plane stiffness coefficients, B_{ij} = coupled stiffness coefficients and D_{ij} = bending stiffness coefficients.

There are two conditions sufficient for hygrothermal stability [147].

Symmetric laminate

The laminate has a stacking sequence that is symmetric about the mid-plane, which means the coupled stiffness matrix equals zero (refer Equation 2-19) [147].

$$[B] = 0 \qquad \text{Equation 2-19}$$

Asymmetric laminate with hygrothermal stability

The asymmetric laminate has equal hygrothermal expansion in all in-plane directions (refer Equation 2-20) AND the non-mechanical shear force and moments are zero (refer Equation 2-21) [147].

$$N_{xx}^{(T,H)} = N_{yy}^{(T,H)} \qquad \text{Equation 2-20}$$

and

$$N_{xy}^{(T,H)} = M_{xx}^{(T,H)} = M_{yy}^{(T,H)} = M_{xy}^{(T,H)} = 0 \qquad \text{Equation 2-21}$$

Symmetric laminates are precluded from extension-bend-twist mechanical coupling because the coupling matrix [B] = 0 (refer Equation 2-23). Asymmetric laminates can exhibit various degrees of extension-bend-twist mechanical coupling because the coupling stiffness matrix is non-zero (refer Equation 2-18). It is also possible to design asymmetric hygrothermally stable stacking sequences with [B] = 0 that do not have mechanical coupling between in-plane and out-of-plane deformations [148].

Balanced laminates have matching +/- off-axis plies with equal stiffness in all in-plane directions. The in-plane stiffnesses A_{16} and A_{26} are zero (refer Equation 2-22) preventing extension-shear coupling. Unbalanced laminates have extension-shear mechanical coupling.

Balanced laminate

$$A_{16} = A_{26} = 0 \qquad \text{Equation 2-22}$$

Traditionally fibre-reinforced laminates are laid up with a balanced quasi-isotropic design to ensure processing and hygrothermal shape stability, quasi-isotropic mechanical properties and to avoid mechanical coupling. The classical laminated theory relationship for a symmetric and balanced lay-up is given in Equation 2-23.

$$\begin{Bmatrix} N_{xx} \\ N_{yy} \\ N_{xy} \\ M_{xx} \\ M_{yy} \\ M_{xy} \end{Bmatrix}^{(T,H)} = \begin{bmatrix} A_{11} & A_{12} & 0 & 0 & 0 & 0 \\ A_{12} & A_{22} & 0 & 0 & 0 & 0 \\ 0 & 0 & A_{66} & 0 & 0 & 0 \\ 0 & 0 & 0 & D_{11} & D_{12} & D_{16} \\ 0 & 0 & 0 & D_{12} & D_{22} & D_{26} \\ 0 & 0 & 0 & D_{16} & D_{26} & D_{66} \end{bmatrix} \begin{Bmatrix} \varepsilon_{xx} \\ \varepsilon_{yy} \\ \gamma_{xy} \\ \kappa_{xx} \\ \kappa_{yy} \\ \kappa_{xy} \end{Bmatrix} \qquad \text{Equation 2-23}$$

However there is a vast and mainly unexplored design space containing all permutations between extension, bend, twist and shear mechanical coupling which can be designed without undesirable hygrothermal instability by utilising Equation 2-20 and Equation 2-21 [149]. Potential applications of hygrothermally stable laminates with mechanical coupling include designing a rotor blade with extension-twist coupling to passively adjust the angle of attack with changes in rotor speed to achieve the best propulsive efficiency [149]. In this PhD project the use of non-symmetric laminates in the design of biomimetic composite joints are applied, as described in chapter four.

2.6.10 Summary of fibre-reinforced composite T-joints

Sections 2.6.1 - 2.6.9 demonstrated the importance of geometric and material parameters on the failure strength and fracture mechanics of fibre-reinforced composite T-joints and 90° brackets. Important geometric parameters that influence the strength of angled joints under bending and tensile loading include:

- Flange/overlaminate radius [104, 106, 108, 115, 116]
- Flange/overlaminate thickness [104, 106, 108, 113, 115, 116, 125]
- Horizontal skin thickness [113]
- Delta-fillet area [114, 144]

Important material parameters influencing angled joint strength include:

- Material selection [126, 127]
- Flange/overlaminate interlaminar tensile strength [104, 106, 108, 125]
- Delta-fillet stiffness [113] and tensile strength [104, 108]
- Flange/overlaminate ply stacking sequence [126, 127]

2.6.10.1 Composite T-joints under bending loading

The key geometric and material based parameters influencing the stress distribution in the critical radius bend/delta-fillet region under bending loading and their influence on T-joint strength are summarised in Table 2-15. Unknowns include the influence of horizontal skin thickness, delta-fillet area, delta-fillet stiffness, and flange ply stacking sequence.

The failure mode of carbon/epoxy T-joints under bending loading is shown in Figure 2-98. A bending moment applied to the stiffener web induces bending and shear forces on the joint that generate high interlaminar tensile and shear stresses within the radius bend due to the stress concentration resulting from the T-joint geometry. These stresses initiate delaminations in the tensile side radius bend, which then propagate through the delta-fillet, flange and stiffener.

Table 2-15 Influence of key parameters in strength of T-joint under bending loading

	Parameter	Specific Influence	T-joint Strength
Geometry	Increasing flange/ overlaminate thickness [108]	Decreases T-joint displacement Decreases in-plane stress in radius bend Decreases interlaminar tensile stress in radius bend Decreases delta-fillet principal stress	Increases (with weight penalty)
	Increasing flange/ overlaminate radius [108]	Decreases T-joint displacement Decreases in-plane stress in radius bend Decreases interlaminar tensile stress in radius bend Delta-fillet principal stress depends on radius size	Increases (limited by space requirements)
	Increasing horizontal skin thickness	Unknown	?
	Increasing delta-fillet area	Unknown	?
Material	Increasing flange/ overlaminate interlaminar tensile strength	Delays initial damage caused by delaminations in the radius bend (according to strength-based delamination criterion [128-130])	Increases
	Increasing delta-fillet stiffness	Unknown	?
	Increasing delta-fillet strength	No change (initial failure occurs in radius bend [104, 107, 113])	No change
	Flange/ overlaminate ply stacking sequence	Variations in $[0_i/90_j]$ alters stress distribution in radius bend [126, 127]	Alters failure mode, & joint strength

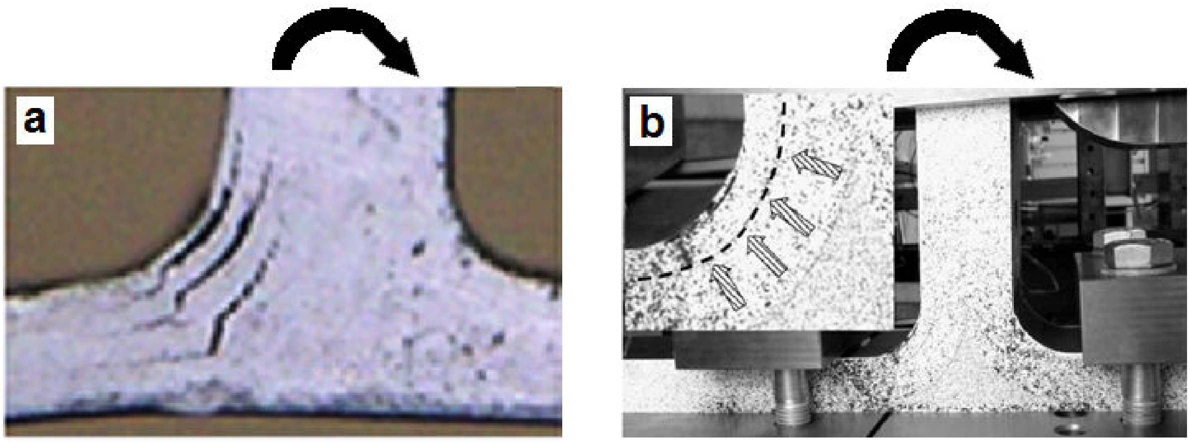

Figure 2-98 Failure modes of CFRP T-joints under bending loading: (a) web thickness ~ 3 mm [107]; and (b) stiffener thickness ~ 60 mm [113]

2.6.10.2 Composite T-joints under tensile loading

The key geometric and material based parameters influencing the stress distribution in the critical radius bend/delta-fillet region under tensile loading and their influence on T-joint strength are summarised in Table 2-16. The influence of most parameters has been researched except for the influence of the flange ply stacking sequence.

Table 2-16 Influence of key parameters in strength of T-joint under bending loading

	Parameter	**Specific Influence**	**T-joint Strength**
Geometry	Increasing flange/ overlaminate thickness [108]	Decreases T-joint displacement In-plane and interlaminar tensile stress in radius bend and delta-fillet principal stress is dependent on radius size	May increase or decrease depending on radius geometry
	Increasing flange/ overlaminate radius [108]	Decreases T-joint displacement In-plane and interlaminar tensile stress in radius bend and delta-fillet principal stress is dependent on radius size	May increase or decrease depending on radius geometry
	Increasing horizontal skin thickness	Decreases T-joint displacement Decreases peak through-thickness strain in the flange/overlaminate [123]	Increases
	Increasing delta-fillet area	Increases principal stress in delta-fillet [114]	Decreases
Material	Increasing flange/ overlaminate interlaminar tensile strength	Depends on how strength is shared between radius bend flange and delta-fillet [104]	Increases if initial failure occurs as delamination in radius bend
	Increasing delta-fillet stiffness	Decreases interlaminar & axial strain in flange/overlaminate radius bend [123]	Increases
	Increasing delta-fillet strength	Depends on how strength is shared between delta-fillet and radius bend flange [104]	Increases if initial failure occurs in delta-fillet
	Flange/ overlaminate ply stacking sequence	Variations in $[0_i/90_j]$ alters stress distribution in radius bend [126, 127]	? Can alter failure mode and joint strength if initial failure occurs in radius bend

Examples of the failure modes of composite T-joints with increasing stiffener web thicknesses are shown in Figure 2-99. In all three cases the first crack initiated in the delta-fillet and propagated either along the horizontal flange/skin interface (refer Figure 2-99b) or in the vertical mid-plane interface (refer Figure 2-99c) or both (refer Figure 2-99a).

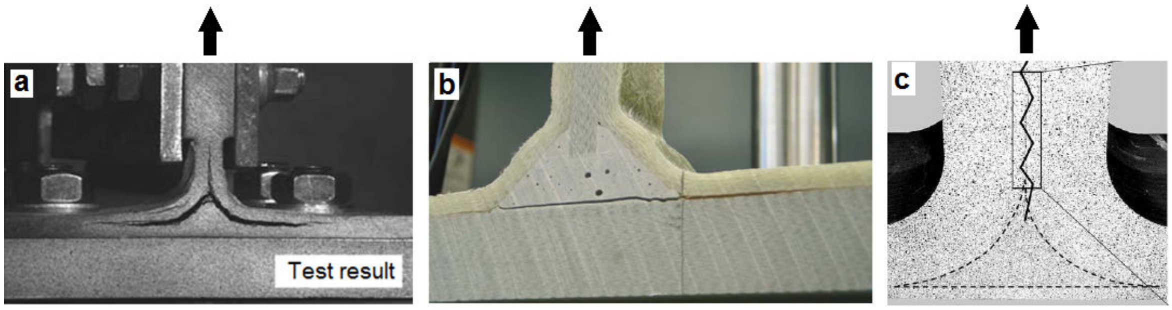

Figure 2-99 Failure modes of fibre reinforced polymer T-joints under tensile loading: (a) carbon/epoxy T-joint [115]; (b) glass/vinylester T-joint; and (c) ultra-thick carbon/epoxy T-joint [113]

2.7 CONCLUSION

Virtually all biological materials are composites containing a ceramic or fibrous strong/stiff phase reinforced by a flaw tolerant bio-polymer phase. Natural materials have a hierarchical structure ranging from the nano- to the macro-length scale. Synergistic effects across the hierarchical length scales produce composites with mechanical properties up to an order of magnitude superior to their constituent materials. Biological materials are commonly strong and stiff as well as being tough and flaw tolerant due to multiple toughening mechanisms generating rising R-curve behaviour. Natural materials respond to the local loading conditions through adaptive growth.

Bio-inspired materials have had some success in mimicking these characteristics, but have so far been unable to replicate the regularity of structure, especially at the nano-length scale that is a feature of nano-scale self-assembly (growth), due to manufacturing limitations [31, 36, 58-60]. Research into bio-inspired structures has produced designs based on the bio-inspired principles of uniform stress and zero shear stress. An adaptive growth strategy was used as a shape optimisation tool to generate a uniform stress in the adhesive of a metal bonded butt-joint [15]. Material optimisation utilising the principle of optimised fibre placement aligned with the force flow was used to increase the strength of circular notched glass and carbon composite panels by minimising shear stresses that cause fibre/matrix rupture [16-18]. In general, however, there is a lack of research into bio-inspired design for composite T-joints for aerospace applications.

Tree branch-trunk joints were chosen as the natural load-bearing joint for detailed investigation because wood is an anisotropic fibre-reinforced composite with a mechanical response consistent with carbon fibre reinforced polymers used in aerospace structures. Furthermore the branch-trunk joints undergo similar loading conditions to aerospace composite joints including static and dynamic bending moments and shear stresses. A carbon fibre/epoxy T-joint was chosen as the representative aerospace composite joint. Experimental and finite element research into the strength, failure modes and fracture mechanics of composite T-joints for aerospace and marine applications has shown the critical zone is the radius bend and delta-fillet region. Composite T-joints fail in this zone under both tension and bending loading due to the high interlaminar tensile and shear stresses resulting from the T-joint geometry coupled with the low interlaminar strength of composite materials. Parametric investigations into T-joints have quantified the effect of joint geometry (flange thickness, flange radius, horizontal skin thickness and delta-fillet area) and material selection (flange interlaminar tensile strength, delta-fillet stiffness and strength), however the effect of laminate stacking sequence is a notable omission (refer Table 2-15).

A detailed review was undertaken into the structure of wood with a focus on relating the architecture of adaptive growth in and around the tree branch to the strength, toughness and fracture mechanics of the tree branch-trunk joint. What has been learned from this review is a bio-inspired aerospace composite T-joint would be hierarchically designed with a more unified approach to integrating material and structure. Shape optimisation and material optimisation would be utilised to achieve the experimentally observed axiom of uniform strain [19] as shown schematically in Figure 2-100.

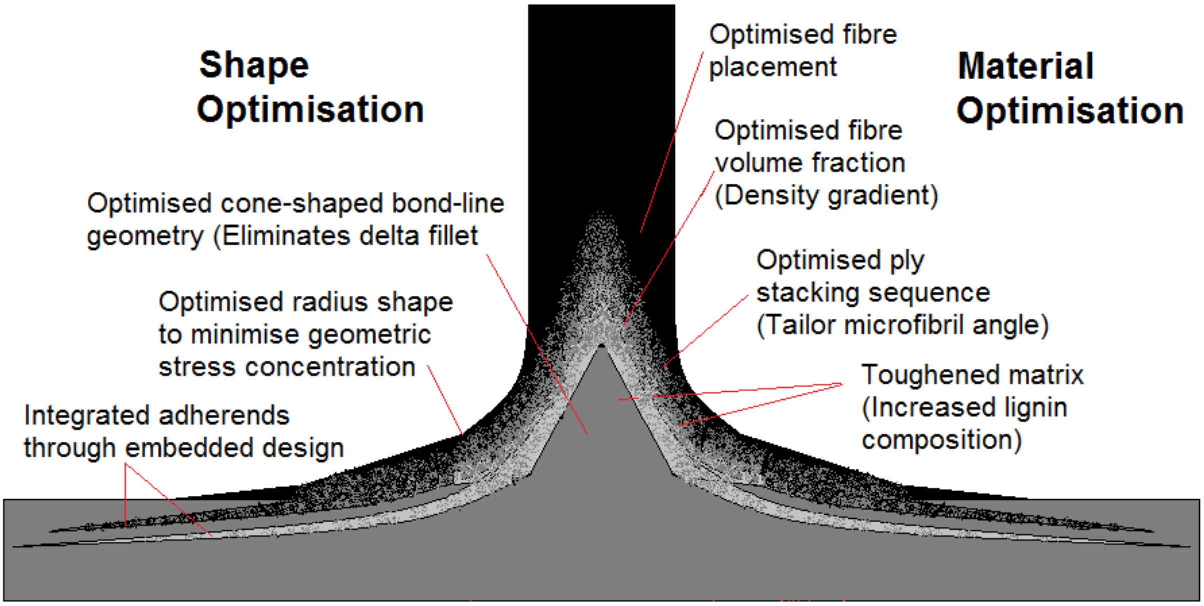

Figure 2-100 Schematic of a bio-inspired composite T-joint concept highlighting shape optimisation and material optimisation features

Shape optimisation would include: i) optimising the radius shape beyond the standard quarter-circle radius fillet to minimise the geometric stress concentration; ii) optimising the bond-line geometry into a cone-shaped design to reduce the stress concentration by increasing the load transfer area and avoiding the formation of a weak delta-fillet; and iii) integrating the adherends through embedded design.

Material optimisation would be an important consideration including: i) optimised fibre placement; ii) tailoring the fibre volume fraction to create a density gradient analogous to adaptive growth in reaction wood with a through-thickness reinforcement to prevent the formation of shear cracks analogous to the radial reinforcement of rays; iii) tailoring ply orientations in the laminate stacking sequence as a 1D simplification of the variation in the 3D helically wound microfibril angle that controls Young's modulus, strength, strain-to-failure and work of fracture in wood; and iv) toughened matrix with a flaw tolerant chemical composition in the vicinity of the joint analogous to changes in the lignin content of wood.

The shape optimisation features of optimised radius geometry [61, 62, 64] and optimised bond-line geometry [15, 63] were discounted as they have previously been investigated. Previous research into improving the toughness and impact damage tolerance of T-joints has considered toughened adhesives and through-thickness reinforcements including z-pins, stitching and 3D woven composites [139, 142, 150-152] which improve the delamination fracture toughness. However the effect of a structural change to integrate the adherends by embedding the flange into the skin has not been considered.

The material optimisation features of optimised fibre placement [16, 18, 92] and toughened matrix [139] were discounted as having already been researched. Optimised fibre volume fraction (density gradient) was ruled out as being too difficult to manufacture, leaving optimised ply stacking sequence to be selected for investigation. T-joint parametric studies have failed to consider the full spectrum of ply angles from -90° to 90° as a design variable altering the stress distribution, failure mode, fracture mechanics and strength of T-joints. This relates back to two ‘golden’ rules of composite design, namely designing laminates with balance (matching +/- off-axis plies) and symmetry about the mid-plane. Traditionally laminates are designed with $[0_i/\pm45_j/90_k]_s$ stacking sequences to ensure processing and hygrothermal shape stability, quasi-isotropic mechanical properties, and to avoid mechanical coupling. However there is a vast and mainly unexplored design space of non-standard ply orientations, including asymmetric hygrothermal laminates that can be used to exploit the full potential of anisotropic composites with potential weight and cost savings.

In summary, the shape optimisation feature of integrated adherends through embedded design and the material optimisation feature of optimised ply stacking sequence were selected for investigation in this PhD project. These two bio-inspired features provided ample scope, both as individual concepts and together as a hierarchical design.

CHAPTER 3:

3 CHARACTERISATION OF THE TREE BRANCH-TRUNK JOINT

3.1 INTRODUCTION

Trees were selected for detailed investigation because wood is an anisotropic composite with a mechanical response similar to CFRP laminates (refer Figure 2-29) [51-53]. Furthermore, tree branch-trunk joints have many structural properties which are desirable in composite joints, including strength, toughness, fatigue resistance and damage tolerance [45-49]. However it is important to note that the design drivers of engineered composite T-joints and tree branch joints are not identical. Composite T-joints are generally designed for ultimate strength, with due consideration given to other properties such as barely visible impact damage (BVID) resistance, stiffness, fatigue and damage tolerance. In contrast, tree branch joints must maintain structural integrity, which requires sufficient static strength to resist the bending moment profile and shear forces as a result of self-weight and wind, fatigue properties sufficient to resist cyclic wind loading, and damage tolerance; although the relative importance of these properties is not quantifiable.

In addition, the structure of trees is complicated by biological considerations such as vascular flow and cell function. Biological processes mean trees are under constant 'structural health monitoring' and have the ability to self-heal, meaning the onset of damage at relatively low loads may be less significant for trees than in engineered composite joints because small cracks in the branch/trunk connection will be instantly located and can be repaired. Therefore, design for resistance against first failure may be less critical in tree joints than in composite T-joints and the tree branch-trunk joint may be optimised towards high damage tolerance and maximum work-of-fracture under the prevailing loading conditions.

Trees respond to the prevailing loading conditions caused by wind gusts and the self-weight of the branch by tailoring both the material properties of the wood cell wall (nano-length scale [54]), wood cell (micro-length scale [53]) and the structural features of the joint (meso and macro-length scales [46, 47]), as discussed in chapter two. This hierarchical strategy of combining elements from the nano-, micro-, meso- and macro-length scales counteracts the strain concentration caused by load transfer across the geometry of the joint where the branch connects to the trunk. As a result of this strategy, trees attain a near iso-strain response across the joint (refer Figure 2-46) [19].

The research into the characterisation of the tree branch-trunk joint considered samples from the species Radiata pine (*Pinus radiata*) which was chosen as a softwood representative of most wood species. The aims were to: i) determine the macro-architecture of the branch-trunk joint; ii) determine the micro-architecture of the branch-trunk joint; iii) determine the damage and failure modes of the branch-trunk under gravity direction and reverse direction bending loading in order to achieve the overall aim; iv) to understand the interaction between the hierarchical architecture and the mechanical response of the tree branch-trunk joint. These aims link back to the central scope of the PhD to determine what architecture and organisational principles observed in natural load bearing structures can be transferred to composite T-joints through biomimetic engineering.

3.2 EXPERIMENTAL METHODOLOGY

Twenty-two freshly cut branch-trunk joints were collected from two softwood trees of the species Radiata pine (*Pinus radiata*) (refer Figure 3-1a) from HVP plantations in Gippsland, Victoria. Tree A was located at 146.217°, -38.217° decimal degrees and tree B was located at 147.055°, -38.233°. The two plantation trees had an identical age (planted in 1994) and growth history to minimize the variability in mechanical properties between specimens. The specimens consisted of a straight section of the trunk about 500 mm long with a single branch about 150 mm long. The diameter of the trunks ranged from 22 – 159 mm with an average diameter of 90 mm ± 39 mm. The diameter of the branches varied from 17 – 45 mm with an average diameter of 30 mm ± 8.7mm. The angle between the branch and the trunk was measured using a protractor (refer Figure 3-1b) and ranged from 46 - 88° with an average of 64° ± 12°. The moisture content of the wood was measured to be in the range of 30 – 38 % by volume, and the wood was not dried prior to mechanical testing (green wood).

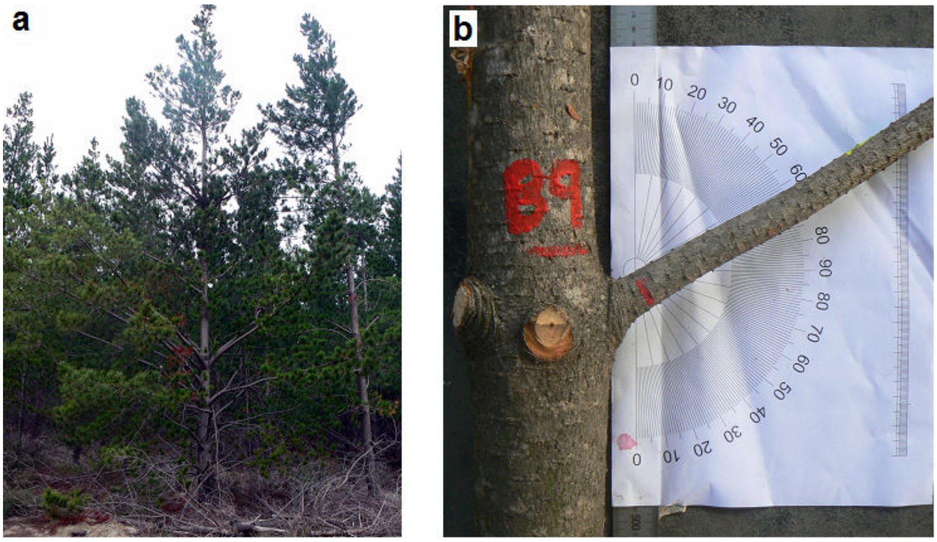

Figure 3-1 (a) Radiata pine tree A; and (b) measuring the angle in the branch-trunk joint specimen

The structural properties of the tree branch-trunk joints were investigated using the test set-up shown in Figure 3-2.

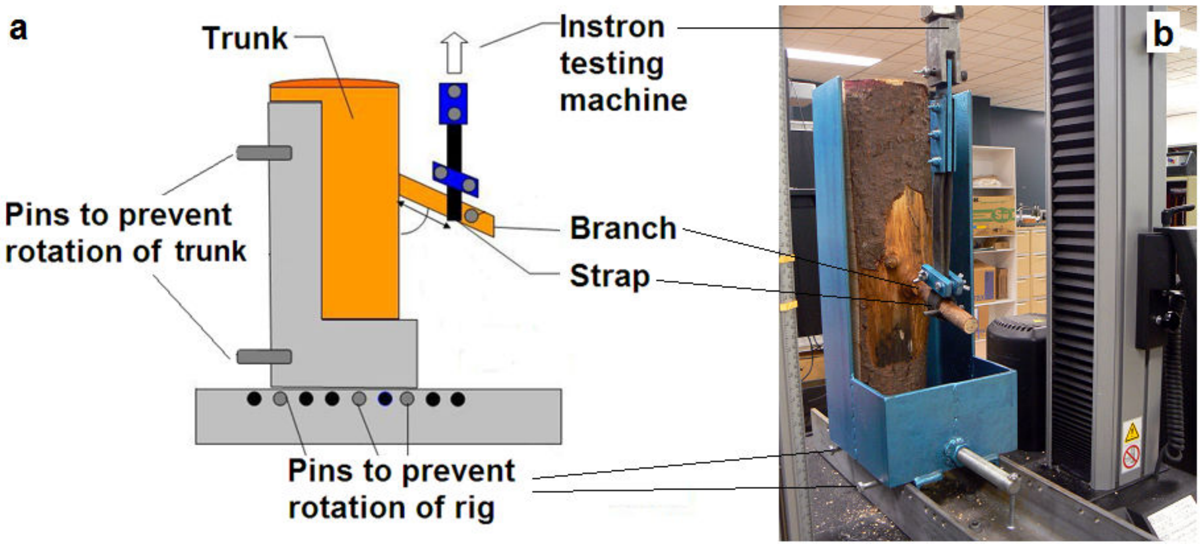

Figure 3-2 (a) Schematic of bending test set-up; and (b) photograph of bending test rig

The bark was removed from the specimen and the trunk was rigidly fixed by bolts to the test frame to ensure it did not move during testing. The branch was loaded at a vertical displacement rate of 3 mm/min via a strap attached to the crossheads of a 50 kN Instron machine. This loading condition induced a bending moment at the connection between the branch and trunk. Eight samples of the branch-trunk joint were tested under bending loading in the same direction as the gravity self-weight of the branch (refer Figure 3-3a) and seven samples in the reverse direction (refer Figure 3-3c). Several branches were bisected along the vertical axis of the trunk and seven bisected samples were tested under bending loading in the same direction as the gravity self-weight of the branch (refer Figure 3-3b).

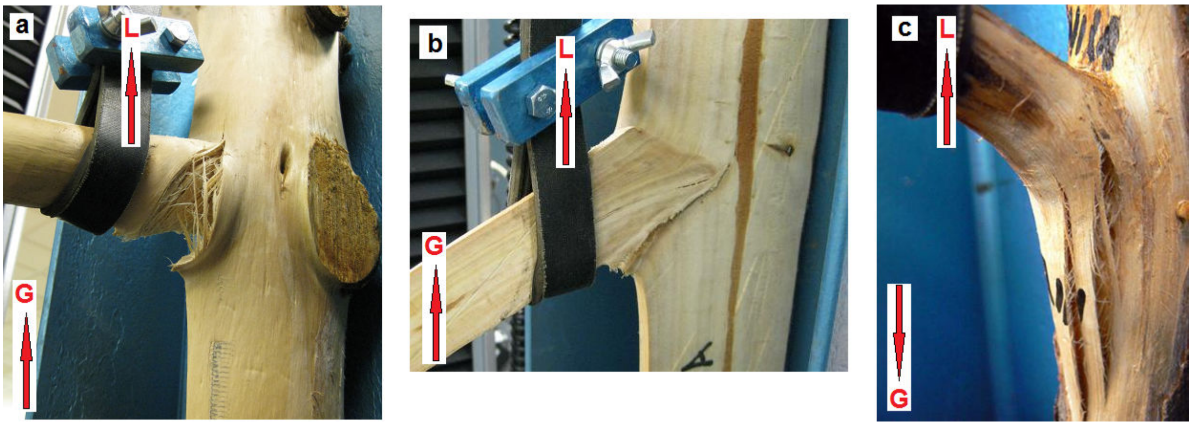

Figure 3-3 Bending loading in: (a) gravity direction on intact joint; (b) gravity direction on bisected joint; and (c) reverse gravity direction on intact joint. L = loading direction and G = gravity direction of the self-weight of the branch

Bending stress was calculated using the flexural formula given in Equation 3-1 with the geometric parameters given in Figure 3-4 where the dashed line represents the branch before the bending load is applied, the solid line represents the trunk and branch shortly before fracture. The moment arm from the base of the branch to the centre of the strap was multiplied by the bending force to calculate the bending moment. The semi-major and semi-minor axes at the base of the elliptical branch were measured with callipers and used to calculate the moment of inertia, assuming constant density. The distance from the neutral plane was calculated by halving the vertical semi-major axis of the branch.

$$\sigma_b = \frac{My}{I} = F \times a \times \frac{r}{I} \qquad \text{Equation 3-1}$$

Where σ_b = bending stress, M = bending moment, y = distance from the neutral plane to tension surface of the branch, I = moment of inertia of the oval branch, F = the critical bending force, a = effective lever arm shortly before breakage and r = major radius of the oval branch.

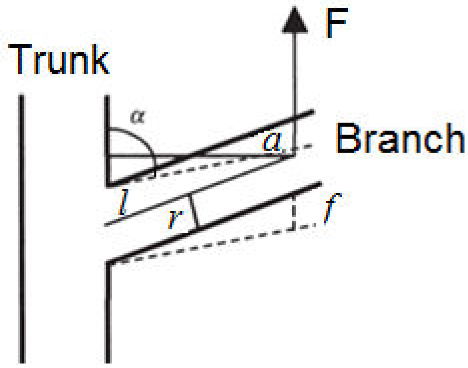

Figure 3-4 Geometric parameters used to calculate bending stress from the experimental data

Tensile testing was used to measure the transverse mechanical properties of branch wood. Twelve dog bone shaped coupons were cut from the tangential-radial plane (refer Figure 3-5a), twenty samples from the radial-longitudinal plane (refer Figure 3-5b) and four samples from the branch-trunk joint (refer Figure 3-5c).

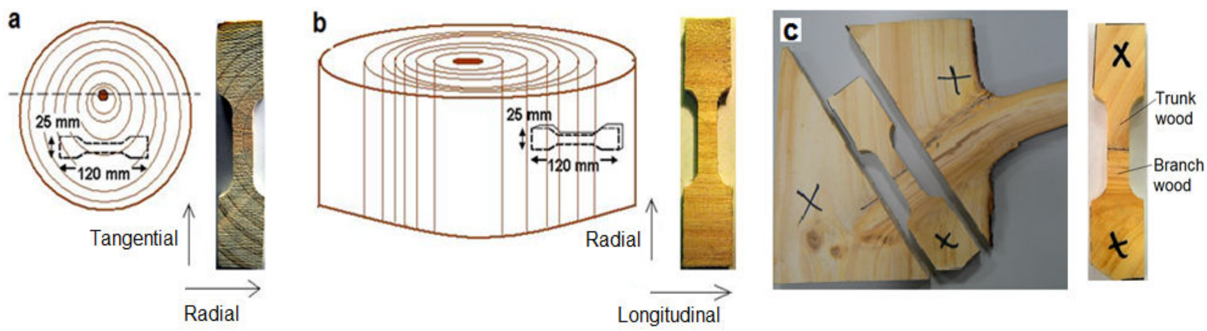

Figure 3-5 Dog bone coupons cut from: (a) tangential-radial plane; (b) radial-longitudinal plane; and (c) across the branch-trunk joint

The dog bone coupons had the geometry and dimensions shown in Figure 3-6a-b. The rectangular tabs were placed in the Instron grips and loaded under tensile load at a displacement rate of 1 mm/min until failure, which occurred in the thin test-section of the dog-bone geometry where an extensometer was attached (refer Figure 3-6c).

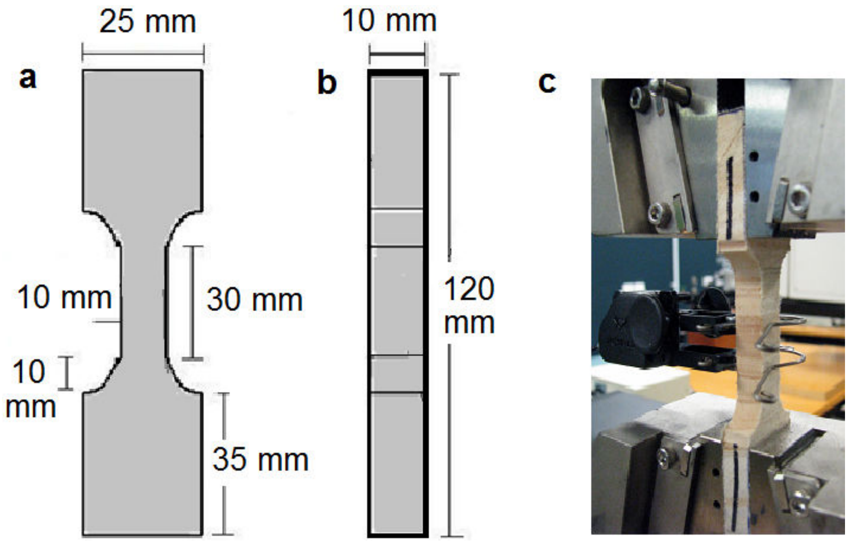

Figure 3-6 Dimensions and geometry of dog bone coupons: (a) front view; (b) side view; and (c) test-set-up for tensile loading with an extensometer attached to measure the strains in the working section

The imaging techniques of x-ray computed tomography (CT), x-ray micro-computed tomography (micro-CT) and scanning electron microscopy (SEM) were used to characterise the internal structural features and fracture surfaces of the tree branch-trunk joint. The internal macro-structural features were analysed with CT using a Siemens Somatom Sensation 64. Two wood branch-trunk joints were selected for macro-scale CT imaging. The two tree branch-trunk joints were scanned in the front (refer Figure 3-7a), side and plan view orientations with a slice width of 0.5 mm, producing about 100 images for each through-thickness scan. The initiation and development of damage in the tree branch joints under increasing bending strain were investigated using micro-CT with a Skyscan 1072 at a resolution of 12 microns (refer Figure 3-7b) and SEM (Philips XL30).

Joint A had a symmetrical branch-trunk joint and had not undergone bending testing. Joint B had an asymmetrical branch-trunk joint and had undergone gravity direction bending testing.

Symmetry could be measured by the location of a feature known as the branch seam. The branch seam is the point where the wood tissue in both the branch and trunk diverges 90° around the radial direction of the branch. It is analogous to the 'stagnation point' in the model of wood grain patterns around the branch utilising streamlines as shown in Figure 2-45b. A symmetrical joint had the branch seam located in the centre of the branch-trunk junction as shown in Figure 3-8a. An asymmetric joint had the branch seam rotated around the elliptical radius of the branch as shown in Figure 3-8b.

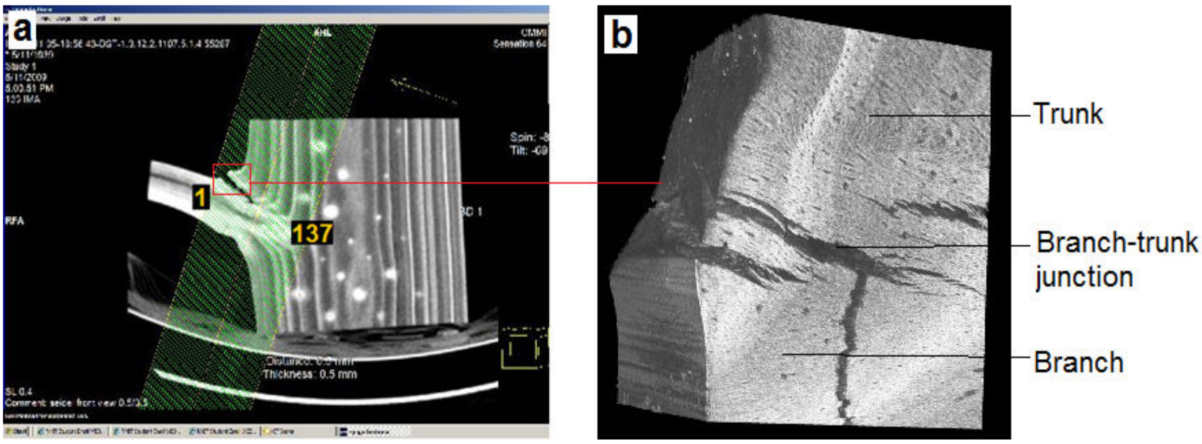

Figure 3-7 (a) CT scan across the front view of Joint B showing cracking damage. 1 = first cross-sectional slice and 137 = last cross-sectional slice; and (b) micro-CT of micro-scale damage across the branch-trunk joint

3.3 RESULTS AND DISCUSSION

3.3.1 Structural properties

CT revealed three main design features which control the mechanical properties of tree joints, as described below.

3.3.1.1 Embedded design with cone-shaped internal branch structure

The tree branch-trunk joint has an embedded design in which the cone-shaped internal branch structure is enclosed internally within the main trunk (refer Figure 3-8a). In contrast, conventional composite T-joints maintain separation between the adherends without any embedment. The cone-shaped internal branch structure increases the effective load transfer area of the joint compared to the butt-shaped connections used in composite T-joints.

The increase in the load transfer area created by the cone-shaped design reduces the stress acting at the branch-trunk interface under an externally applied load and is analogous to the shape attained by optimisation of a butt-joint in tension (refer Figure 2-22 and Figure 2-23). The cone-shaped structure also provides increased toughness by forcing interfacial cracks between the branch and trunk to grow in mode II (shear) rather than in mode I (crack opening tension). The fracture toughness mode ratio (G_{IIc}/G_{Ic}) of freshly cut *Pinus radiata* is about 11 [153], thus forcing crack growth to occur under the mode II condition which greatly increases the fracture toughness of the tree joint.

Figure 3-8b shows the internal structure of an asymmetric branch-trunk joint. The branch is curved down due to external loading strains in the direction indicated by the arrow, most likely caused by a prevailing wind load on the branch. The architecture and structural properties of the branch-trunk joint are dependent on the external loading conditions acting on the tree which govern adaptive growth, as discussed in chapter two.

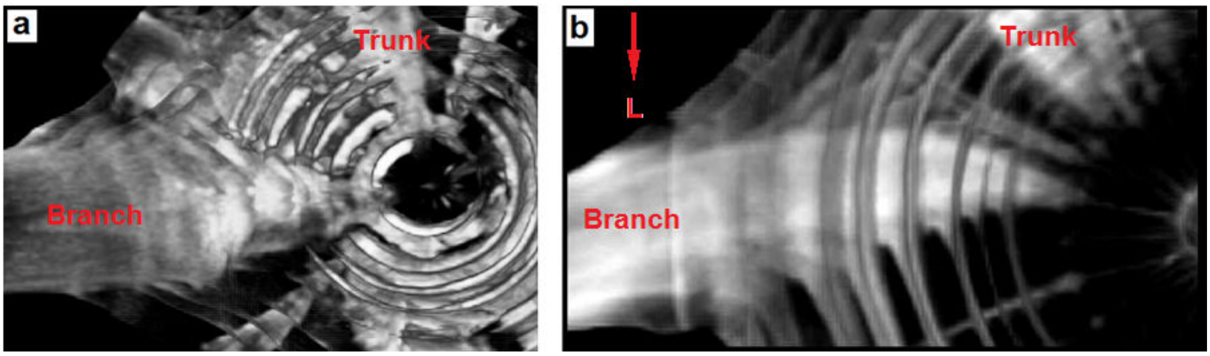

Figure 3-8 CT image of the plan view showing cone-shaped internal branch structure: (a) symmetric branch-trunk joint (joint A); and (b) asymmetric branch-trunk joint (joint B). L refers to loading direction on branch

3.3.1.2 Three-dimensional fibre lay-up

Figure 3-9 shows fibrils in the wood grain tissue are arranged in a complex three-dimensional lay-up which is aligned along the principal directions of applied stress. The fibrils aligned along the trunk extend both laterally (refer Figure 3-9a) and forward (refer Figure 3-9b) at the joint to fully encase the branch in a 'ball and socket' union that supports the branch and aids load transfer. In contrast, engineered composite joints are restricted to a two-dimensional fibre pattern along the planes of the adherends.

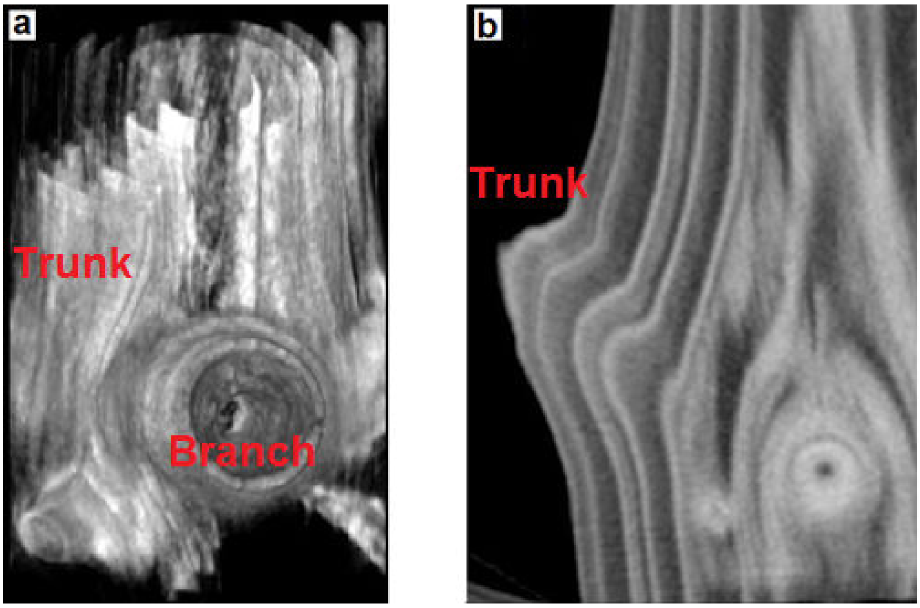

Figure 3-9 CT image of the 3D fibril lay-up of the wood grain tissue: (a) front view showing the trunk tissue ('socket') extending laterally around the branch ('ball') to encase the branch in a 'ball-and-socket' type union; and (b) side view showing the trunk tissue extending forwards

3.3.1.3 Variable density

The density of wood, which is defined by the packing density governed by the wood cell (tracheid) shape, diameter and wall thickness, changes through the joint as shown qualitatively in the CT image presented in Figure 3-10. Brighter spots indicate zones of higher density. The highest density is located in regions of maximum tensile and compressive stress under bending loading caused by the self-weight of the branch, which coincides with the location where the wood fibrils undergo directional change from the trunk to branch. Dark area indicating lower density is located at the neutral axis of the branch in the area of zero bending strain. Density variation can be interpreted as a change in fibre volume fraction across the joint. This reduces the mismatch in the elastic moduli between fibrils aligned with the trunk and branch directions, and thereby creates near iso-strain conditions through the joint. In contrast, engineered composite joints maintain a uniform fibre volume fraction across the plies in the radius bend, resulting in a large stiffness discontinuity between the radius bend and the delta-fillet region.

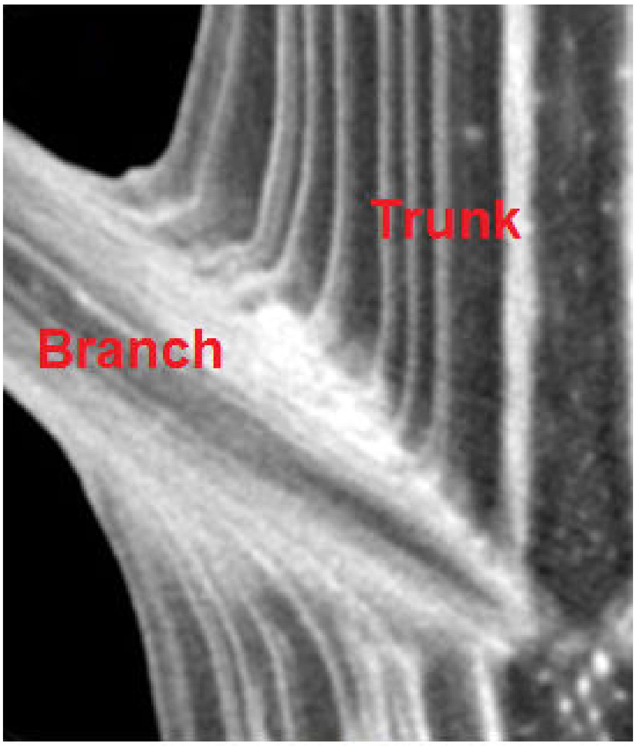

Figure 3-10 CT image of the side view of the tree branch-trunk joint showing variation in fibril density across branch-trunk joint

In addition, periodically varying Young's modulus across the earlywood/latewood growth rings provides an extrinsic toughening mechanism for arresting crack growth by reducing the crack driving force [26].

It has previously been shown by a direct strain measurement technique (ESPI) that uniform strain is achieved across the branch-trunk joint of a similar softwood species [19]. The three design features of embedded design, three-dimensional fibre lay-up and variable density work together to counteract the stress concentration caused by the tree joint geometry. Furthermore, these design features provide high damage tolerance in green wood by restricting unstable crack growth through the otherwise brittle cellular structure of the wood.

3.3.2 Mechanical properties and failure modes

3.3.2.1 Gravity direction bending load

The mechanical response of the tree branch-trunk joint under a bending moment acting in the gravity direction corresponding to the self-weight of the branch was determined using the test set-up shown in Figure 3-2. Typical bending load-displacement curves for the tree branch and conventional CFRP T-joint are presented in Figure 3-11 and the damage modes and failure mechanisms of tree joints loaded under gravity direction bending loading are shown in Figure 3-12. The load-displacement curves have been normalized to their maximum bending load, although a quantitative comparison is meaningless because of the different sample sizes and shapes. However, the curves can be used to qualitatively compare the loading response of a tree branch joint to a conventional carbon/epoxy composite T-joint.

The tree joint shows linear-elastic deformation followed by inelastic deformation with increasing displacement prior to peak load. The inelastic deformation occurs over a large displacement range which indicates that significant permanent deformation occurs in the tree joint before it reaches ultimate strength. This inelastic deformation correlates to the damage mode of radial cracking around the tensile side of the branch circumference at the interface of the branch and trunk growth rings as shown in Figure 3-12a. In contrast, the composite T-joint exhibits linear-elastic behaviour with increasing displacement until the ultimate load, when an abrupt drop in load-carrying capacity occurs due to unstable delamination cracking along the flange-skin bond-line.

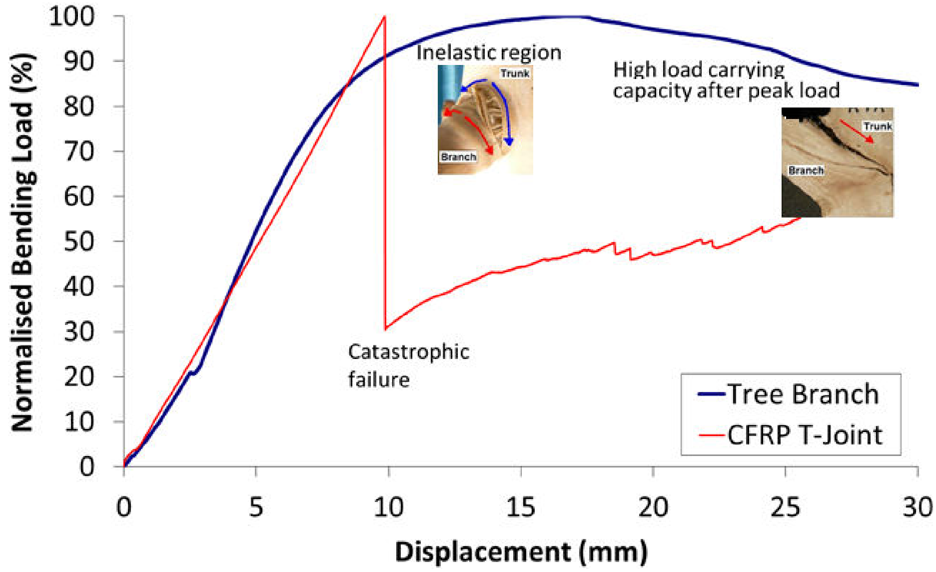

Figure 3-11 Typical bending load-displacement curve for tree branch-trunk joint and CFRP T-joint

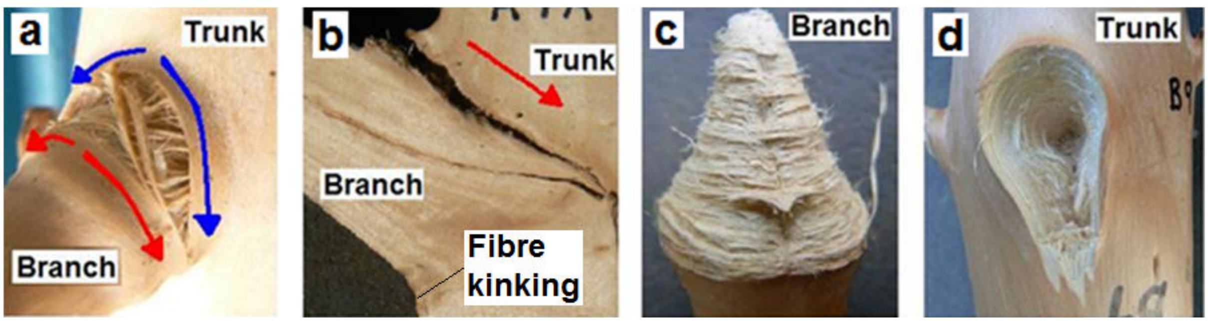

Figure 3-12 Gravity direction bending-induced damage modes in the tree-branch joint: (a) radial cracking around the tensile side of the branch circumference; (b) longitudinal cracking along the internal branch-trunk junction; (c) branch fracture surface; and (d) trunk fracture surface after complete joint failure

The tree joint does not fail catastrophically at the peak load. Instead, the tree joint retains high load-bearing capacity with increasing displacement after the onset of first failure, which is indicative of stable damage growth. This correlates with the damage mode of longitudinal cracking along the branch-trunk junction where there are no continuous fibres between the branch and the trunk, as shown in Figure 3-12b. Fibril kinking is visible on the compression side of the joint. The branch-trunk junction is the pre-determined point of weakness forcing the crack to growth in mode II (shear) rather than mode I (crack opening tension). As mentioned, wood is about 11 times tougher in shear [153] so forcing the crack to grow in mode II is advantageous to the toughness of the joint. Figure 3-12b also shows the secondary damage mode of local buckling and kinking of fibrils on the compression side of the branch. A cross-section through-the-thickness of the side view of the branch-trunk joint showing the progression of the cone-shaped crack path is given in Figure 3-13.

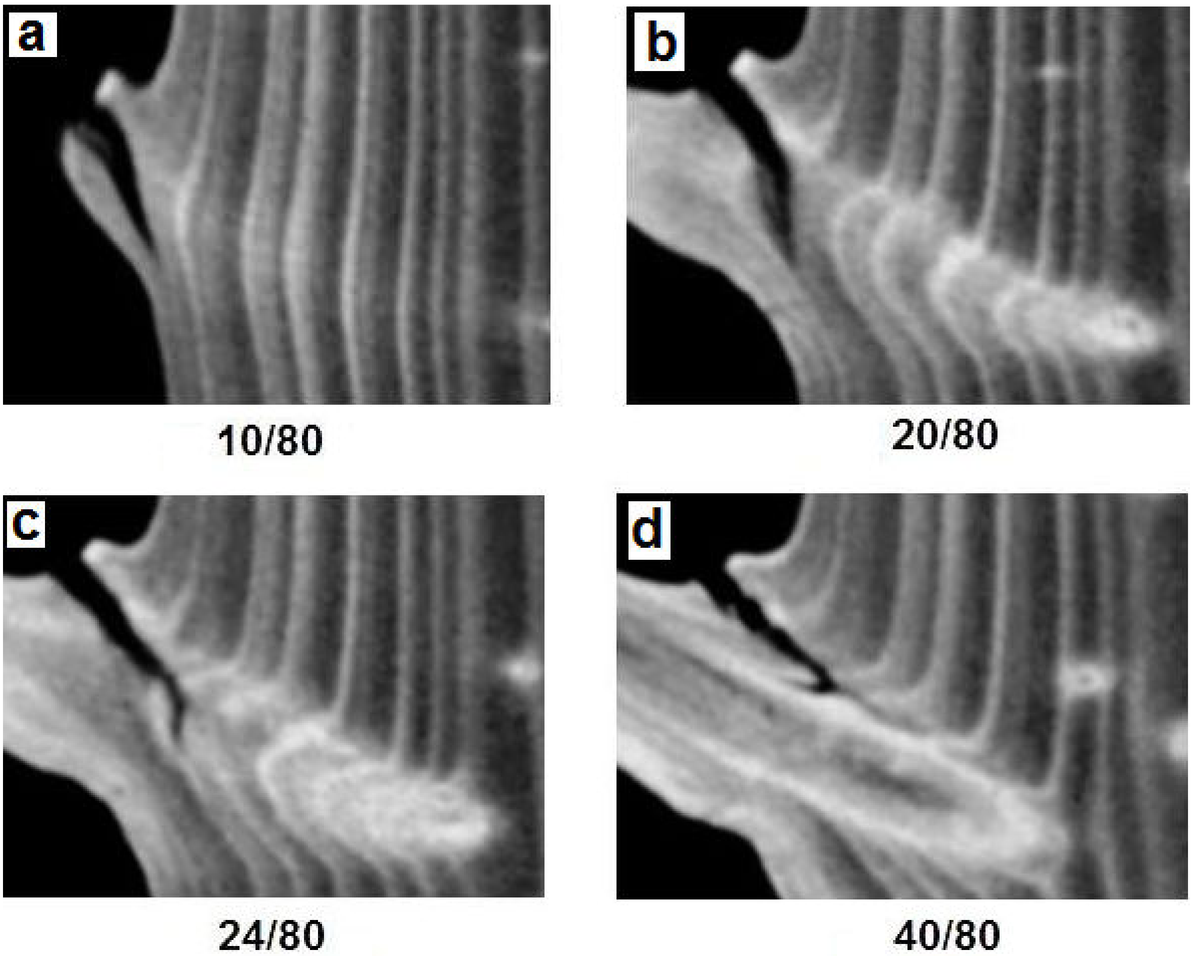

Figure 3-13 CT images of the side view of the branch-trunk joint showing development of crack through-the-thickness of the joint. Bright zones indicate areas of highest density: (a) image 10/80; (b) image 20/80; (c) imagine 24/80; and (d) image 40/80 (mid-point)

In Figure 3-13a, image 10/80 shows the appearance of the branch growth rings and location of the crack path propagating in the radial direction around the branch. In Figure 3-13b, image 20/80 shows the cone-shaped internal branch architecture with higher density growth rings and the location of crack path follows both longitudinal and radial directions in and around the branch. In Figure 3-13c, image 24/80 shows the location of the crack path transitioning from the radial to the longitudinal direction. In Figure 3-13d, image 40/80 at the centre of the branch cross-section shows the crack path dominated by the longitudinal direction.

The crack continues to propagate both radially and longitudinally along the three-dimensional cone-shaped fracture surface across the branch-trunk junction, retaining the capacity to transfer load as cracking proceeds over large displacements beyond the peak load. Final failure occurs with complete pull-out of the branch. Both the branch and trunk exhibit rough, fibrous, corrugated fracture surfaces after complete joint failure (refer Figure 3-12c-d). This failure mode is consistent with observations of branch failure occurring in nature (refer Figure 3-14).

This testing shows that tree joints have high residual strength after peak load and can be deformed over a large strain beyond the onset of cracking, indicating high damage tolerance. In the tree, material and structure work in synergy to resist unstable crack growth. The bending testing revealed that green tree branch joints deform via inelastic (non-brittle) fracture processes, despite the constituent of the wood fibrils (cellulose) and the fibril binder (hemi-cellulose and lignin) both being intrinsically brittle.

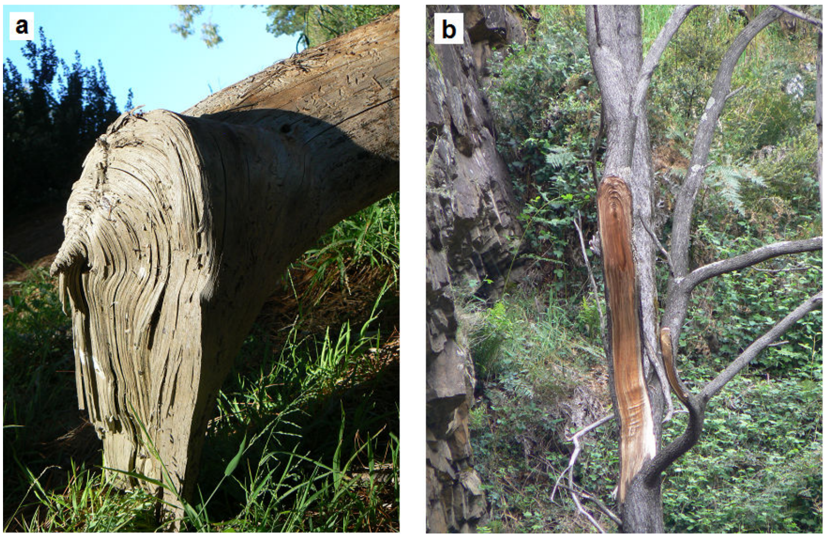

Figure 3-14 Natural branch-trunk joint fractures observed in nature showing: (a) branch fracture surface showing cone-shaped internal branch architecture; and (b) trunk fracture surface after branch has pulled out

The mechanical responses of the symmetric joint from Figure 3-15a and the asymmetric joint from Figure 3-15b are given in Figure 3-16. The two branch-trunk joints showed similar stiffness, although the bending strength of the asymmetric joint was greatly reduced. The maximum bending strength of the asymmetric joint was about one-third of the symmetric joint. An observation from the gravity direction bending mechanical testing was that the joint properties were highly dependent on alignment of the loading direction with the symmetry of the joint. This was due to the misalignment between the tree joint architecture and the loading direction. Where the symmetric joint architecture was aligned with the loading direction of the vertical shear force, the joint showed superior strength because fibrils on both sides of the joint seam were equally loaded. Where the joint architecture was misaligned with the loading direction the fibrils on one side of the branch seam had to take a disproportionate amount of load, becoming overloaded and consequently failing under a reduced load.

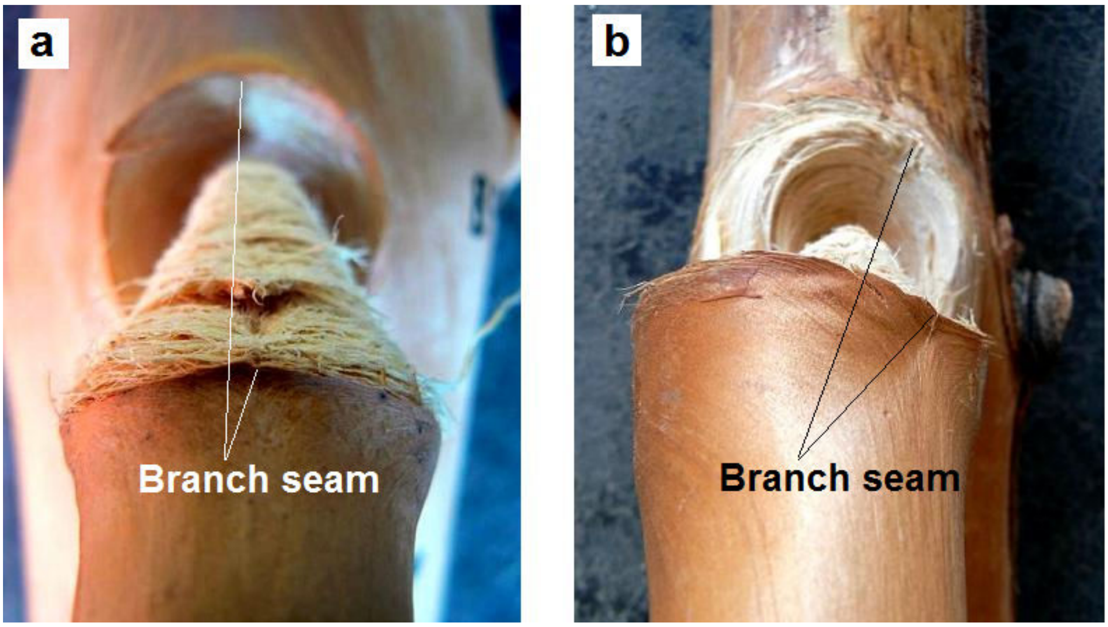

Figure 3-15 (a) Branch seam aligned with the vertical loading direction showed superior bending strength and toughness compared to (b) branch seam misaligned with the vertical loading direction.

This asymmetric branch-trunk joint was probably subject to eccentric loading conditions such as a prevailing wind side load and tailored the architecture of the joint to the conditions under which the tree grew. The misalignment between the branch seam and the loading direction was an artificial construct of the testing in which the asymmetric joint was tested in a way in which it was never adapted to be loaded. If the loading direction was rotated to align with the branch architecture the ‘asymmetric’ joint would almost certainly exhibit similar strength to the ‘symmetric’ joint.

Figure 3-16 Gravity direction bending strength of tree branch-trunk joints was strongly dependent on the alignment of the branch-trunk junction ‘branch seam’ with the loading direction

3.3.2.2 Bisected branch-trunk joint under gravity bending load

Gravity direction bending testing was conducted on tree branch-trunk joints bisected about the longitudinal axis of the tree trunk utilising the same test fixture (refer Figure 3-17a). The failure modes were the same as those observed for the intact joint as discussed in section 3.3.2.1. This involved damage to the tensile side radius bend with cracking in the radial direction around the branch-trunk growth ring interface (refer Figure 3-17b) followed by cracking along the longitudinal branch-trunk junction (refer Figure 3-17c) with a half cone-shaped fracture surface (refer Figure 3-17d).

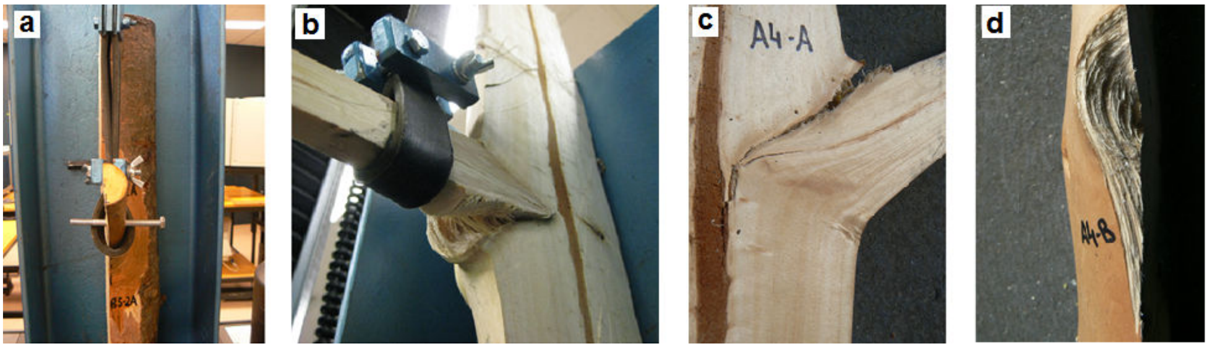

Figure 3-17 Bisected branch-trunk joint under gravity direction bending loading: (a) test set-up; (b) initial failure mode of radial cracking around the branch tensile side radius bend; (c) longitudinal cracking on tension side and fibril kinking on the compression side; and (d) cone-shaped trunk fracture surface

The mechanical response is given in the bending load-displacement curve shown in Figure 3-18. Taking into account the reduced area the bisected branch joint attained a similar bending strength compared to the intact branch joint. However the bisected joint showed reduced load carrying capacity following peak load (damage tolerance), compared to the intact joint (refer Figure 3-18). This was due to a reduction in the stability of the bisected joint where the branch was free to move laterally about the longitudinal axis of the trunk.

Figure 3-18 The intact branch and bisected branch-trunk joint have roughly equal bending strength but the bisected branch showed reduced load-carrying capacity following peak load

3.3.2.3 Reverse bending load

Under reverse bending loading opposing the gravity self-weight of the branch the failure mode was markedly different due to the reversal of the tensile and compressive forces acting on the branch architecture. In the gravity loading direction there are no continuous fibrils running from the branch into the trunk on the tensile side of the joint and consequently the branch pulls out along the cone-shaped branch-trunk junction (refer Figure 3-15). In contrast, under reverse bending loading there are continuous fibrils running between the branch and trunk on the tensile side of the joint. As the branch displacement increased the tensile stress was taken up by these wood grain fibrils. Eventually the interlaminar tensile and shear stresses induced by the geometry of the joint caused delamination between the wood grain fibres. The initial delamination in the tree was observed about one-third through-the-thickness of the tensile side radius bend of the branch as shown in Figure 3-19a, which was similar to the initial delamination failure location in the carbon/epoxy T-joint under bending load (refer Figure 3-19b). The final failure to the tree joint involved extensive delamination in this radius zone which propagated downwards causing widespread damage in the trunk (refer Figure 3-20a) which was similar to the final failure mode of the composite T-joint under bending (refer Figure 3-20b). The damage to the trunk under reverse loading was greater than under gravity direction loading (refer Figure 3-12d) in which the tree is adapted so branch failure does not cause catastrophic damage to the entire tree.

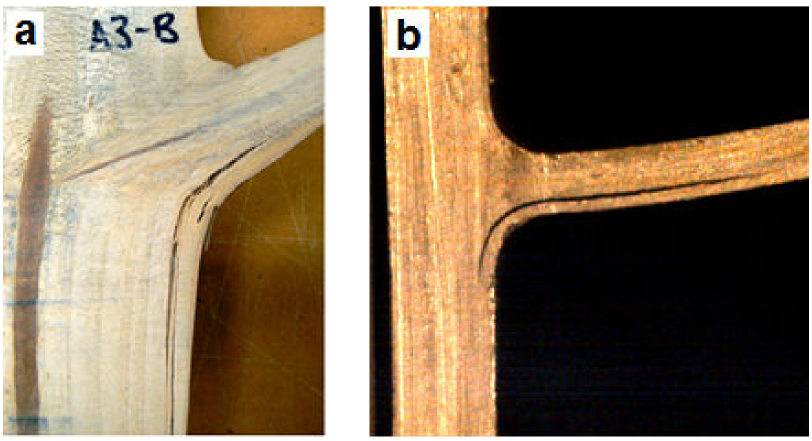

Figure 3-19 Initial failure mode of delamination: (a) tree branch-trunk joint under reverse bending loading compared to (b) composite T-joint

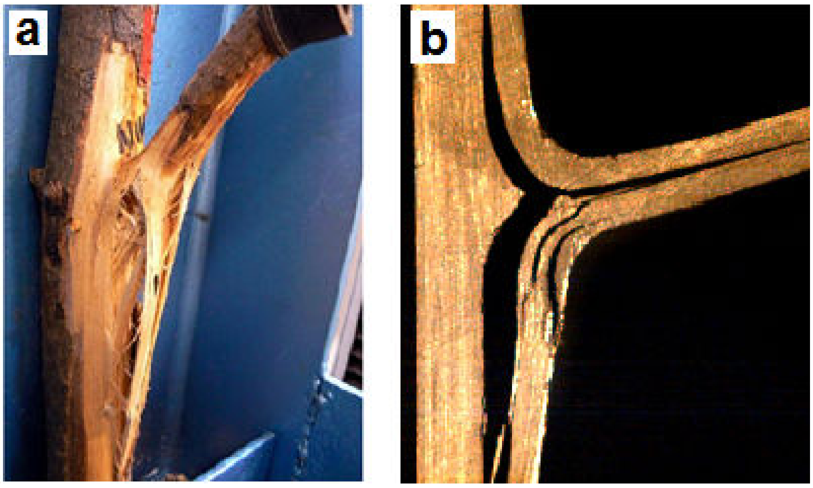

Figure 3-20 Final failure mode of multiple delamination failure: (a) tree branch-trunk joint under reverse bending loading with extensive damage to the trunk compared to (b) composite T-joint

The mechanical response is given in the bending load-displacement curve shown in Figure 3-21. The initial linear-elastic stiffness is similar in comparison to the gravity direction loading configuration. The gravity loaded joint enters the inelastic phase (corresponding to the initiation of the radial cracking damage mode around the interface of the branch-trunk joint - refer Figure 3-12a) at a lower displacement compared to the reverse loaded joint (corresponding to wood fibril delamination - refer Figure 3-19a). In comparison, the bending strength of the joint under reverse loading is similar but after the onset of delamination damage the strength decreased rapidly and the toughness and ductility was greatly reduced. The gravity direction loaded joint maintains a higher load carrying capacity (damage tolerance) over a much larger bending displacement. This is due to combined micro-level toughening mechanisms of the wood and the macro-level joint architecture resulting in controlled crack growth along the cone-shaped internal branch structure.

Table 3-1 compares the average bending strength of the tree branch-trunk joint under both gravity direction and reverse bending loading to the bending strength of wood. Omitting the asymmetric gravity direction specimens in which the misalignment between the branch seam and the loading direction was greater than 5° (which caused artificially premature failure) the joint is perfectly efficient in terms of being equal to the strength of the material (wood). This is achieved in both the gravity and reverse gravity directions, despite the very different architectures in the joint.

Figure 3-21 The bending strength under reverse gravity loading is slightly higher but the toughness, ductility and damage tolerance of the joint is greatly reduced

Table 3-1 Bending strengths of wood and the branch-trunk joint

	Bending strength (MPa)	**Excluding joints with asymmetric branch seam misalignment >5°**	**Percentage of bending strength of wood**
Pinus radiata [50]	41.9		
Branch-trunk joint under gravity direction bending load	31.7 ± 10.4	40.0 ± 10.7	76% (96%)
Branch-trunk joint under reverse bending load	43.1 ± 12.2		103%

3.3.3 Transverse mechanical properties in the branch-trunk joint

Representative tensile stress-strain curves from the dog bone coupons taken from the transverse directions in and close to the branch-trunk joint are shown in Figure 3-22. The radial-longitudinal (R-L) and the branch-trunk joint samples showed close to linear-elastic mechanical behaviour prior to failure. The tangential-radial (T-R) samples showed some inelastic deformation prior to failure.

Figure 3-22 Representative transverse tensile stress-strain curves for *Pinus radiata*

The tensile mechanical properties of the transverse samples are given in Figure 3-23 with standard deviations. The coupons from the tangential-radial plane had the lowest tensile strength and modulus which is consistent with results from literature (refer Table 2-7). The wood was about four times stiffer and three times stronger in the radial-longitudinal plane due to the presence of rays reinforcing the radial direction; however the tensile strength results showed a large amount of scatter. The branch-trunk junction showed the highest average modulus and strength, also with high scatter. This was probably due to variation in the age and diameter of the different branch-trunk joints of the four samples (although the trees were all the same age the branches taken from different locations on the trunk were of various levels of maturity). The tensile strength was similar to the radial-longitudinal plane, however the modulus was three times greater than the radial-longitudinal plane and about 12 times stiffer compared to the tangential-radial plane.

Figure 3-23 Tensile strength versus Young's modulus for transverse wood from the branch-trunk joint sourced from the tangential-radial plane; radial-longitudinal plane; and branch-trunk junction. Error bars indicate one standard deviation

The failure modes are shown in Figure 3-24. In the tangential-radial and longitudinal-radial planes failure occurred in the centre of the working section of the dog bone coupons. In the branch-trunk specimens the failure mode was the same as that observed in the branch-trunk joint under gravity direction bending load, with the crack occurring at the branch-trunk junction. This is a strategic failure point. Tensile stress is only resisted by the transverse strength of wood because there are no continuous fibrils across this interface. Scanning electron micrographs shown in Figure 3-25 revealed the failure mode at the branch-trunk junction is trans-wall failure along the longitudinal tracheid axis (refer Figure 2-38) exposing the inside of the tracheid, together with some fibre pull-out. Previous research showed that adaptive growth in and around the branch-trunk joint is manifested by changes to the chemical composition, primarily through increases in the lignin content [77]. The test results show that wood has the highest tensile transverse properties across the branch-trunk joint.

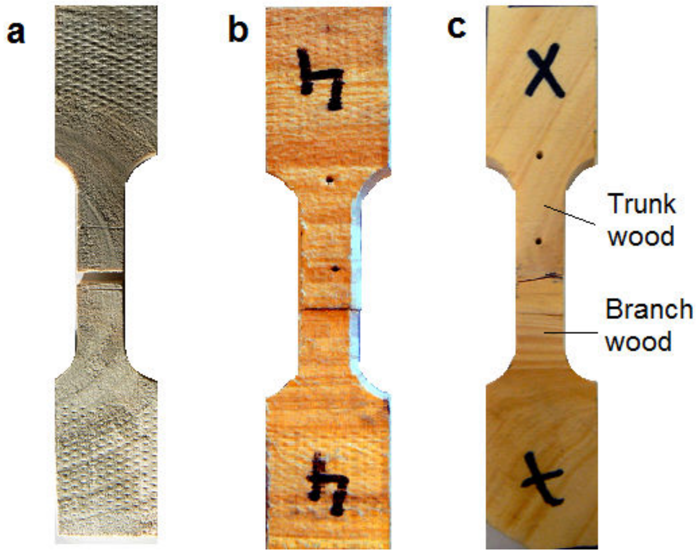

Figure 3-24 Transverse failure mode of wood until tensile loading: (a) tangential-radial plane; (b) longitudinal-radial plane; and (c) branch-trunk junction

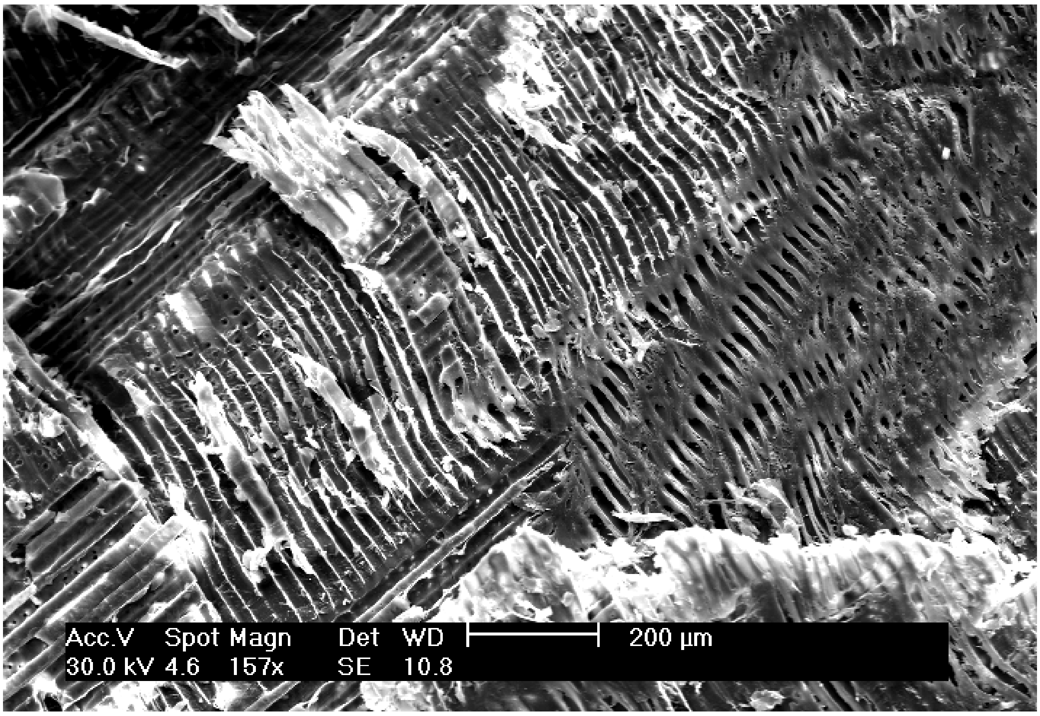

Figure 3-25 Trans-wall failure (splitting along the longitudinal tracheid axis) in the branch-trunk fracture surface exposing the inside of the tracheid together with some fibril pull-out. Resolution = 200 µm

3.3.4 Toughening mechanisms

The initiation and development of damage in the tree branch joint under increasing bending strain was investigated using scanning electron microscopy (SEM) and x-ray micro-computed tomography (micro-CT). Gravity direction bending testing was stopped at the peak load and 12 mm samples were cut from the tensile side branch-trunk junction and scanned using micro-CT, which allows non-destructive imaging through-the-thickness of the sample. Several micro-damage modes and toughening processes occur in the tree joint under bending: including fibril bridging, crack branching and deflection, and fibril pull-out.

3.3.4.1 Fibril bridging

Micro-CT images from the front view (perpendicular to the branch) showed significant bridging of individual fibrils and ligaments of the wood across single (refer Figure 3-26a) and multiple (refer Figure 3-26b) crack fronts.

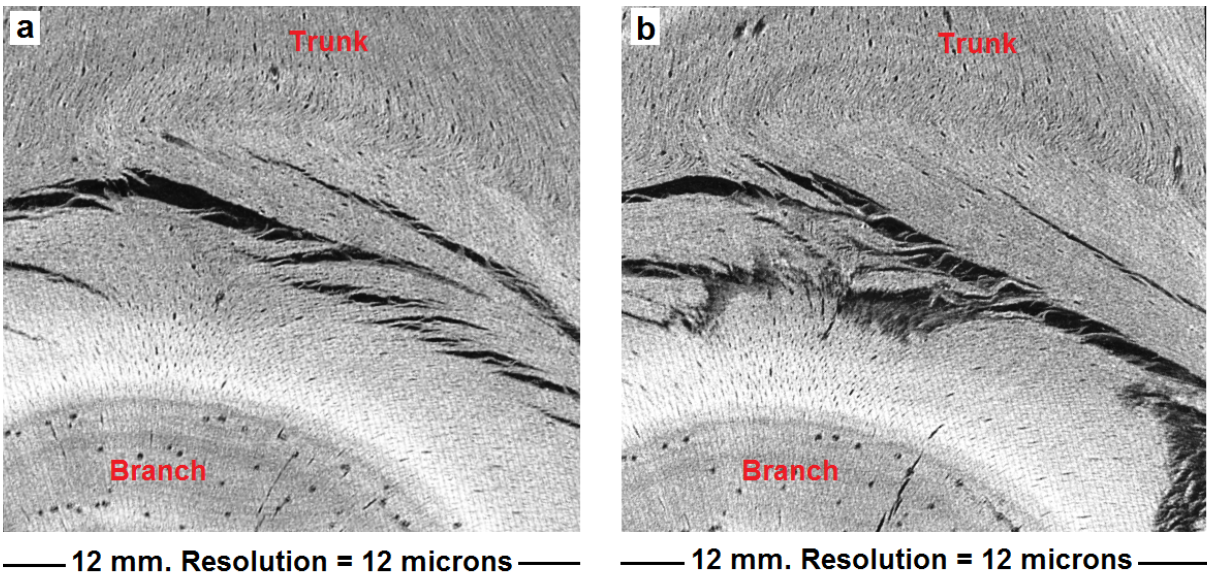

Figure 3-26 Micro-CT front view cross-section of branch-trunk joint showing fibre across: (a) one main crack front; and (b) multiple crack fronts opened up by crack branching and deflection

The high density of wood fibrils and ligaments bridging the crack generates traction loads that resist the opening and propagation of the crack, thereby stabilising the fracture process. In this way the resistance to cracking increases with crack extension (rising R-curve behaviour), which promotes high toughness in the brittle wood material by encouraging crack deflection and crack branching.

3.3.4.2 Crack branching and deflection

The side-view (parallel to the branch) images show clear evidence of the toughening mechanisms of crack branching and deflection. Crack deflection occurs when the crack splits into multiple crack fronts. Figure 3-27a shows two main crack fronts and Figure 3-27b shows three main crack fronts.

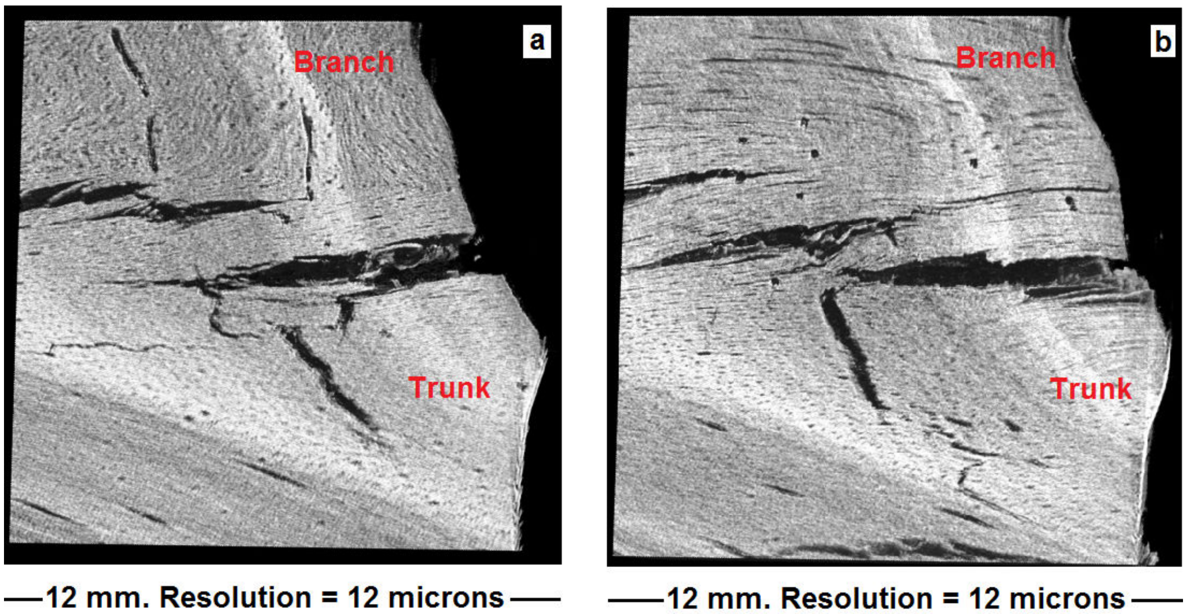

Figure 3-27 Micro CT side view cross-section of branch-trunk joint showing crack deflection and branching: (a) two crack fronts; and (b) three crack fronts

Crack branching and deflection occurs as a result of rising R-curve behaviour (refer Figure 2-6). As the crack extends, toughening mechanisms such as fibril bridging increase the material resistance to further crack extension and the crack growth is slowed down or arrested. Cracking preferentially occurs where the material resistance to crack extension is lower, opening up new crack fronts. Cracking occurs over a large volume and extensive crack branching and crack deflection increase the strain energy release rate per unit volume of wood.

3.3.4.3 Fibre pull-out

SEM revealed fibril pull-out throughout the branch fracture surface (refer Figure 3-28) and in particular along the seam of the branch-trunk junction (refer Figure 3-29).

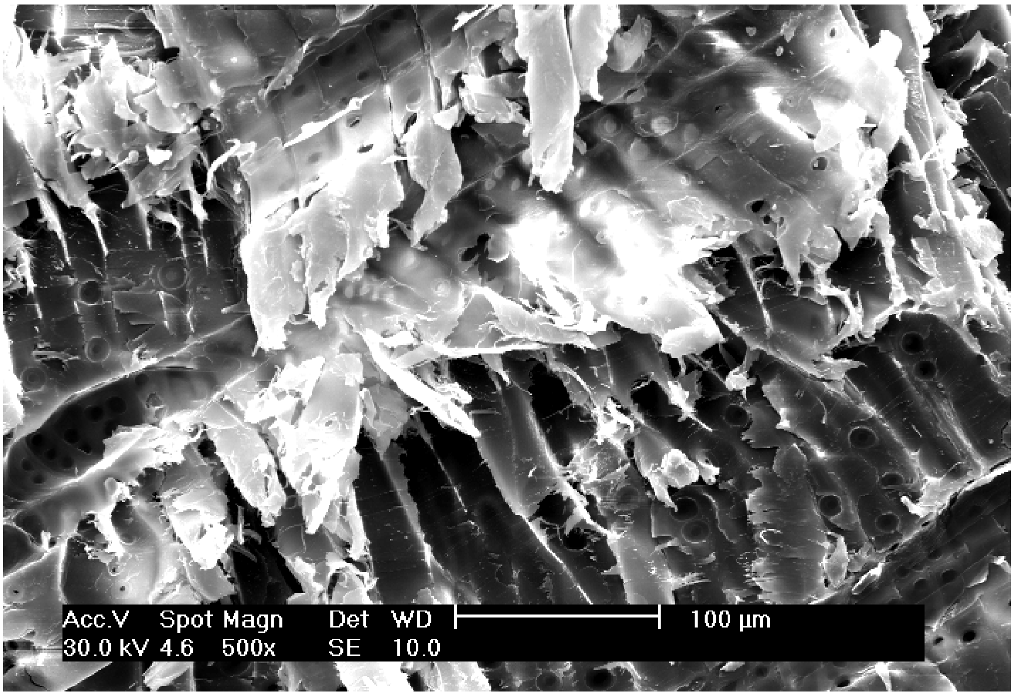

Figure 3-28 Detail of rough, fibrous branch fracture surface showing fibril pull-out in tracheids. Resolution = 100 µm

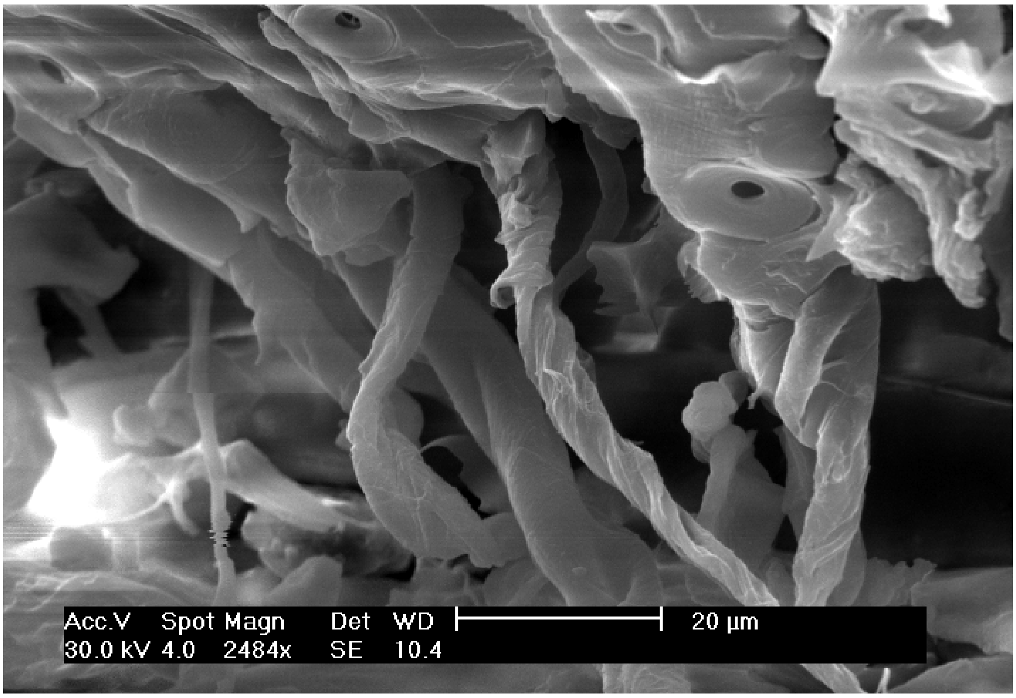

Figure 3-29 Detail of branch-joint seam. Fibril bridging and pull-out is especially prevalent in this location. Resolution = 20 μm

Fibre pull-out is a damage mechanism that absorbs a high amount of strain energy, contributing to increased toughness. Fibril pull-out, together with extensive fibril bridging, crack deflection, and crack branching across the main crack on the tensile branch-trunk junction are the main micro-level toughening mechanisms in the branch-trunk joint.

3.4 SUMMARY AND CONCLUSIONS

Tree branch-trunk joints are characterised by a strongly hierarchical structure in which features at the nano-, micro-, meso- and macro-length scales interact in synergy to produce desirable properties such as high strength, stiffness, toughness and damage tolerance. The main macro-structural features of tree branch-trunk joints as identified through x-ray computed tomography are: (i) integrated adherends with the cone-shaped internal branch structure embedded to the centre of the trunk forcing crack growth under mode II rather than mode I conditions; (ii) three-dimensional fibril lay-up with trunk fibrils extending forward and laterally to support the branch in a 'ball and socket' type union; and (iii) controlled variation in fibril density (fibre volume fraction) across the joint, where the highest density coincides with locations of maximum bending stress and where fibrils undergo directional change, thus reducing modulus discontinuities between fibrils aligned with the branch and trunk directions.

Mechanical testing of tree-branch joints under gravity direction bending loading revealed inelastic deformation behaviour and high residual strength following peak load, indicative of high toughness and damage tolerance. This is despite the fact that, similar to carbon fibre composites, the constituent material of wood fibrils (cellulose) is brittle. In contrast, CFRP T-joints experience brittle failure under bending loading. The strength of the tree branch-trunk joint is highly dependent on the alignment of the symmetry of the branch-trunk architecture with the loading direction, indicating that the architecture of the tree joint is adapted to the external loading conditions. The bisected branches showed a reduction in toughness and damage tolerance due to the removal of the supporting 3D fibre structure. Under reverse gravity loading the tree joint failed due to delaminations in the continuous fibres running between the branch and the trunk. Under reverse loading the joint had reduced inelastic strain absorption, damage tolerance and toughness and did not retain high loading capability over large bending displacements. The bending strength of the tree branch-trunk joint approaches the same strength as the constituent material (wood), maximising the efficiency of the joint.

X-ray micro-computed tomography and SEM imaging revealed the main toughening mechanisms in tree branch joints at the micro-level are: (i) large-scale crack bridging by wood fibrils and ligaments that generate traction forces which resist damage growth and generate rising R-curve behaviour; (ii) extensive crack branching and deflection creating a large strain energy per volume of material as a result of rising R-curve behaviour; and (iii) extensive fibril pull-out across the branch-trunk fracture surface and particularly along the branch seam, which also contributes to rising R-curve behaviour.

Wood has a hierarchical structure in which features at the nano-, micro-, meso- and macro-length scales interact in synergy to produce desirable properties [4, 9, 42, 154]. The micro-level damage mechanisms together with the macro-level structural features are the primary toughening mechanisms generating a high load-bearing capacity beyond the peak load. These toughening processes are not operative in any significant way in conventional fibre-reinforced composite T-joints. They give a physical explanation for the high levels of inelastic strain energy, toughness and damage tolerance observed during mechanical testing of the tree branch-trunk joint under gravity direction bending load; properties which are not found within a conventional fibre-reinforced composite T-joint.

The research work presented in this chapter is used as the basis for the biomimetic design of aerospace structural T-joints made of carbon fibre-epoxy laminate to achieve increased strength (chapter four) and damage tolerance (chapter five).

CHAPTER 4:

4 T-JOINT STRENGTH IMPROVEMENT THROUGH BIOMIMETIC OPTIMISATION AND DESIGN OF EXPERIMENTS

4.1 INTRODUCTION

The opportunity exists to apply bio-inspired design methods to increase the strength of composite T-joints by mimicking the material optimisation observed in tree branch-trunk joints to attain near iso-stress conditions across the joint [19]. In this study, material optimisation refers to an optimised distribution of the stiffness and strength properties of orthotropic composites to alleviate the geometric stress concentration caused by structural details such as the radius bend. Imaging work discussed in chapter three and previous investigations into tree branch-trunk joints described in chapter two show that this is achieved via changes at the material (cellular) level through tailoring the fibre volume fraction (density) and fibre orientation [45, 46, 77, 83, 84, 102]. Tailoring the fibre orientation is the more easily implemented of these two options using conventional composite manufacturing processes. Variations to the fibre volume content across a composite structure are difficult to manufacture in a controlled and precise manner.

Minimising the in-plane discontinuity in the mechanical properties of stiffness and strength across the thickness of the laminate reduces the interlaminar stresses [66]. Mechanical continuity in in-plane mechanical properties can be achieved through a helicoidal lay-up in which the orientation of each ply changes by 10° from the adjacent ply across the stacking sequence [66]. However the disadvantage of this approach is that the resulting laminate is essential isotropic, once again bringing us back to 'black Aluminium' and negating the advantages of anisotropic materials in which the stiffness can be tailored to the loading direction.

The objective of this study is to use optimisation tools to find a laminate stacking sequence that minimises interlaminar stresses within prescribed stiffness constraints, without simply generating an isotropic laminate as occurs through a helicoidal laminate stacking sequence. The aim is to evaluate the hypothesis that the damage initiation load (and consequently absorbed elastic strain energy) of composite T-joints under bending can be improved using the bio-inspired design strategy of optimised fibre orientation, which is based on the biomimetic principle of uniform strain. It is postulated that a reduction in the maximum interlaminar tensile stress within the critical radius bend/delta-fillet region affected by the geometric stress concentration will delay the onset of delamination damage in the radius bend and thereby increase the T-joint strength. It is acknowledged that previous work shows matrix cracking will precede delamination in L-joints [130]. However, delamination failure is considered to be the first critical failure mode because (unlike matrix cracking) it results in a reduction in both the load carrying capacity and stiffness of the joint.

Most T-joint parametric studies have not considered the full spectrum of ply angles from -90° to +90° as a design variable affecting the stress distribution, failure mode, fracture mechanics and strength of composite T-joints. This relates back to the two 'golden rules' of composite laminate design, namely designing laminates with balance (matching +/- off-axis plies) and symmetry about the mid-plane [145]. Traditionally, laminates are often designed with $[0_i/\pm45_j/90_k]_s$ stacking sequences to ensure processing stability [146], hygrothermal shape stability [147], quasi-isotropic mechanical properties, and to avoid mechanical coupling [149]. However there is a vast and mainly unexplored design space of non-standard (non-quasi-isotropic) ply orientations, including asymmetric hygrothermal laminates that can be used to exploit the full potential of anisotropic composites with potential weight and cost savings [145].

The mechanical performance of a composite T-joint with four different stiffener laminate stacking patterns is compared using perturbation finite element analysis. FEA is coupled with numerical optimisation and design of experiments (DoE) analysis to generate improved bio-inspired, quasi-isotropic and hygrothermally stable stiffener laminate designs.

The improved designs are validated by experimental bending and tensile testing. The carbon fibre composite T-joint was optimised under the external loading condition of bending because this type of loading most closely resembles the natural loading condition of the self-weight of the tree branch (discussed in chapter three) and is easily reproducible using available laboratory resources. While this load case is not necessarily a real world loading condition for aerospace structures, this work assesses the concept that the damage initiation load and absorbed elastic strain energy of composite T-joints can be improved by optimising the material properties to the prevailing loading conditions (mimicking the tailoring of microfibril angles that exists in and around tree branch-trunk joints). The methodology can be easily adapted to accommodate a real world loading condition.

4.2 RESEARCH METHODOLOGY

4.2.1 Linear perturbation finite element analysis

Finite element analysis (FEA) using the software PATRAN 2012.1.2 as the pre-processor and SIMULIA ABAQUS 6.9-2 as the solver and post-processor was performed on a unidirectional carbon/epoxy T-joint under bending and tensile perturbation loading.

Figure 4-1 shows the FE model of the composite T-joint. The T-joint consists of a 70 mm high 16 ply unidirectional carbon/epoxy prepreg stiffener web laminate bonded by co-curing without film adhesive to a 230 mm long 16 ply carbon/epoxy prepreg skin laminate having the lay-up $[45/0/-45/90/90/-45/0/45]_s$. The stacking sequence of the stiffener laminate of the baseline T-joint (Design A) is $[45/0/-45/90/90/-45/0/45]_{s.}$ Three other T-joint stiffener laminate stacking sequence design concepts are compared to this baseline design.

The FE model had the geometry, boundary conditions, coordinate systems and ply angle definitions given in Figure 4-1. The stiffener flange overlaps the skin by 15 mm followed by a flange run-out at an angle of 5°. Both the stiffener and skin laminates are approximately 2.8 mm thick. This geometry was chosen as representative of the dimensions of aerospace structural T-joints following composite design rules (e.g. 5° flange run-out and minimum 0.125 inch radius bend) and also to comply with existing tooling and test rigs. The T-joint was constructed as a 3D model because the 2D elements in the pre-processor did not support the input of the ply orientation in the orthotropic material properties.

The T-joint was modelled ply-by-ply (refer Figure 4-2) with one element across the through-thickness direction of each ply and two elements across the width direction. The composite plies were constructed from HEX-20 solid elements. Each ply in the radius bend was modelled with 30 elements in the tangential direction. The delta-fillet region was modelled using HEX-20 and TRI-15 solid elements to model unidirectional carbon/epoxy tape oriented in the direction of the stiffener blade, replicating the construction of the T-joint test specimens used to validate the FE model. The mesh discretisation of the FEA T-joint model as a whole was verified to generate global stiffness properties (for example refer Figure 6-18) consistent with the calculated bending stiffness of the laminate. The mesh discretisation of the FEA in the critical radius bend and delta-fillet region was validated to generate interlaminar tensile stresses (for example refer Figure 6-20) consistent with the interlaminar tensile failure strength of the material at the experimentally determined failure displacement (refer Chapter 6). The elements had the orthotropic properties of the unidirectional carbon/epoxy prepreg used in the experimental joints (Lavender VTM264) and these are given in Table 4-1. This material was chosen as being representative of a typical aerospace unidirectional prepreg material, consisting of T700 carbon fibre reinforcement and HS200 epoxy resin.

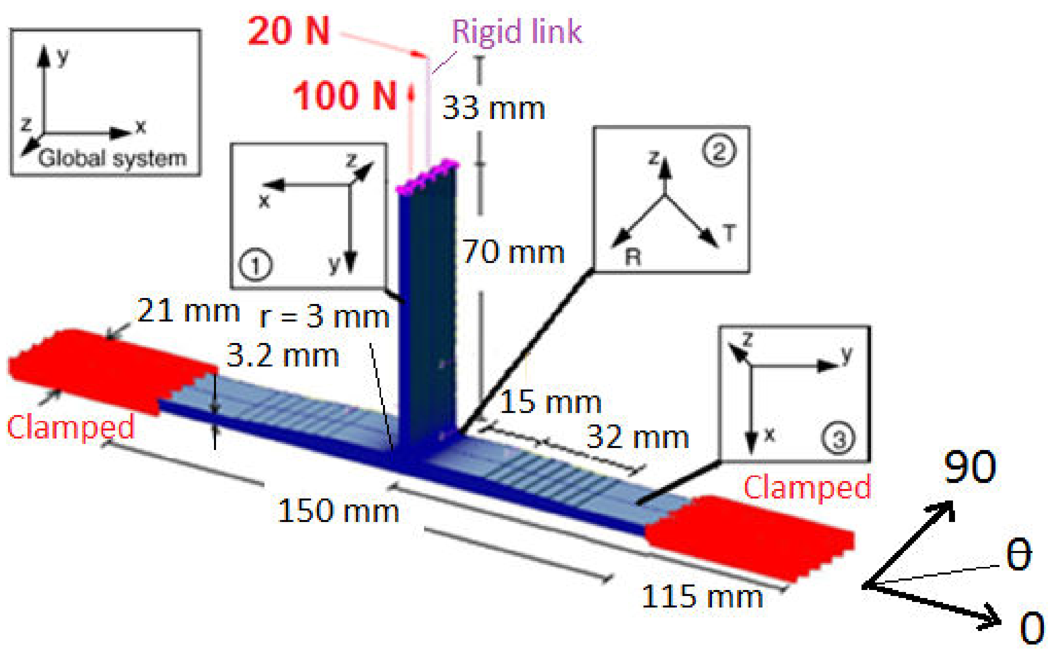

Figure 4-1 Finite element model of composite T-Joint showing the geometry, boundary conditions, coordinate systems and ply angle definition

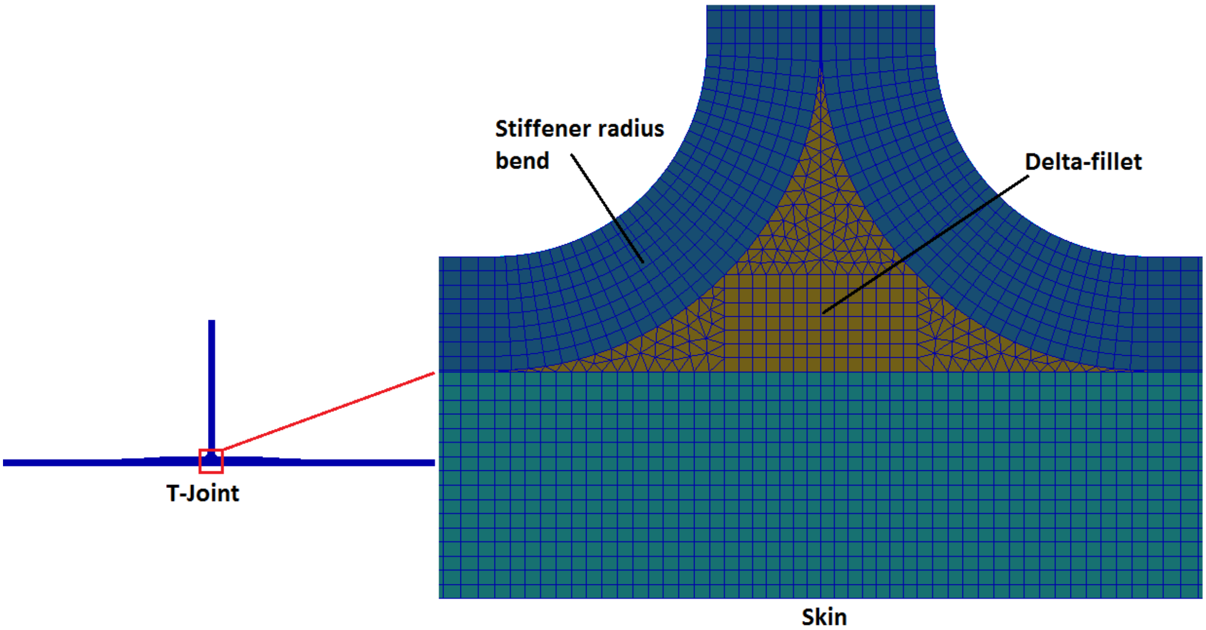

Figure 4-2 Finite element model of composite T-Joint showing mesh detail: dark blue = stiffener radius bends, light blue = skin and orange = delta-fillet region. In the stiffener radius bends and skin laminates each element represents one ply.

The boundary conditions applied to the FE model of the T-joint involved clamping the skin on either side of a working section of 150 mm containing the stiffener web by fixing the 3D solid elements of the skin to prevent displacement in all directions. Bending and tensile forces were applied to perturb the T-joint within the linear elastic range. Perturbation FE analysis was used to minimise the run-time of the optimisation loop. A bending load of 20 N was applied perpendicular to the stiffener at a node located 33 mm from the free edge of the stiffener web tip and 103 mm from the stiffener flange (refer Figure 4-1). The bending force was applied to the free edge nodes at the top of the stiffener via a rigid link to mimic the experimental test set-up. This force induced bending and shear stresses along the stiffener web. The tensile load was a 100 N pull-off force applied to the centre of the free edge of the tip of the stiffener web. This force induced symmetric stresses in both radius bends. Linear elastic FEA was used to determine the internal stress distributions and the locations of the peak interlaminar tensile and shear stresses in the radius bend/delta-fillet region under the bending and tensile loads.

Table 4-1 Material property values of the unidirectional carbon/epoxy laminate used in the finite element analysis [155]

Material Property	Value
Cured ply thickness	0.2 mm*
E_{11}	117 GPa*
E_{22}	7.47 GPa*
E_{33}	7.47 GPa**
v_{12}	0.33*
v_{13}	0.02***
v_{23}	0.33**
G_{12}	4.07 GPa*
G_{13}	4.07 GPa**
G_{23}	2.31 GPa*

*experimentally determined, **assumption, ***calculated analytically

4.2.2 Bio-inspired optimisation and design of experiments

A numerical optimisation program was developed using the ESTECO software modeFRONTIER v 4.3. Both optimisation and design of experiment methodologies were explored for the problem of improving the stiffener ply stacking sequence. The program evaluated the resultant peak interlaminar tensile stress (σ_{33}) within the T-joint radius bend/delta-fillet region as determined by finite element perturbation analysis. Previous work confirmed that delamination damage in T-joints under bending and tensile loading occurs in the stiffener radius bend, which is the reason why only the stiffener laminate was optimised [104, 106, 107, 127, 130, 156-158].

The stiffener of the T-joint was modelled with the following four design concepts for the 16 ply stacking sequence:

Design A: Baseline quasi-isotropic: stacking pattern = $[45/0/\text{-}45/90/90/\text{-}45/0/45]_s$

Design B: Bio-inspired optimised: stacking pattern = $[\theta_1/\theta_2/\text{-}\theta_2/\text{-}\theta_1/\theta_3/\theta_4/\text{-}\theta_4/\text{-}\theta_3]_s$

Design C: Improved quasi-isotropic DoE: stacking pattern = $[0_i/\pm45_i/90_i]_s$

Design D: Hygrothermally stable DoE: stacking pattern = $[\theta/(\theta\text{–}90)_2/\theta/\text{-}\theta/(90\text{–}\theta)_2/\text{-}\theta]_s$

Designs B - D were restrained to maintain similar global in-plane and bending stiffness properties compared to the baseline Design A. In order to evaluate the stiffness constraints, the in-plane and bending stiffness matrices (refer Equation 4-1) were calculated using classical laminated theory (CLT) using Equation 4-2 to Equation 4-6. CLT assumes rigid bonds between plies of different orientations and also assumes that strains are continuous through-the-thickness of the laminate.

$$\begin{bmatrix} A_{11} & A_{12} & A_{16} & 0 & 0 & 0 \\ A_{12} & A_{22} & A_{26} & 0 & 0 & 0 \\ A_{16} & A_{26} & A_{66} & 0 & 0 & 0 \\ 0 & 0 & 0 & D_{11} & D_{12} & D_{16} \\ 0 & 0 & 0 & D_{12} & D_{22} & D_{26} \\ 0 & 0 & 0 & D_{16} & D_{26} & D_{66} \end{bmatrix}$$

Equation 4-1

Where $[A_{ij}]$ = in-plane stiffness matrix, $[D_{ij}]$ = bending stiffness matrix and $[B_{ij}]$ = coupled stiffness matrix = $[0]$ because the laminate is symmetric about the mid-plane.

$$\begin{bmatrix} Q_{11}(0) & Q_{12}(0) & 0 \\ Q_{12}(0) & Q_{22}(0) & 0 \\ 0 & 0 & Q_{66}(0) \end{bmatrix} = \begin{bmatrix} \frac{1}{E_1} & -\frac{\nu_{21}}{E_2} & 0 \\ -\frac{\nu_{12}}{E_1} & \frac{1}{E_2} & 0 \\ 0 & 0 & \frac{1}{G_{12}} \end{bmatrix}^{-1}$$

Equation 4-2

Where $Q_{ij}(0)$ = single ply stiffness at 0° ply orientation, E_1 = in-plane Young's modulus, E_2 = transverse Young's modulus, G_{12} = Shear modulus, ν_{12} = Poisson's ratio in the in-plane-transverse plane and ν_{12} = Poisson's ratio in the transverse-in-plane plane.

$$\begin{bmatrix} Q_{11}(\theta) \\ Q_{12}(\theta) \\ Q_{22}(\theta) \\ Q_{16}(\theta) \\ Q_{26}(\theta) \\ Q_{66}(\theta) \end{bmatrix} = \begin{bmatrix} c^4 & 2c^2s^2 & s^4 & 4c^2s^2 \\ c^2s^2 & c^4+s^4 & c^2s^2 & -4c^2s^2 \\ s^4 & 2c^2s^2 & c^4 & 4c^2s^2 \\ c^3s & -cs\left(c^2-s^2\right) & -cs^3 & -2cs\left(c^2-s^2\right) \\ cs^3 & cs\left(c^2-s^2\right) & -c^3s & 2cs\left(c^2-s^2\right) \\ c^2s^2 & -2c^2s^2 & c^2s^2 & \left(c^2-s^2\right)^2 \end{bmatrix} \begin{bmatrix} Q_{11}(0) \\ Q_{12}(0) \\ Q_{22}(0) \\ Q_{66}(0) \end{bmatrix}$$ Equation 4-3

Where $Q_{ij}(\theta)$ = single ply stiffness at θ° ply orientation, $c = \cos(\theta)$ and $s = \sin(\theta)$.

$$A_{ij} = \sum_{k-1}^{n} Q_{ij}(\theta_k)(h_k - h_{k-1})$$ Equation 4-4

$$A_{ij} = \frac{1}{2}\sum_{k-1}^{n} Q_{ij}(\theta_k)\left(h_k{}^2 - h_{k-1}{}^2\right)$$ Equation 4-5

$$D_{ij} = \frac{1}{3}\sum_{k-1}^{n} Q_{ij}(\theta_k)\left(h_k{}^3 - h_{k-1}{}^3\right)$$ Equation 4-6

Where k = ply number, and h_k and h_{k-1} are defined in Figure 4-3 where t = laminate thickness.

Figure 4-3 Definition of laminate geometry used in classical laminate theory

All four laminate stacking sequence design concepts are balanced and symmetric across the T-joint stiffener laminate without mechanical coupling (*[B]* matrix is equal to zero). However the T-joint stiffener is comprised of two back-to-back L-shaped flanges and across the 8 ply radius bend of the L-shaped flanges there may be mechanical coupling. Designs B, C and D are not symmetric across the 8 ply radius bend, although design D is a special class of laminate that is not symmetric but fulfils the conditions necessary for hygrothermal stability. Designs B and C are not hygrothermally stable across the radius bend, which will cause some post-cure warping and residual thermal stresses in the radius bend/delta-fillet region due to the temperature difference between cure (120°C) and testing (~20°C). In addition, Designs B, C and D have various degrees of mechanical coupling, which can be ascertained by the coupled *[B]* stiffness matrix.

4.2.2.1 Multi-objective simulated annealing (MOSA) – Design B

For Design B the optimiser algorithm was Multi-Objective Simulated Annealing (MOSA) and each optimisation program was run for 100 iterations (which took about 3 hours run-time). The optimiser was capable of varying the ply angle of each ply in the T-joint stiffener laminate from 0° – 90° in increments of 2°. The optimisation program was run with the single objective of minimising the peak interlaminar tensile stress (σ_{33}) in the T-joint radius bend (refer Equation 4-7).

$$[(\sigma_{33})] \rightarrow min \qquad \text{Equation 4-7}$$

The interlaminar tensile strength of the carbon/epoxy laminate was assumed to be constant across the T-joint. The program was capable of tracking any change in the location of the peak interlaminar stress in the radius bend as the optimisation progressed. The peak interlaminar tensile and shear stresses in the bio-inspired T-joint (Design B) were compared to the peak interlaminar tensile and shear stresses in the baseline quasi-isotropic T-joint (Design A).

The optimisation program is considered to be bio-inspired in three ways:

i) the optimisation algorithm in which the material properties were altered in order to fit the external loading conditions (analogous to evolutionary optimisation – 'survival of the best fit') [5];

ii) the optimisation objective function, which was set to minimise the peak interlaminar stress (analogous to strain under elastic loading conditions), and thus attain a uniform strain distribution which is a principle observed in structural joints found in nature [19, 46, 156]; and

iii) the technique to minimise the geometric interlaminar stress concentration through ply angle changes to alter the orthotropic stiffness and strength properties of the laminate. This is bio-inspired from the observations that in and around the tree branch-trunk joint the S2 microfibril angle in the wood cell wall (together with changes in density) is altered to achieve the uniform strain field [19, 46]. The interlaminar elastic moduli of carbon fibre reinforced polymer (CFRP) laminates is generally insensitive to changes in the ply orientation (i.e. isotropic in the through-thickness direction) and therefore an objective function based on minimising interlaminar stress is equivalent to an objective function based on minimising interlaminar strain, assuming linear elastic stress-strain behaviour prior to delamination damage initiation.

A schematic of the bio-inspired optimisation program is given in Figure 4-4. There are four ply angle input variables. The 16 ply stiffener laminate pattern = $[\theta_1/\theta_2/-\theta_2/-\theta_1/\theta_3/\theta_4/-\theta_4/-\theta_3]_s$, where the symbols $\theta_1 - \theta_4$ represent the four ply angle input variables. This stacking sequence was used due to the design requirement for a balanced (with matching +/- off-axis plies) and mid-plane symmetric ply stacking configuration to prevent warping of the stiffener web during production and testing. This sequence was determined to be the laminate stacking pattern that provided the highest reduction in the peak interlaminar tensile stress when compared to alternative symmetrical and balanced patterns $[\theta_1/\theta_2/\theta_3/\theta_4/-\theta_4/-\theta_3/-\theta_2/-\theta_1]_s$, $[\theta_1/\theta_2/\theta_3/\theta_4/-\theta_1/-\theta_2/-\theta_3/-\theta_4]_s$, $[\theta_1/\theta_2/-\theta_1/-\theta_2/\theta_3/\theta_4/-\theta_3/-\theta_4]_s$, and $[\theta_1/-\theta_1/\theta_2/-\theta_2/\theta_3/-\theta_3/\theta_4/-\theta_4]_s$.

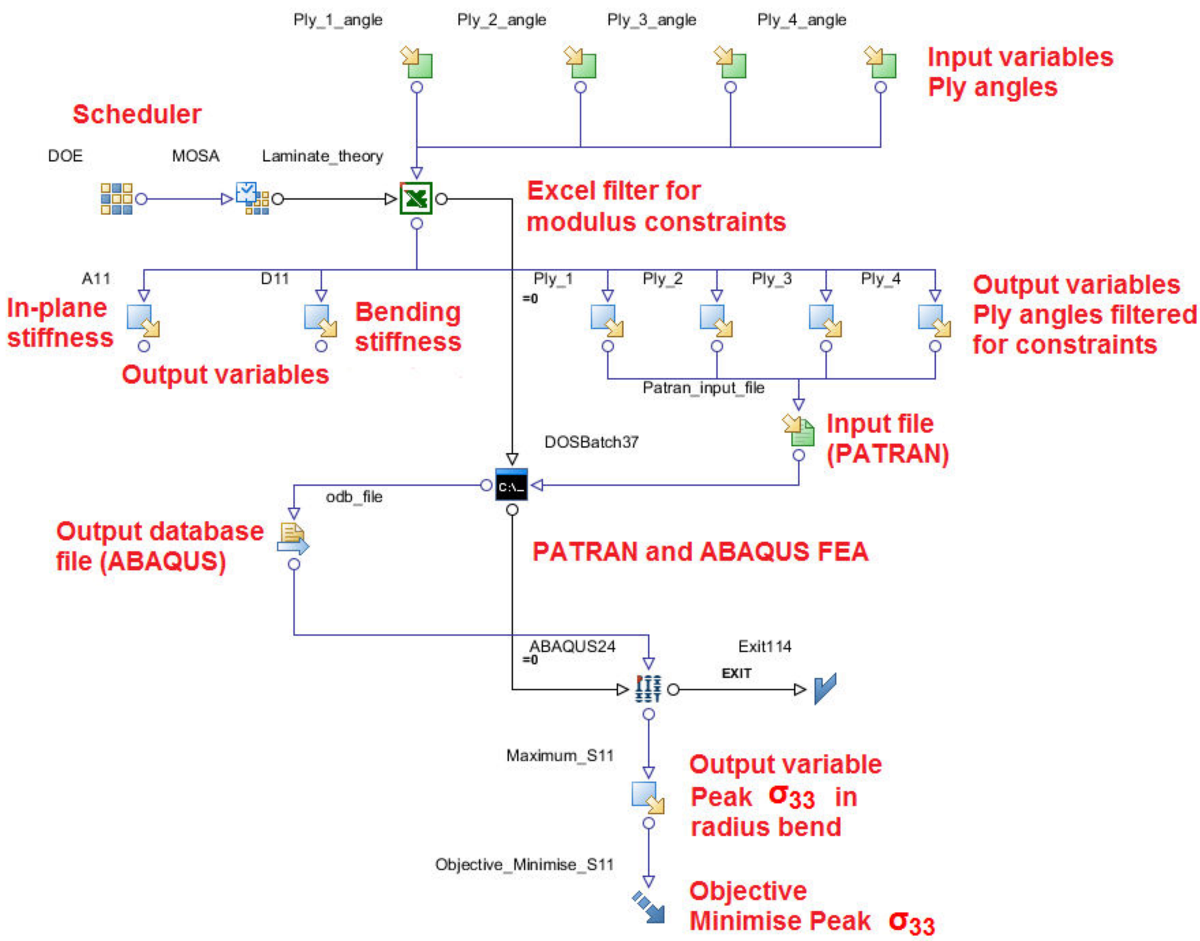

Figure 4-4 Schematic of modeFRONTIER bio-inspired optimisation loop used for the stiffener laminate ply analysis of T-Joint Design B

The initial design was an arbitrary value that fulfilled the global stiffness constraints, and was set to $[20/60/-60/-20/40/36/-36/-40]_s$. It was found that if the initial value of ply 1 was set below 40° the optimisation would trend towards ply 1 = 0°, but if the initial value of ply 1 was set above 50° the optimisation would trend towards ply 1 = 90° (even though the objective result was not as good as when the optimisation trended towards ply 1 = 0°), as the MOSA algorithm could not bounce out of the local maxima that occurs at $\theta = 45°$. The design of experiments approach discussed in section 4.2.2.2 avoided the optimisation problem of setting the initial design.

The plies in the radius bend were numbered from 1 - 8 according to the convention shown in Figure 4-5, with ply 1 on the free edge of the outer radius bend and ply 8 adjacent to the delta-fillet region.

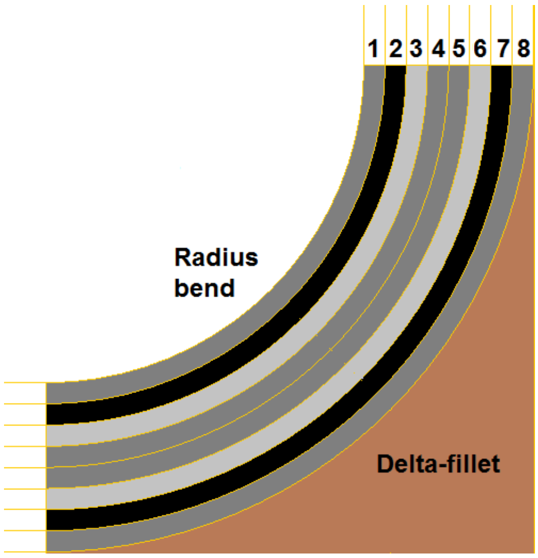

Figure 4-5 8 ply radius bend ply numbering convention

In order to compare T-joints with similar global structural properties, and potentially enable bio-inspired optimised designs to be retro-fitted into existing structures with minimal re-design, the in-plane (A_{11}) and bending (D_{11}) stiffness values of the stiffener web laminate of the optimised T-joint were both constrained to within 10% of the baseline quasi-isotropic stiffener web laminate. The optimisation program thus had the following constraints:

i) Stiffener web laminate stacking pattern $[\theta_1/\theta_2/-\theta_2/-\theta_1/\theta_3/\theta_4/-\theta_4/-\theta_3]_s$ with symmetry and balance to prevent warping and mechanical coupling.
ii) In-plane (A_{11}) stiffness of the bio-inspired optimised laminate constrained within ±10% of the baseline Design A T-joint.
iii) Bending (D_{11}) stiffness of the bio-inspired T laminate constrained within ±10% of the baseline Design A T-joint.

In the optimisation loop the four ply angle input variables pass through an Excel spread sheet that applies the global stiffness constraints and the in-plane (A_{11}) and bending (D_{11}) stiffness values are read as output variables (refer Figure 4-4). The filtered ply angle output variables that fulfil the global stiffness constraints are transferred into the PATRAN input file for the finite element analysis using ABAQUS as the solver. The output database file is connected to the ABAQUS post-processor that reads the peak interlaminar tensile stress in the T-joint radius bend, which alters as the ply angles change according to the scheduler, which is set to the multi-objective simulated annealing (MOSA) optimisation algorithm for 100 iterations. Approximately one-third of the iterations fulfilled the global stiffness constraints. The peak interlaminar tensile stress in the T-joint radius bend is read as the output variable from the ABAQUS node. The objective node attached to this output variable is set to minimise the peak interlaminar tensile stress in the T-joint radius bend.

4.2.2.2 Design of experiments (DoE) – Designs C and D

The methodology of design of experiments (DoE) was first proposed by Ronald Fisher in 1935 [159]. DoE is used very broadly in many applications across both the natural and social sciences to systematically explore the intervention or 'treatment' of objects known as 'the experimental units'. DoE involves the systematic exploration of the design space of parametric systems, which can be either discrete or continuous. The input variable, also known as the 'parameter' or 'factor' is sampled at discrete levels, with more important input parameters generally sampled at more levels, with the aim to determine trends between the input and output variables [160].

In engineering applications DoE is mostly used in conceptual design, in order to explore as much of the design space as is required for proof of concept. The most complete method of DoE is known as 'full factorial', in which every input variable is tested at each level together with every level of every other input variable. This leads to n experiments according to Equation 4-8 [160].

$$n = l^k \qquad \text{Equation 4-8}$$

Where n = number of experiments in the DoE, l = number of levels that each input variable is sampled at and k = number of input variables in the DoE.

The number of experiments in full factorial DoE increases exponentially with the number of input variables, therefore full-factorial DoE is not always practical. For example, to perform a full factorial DoE in place of the ply optimisation considered in this chapter, the four ply angle input variables would need to be sampled at 46 levels in order to consider all ply angles between 0 - 90° at 2° intervals, resulting in 46^4 = 4,477,456 experiments. Considering the FE model for each experiment required about one minute run-time, performing the full factorial analysis would have required a run-time of a little over 9 years! In contrast, the 100 iteration optimisation program took about three hours to run, which is approximately 0.004% of the computing cost.

For T-joint design concepts C and D, the DoE methodology was computationally more efficient due to the restricted design space. Two DoE programs were developed that were similar in structure to the optimisation program shown in Figure 4-4. The main difference was the DoE programs did not have an objective node. The first was a fractional factorial DoE that considered quasi-isotropic ply orientations. There were 8 ply angle input variables considering the four traditional quasi-isotropic ply orientations of [0/±45/90]. The DoE was constrained so that all designs contained equal numbers of 0°, +45°, -45° and 90° plies in order to preserve the same in-plane stiffness (A_{11}) as the baseline T-joint design. The second constraint was the difference in the ply angle between adjoining plies could not vary by more than 45°. The bending stiffness (D_{11}) was not constrained. The eight experiments that were considered in the fractional factorial quasi-isotropic DoE are given in Table 4-2.

The second DoE program was a full-factorial hygrothermally stable DoE. The DoE considered one ply angle input variable in the asymmetric hygrothermally stable laminate stacking pattern $[\theta/(\theta–90)_2/\theta/-\theta/(90–\theta)_2/-\theta]_s$. This was determined to be the pattern that resulted in the lowest peak interlaminar tensile stress when compared to alternative asymmetric hygrothermally stable laminate stacking patterns of $[\theta/(\theta–90)/-\theta/(90–\theta)/(\theta–90)/\theta/(90–\theta)/-\theta]_s$ and $[\pm\theta/\pm(\theta–90)/\pm\theta/\pm(\theta–90)]_s$. These three 8 ply asymmetric hygrothermally stable laminates were discovered by Cross et al. [147]. The single ply angle input variable in the DoE was the ply angle θ, which was varied by the DoE program between 0° – 90°, in increments of 2°, which generated 46 levels. Therefore the total number of experiments in the DoE was $46^1 = 46$, which was not computationally expensive and thereby justified the decision for a full factorial DoE.

Table 4-2 Experiments in the quasi-isotropic DoE

DoE	Ply 1	Ply 2	Ply 3	Ply 4	Ply 5	Ply 6	Ply 7	Ply 8
1	0°	45°	90°	-45°	0°	45°	90°	-45°
2	0°	45°	90°	-45°	-45°	90°	45°	0°
3	45°	0°	-45°	90°	45°	0°	-45°	90°
4	45°	0°	-45°	90°	90°	-45°	0°	45°
5	45°	90°	-45°	0°	45°	90°	-45°	0°
6	45°	90°	-45°	0°	0°	-45°	90°	45°
7	90°	45°	0°	-45°	90°	45°	0°	-45°
8	90°	45°	0°	-45°	-45°	0°	45°	90°

4.2.3 Fabrication and experimental procedure

The fabrication of the experimental specimens is shown in Figure 4-6. After cutting out the unidirectional carbon/epoxy prepreg to the required sizes, the plies were laid up on two L-shaped aluminium tools with machined 3 mm radius bends (refer Figure 4-6a). The L-pieces were de-bulked for five minutes after every fourth ply was laid down (refer Figure 4-6b). After laying up 8 stiffener plies on each L-piece the two L-pieces were joined together across the stiffener and clamped (refer Figure 4-6c). The delta-fillet region at the base of the stiffener was filled with a triangular 'noodle' formed from the unidirectional carbon/epoxy prepreg to minimise the formation of a void or resin-rich zone.

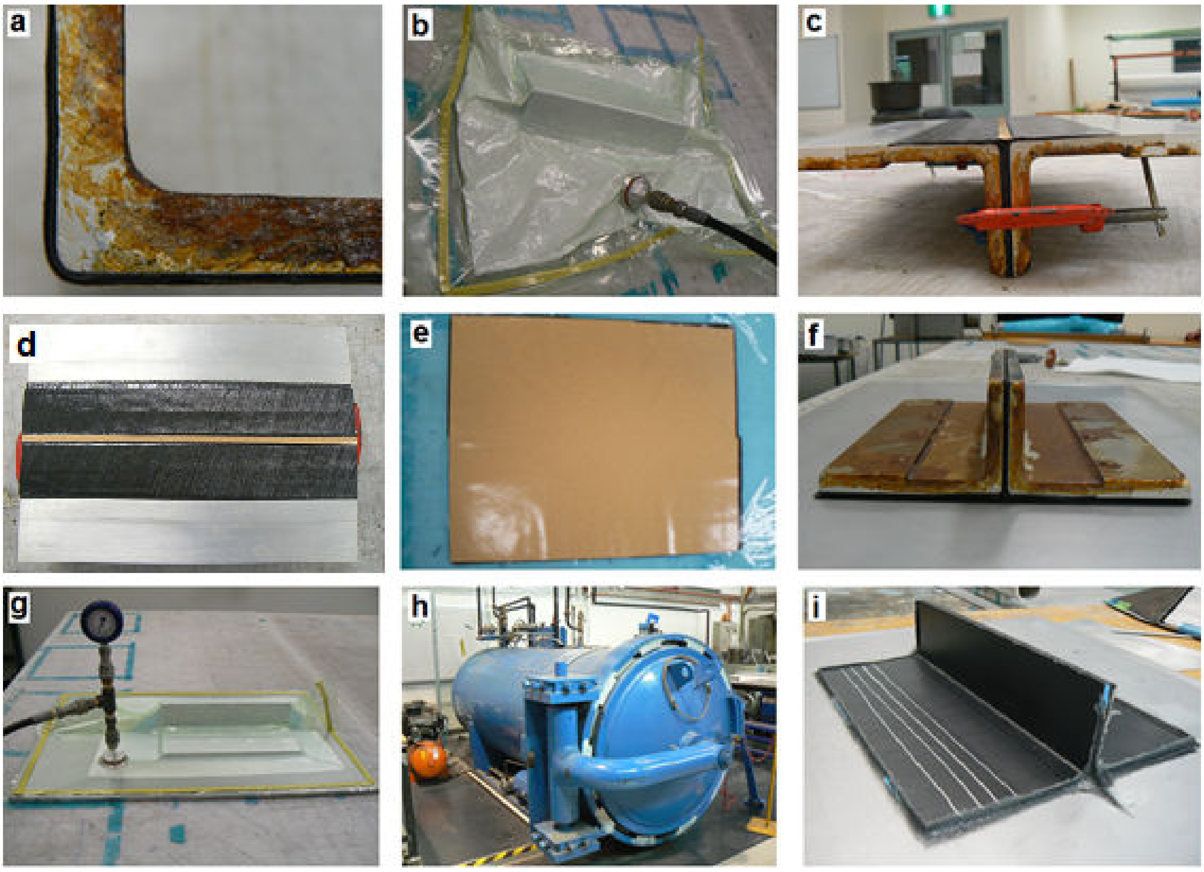

Figure 4-6 Production process to fabricate composite T-joints: (a) L-shaped aluminium tools with machined 3 mm radius bends; (b) de-bulking; (c) clamped L-pieces; (d) formation of 'noodle'; (e) rectangular skin; (f) assembly of L-pieces and skin; (g) lay-up under vacuum release; (h) autoclave; and (i) T-joint part

The area of the delta-fillet (refer Figure 4-7) was approximated by calculating the area of a rectangle of length $2r_i$ x width r_i and subtracting two quarters of the area of a circle with radius r_i where r_i = inner radius as given by Equation 4-9.

$$Delta - fillet\_area \approx 2r_i^2 - 2 \times \left(\frac{\pi r_i^2}{4} \right) \quad \text{Equation 4-9}$$

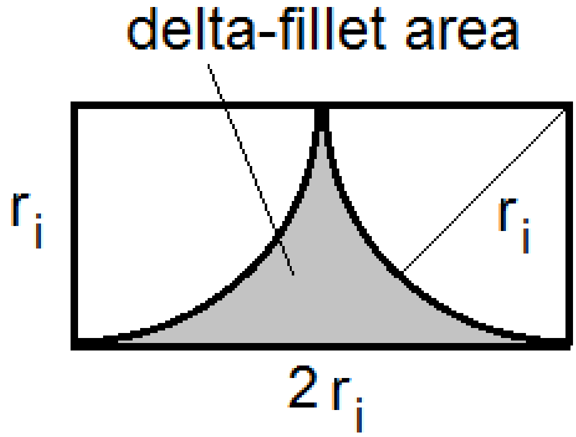

Figure 4-7 Schematic of delta-fillet area

The 16 ply rectangular skin was laid up separately and also de-bulked after every fourth ply (refer Figure 4-6e). The clamped back-to-back L-pieces were placed on top of the flat skin and together they were placed on a flat aluminium tool (refer Figure 4-6f). The skin and flange of the T-joint were bonded by co-curing without film adhesive. Release film and breather material were placed on top of the T-joint laid up on the tool. A vacuum bag was placed over the top and secured with mastick and checked for leaks (refer Figure 4-6g). The bagged tool was placed in the autoclave for 1 hour at 620 kPa (90 psi) (refer Figure 4-6h). After curing the T-joint was de-bagged and the aluminium tooling was removed. The T-joint part was subsequently cut into 12 x 21 mm wide T-joint specimens using a diamond saw.

The boundary conditions for the experimental testing were the same as those applied in the finite element model (refer Figure 4-8). The skin was clamped on either side of a 150 mm working section containing the stiffener web. Bending and tensile tests were performed using a 50 kN Instron testing machine.

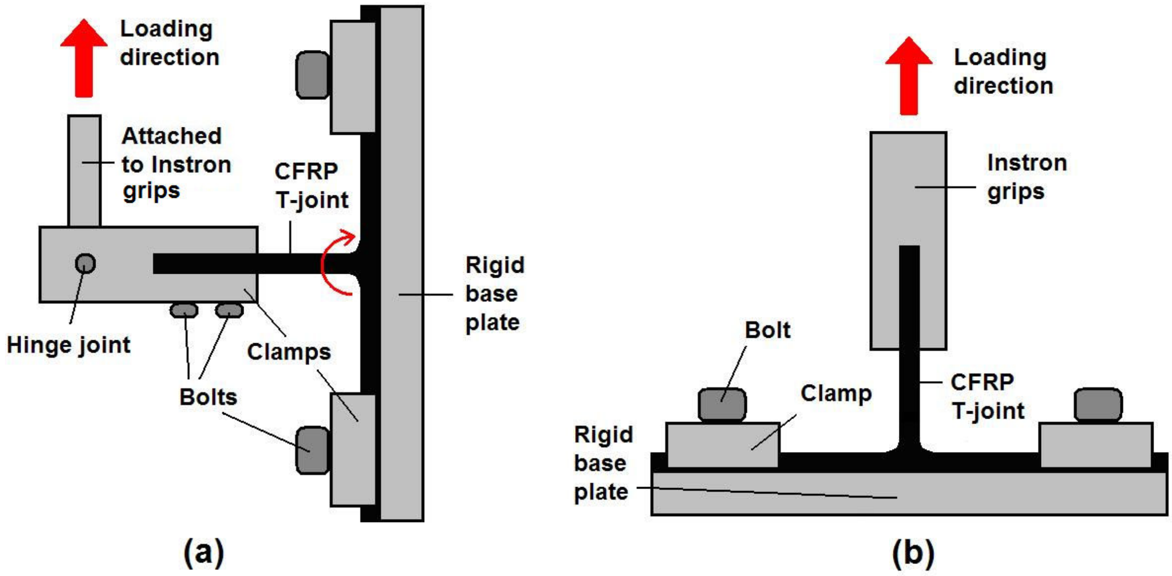

Figure 4-8 Schematic of experimental test set-up; (a) bending load case; and (b) tension load case

Bending tests were performed by applying a bending force perpendicular to the stiffener web via a clamp attached to the Instron cross-heads with the skin clamped, as shown schematically in Figure 4-8a. The load was applied at a rate of 3 mm/min to a maximum displacement of 25 mm, at which point the test was stopped. The design of the specimens with an overlaminate connecting the stiffener to the skin meant the stiffener did not detach following failure. The applied load induced bending and shear stresses along the stiffener and a bending moment in the radius bend/delta-fillet region of the T-joints. Tensile tests were performed by clamping the Instron cross-heads 50 mm along the stiffener web and applying a tensile pull-off force, shown schematically in Figure 4-8b. The tensile load was applied at a rate of 1 mm/min.

Six samples of the conventional and bio-inspired T-joints were tested under each load case in nominally identical conditions, and the mechanical responses at damage initiation were compared to the interlaminar stress distribution predicted using the FEA.

4.3 RESULTS AND DISCUSSION

4.3.1 Bio-inspired optimisation: Design B

The result of the optimisation loop modelling was design B (bio-inspired optimised) had a stiffener laminate stacking pattern of $[12/84/-84/-12/36/60/-60/-36]_s$. The progress of the optimisation with successive iterations is shown in Figure 4-9.

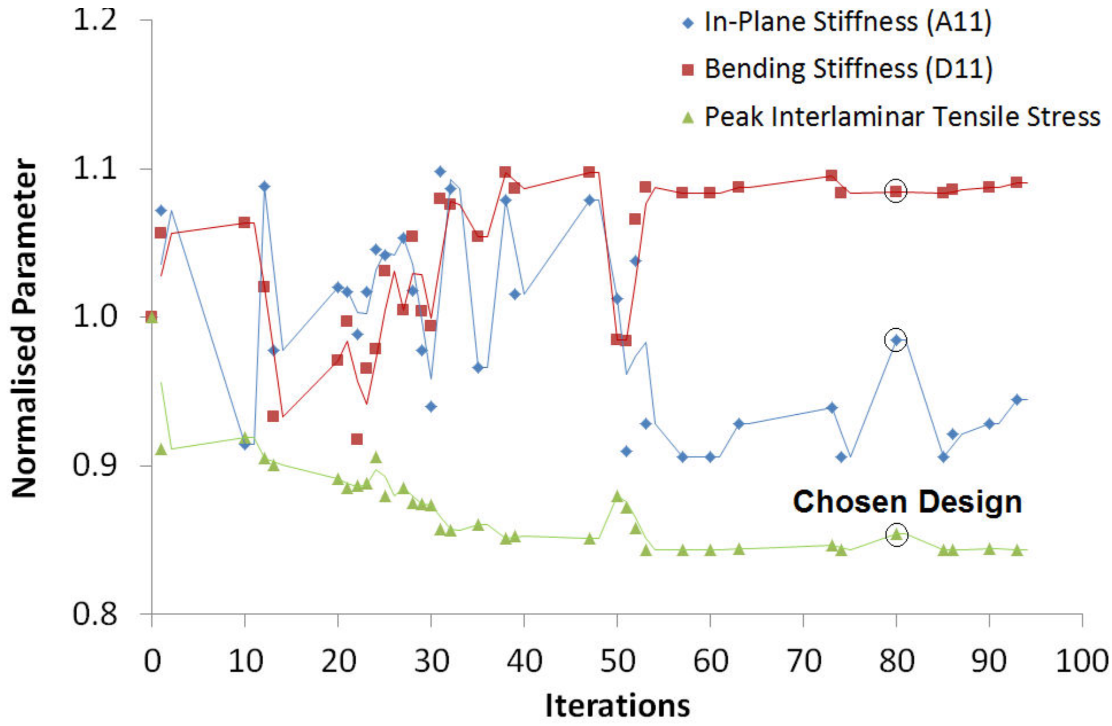

Figure 4-9 Progression of the optimisation program for design B across 100 iterations

Each parameter is normalised to the value in the baseline T-joint (Design A). Out of 100 iterations approximately one-third fulfilled the global stiffness constraints. The in-plane (A_{11}) and bending (D_{11}) stiffness values oscillate ±10% about the normalised baseline quasi-isotropic values, representing the actual values of 158.9 GPa.mm (A_{11}) and 142.9 GPa.mm^3 (D_{11}). As the optimisation progressed the bending stiffness of design B was maximised close to +10% due to the optimisation program replacing ply 1 with a high stiffness 12° ply to reduce the in-plane bending strain. The in-plane stiffness was minimised close to -10% because lower stiffness laminates attract less load. The peak interlaminar tensile stress decreased quickly as the MOSA algorithm progressed, reaching a value close to the minimum after less than 60 iterations.

Figure 4-10 shows that after about 60 iterations the ply angle input variables only varied by a small amount (in the order of 5°).

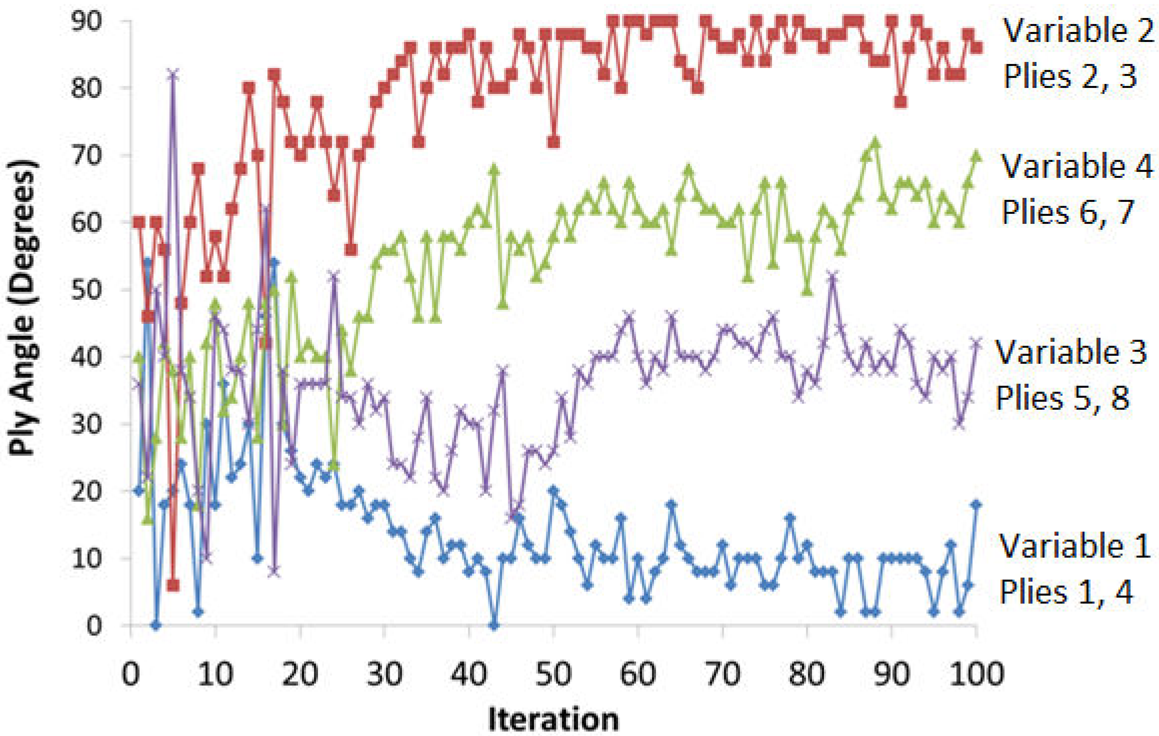

Figure 4-10 Variation of ply angle input variables as the optimisation for design B progressed to 100 iterations

It can be seen that the optimisation was stable and small changes in the ply angles did not cause large variations in the peak interlaminar tensile stress. This is significant because during production small variations in the ply angles in the laminate can be introduced, with misalignments up to about 5°. Iteration 80 with a peak interlaminar tensile stress 15% lower than design A (baseline) was chosen for FE analysis and experimental validation because the in-plane (A_{11}) stiffness was closer to the baseline than other iterations with a comparable value of the peak interlaminar tensile stress. Iteration 80 had a stiffener laminate stacking pattern of $[12/84/-84/-12/36/60/-60/-36]_s$, compared to design A (baseline) with a stiffener laminate sequence of $[45/0/-45/90/90/-45/0/45]_s$.

Table 4-3 summarises the effect size of each ply input angle variable in the optimisation. The effect size quantifies the strength of the relationship between the input variables (stiffener laminate ply angles) and the output variable (peak interlaminar tensile stress in the T-joint radius bend). Low absolute values indicate that there is a weak relationship between the input and output variables so it is possible to ignore that variable in the optimisation process. Significance is a parameter that indicates the confidence that the effect size result is true. A low value of significance does not necessarily mean that the input variable is important, but that the size effect parameter is probably reliable.

Figure 4-11 shows that variables 1, 2 and 3 (representing the orientation of plies 1, 2, 3, 4, 5 and 8 in the stiffener laminate) have the greatest effect on the peak interlaminar tensile stress in the T-joint radius bend. This means that misalignment errors in laying down these plies would have roughly the same effect on the interlaminar tensile stress. Variable 4 corresponding to plies 6 and 7 in the laminate stacking sequence has only has a minor effect size. The effect size data shows the optimisation is fairly insensitive to the orientation of plies 6 and 7 (60°), and therefore the orientation of these plies could be adjusted to produce the desired stiffness properties in the laminate without significantly affecting the peak interlaminar tensile stress.

Table 4-3 Effect size and significance of optimisation ply angle variables

Optimisation Ply Angle Variable	**Ply Number in Radius Bend Laminate Stacking Pattern**	**Effect Size**	**Significance**
θ_1	1,4	0.33 (31.8%)	0.000
θ_2	2,3	0.32 (31.5%)	0.000
θ_3	5,8	0.31 (29.7%)	0.000
θ_4	6,7	0.07 (7%)	0.140

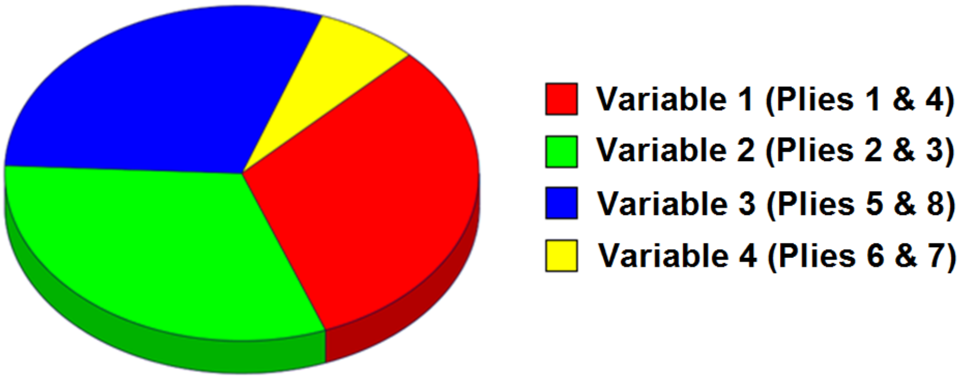

Figure 4-11 Pie chart of the effect size of each optimisation variable

4.3.2 Design of experiments: Designs C and D

4.3.2.1 Improved quasi-isotropic DoE (Design C)

The results of the fractional factorial quasi-isotropic DoE for design C are given in Table 4-4 (with the baseline design A highlighted in grey). The quasi-isotropic T-joint laminate sequences are given in Table 4-2. Since all of the different quasi-isotropic laminate designs ('experiments') had equal proportions of 0/±45/90 plies, the in-plane stiffness (A_{11}) was constant. However depending on the location of the plies in the stacking pattern, the bending stiffness (D_{11}) was variable.

Figure 4-12 and Figure 4-13 show that the reductions in both the interlaminar tensile and shear stresses roughly correlate to an increase in the bending stiffness of the stiffener laminate. Although the results are not exactly linear, they can be approximated by a linear relationship with a degree of scatter. This is the same relationship found for design B (bio-inspired optimised) in which the bending stiffness D_{11} trended towards the maximum allowable of +10% of the baseline value (refer Figure 4-9) because a high stiffness ply was placed in ply 1. Placing a high stiffness 0° ply in ply 1 (at the maximum distance from the neutral axis) increases the in-plane stiffness of the ply that undergoes maximum tensile strain under bending load, resulting in a more homogenous strain field.

Table 4-4 Stiffness properties and FEA peak interlaminar tensile and shear stresses of design C (quasi-isotropic DoE). (Percentages are based on comparison to the baseline quasi-isotropic design highlighted in grey).

DoE	A_{11} (GPa.mm)	D_{11} (GPa.mm^3)	Peak σ_{33} in T-joint radius bend (MPa)	Peak τ_{13} in T-joint radius bend (MPa)
1	158.9	174.0 (22%)	6.67 (-15%)	-6.81 (-16%)
2	158.9	156.6 (9.6%)	7.07 (-10%)	-7.87 (-3%)
3	158.9	153.6 (7.5%)	7.62 (-3%)	-8.37 (3%)
4	158.9	142.9 (0.0%)	7.87 (0%)	-8.10 (100%)
5	158.9	104.2 (-27%)	8.05 (2.3%)	-11.91 (47%)
6	158.9	121.7 (-15%)	8.00 (1.7%)	-10.04 (24%)
7	158.9	110.5 (-23%)	8.08 (2.6%)	-9.12 (13%)
8	158.9	121.3 (-15%)	7.62 (-3%)	-9.57 (18%)

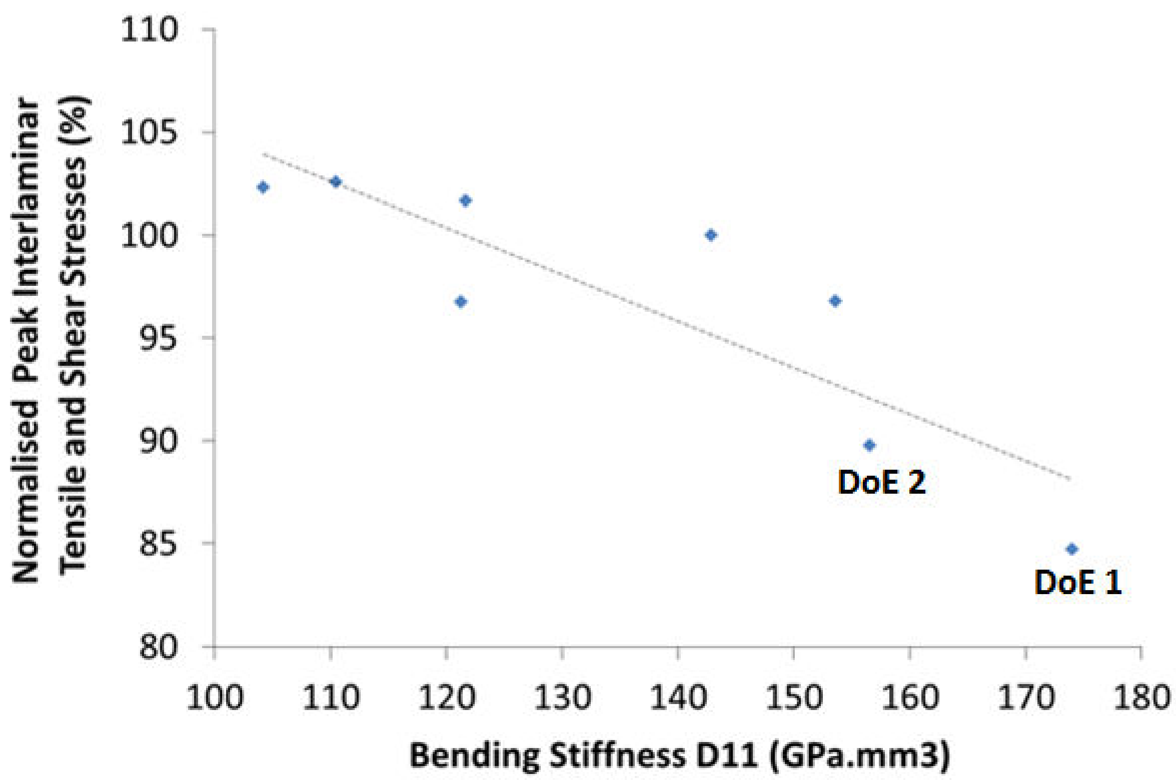

Figure 4-12 Normalised peak interlaminar tensile stress vs bending stiffness for design C (quasi-isotropic DoE)

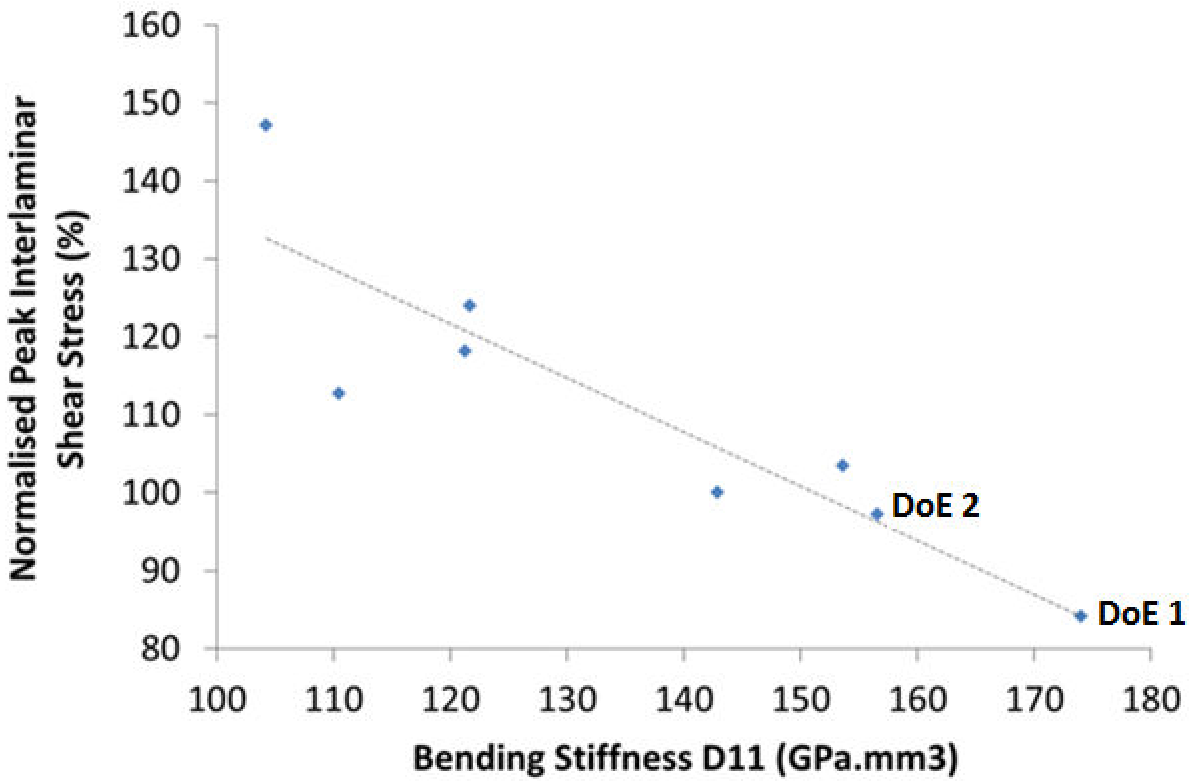

Figure 4-13 Normalised peak interlaminar shear stress vs bending stiffness for design C (quasi-isotropic DoE)

DoE 1 with a stiffener ply stacking pattern of $[0/45/90/-45/0/45/90/-45]_s$ exhibited the highest reductions in the peak interlaminar tensile and shear stresses (refer Table 4-4). The peak interlaminar tensile stress (σ_{33}) was reduced by 15% and the peak interlaminar shear stress (τ_{13}) was reduced by 16% compared to the baseline quasi-isotropic T-joint. However, the bending stiffness D_{11} was 22% higher than the baseline quasi-isotropic laminate, which is outside the 10% upper limit in the bio-inspired optimisation program. If the bending stiffness D_{11} was constrained to values within ±10% of the baseline design A, the best result from the quasi-isotropic DoE was experiment 2, with the stacking pattern of $[0/45/90/45/-45/90/45/0]_s$ which reduced the peak interlaminar tensile and shear stresses by 10% and 3%, respectively (refer Table 4-4).The effect size and the significance are given in Table 4-5.

The influence of the ply angle input variables on the output variables of peak interlaminar tensile stress and shear stress is shown in Figure 4-14a and Figure 4-14b, respectively. Together these results reveal that the most important plies in design C to reduce the peak interlaminar tensile and shear stresses are plies 1 and 3. They both have an effect size on the peak interlaminar tensile stress of 25%. The effect on the peak interlaminar shear stress of both plies 1 and 3 is 27%. These results explain why the same laminate design (experiment 1) results in the largest reduction in both the peak interlaminar tensile and shear stresses. This coupling, based on the bending stiffness D_{11}, is fortuitous because it means that changes in the stiffener laminate stacking pattern work in harmony to reduce both the interlaminar tensile and shear stresses that contribute to the interactive stress concentration that initiates delamination damage in the T-joint radius bend.

Table 4-5 Effect size and significance of each ply angle input variable in design C (quasi-isotropic DoE)

Ply Number	Effect size on peak interlaminar tensile stress (σ_{33})	Significance	Effect size on peak interlaminar shear stress (τ13)	Significance
1	1.0 (25%)	0.001	2.2 (27%)	0.042
2	0.2 (4%)	0.361	1.0 (12%)	0.242
3	1.0 (25%)	0.001	2.2 (27%)	0.042
4	0.2 (4%)	0.361	1.0 (12%)	0.242
5	0.6 (14%)	0.060	0.8 (10%)	0.256
6	0.3 (7%)	0.229	0.1 (1%)	0.471
7	0.6 (14%)	0.060	0.8 (10%)	0.256
8	0.3 (7%)	0.229	0.1 (1%)	0.471

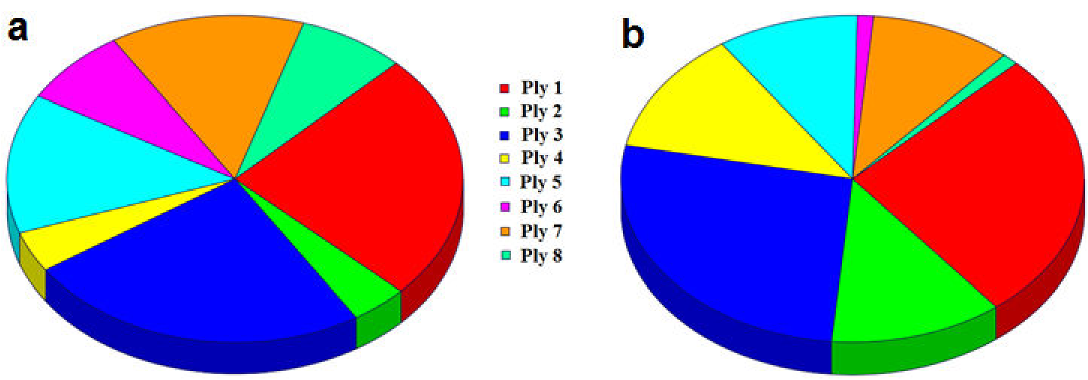

Figure 4-14 Effect size of ply angle input variables on design C: (a) peak interlaminar tensile stress in the T-joint radius bend; and (b) peak interlaminar shear stress in the T-joint radius bend

4.3.2.2 Hygrothermally stable (Design D)

Figure 4-10 shows the variation in the peak interlaminar tensile and shear stresses in the T-joint radius bend (normalised by the values in the baseline quasi-isotropic design) for the hygrothermally stable stacking pattern $[\theta/(\theta–90)_2/\theta/-\theta/(90–\theta)_2/-\theta]_s$ of design D. The minimum normalised interlaminar tensile and shear stresses occur at θ = 0°. This corresponds to a ply lay-up of 0°/90° for the first two plies, echoing the results of the bio-inspired optimisation where the optimisation trended towards 0°/90° but was constrained by the in-plane and bending constraints to values of 12°/84° for the first two plies. The interlaminar shear stress curve approximates a gull wing shape with a maximum at θ = 45° and the interlaminar tensile stress curve is relatively flat. In the bio-inspired optimisation program the results depended on the initial design.

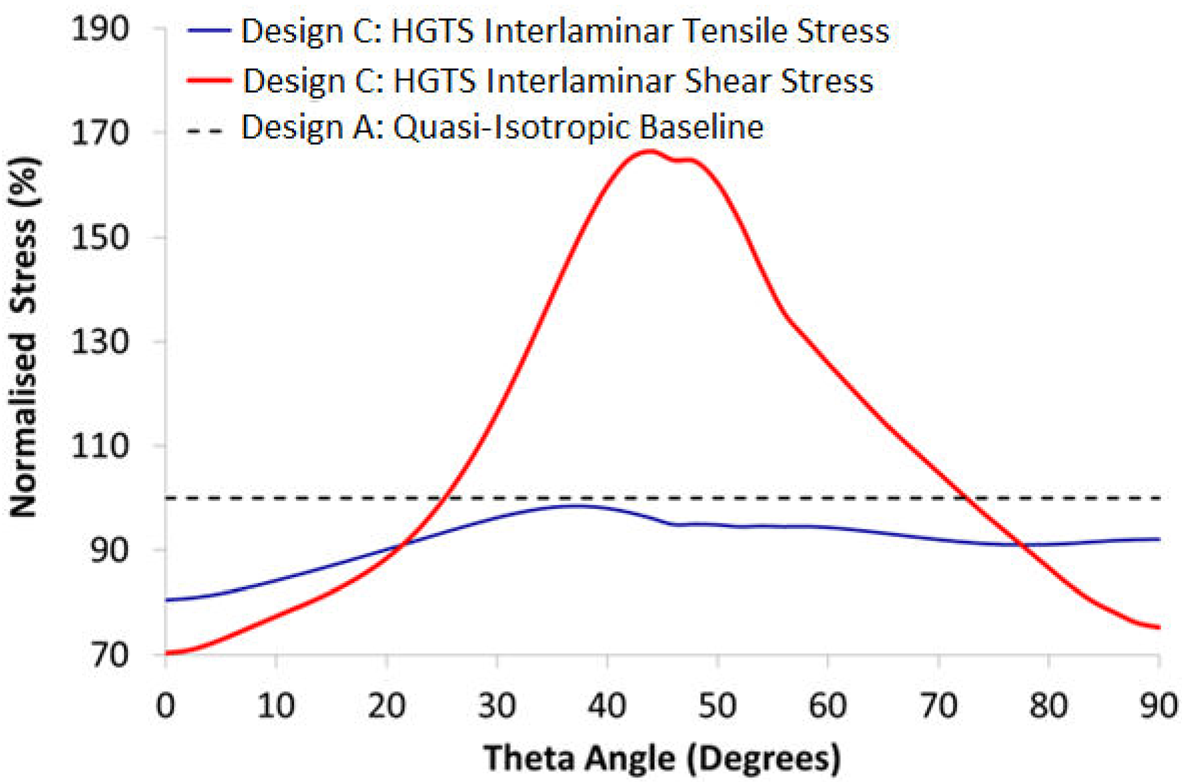

Figure 4-15 Normalised interlaminar tensile and shear stresses in the hygrothermally stable DoE (design D) compared to the baseline quasi-isotropic laminate (design A)

Figure 4-16 shows the same results as Figure 4-15**,** but in this case the laminate stiffness constraints of A_{11}, D_{11} = ±10% of baseline quasi-isotropic design are included. Applying these constraints eliminates a significant portion of the curves. The hygrothermally stable laminate only fulfils the global stiffness constraints for 18° ≤ θ ≤ 26°. The value of θ that produces the largest reduction in both the peak interlaminar tensile and shear stresses in the T-joint radius bend is the smallest angle of θ = 18°. Therefore, the hygrothermally stable stacking sequence for the stiffener laminate (design D) considered for FE analysis and experimental validation was $[18/\text{-}72/\text{-}72/18/\text{-}18/72/72/\text{-}18]_S$.

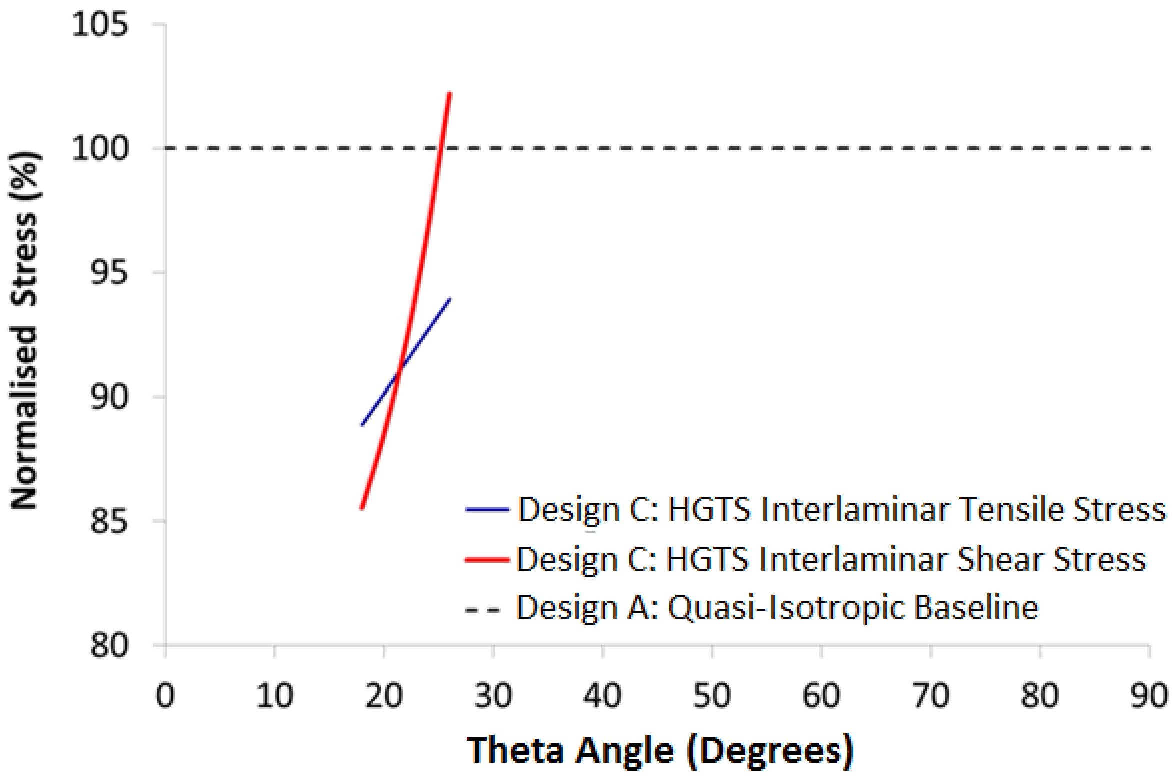

Figure 4-16 Normalised interlaminar tensile and shear stresses with global laminate stiffness constraints – hygrothermally stable DoE compared to baseline quasi-isotropic design

4.3.3 Finite element analysis of T-joints

4.3.3.1 Bending load case

Based on the analysis presented above, four stiffener laminate stacking sequences were evaluated using FEA. Figure 4-17 compares the interlaminar tensile stress distribution across the radius bends and delta-fillet region in the T-joint. The stress distributions are shown for the case of a 20 N elastic perturbation bending load applied to the stiffener (refer Figure 4-8). The figures show a 2D slice encompassing the peak interlaminar tensile stress which occurred at the mid-point across the width of the T-joint. The curved arrow indicates the direction of the bending moment induced by the applied load on the stiffener web.

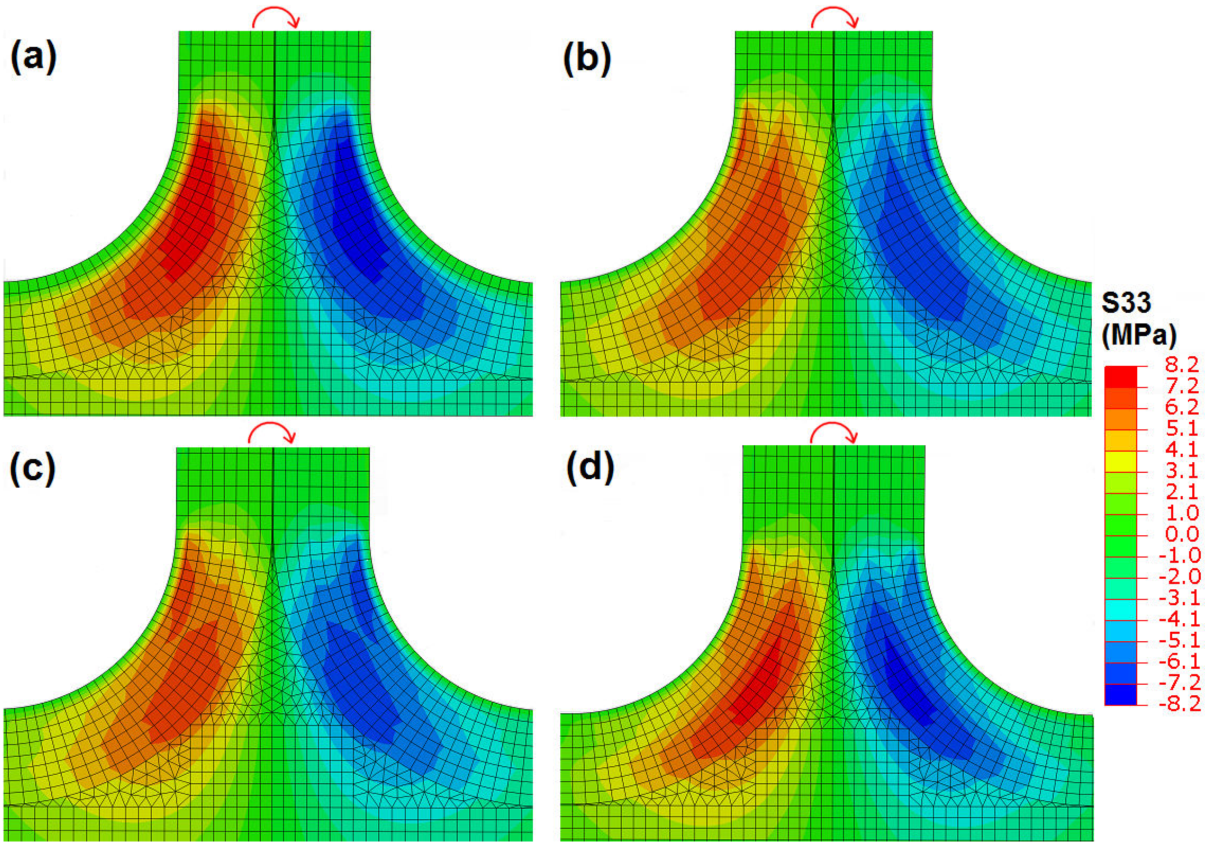

Figure 4-17 FEA interlaminar tensile stress (σ_{33}) distribution: (a) baseline quasi-isotropic (design A); (b) bio-inspired optimised (design B); (c) quasi-isotropic DoE (design C); and (d) hygrothermally stable DoE (design D)

The interlaminar tensile stress concentration occurs at about the mid-point both tangentially and radially across the radius bend. The FE analysis revealed that the interlaminar tensile stress was more evenly distributed across the radius of the design B (bio-inspired optimised - refer Figure 4-17b), design C (quasi-isotropic DoE - refer Figure 4-17c) and design D (hygrothermally stable DoE - refer Figure 4-17d) joints compared to design A (baseline - refer Figure 4-17a). While a completely uniform interlaminar tensile stress distribution (without any localised regions of concentrated stress) was not attained in the optimised T-joints, a significant reduction in the peak interlaminar tensile stress was achieved by altering the ply stacking pattern of the stiffener laminate.

The location of peak interlaminar tensile stress was also influenced by the laminate stacking pattern. Figure 4-18 shows the peak interlaminar tensile stress across the T-joint radius bend (which was 1.6 mm thick) for the 4 different laminate stacking sequence concepts.

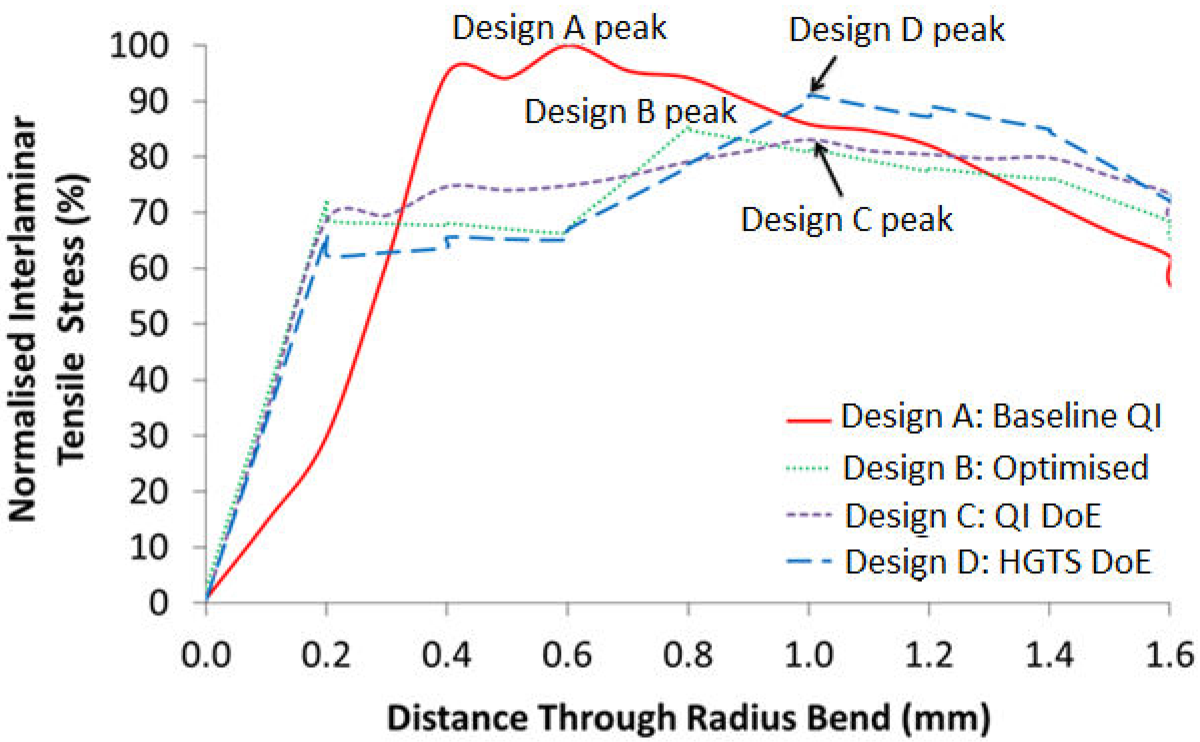

Figure 4-18 FEA interlaminar tensile stress (σ_{33}) distribution for the 4 stiffener laminate concepts

In design A (baseline quasi-isotropic), the peak occurs between ply 3 (-45°) and ply 4 (90°). In design B (bio-inspired optimised), the peak occurs between ply 4 (-12°) and ply 5 (36°). In design C (improved quasi-isotropic DoE), the peak occurs between ply 5 (0°) and ply 6 (45°). In design D (hygrothermally stable DoE), the peak also occurs between ply 5 (-18°) and ply 6 (72°). Designs B, C and D have a higher interlaminar tensile stress in ply 1 (free edge radius bend ply) compared to design A because ply 1 is stiffer than the baseline.

Figure 4-19 compares the interlaminar shear stress distribution across the radius bend and delta-fillet regions in the T-joints under the applied bending load. The figure shows a 2D slice encompassing the peak interlaminar shear stress which occurred at the free edge across the width of the T-joints.

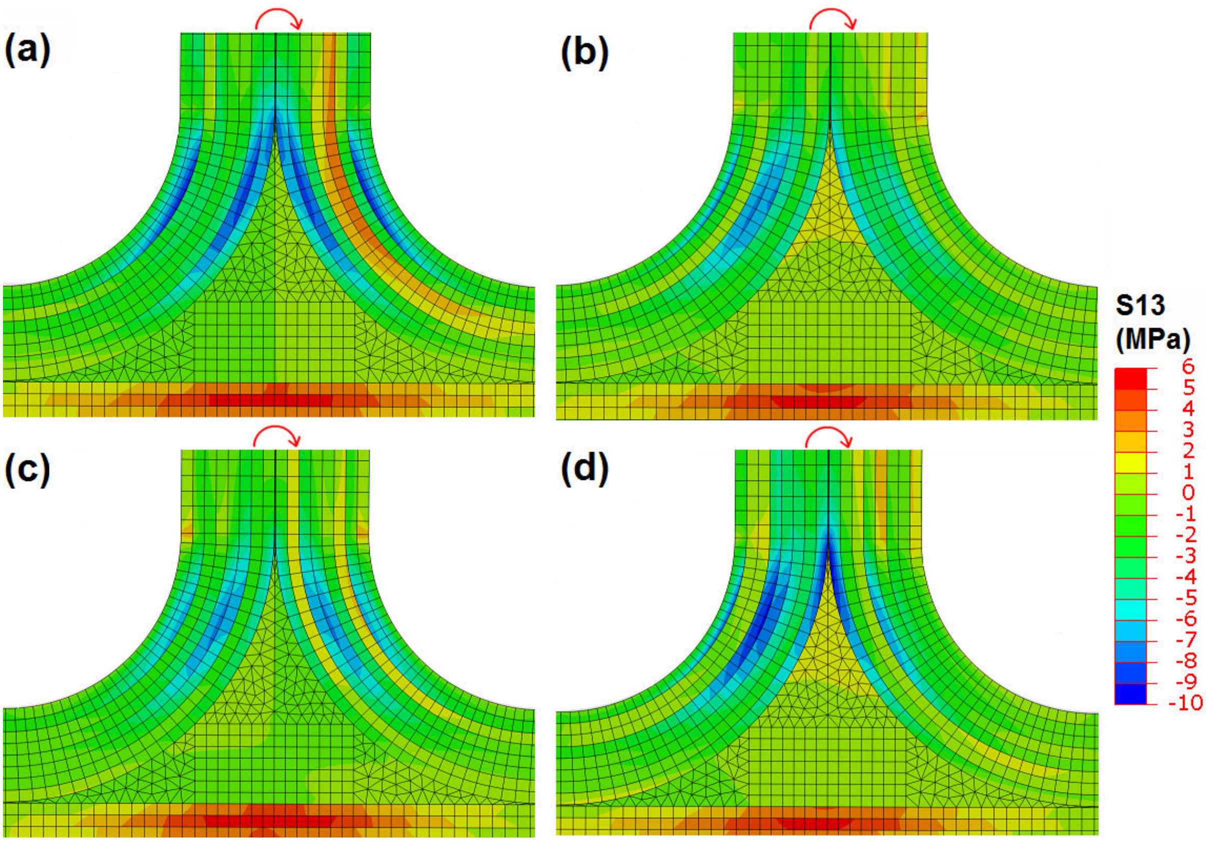

Figure 4-19 FEA interlaminar shear stress (τ_{13}) distribution: (a) baseline quasi-isotropic (design A); (b) bio-inspired optimised (design B); (c) quasi-isotropic DoE (design C); and (d) hygrothermally stable DoE (design D)

Although the interlaminar shear stress was not a driving design factor in the optimisation objective, there was a significant reduction in the peak interlaminar shear stress, particularly in design B (bio-inspired optimised - refer Figure 4-19b) and design C (improved quasi-isotropic DoE - refer Figure 4-19c). The interlaminar tensile and shear stresses both contribute to the interactive interlaminar stress concentration that initiates delamination damage in the radius bend, and therefore any reduction in the shear stress should increase the failure initiation load of the T-joint.

The distribution of the interlaminar shear stress across the radius bend was also altered by the change in laminate stacking sequence, with the peak shear stress coinciding with the highest stiffness plies. Figure 4-20 shows the peak interlaminar shear stress across the radius bend for the four laminate stacking concepts. In design A the peak shear stress occurs between ply 2 (0°) and ply 3 (-45°). In design B the peak stress occurs between ply 1 (12°) and ply 2 (84°). In design C the peak stress occurs between ply 5 (0°) and ply 6 (45°). In design D the peak stress occurs between ply 4 (18°) and ply 5 (-18°).

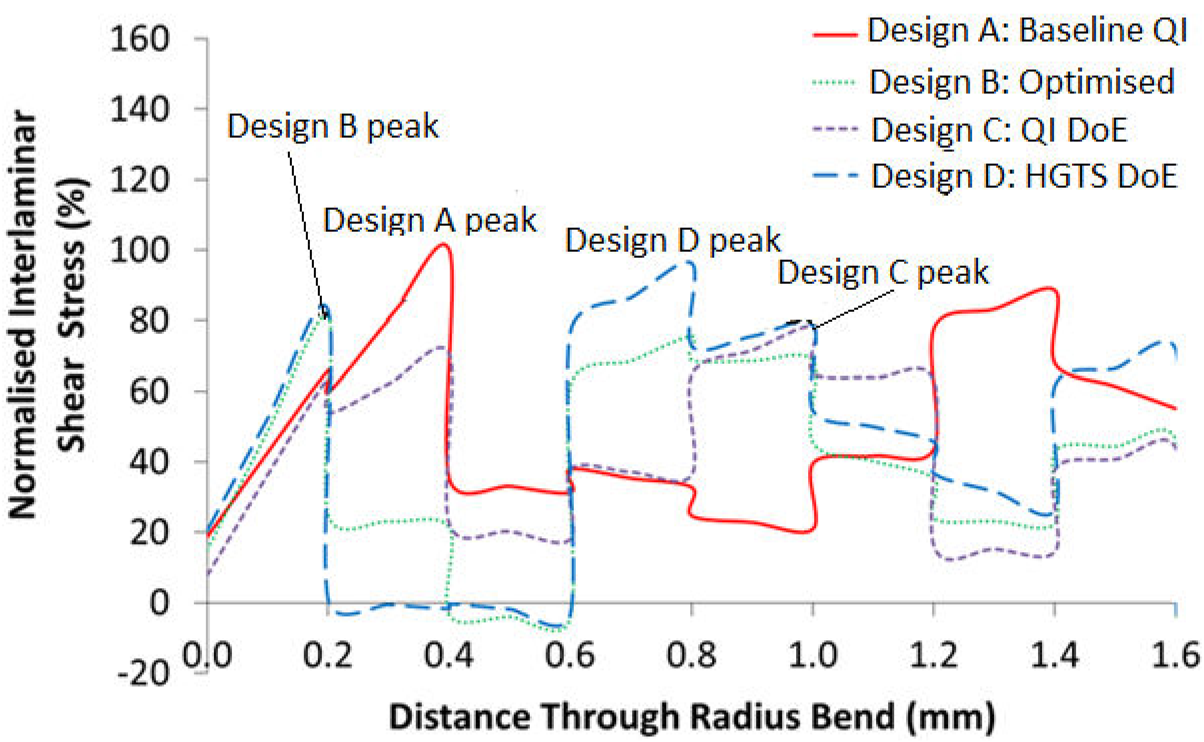

Figure 4-20 FEA interlaminar shear stress (τ_{13}) distribution for the 4 stiffener laminate concepts

Table 4-6 summarises the stiffness and interlaminar shear stress values for the four stiffener laminate design concepts based on the FEA under the bending perturbation load of 20 N. For designs B and D the global stiffness values were within the prescribed constraint of ±10% of the baseline conventional quasi-isotropic T-joint. In design C the bending stiffness was 22% higher than the baseline, thus exceeding the global bending stiffness constraint. Designs B, C and D all achieved a reduction in both the peak interlaminar tensile stress (varying between 11 - 17%) and the peak interlaminar shear stress (varying between 4 – 22%).

Table 4-6 Comparison of the stiffness properties and peak interlaminar and shear stresses for the four stiffener stacking sequences under bending load (change from baseline design %)

Stiffener Laminate Stacking Pattern	**A_{11} (GPa.mm)**	**D_{11} (GPa.mm^3)**	**Peak σ_{33} (MPa)**	**Peak τ_{13} (MPa)**	**Σ reduction in peak stresses**
Design A: Baseline quasi-isotropic $[45/0/-45/90/90/-45/0/45]_s$	158.9	142.9	8.35	-9.85	
Design B: Bio-inspired optimised: 4 variables: $[\theta_1/\theta_2/\theta_3/\theta_4]$ $[12/84/-84/-12/36/60/-60/-36]_s$	150.5 (-5.3%)	155.8 (9.0%)	7.12 (-15%)	-7.97 (-19%)	-34%
Design C: Quasi-isotropic DoE: 4 variables: [0/±45/90] $[0/45/90/-45/0/45/90/-45]_s$	158.9 (0.0%)	174.0 (22%)*	6.93 (-17%)	-7.70 (-22%)	-39%
Design D: Hygrothermally stable DoE: 1 variable: $[\theta/(\theta–90)]$ $[18/-72/-72/18/-18/72/72/-18]_s$	171.8 (8.1%)	152.3 (6.6%)	7.42 (-11%)	-9.48 (-4%)	-15%

* Exceeds constraint

All three alternate stiffener laminate designs have a higher bending stiffness compared to the baseline design. The higher bending stiffness could mean that the T-joints attract more load for the same displacement, somewhat negating the increase in strength. This can only be established through analysis and testing of larger structures.

The sum of the percentage reduction in the peak interlaminar tensile and shear stresses compared to the baseline is taken as an estimate of the improvement in the failure initiation load. The FE analysis predicts that disqualifying design C (which exceeds the laminate stiffness constraints) design B (bio-inspired optimised) will have the highest increase in bending failure load.

4.3.3.2 Tension load case

Figure 4-21 compares the interlaminar tensile stress distribution for the four laminate design concepts under a tensile load applied to the stiffener.

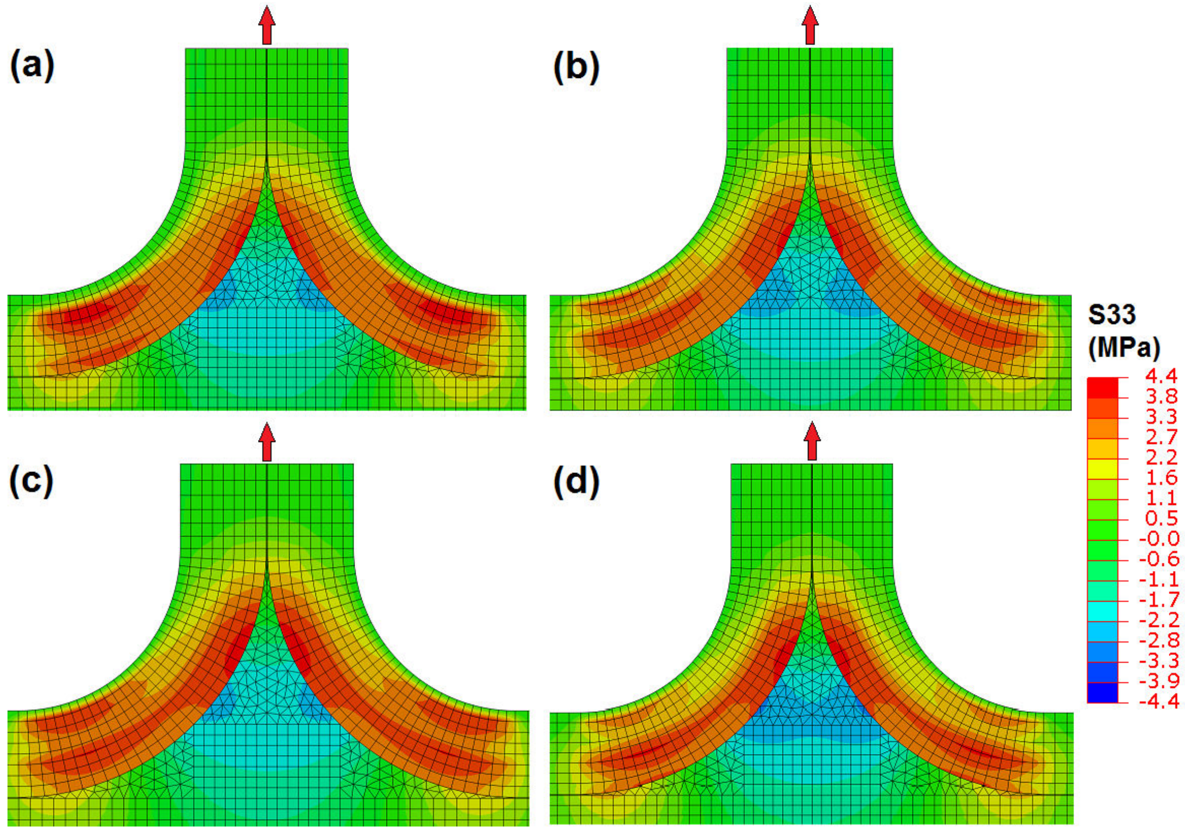

Figure 4-21 FEA interlaminar tensile stress (σ_{33}) distribution: (a) baseline quasi-isotropic (design A); (b) bio-inspired optimised (design B); (c) quasi-isotropic DoE (design C); and (d) hygrothermally stable DoE (design D)

The figures show a 2D slice encompassing the peak interlaminar tensile stress which occurred at the mid-point across the width of the T-joints. The arrow indicates the direction of the tensile force applied to the stiffener web. The stress distribution was similar for all the laminate stacking patterns, with two interlaminar tensile stress concentrations (indicated by red shading). One stress concentration occurs within the radius bend and the other occurs at the radius bend/delta-fillet interface

Figure 4-22 compares the interlaminar shear stress distribution across the radius bend and delta-fillet regions in the T-joint for the four different stiffener laminate stacking sequence concepts under the tensile load. The highest interlaminar shear stresses occur in the stiffest plies: in the 0° plies (ply 2 and ply 7) in design A (refer Figure 4-22a), ±12° plies (plies 1, 4, 5 and 8) in design B (refer Figure 4-22b), 0° plies (ply 1 and ply 5) in design C (refer Figure 4-22c) and ±18° plies (plies 1, 4, 5 and 8) in design D (refer Figure 4-22d).

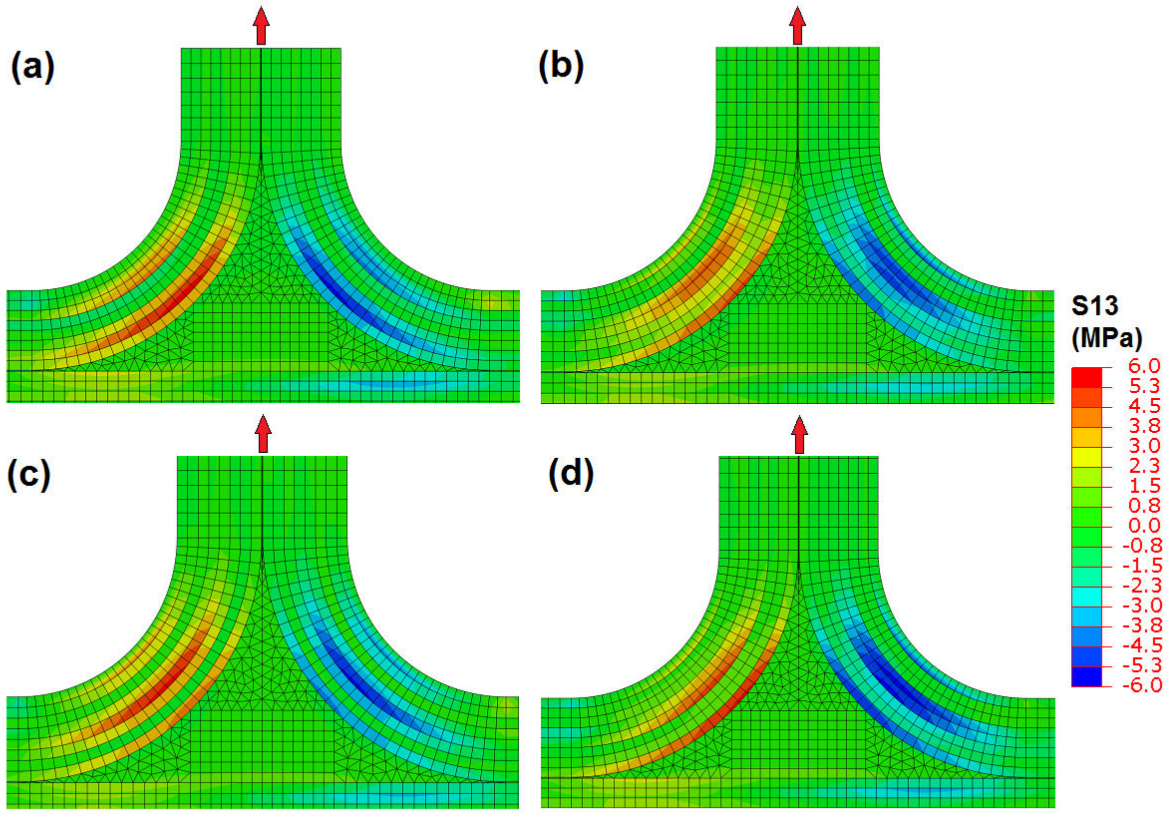

Figure 4-22 FEA interlaminar shear stress (τ_{13}) distribution: (a) baseline quasi-isotropic (design A); (b) bio-inspired optimised (design B); (c) quasi-isotropic DoE (design C); and (d) hygrothermally stable DoE (design D)

Table 4-7 summarises the stiffness and interlaminar shear stress values calculated using the FE model for the T-joints under the tensile perturbation load of 100 N. Designs B, C and D all achieved a modest reduction in the peak interlaminar tensile stress of between 2.9 – 5.3%.

The sum of the percentage reduction in the peak interlaminar tensile and shear stresses predicts a small improvement for designs B, C and D under tensile load compared to the baseline design A. The FE analysis predicts that the bio-inspired design B will have the highest increase in tensile failure load, followed by design C and then design D.

Table 4-7 Comparison of the stiffness properties and peak interlaminar and shear stresses for the four stiffener stacking sequences under tensile load (bracketed numbers refer to change from baseline design %)

Stiffener Laminate Stacking Pattern	**A_{11} (GPa. mm)**	**D_{11} (GPa. mm^3)**	**Peak σ_{33} (MPa)**	**Peak τ_{13} (MPa)**	**Σ Difference in Peak Stresses**
Design A: Baseline quasi-isotropic $[45/0/-45/90/90/-45/0/45]_s$	158.9	142.9	4.16	5.72	
Design B: Bio-inspired optimised: 4 variables: $[\theta_1/\theta_2/\theta_3/\theta_4]$ $[12/84/-84/-12/36/60/-60/-36]_s$	150.5 (-5.3%)	155.8 (9.0%)	3.94 (-5.3%)	5.35 (-6.5%)	-11.8%
Design C: Quasi-isotropic DoE: 4 variables: [0/±45/90] $[0/45/90/-45/0/45/90/-45]_s$	158.9 (0.0%)	174.0 (22%)*	4.04 (-2.9%)	5.67 (-0.9%)	-3.8%
Design D: Hygrothermally stable DoE: 1 variable: [θ/(θ–90)] $[18/-72/-72/18/-18/72/72/-18]_s$	171.8 (8.1%)	152.3 (6.6%)	4.02 (-3.4%)	5.86 (2.4%)	-1.0%

* Exceeds constraint

4.3.4 Experimental results

Mechanical tests were performed on the four stiffener laminate design concepts to validate the results from the FE model and also to determine their failure properties and damage behaviour. Figure 4-23 shows the definition of the flange, stiffener and width dimensions.

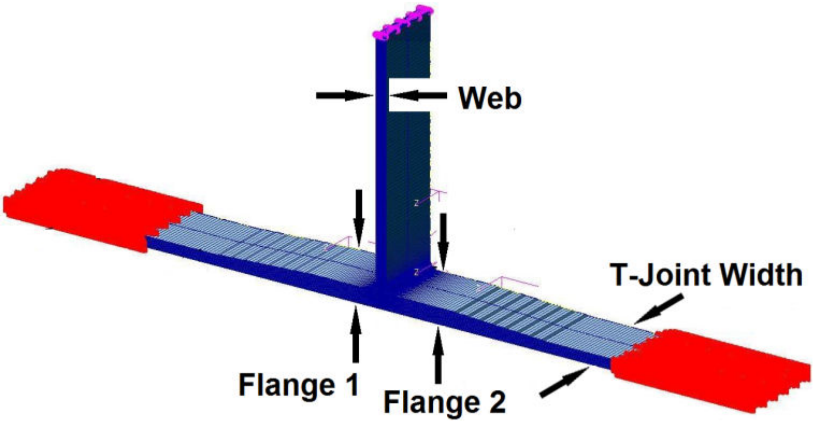

Figure 4-23 Measured dimensions of T-joint experimental samples

The dimensions of the T-joint specimens used in the experimental testing are given in Table 4-8 for bending and Table 4-9 for tension loading. The only significant difference between the T-joint types was the stiffener web thickness of the hygrothermally stable joint samples which was between 10 – 13% less than the other joint specimens.

Table 4-8 Dimensions of T-joint samples used in the experimental bending testing (bracketed numbers refer to change from baseline design %)

	Design A Baseline Quasi-Isotropic	**Design B Bio-Inspired Optimised**	**Design C Quasi-Isotropic DoE**	**Design D Hygrothermally Stable DoE**
Flange 1 thickness t_1 (mm)	5.20	5.07 (-2.5%)	5.14 (-1.2%)	5.05 (-2.9%)
Flange 2 thickness t_2 (mm)	5.21	5.07 (-2.7%)	5.13 (-1.4%)	5.10 (-2.1%)
Stiffener web thickness t_3 (mm)	3.19	3.15 (-1.3%)	3.06 (-4.0%)	2.86 (-10%)
T-joint width w (mm)	20.59	20.59 (0.0%)	20.29 (-1.5%)	21.15 (2.7%)
T-joint flange area $=(t_1+t_2)/2*w$ (mm^2)	107.1	104.4 (-2.5%)	104.16 (-2.8%)	107.29 (0.2%)

Table 4-9 Dimensions of T-joint samples used in the experimental tensile testing (bracketed numbers refer to change from baseline design %)

	Design A Conventional Quasi-Isotropic	Design B Bio-Inspired Optimised	Design C Quasi-Isotropic DoE	Design D Hygrothermally Stable DoE
Flange 1 thickness t_1 (mm)	5.10	5.27 (3.3%)	5.25 (2.9%)	5.14 (0.8%)
Flange 2 thickness t_2 (mm)	5.10	5.26 (3.3%)	5.24 (2.8%)	5.19 (1.8%)
Stiffener web thickness t_3 (mm)	3.21	3.16 (-1.5%)	3.05 (-4.9%)	2.89 (-13%)
T-joint width w (mm)	20.87	20.21 (-3.2%)	20.27 (-2.9%)	20.80 (-0.3%)
T-joint flange area $=(t_1+t_2)/2*w$ (mm^2)	106.3	106.4 (0.1%)	106.2 (-0.1%)	107.35 (0.9%)

The experimental test results were analysed based on seven metrics (refer Figure 4-24):

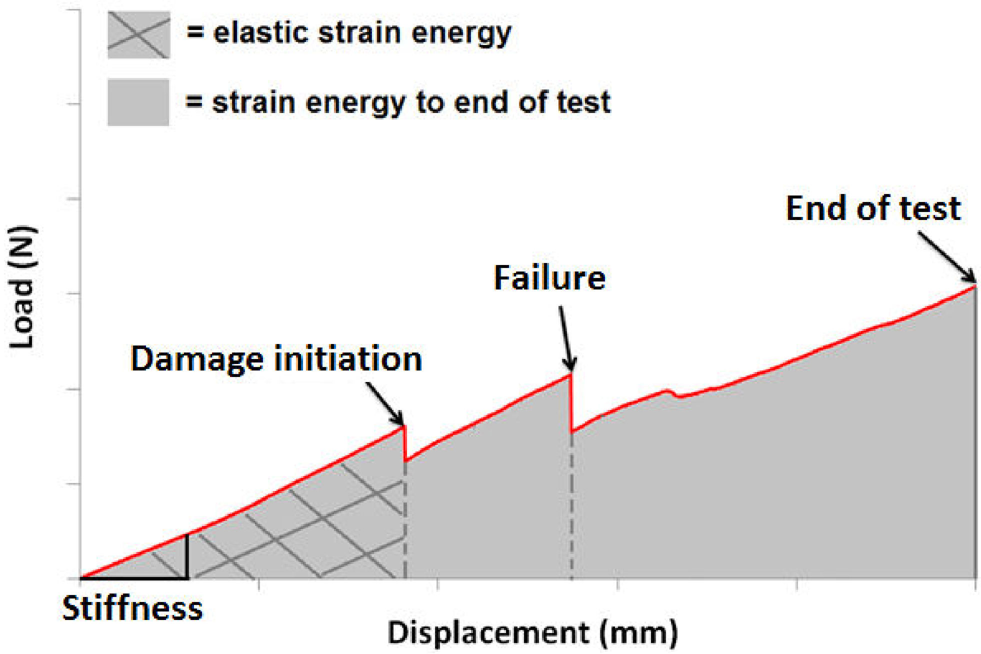

Figure 4-24 Definition of experimental analysis metrics for T-joint performance

- Stiffness = slope of load-displacement curve up to 5 mm (bending) or 2 mm (tensile) displacement;
- Damage initiation load;
- Displacement at damage initiation;
- Failure load = max load before failure mode of crack propagating through delta-fillet region;
- Displacement at failure load
- Elastic strain energy = area under load-displacement curve up to damage initiation load; and
- Strain energy to end of test = area under load-displacement curve up to 25 mm (bending) or 7 mm (tensile) displacement.

4.3.4.1 Bending load case

Mechanical bend tests were performed on the composite T-joint to validate the FE analysis by experimentally determining the change in structural performance for four stiffener laminate stacking design concepts. Representative bending load-displacement curves for the four concepts are given in Figure 4-25. The main features of the curves are: (i) the bending stiffness *k*, which is defined by the gradient of the linear portion of the curve; (ii) the damage initiation load (indicated by the arrows in Figure 4-25); and (iii) the failure mode, which was either a one-step failure mode whereby damage initiation coincided with failure load or a two-step progressive failure mode.

Table 4-10 summarises the bending experimental results based on the seven test metrics. As predicted by classical laminated theory, design C (quasi-isotropic DoE) was the only design that exceeded the bending stiffness constraint of ±10% of the baseline design A. Designs B, C and D all showed significant improvement in the damage initiation load compared to the baseline design A. Designs B and C had similar results in terms of damage initiation load, failure load, elastic strain energy and absorbed strain energy to 25 mm displacement (end of test). However design B achieved these results within the prescribed global in-plane and bending stiffness constraints, while design C did not.

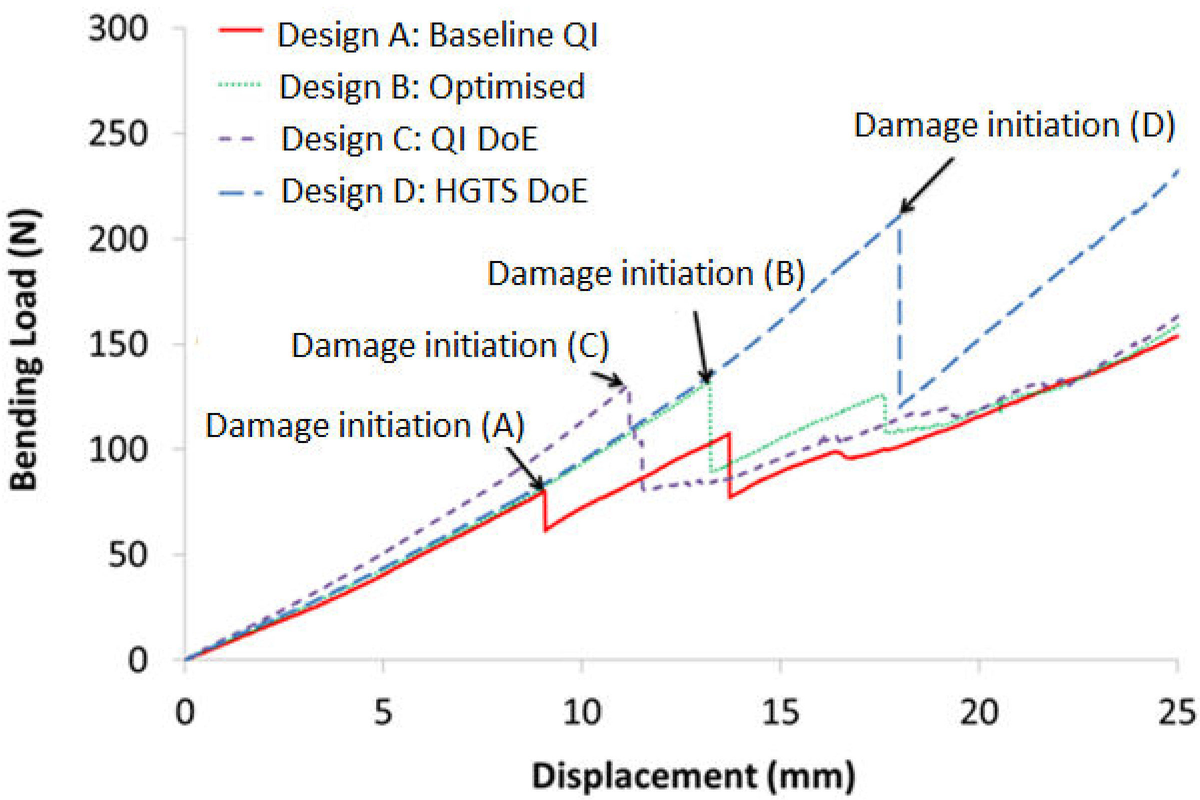

Figure 4-25 Representative bending load-displacement curves for designs A, B, C and D

The percentage improvement in damage initiation load in design B (41%) and design C (48%) could be approximated by the sum of the percentage reduction in the peak interlaminar tensile and shear stresses in the radius bend derived from the FEA of 34% for design B and 39% for design C.

The outlier in the experimental results was design D which exhibited a 126% increase in damage initiation load and 306% increase in elastic strain energy compared to the baseline design A (refer Table 4-10), despite the FEA model predicting the sum of the reduction in the peak interlaminar tensile and shear stresses in the T-joint radius bend to be just 25% (refer Table 4-6). In addition, design D was the only design that achieved a significant improvement in failure load compared to the baseline design A. This was attributed to the hygrothermal stability of the design D laminate compared to the bio-inspired optimised (design B) and quasi-isotropic DoE (design C) laminates.

Table 4-10 Comparison between the experimental structural properties of designs A, B, C and D under bending [The number in the square brackets is the standard deviation based on six measurements]. (The number in the round brackets is the percentage difference from the baseline conventional quasi-isotropic T-joint)

	Design A **Conventional Quasi-Isotropic T-Joint**	**Design B** **Bio-Inspired Optimised T-Joint**	**Design C** **Quasi-Isotropic DoE T-Joint**	**Design D** **Hygrothermally Stable DoE T-Joint**
Stiffness *k* (N/mm)	8.38 [±0.85]	8.94 [±0.72] (7%)	9.50 [±0.51] (13%)	7.91 [±0.77] (-6%)
Damage initiation load (N)	85 [±13]	120 [±14] (41%)	126 [±18] (48%)	192 [±30] (126%)
Displacement at damage initiation (mm)	8.88 [±0.93]	11.4 [±1.15] (28%)	11.9 [±1.5] (34%)	17.6 [±1.2] (98%)
Failure load (N)	126 [±30]	125 [±20] (-0.8%)	126 [±18] (0.0%)	194 [±32] (54%)
Displacement at failure load (mm)	15.3 [±3.3]	17.7 [±1.4] (16%)	11.9 [±1.5] (-22%)	18.1 [±2.1] (18%)
Elastic strain energy (J)	361 [±84]	634 [±122] (76%)	689 [±159] (91%)	1467 [±298] (306%)
Strain energy to 25 mm displacement (end of test) (J)	2227 [±167]	2220 [±168] (-0.3%)	2260 [±84] (1.5%)	2576 [±317] (16%)

Table 4-11 summarises the hygrothermal and mechanical coupling properties of the four stiffener laminate design concepts across the 8 ply radius bend laminate of the T-joint. Designs B and C are not hygrothermally stable across the 8 ply radius bend laminate, which will cause some post-cure warping and residual thermal stresses in the radius bend/delta-fillet region. Designs A and D will not have this problem. In addition, designs B and C are completely coupled in all permutations of the extension-bend-twist planes in the 8 ply radius bend. However, design D is less coupled, with mechanical coupling occurring only in the extension-twist plane.

Table 4-11 Summary of hygrothermal stability and mechanical coupling of the four design concepts

8 Ply Radius Bend Laminate	Symmetric ?	Hygro-thermally Stable?	Mechanical Coupling?	Coupled *[B]* matrix
Design A Baseline quasi-isotropic [45/0/-45/90/90/-45/0/45]	Yes	Yes	No	$\begin{bmatrix} 0 & 0 & 0 \\ 0 & 0 & 0 \\ 0 & 0 & 0 \end{bmatrix}$
Design B Bio-inspired optimised [12/84/-84/-12/36/60/-60/-36]	No	No	Yes	$\begin{bmatrix} -7.14 & 6.0 & -7.09 \\ 6.0 & -4.9 & 7.9 \\ -7.09 & 7.9 & 6.0 \end{bmatrix}$
Design C Quasi-isotropic DoE [0/45/90/-45/0/45/90/-45]	No	No	Yes	$\begin{bmatrix} -10.9 & 2.1 & -4.4 \\ 2.1 & 6.7 & -4.4 \\ -4.4 & -4.4 & 2.1 \end{bmatrix}$
Design D Hygrothermally stable DoE [18/-72/-72/18/-18/72/72/-18]	No	Yes	Yes	$\begin{bmatrix} 0 & 0 & -7.9 \\ 0 & 0 & 7.9 \\ -7.9 & 7.9 & 0 \end{bmatrix}$

High speed photographic images of the failure modes at damage initiation, failure load and end of test (25 mm bending displacement) are given for designs A, B, C and D (refer Figure 4-26 to Figure 4-29). All four stiffener laminate design concepts had similar failure modes with damage initiating as delaminations in the tensile side of the radius bend and failure load (if a progressive failure mode) corresponding to a load drop caused by a crack propagating through the radius bend/delta-fillet interface. At the end of the bending test this main crack had propagated along the tensile side stiffener flange/skin bond-line under mode I (opening), across the radius bend/delta-fillet regions, and within the stiffener web. This dominant crack also propagated along the compression side stiffener flange/skin bond-line, but did not grow as quickly due to the crack propagation being dominated by mode II (shear).

Designs A and B had a two-step progressive failure mode, and designs C and D both had a one-step failure mode in which the radius bend delaminations (damage initiation) and radius bend/delta-fillet interface cracking (failure) occurred almost simultaneously. High speed photography showed that in fact the delamination in the radius bend initiated first (refer Figure 4-28a) followed by the radius bend/delta-fillet interface crack approximately 0.001 second later (refer Figure 4-28b).

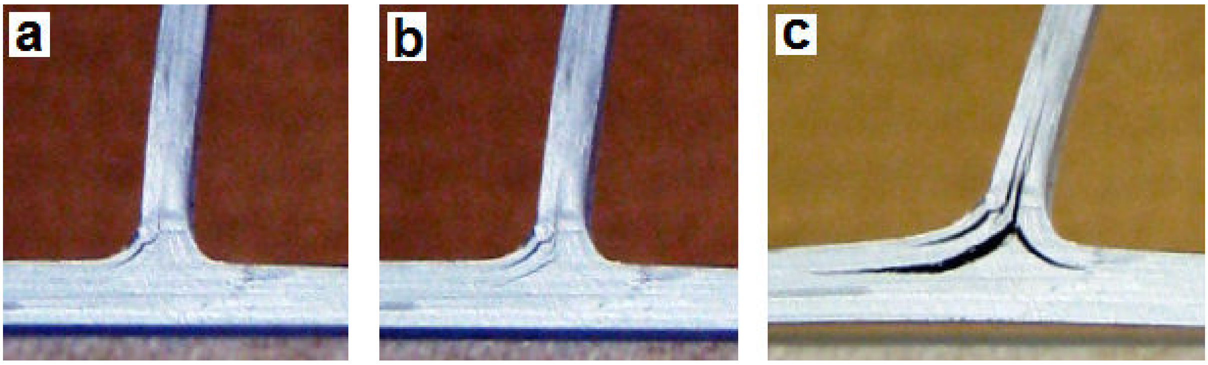

Figure 4-26 Damage and failure modes under bending testing: baseline quasi-isotropic (design A): (a) delamination damage initiation; (b) failure load; and (c) end of bending test at 25 mm displacement

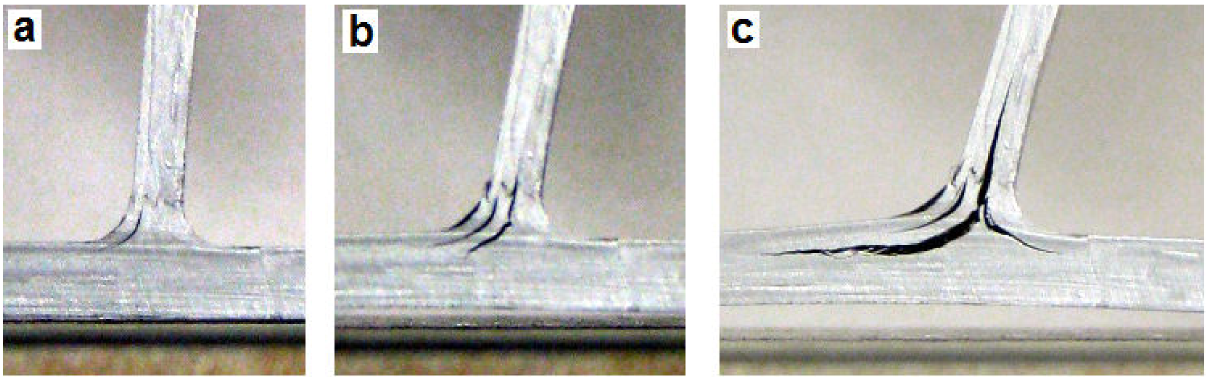

Figure 4-27 Damage and failure modes under bending testing: bio-inspired optimised (design B): (a) delamination damage initiation; (b) failure load; and (c) end of bending test at 25 mm displacement

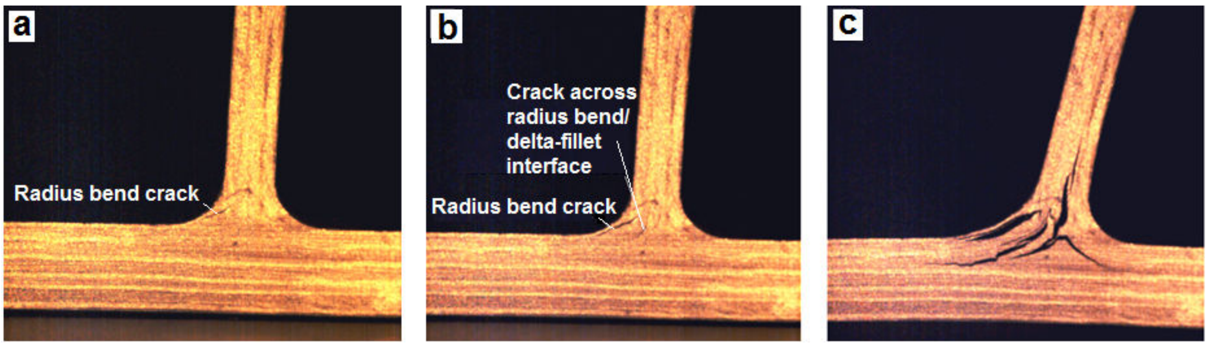

Figure 4-28 Damage and failure modes under bending testing: quasi-isotropic DoE (design C): (a) radius bend delamination initiation followed 0.001 sec later by; (b) cracking across the radius bend/delta-fillet interface; and (c) end of bending test at 25 mm displacement

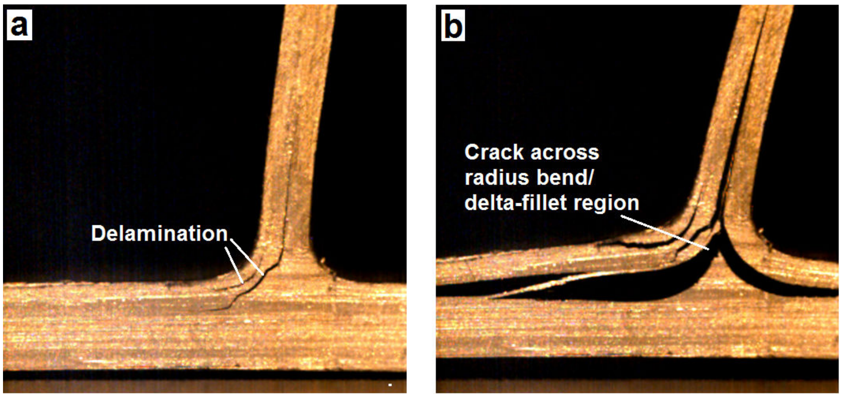

Figure 4-29 Damage and failure modes under bending testing: hygrothermally stable (design D): (a) damage initiation radius bend delaminations; and (b) end of bending test at 25 mm displacement

4.3.4.2 Tension load case

Representative experimental tensile load-displacement curves for designs A, B, C and D are given in Figure 4-30. The failure mode for all four stiffener laminate design concepts was similar and occurred in a multi-step process. Damage initiation corresponded to delaminations that occurred in one or both radius bends and/or cracking at the radius bend/delta-fillet interface as shown in Figure 4-31 to Figure 4-34. The initiation of these delamination cracks corresponded to the load drops in the tensile load-displacement curves, with some samples showing only one large load drop (indicating simultaneous delamination in radius bend and across the radius bend/delta-fillet interface) and other samples exhibiting multiple small load drops corresponding to the progressive development of these cracks. The damage initiation failure mode was different compared to the bending load case, where failure was consistently observed to be delamination cracking within the tensile side radius bend. In contrast, under tensile loading first failure in some cases occurred due to radius bend delaminations, and in other cases due to cracking at the delta-fillet interface and in other instances a combination of both.

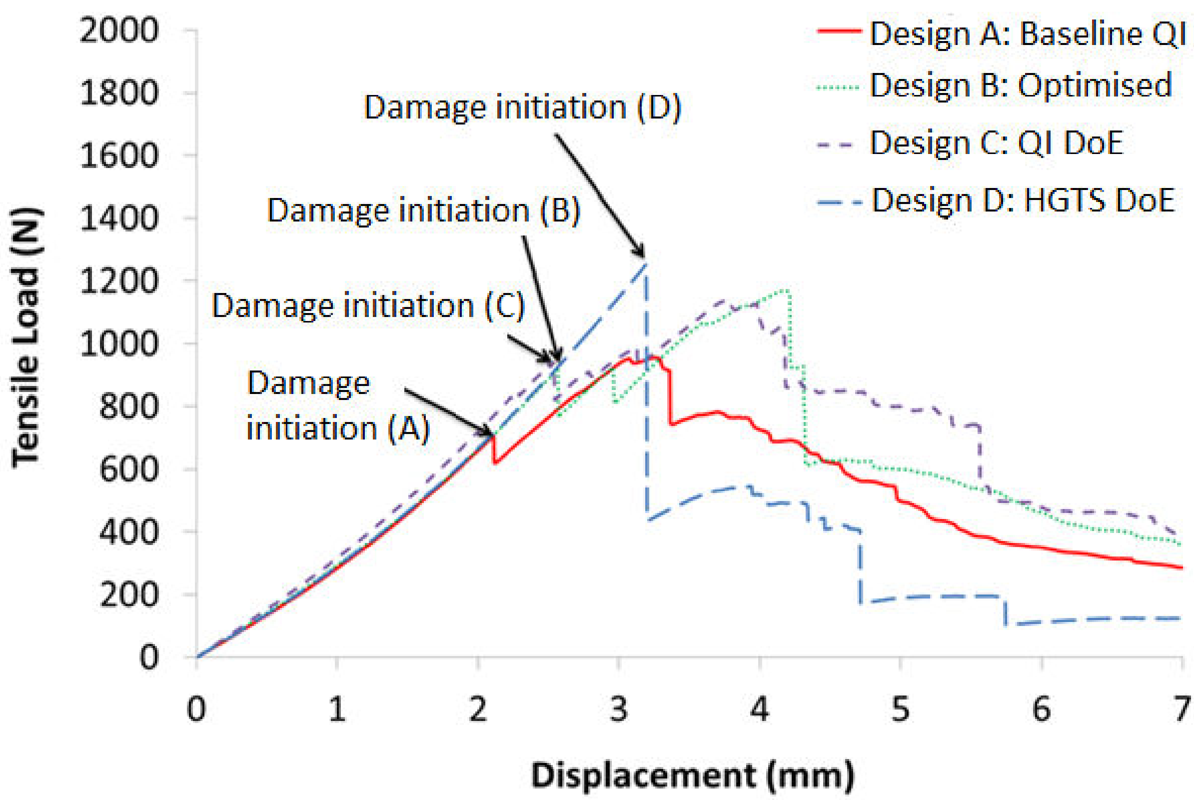

Figure 4-30 Representative tensile load-displacement curves for designs A, B, C and D

Final failure occurred when the crack at the radius bend/delta-fillet interface propagated either above or below (refer Figure 4-31b) the delta-fillet 'noodle' to the stiffener flange/skin bond-line to form the dominant horizontal crack. This crack opened up quickly, reflecting the absence of crack stoppers coupled with the low interlaminar fracture toughness of unidirectional carbon/epoxy laminate. Testing was stopped at 7 mm tensile displacement with the samples exhibiting a well-developed crack between the stiffener web/skin bond-line, another well-developed main crack within the stiffener web, and several secondary cracks in the radius bend region (refer Figure 4-31b). The tensile failure mode of the bio-inspired optimised (for bending) design B was the same as the baseline design A for both damage initiation (refer Figure 4-32a) and end of test (refer Figure 4-32b).

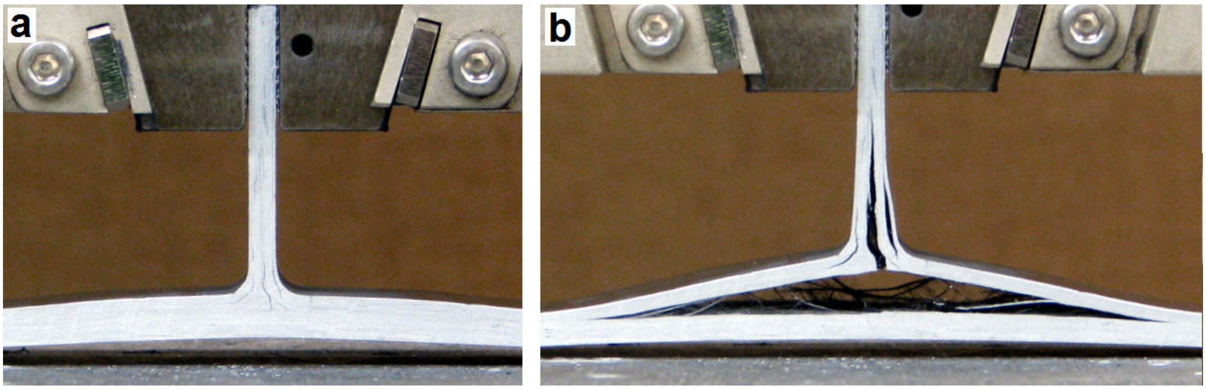

Figure 4-31 Design A under tensile loading: (a) damage initiation showing mixture of radius bend and radius bend/delta-fillet interface cracks; and (b) end of test at 7 mm tensile displacement

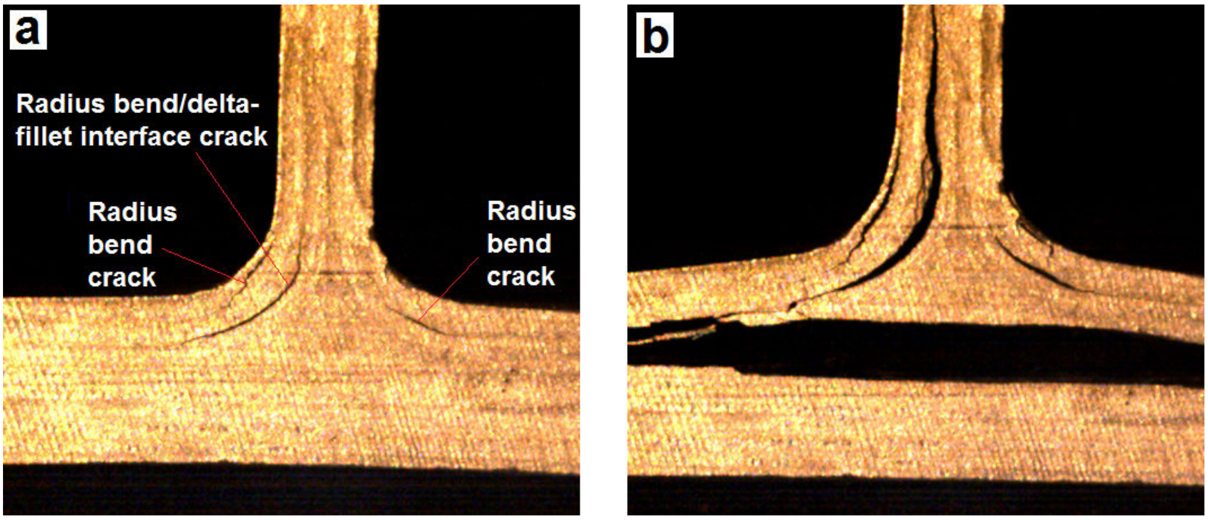

Figure 4-32 Damage and failure modes under tensile loading - bio-inspired optimised T-joint (Design B): (a) damage initiation showing mixture of radius bend and radius bend/delta-fillet interface cracks; and (b) end of test at 7 mm tensile displacement

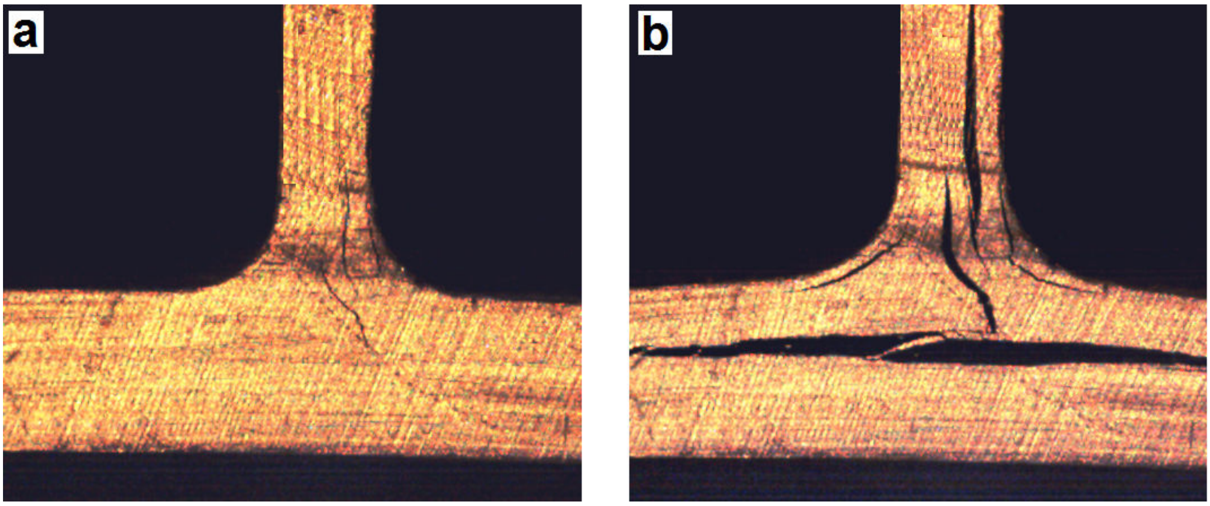

Figure 4-33 Design C damage and failure modes under tensile loading: (a) radius bend delamination and radius bend/delta-fillet interface cracking occurred simultaneously; and (b) end of bending test at 7 mm displacement

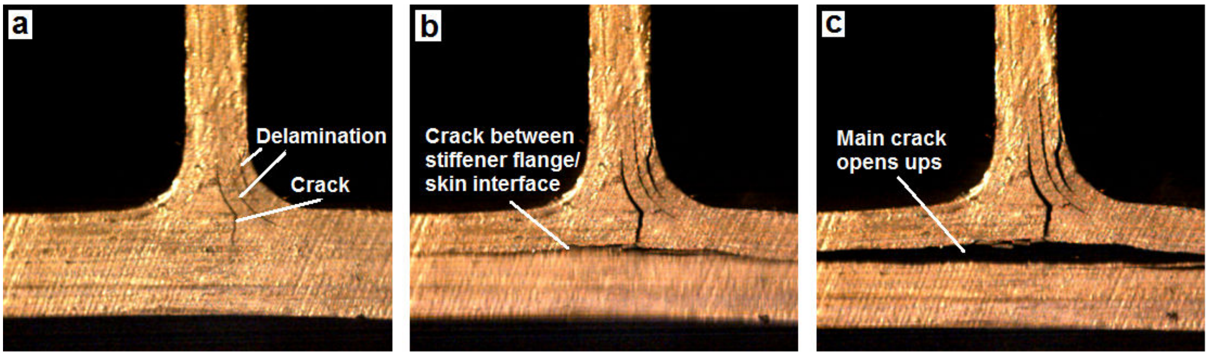

Figure 4-34 Design D damage and failure modes under tensile testing: (a) damage initiation with two radius bend delaminations and a crack across the radius bend/delta-fillet interface; (b) 0.0004 seconds later the crack propagates down through the delta-fillet 'noodle' to the stiffener flange/skin bond-line; and (c) 0.0004 seconds later uncontrolled propagation of the dominant stiffener flange/bond-line crack

Table 4-12 summarises the tensile experimental results for the four T-joint designs. As predicted by FEA, the results show that designs B and C had better mechanical performance with a higher damage initiation load under tensile loading in comparison with the baseline design A. The failure loads were approximately the same. Once again, design D performed well beyond the FEA prediction with a 84% increase in damage initiation load and 144% increase in elastic strain energy compared to design A. Again this was attributed to the absence of residual thermal stresses and reduced mechanical coupling in the radius bend of due to the special properties of the hygrothermal stiffener laminate in design D.

Table 4-12 Comparison between the experimental structural properties of designs A, B, C and D under tension. [The number in the square brackets is the standard deviation based on six measurements]. (The number in the round brackets is the percentage difference from the baseline conventional quasi-isotropic T-joint)

	Design A Conventional Quasi-Isotropic T-Joint	Design B Bio-Inspired Optimised T-Joint	Design C Quasi-Isotropic DoE T-Joint	Design D Hygrothermally Stable DoE T-Joint
Stiffness (N/mm)	257 [±44]	288 [±12] (12%)	303 [±10] (18%)	302 [±8] (18%)
Load at damage initiation (N)	707 [±55.3]	889 [±166] (26%)	927 [±9.8] (31%)	1300 [±90] (84%)
Displacement at damage initiation (mm)	2.30 [±0.34]	2.49 [±0.25] (8.3%)	2.52 [±0.09] (10%)	3.20 [±0.11] (39%)
Failure load (N)	1069 [±44.9]	1261 [±120] (18%)	1075 [±55] (0.6%)	1316 [±90] (23%)
Displacement at failure load (mm)	4.01 [±0.50]	4.09 [±0.40] (2.0%)	3.61 [±0.23] (-10%)	3.30 [±0.08] (-18%)
Elastic strain energy (J)	748 [±119]	1022 [±278] (37%)	1082 [±54] (45%)	1822 [±167] (144%)
Strain energy to 7 mm displacement (J)	3910 [±238]	4122 (±180) (5.4%)	4229 (±236) (8%)	3042 (±179) (-22%)

4.4 SUMMARY AND CONCLUSIONS

The research presented in this chapter has proven that tailored design of the stiffener ply stacking pattern by numerical optimisation or design of experiments can improve the mechanical properties of composite T-joints under bending and tension loads. A bio-inspired optimisation program was applied to the stiffener laminate stacking sequence of a T-joint. The optimisation program was bio-inspired in three ways: (i) the optimisation algorithm which altered the material in order to fit the external loading conditions (analogous to evolutionary optimisation – survival of the best fit) [5]; (ii) the optimisation objective function, which was set to minimise the peak interlaminar tensile stress (analogous to strain under elastic loading conditions), and thus attain a more uniform strain distribution - a principle observed in structural joints found in nature [19, 46, 156]; and (iii) the technique to minimise peak interlaminar tensile stress through changes to the ply orientations in the laminate stacking pattern is bio-inspired from the observations of the tailoring of the microfibril angle of wood in and around the branch-trunk joint to help achieve a uniform strain field [19, 46]. The optimisation program was simplified to a reduced factorial quasi-isotropic design of experiments and a full factorial hygrothermally stable DoE applied to design the stiffener laminate stacking pattern.

FE modelling revealed that the optimisation and DoE methodologies successfully tailored the laminate stacking pattern of the T-joint stiffener to the external loading conditions of a shear force and bending moment. The bio-inspired optimised and DoE stiffener laminates were capable of mimicking (in part) the biological principle of uniform strain that exists within biological structural joints such as the tree branch-trunk joint. The optimisation and DoE programs all placed a high stiffness ply in the location of ply 1 at the free edge of the outer radius bend in the region that undergoes maximum tensile strain under bending load. This resulted in significant decreases to both the peak interlaminar tensile and shear stresses in the T-joint radius bend and an increase in the interlaminar tensile and shear stresses in other plies. This is equivalent to generating a more uniform stress field. Increasing the loading of each ply to a higher and more homogenous fraction of the applied stress explains how the optimised designs were able to absorb more elastic energy prior to delamination damage initiation. Under a different load case of a tensile load applied to the stiffener web FEA predicted a small reduction in the peak interlaminar stresses in the radius bend for the optimised (for bending) and DoE designs.

The results of the experimental bending tests showed that all T-joint designs are susceptible to radius bend delaminations, which initiate at relatively low applied loads due to the high geometric interlaminar stress concentration coupled with the poor through-thickness strength properties of the carbon/epoxy composite. Altering the stiffener ply stacking pattern through optimisation or DoE methodologies increased both the load and displacement at damage initiation and absorbed elastic strain energy compared to the baseline T-joint, without significantly affecting the global stiffness properties. The reduction in the peak interlaminar stresses in the bio-inspired optimised and DoE joint designs under tensile loading was also validated experimentally to improve both the tensile damage initiation load and absorbed elastic strain energy. In both the bending and tensile load cases the bio-inspired optimised T-joint did not exhibit a significantly different failure load or total absorbed strain energy to the end of test compared to the baseline.

The experimental results revealed the bending load case exhibited a consistent damage initiation failure mode of delamination in the radius bend. For this load case the sum of the reduction in the peak interlaminar tensile and shear stresses could be used to estimate the improvement in the damage initiation load for the optimised and quasi-isotropic DoE T-joint designs. The hygrothermally stable DoE T-joint with just one ply angle variable exhibited the best mechanical properties, with its superior performance under both bending and tensile load cases far exceeding the predictions from the FE model. This was attributed to the reduction in residual thermal stresses across the radius bend due to the hygrothermally stable ply stacking pattern of the laminate. These results indicate that it is important to eliminate post-curing residual thermal stresses as a result of hygrothermal instability and mechanical coupling across the T-joint radius bend in order to increase the mechanical properties.

Based on this research, bio-inspired optimisation has proven an effective technique to improve the damage initiation strength of composite T-joints without incurring stiffness, weight or cost penalties. Changing the laminate ply stacking pattern of the T-joint to tailor the internal stiffness and strength properties to suit the external loading conditions is more feasible than many other methods (e.g. tailoring the internal material properties by altering the fibre volume fraction or fibre stiffness through hybrid material selection) using current composite manufacturing methods. It is believed that this bio-inspired optimisation methodology is flexible and can be applied to improve the damage initiation strength and elastic strain energy absorption of T-joints under other loading conditions (e.g. anti-symmetric bending), and other joint designs (e.g. L-shaped joints and 90° angle brackets).

Chapter 5:

5 T-JOINT DAMAGE TOLERANCE IMPROVEMENT THROUGH BIOMIMETIC EMBEDDED DESIGN

5.1 INTRODUCTION

In chapter four the damage initiation strength of a carbon/epoxy composite T-joint was improved using the bio-inspired optimisation methodology of tailoring the stiffener laminate stacking pattern to the prevailing loading conditions of a bending moment on the stiffener to delay delamination damage initiation in the radius bend. This approach successfully lowered the peak interlaminar tensile and shear stresses in the radius bend of the T-joint. However, the results also showed that altering the stiffener laminate stacking pattern produced no change to the damage tolerance of the T-joint as evidenced by similar results for the failure load and total absorbed energy at the end of test.

In chapter three the structural features in the tree branch-trunk joint that contribute to high damage tolerance were characterised: (i) optimised external radius geometry; (ii) optimised internal bond-line geometry (cone-shaped internal branch structure); and (iii) integrated adherends with the branch integrated into centre of the trunk through embedded design. The structural features of optimised radius geometry [61, 62, 64] and optimised bond-line geometry [15, 63] were discounted from further study as they have previously been investigated. Thus embedded design was chosen for further investigation as a bio-inspired structural feature capable of improving the damage tolerance of composite T-joints. Damage tolerance is defined in this study as the load-bearing capacity of a composite T-joint containing damage.

Research by Shigo [96] and x-ray computed tomography (CT) imaging from chapter three showed the branch is embedded to the centre of the tree trunk. Idealising the three-dimensional tree as a two-dimensional composite T-joint, the stiffener flange (analogous to the branch) is integrated to a depth of 50% of the skin (analogous to the trunk). In this chapter the bio-inspired concept of embedded design is appropriated with the objective of increasing the damage tolerance of the T-joint. The aim of the study presented in this chapter is to design and evaluate a bio-inspired composite T-joint with stiffener flange plies embedded to a varying percentage of the skin depth. The efficacy of the bio-inspired embedded design in regards to improving the damage tolerance was evaluated for T-joints made using both unidirectional and fabric carbon/epoxy prepreg material systems. The structural properties and damage modes of the bio-inspired embedded T-joint designs were experimentally measured and numerically analysed using non-linear finite element modelling.

5.2 EXPERIMENTAL METHODOLOGY

5.2.1 Bio-inspired embedded design and T-joint fabrication

Two T-joint designs were constructed from unidirectional prepreg VTM264 (T700 fibre/HS200 resin) and six designs were made using fabric prepreg (Hexcel T-300 fibre based 6K five-harness satin weave fabric AGP370-5H/3501-6 resin). The unidirectional specimens were designed to mimic the presumably biologically superior 50% integration of the tree branch into the trunk discussed in chapter three. They consisted of a conventional T-joint (refer Figure 5-1a) with a 32 ply stiffener web laminate and a geometrically equivalent 50% embedded T-joint (refer Figure 5-1b) with the stiffener flange embedded to a depth of 50% of the skin thickness. In both these conventional and embedded T-joints the stiffener had a 3 mm outer radius (r_o) with a stacking sequence of $[45/0/-45/90/90/-45/0/45]_{2s}$ and was connected via the flange to a 16 ply quasi-isotropic skin. Compared to the T-joints tested in chapter four the stiffener web thickness is doubled due to the embedded layers.

The fabric specimens were designed to assess the efficacy of the level of integration (25% to 75%) of the flange into the skin, and also to assess the efficacy of fabric compared to unidirectional prepreg for bio-inspired embedded design. The fabric T-joints consisted of conventional 8, 16 and 24 ply stiffener laminates and geometrically equivalent 25%, 50% and 75% embedded T-joints. All six conventional and embedded T-joint designs (refer Figure

5-2) had a stiffener laminate with a 3 mm outer radius (r_o) connected via the flange to an 8 ply quasi-isotropic fabric skin having the lay-up [±45, 0/90, ±45, 0/90]$_s$.

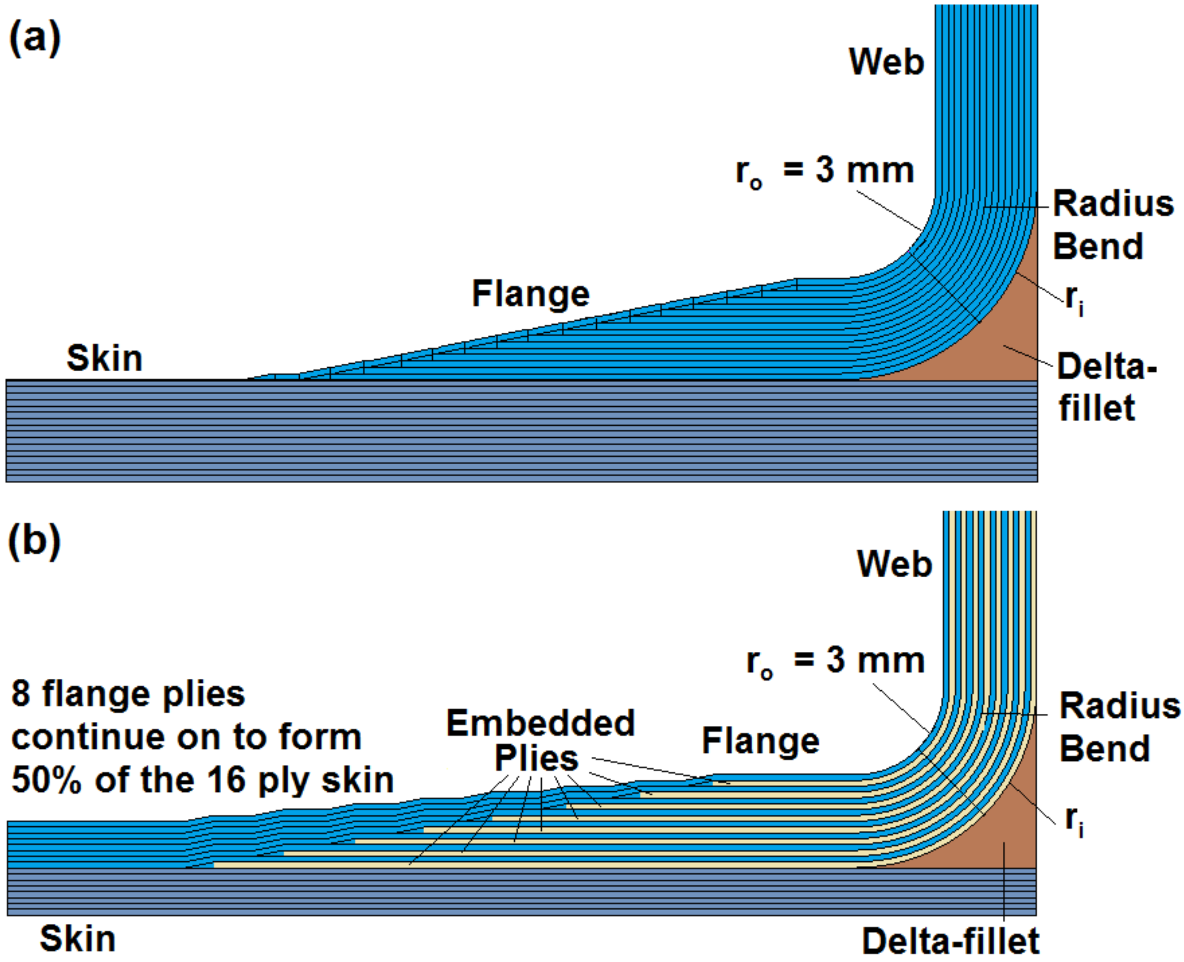

Figure 5-1 Unidirectional conventional and bio-inspired embedded T-joint designs: (a) 32 ply conventional T-joint; and (b) 50% embedded T-joint. r_o = outer radius and r_i = inner radius.

The number of plies in the T-joint stiffener web laminate increased with progressive embedment of the flange plies into the skin. In order to minimise the variables, each bio-inspired embedded T-joint was compared to a geometrically equivalent conventional T-joint with the same number of plies in the stiffener laminate and the same stacking sequence. The 25% embedded and geometrically equivalent 8 ply conventional T-joints had the same 8 ply stiffener laminate with the lay-up [±45, 0/90, ±45, 0/90]$_s$. The 50% embedded and equivalent 16 ply conventional T-joints had a 16 ply stiffener laminate both having the lay-up of

[±45, 0/90, 0/90, ±45]$_{2S}$. The 75% embedded and equivalent 24 ply conventional T-joints had a 24 ply stiffener having the lay-up [±45, 0/90, 0/90, ±45, ±45, 0/90]$_{2S}$. In Figure 5-2a (with symmetry about the vertical axis) the skin of the 25% embedded T-joint consists of 25% stiffener flange plies and 75% skin plies. In Figure 5-2b the skin of the 50% embedded T-joint consists of 50% stiffener flange plies and 50% skin plies and in Figure 5-2c the skin of the 75% embedded T-joint consists of 75% stiffener flange plies and 25% skin plies.

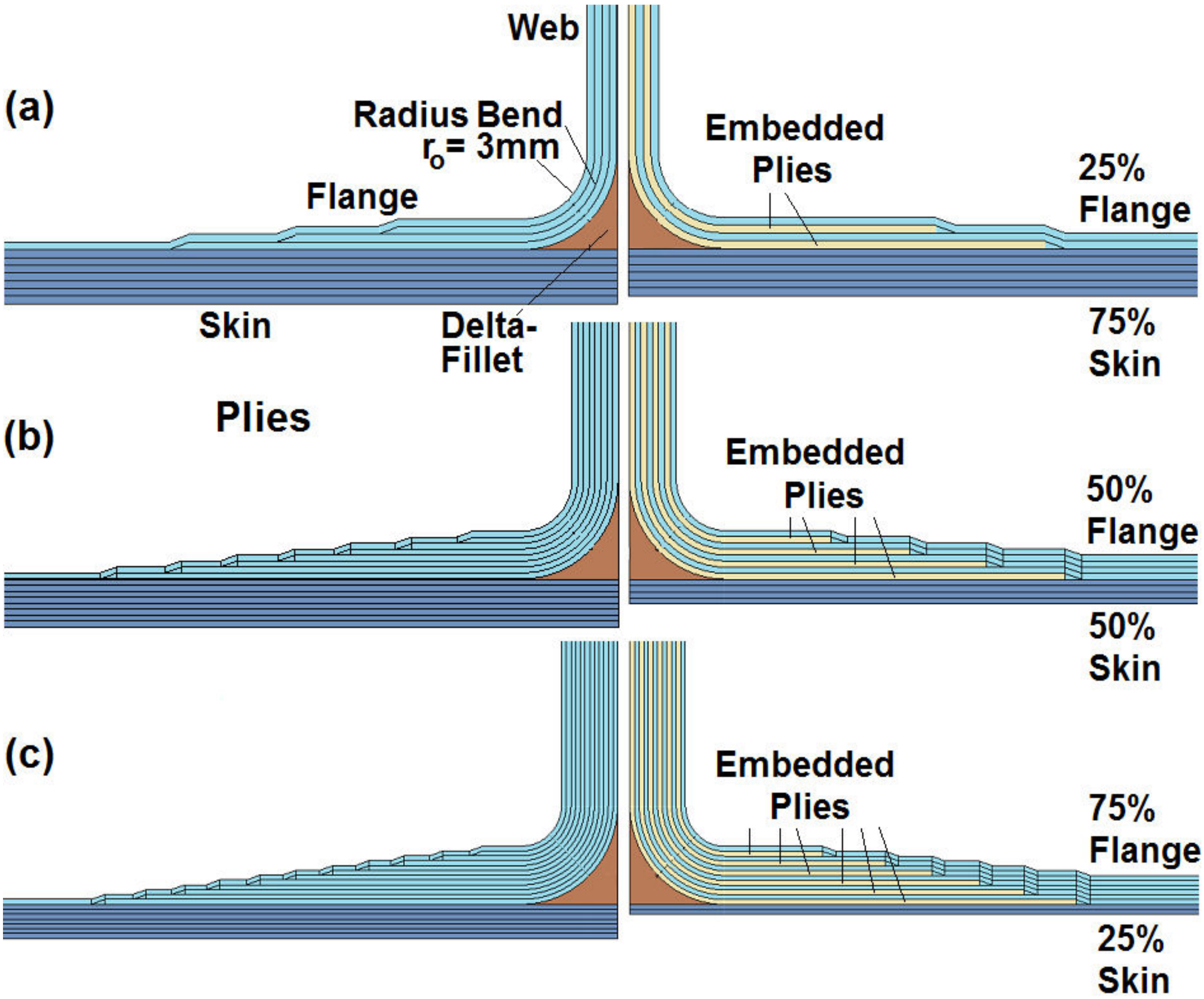

Figure 5-2 Fabric carbon/epoxy conventional and embedded T-joints: (a) left: 8 ply conventional; compared to right: 25% embedded T-joint; (b) left: 16 ply conventional; compared to right: 50% embedded T-joint; and (c) left: 24 ply conventional; compared to right: 75% embedded T-joint. r_o = outer radius

The area of the delta-fillet 'noodle' was calculated as described in chapter four. The area of the delta-fillet increased with the thickness of the stiffener web laminate due to the increasing inner radius r_i. However, the delta-fillet area was the same for the bio-inspired embedded and geometrically equivalent conventional T-joint designs. This eliminated size effects of the delta-fillet region as a variable influencing the initiation of damage in the radius bend/delta-fillet region when comparing the conventional and embedded T-joints. The delta-fillet area under the stiffener was modelled as carbon/epoxy prepreg fabric oriented along the stiffener web (z-direction), replicating the fabrication of the T-joint test specimens.

The geometric variables of stiffener flange thickness (t_1 and t_2) and stiffener thickness of the conventional and embedded fabric T-joint designs are shown in Figure 5-3 and given in Table 5-1. The stiffener web thickness of the conventional and embedded T-joints was the same. However the flange thickness was different due to the effect of the embedded design in which some plies formed both part of the flange and part of the skin (refer Figure 5-2). Therefore the results of the mechanical testing were normalised by the area of the T-joint flange, which was calculated as given by Equation 5-1, in order to compare designs with equivalent material in the joint.

$$Flange/skin\_area = \frac{(t_1 + t_2)}{2} \times w \qquad \text{Equation 5-1}$$

Where t_1 = thickness of flange 1, t_2 = thickness of flange 2 and w = T-joint width as defined in Figure 5-3.

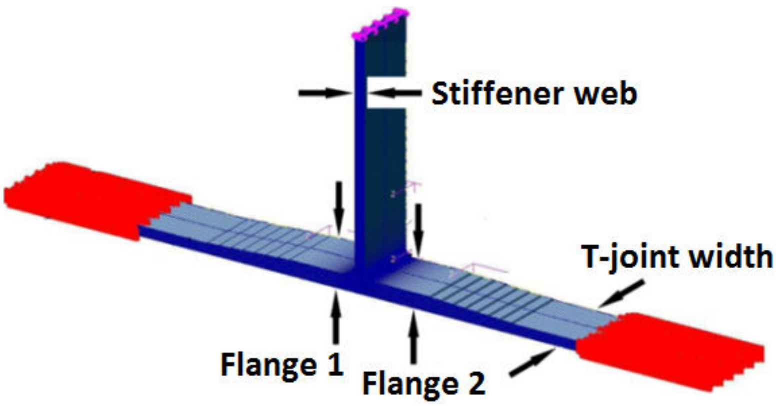

Figure 5-3 Dimensions of T-joint flange area

Table 5-1 Geometry of conventional and embedded T-joints with increasing stiffener web thickness

T-Joints	Stiffener Web Thickness (mm)	Flange Thickness t_1 and t_2 (mm)
Fabric 8 ply conventional	2.8 (8 plies)	4.2 (12 plies)
Fabric 25% embedded	2.8 (8 plies)	3.5 (10 plies)
Fabric 16 ply conventional	5.6 (16 plies)	5.6 (16 plies)
Fabric 50% embedded	5.6 (16 plies)	4.2 (12 plies)
UD 32 ply conventional	6.4 (32 plies)	6.4 (32 plies)
UD 50% embedded	6.4 (32 plies)	4.8 (24 plies)
Fabric 24 ply conventional	8.4 (24 plies)	7.0 (20 plies)
Fabric 75% embedded	8.4 (24 plies)	4.9 (14 plies)

5.2.2 Experimental procedure

The composite T-joints were tested under bending, tensile and compressive loads that were applied using a 50 kN Instron test machine (refer Figure 5-4). The bending and tensile testing was conducted as described in chapter four. Under compressive loading, the T-joint skin was clamped between the Instron grips and subjected to compression at a loading rate of 0.5 mm/min (refer Figure 5-4c). Four samples were tested under bending, tensile and compressive loading for the two different unidirectional T-joint designs. Eight samples were tested under bending, tensile and compressive loading for the six different fabric T-joint designs.

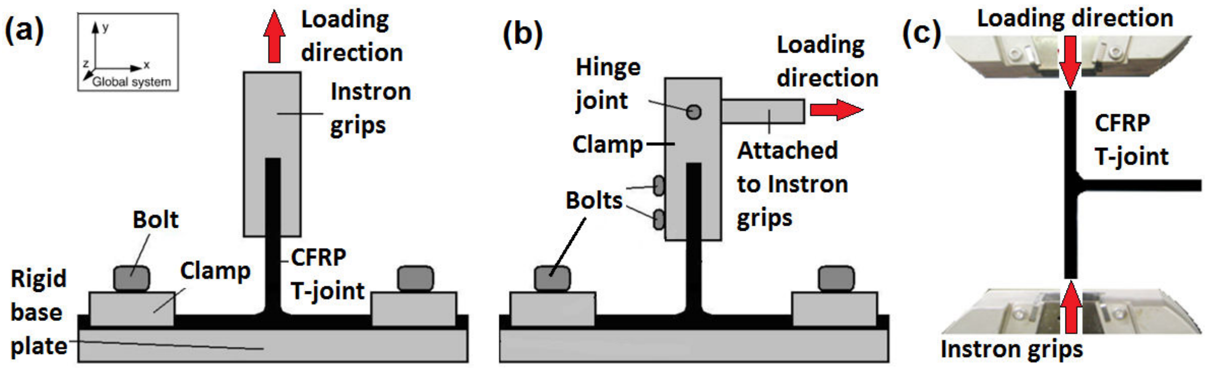

Figure 5-4 Experimental test set-up: (a) tensile; (b) bending; and (c) compressive loading

5.2.3 Non-linear finite element analysis

The boundary conditions and large deformations during testing of the T-joints induced non-linear effects in the bending and tensile loading cases. Therefore non-linear FE analysis was used to model the bending and tensile experimental tests up to the average damage initiation load as obtained from the experimental testing. The non-linear FE analysis was used to determine the effect of the embedded geometry on the interlaminar tensile and shear stress fields in the radius bend/delta-fillet region and the subsequent influence on the damage initiation load of the T-joints. The FE analysis also gave information about the ply failure location and the failure mode (e.g. interlaminar shear dominated, mixed-mode or interlaminar tensile dominated). These results were analysed using Long's strength-based criterion to predict the location of delamination damage within the plies of the radius bend.

The geometry of the FE model was as described in section 5.2.1. All eight T-joint designs were modelled. The material properties used in the FE analysis are given in Table 5-2. The meshing of the FE model was the same as described in chapter four. The non-linear analysis was displacement controlled. The boundary conditions for the non-linear analyses are given in Figure 5-5. In the bending load case, the average damage initiation displacement was applied perpendicular to the stiffener web at the node 103 mm from the flange representing the hinge joint shown in Figure 5-5a. The bending displacement was applied to the free edge nodes at the top of the stiffener web via a rigid link. The displacement in the y-direction was fixed to simulate the experimental test conditions in which the attachment to the Instron grips was fixed in one plane (refer Figure 5-4b). Under large bending displacements the test rig induced a secondary tensile load on the stiffener web as it rotated and stretched. In the tensile load case (refer Figure 5-5b), the average damage initiation tensile (pull-off) displacement was applied to the centre of the free edge of the stiffener web tip.

Table 5-2 Unidirectional and fabric carbon/epoxy composite material properties used in the finite element analysis of the T-joints

Material Property	**Unidirectional Prepreg (Lavender VTM264)**	**Fabric Prepreg (Hexcel AGP370-5H/3501)**
Cured ply thickness	0.2 mm*	0.35*
In-plane Young's modulus E_{11}	117 GPa*	53.8 GPa*
Transverse Young's modulus E_{22}	7.47 GPa*	53.8 GPa*
Interlaminar Young's modulus E_{33}	7.47 GPa**	9.5 GPa**
Poisson's ratio v_{12}	0.33*	0.25**
Poisson's ratio v_{13}	0.02***	0.044***
Poisson's ratio v_{23}	0.33**	0.25**
In-plane shear modulus G_{12}	4.07 GPa*	5.0 GPa**
Interlaminar shear modulus G_{13}	4.07 GPa**	5.0 GPa**
Interlaminar shear modulus G_{23}	2.31 GPa*	5.0 GPa**

*experimentally determined, **assumption, ***calculated analytically

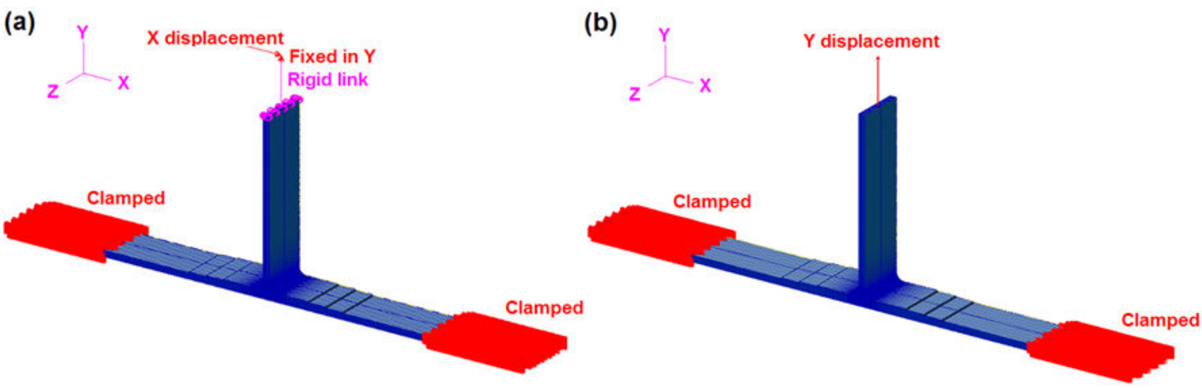

Figure 5-5 Boundary conditions in the non-linear FE model of T-Joint: (a) bending; and (b) tension

5.3 RESULTS AND DISCUSSION

5.3.1 Experimental results

The experimental test results were normalised by the T-joint flange area (calculated using Equation 5-1) in order to compare the mechanical properties of the embedded and conventional T-joints specific to the amount of material in the joint. The results were analysed based on four metrics (refer Figure 5-6): (i) normalised damage initiation load; (ii) normalised failure load; (iii) normalised inelastic strain energy (defined as ductility); and (iv) normalised strain energy to failure (defined as toughness).

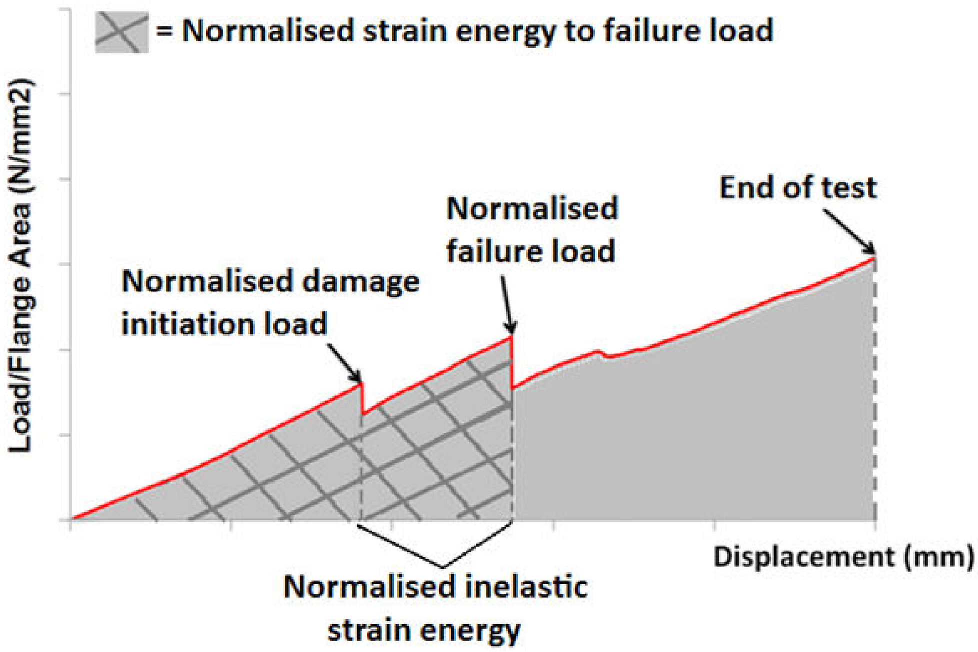

Figure 5-6 Definition of four analysis metrics used to assess T-joint performance

Damage initiation load was defined as the load at which the first load drop occurred. Failure load was defined as the maximum load sustained before failure caused by cracking through the delta-fillet region to the stiffener flange/skin bond-line (equivalent to peak load). The normalised inelastic strain energy was measured as the area under the normalised load-displacement curve between damage initiation and failure load and was used to define the 'ductility' of the joint. A T-joint in which the damage initiation load coincided with the failure load had a normalised inelastic strain energy value of zero, which indicated completely brittle failure. Normalised strain energy to failure was measured as the total area under the normalised load-displacement curve up to the failure load and defined the toughness of the T-joint.

5.3.1.1 Bending load case

The normalised bending load-displacement curves for the bio-inspired embedded composite T-joints are compared to the geometrically equivalent conventional joints in Figure 5-7. Normalising the bending load by the flange area collapsed the curves so the embedded and conventional T-joints had similar normalised stiffness. Figure 5-7a shows that the bending load-displacement curves of the thinnest joints had the highest failure displacement. The load-displacement curves are clearly non-linear after exceeding approximately 7 mm of bending displacement due to the constraint of the fixed hinge height which fixed the Instron cross-head in the y-direction. Both T-joint designs experienced brittle failure (damage initiation load is equal to failure load). The small level of integration did not significantly alter the failure characteristics of the embedded T-joint. Figure 5-7b shows that there was an earlier onset of damage in the 50% embedded T-joint, with the damage initiation load reduced by 36% compared to the equivalent conventional joint. Damage was initiated by delamination cracks developing at lower applied loads in the radius bend. However, after damage initiation the 50% embedded T-joint retained load-bearing capacity (damage tolerance) and attained the same normalised peak load as the conventional joint by absorbing inelastic strain energy. Figure 5-7c shows similar results for the unidirectional 50% embedded and geometrically equivalent conventional T-joints, although the normalised failure load is higher for the unidirectional samples. Figure 5-7d shows a similar trend for the 75% embedded T-joint, however this joint did not attain the same normalised peak load compared to the fabric 24 ply conventional joint suggesting the reduction in the continuous skin plies caused by the 75% level of integration may be too high to maintain the same normalised failure load.

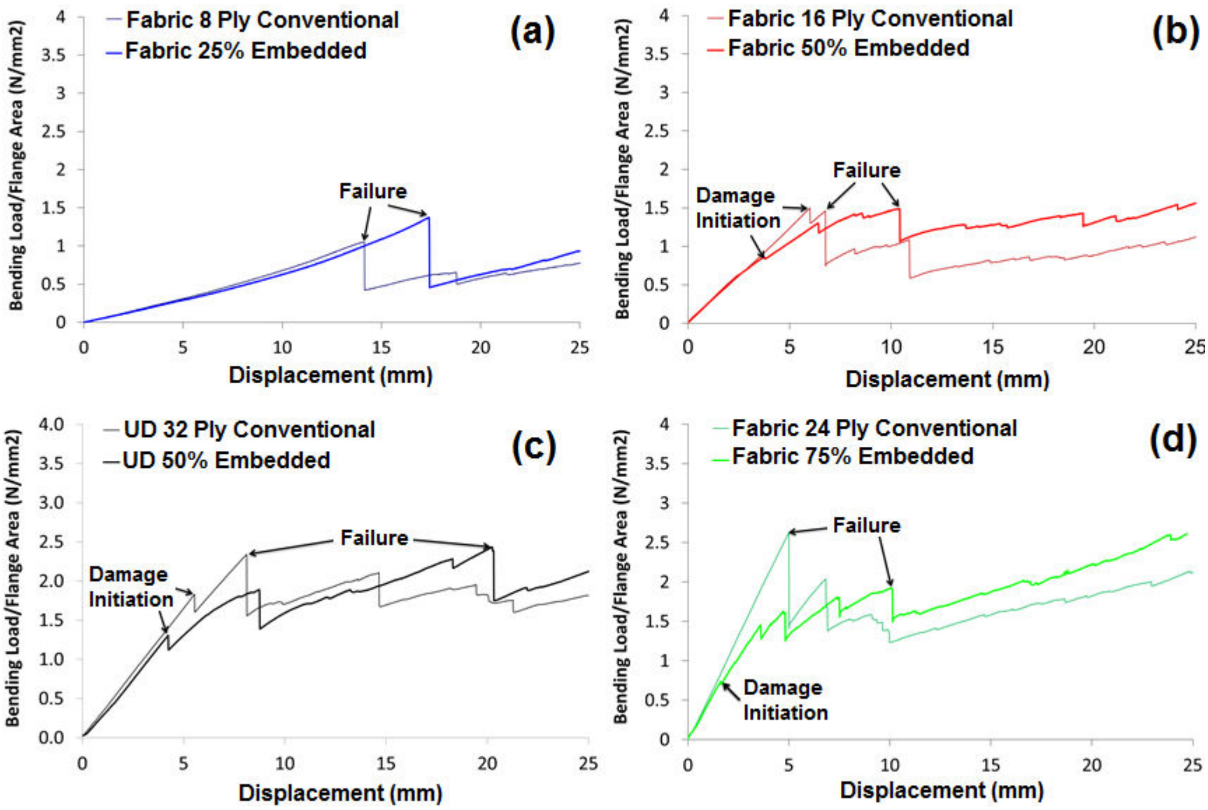

Figure 5-7 T-joint normalised bending load-displacement curves: (a) fabric 8 ply conventional and 25% embedded; (b) fabric 16 ply conventional and 50% embedded; (c) unidirectional 32 ply conventional and 50% embedded; and (d) fabric 24 ply conventional and 75% embedded T-joints

The initiation and growth of damage in the T-joints was monitored over the course of the bending tests. Regardless of the joint design the damage always initiated in one of two modes: (i) delamination cracking approximately one-third through-the-thickness of the radius bend (refer Figure 5-8a); or (ii) simultaneous delamination cracking in the radius bend and cracking across at the delta-fillet interface (refer Figure 5-8b).

The frequency of these failure modes is given in Figure 5-9. In the fabric 8 ply conventional T-joint the damage initiated 5/8 times simultaneously in the radius bend and at the delta-fillet interface. In the fabric 25% embedded T-joint, the damage initiated 4/8 times simultaneously in the radius bend and at the delta-fillet interface. For the remaining T-joints the increasing interlaminar stresses caused by increasing stiffener web thickness caused first damage to always initiate as delamination cracks in the radius bend.

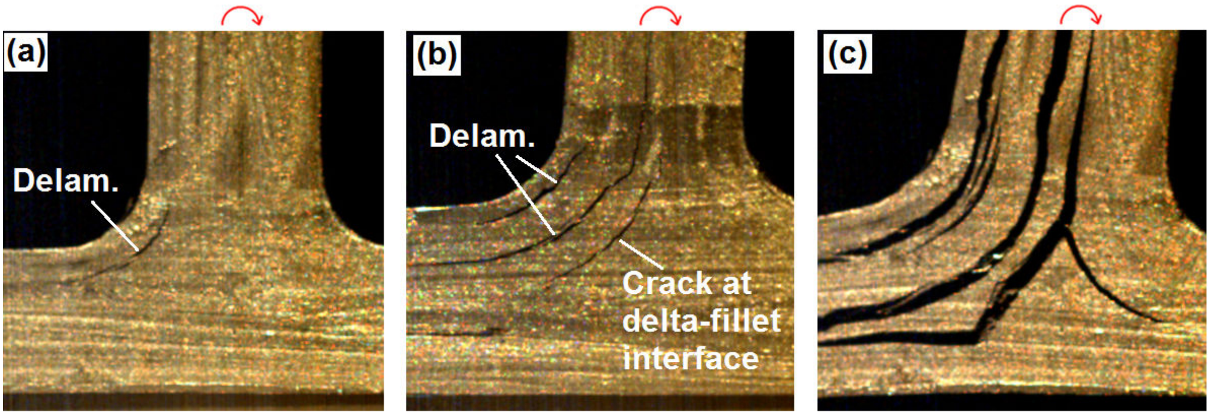

Figure 5-8 Damage initiation under bending loading: (a) radius bend delamination; (b) simultaneous radius bend delaminations and cracking at the delta-fillet interface; and (c) end of test

Figure 5-9 Damage initiation modes for the conventional and bio-inspired embedded T-joints under bending loading

The fabric and unidirectional conventional T-joints generally had limited or no further load-bearing capacity once initial damage had been sustained due to rapid and large-scale crack growth along the stiffener flange/skin bond-line. As the damage progressed, intra-ply cracking and inter-ply delaminations occurred in the tensile side of the radius bend. The load drop following the failure load was typically due to the main crack propagating through the resin-rich delta-fillet interface to the stiffener flange/skin bond-line (refer Figure 5-10).

The test results indicate that the embedded T-joints are unlikely to experience catastrophic failure because the failure load is higher than the damage initiation load. Therefore, mimicking tree joints with high levels of integration (50% or 75% embedded) of flange plies into the skin resulted in superior damage tolerance as defined by load-bearing capability following first failure in the composite T-joint. A low level of integration (25% embedded) had little or no beneficial effect.

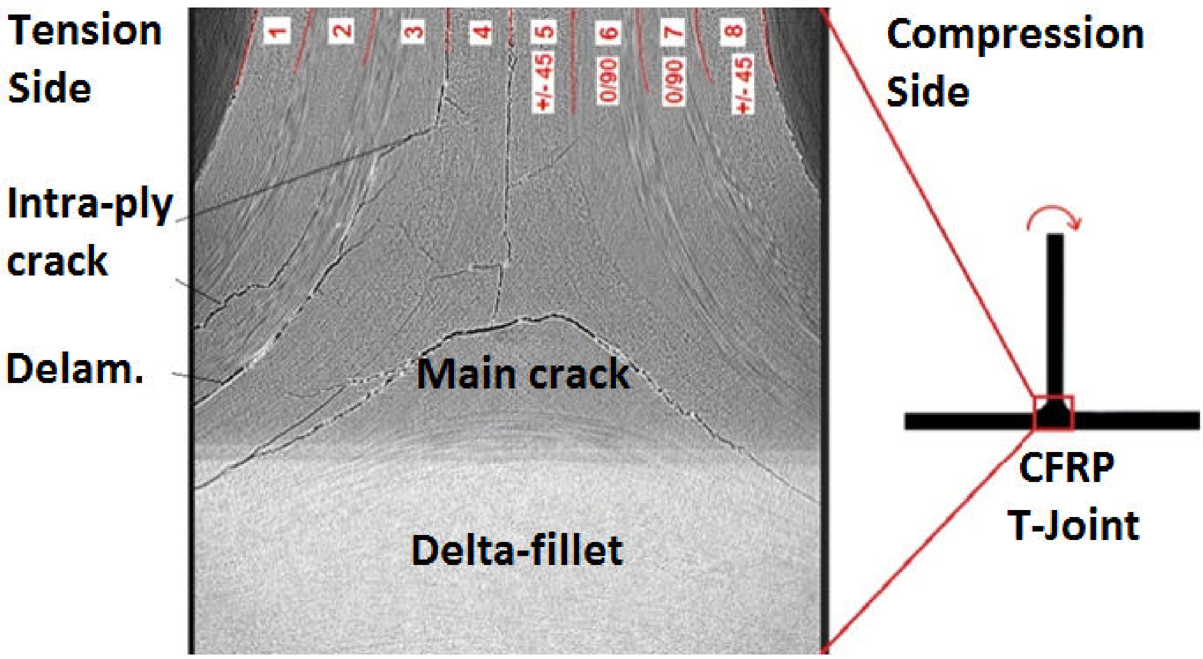

Figure 5-10 Micro-CT image of the damage region of a fabric 25% embedded T-joint failed under bending showing delaminations and intra-ply cracking in the tensile side radius bend and the main crack propagating across the radius bend/delta-fillet interface

The radius bend/delta-fillet region is the main point of weakness for all T-joint designs because of the high geometric interlaminar stress concentration and the large mismatch between the elastic properties of the stiffener web radius bend (high axial modulus) and delta-fillet region (low transverse modulus), as discussed in chapter two [104, 108-113]. The bio-inspired embedded T-joint design does not alter the location of the geometric stress concentration or the mismatch between the elastic properties of the radius bend and delta-fillet region, and consequently the location of damage initiation was not changed significantly by the bio-inspired embedded design. In tree branch-trunk joints the modulus mismatch between fibrils aligned with the trunk and branch directions is reduced by the density gradient across the joint (refer chapter three). It might be possible to vary the fibre volume fraction across the radius bend/delta-fillet interface to smooth the modulus transition in this region and thereby improve the damage initiation load by reducing the geometric stress concentration, although this was not investigated in the PhD project.

A summary of the results from the bending testing is given in Table 5-3. The damage initiation load was lower for all the embedded T-joints with the exception of the fabric 25% embedded T-joint. The normalised failure loads were generally similar for the embedded and conventional T-joints; however the normalised failure load of the T-joint with 75% embedded plies was about 30% lower compared to the 24 ply conventional T-joint.

Ductile-type failure behaviour of the T-joints was quantified using the normalised inelastic strain energy. Embedding flange plies into the skin caused more extensive crack deflection and crack branching (refer Figure 5-11), similar to the toughening mechanisms observed in tree joints in chapter three. Increasing the percentage of embedded plies resulted in a more stable and progressive failure mode following damage initiation by partially stabilising and inhibiting the main crack path between the flange and skin. This resulted in a more ductile-type failure with higher load-bearing capability after initial failure. Under bending loading the 75% embedded T-joint showed the largest increase in normalised inelastic strain energy; absorbing on average over six times the inelastic strain energy of the equivalent conventional joint.

Table 5-3 Comparison between the structural properties of the bio-inspired embedded and geometrically equivalent conventional T-joints under bending loading. [± Standard deviation based on 8 samples for the fabric and 4 samples for the unidirectional T-joints]. (Percentage change compared to geometrically equivalent conventional T-joint)

T-joint	Damage Initiation Load (N)	Norm. Damage Initiation Load (N/mm^2)	Norm. Failure Load (N/mm^2)	Norm. Inelastic Strain Energy (Ductility) (J/mm^2)	Norm. Strain Energy to Failure Load (Toughness) (J/mm^2)
Fabric 8 ply conventional	86.4 [±29]	1.03 [±0.34]	1.09 [±0.29]	3.13 [±3.18]	9.89 [±2.64]
Fabric 25% embedded	105.5 [±27] (22%)	1.38 [±0.34] (34%)	1.39 [±0.33] (27%)	1.31 [±2.75] (-58%)	11.4 [±2.38] (15%)
Fabric 16 ply conventional	131 [±62]	1.08 [±0.53]	1.30 [±0.30]	2.19 [±2.40]	5.15 [±0.64]
Fabric 50% embedded	84 [±22] (-36%)	0.93 [±0.25] (-14%)	1.34 [±0.15] (3%)	5.07 [±3.09] (132%)	7.76 [±2.01] (51%)
UD 32 ply embedded	268 [±9.1]	1.93 [±0.14]	2.27 [±0.09]	11.8 [±8.86]	17.5 [±9.49]
UD 50% embedded	187 [±42] (-30%)	1.62 [±0.35] (-16%)	2.24 [±0.19] (-1%)	20.6 [±7.48] (75%)	24.9 [±6.19] (42%)
Fabric 24 ply conventional	275 [±143]	1.90 [±0.48]	2.63 [±0.18]	1.35 [±1.52]	8.39 [±1.57]
Fabric 75% Embedded	159 [±20] (-42%)	1.44 [±0.19] (-24%)	1.92 [±0.20] (-27%)	9.87 [±4.31] (631%)	12.8 [±4.24] (53%)

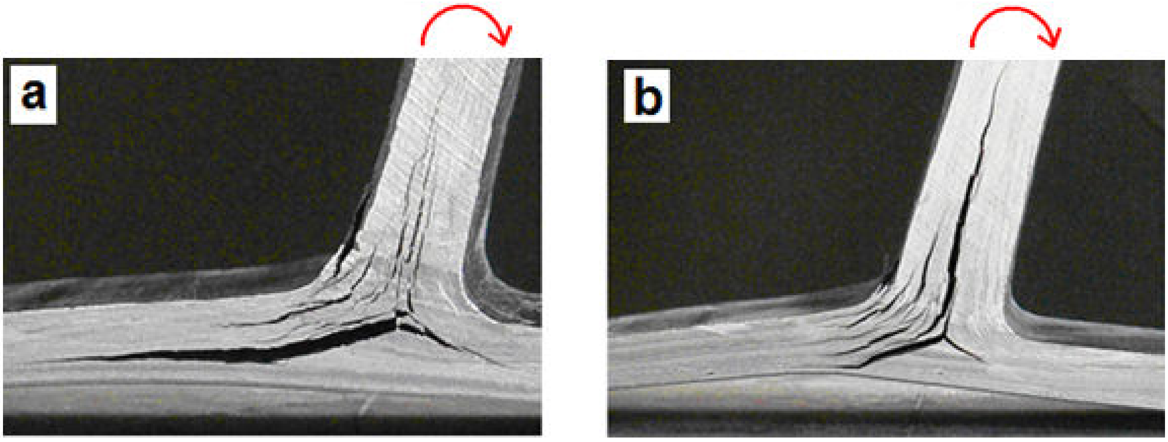

Figure 5-11 Increased crack branching and crack deflection inhibits growth of main crack along flange/skin bond-line under bending loading: (a) 24 ply conventional T-joint; and (b) 75% embedded T-joint

The development of multiple cracks through crack branching and deflection also increased the normalised strain energy to failure absorbed by the bio-inspired embedded T-joints, which was defined as a measure of toughness. The embedded T-joints all exhibited higher toughness, absorbing about 50% more strain energy to failure than the conventional T-joints.

The unidirectional 50% embedded and fabric 50% embedded T-joints performed similarly, however in absolute terms the unidirectional T-joints had higher damage initiation and peak loads. This is attributed to the higher stiffness of the unidirectional fibres, which had less fibre waviness compared to the woven specimens resulting in less strain in the T-joint for a given applied load.

5.3.1.2 Tension load case

The normalised tensile load-displacement curves for the bio-inspired embedded T-joints are compared to the conventional T-joint in Figure 5-12.

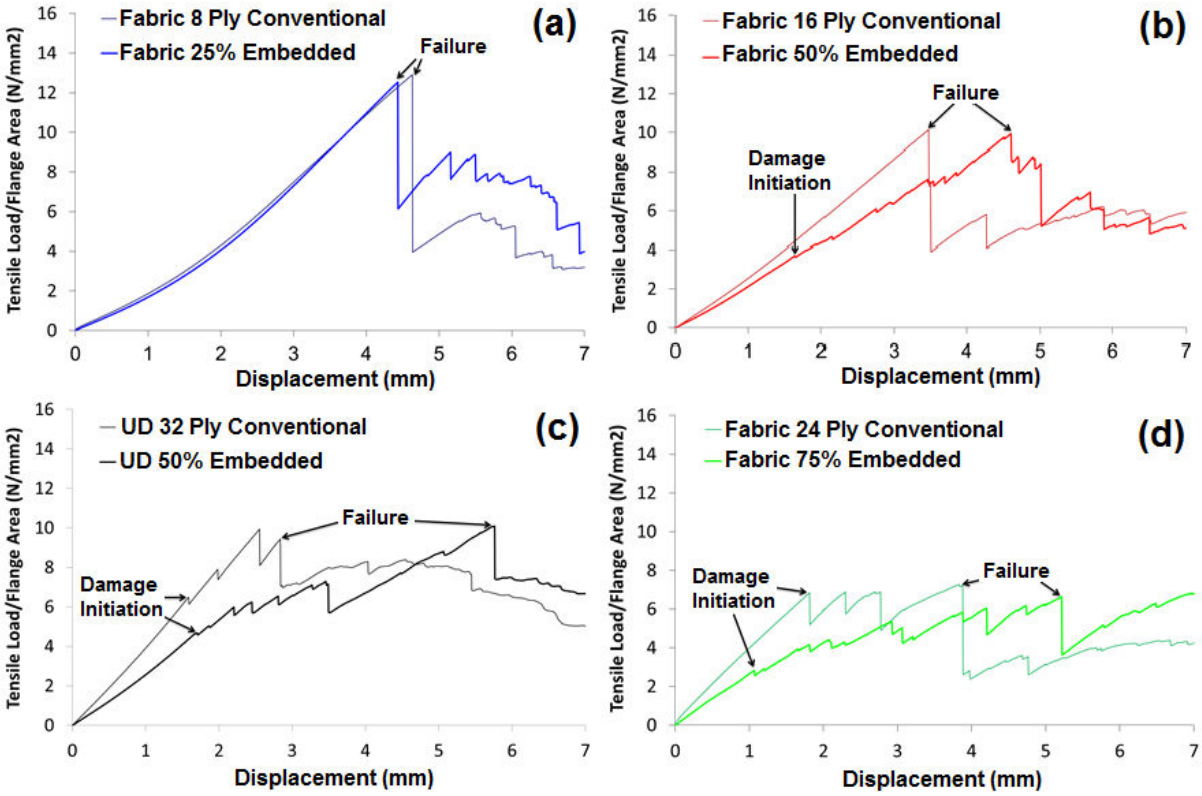

Figure 5-12 Normalised tensile load-displacement curves: (a) fabric 8 ply conventional and 25% embedded T-joints; (b) fabric 16 ply conventional and 50% embedded T-joints; (c) unidirectional 32 ply conventional and 50% embedded T-joints; and (d) fabric 24 ply conventional and 75% embedded T-joints

All the experimental results show some non-linear behaviour due to the boundary conditions and joint geometry; however this was most pronounced in the thinnest (8 ply) samples which experienced the highest tensile failure displacement. Figure 5-12a shows that embedding 25% of the flange plies into the skin had no significant influence on the tensile properties due to the similarity to the conventional T-joint design. This finding is the same as the bending load condition. Figure 5-12b to Figure 5-12d show the tensile load response of fabric and unidirectional T-joints with 50% or 75% integration followed a similar trend to the bending load case, with a reduction in the damage initiation load and a similar normalised failure load compared to the conventional joint. The results for the unidirectional and fabric T-joints were both qualitatively and quantitatively similar.

Unlike the bending load case the T-joints did not have the same normalised initial stiffness. The embedded T-joints had a reduced stiffness compared to the conventional joints. This was attributed to the conventional joints having a longer stiffener flange run-out due to the requirement to taper all the stiffener flange plies, as opposed to the embedded designs in which a percentage of the stiffener plies did not run-out but formed part of the skin. The longer stiffener run-out increased the stiffness of the skin in the conventional T-joints and hence increased the tensile stiffness of the T-joint pull-off tests.

A summary of the tensile performance of all the embedded and conventional T-joints is contained in Table 5-4. The 50% embedded T-joint showed the largest reduction in damage initiation load (55%) compared to the 16 ply conventional design. The reduction for the 75% embedded design was also significant at 43%. There was no significant difference in the normalised tensile failure load for all three levels of integration.

As was observed in the bending load case, the 50% and 75% embedded T-joints showed increased normalised inelastic strain energy (defined as ductility) and normalised strain energy to failure (defined as toughness) due to an ability to sustain load carrying capacity following the initiation of delamination cracks in the radius bend. The normalised inelastic strain energy was zero for both the 8 ply conventional and 25% embedded T-joints, indicating completely brittle failure. The 50% and 75% embedded T-joints showed significant improvement in ductility of between 120 – 200%. These results demonstrate that mimicking tree branch connections by integrating the flange plies into the skin of the T-joint improved the tensile load-bearing capacity after first failure, and thereby enhanced the damage tolerance.

The development of damage in the conventional and bio-inspired embedded T-joints under tensile loading showed many similarities to the bending load case described earlier. Delamination damage initiated in the radius bend and at the delta-fillet interface due to the geometric stress concentration and the large mismatch in the elastic moduli due to the different orientation of the fibres in the radius and delta-fillet region. This region is the same for both the conventional and embedded T-joint designs. The damage initiation modes are shown in Figure 5-13, and involved cracking at the delta-fillet interface (refer Figure 5-13a) or simultaneous radius bend and delta-interface cracking (refer Figure 5-13b). The frequency of these failure modes for the T-joints is given in Figure 5-14. In the 8 ply conventional and 25% embedded T-joints the damage always initiated at the delta-fillet interface. For the remainder of the T-joint samples the damage initiated as simultaneous radius bend delaminations and cracking at the delta-fillet interface.

Table 5-4 Comparison between the structural properties of the bio-inspired embedded and equivalent conventional T-joints under tension loading. [± Standard deviation based on 8 samples for the fabric and 4 samples for the unidirectional T-joints]. (Percentage change compared to geometrically equivalent conventional T-joint)

T-Joint	Damage Initiation Load (N)	Norm. Damage Initiation Load (N/mm^2)	Norm. Failure Load (N/mm^2)	Norm. Inelastic Strain Energy (Ductility) (J/mm^2)	Norm. Strain Energy to Failure Load (Toughness) (J/mm^2)
Fabric 8 ply conventional	1186 [±178]	14.3 [±2.14]	14.3 [±2.25]	0.0 [±0.0]	30.7 [±10.7]
Fabric 25% embedded	1131 [±180] (-5%)	14.7 [±2.35] (3%)	14.8 [±2.30] (3%)	0.0 [±0.0] (0%)	31.4 [±9.1] (2%)
Fabric 16 ply conventional	707 [±351]	5.91 [±2.94]	8.15 [±1.17]	5.50 [±45.48]	13.5 [±3.34]
Fabric 50% embedded	315 [±51] (-55%)	3.52 [±0.57] (-40%)	8.06 [±1.07] (-1%)	15.2 [±2.55] (176%)	18.4 [±2.22] (36%)
UD 32 ply embedded	876 [±33]	6.38 [±0.13]	9.02 [±0.81]	8.70 [±2.69]	13.7 [±2.79]
UD 50% embedded	604 [±116] (-31%)	5.50 [±1.08] (-16%)	9.40 [±0.65] (4%)	26.2 [±3.74] (201%)	31.1 [±2.77] (127%)
Fabric 24 ply conventional	545 [±402]	3.70 [±2.73]	6.91 [±0.18]	13.4 [±3.72]	17.8 [±6.48]
Fabric 75% Embedded	313 [±54] (-43%)	2.86 [±0.49] (-23%)	7.33 [±1.22] (6%)	29.7 [±8.53] (122%)	31.5 [±8.20] (77%)

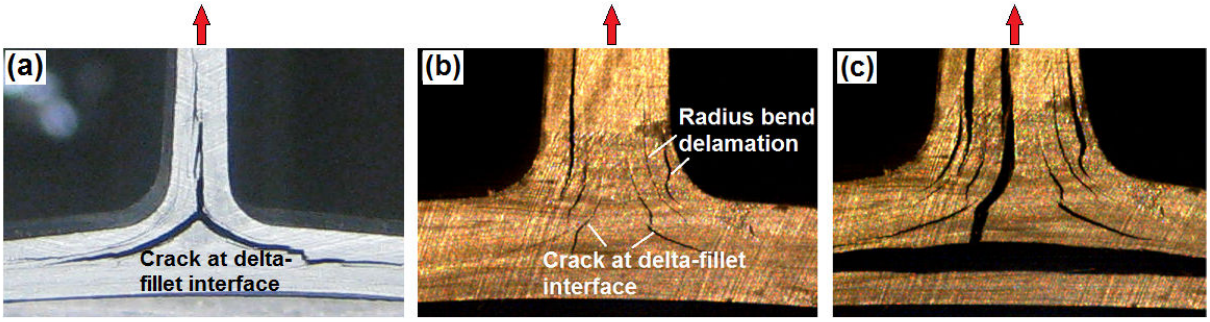

Figure 5-13 Failure modes of the T-joints under tensile loading: (a) cracking across delta-fillet interface; (b) simultaneous radius bend and delta-fillet interface cracking; and (c) end of test

Figure 5-14 Damage initiation modes for the conventional and embedded T-joints under tensile loading

The conventional T-joints experienced brittle failure due to unstable growth of a single, dominant crack along the stiffener flange/skin bond-line. In contrast, multiple cracking (rather than a single crack) occurred in the embedded T-joints containing 50% or 75% embedded plies. The development of multiple cracks increased the strain energy release rate per volume of material, thereby slowing the spread of damage along the stiffener flange/skin bond-line which resulted in higher tensile load-bearing capacity following first failure. The normalised strain energy to failure load increase was proportional to the level of integration in the bio-inspired T-joints up to a maximum 77% improvement for the 75% embedded design (refer Table 5-4). This indicates that more energy was required to pull-out the increasingly embedded T-joints under tensile load. Final failure occurred with the main crack propagating along the stiffener flange/skin bond-line and into the vertical stiffener web.

In summary, implementing the bio-inspired structural feature of embedded design improved the damage tolerance, ductility and toughness of the T-joints under both bending and tensile loading. Both conventional and embedded designs attained the same normalised failure load. However, the embedded design triggered an earlier onset of damage initiation, which is a disadvantage as design rules can assume that composite materials will experience brittle failure, thus damage initiation is often defined as the design load. The cause of the early onset damage initiation was investigated using non-linear FE analysis in section 5.3.2, and the effect is eliminated in chapter six through hierarchical design.

5.3.1.3 Compression load case

The normalised compressive load-displacement curves for the embedded T-joints are compared to the conventional joints in Figure 5-15. After an initial linear-elastic region of loading the skin deformed until the stiffener flange/skin area buckled in a half-sine wave, causing an abrupt loss of compressive load carrying capacity. Under compressive loading the skin failed in one of three buckling modes depending on the test boundary conditions:

- Stiffener web pointing up (refer Figure 5-16b);
- Stiffener web pointing down (refer Figure 5-16c); or
- Stiffener web straight (refer Figure 5-16d),

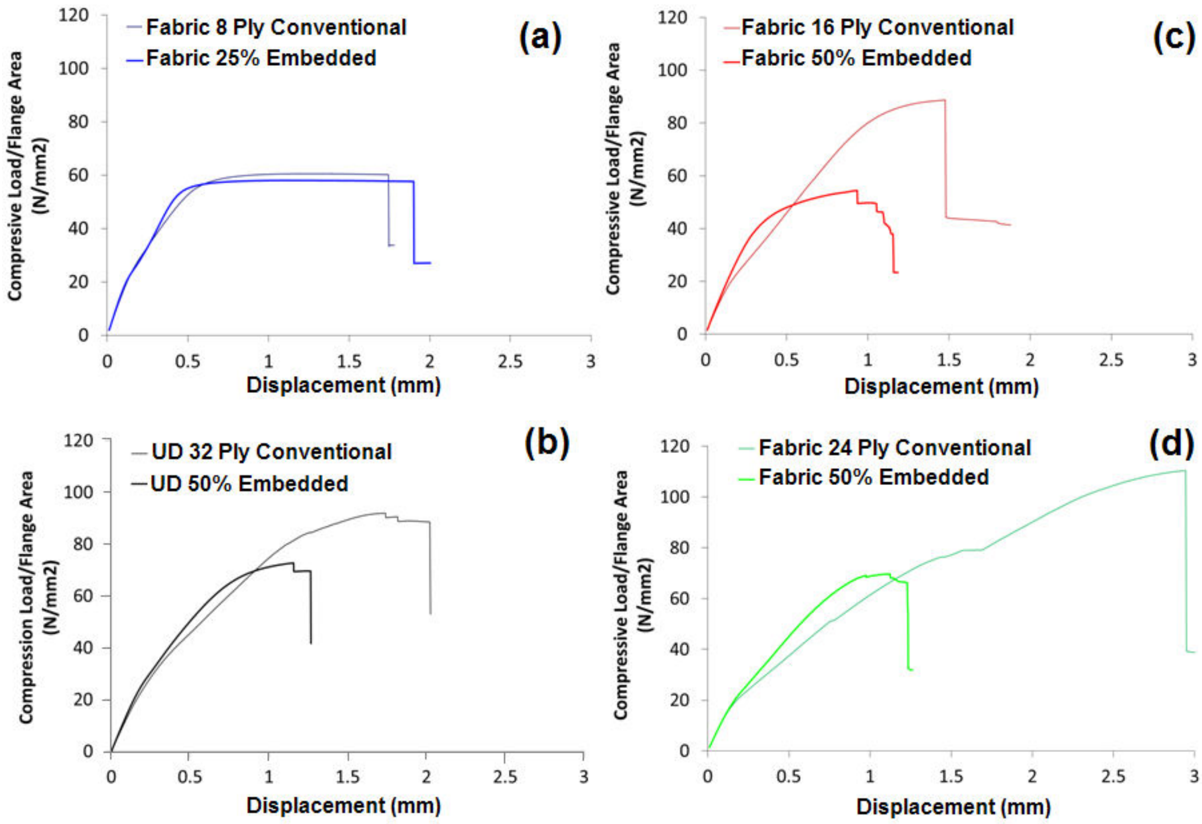

Figure 5-15 T-joint normalised compressive load-displacement curves: (a) fabric 8 ply conventional and 25% embedded; (b) fabric 16 ply conventional and 50% embedded; (c) unidirectional 32 ply conventional and 50% embedded; and (d) fabric 24 ply conventional and 75% embedded

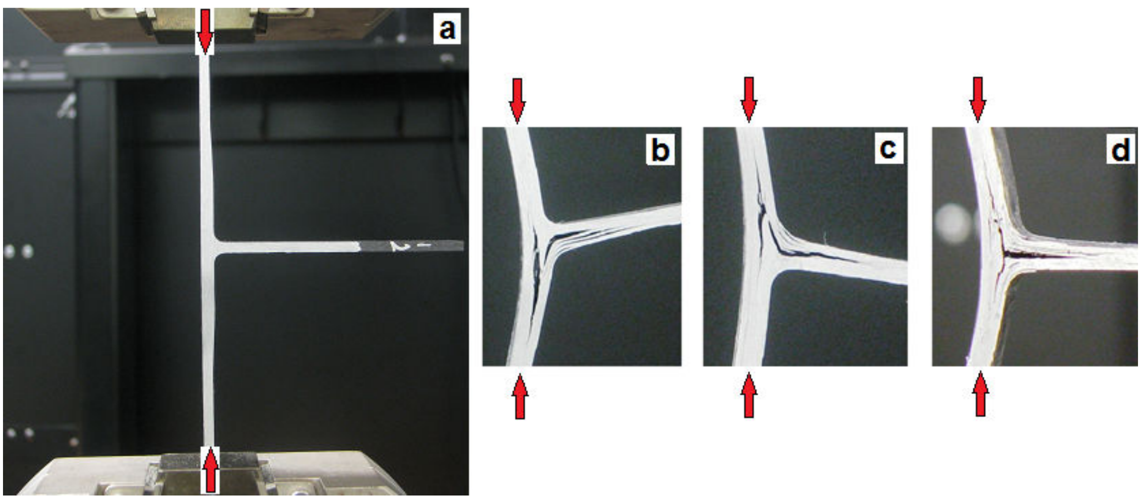

Figure 5-16 (a) Compressive testing and buckling failure modes: stiffener (b) stiffener web pointing up; (c) stiffener web pointing down; and (d) stiffener web straight

The structural properties of the embedded and conventional T-joints under compressive load are contained in Table 5-5. There was almost no difference between the 8 ply conventional and 25% embedded T-joints due to the similarity of the two designs. There was a significant reduction in the normalised compressive strength of the 50% embedded and 75% embedded T-joints compared to their conventional designs due to the reduction in continuous skin plies in the eight ply skin.

Table 5-5 Comparison between the structural properties of the embedded and conventional T-joints under compressive loading. [± Standard deviation based on 8 samples for the fabric and 4 samples for the unidirectional T-joints]. (Percentage change compared to geometrically equivalent conventional T-joint)

T-Joint	Failure Load (N)	Normalised Failure Load (N/mm^2)	Normalised Strain Energy to Failure Load (Toughness) (J/mm^2)
Fabric 8 ply conventional	5021 [±115]	60.0 [±1.52]	77.7 [±8.44]
Fabric 25% embedded	4636 [±426] (-8%)	60.3 [±4.57] (0.5%)	81.5 [±10.3] (5%)
Fabric 16 ply conventional	10052 [±524]	87.2 [±2.40]	85.3 [±8.0]
Fabric 50% embedded	3677 [±441] (-63%)	49.5 [±3.08] (-43%)	38.8 [±6.57] (-55%)
UD 32 ply embedded	12713 [±700]	90.6 [±2.78]	111.2 [±22.1]
UD 50% embedded	7038 [±1697] (-45%)	64.9 [±10.8] (-28%)	62.6 [±25.5] (-44%)
Fabric 24 ply conventional	15771 [±179]	109.8 [±0.57]	241 [±44.6]
Fabric 75% Embedded	7017 [±382] (-56%)	67.1 [±4.10] (-39%)	55.1 [±4.75] (-77%)

Figure 5-17 shows an approximate linear increase in the normalised compressive strength capability of the conventional T-joints corresponding to the increased material in the stiffener stabilizing the skin against buckling. The 32 ply unidirectional conventional T-joint attained about the same normalised compressive strength as the 16 ply fabric T-joint. The unidirectional 50% embedded T-joint had a slightly higher compressive load capability compared to the fabric 50% embedded. There was no significant reduction in the compressive load carrying capacity of all the embedded T-joints in comparison to the baseline fabric 8 ply conventional T-joint (refer Figure 5-17).

Figure 5-17 Normalised compressive strength for conventional and embedded T-joints

Increasing the percentage of embedded plies had two contrasting effects on the T-joint. Increasing the number of stiffener web plies improved the buckling resistance by increasing the moment of inertia of the stiffener web, whilst simultaneously degrading the in-plane stiffness of the skin by reducing the number of continuous skin plies. The reduction in the number of continuous skin plies had the greatest effect (in absolute terms) on the buckling capability of the skin of the fabric 50% embedded T-joint, which was about 40% lower than the geometrically equivalent 16 ply conventional design.

Reduction in in-plane properties is a typical trade-off for improvement in the toughness and damage tolerance of composite joints. Toughening techniques that show this inverse relationship between toughness and in-plane properties include stitching, tufting, 3D weaving and z-pinning [1, 2]. The compressive test results show that increasing the damage tolerance, ductility and toughness of the T-joint through bio-inspired embedded design does not have a significantly detrimental effect on the in-plane properties of the skin due to the stabilising effect of the increasing stiffener web thickness. However the increased stiffener web thickness increases the weight of the design.

5.3.2 Finite element analysis of T-joint

The experimental results showed that implementing the bio-inspired structural feature of embedded design has the advantages of improving the damage tolerance, ductility and toughness of composite T-joints. However, the embedded design has the disadvantage of triggering damage initiation at lower applied loads compared to the equivalent conventional design. The causes of the reduction in the damage initiation load were investigated using finite element analysis (FEA). Non-linear FE modelling was required to analyse the non-linear deformation of the T-joint in order to accurately model the load-displacement curves up to the damage initiation load.

Non-linear FE analysis was performed on the conventional and bio-inspired T-joints for the bending and tensile load cases to quantify the effect of the embedded design at varying levels of integration on the interlaminar tensile and shear stress distribution in the radius bend region at the damage initiation load. Quantifying the change in peak interlaminar stresses in the radius bend region of the embedded T-joint designs enabled a prediction of the reduction in damage initiation load compared to the geometrically equivalent conventional T-joint.

The FEA results were used to predict the onset of delamination damage and the failure location for the different T-joint designs. Long's criterion (refer Equation 5-2) quantifies the interaction between the interlaminar tensile and interlaminar shear stresses in relation to the allowable strength values in order to predict the initiation of mixed mode I/II delamination damage in laminates [157]. Long's criterion was used for the prediction of the location of delamination damage initiation at the ply level in the T-joint radius bend.

$$\left(\frac{\sigma_{33}}{Z_t}\right)+\left(\frac{\tau_{13}}{S_{13}}\right)^2 \geq 1 \qquad \text{Equation 5-2}$$

Where σ_{33} = interlaminar tensile stress, τ_{13} = interlaminar shear stress, Z_t = interlaminar tensile strength and S_{13} = interlaminar shear strength.

The manufacturer's datasheet gave the interlaminar shear strength (S_{13}) of the unidirectional carbon/epoxy prepreg VTM264 to be 84.3 MPa. This value was used for both the unidirectional and fabric prepregs [155]. The interlaminar tensile strength is sensitive to volumetric effects [106, 125, 134]; a specimen with a larger volume has a reduced interlaminar tensile strength because of the increased probability of the sample containing more numerous and larger flaws. Shivakumar et al. [125] experimentally determined the interlaminar tensile strength of AS4/3501-6 carbon/epoxy prepreg (the same resin system as the fabric samples in the present study) to be 47.6 MPa for samples of equivalent thickness to the 8 ply samples and 23.4 MPa for samples of equivalent thickness to the 16 ply samples. Consequently, the value of Z_t = 47.6 MPa was used for the 8 ply conventional and 25% embedded T-joints and 23.4 MPa was used for the 16 and 32 ply T-joints.

5.3.2.1 Bending load case

The normalised bending load-displacement curves obtained from non-linear FE analysis up to the average damage initiation load are compared to the experimental results in Figure 5-18. The numerical results show good agreement with experimental results. For the 8 ply conventional (refer Figure 5-18a) and 25% embedded (refer Figure 5-18b) T-joints, the numerical analysis accurately predicts the non-linear elastic region caused by the high failure displacement and boundary conditions.

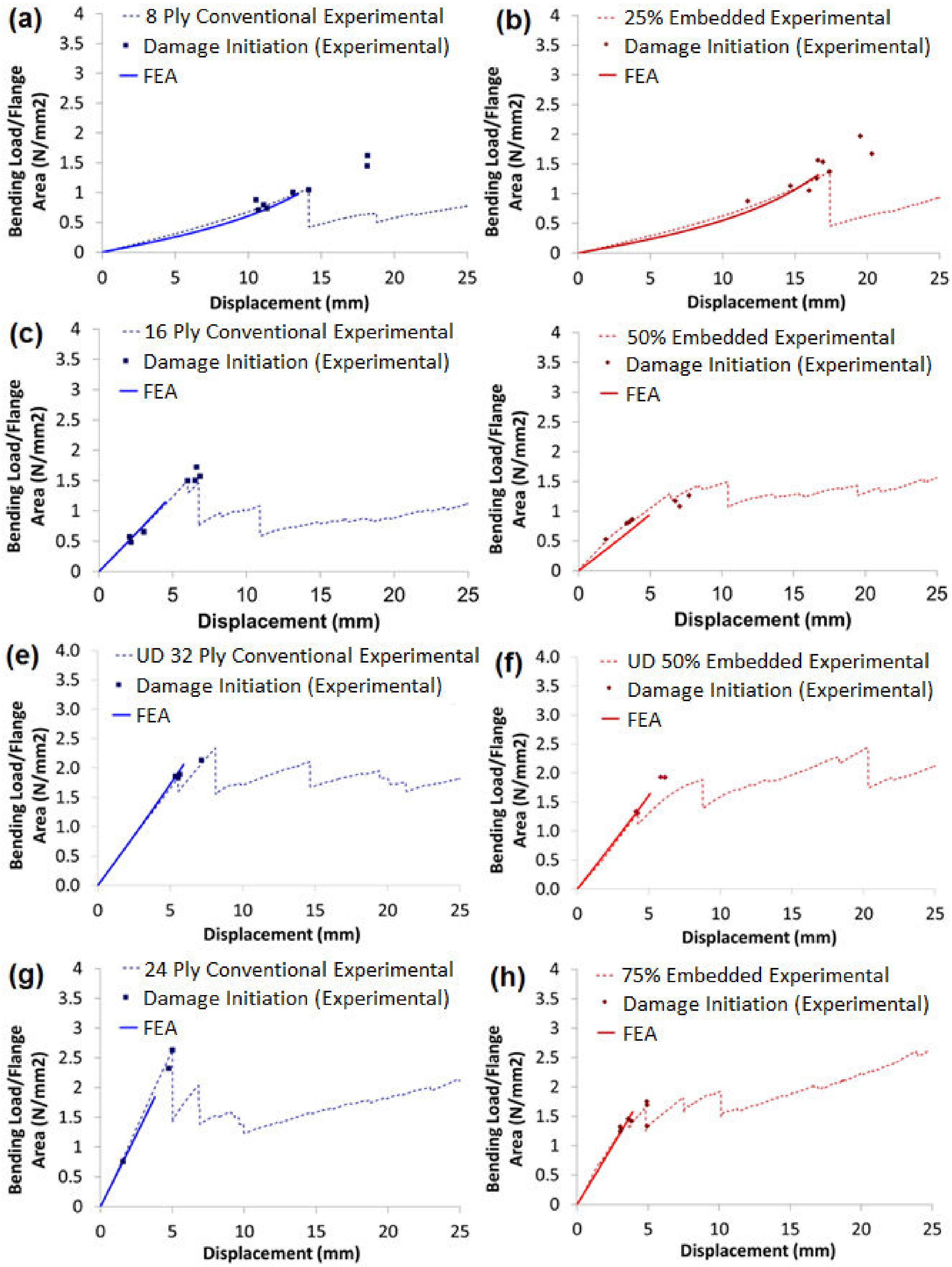

Figure 5-18 Non-linear FEA compared to experimental results under bending load: fabric (a) 8 ply conventional; (b) 25% embedded; (c) 16 ply conventional; (d) 50% embedded; (e) UD 32 ply conventional; (f) UD 50% embedded; (g) 24 ply conventional; and (h) 75% embedded T-joints

For the other T-joints, the damage initiation occurred below about 5 mm displacement and non-linear effects are less pronounced. For all designs, the FEA accurately calculated the initial stiffness of the T-joints under bending load.

FEA was used to model the stress distribution of the embedded and conventional T-joints. For each joint pair, stresses are evaluated at the damage initiation load of the embedded design as obtained from the experimental results. Comparing the interlaminar tensile and shear stress distributions across the radius bend and delta-fillet region at the same applied load enabled a detailed comparison of the effect of the embedded design on the interlaminar geometric stress concentration. The interlaminar tensile stress distributions within the embedded and conventional T-joints under bending are shown in Figure 5-19. The damage initiation load of the embedded design was lower than the equivalent conventional design, with the exception of the fabric 25% embedded design.

The analysis predicts that the peak interlaminar tensile stress occurs at approximately the mid-point both tangentially and radially across the radius bend. At all levels of integration the peak interlaminar tensile stress is higher in the embedded T-joint compared to the conventional joint for the same applied bending load. This explains the reduction in the damage initiation load. The value of the peak interlaminar tensile stress decreased and the location of the peak stress shifted from the inner radius towards the outer radius for increasing stiffener web thickness. This findings agrees with the work by Ko [143] who found that the location of maximum interlaminar tensile stress shifted towards the outer radius of a 90° curved beam as the ratio of the outer radius to the inner radius increases.

The FEA also shows the effect of the boundary conditions in which the applied bending displacement was fixed in the y-direction by the design of the Instron test rig (refer Figure 5-4 and Figure 5-5). At high displacements, as experienced by the 8 ply conventional (refer Figure 5-19a) and fabric 25% embedded (refer Figure 5-19b) T-joints, these test conditions induced a secondary tensile stress on the stiffener web as it rotated and stretched, which reduced the interlaminar compressive stress and increased the interlaminar shear stress in the right hand side radius bend.

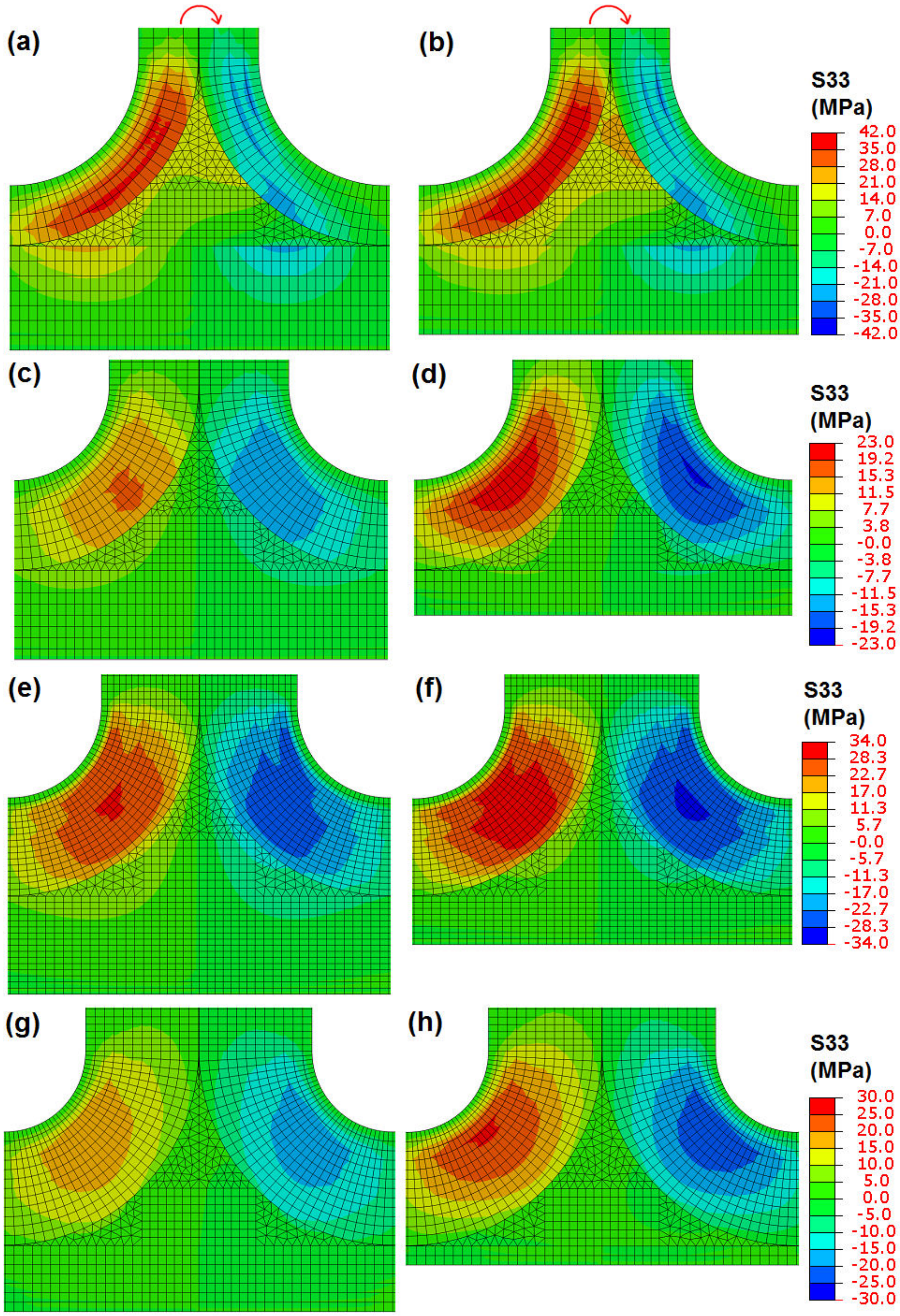

Figure 5-19 FEA peak interlaminar tensile stress (σ_{33}) distribution under bending load: fabric (a) 8 ply conventional; and (b) 25% embedded. Damage initiation load = 106 N; (c) 16 ply conventional; and (d) 50% embedded. Damage initiation load = 84 N; (e) unidirectional 32 ply conventional; and (f) unidirectional 50% embedded. Damage initiation load = 187 N; (g) 24 ply conventional; and (h) 75% embedded. Damage initiation load = 159 N

The T-joints with higher levels of integration of the embedded design also had thicker stiffener webs. Increasing the number of stiffener web plies increases the bending stiffness of the stiffener web, which mitigates the loss in the in-plane stiffness of the skin caused by the reduction in the continuous skin plies. These dual factors of increasing the stiffener web stiffness but decreasing the in-plane skin stiffness in the embedded T-joints explain why there is a slight percentage decrease in the interlaminar tensile stress concentration in the 75% embedded joint compared to the 50% embedded joint (refer Table 5-6).

The interlaminar shear stress distributions in the embedded and conventional T-joints encompassing the location of peak interlaminar shear stress are shown in Figure 5-20. The absolute (ignoring the sign) peak interlaminar shear stress was concentrated at the intersection of the radius bends at the top of the delta-fillet region. Once again the FEA results show that for the same applied bending load, the peak interlaminar shear stress was higher in the embedded T-joint compared to the conventional joint. As explained previously, this stress concentration is responsible for the lower failure initiation loads for the embedded T-joints. The increase in both the interlaminar tensile and shear stresses in the embedded T-joints compared to the conventional joints was due to the reduction from seven continuous skin plies plus an overlaminate (conventional) to six continuous skin plies (25% embedded), to four (fabric 50% embedded), or to two (75% embedded), thereby reducing the stiffness of the skin. This increased the flexibility of the T-joint under load, which in turn increased the strains and stresses in the radius bend and delta-fillet region for the same applied load. Another effect of the embedded design was increasing the number of stiffener laminate plies from 8 (25% embedded) to 16 (50% embedded) to 24 (75% embedded), which increases the bending stiffness of the stiffener web. Therefore, increasing the level of integration of the embedded design progressively increases the stiffener web stiffness but simultaneously decreases the skin stiffness.

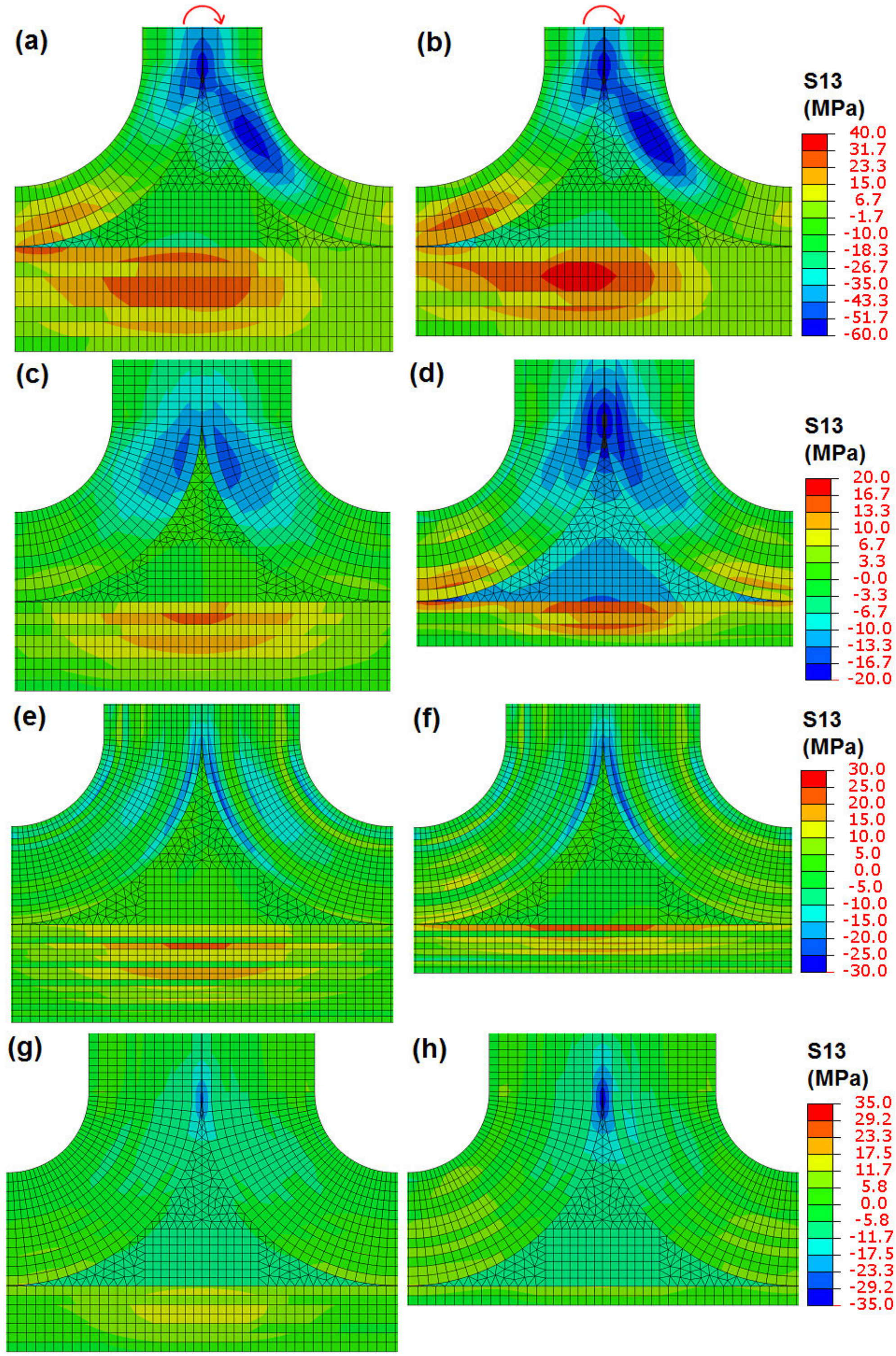

Figure 5-20 FEA peak interlaminar shear stress (τ_{13}) distribution under bending load: fabric (a) 8 ply conventional; and (b) 25% embedded. Damage initiation load = 106 N; (c) 16 ply conventional; and (d) 50% embedded. Damage initiation load = 84 N; (e) unidirectional 32 ply conventional; and (f) unidirectional 50% embedded. Damage initiation load = 187 N; (g) 24 ply conventional; and (h) 75% embedded. Damage initiation load = 159 N

Table 5-6 summarises the peak values of the interlaminar tensile (σ_{33}) and interlaminar shear (τ_{13}) stresses of the embedded and conventional T-joints at the damage initiation load of the embedded joint.

Table 5-6 Summary of the FEA peak interlaminar tensile and shear stresses and comparison to the experimentally determined reduction in damage initiation load.

T-joint	Load (N)	Peak σ_{33} in Radius Bend (MPa)	Peak τ_{13} at Delta-Fillet (MPa)	Failure Mode Observed During Testing	Δ Damage Initiation Load Compared to Conventional (%)
Fabric 8 ply conventional	106*	38.4	-84.2	Mixed delta-fillet and radius bend	
Fabric 25% embedded	106*	41.2 (7%)	-85.3 (1%)	Mixed delta-fillet and radius bend	22%
Fabric 16 ply conventional	84**	15.8	-14.9	Radius bend delamination	
Fabric 50% embedded	84**	22.3 (41%)	-21.0 (41%)	Radius bend delamination	-36%
UD 32 ply conventional	187***	29.1	-21.6	Radius bend delamination	
UD 50% embedded	187***	33.2 (14%)	-23.6 (9%)	Radius bend delamination	-32%
Fabric 24 ply conventional	159****	19.1	-24.4	Radius bend delamination	
Fabric 75% embedded	159****	26.5 (39%)	-33.0 (35%)	Radius bend delamination	-42%

*Damage initiation load of 25% embedded T-joint, **Damage initiation load of 50% embedded T-joint, ***Damage initiation load of 50% embedded unidirectional T-joint, ****Damage initiation load of 75% embedded T-joint

Under bending load the peak interlaminar tensile stress occurs in the radius bend and the peak interlaminar shear stress occurs at the delta-fillet interface. Therefore the reduction in damage initiation load will be either σ_{33} or τ_{13} dominated, depending on the failure location. In the 25% embedded T-joint, the small change in the T-joint geometry results in minimal changes to the peak interlaminar tensile and shear stresses, suggesting any difference in the mechanical performance should be marginal. In the remaining T-joints there are significant increases in both peak interlaminar stresses in the embedded design causing the reduction in the damage initiation loads.

The FE analyses were compared against the experimental results. The 25% embedded T-joints had a higher damage initiation load compared to the conventional T-joint. However, during experimental bend tests the failure mode was observed to be controlled by the quality of the radius bend/delta-fillet interface, which is susceptible to voids and resin-rich regions during manufacturing, resulting in significant standard deviations. The damage initiation for the other T-joint designs was observed during the experiments to occur as delaminations in the radius bend, which indicates it was interlaminar tensile stress dominated. Therefore the change in the peak interlaminar tensile stress was used to predict the reduction in the damage initiation load. The fabric 50% embedded T-joints had good correlation between the increase in the peak interlaminar tensile stress (41%) and the average experimental reduction in the damage initiation load (-36%). The unidirectional 50% embedded T-joint had a 32% reduction in average damage initiation load which was significantly larger than the 14% change in the peak interlaminar tensile stress. This suggests that the unidirectional 50% embedded T-joint possibly experienced a mixed mode failure in which interlaminar shear contributed to the initiation of delamination damage. The 75% embedded T-joint also showed good correlation between the increase in the peak interlaminar tensile stress (39%) and the average experimental reduction in the damage initiation load (-42%).

For further investigation of the failure location and failure mode, Long's criterion was evaluated at the damage initiation load for each T-joint design. Two different failure modes were observed for the thin-webbed 8 ply conventional and 25% embedded T-joints (refer Figure 5-9), therefore Long's failure criterion was calculated at two locations: along the radial path encompassing peak interlaminar tensile stress (refer Figure 5-21a) and the radial path encompassing peak interlaminar shear stress (refer Figure 5-21b), as determined by the non-linear FEA. For the remaining T-joints Long's criterion was calculated along the radial path encompassing peak interlaminar tensile stress at the mid-point of the radius bend.

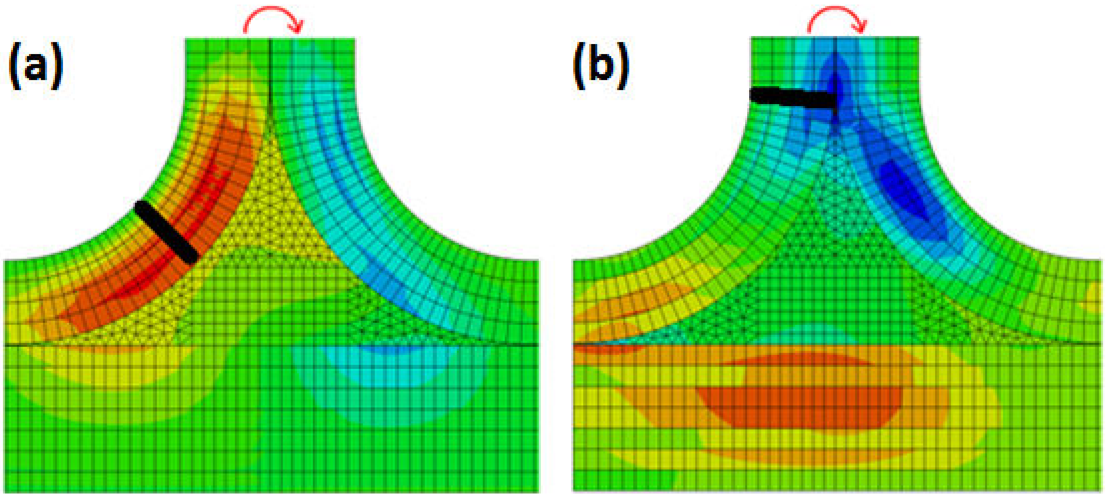

Figure 5-21 Black line indicates location of radial path encompassing: (a) peak interlaminar tensile stress; and (b) peak interlaminar shear stress

Figure 5-22 shows the failure analysis of the embedded and conventional T-joints using Long's strength-based delamination failure criterion [129]. When Long's criterion = 1 it is assumed that failure occurs, when the criterion > 1 it is underestimating the failure load or overestimating the interlaminar strength and when it is < 1 it is overestimating the failure load or underestimating the interlaminar strength.

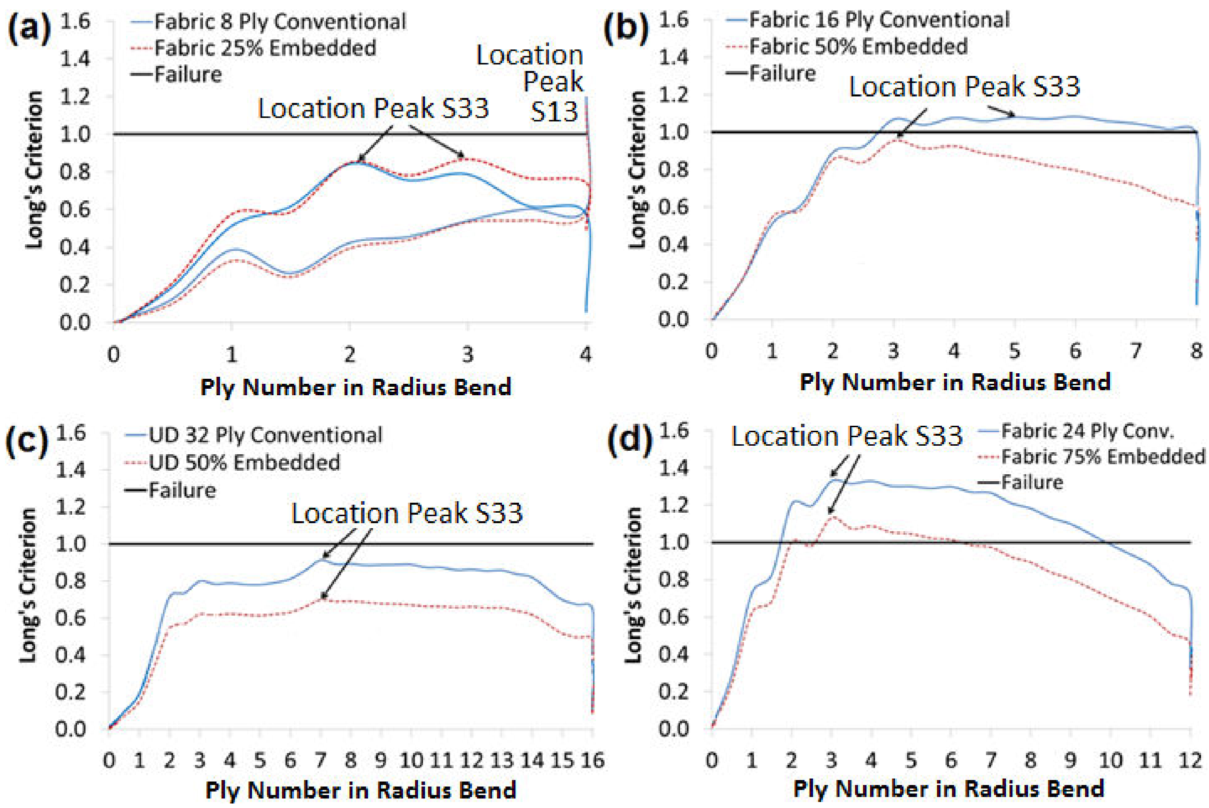

Figure 5-22 Long's criterion under bending load: fabric (a) 8 ply conventional at 86 N and 25% embedded at 106 N; (b) 16 ply conventional at 131 N and 50% embedded at 84 N; (c) unidirectional 32 ply conventional at 268 N and 50% embedded at 187 N; and (d) 24 ply conventional at 275 N and 75% embedded at 159 N. S33 = interlaminar tensile stress and S13 = interlaminar shear stress.

The information from the non-linear FEA concerning the peak interlaminar tensile and shear stresses and the predicated failure mode and location under bending load from Long's criterion are summarised in Table 5-7. The results show that the damage initiation in the 8 ply conventional and 25% embedded T-joints is interlaminar shear dominated, with the shear stress exceeding the shear strength at the radius bend/delta-fillet interface. However, Figure 5-22a shows that while Long's criterion exceeds 1 at the delta-fillet interface failure, there is also a significant superposition of interlaminar stresses in the radius bend between plies 2 - 3, which may cause further delamination failure following failure of the delta-fillet interface. This is supported by the experimental results that show multiple cracking in this region (refer Figure 5-9 and Table 5-6).

Table 5-7 Summary of the failure modes of the conventional and embedded T-joints at the bending damage initiation load

T-joint	Exp. Damage Initiation Load (N)	FEA Peak σ_{33} (MPa)	FEA Peak τ_{13}*** (MPa)	Failure Mode (FEA)	Peak Long's Criterion	Failure Location (Long's Criterion)
Fabric 8 ply conventional	86	31.7 (56% Z_t*)	-88.3 (105% S_{13})	τ_{13} dominated	1.22	Delta-fillet interface
Fabric 25% embedded	106	41.2 (73% Z_t*)	-85.3 (101% S_{13})	τ_{13} dominated	1.15	Delta-fillet interface
Fabric 16 ply conventional	131	25.1 (107% Z_t**)	-24.6 (29% S_{13})	σ_{33} dominated	1.08	Plies 3 - 8
Fabric 50% embedded	84	22.3 (95% Z_t**)	-33.4 (40% S_{13})	σ_{33} dominated	0.95	Plies 3 - 4
UD 32 ply conventional	268	42.0 (88% Z_t*)	-30.7 (36% S_{13})	σ_{33} dominated	0.91	Plies 7 - 13
UD 50% embedded	187	33.2 (70% Z_t*)	-23.6 (28% S_{13})	σ_{33} dominated	0.70	Plies 7 - 13
Fabric 24 ply conventional	275	32.3 (137% Z_t**)	-44.2 (52% S_{13})	σ_{33} dominated	1.33	Plies 3 - 6
Fabric 75% embedded	159	26.5 (133% Z_t**)	-35.8 (42% S_{13})	σ_{33} dominated	1.13	Plies 3 - 4

*Z_t = 47.6 MPa, ** 23.4 MPa [125]. ***S_{13} = 84.3 MPa [155]

The damage initiation in the fabric 16 ply conventional and 50% embedded T-joints is interlaminar tensile dominated and occurs in the radius bend. Figure 5-22b shows Long's criterion reaches a peak for the conventional T-joint between plies 3 – 8 and between plies 3 – 4 for the 50% embedded T-joint, indicating the likely location of delamination damage.

The damage initiation in the unidirectional 32 ply conventional and 50% embedded T-joints is dominated by the interlaminar tensile stress and occurs in the radius bend. Figure 5-22c shows Long's criterion reaches a peak between plies 7 – 13 in both the conventional and 50% embedded T-joints.

The damage initiation in the 24 ply conventional and 75% embedded T-joints is interlaminar tensile dominated and occurs in the radius bend. Figure 5-22d shows Long's criterion reaches a peak for the conventional T-joint from plies 3 – 6 and for the 75% embedded T-joints at ply 3, indicating the likely location of delamination damage.

The peak value of Long's criterion varied between 0.7 – 1.33 with an average value of 1.06. In general the Long's criterion accurately predicted the failure value of 1.0 at the damage initiation load. For the unidirectional samples the values of Long's criterion < 1 suggest the T-joint may have failed prematurely, possibly due to flaws such as voids or resin-rich regions, or the value of Z_t = 47.6 MPa may have been slightly high. Long's criterion was useful in determining the location of the interactive interlaminar stress concentration likely to be the site of damage initiation. Comparison with experimental observations shows Long's failure criterion predicts the location of the failure accurately for the different T-joint designs.

In summary, the thin-webbed T-joints are limited by the high interlaminar shear stresses that occur at high bending displacement at the delta-fillet interface. These reduce as the T-joint stiffener web gets thicker. The limiting factor for thick-webbed composite T-joints under bending is the high interlaminar tensile stresses that occur in the radius bend coupled with decreasing interlaminar tensile strength proportional to the thickness of the laminate.

5.3.2.2 Tension load case

The normalised FEA tensile load-displacement curves calculated up to the damage initiation load are compared to the experimental curves in Figure 5-23. Once again, the curves predicted by FEA show good agreement with the experimental results. For the 8 ply conventional (refer Figure 5-23a) and fabric 25% embedded joints (refer Figure 5-23b), the FEA accurately calculates the initial non-linear elastic region of the curves caused by the large deformations of the T-joints. For applied displacements larger than 3 mm, the FEA starts to diverge from the experiment, predicting higher stiffness and therefore higher loads at the same displacement.

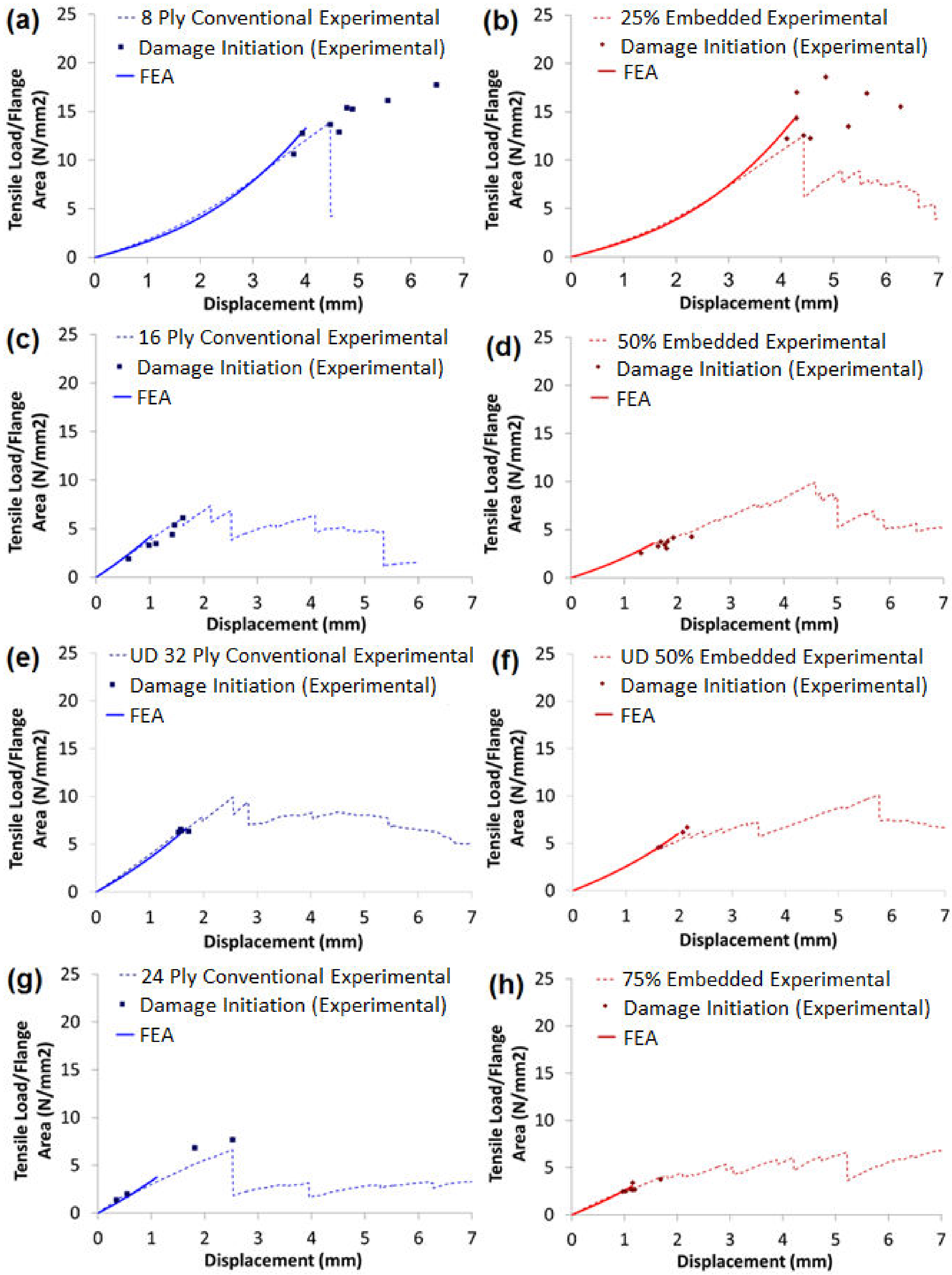

Figure 5-23 Non-linear FEA compared to experimental normalised tensile load-displacement curves: fabric (a) 8 ply conventional; (b) 25% embedded; (c) 16 ply conventional; (d) 50% embedded; (e) unidirectional 32 ply conventional; (f) unidirectional 50% embedded; (g) 24 ply conventional; and (h) 75% embedded T-joints

This divergence is caused by the boundary conditions, which in the FEA are modelled with the skin being perfectly clamped, with zero displacement in the x, y and z directions. In reality, the clamping condition was not perfect and allowed some displacement in the in-plane skin direction, which would 'soften' the non-linear effects as seen with the experimental results. The boundary conditions could be more precisely modelled by rotational springs with variable spring stiffness. However, in all cases the FEA accurately predicted the initial stiffness of the T-joint up to the damage initiation load.

The interlaminar tensile stress distributions under tensile load within the embedded and conventional T-joints are shown in Figure 5-24. The applied load is the average damage initiation load for the embedded T-joint. In all cases the peak interlaminar tensile stress is higher in the embedded T-joint, and the value of the peak interlaminar tensile stress decreases with increasing stiffener laminate thickness. The FEA also shows that there are two locations of peak interlaminar tensile stress. The first location is at the intersection of the radius bends at the top of the delta-fillet. The second location is in the radius bend about one-third tangentially around the radius from the stiffener flange. As the stiffener web increases in thickness, the radius bend stress concentration increases in relation to the delta-fillet interface stress concentration. The increase in the peak interlaminar tensile stress is slightly higher in the unidirectional 50% embedded T-joint compared to the fabric 50% embedded T-joint.

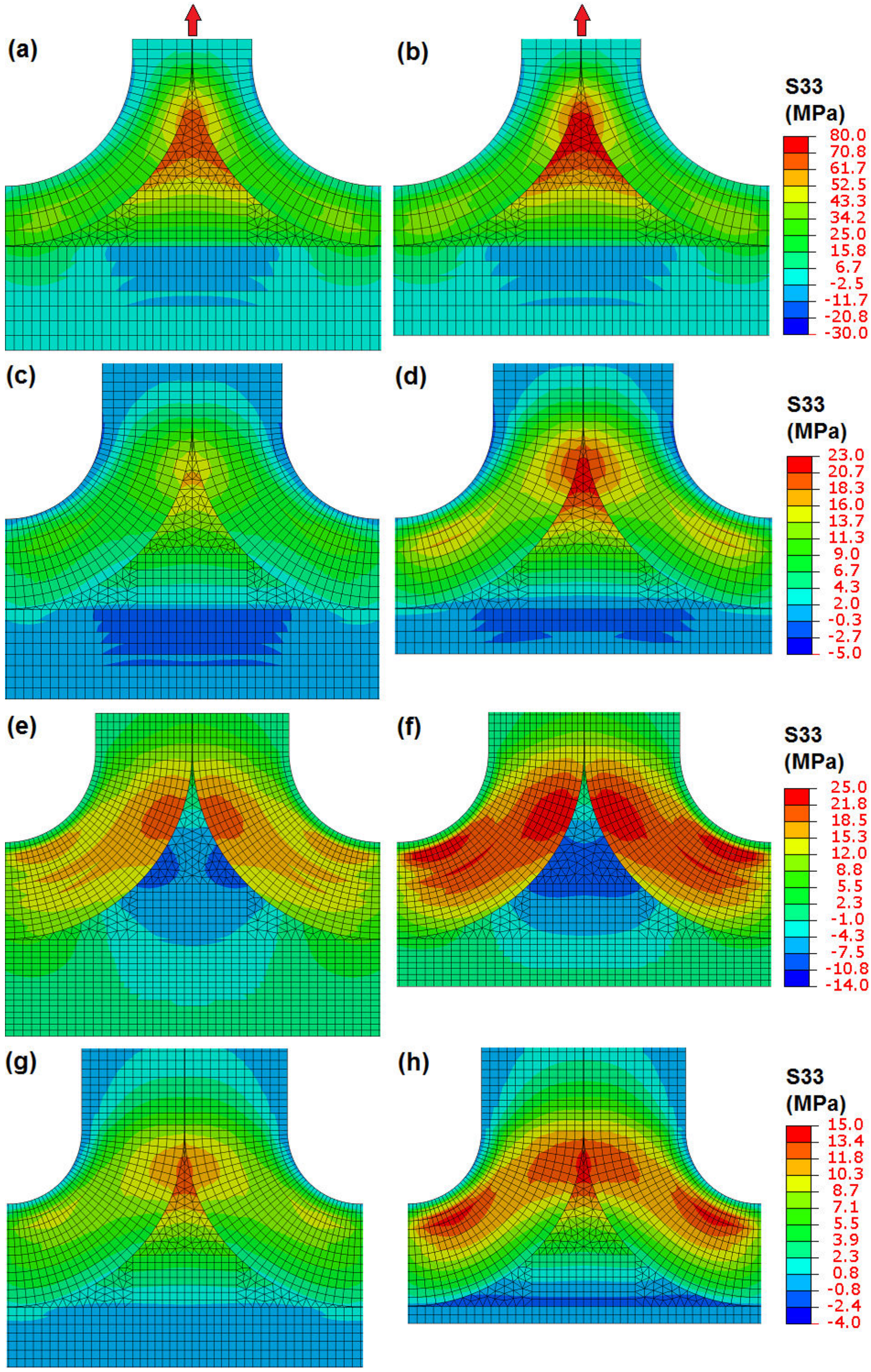

Figure 5-24 FEA peak interlaminar tensile stress (σ_{33}) distribution under tensile load: fabric (a) 8 ply conventional; and (b) 25% embedded. Damage initiation load = 1131 N; (c) 16 ply conventional; and (d) 50% embedded. Damage initiation load = 315 N; (e) unidirectional 32 ply conventional; and (f) unidirectional 50% embedded. Damage initiation load = 604 N; (g) 24 ply conventional; and (h) 75% embedded. Damage initiation load = 313 N

The interlaminar shear stress distributions under tensile load within the embedded and conventional T-joints are shown in Figure 5-25. The results show that the peak shear stress was higher in the bio-inspired embedded T-joints compared to the equivalent conventional joint for the same applied load. The peak shear stress was concentrated at the tangential mid-point of the radius bend in the 0/90° plies in the fabric joints and in the 0° plies in the unidirectional joints. The increase in the peak shear stress was higher in the fabric 50% embedded T-joint compared to the unidirectional 50% embedded joint.

The increase in both the peak interlaminar and tensile shear stresses in the embedded T-joint compared to the equivalent conventional T-joint was again attributed to the reduction in skin stiffness due to the reduction in the number of continuous skin plies in the embedded designs from six (25% embedded) to four (fabric 50% embedded) to two plies (75% embedded). This resulted in increased flexibility for the embedded T-joint under a given applied tensile load. However, there is a balance between the reduction in skin stiffness and increasing the number of stiffener laminate plies from 8 (25% embedded) to 16 (50% embedded) to 24 (75% embedded), which increases the bending stiffness of the stiffener web. Table 5-8 summarises the maximum value of the interlaminar tensile (σ_{33}) stress in both the radius bend and at the delta-fillet interface and the peak interlaminar shear (τ_{13}) stress in the radius bend of the embedded and conventional T-joints.

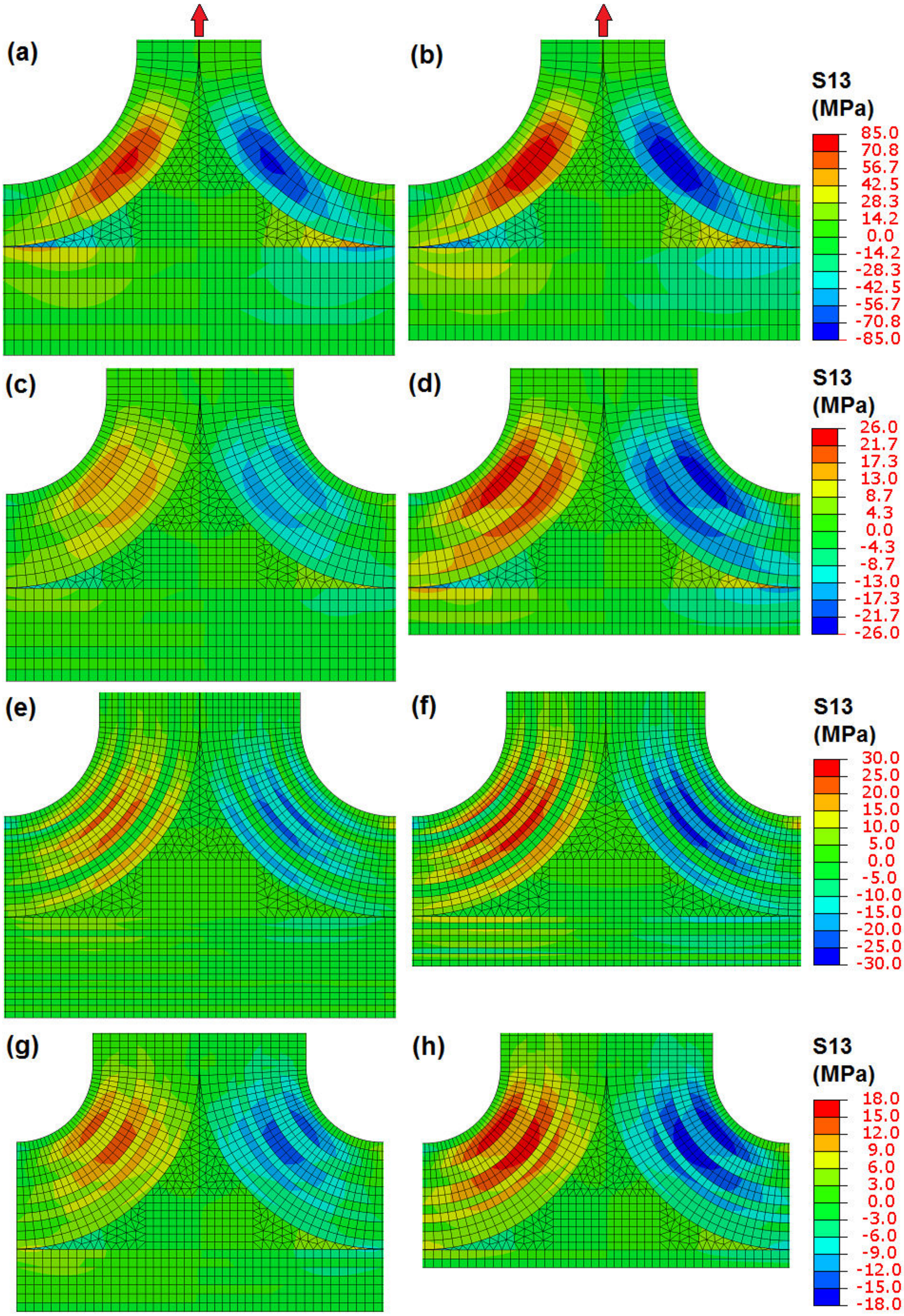

Figure 5-25 FEA peak interlaminar shear stress (τ_{13}) distribution under tensile load: fabric (a) 8 ply conventional; and (b) 25% embedded. Damage initiation load = 1131 N; (c) 16 ply conventional; and (d) 50% embedded. Damage initiation load = 315 N; (e) unidirectional 32 ply conventional; and (f) unidirectional 50% embedded. Damage initiation load = 604 N; (g) 24 ply conventional; and (h) 75% embedded. Damage initiation load = 313 N

Table 5-8 Summary of the FEA peak interlaminar tensile and shear stresses in the radius bend of the conventional and bio-inspired embedded T-joints at the damage initiation load and validation of FEA comparing peak interlaminar stresses in radius bend with the experimentally determined reduction in damage initiation load under tension.

T-joint	Damage Initiation Load (N)	Peak σ_{33} in Radius Bend (MPa)	Peak σ_{33} in Delta-Fillet (MPa)	Peak τ_{13} Radius Bend (MPa)	ΣΔ (Peak σ_{33} + Peak τ_{13}) in Radius Bend	Δ Damage Initiation Load Compared to Conventional T-Joint (%)
Fabric 8 ply conventional	1131*	40.8	56.5	75.6		
Fabric 25% embedded	1131*	45.2	62.4 (10%)	84.0 (10%)		-5%
Fabric 16 ply conventional	315**	11.0	14.4	17.6		
Fabric 50% embedded	315**	17.3	21.9 (52%)	25.6 (45%)		-55%
UD 32 ply conventional	604***	18.6	20.1	23.5		
UD 50% embedded	604***	25.2 (25%)	23.9	29.5 (26%)	51%	-31%
Fabric 24 ply conventional	313****	10.0	12.5	13.7		
Fabric 75% embedded	313****	15.0 (20%)	14.0	17.9 (31%)	51%	-43%

*Damage initiation load of 25% embedded T-joint, **Damage initiation load of 50% embedded T-joint, ***Damage initiation load of 50% unidirectional embedded T-joint, ****Damage initiation load of 75% embedded T-joint

The interlaminar tensile stress concentration is highest at the delta-fillet interface for all joint designs except for the unidirectional 50% embedded and the fabric 75% embedded T-joints. For these two designs, in which the peak interlaminar tensile stress occurs in the radius bend, there is a significant superposition with the peak interlaminar shear stress, which also occurs in the radius bend, resulting in an interactive interlaminar stress concentration. The increase in the peak interlaminar tensile stress in the fabric 25% and 50% embedded T-joints showed good correlation with the average experimental reduction in the damage initiation load. The summation of the increase in the peak interlaminar tensile and shear stresses provided a conservative prediction of the average reduction in damage initiation load obtained from the experimental tests. This is to be expected as the peak interlaminar tensile and shear stresses were not exactly coincident in the T-joint radius bend.

Long's failure criterion was calculated at two locations across the radius bend encompassing the interlaminar tensile stress concentrations as determined by the non-linear FEA, as shown in Figure 5-26.

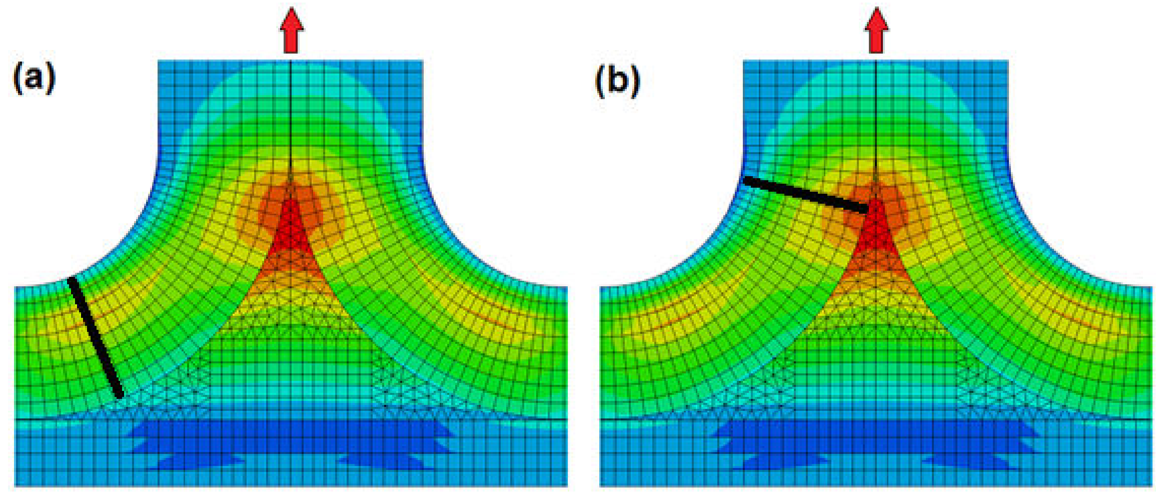

Figure 5-26 Black line indicates location of path encompassing peak interlaminar tensile stress: (a) in radius bend; and (b) at delta-fillet interface

Long's criterion calculated at the average damage initiation load as obtained from the experimental testing across the two paths of peak interlaminar tensile stress is given in Figure 5-27.

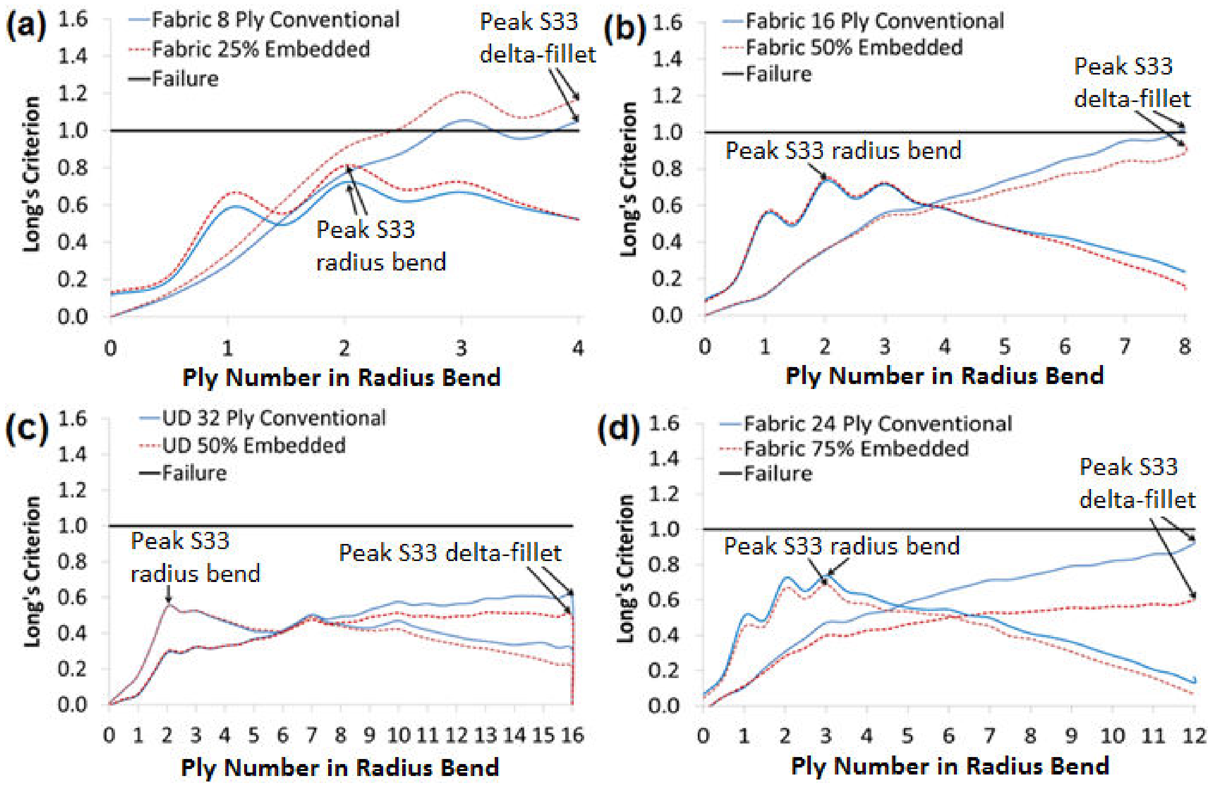

Figure 5-27 Long's criterion: fabric (a) 8 ply conventional at 1186 N and 25% embedded at 1131 N; (b) 16 ply conventional at 707 N and 50% embedded at 315 N; (c) unidirectional 32 ply conventional at 876 N and 50% embedded at 604 N; and (d) 24 ply conventional T-joint at 545 N and 75% embedded T-joint at 313 N

The information from the non-linear FEA concerning the peak interlaminar tensile and shear stresses and the information from Long's criterion concerning failure mode and location under tensile loading is summarised in Table 5-9. The results show that at the damage initiation load the 8 ply conventional and 25% embedded T-joints fail by exceeding the interlaminar tensile strength at the delta-fillet interface. Almost simultaneously, the interlaminar shear strength is also exceeded in the radius bend. Figure 5-27a shows there is also an interactive stress concentration in the radius bend at ply 2, which may cause delamination failure after delta-fillet cracking. These results suggest damage will occur at the delta-fillet interface, with potential for damage initiation following closely in the radius bend, as observed during experimental testing (refer Figure 5-14).

Table 5-9 Summary of the failure modes of the conventional and bio-inspired embedded T-joints at the tensile damage initiation load

T-joint	Exp. Damage Initiation Load (N)	FEA Peak σ_{33} (MPa)	FEA Peak τ_{13} (MPa)	Failure Mode (FEA)	Peak Long's Criterion	Failure Location (Long's Criterion)
Fabric 8 ply conventional	1186	56.5** (119% Z_t)	75.6* (90% S_{13})	Exceeds $\mathbf{Z_t}$ at delta-fillet. High $\mathbf{S_{13}}$ in radius bend	1.08	Ply 3 & delta-fillet interface
Fabric 25% embedded	1131	62.4** (131% Z_t)	84.0* (99% S_{13})	Exceeds $\mathbf{Z_t}$ at delta-fillet. High $\mathbf{S_{13}}$ in radius bend	1.21	Ply 3 & delta-fillet interface
Fabric 16 ply conventional	495	23.8** (102% Z_t)	27.5* (33% S_{13})	$\boldsymbol{\sigma_{33}}$ dominated at delta-fillet interface	1.02	Delta-fillet interface
Fabric 50% embedded	315	21.9** (94% Z_t)	25.6* (30% S_{13})	$\boldsymbol{\sigma_{33}}$ dominated at delta-fillet interface	0.94	Delta-fillet interface
UD 32 ply conventional	876	27.8** (58% Z_t)	32.3* (38% S_{13})	$\boldsymbol{\sigma_{33}}$ dominated in radius bend and at delta-fillet interface	0.61	Plies 2 - 3 & delta-fillet interface
UD 50% embedded	604	25.2* (53% Z_t)	12.4* (15% S_{13})	$\boldsymbol{\sigma_{33}}$ dominated in radius bend and at delta-fillet interface	0.55	Plies 2 - 3 & delta-fillet interface
Fabric 24 ply conventional	545	21.6** (92% Z_t)	21.1* (25% S_{13})	$\boldsymbol{\sigma_{33}}$ dominated in radius bend at delta-fillet interface	0.92	Plies 2 - 3 & delta-fillet interface
Fabric 75% embedded	313	15.0* (64% Z_t)	17.9* (21% S_{13})	$\boldsymbol{\sigma_{33}}$ dominated in radius bend and at delta-fillet interface	0.70	Plies 2 - 3 & delta-fillet interface

* occurs in radius bend, ** occurs at delta-fillet interface

The failure of the fabric 16 ply conventional and 50% embedded T-joints is interlaminar tensile dominated at the delta-fillet interface. Figure 5-27b shows Long's criterion reaches a peak for these two T-joints at the delta-fillet interface. There is also an interactive stress concentration between plies 3 – 4, indicating the likely location of any delamination damage.

Figure 5-27c shows Long's criterion reaches a peak between plies 2 - 3 in the radius bend and between plies 12 – 16 up to the delta-fillet interface for both the unidirectional 32 ply conventional and 50% embedded T-joints. The failure is dominated by the interlaminar tensile stress. Delamination damage and cracking across the delta-fillet interface are predicted to initiate simultaneously, and it was also observed in the experimental tests. While the failure location is predicted accurately, the failure load is overestimated using Long's criterion. The results suggest either the UD specimens failed prematurely due to flaws such as voids or resin-rich regions or the estimated interlaminar tensile strength of 47.6 MPa was over-predicted.

Figure 5-27d shows Long's criterion reaches a peak between plies 2 - 3 in the radius bend and at the delta-fillet interface for both the fabric 24 ply conventional and 75% embedded T-joints. The failure is dominated by the interlaminar tensile stress. Delamination damage and cracking across the delta-fillet interface are predicted to initiate almost simultaneously as observed in the experimental tests.

In summary, under tensile loading multiple failure modes occur simultaneously in the radius bend and at the delta-fillet interface due to the superposition of interlaminar tensile and shear stresses. The thin-webbed 8 ply composite T-joints represent an optimum design as both the interlaminar tensile and shear strengths are exceeded simultaneously. The thick-webbed composite T-joints are limited by the high interlaminar tensile stresses that occur in the radius bend and at the delta-fillet interface.

The peak value of Long's criterion varied between 0.61 – 1.21 with an average value of 0.88. In general the Long's criterion accurately predicted the failure value of 1.0 at the damage initiation load for the fabric T-joints. Long's criterion was useful in explaining the underlying physics of the multiple failure modes in the radius bend and delta-fillet region observed during the experimental testing of the embedded and conventional T-joints.

5.4 SUMMARY AND CONCLUSIONS

The experimental test results showed that under both bending and tensile loading damage initiated in the radius bend/delta-fillet zone with delaminations forming in the radius and cracking occurring at the delta-fillet interface of the T-joint. This damage was caused by the geometric stress concentration and a large mismatch in elastic moduli due to the different orientation of the carbon fibres in the radius bend and delta-fillet 'noodle' regions.

Embedded design in which the stiffener flange is partially integrated into the skin increases the inelastic strain energy (ductility), strain energy to failure load (toughness) and damage tolerance of T-joints under both bending and tensile loading. More energy is required to fail the joint with higher levels of embedment.

Integrating the stiffener flange and skin plies up to 25% embedment is a small change to the design that does not significantly alter the mechanical properties of the T-joint. The 50% embedded T-joint design stands out as absorbing significantly higher inelastic strain energy and strain energy to failure load under both bending and tension loading whilst maintaining the same normalised failure load as the equivalent conventional design. The 75% embedded T-joint design had the highest tensile performance in terms of ductility and damage tolerance, because the flange is embedded deep into the skin and therefore requires a large amount of energy to pull it out. This T-joint might be appropriate in designs where high tensile ductility and damage tolerance are key requirements; however the normalised bending failure load is reduced. In addition, increasing the percentage of embedment requires more stiffener web plies. Thus it is important to consider whether a bio-inspired embedded design suits the existing design of weight-critical structures.

Improvements in ductility, toughness and damage tolerance were attributed to the embedded design inducing crack deflection and crack branching (similar to the tree branch-trunk joint). This increased the strain energy release rate per volume of material, which partially stabilised the crack growth process along the stiffener flange/skin bond-line. In comparison, a single dominant crack along the stiffener flange/skin bond-line induced brittle failure of the conventional T-joint.

Bio-inspired embedded design is effective for T-joints fabricated from either fabric or unidirectional carbon/epoxy prepreg materials. The experimental results for the fabric and unidirectional 50% embedded T-joints were qualitatively similar, with the unidirectional specimens exhibiting slightly higher mechanical properties due to the reduced fibre waviness.

The embedded T-joint design has the disadvantages of a reduction in the normalised damage initiation load under both tensile and bending loading and a reduction in the in-plane compressive strength of the skin compared to the geometrically similar conventional design. The loss in compressive strength arises from the reduction in the number of continuous skin plies in the embedded design and is somewhat mitigated by the increase in the number of stiffener web plies with increasing embedment.

Non-linear FE analysis showed that the reduction in the normalised damage initiation load of the embedded T-joint design is caused by an increase in the interlaminar tensile and shear stresses in the radius bend/delta-fillet region. This is due to the reduction from seven continuous skin plies plus an overlaminate (no embedded plies) to six (25% embedded), to four (fabric 50% embedded), and finally to two (75% embedded). The reduction in continuous skin plies reduces the stiffness of the skin. This increases the flexibility of the T-joint under load which thereby increases the strains and stresses in the radius bend and delta-fillet region.

In both the bending and tensile load cases, the percentage reduction in the damage initiation load of the embedded T-joint correlated with the percentage increase in the peak interlaminar tensile stress in the radius bend or the sum of the percentage increase in the peak interlaminar tensile and shear stresses if these peak stresses were superimposed at the failure location.

The non-linear FEA investigation revealed information about the failure mode and exact location of failure within the radius bend/delta-fillet region of the conventional and embedded T-joint designs. Under bending load, the damage initiation in the thin-webbed 8 ply T-joints is dominated by the high interlaminar shear stresses that occur at high bending displacement at the delta-fillet interface. These stresses decrease as the T-joint stiffener web gets thicker. Damage initiation in the thicker T-joints is dominated by high interlaminar tensile stresses that occur in the radius bend. Under tensile loading multiple failure modes occur with delamination damage in the radius bend and cracking at the delta-fillet interface occurring simultaneously. The thin-webbed 8 ply T-joints represent an optimum design as the interlaminar tensile and shear strengths are both exceeded simultaneously. Damage initiation in the medium-thickness T-joints is dominated by the interlaminar tensile stresses at the delta-fillet interface. Damage initiation in the thick-webbed T-joints is dominated by high interlaminar tensile stresses that occur in both the radius bend and at the delta-fillet interface.

Mimicking the 50% integration of the tree branch into the trunk discussed in chapter three (which could be considered a natural optimum) produced significant improvements in ductility, toughness and damage tolerance with a reduced weight increase in comparison to the 75% embedded design. While inspiration for the embedded composite T-joint design came from the design of tree branch joints, there are several major differences between the tree branch-trunk joint and the composite T-joint. Trees have the ability to self-heal, meaning the onset of damage at relatively low loads resulting in small cracks might be less significant than in engineered composite joints because the branch-trunk joint can repair itself. Furthermore, computed tomography shows that the fibril lay-up to the tree branch embedded to the centre of the trunk is three-dimensional. In comparison, the fibre lay-up to the embedded composite T-joint is only two-dimensional due to manufacturing limitations. Improvements in manufacturing techniques that can produce T-joints with three-dimensional fibre lay-ups may enable more complex damage tolerant designs.

The results show that only implementing the biomimicked feature of embedded design at the structural level improves ductility, toughness and damage tolerance under both bending and tensile load at the expense of early onset damage initiation and reduced in-plane properties. The bio-inspired principle of hierarchical design indicates that refinement of material properties (as discussed in chapter four) provides a solution to compensate for the interlaminar stress concentration in the radius bend of the embedded joint design in order to mitigate the early onset damage. The hierarchical approach to bio-inspired design of composite T-joints using both embedded design and optimised stiffener ply stacking sequence is investigated in the following chapter.

CHAPTER 6:

6 HIERARCHICAL DESIGN OF COMPOSITE T-JOINTS

6.1 INTRODUCTION

A characteristic feature of biological structures is hierarchical design, which enables maximum structural efficiency to be extracted by converting relatively weak or brittle constituents into strong and tough composite materials [4]. Hierarchical design allows cracks to initiate and propagate over several length scales which promotes high toughness and damage tolerance. The approach is so effective that the fracture toughness of biological composites such as nacre is more than an order of magnitude higher than the constituent materials [36, 161]. Figure 2-16 shows the five layers of structural hierarchy in wood from the nano- to macro-length scales: (1) molecular nano-crystallines of cellulose in the microfibrils; (2) composite microfibrils comprised of cellulose, hemi-cellulose and lignin; (3) concentric lamellae of aligned microfibrils surrounding the hollow wood cell; (4) cellular structure comprising the grain of wood; and (5) macro-structure of the growth rings with seasonally varying density as a result of periodic changes to the diameter and wall thickness of the wood cells

Through the transformative process of hierarchical design, weaknesses in the constituent materials and localised stress concentrations can be overcome by the architecture of the material and structure of the composite. In chapter four the strength of unidirectional carbon/epoxy T-joints under bending and tension loading was improved by reducing the geometric interlaminar stress concentration across the radius bend through bio-inspired optimisation of the fibre orientation across the laminate stacking sequence. This approach was based on the observed optimisation of internal material properties within biological load-bearing structures such as trees [46, 47]. The advantage of this approach is that the damage initiation strength was improved without cost or weight penalties. The disadvantage was that the T-joint continued to undergo brittle failure due to the low interlaminar fracture toughness of the carbon/epoxy prepreg material.

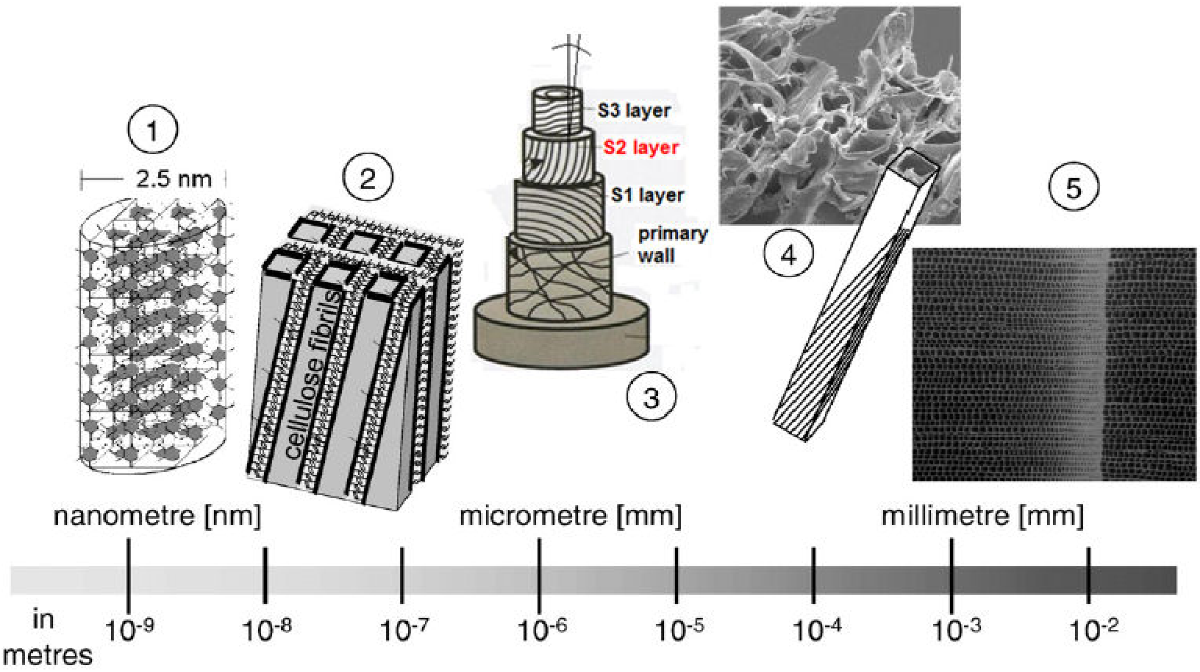

Figure 6-1 Hierarchical structure of wood [24]

In chapter five the toughness and damage tolerance of T-joints was improved through biomimetic design in which the plies of the stiffener flange and skin were integrated by partially embedding flange plies into the skin laminate. This approach was based on the concept of creating a more integrated T-joint at the structural level. The advantage of the design is more energy is required to pull-out the stiffener under tensile and bending loading due to crack deflection and crack branching increasing the strain energy release rate across the flange area. The disadvantage is the reduction in the damage initiation load due to delaminations initiating prematurely in the radius bend due to an increase in the interlaminar tensile and shear stresses caused by a reduction in skin stiffness.

In summary, the bio-inspired optimisation of the stiffener laminate ply stacking sequence described in chapter four increased the strength of the T-joint without improving toughness whereas the biomimetic embedded design described in chapter five improved the toughness of the T-joint at the expense of strength. The obvious solution to overcome the deficiencies in each approach is to create a hierarchical composite T-joint design combining ply (material) optimisation in conjunction with integrated embedded structural design.

The objective of the study presented in this chapter is to evaluate the efficacy of combining material and structural changes to the T-joint in a single hierarchical design. The hypothesis is that combining the biomimetic approaches of strength improvement through ply angle optimisation together with damage tolerance improvement through embedded design will result in a hierarchically designed composite T-joint that is both strong and tough. In this chapter the hierarchical T-joint is defined as the joint that combines the optimised orientation of the plies in the stiffener laminate (for increased strength) and embedding of stiffener plies into the skin (for increased toughness).

6.2 ANALYSIS AND EXPERIMENTAL METHODOLOGY

6.2.1 Non-linear finite element analysis

Non-linear FE analysis was conducted according to the description given in chapter five to determine the interlaminar and tensile stress distributions at damage initiation and to determine the failure location at the ply-level within the T-joints.

6.2.2 Optimisation analysis

The optimisation model was constructed according to the description given in chapter four with the following modifications. In the hierarchical optimisation the stiffener web laminate was constructed from 32 plies of unidirectional carbon/epoxy prepreg (i.e. double the thickness of the optimised T-joint described in chapter four). Consequently, for the hierarchical optimisation there were eight ply angle input variables (instead of four) and the optimisation was run for 200 iterations instead of 100 iterations.

The 32 ply stiffener laminate had the ply stacking pattern $[\theta_1/\theta_2/\theta_3/\theta_4/-\theta_4/-\theta_3/-\theta_2/-\theta_1/\theta_5/\theta_6/\theta_7/\theta_8/-\theta_8/-\theta_7/-\theta_6/-\theta_5]_s$, where the symbols θ_1 – θ_8 represent the 8 ply angle input variables. The hierarchical design was compared to a baseline quasi-isotropic lay-up of $[45/0/-45/90/90/-45/0/45]_{2S}$. As described in chapter four, the optimisation program was run with the single objective of minimising the peak interlaminar tensile stress (σ_{33}) in the T-joint radius bend without violating the constraints of keeping the in-plane and bending stiffness values of the stiffener laminate within ±10% of the baseline (quasi-isotropic) stiffener design. The initial design was an arbitrary design that fulfilled the global stiffness constraints and was set to $[20/40/50/60/-60/-50/-40/-30/24/34/44/54/-54/-44/-34/-24]_s$. The plies in the radius bend were numbered from 1 – 16 (refer Figure 6-2), with ply 1 on the free edge of the outer radius bend and ply 16 adjacent to the delta-fillet region in the inner radius bend.

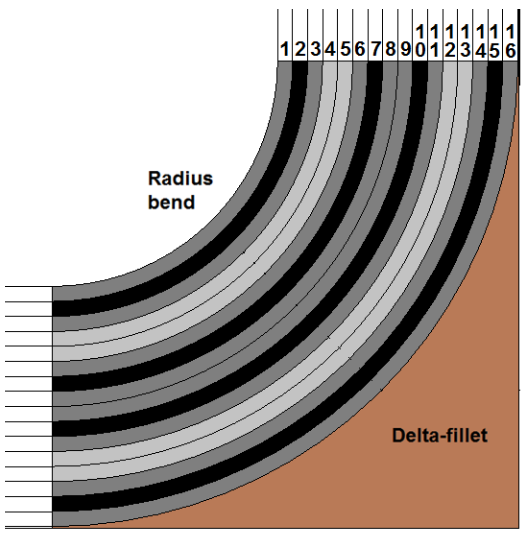

Figure 6-2 16 ply radius bend ply numbering convention

6.2.3 Experimental testing

Test specimens were tested to evaluate the hypothesis of increased strength and toughness in the hierarchical design compared to the baseline and to validate the non-linear FE model. The

T-joints were fabricated from VTM264 unidirectional carbon fibre/epoxy prepreg and cured according to the procedure described in chapter four. The baseline T-joint had a 32 ply stacking sequence of $[45/0/-45/90/90/-45/0/45]_{2s}$ for the stiffener laminate. The hierarchical T-joint had a stacking pattern of $[0/36/70/84/-84/-70/-36/0/12/50/50/74/-74/-50/-50/-12]_s$ for the stiffener, as derived from the optimisation analysis described in section 6.3.1. The T-joint specimens were tested under stiffener bending and tension loading to failure, with the test method described in full in chapters four and five. Four samples of both T-joints types were tested under bending and a further four samples tested under tension load.

6.3 RESULTS AND DISCUSSION

6.3.1 Optimisation analysis

The progression of the hierarchical optimisation across 200 iterations is shown in Figure 6-3. In Figure 6-3a the three parameters of peak interlaminar tensile stress and in-plane and bending stiffnesses were normalised to the value in the baseline T-joint. In Figure 6-3b the peak interlaminar tensile stress was normalised by multiplying by the ratio of the conventional and hierarchical flange areas to account for the differing amounts of material in the baseline and hierarchical T-joints. Approximately one-third of the iterations fulfilled the global stiffness constraints. The in-plane (A_{11}) and bending (D_{11}) stiffness values of the stiffener laminate both oscillated ±10% about the normalised baseline value of 1.0.

The peak interlaminar tensile stress decreased as the optimisation progressed towards completion. Comparing the stress values directly, Figure 6-3a shows that in the initial design the peak interlaminar tensile stress was about 20% higher than the baseline T-joint and declined to a minimum of 6% higher at the end of the optimisation process. Comparing the stress values normalised for flange area, Figure 6-3b shows the initial design is about the same as the baseline design and the optimisation modelling reduces the peak down to 20% less than the baseline. In general, the optimised designs in which the peak interlaminar tensile stress was minimised correlated with designs in which the in-plane stiffness A_{11} trended towards the minimum normalised value of 0.9.

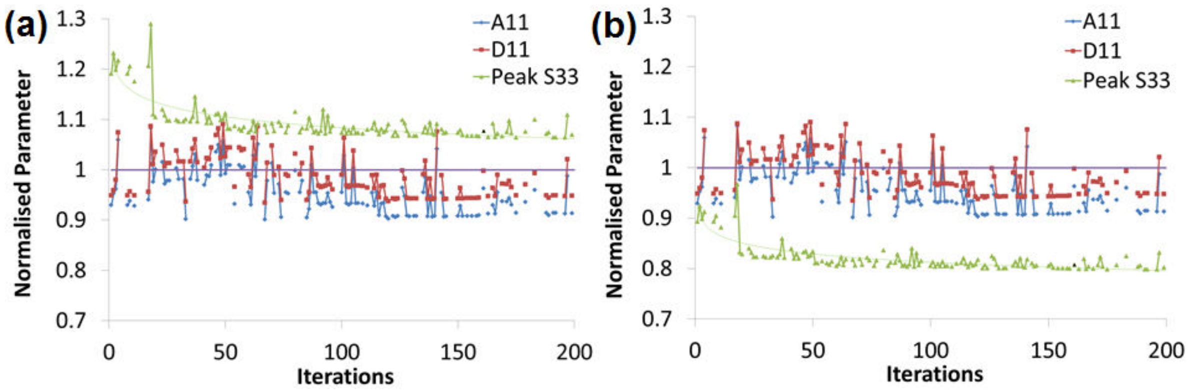

Figure 6-3 Progression of the hierarchical optimisation program across 200 iterations (a) normalised to baseline values; and (b) normalised to flange area in conventional and embedded T-joints. A_{11} = laminate in-plane stiffness, D_{11} = laminate bending stiffness and S_{33} = peak interlaminar tensile stress in the radius bend.

Iteration 160 was chosen for further FE analysis and experimental validation because the in-plane and bending stiffness values were closer to the baseline design than other designs with comparable values of the peak interlaminar tensile stress. Iteration 160 had a laminate stacking pattern of $[0/36/70/84/-84/-70/-36/0/12/50/50/74/-74/-50/-50/-12]_s$. The laminate properties and peak interlaminar tensile and shear stresses of the baseline and hierarchical optimised T-joints are compared in Table 6-1.

Table 6-1 Hierarchical optimisation results (Percentages in brackets are based on comparison to the baseline conventional quasi-isotropic T-joint)

	Baseline T-Joint	**Hierarchical T-Joint**
T-joint stiffener web laminate stacking pattern	$[45/0/-45/90/90/-45/0/45/45/0/-45/90/90/-45/0/45]_s$	$[0/36/70/84/-84/-70/-36/0/12/50/50/74/-74/-50/-50/-12]_s$
In-plane stiffness A_{11} (GPa.mm)	317.8	306.0 (-3.7%)
Bending stiffness D_{11} (GPa.mm^3)	1099	1096 (-0.3%)
Peak interlaminar tensile stress σ_{33} (MPa) in T-joint radius bend under 20 N perturbation load	3.41	3.67 (8%)
Peak σ_{33} x 50% embedded flange area/baseline flange area (MPa)		2.75 (-19%)

Figure 6-4 gives the value of each ply angle input variable as the optimisation progressed. The 8 ply angle input variables ($\theta_1 - \theta_8$) correspond to the stiffener laminate stacking pattern $[\theta_1/\theta_2/\theta_3/\theta_4/-\theta_4/-\theta_3/-\theta_2/-\theta_1/\theta_5/\theta_6/\theta_7/\theta_8/-\theta_8/-\theta_7/-\theta_6/-\theta_5]_s$.

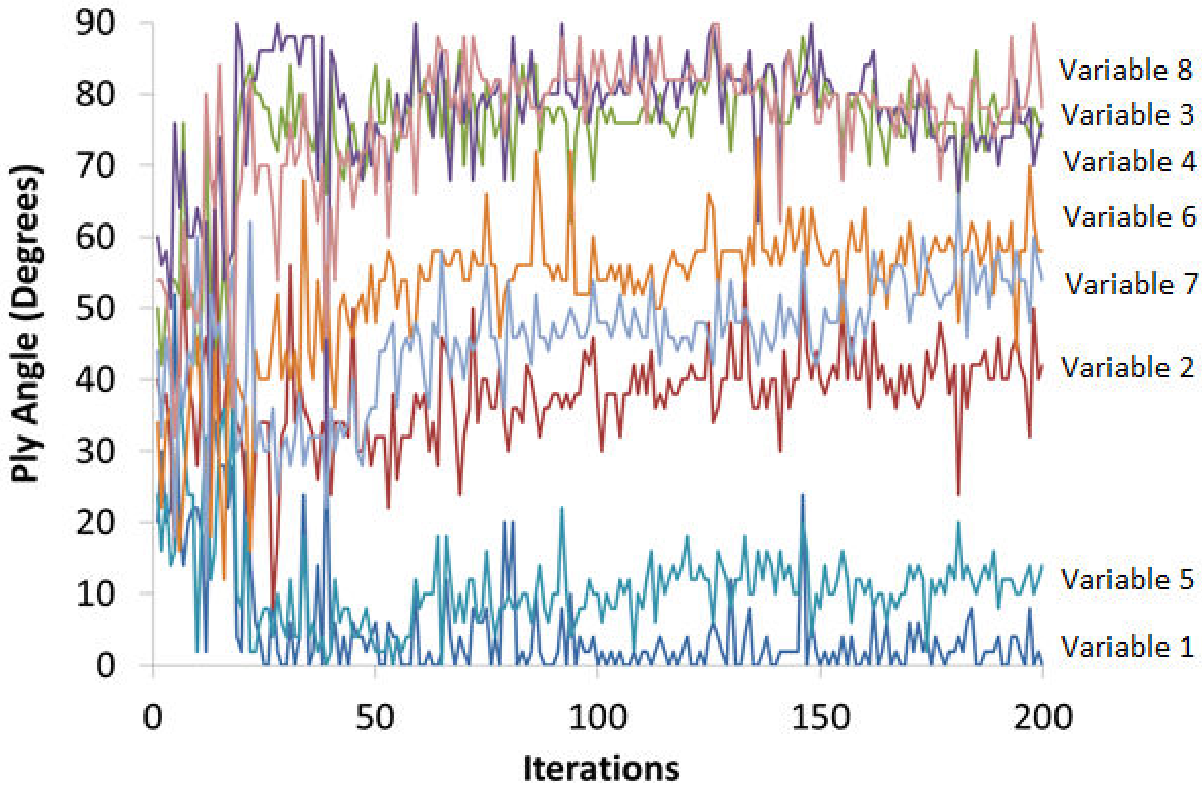

Figure 6-4 Variation of ply angle input variables as the hierarchical optimisation progressed

Figure 6-4 shows that early in the optimisation the simulated annealing algorithm has a ‘hot temperature’ and each iteration has a large step size of about 25°. As the optimisation progresses the ‘temperature’ cools and at around 100 iterations the step size has reduced to about 5 - 10°. The optimisation then stabilises with small fluctuations in ply angles which did not cause large variations in the interlaminar tensile stress distribution. This is significant because small variations in the ply angles can be inadvertently introduced during lay-up of plies in the manufacture of composite structures, with misalignments up to about 5°. Figure 6-4 shows that variable 1 (corresponding to ply angles 1 and 8) trended towards an orientation of 0°. The trend of placing a stiff ply with a low orientation in ply 1 was also observed in the bio-inspired optimisation and DoE described in chapter four.

Figure 6-5 shows the variation in the peak interlaminar tensile stress (normalised to the baseline value) versus the orientation of ply 1. The minimum peak interlaminar tensile stress occurs at the ply 1 orientation of 0°. Placing a high stiffness 0° ply at the free edge of the radius bend maximises the in-plane stiffness in the ply that undergoes maximum tensile strain, which helps to homogenise the strain field across the bend region. The high stiffness ply 1 also attracts more interlaminar tensile stress, which helps to homogenise the stress field across the full radius bend.

Figure 6-5 Variation of peak interlaminar tensile stress in T-joint radius bend as a function of the orientation of the outer radius ply 1

Figure 6-6 shows the variation in the ply angle orientation across the 16 ply radius bend laminate for the baseline and hierarchical T-joints. Figure 6-6a shows within the baseline T-joint there is an oscillation in the ply stacking pattern with 3 local maxima and 4 local minima. Figure 6-6b shows that in the hierarchical joint there is an oscillation in the stacking pattern with just 2 local maxima and 2 local minima. This shows there is less variation between adjacent plies in the hierarchical joint, which helps minimise the interlaminar stresses [66].

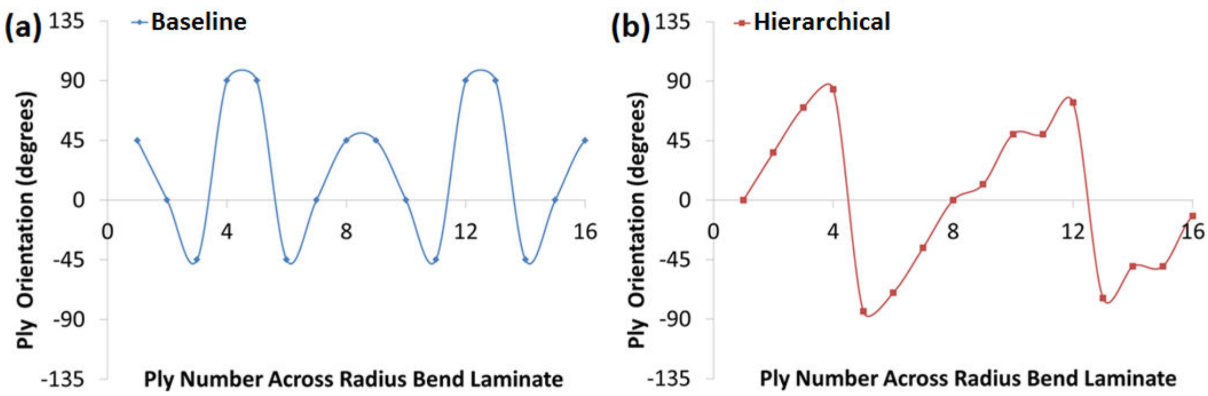

Figure 6-6 Variation of the ply angle across the 16 ply T-joint radius bend laminate for the: (a) baseline; and (b) hierarchical T-joints

Figure 6-7 presents the difference in the ply orientation between adjacent plies across the 16 ply radius bend laminate for the baseline and hierarchical T-joints. In the baseline T-joint the difference in ply angle between adjacent plies is 45°. In the hierarchical T-joint the largest difference in ply angle between adjacent plies is 38°, which occurs between ply 9 (12°) and ply 10 (50°). Thus the hierarchical optimisation reduces the misorientation between adjacent plies across the radius bend, which should 'smooth' the stiffness transition through this region of the T-joint.

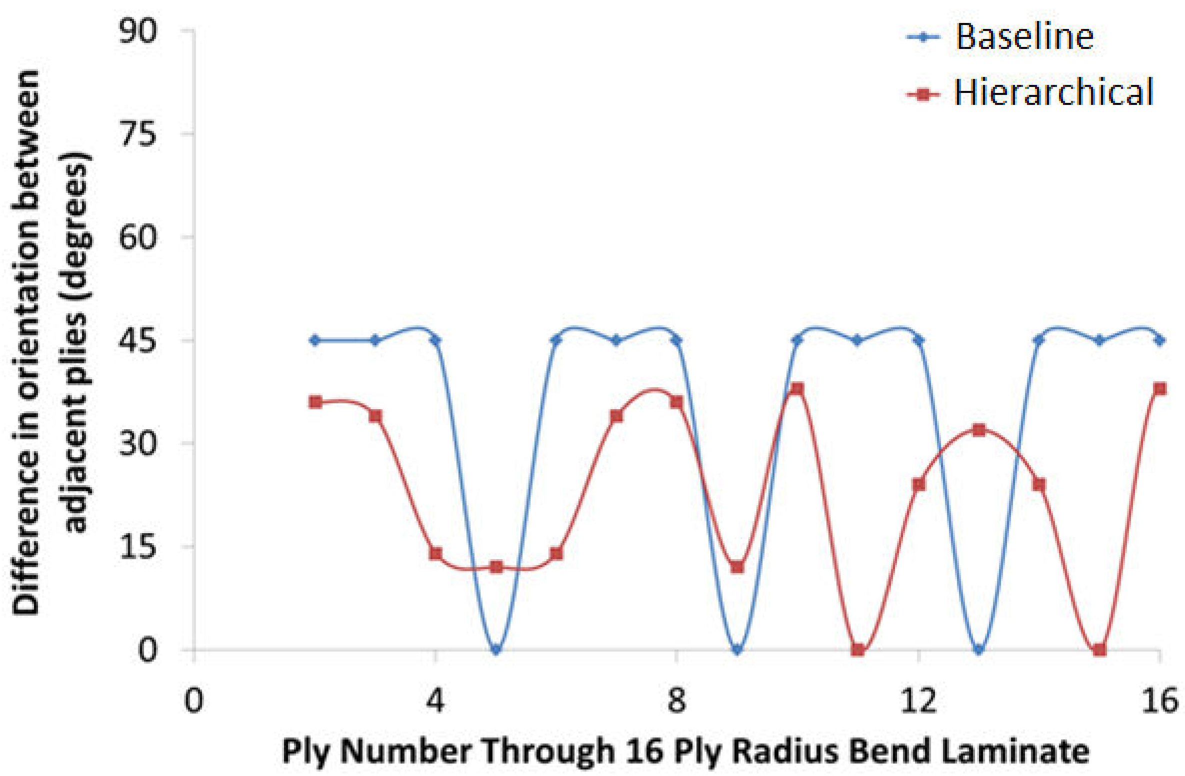

Figure 6-7 Difference in orientation between adjacent plies across the 16 ply T-joint radius bend laminate for the baseline and hierarchical T-joints

Table 6-2 summarises the effect size of each ply angle input variable in the hierarchical optimisation of the laminate used in the radius bend region. The effect size quantifies the relationship between the input variables (ply angles) and the output variable (peak interlaminar tensile stress in the T-joint radius bend). Low values indicate no relationship between the input and output variables so it is possible to ignore that variable in the optimisation process. Low significance indicates that the values of the size effect parameters are probably reliable.

Figure 6-8 shows that variables 1 and 3 (representing plies 1, 3, 6 and 8) have the greatest effect on the peak interlaminar tensile stress in the radius bend of the hierarchical T-joint. The effect size data shows the hierarchical optimisation is fairly insensitive to the orientation of variables 2 and 7 (representing plies 2, 7, 11 and 14), and therefore the orientation of these plies could be adjusted to produce the desired global stiffness properties in the laminate without significantly affecting the peak interlaminar tensile stress.

Table 6-2 Effect size and significance of each ply angle input variable in the hierarchical optimisation

Optimisation Ply Angle Variable	Ply Number in Radius Bend Laminate Stacking Pattern	Effect Size	Significance
θ_1	1,8	0.437 (20%)	0.000
θ_2	2,7	0.041 (2%)	0.070
θ_3	3,6	0.437 (20%)	0.000
θ_4	4,5	0.309 (14%)	0.000
θ_5	9,16	0.307 (14%)	0.001
θ_6	10,15	0.210 (10%)	0.000
θ_7	11,14	0.084 (4%)	0.000
θ_8	12,13	0.36 (16%)	0.000

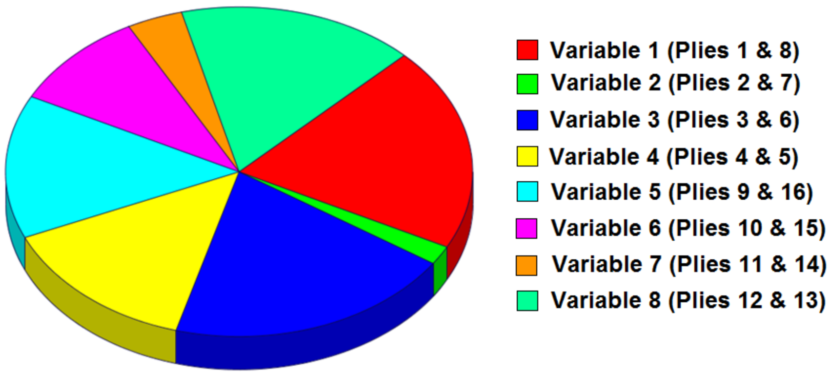

Figure 6-8 Effect size of each ply angle input variable in the hierarchical optimisation of the stiffener laminate

6.3.2 Experimental results of T-joint testing

6.3.2.1 Bending load case

Bending and tension tests were performed on the baseline and hierarchical T-joints to determine any improvement to the mechanical properties achieved through the bio-inspired design changes of optimised ply stacking in the stiffener laminate and integrated embedded stiffener design.

The geometry and dimensions of the T-joint samples used in the experimental bending tests are shown in Figure 6-9 and given in Table 6-3, respectively. The flange thickness of the hierarchical T-joint was 20% less than the baseline joint because the flange was embedded to a depth of 50% within the skin. The hierarchical T-joint also had a slightly thinner stiffener web compared to the baseline joint. Overall the flange area of the hierarchical T-joint was 23% smaller than the baseline T-joint. The mechanical properties obtained from the experimental tests were normalised by the flange area in order to compare specific properties taking into account the amount of material in the joint.

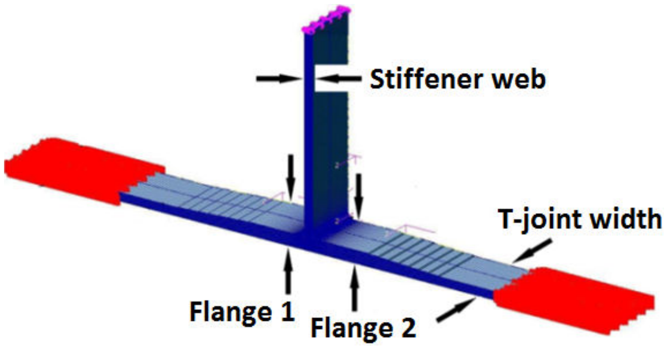

Figure 6-9 Dimensions of T=joint flange area

Table 6-3 Dimensions of T-joint samples

	Baseline T-Joint	Hierarchical T-Joint	Dimension Difference Δ%
Flange 1 thickness t_1 (mm)	6.42 [±0.14]	5.12 [±0.13]	-20%
Flange 2 thickness t_2 (mm)	6.44 [±0.16]	5.16 [±0.12]	-20%
Stiffener web thickness t_3 (mm)	6.36 [±0.04]	5.91 [±0.03]	-7.1%
T-joint width w (mm)	21.37 [±0.25]	20.65 [±0.20]	-3.4%
T-joint flange area $=(t_1+t_2)/2*w$ (mm^2)	137.3 [±3.61]	106.2 [±2.34]	-23%

Representative normalised bending load-displacement curves for the two designs are shown in Figure 6-10. Under bending the optimised stiffener ply stacking sequence improved the damage initiation load and the 50% integration of the stiffener flange plies into the skin led to improved toughness. Thus the hierarchical T-joint was both stronger and tougher than the baseline T-joint design.

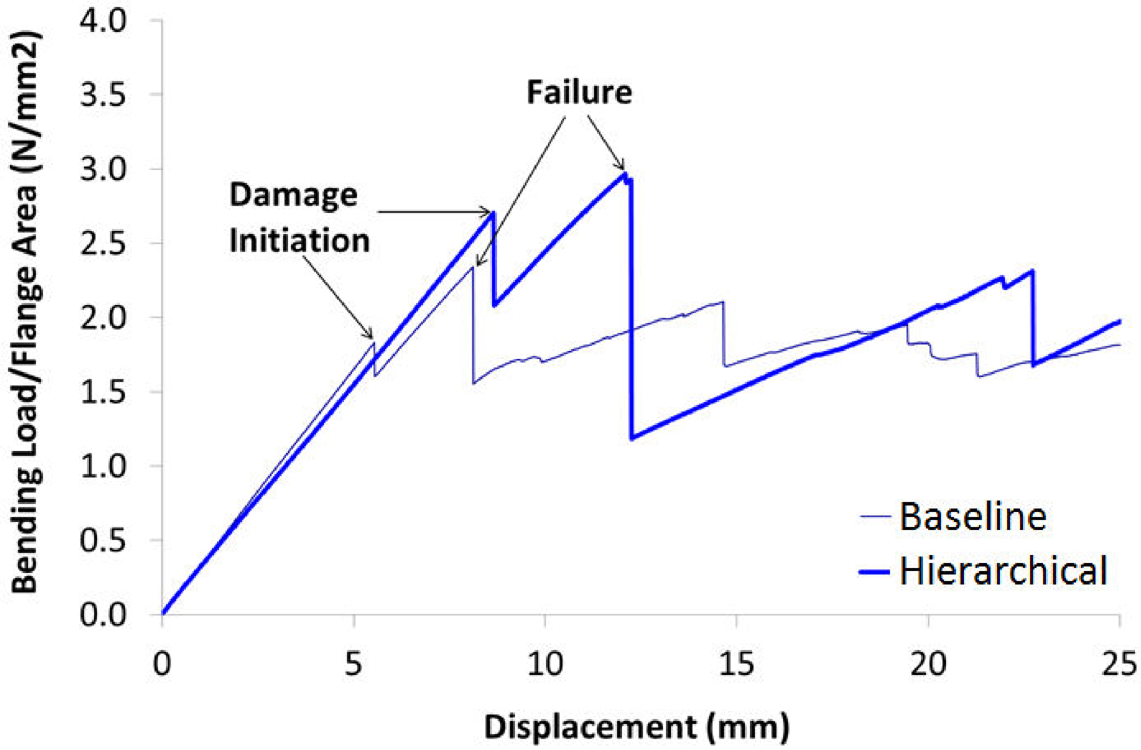

Figure 6-10 Representative bending load-displacement curves for the baseline and hierarchical T-joints

A summary of the experimental results is given in Table 6-4. The normalised bending stiffness *k*, (gradient of the linear portion of the curve) was -3.1% less for the hierarchical T-joint when compared to the baseline joint, thereby validating the classical laminated theory prediction of -3.7% bending stiffness. The load at first failure for both T-joints was about the same. Taking into account the reduced flange area, the normalised load at first failure was 38% higher for the hierarchical T-joint. The normalised failure load was the same for both T-joints, which further supports the findings of the ply optimisation study presented in chapter four that concluded the ply orientation does not significantly alter the failure (peak) load and the embedded design study in chapter six that concluded that the 50% embedded design also does not significantly alter the failure (peak) load. The normalised elastic strain energy of the hierarchical T-joint was 100% higher than the baseline, the normalised inelastic strain energy (ductility) was 93% higher and the normalised strain energy to failure (toughness) was 95% higher than the baseline T-joint. However there was no significant difference between the normalised strain energy to 25 mm displacement (end of test) for the two T-joints.

Table 6-4 Comparison between the structural properties of the baseline and hierarchical T-joints under bending loading [± standard deviation based on 4 samples]

	Baseline T-Joint	**Hierarchical T-Joint**	**Δ**
Normalised stiffness *k* (N/mm^3)	0.32 [±0.03]	0.31 [±0.01]	-3.1%
Damage initiation load (N)	268 [±9.1]	281 [±24]	5%
Normalised damage initiation load (N/mm^2)	1.93 [±0.14]	2.67 [±0.25]	38%
Damage initiation displacement (mm)	5.93 [±0.82]	8.56 [±0.78]	44%
Normalised failure load (N/mm^2)	2.27 [±0.09]	2.23 [±0.27]	-1.8%
Failure displacement (mm)	12.2 [±5.34]	21.2 [±1.86]	74%
Normalised elastic strain energy (J/mm^2)	5.69 [±1.08]	11.4 [±1.97]	100%
Normalised inelastic strain energy (J/mm^2)	11.8 [±8.86]	22.8 [±5.99]	93%
Normalised strain energy to failure (J/mm^2)	17.5 [±9.49]	34.2 [±4.69]	95%
Normalised strain energy to 25 mm displacement (end of test) (J/mm^2)	40.0 [±1.05]	41.0 [±4.55]	2.5%

High speed photography shows the damage initiation and failure modes of the baseline (refer Figure 6-11) and hierarchical (refer Figure 6-12) T-joints under bending load. In both T-joints damage initiated as a delamination in the tensile radius bend, about one-third distance radially from the outer radius (refer Figure 6-11a and Figure 6-12a). At the failure load drop several additional delaminations and a crack across the radius bend/delta-fillet interface initiated (refer Figure 6-11b and Figure 6-12b). At the end of the test (after 25 mm bending displacement) the dominant crack opened up the stiffener flange/skin bond-line and within the stiffener web (refer Figure 6-11c and Figure 6-12c). There was some evidence of crack branching and deflection in the hierarchical T-joint.

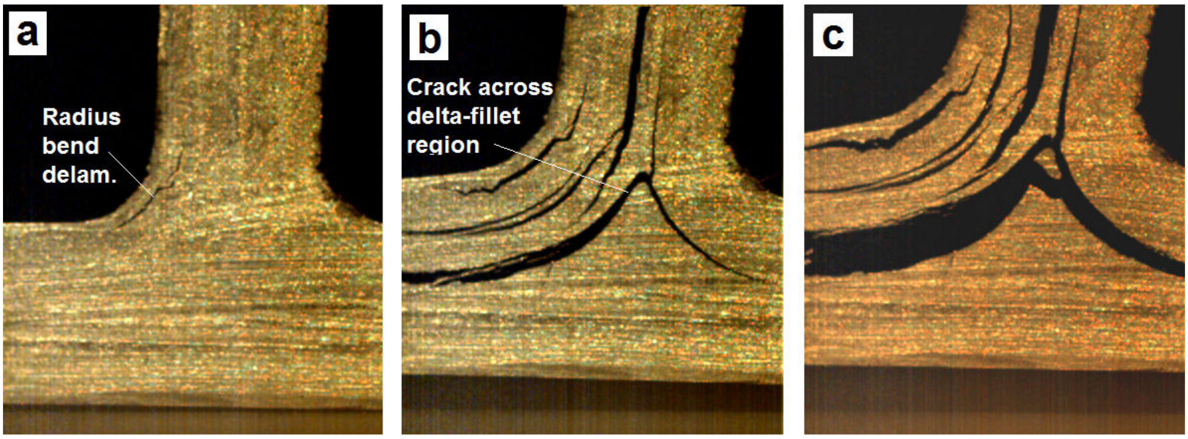

Figure 6-11 Damage and failure modes under bending: baseline T-joint at the: (a) delamination damage initiation load; (b) failure load drop; and (c) end of test at 25 mm displacement

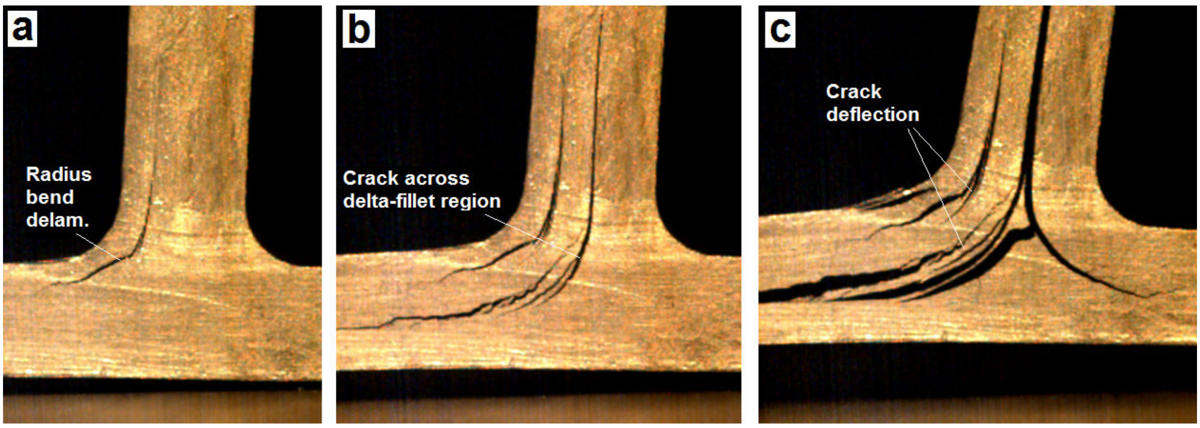

Figure 6-12 Damage initiation and failure modes under bending: hierarchical T-joint at the: (a) delamination damage initiation load; (b) failure load drop; and (c) end of test

6.3.2.2 Tension load case

Representative normalised tensile load-displacement curves for the two T-joints are shown in Figure 6-13. Under tension loading the hierarchical T-joint exhibited both improved damage initiation strength and improved failure displacement - indicating better ductility and toughness. A summary of the experimental results is given in Table 6-5. In contrast to the bending load case the tensile T-joints did not have the same normalised initial stiffness. This was consistent with results discussed in chapter five (refer section 5.3.1.2).

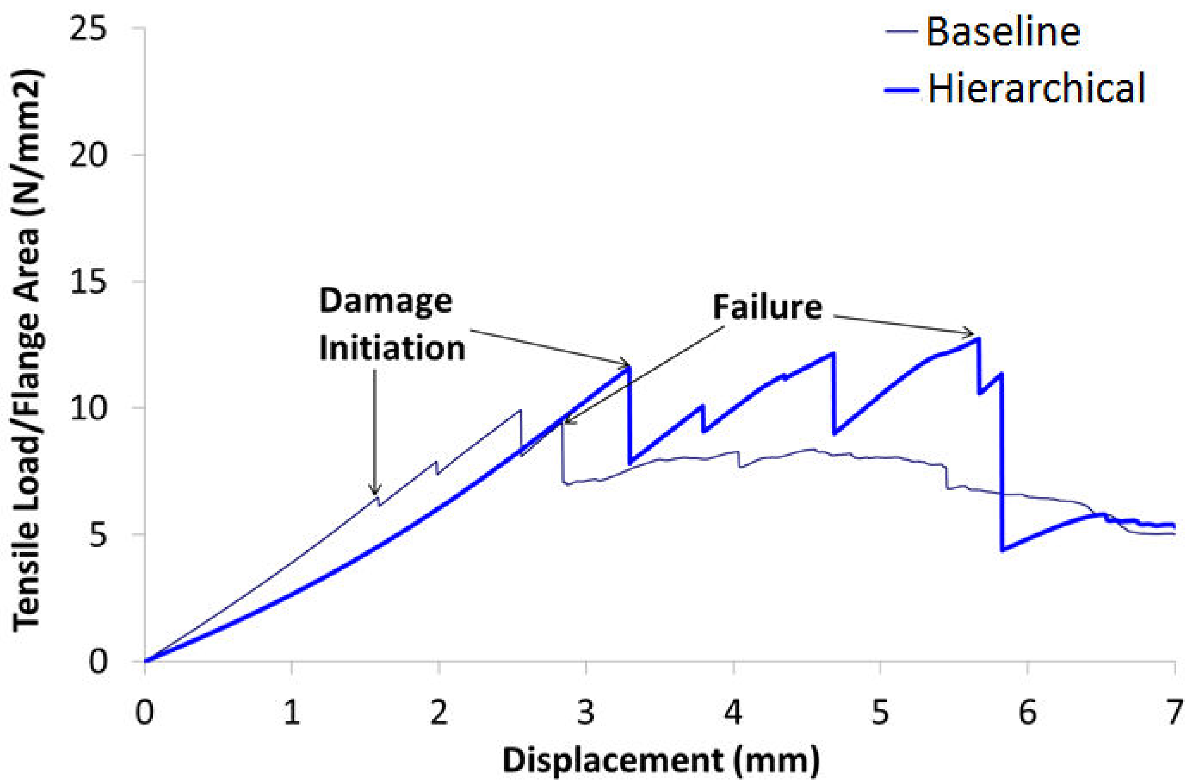

Figure 6-13 Representative tensile load-displacement curves for the baseline and hierarchical T-joints

Table 6-5 Comparison between the structural properties of the baseline and hierarchical T-joints under tension loading [± standard deviation based on 4 samples]

	Baseline T-Joint	**Hierarchical T-Joint**	**Δ**
Normalised stiffness *k* (N/mm^3)	3.82 [±0.24]	2.65 [±0.10]	-31%
Damage initiation load (N)	876 [±33]	1115 [±168]	27%
Normalised damage initiation load (N/mm^2)	6.38 [±0.13]	10.5 [±1.67]	65%
Damage initiation displacement (mm)	1.61 [±0.08]	3.02 [±0.38]	88%
Normalised failure load (N/mm^2)	9.02 [±0.81]	11.7 [±0.98]	30%
Failure displacement (mm)	2.74 [±0.31]	5.25 [±0.70]	92%
Normalised elastic strain energy (J/mm^2)	4.98 [±0.26]	14.4 [±3.56]	189%
Normalised inelastic strain energy (J/mm^2)	8.7 [±2.69]	16.3 [±9.01]	87%
Normalised strain energy to failure (J/mm^2)	13.7 [±2.79]	27.8 [±14.8]	103%
Normalised strain energy to 7 mm displacement (end of test) (J/mm^2)	45.9 [±1.13]	47.3 [±3.98]	3.1%

There was an improvement in the damage initiation load and normalised failure load of 27%, resulting in an increase in the absorbed elastic strain energy of nearly 200%. The normalised inelastic strain energy (ductility) and normalised strain energy to failure (toughness) were about the same as the bending load case with around 100% improvement for the hierarchical T-joint. Again, the normalised strain energy to the end of test was not significantly different between the two T-joint designs.

High speed photography was used to observe the damage initiation and failure modes of the baseline (refer Figure 6-14) and hierarchical (refer Figure 6-15) T-joints under tensile load. The damage mode is similar and initiated as delaminations in the radius bend together with cracking at the delta-fillet interface (refer Figure 6-14a and Figure 6-15a). After the final failure load drop several more delaminations and a crack through the delta-fillet region were visible (refer Figure 6-12b). At the end of test (after 7 mm tensile displacement), the main crack had opened up along the stiffener flange/skin bond-line, and within the stiffener web (refer Figure 6-14b and Figure 6-15c).

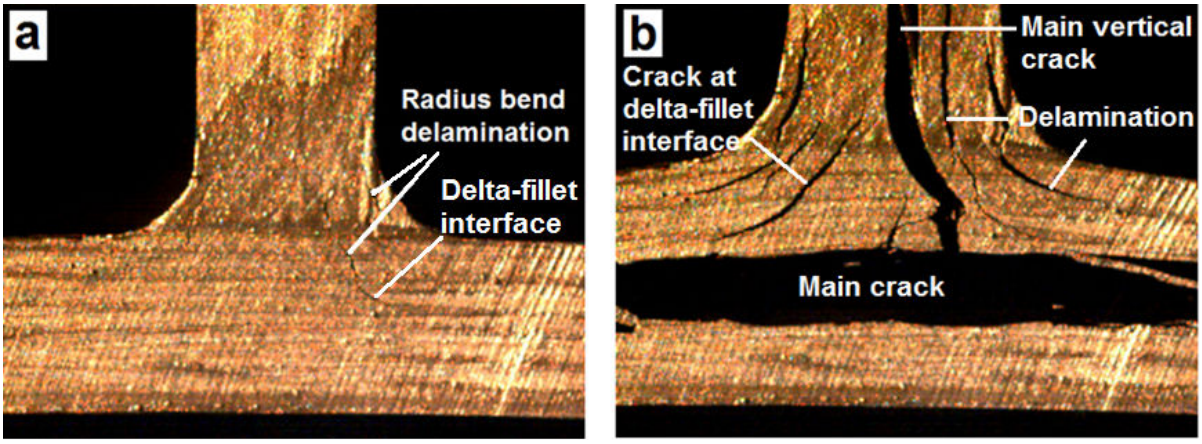

Figure 6-14 Baseline T-joint under tensile loading: (a) damage initiation; and (b) end of test

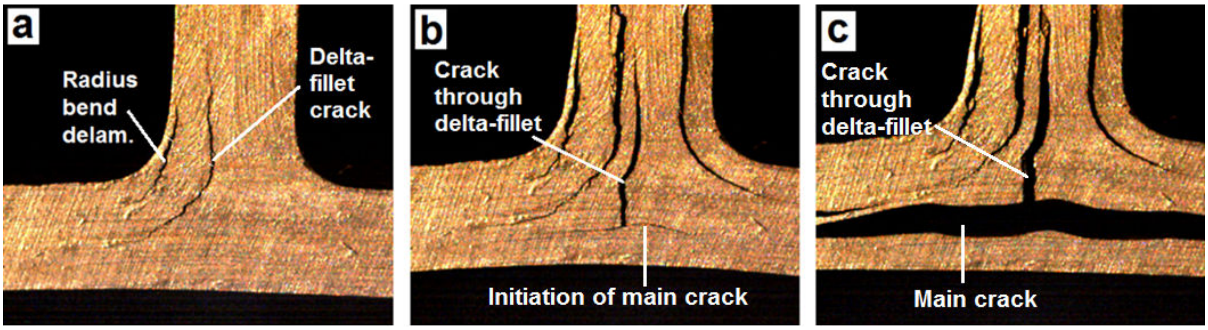

Figure 6-15 Hierarchical T-joint under tensile loading: (a) damage initiation; (b) failure load drop showing crack through delta-fillet; and (c) end of test

6.3.2.3 Summary of experimental results and observations

The mechanical performance of the hierarchical design in comparison to the baseline T-joint design is summarised for the bending and tensile load cases in Figure 6-16 and Figure 6-17, respectively. Improvements in damage tolerance are gained without loss of strength as measured by either the damage initiation or failure loads.

Figure 6-16 Performance of hierarchical T-joint under bending load

Figure 6-17 Performance of hierarchical T-joint under tension load

6.3.3 Finite element analysis of T-joints

Non-linear FE analysis was performed on the conventional and hierarchical T-joints to quantitatively predict the effect of the embedded design and the optimised stiffener laminate stacking sequence on the interlaminar tensile and shear stress distribution in the radius bend region. Stress contour plots were compared at the normalised failure load of the conventional T-joint. This failure load was chosen as it represents the lower failure load of the two T-joint designs.

Stress distributions were also compared between the T-joint designs to evaluate the accuracy of the FE model in predicting the load and ply-level location of delamination damage. Long's criterion was used to predict delamination cracking at the ply level according to the description given in chapter five. Long's criterion was calculated using the interlaminar stress distribution in the radius bend determined by the non-linear FE analysis. Where Long's criterion = 1 it is assumed that failure occurs. If Long's criterion > 1 the interlaminar stresses are underestimated or the interlaminar strengths are overestimated and Long's criterion < 1 indicates the interlaminar stresses are overestimated or the interlaminar strengths are underestimated.

6.3.3.1 Bending load case

Figure 6-18 and Figure 6-19 compare the experimental and FEA normalised bending load-displacement curves. The FEA shows good agreement with the experimental results by accurately predicting the bending stiffness of both the baseline T-joint (refer Figure 6-18) and hierarchical T-joint (refer Figure 6-19).

FEA was then used to model the internal interlaminar stress distribution in the conventional and hierarchical T-joint designs. Comparing the interlaminar tensile and shear stress distributions across the radius bend and delta-fillet region at the same normalised applied load enabled a qualitative and quantitative comparison of the effect of the optimised stiffener ply stacking sequence and embedded design on the geometric stress concentration.

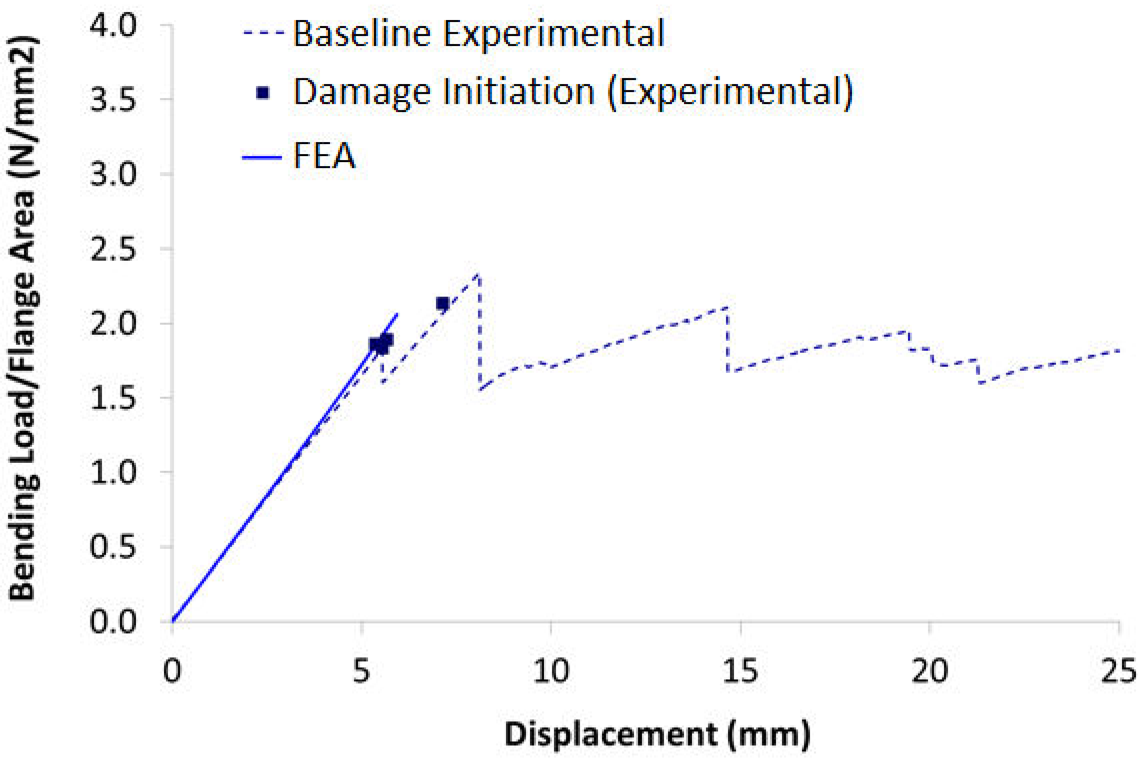

Figure 6-18 Experimental and FEA results for baseline T-joint design under bending load

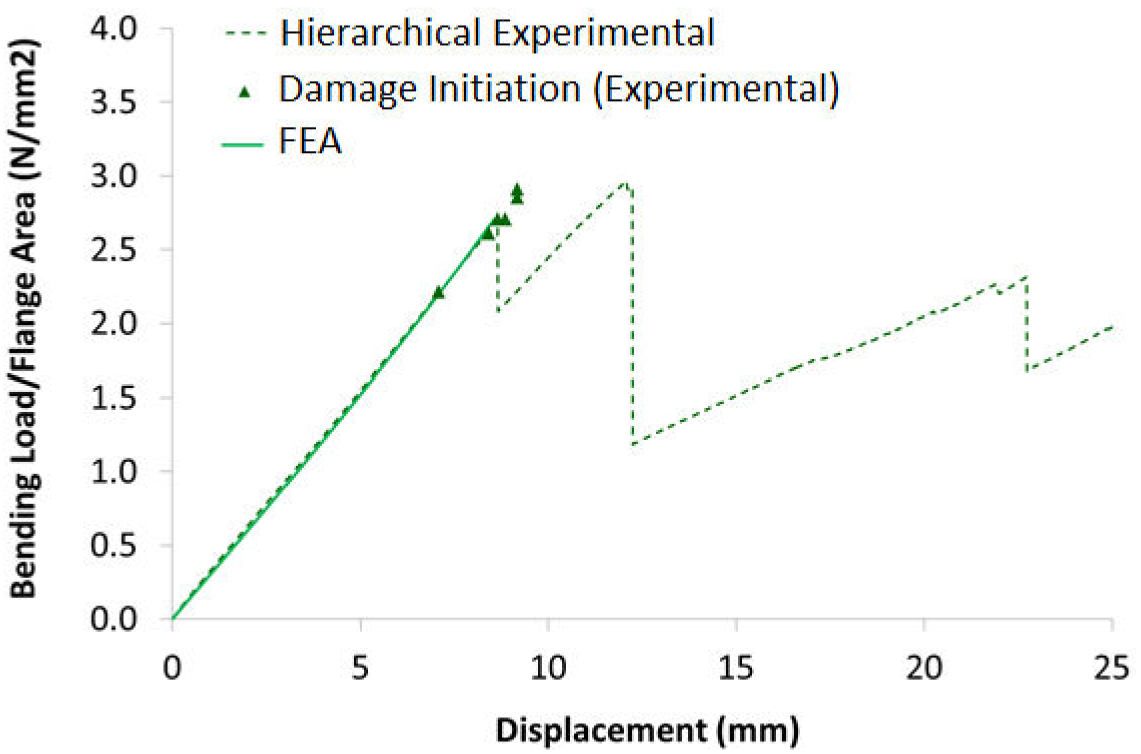

Figure 6-19 Experimental and FEA results for hierarchical T-joint design under bending load

The FEA results for the interlaminar tensile stress distribution are shown in Figure 6-20. The results indicate that the peak interlaminar tensile stress is located approximately mid-way both radially across and tangentially around the radius bend. The peak interlaminar tensile stress in the hierarchical design (refer Figure 6-20b) is significantly lower than the baseline design (refer Figure 6-20a) due to the optimised stiffener laminate ply stacking pattern.

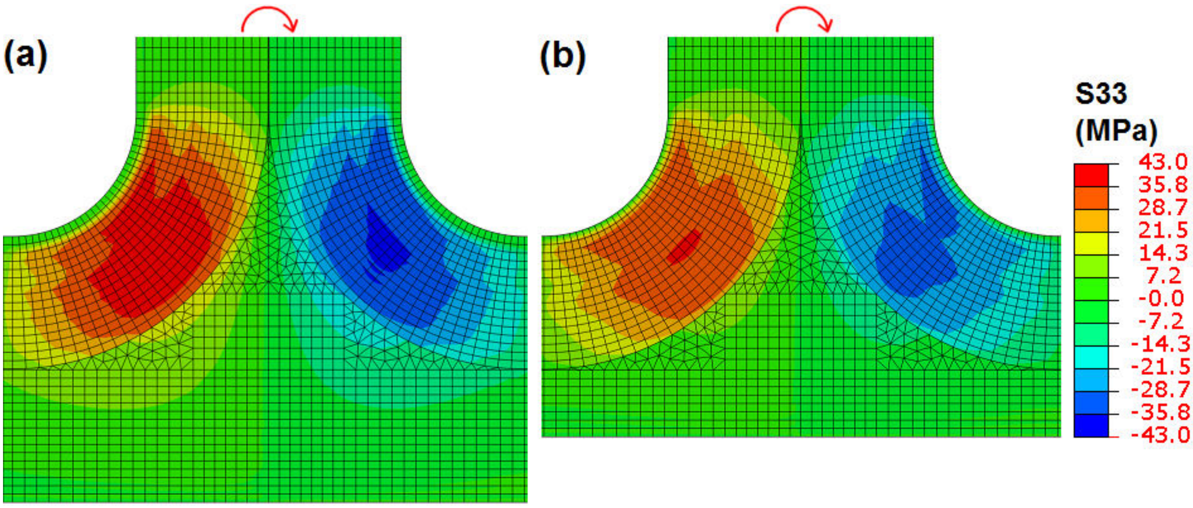

Figure 6-20 FEA peak interlaminar tensile stress (σ_{33}) distribution under the normalised bending damage initiation load of the conventional T-joint of 1.93 N/mm^2: (a) conventional; and (b) hierarchical designs

Figure 6-21 compares the interlaminar shear stress distribution across the T-joint radius bend and delta-fillet region for the two T-joint designs (refer Figure 6-21a and Figure 6-21b). The FEA results indicate the interlaminar shear stress concentrations in the radius bend and at the delta-fillet interface are lower for the hierarchical T-joint.

Table 5-6 summarises the FEA results. The combined reductions in the peak interlaminar tensile and shear stresses in the hierarchical T-joint reduce the interactive stress concentration that initiates mixed-mode delamination damage initiation, thereby improving the damage initiation load.

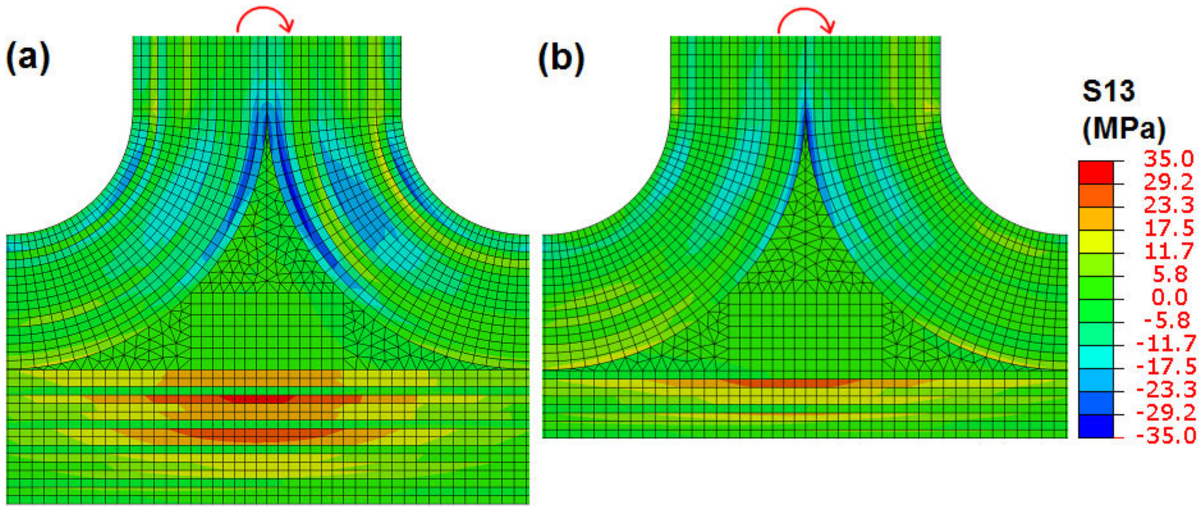

Figure 6-21 FEA peak interlaminar shear stress (τ_{13}) distribution under the normalised bending damage initiation load of the conventional T-joint of 1.93 N/mm^2: (a) conventional; and (b) hierarchical designs

Table 6-6 Summary of the FEA peak interlaminar tensile and shear stresses in the radius bend of the baseline and hierarchical T-joints under bending

T-joint	Norm. Load (N/mm^2)	Peak σ_{33} in Radius Bend (MPa)	Δ Peak σ_{33} (%)	Peak τ_{13} at Delta-Fillet (MPa)	Δ Peak τ_{13} (%)	ΣΔ (Peak σ_{33} + Peak τ_{13})	Δ Experimental Norm. Damage Initiation Load (%)
Baseline	1.93*	42.5		-30.7			
Hierarchical	1.93*	36.4	-17%	-28.7	-7%	-24%	38%

* Average normalised bending damage initiation load of conventional T-joint from experimental tests

These FEA results predict that under bending load the hierarchical T-joint will not fail prematurely compared to the baseline T-joint as was observed for the embedded joint design without ply optimisation (refer chapter five). This prediction is validated by the experimental testing. The sum of the reduction in the peak interlaminar stresses is -24%, which provides a conservative estimate for the average increase in the normalised damage initiation load obtained from the experimental bending tests of 38%.

To further analyse the onset and location of delamination damage, Long's strength-based delamination criterion [129] was calculated at the bending damage initiation load of the conventional (268 N) and hierarchical (281 N) T-joints. Long's criterion was calculated at two locations; along the radial path encompassing peak interlaminar tensile stress, which occurs at about the mid-point both radially across and tangentially around the radius bend (refer Figure 6-22a) and along the radial path encompassing peak interlaminar shear stress, which occurs at the top of the delta-fillet interface (refer Figure 6-22b). Long's criterion is plotted in Figure 6-23.

The information from the non-linear FE analysis concerning the peak interlaminar tensile and shear stresses and the information from Long's criterion concerning the predicted failure mode and ply-level location under bending load are summarised in Table 6-7. The results show that the failure is dominated by the peak interlaminar tensile stress, which occurs at about the mid-point both tangentially and radially across the radius bend (refer Figure 6-20). Failure generally occurs when the interlaminar tensile strength in the radius bend is exceeded. The results indicate that damage should initiate in the radius bend and is unlikely at initiate at the delta-fillet interface. Long's criterion indicates there is a broad band of an interactive interlaminar stress concentration in the radius bend from about plies 2 – 14 over which delamination could occur. This accounts for the multiple delamination cracks occurring within the radius bend region of the T-joint designs (ref Figure 6-11 and Figure 6-12).

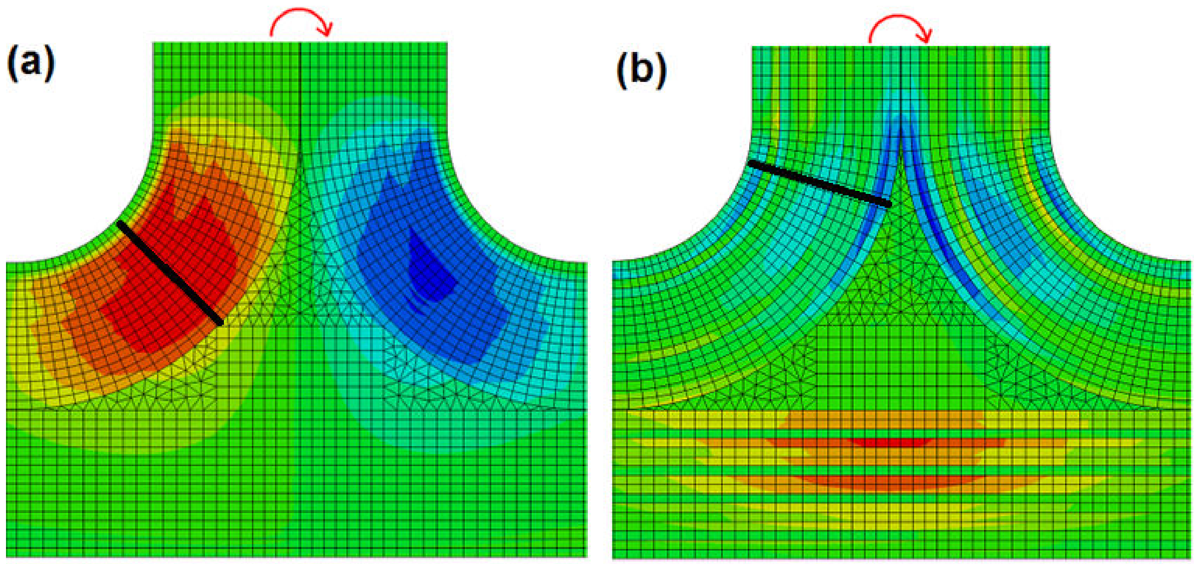

Figure 6-22 Paths of peak stress: (a) interlaminar tensile stress; and (b) interlaminar shear stress

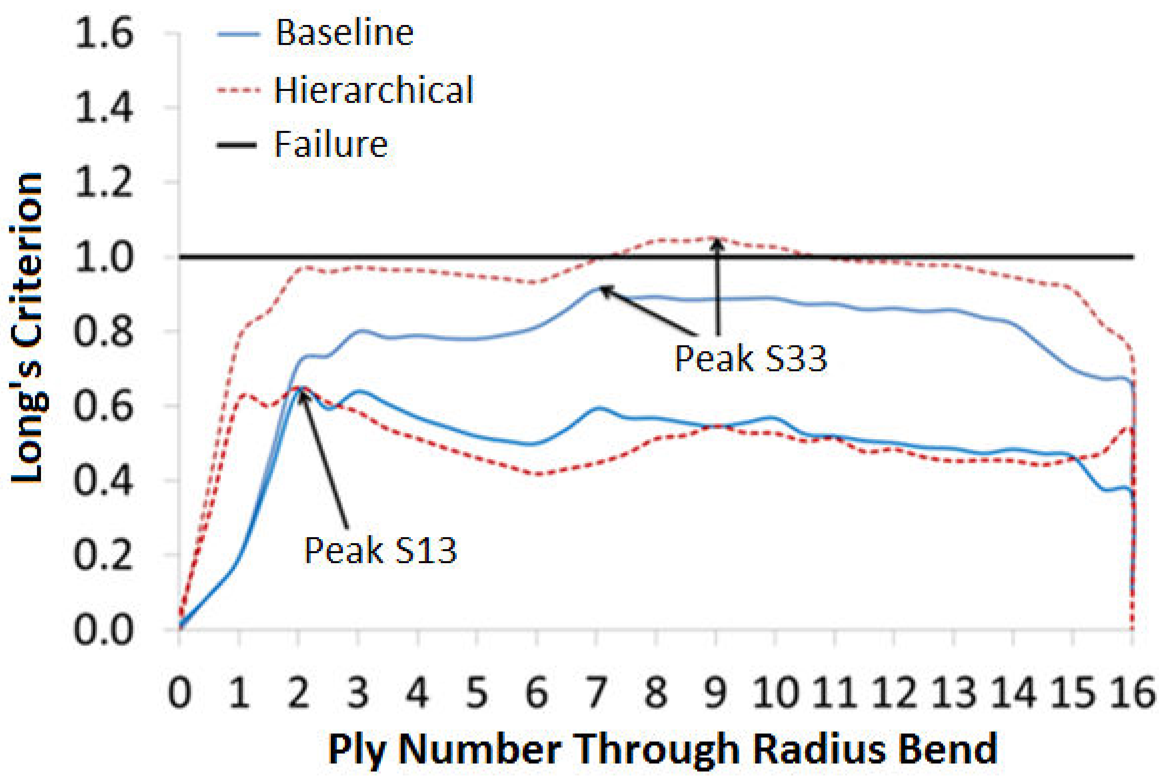

Figure 6-23 Long's criterion under bending load: failure load of 268 N for baseline T-joint and failure load of 281 N for hierarchical T-joint. S33 = interlaminar tensile stress and S13 = interlaminar shear stress

Table 6-7 Summary of the failure modes of the baseline and hierarchical T-joints at the bending damage initiation load

T-joint	Exp. Damage Initiation Load (N)	FEA Peak σ_{33} (MPa)	% of Z_t*	FEA Peak τ_{13} (MPa)	% of S_{13}*	Failure Mode (FEA)	Failure Location (Long's Criterion)
Baseline	268	42.0	88%	-30.7	36%	σ_{33} dominated in radius bend	Between plies 2 - 14
Hierarchical	281	49.9	105%	-38.0	45%	σ_{33} dominated in radius bend	Between plies 3 - 13

*Z_t = 47.6 MPa [125]. **S_{13} = 84.3 MPa [155]

6.3.3.2 Tension load case

Figure 6-24 and Figure 6-25 compare representative experimental normalised tensile load-displacement curves compared to the non-linear FE analysis for the baseline and hierarchical T-joints. In comparison to the bending load case the tensile results shows more obvious non-linear deformation, especially above displacements of about 1 mm. The non-linear behaviour is caused by the boundary conditions of the clamped skin, which resists the extension of the skin as the T-joint is loaded in tension.

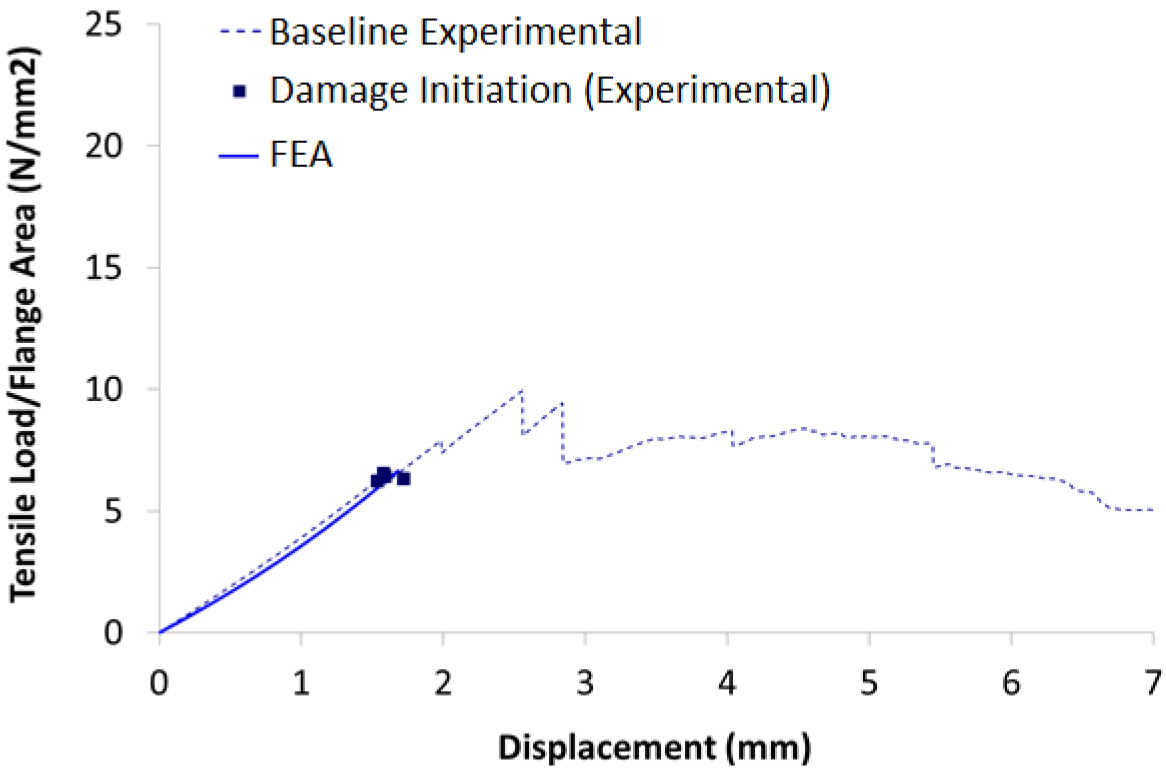

Figure 6-24 Non-linear FEA compared to experimental results under tensile load for baseline T-joint

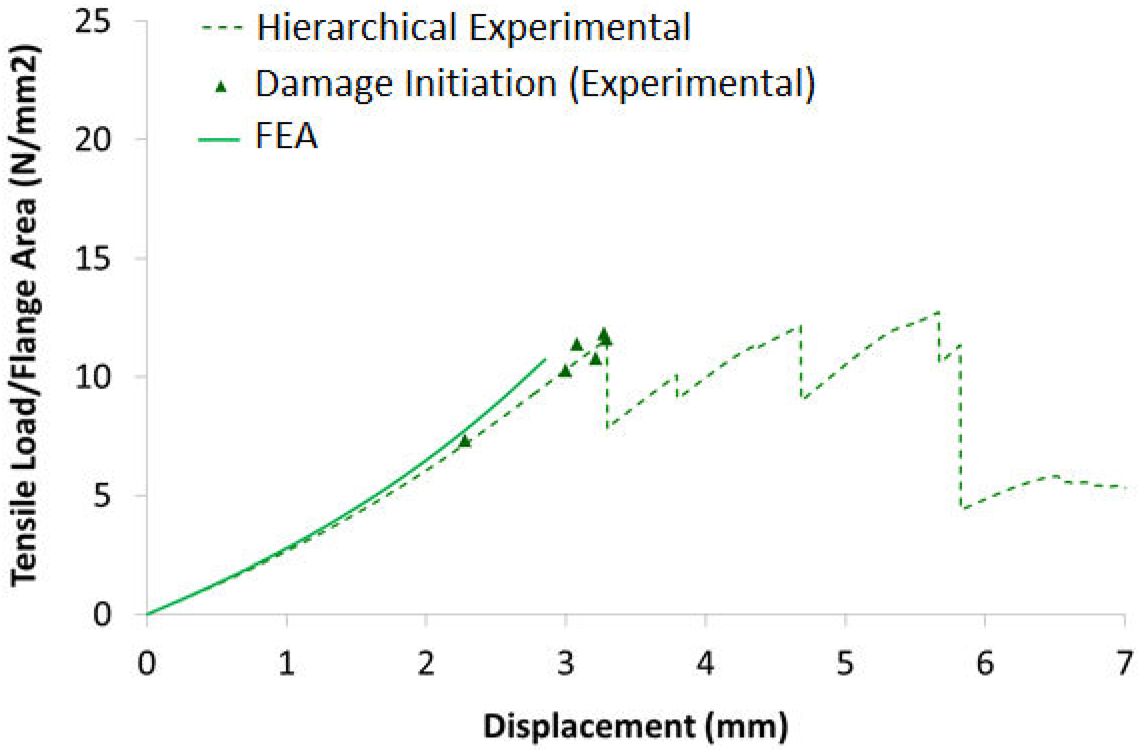

Figure 6-25 Non-linear FEA compared to experimental results under tensile load for hierarchical T-joint

The FEA shows good agreement with the experimental results, accurately predicting the stiffness of both the baseline (refer Figure 6-24) and hierarchical T-joint (refer Figure 6-25) up to about 2 mm displacement. At higher displacements, the FEA predicts higher stiffness than the experiment results due to the boundary conditions being modelled as perfect clamps. In reality, the clamp allows some displacement in the in-plane skin direction which 'softens' the non-linear response, as seen in the experimental results. However, the perfect clamp approach was considered sufficient for the comparison of the interlaminar stresses in the radius bend of both types of T-joints under tension loading.

FEA was used to compare the internal interlaminar tensile stress distribution in the baseline and hierarchical T-joints at the average damage initiation load of the baseline T-joint of 6.38 N/mm^2 (refer Figure 6-26). The FEA results indicate similar stress distributions, with the peak interlaminar tensile stress at the delta-fillet interface in the hierarchical T-joint slightly lower than the baseline T-joint. However, the peak interlaminar tensile stress in the radius bend is slightly higher in the hierarchical T-joint.

The interlaminar shear stress distributions in the two T-joint designs are given in Figure 6-27. The interlaminar shear stress concentrations are located in the high stiffness 0° plies in the baseline and 12° plies in the hierarchical T-joints. The peak interlaminar shear stress is 8% lower in the hierarchical T-joint.

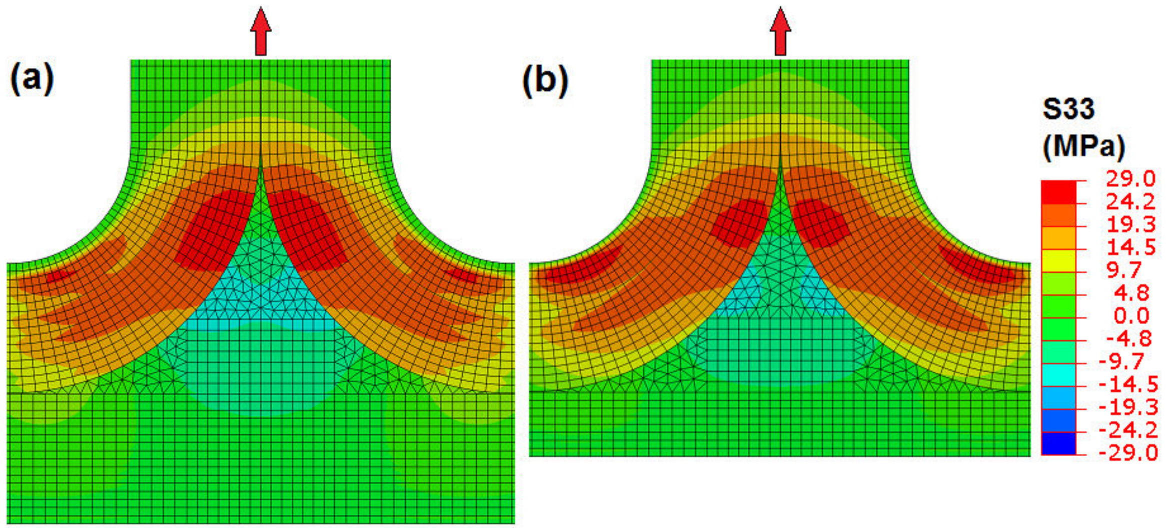

Figure 6-26 FEA interlaminar tensile stress (σ_{33}) distribution under the normalised tensile damage initiation load of the baseline T-joint of 6.38 N/mm^2: (a) baseline; and (b) hierarchical T-joints

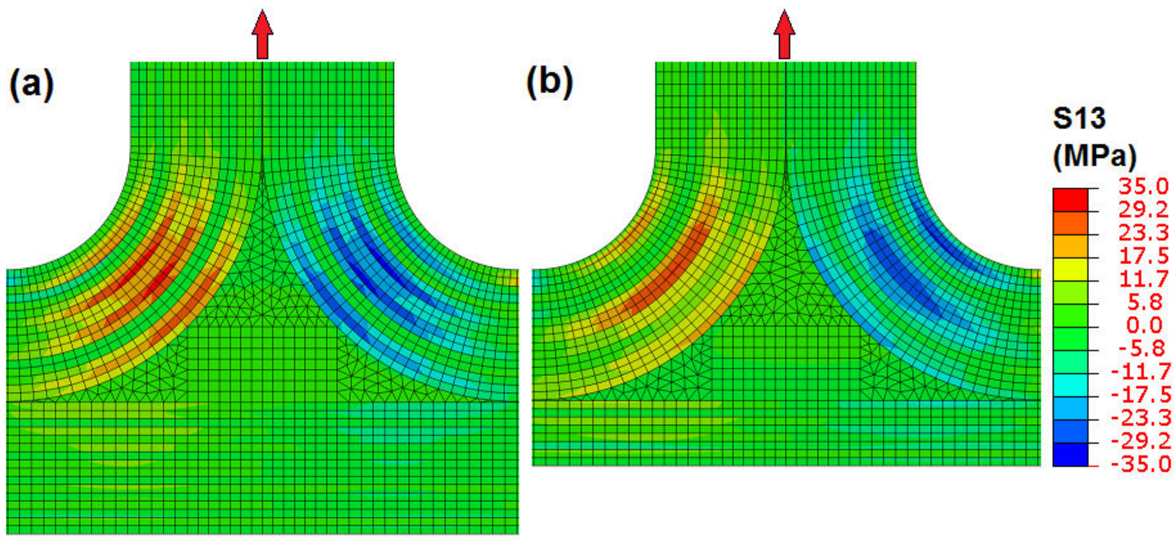

Figure 6-27 FEA interlaminar shear stress (τ_{13}) distribution under the normalised tensile damage initiation load of the baseline T-joint of 6.38 N/mm^2: (a) baseline; and (b) hierarchical T-joints

Table 6-8 summarises the FEA results. The analysis indicates a small reduction (-5%) in the interactive stress concentration that causes mixed-mode delamination damage in the hierarchical T-joint. Thus the FEA predicts that the introduction of ply optimisation will mean the hierarchical T-joint will fail at a higher load compared to the baseline T-joint. This prediction was validated by the experimental testing.

Table 6-8 Summary of the FEA peak interlaminar tensile and shear stresses in the radius bend of the baseline and hierarchical T-joints at the normalised tensile damage initiation load of the conventional T-joint

T-joint	Norm. Load (N/mm^2)	Peak σ_{33} (MPa)	Δ Peak σ_{33} (%)	Peak τ_{13} (MPa)	Δ Peak τ_{13} (%)	ΣΔ (Peak σ_{33} + Peak τ_{13})	Δ Experimental Norm. Damage Initiation Load (%)
Baseline	6.38*	27.8**		32.3***			
Hierarchical	6.38*	28.6***	3%	29.8***	-8%	-5%	65%

* Average normalised bending damage initiation load of conventional T-joint from experimental tests
** Occurs at delta-fillet interface, *** Occurs in radius bend

However, the experimental data shows a much larger increase in the normalised tensile damage initiation load than predicted by FEA. For further evaluation of the likely causes, Long's strength-based delamination damage criterion was calculated at the tensile damage initiation load of the baseline (876 N) and hierarchical (1115 N) T-joints. Long's criterion was calculated along the radial paths encompassing peak interlaminar tensile stress in the radius bend (refer Figure 6-28a) and at the delta-fillet interface (refer Figure 6-28b), as determined by the non-linear FE analysis (refer Figure 6-29).

The information from Long's criterion concerning the peak interlaminar tensile and shear stresses and the predicted failure mode and location under tension loading are summarised in Table 6-9. The results predict two failure modes occurring simultaneously in both the radius bend and at the delta-fillet interface, which was validated by the experimental tests (refer Figure 6-14 and Figure 6-15).

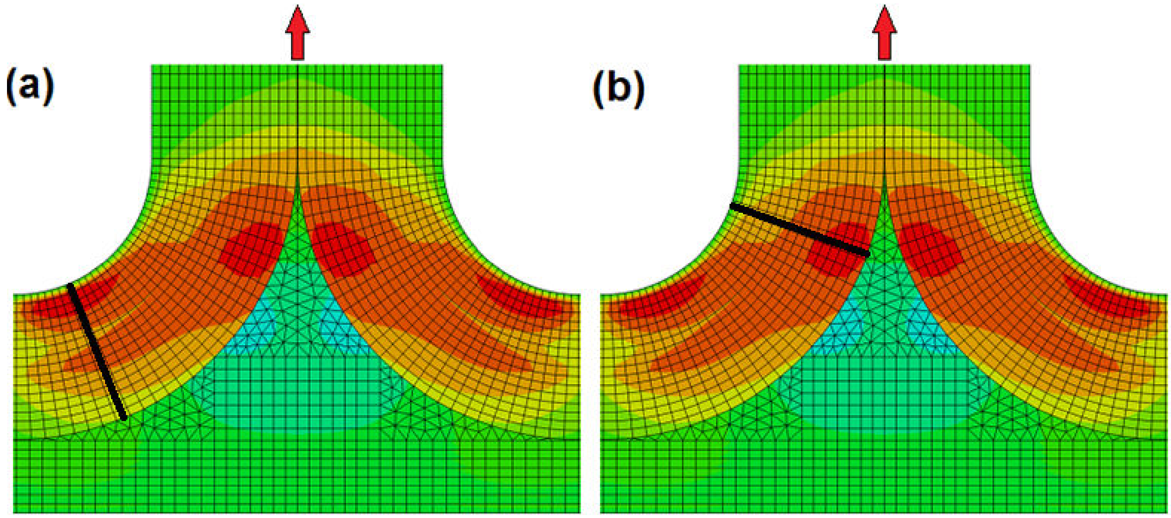

Figure 6-28 Paths of peak interlaminar tensile stress in the: (a) radius bend; and (b) at the delta-fillet interface

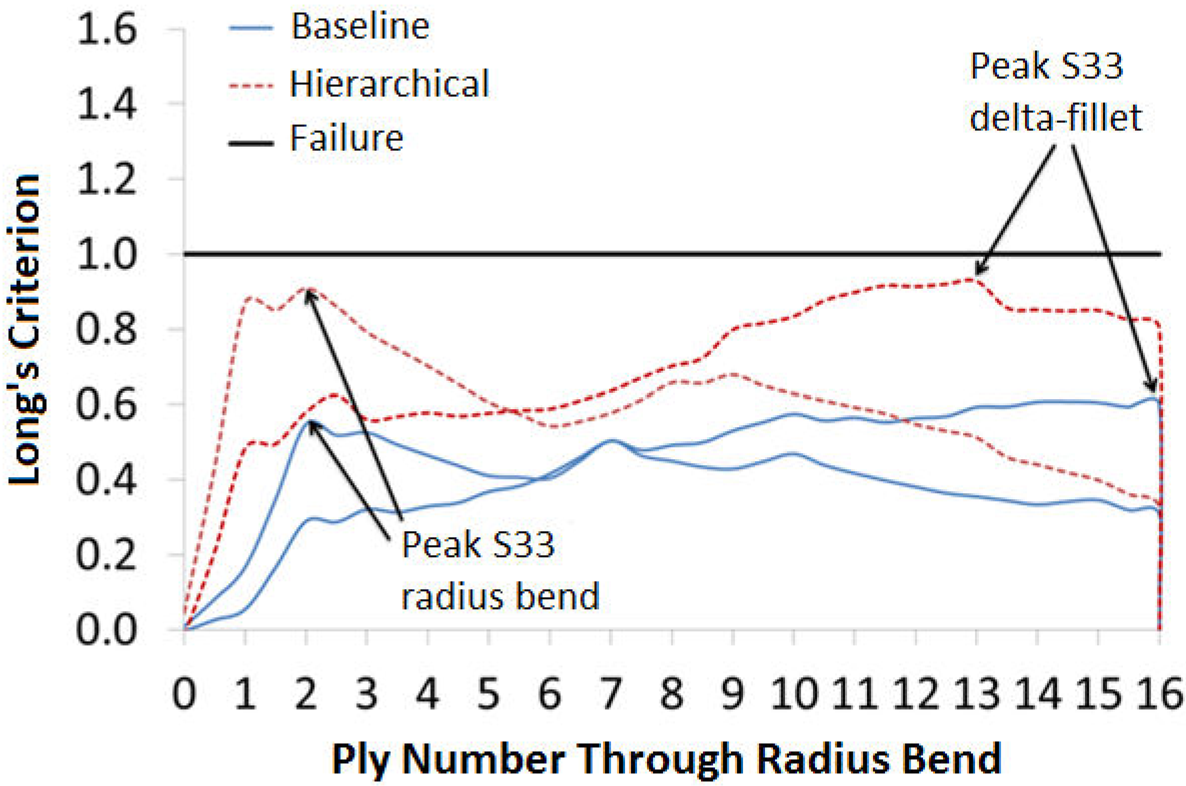

Figure 6-29 Long's criterion at the failure load under tensile load: 876 N for baseline T-joint and 1115 N for hierarchical T-joint. S33 = interlaminar tensile stress.

Table 6-9 Summary of the tensile failure modes of the baseline and hierarchical T-joints

T-joint	Exp. Damage Initiation Load (N)	FEA Peak σ_{33} (MPa)	% of Z_t	FEA Peak τ_{13} (MPa)	% of S_{13}	Failure Mode (FEA)	Failure Location (Long's Criterion)
Conventional	876	27.8**	58%	32.3*	38%	σ_{33} dominated in radius bend and at delta-fillet interface	Plies 2 - 3 and delta-fillet interface
Hierarchical	1115	40.9*	86%	43.6*	52%	σ_{33} dominated in radius bend and at delta-fillet interface	Plies 1 – 2 and plies 11 – 13 and delta-fillet interface

* occurs in radius bend, ** occurs at delta-fillet interface

While Long's criterion for the hierarchical T-joint is within 10% of the failure prediction value of 1 (refer Figure 6-29), the failure load of the baseline T-joint is under-predicted. This is attributed to the volumetric sensitivity of the interlaminar tensile strength, as discussed in chapter five [106, 125, 162]. Reduced interlaminar tensile strength correlates with thicker specimens, due to the higher probability of more numerous and larger flaws. Table 6-3 shows the stiffener web in the hierarchical T-joint was 7% thinner than the baseline T-joint. The tensile experimental and FEA results indicate the baseline T-joint failed at an interlaminar tensile strength of approximately the value used in chapter five for thick samples of 23.4 MPa and the hierarchical T-joint failed at an interlaminar tensile strength of about the value used in chapter five for thin samples of 47.6 MPa. Therefore it is important to note any increase in the cured ply thickness of T-joints as this can be an indicator of a reduction to interlaminar tensile strength. However, it should be noted that the FEA results predict that damage will initiate in the hierarchical T-joint at a higher load compared to a fully compacted baseline T-joint.

6.4 SUMMARY AND CONCLUSIONS

Hierarchical design is a defining characteristic of biological materials in which material and structural changes work in synergy to produce outstanding strength and toughness. A hierarchical T-joint was created by combining the ply-level bio-inspired design concept of optimised stiffener laminate stacking sequence with the structural-level bio-inspired design concept of integrating the flange plies into the skin through embedded design. In chapter four optimising the stiffener ply stacking pattern was found to increase the damage initiation load by tailoring the internal stiffness properties of the stiffener laminate to minimise the geometric interlaminar stress concentration under the applied bending load. However this approach did not improve the damage tolerance of the T-joint. In chapter five, the embedded design concept was found to improve the ductility and toughness of the T-joint at the expensive of a reduction in the damage initiation load under both bending and tensile load.

In combining these two biomimetic design strategies the disadvantage of increasing the interlaminar stresses in the radius bend and delta-fillet regions through the embedded design was overcome by decreasing the geometric interlaminar stress concentrations in these critical zones through the optimised stiffener laminate stacking sequence. Similarly, the advantage of the improvement in damage tolerance in the embedded T-joint overcame the disadvantage of the optimised T-joint exhibiting brittle failure. Hierarchical design enabled the production of a bio-inspired carbon/epoxy composite T-joint that is both strong and tough. Thus, the hierarchical composite T-joint was bio-inspired in three ways: at the material (ply) level, at the structural level, and in the interaction between the two levels.

Elucidating how nature extracts maximum efficiency through hierarchical design provides engineers with an enormous opportunity to apply these concepts to a wide range of materials and manufacturing conditions, thereby driving next-generation improvements in engineered composite structures. As a final challenge, looking into the future the new frontier lies in the synthesis of bio-inspired materials through manufacturing processes that are characteristic of biological systems i.e. nano-scale self-assembly. This will enable implementation of the full four levels of hierarchy observed in nature: including architectures featuring a number of toughening and strengthening mechanisms at each of the nano-, micro-, meso- and macro-length scales. Although this approach presents enormous challenges, mastering control over the fundamental mechanisms of self-assembly exemplified by the growth of biological structures will eventually lead to new composite materials and structures with extraordinary properties.

CHAPTER 7:

7 IMPACT DAMAGE TOLERANCE

7.1 INTRODUCTION

Chapters four to six considered the mechanical performance of novel bio-inspired composite T-joints under low strain rate loading conditions. The studies revealed that once damage has initiated in the bio-inspired T-joints (with optimised ply pattern or embedded design or a combination of the two) due to over-loading they retained higher load-carrying capacity than the baseline conventional T-joint designs. This behaviour is indicative of improved damage tolerance in the bio-inspired joints, which is a beneficial property for aircraft composite structures. Damage tolerance under impact (dynamic) loading is also an important property due to the requirement for structures to retain mechanical performance in the presence of in-service impact damage resulting from events such as hailstorms, tools dropped during maintenance or debris on the runway. In-service repair of thin-gauge composite joints that sustain impact damage is expensive and in order to minimise the repair costs the allowable impact damage limits must be maximised [163].

This chapter presents a preliminary study of the impact damage tolerance of the bio-inspired T-joint design concepts. The low energy impact (from 2 – 14 J) resistance and impact damage tolerance of bio-inspired composite T-joints is evaluated. Generally impact will cause mixed-mode failures; however, the dominant failure mode under low energy loading is delamination. Impact damage tolerance can be defined by two parameters:

- Impact resistance, or the ability to absorb the energy of impact without sustaining significant damage; and
- Impact damage tolerance, or residual mechanical properties after impact damage.

In chapter five the embedded T-joint design improved the damage tolerance of T-joints under quasi-static bending and tensile loading. However, the embedded design reduces the bending modulus of the skin due to the reduction in the number of continuous skin plies. The bending modulus of the skin is an important parameter influencing energy absorption and damage tolerance under impact loading. A skin with a high bending modulus can absorb more energy for a given deflection. This can lead to an increased peak force from the contact pressures under impact, which increases interlaminar stresses that initiate delamination damage. For this reason the impact resistance and impact damage tolerance of a conventional quasi-isotropic T-joint are compared to the 50% embedded quasi-isotropic T-joint. In addition, the bio-inspired optimised design of the stiffener laminate stacking sequence is compared to a baseline conventional quasi-isotropic design.

7.2 EXPERIMENTAL METHODOLOGY

7.2.1 Fabrication of T-joints

Four types of T-joints were fabricated for impact testing:

- Baseline unidirectional T-joint with a quasi-isotropic stiffener laminate stacking pattern, and this was compared to the;
- Bio-inspired optimised unidirectional T-joint with a bio-inspired optimised stiffener laminate stacking sequence.
- Baseline conventional quasi-isotropic T-joint fabricated from fabric carbon/epoxy prepreg, and this was compared to the;
- Bio-inspired fabric 50% embedded T-joint.

The first two T-joints were fabricated from unidirectional T700 carbon fibres/HS200 epoxy resin (Lavender VTM264) tape and the last two T-joints were made using T300 fibre based 6K five-harness satin weave fabric (Hexcel AGP370-5H). These materials are described in detail in chapters four and five.

The hierarchical T-joint design incorporating both stiffener/skin integration (50% embedded design) and optimised stiffener laminate stacking sequence was not tested because the impact results indicated that the optimised (for bending) stiffener laminate stacking sequence did not influence the impact damage tolerance of the T-joint.

7.2.2 Experimental procedure

7.2.2.1 Impact resistance testing

Impact testing was performed on T-joint specimens with the same dimensions as the specimens used in the quasi-static testing described in chapters four and five. In general the impact performance of the small (21 mm) width T-joint specimens is significantly worse than a stiffened panel that is constrained by the global structure due to the difference in boundary conditions and the inability of damage to grow in three dimensions. The impact testing was performed to provide a qualitative and quantitative comparison of how the bio-inspired T-joints differ from the baseline T-joints under impact loading, rather than provide a quantitative analysis of how the bio-inspired T-joints would perform as part of a large stiffened panel structure.

The impact testing was performed using the test rig shown in Figure 7-1a. The impact testing was performed without pre-load applied to the T-joint specimens. The impactor was a steel circular ball with a 0.5 inch (12.7 mm) diameter (refer Figure 7-1b) and the combined weight of the impactor and sled was 1.196 kg. The impactor ball was set to the height above the T-joint skin that produced the desire impact energy calculated using Equation 7-1.

$$h = \frac{E}{mg}$$ Equation 7-1

Where h = the drop height (m), E = impact energy (J), m = combined weight of the impactor ball and sled (kg) and g = acceleration due to gravity = 9.81 m/s^2

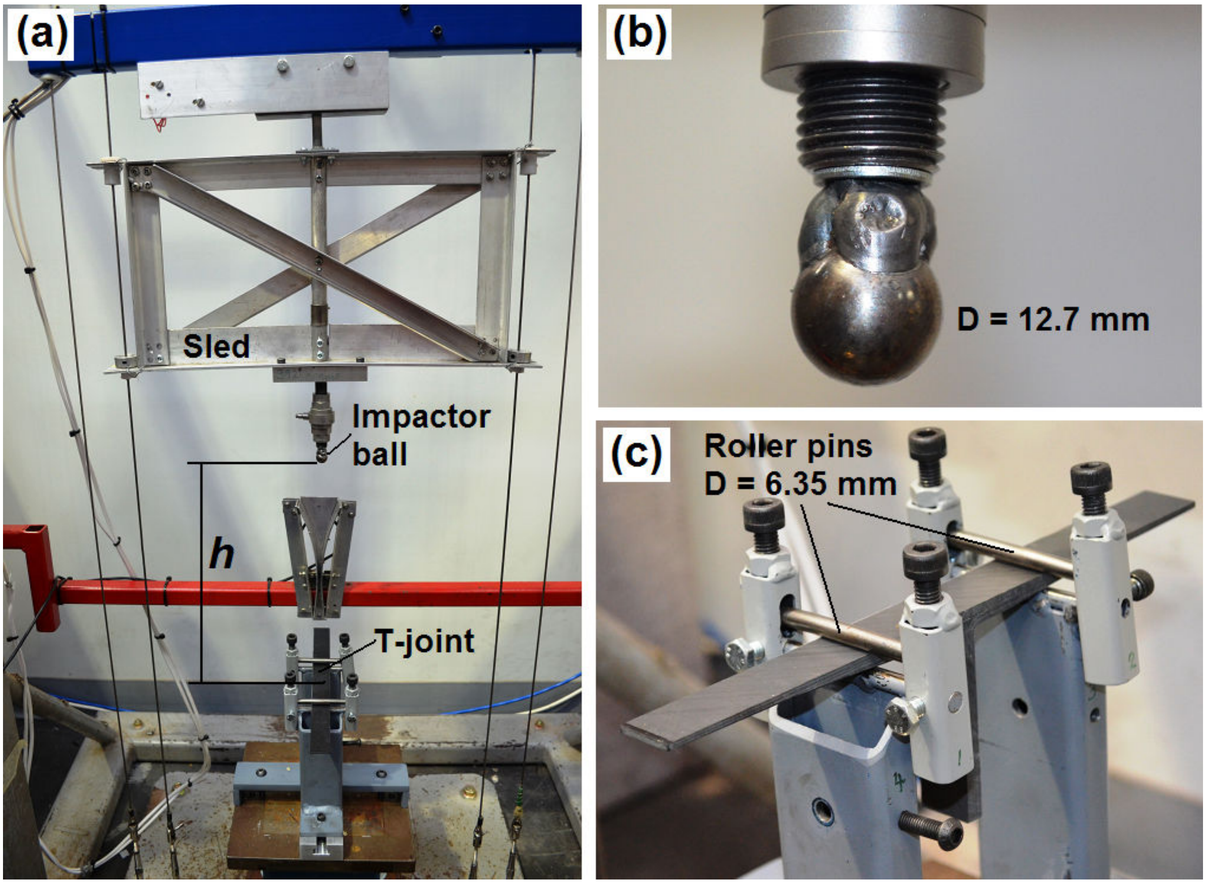

Figure 7-1 Impact test rig: (a) general view of rig showing sled, impactor ball, T-joint and definition of drop height (h); (b) close up of half inch diameter impactor ball; and (c) boundary conditions of T-joint in impactor test rig in which skin was pinned by two quarter inch diameter rollers

Table 7-1 summarises the impact test matrix. Two samples were tested for each incident impact energy level, with energies ranging from 2 to 14 J. The T-joint was placed in the test rig and secured by two pairs of quarter inch (6.35 mm) diameter rollers which pinned the skin at the location of the roller but allowed the skin to flex in response to the impact of the ball (refer Figure 7-1c). This clamping condition is different to the static tests conducted in chapters four to six where the T-joint skin was clamped. After the impactor ball was released, sensors in the impactor test rig measured and recorded the inbound and rebound velocities of the impactor which enabled the energy absorbed by the T-joint and rig to be calculated. The impactor ball and sled were caught after rebounding from the T-joint skin to prevent double impact.

Table 7-1 Summary of impact resistance testing test matrix

Impact energy *E* (J)	Drop height *h* (m)	Impact velocity (m/s)
2	0.17	1.83
4	0.34	2.59
6	0.51	3.17
8	0.68	3.66
10	0.85	4.09
14	1.19	4.84

After impact testing the samples were photographed and then examined using a Rational™ DC-300 digital travelling microscope with x-y measurement capability. The crack length along the (horizontal) stiffener flange/skin bond-line and (vertical) stiffener web were measured using a travelling microscope to within 0.01 mm. Radial cracks were not considered. These two crack lengths were used to quantitatively assess the size of the damage zone and thereby the impact resistance of the T-joints.

7.2.2.2 Post-impact damage tolerance

Post-impact damage tolerance is an important parameter for certification of aircraft composite structures. The residual strength must exceed ultimate load when the impact event causes barely visible impact damage (BVID) and the residual strength must exceed the design load when the impact causes visible damage (VID).

Tensile (stiffener pull-off) tests were performed using a 50 kN Instron testing machine to measure the post-impact strength of the T-joints. The skin of the T-joint was clamped on either side of a 150 mm working section containing the stiffener web. Tensile tests were performed by applying a pull-off force to the T-joint stiffener web, as shown schematically in Figure 7-2. The tensile load was applied at a rate of 1 mm/min. The testing was used to determine the residual peak strength of the T-joints, which was defined in this study as the impact damage tolerance.

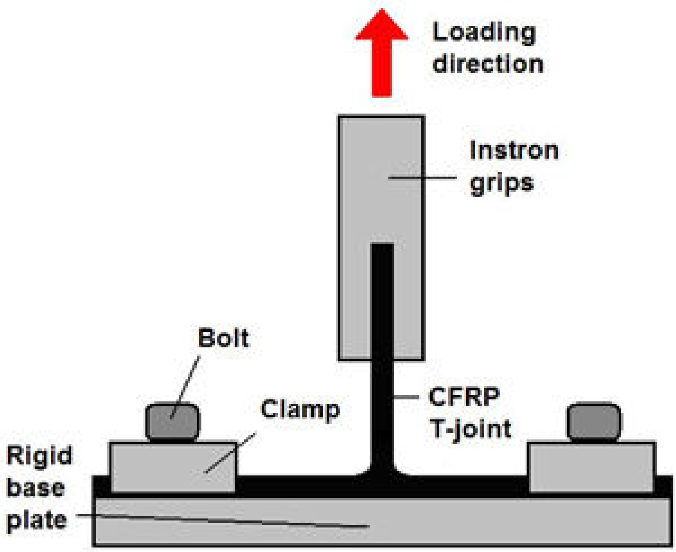

Figure 7-2 Schematic of post-impact residual strength testing of the T-joints

7.2.3 Finite element analysis of T-joints

The impact testing was modelled with a non-linear geometry dynamic explicit FE model constructed using the software SIMULIA ABAQUS 6.9-2. FEA was used to assess the elastic stresses in the T-joints during the lowest energy (2 J) impact event, and the propagation of damage was not modelled. This enabled a comparison of the dynamic elastic contact force and internal stresses within the baseline and bio-inspired T-joint designs.

The geometry and material properties of the FE model of the unidirectional baseline and bio-inspired optimised T-joints were as described in chapter four. The geometry and material properties of the FE model of the fabric baseline and bio-inspired embedded T-joints were as described in chapter five. The meshing was as described in chapter four with the modification that linear HEX-8 and TRIA-6 reduced integration solid elements were used because ABAQUS/Explicit 6.9-2 uses a lumped mass matrix scheme and thus supports linear elements only. The quasi-static properties of the carbon/epoxy composite materials were used in the dynamic analysis of the T-joints i.e. strain rate effects were ignored.

The impactor ball was modelled as a half sphere 3D analytical rigid surface, as shown in Figure 7-3. The impactor was given an initial velocity equivalent to a 2 J incident energy impact. The T-joint was fixed in the Y and Z directions across 1 mm of the mesh at the locations indicated in Figure 7-3, which corresponded with the physical test conditions in which the T-joint was secured by 0.25 inch (6.35 mm) diameter rollers which allowed the skin to flex in response to the impact load.

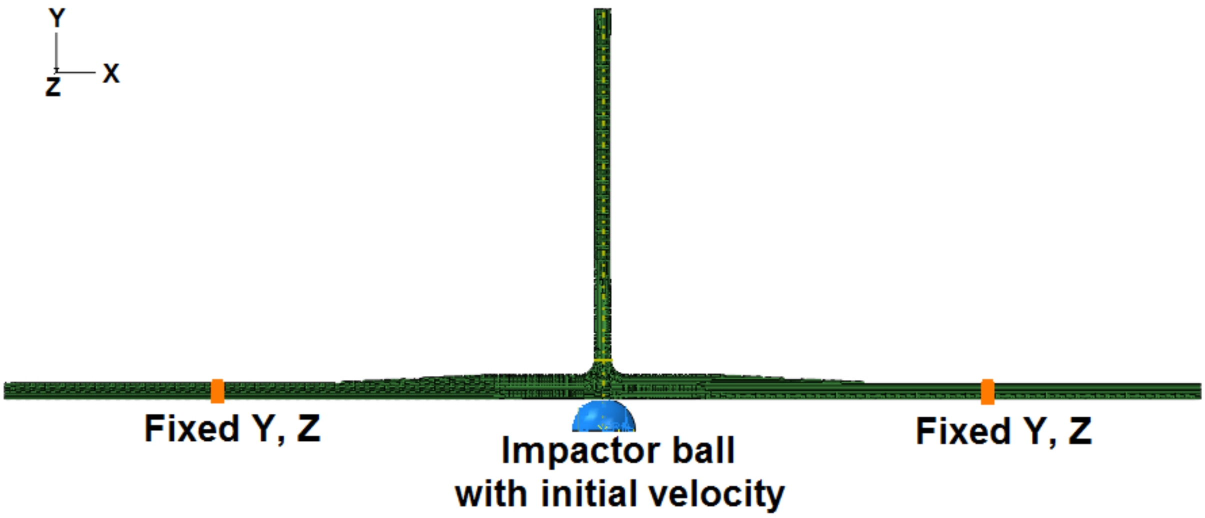

Figure 7-3 FEA impact model boundary conditions

7.3 RESULTS AND DISCUSSION

7.3.1 Experimental results

7.3.1.1 Impact damage resistance of T-joints

The effect of incident impact energy on the damage sustained by the four types of T-joints is shown in Figure 7-4. Figure 7-4a shows the length of the damage zone along the stiffener flange/skin bond-line. The unidirectional baseline, unidirectional optimised and fabric baseline T-joints experienced approximately the same damage size at each impact energy level. The fabric embedded T-joint sustained about half the damage size of the other T-joints.

Figure 7-4b shows the length of the impact-induced damage within the stiffener web of the different T-joints. There is no difference between the impact resistance of the baseline and bio-inspired designs. The unidirectional baseline and optimised T-joints sustained about the same stiffener web damage at each energy level, which was about half that of the fabric baseline and embedded joints.

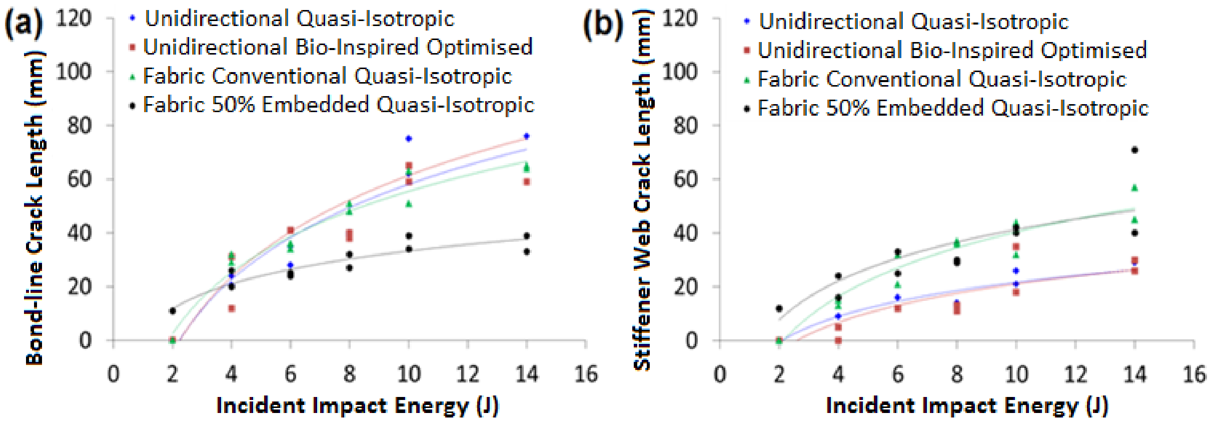

Figure 7-4 Impact testing results for unidirectional and fabric T-joints: (a) bond-line damage zone v impact energy; and (b) stiffener web damage zone v incident impact energy

Figure 7-5 shows the effect of absorbed impact energy on the size of the bond-line damage zone for the T-joints. The absorbed impact energy was determined from the difference between the inbound and outbound velocities of the impactor. The results show a similar trend to Figure 7-4. There is no difference between the unidirectional baseline and optimised joints. The fabric 50% embedded T-joint shows reduced bond-line damage zone compared to the baseline fabric joint for the same absorbed impact energy.

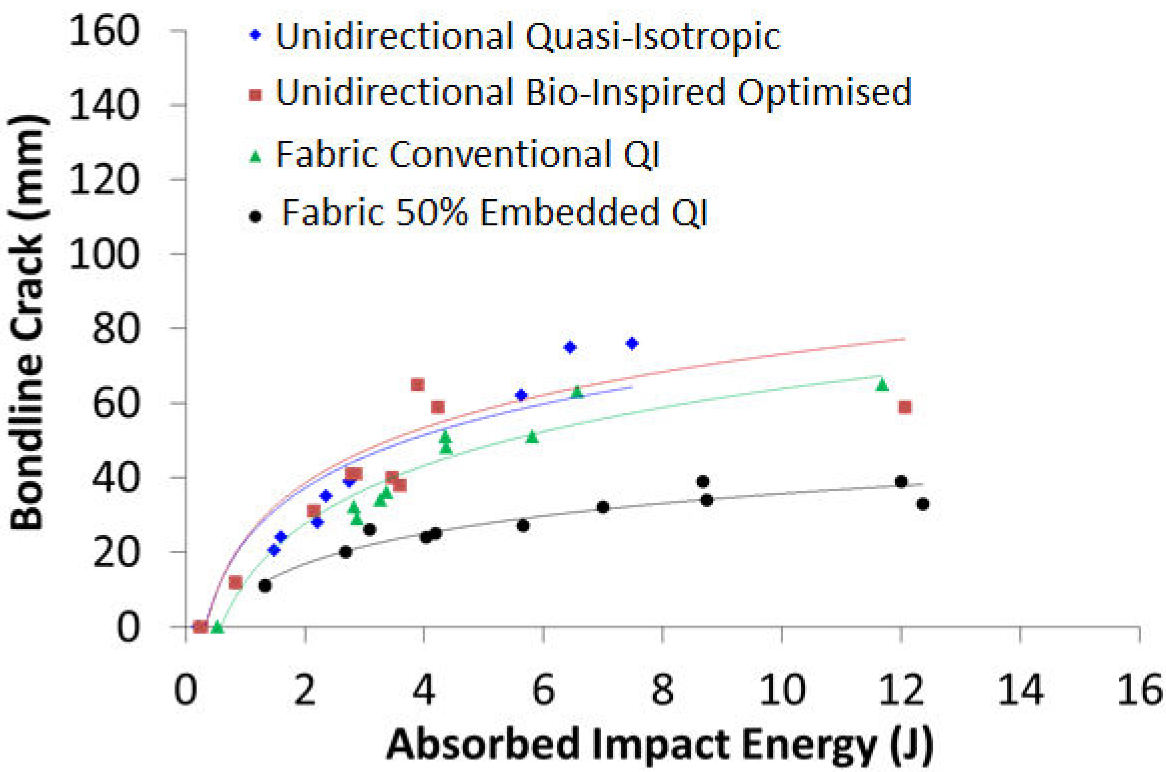

Figure 7-5 Bond-line damage zone versus absorbed impact energy

Figure 7-6 and Figure 7-7 show the impact damage in the unidirectional baseline and optimised T-joints after a 10 J incident energy impact. There are delaminations in the radius bend region, a dominant crack along the stiffener flange/skin bond-line and another main crack within the stiffener web of both T-joints. In the baseline T-joint the crack propagates over the delta-fillet, whereas in the optimised T-joint the crack propagates under the delta-fillet; however, both of these failure modes were observed in both T-joint designs. The baseline T-joint has some external visible skin damage in the form of a shear crack and a skin delamination, whereas the optimised T-joint does not.

Figure 7-8 and Figure 7-9 show the fabric conventional and embedded T-joints after the 10 J incident energy impact.

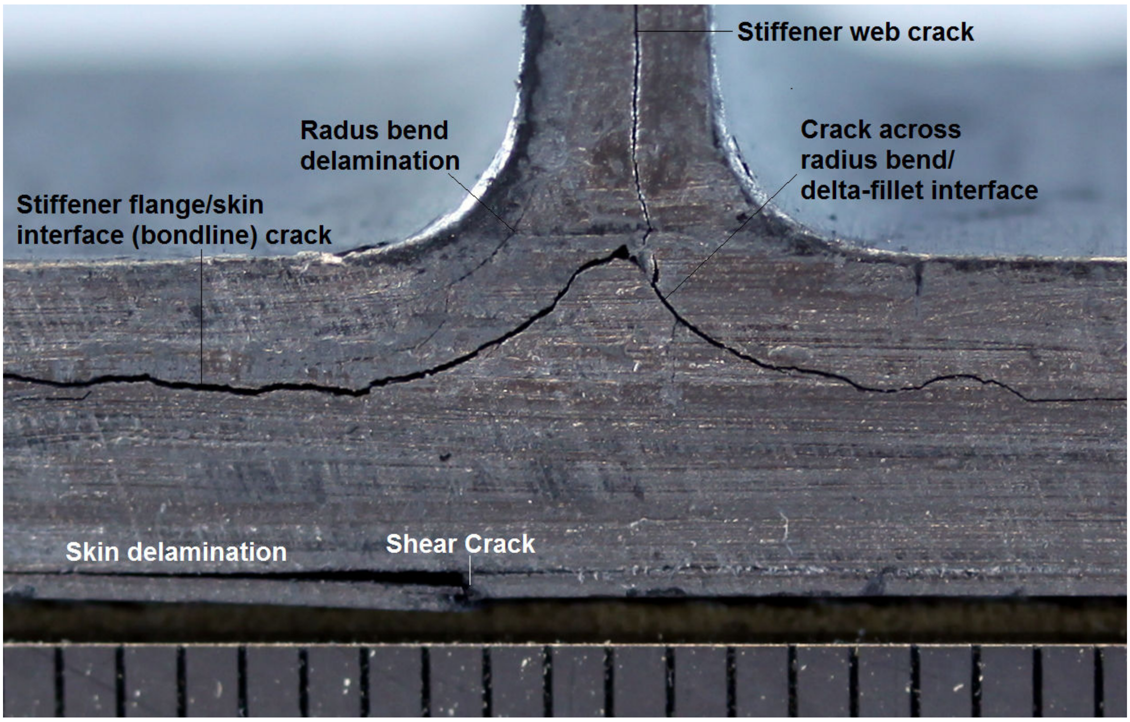

Figure 7-6 Unidirectional baseline T-joint after 10 J incident energy impact

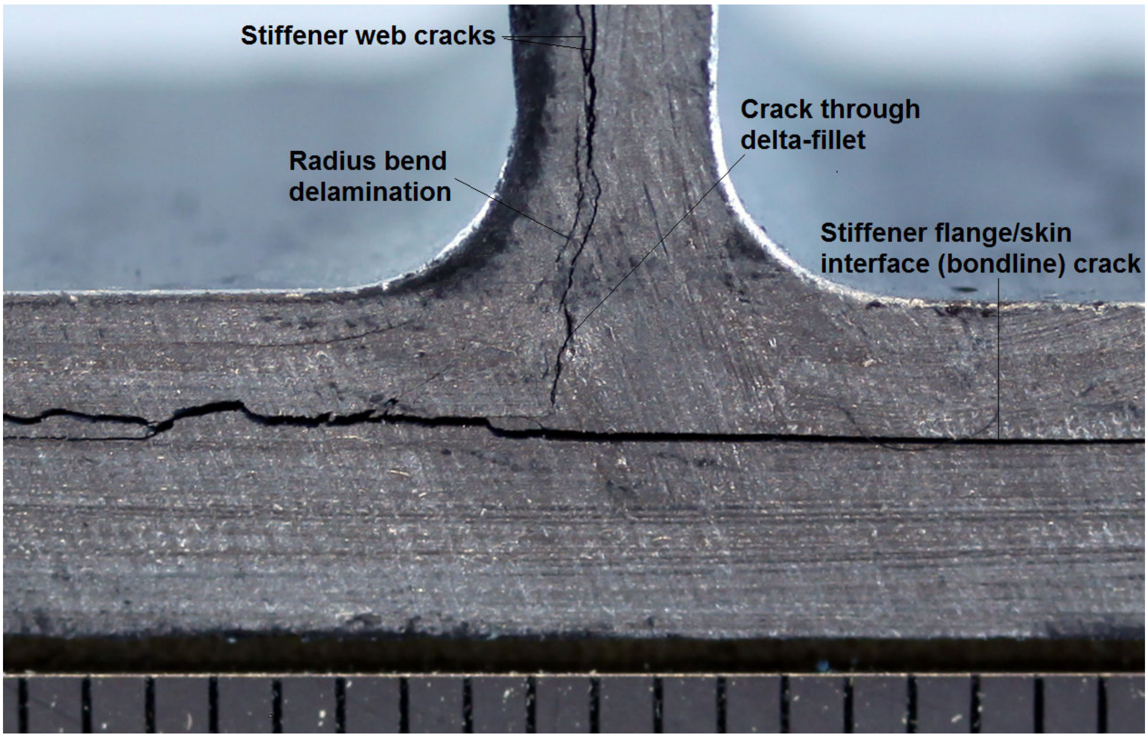

Figure 7-7 Unidirectional bio-inspired optimised T-joint after 10 J incident energy impact

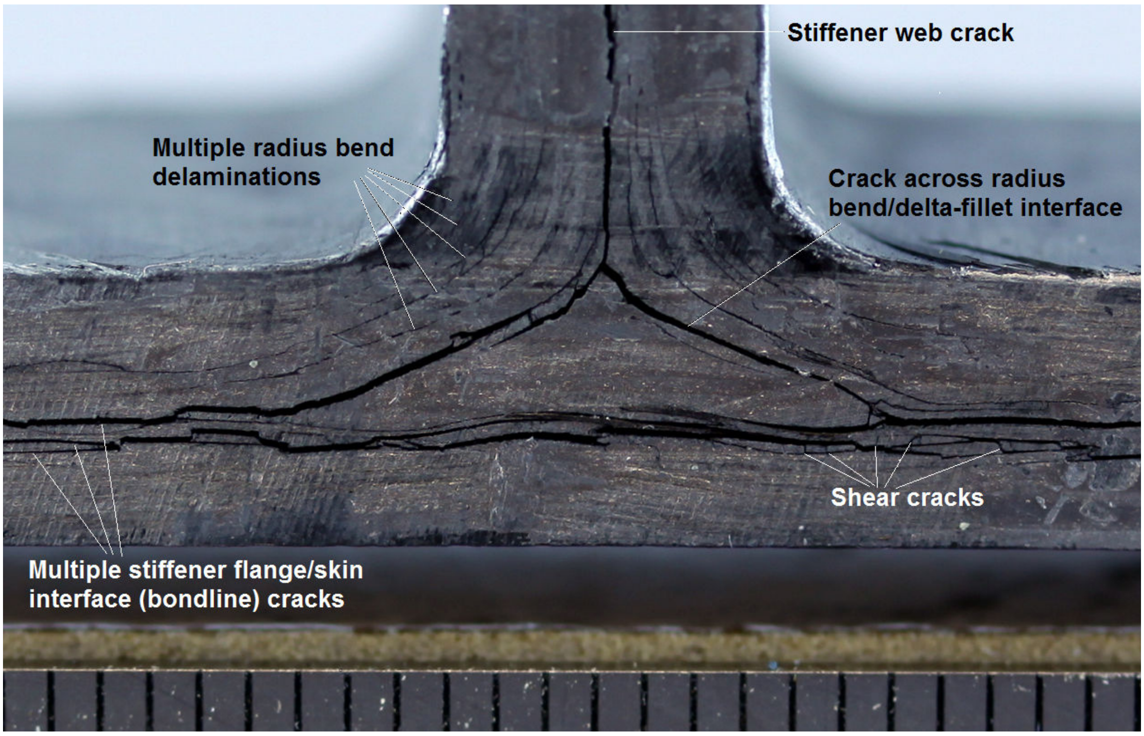

Figure 7-8 Fabric baseline T-joint after 10 J incident energy impact

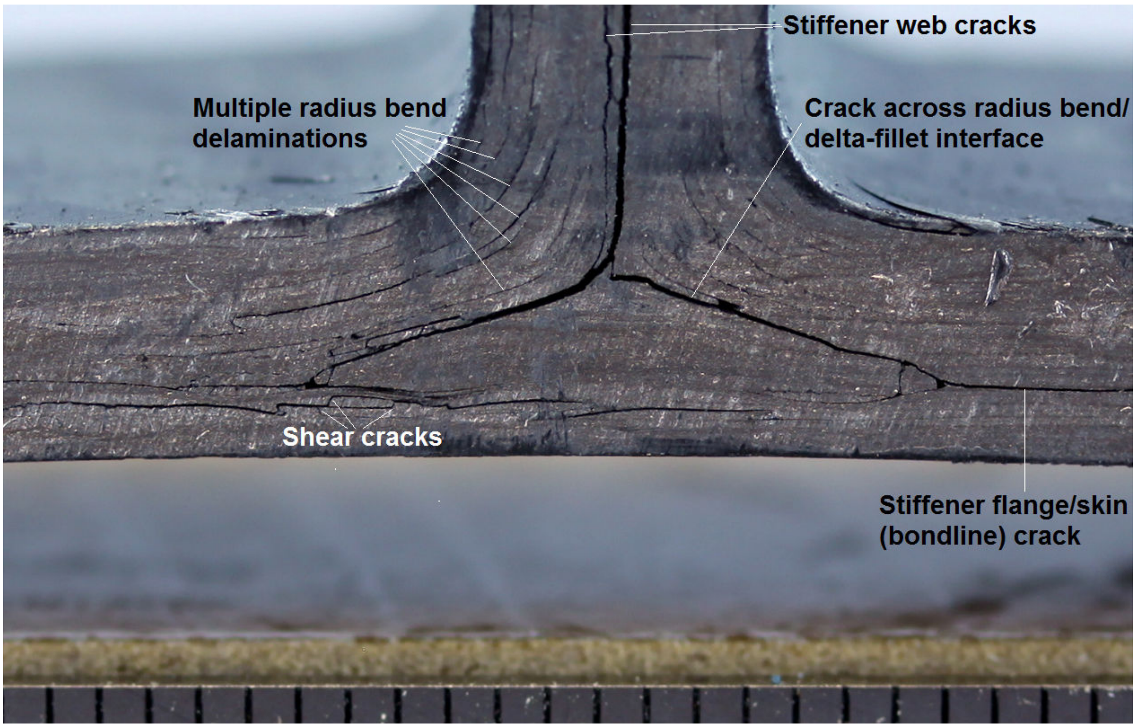

Figure 7-9 Fabric embedded T-joint after 10 J incident energy impact

In comparison to the unidirectional T-joints, there is substantially more damage in the radius bend region with delaminations visible at almost every ply interface. In both the baseline and bio-inspired embedded T-joints there are main cracks propagating along the stiffener flange/skin bond-line and a dominant crack propagating within the centre of the stiffener web, cracking both over and under the delta-fillet and shear cracks within the skin just below the bond-line. In the fabric baseline T-joint the main crack along the stiffener flange/skin bond-line is about 60 mm long whereas in the embedded T-joint it is only about 35 mm long. This difference is attributed to the lower bending stiffness and increased crack branching and increased number of stiffener flange/skin interfaces in the bio-inspired embedded design.

The results show no difference in the impact damage resistance of the unidirectional T-joints with a baseline quasi-isotropic and optimised stiffener laminate stacking sequences. However if the laminate stacking sequence of the skin laminate (as opposed to the stiffener) was optimised to resist impact loading by minimising the interlaminar stresses it is expected that the impact damage resistance would be improved [66]

7.3.1.2 Post-impact damage tolerance

The post-impact tensile stiffness and residual tensile strength was used to quantify the post-impact damage tolerance of the T-joints. Representative tensile load-displacement curves for the baseline unidirectional T-joint at incident energy levels from 2 – 14 J are shown in Figure 7-10. As expected, both the tensile stiffness and strength decreased with increasing impact incident energy due to the greater amount of damage sustained in the T-joint.

The post-impact stiffness of the T-joints versus the bond-line damage length is compared in Figure 7-11. Figure 7-11a shows that there is no difference in stiffness reduction for the unidirectional baseline and bio-inspired optimised T-joints. Figure 7-11b shows the reduction in normalised stiffness with increased damage zone for the fabric baseline and 50% embedded T-joints. As observed in the quasi-static tensile testing discussed in chapter five, the normalised stiffness of the 50% embedded T-joint is less than the geometrically equivalent baseline design due to the longer stiffener flange ramp increasing the skin stiffness in the baseline T-joint design.

Figure 7-10 Post-impact tensile testing results for unidirectional baseline T-joint. Energy levels represent incident impact energy.

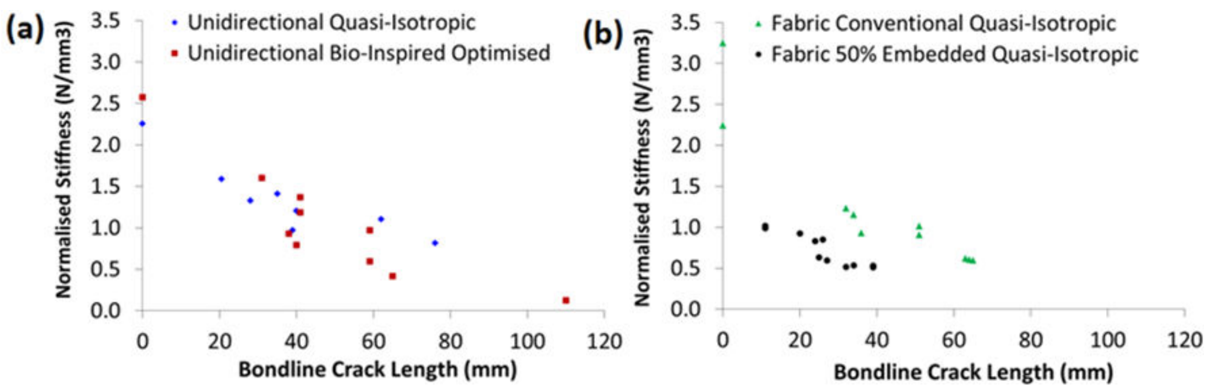

Figure 7-11 Post-impact tensile testing results: normalised stiffness of (a) unidirectional baseline and optimised T-joints; and (b) fabric baseline and 50% embedded T-joints

Figure 7-12 shows the normalised post-impact tensile strengths of the T-joints containing different amounts of delamination cracking along the skin/stiffener flange bond-line. The residual strengths of the different T-joints fall along a common curve, revealing that the joint design does not significantly affect the damage tolerance. In all four T-joint designs the length of the bond-line crack length could be used to predict the residual tensile strength of the T-joint.

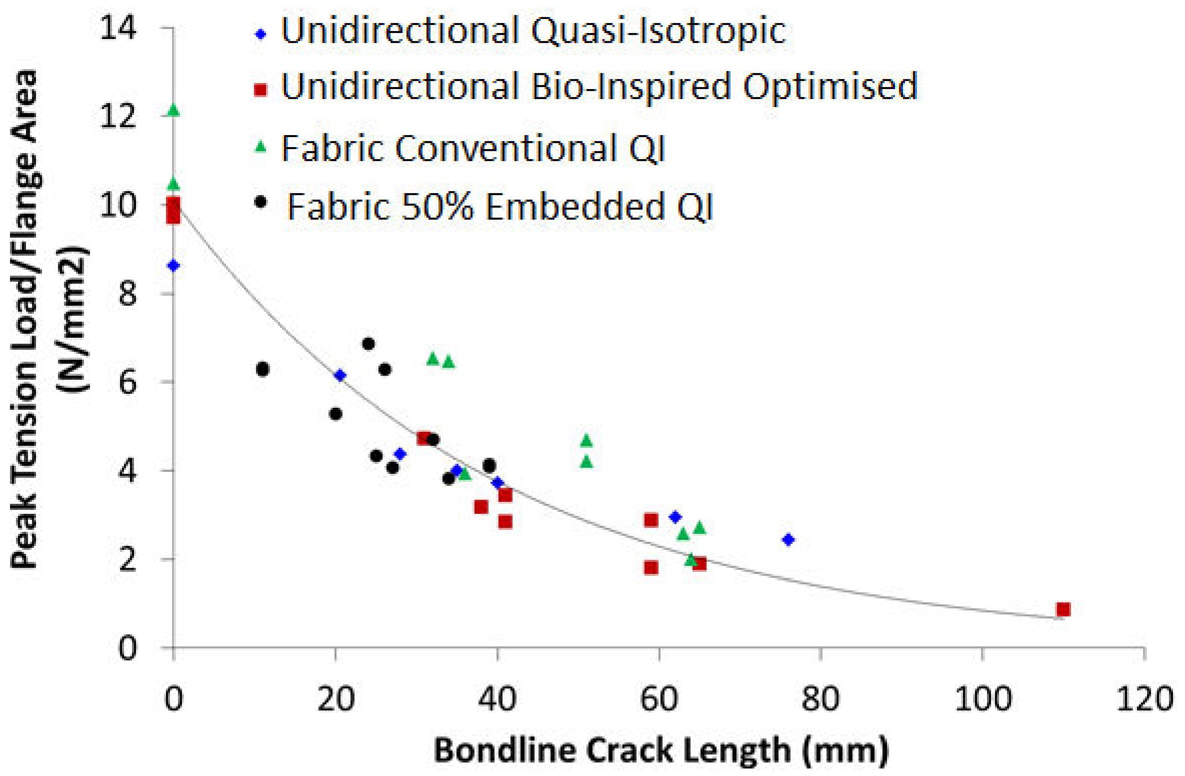

Figure 7-12 Post-impact normalised residual tensile strengths of the T-joints with increasing bond-line damage

In summary, the experimental results show that the fabric 50% embedded T-joint has superior impact damage resistance compared to the other T-joint designs. However, there is no significant difference in the post-impact damage tolerance between all four T-joint designs considered in this preliminary study, revealing that neither optimised design of the stiffener laminate stacking sequence nor integration of the stiffener flange and skin plies through embedded design influences the post-impact damage tolerance.

7.3.2 Finite element analysis of impact loading of T-joints

Figure 7-13 shows the FEA dynamic contact force-time curves for the unidirectional baseline and optimised T-joints calculated using the FE model for a low energy elastic impact event (2 J). The two curves are similar, and in both cases the initial impact perturbs the T-joint skin so that the skin loses contact with the impactor that results in a 'double bounce' in which the contact force returns to zero before increasing as the impactor ball re-contacts the T-joints. The contact curves for both T-joints have similar peak forces, time domain and frequency responses. These FE results indicate there was no significant difference between the unidirectional baseline and optimised T-joints.

Figure 7-14 shows the FEA impact force-time curve for the fabric baseline and 50% embedded T-joints. There are significant differences between the two curves, with the baseline joint experiencing a much higher peak force than the 50% embedded T-joint. The contact time for the baseline T-joint is shorter and the frequency of the oscillations is longer compared to the 50% embedded T-joint.

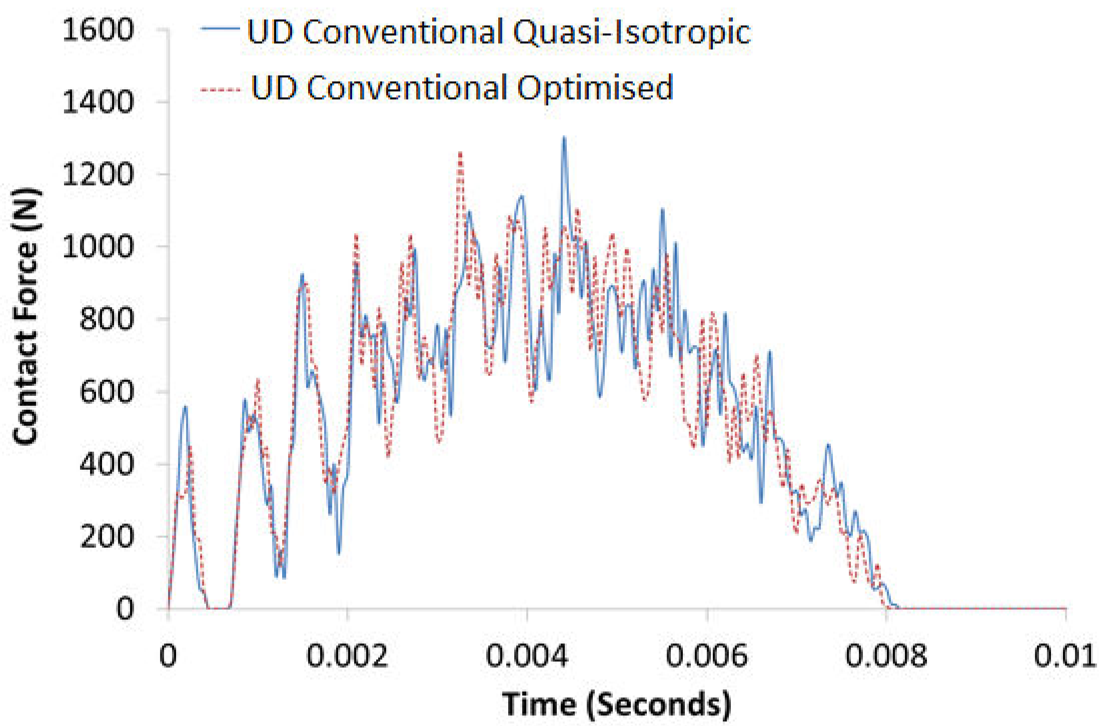

Figure 7-13 Contact force versus time for unidirectional base-line and optimised T-joints under 2 J impact

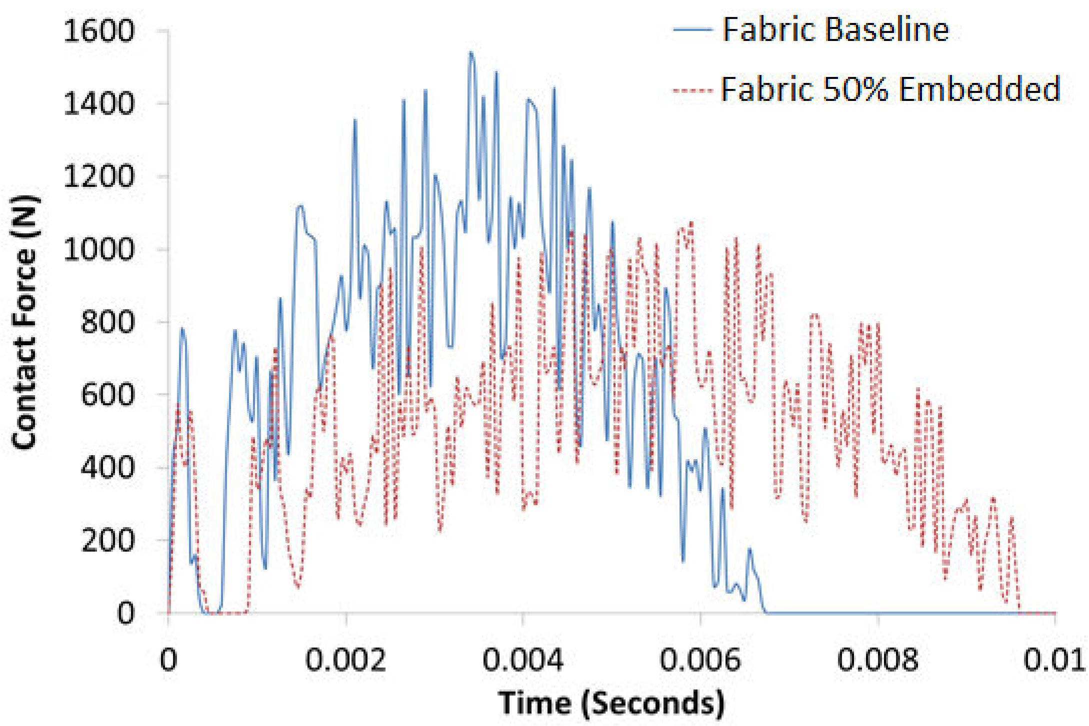

Figure 7-14 Contact force versus time for fabric baseline and 50% embedded T-joints under 2 J impact

These differences are mainly due to the difference in the skin bending stiffness of the two T-joint designs, which are summarised in Table 7-2. The unidirectional baseline and optimised T-joints have only a small difference in the stiffener stiffness properties and no difference in the skin properties, which accounts for their similar impact force-time curves. In contrast, the skin of the 50% embedded T-joint (4 fabric plies) is much thinner than the baseline T-joint (8 fabric plies) and therefore it has a lower bending stiffness, which results in higher displacement under impact loading.

The calculated displacement of the impactor throughout the 2 J incident energy impact loading event on the T-joints is shown in Figure 7-15. The displacement of the ball can be used to estimate the displacement of the T-joint skin under impact, since after the 'double bounce' they were in contact. Until approximately 0.001 seconds all designs show a similar trend. As discussed, the peak displacement of the unidirectional baseline (5.19 mm) and optimised (5.08 mm) T-joints are almost identical because their stiffness properties are similar. The fabric baseline T-joint experiences less displacement compared to the unidirectional joints because of the high stiffness of the stiffener (refer Table 7-2). The fabric

50% embedded T-joint showed much higher peak displacement under impact compared to the fabric baseline joint because of the reduced bending stiffness of the skin (refer Table 7-2). The increased displacement in the more flexible 50% embedded T-joint explains why the contact time was higher and the peak contact force was lower compared to the fabric baseline T-joint.

Table 7-2 Comparison of the stiffness properties in the stiffener and skin of the four T-joint designs

T-Joint Design	Stiffener			Skin Under Stiffener		
	No. Plies	A_{11} (GPa.mm)	D_{11} (GPa. mm^3)	No. Plies	A_{11} (GPa.mm)	D_{11} (GPa.mm^3)
UD baseline	16	158.9	142.9	16	158.9	142.9
UD optimised	16	150.5 (-5%)	155.8 (9%)	16	158.9 (0%)	142.9 (0%)
Fabric baseline	16	275.1	713.3	8	137.6	84.2
Fabric 50% embedded	16	275.1 (0%)	713.3 (0%)	4	68.8 (-50%)	11.2 (-87%)

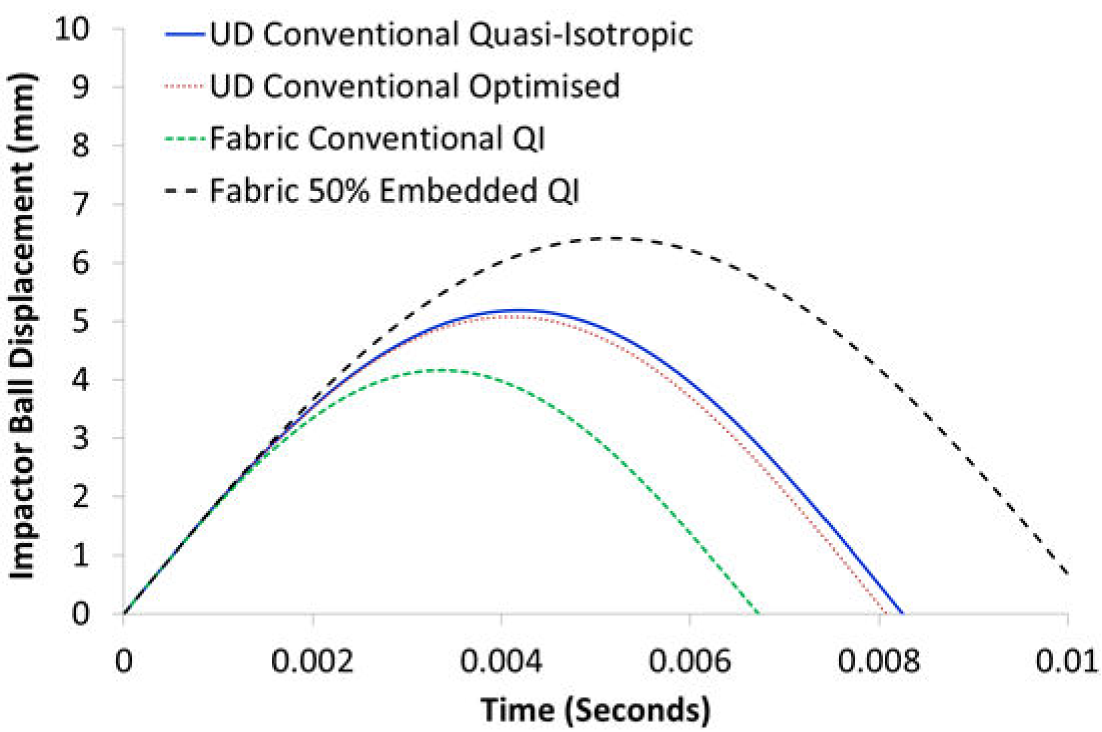

Figure 7-15 FEA of the impactor ball displacements for the four T-joint designs at the impact energy of 2 J

FEA was used to examine the interlaminar tensile and shear stress distribution in the T-joint radius bend and delta-fillet regions at the respective peak contact forces under impact. Figure 7-16 shows the elastic interlaminar tensile stress distribution for the four T-joints, which is similar to the quasi-static tensile stress distribution discussed in chapters four and five. The stress contours are set to the value of the interlaminar tensile strength used in chapter five, which is 47.6 MPa for the unidirectional T-joints and 23.4 MPa for the fabric T-joints.

The elastic interlaminar tensile stress distributions for the unidirectional baseline (refer Figure 7-16a) and unidirectional optimised (refer Figure 7-16b) T-joints are very similar. The stress does not exceed the interlaminar tensile strength, and therefore FEA predicts no damage. This was validated by experimental observation (refer Figure 7-16e and Figure 7-16f).

Despite the significant difference in the peak contact force (refer Figure 7-14), the elastic interlaminar tensile stress distributions of the fabric baseline (refer Figure 7-16c) and fabric 50% embedded (refer Figure 7-16d) T-joints are remarkably similar. The results show that the interlaminar tensile strength of the composite is exceeded in the radius bend, at the delta-fillet interface, and within the delta-fillet region. This was also validated by experimental observation with damage visible in both fabric T-joints following impact at 2 J incident impact energy (refer Figure 7-16g and Figure 7-16h). Based on the experimental observations, there was more cracking visible within the 50% embedded T-joint.

Although damage was not modelled, this observation suggests evidence of crack branching/deflection in the 50% embedded T-joint, as observed in the quasi-static experimental results in chapter five. It is possible that the 50% embedded design alters the toughness of the T-joint so that damage that would normally propagate along the stiffener flange/skin bond-line is deflected towards the radius and stiffener web where there are no embedded plies. It might be possible to strategically embed parts of a primary composite structure in order to transfer impact damage towards less crucial secondary structure. This could be investigated further using FE analysis that incorporates damage modelling.

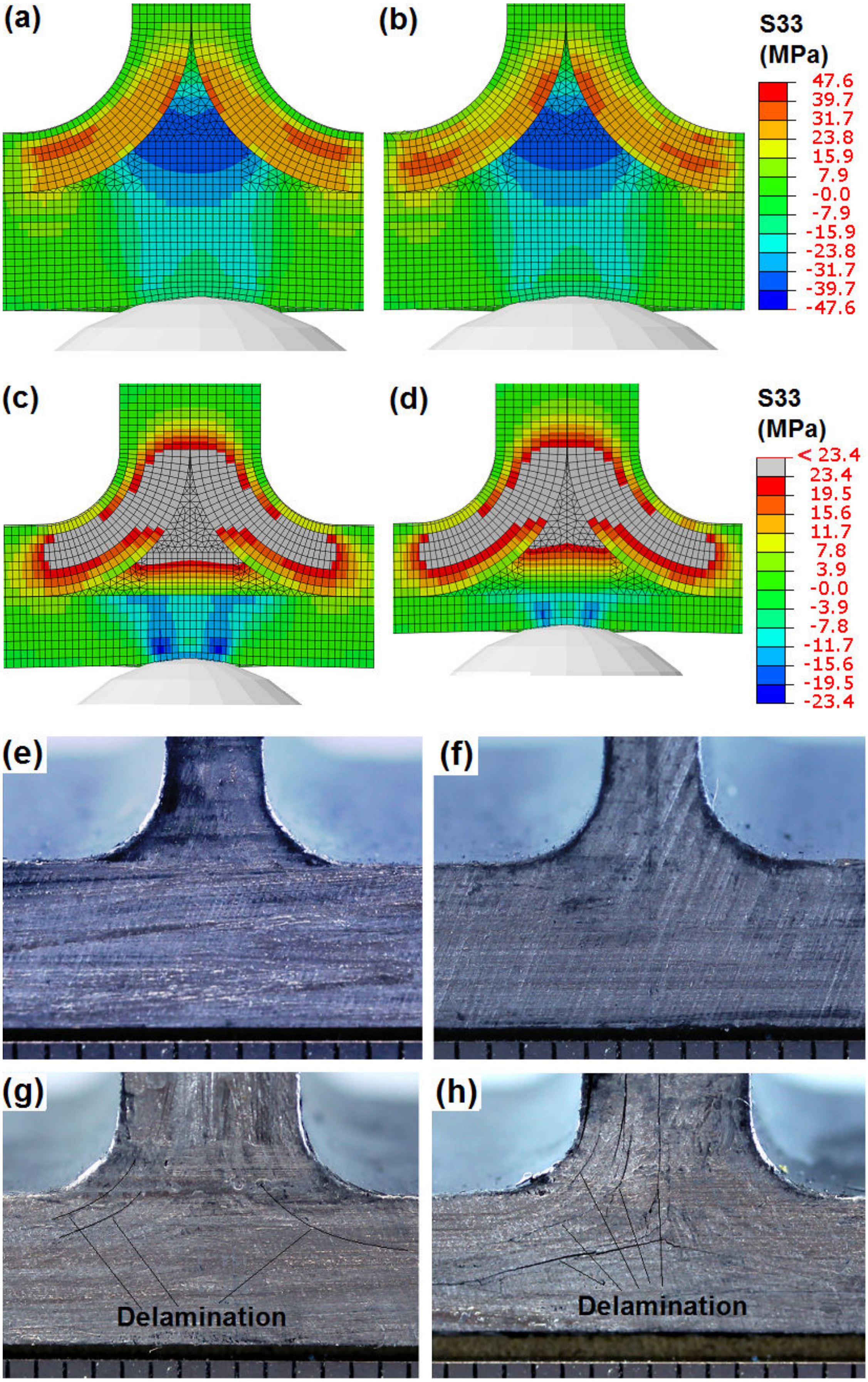
(a)
(b)
S33
(MPa)
47.6
39.7
31.7
23.8
15.9
7.9
-0.0
-7.9
-15.9
-23.8
-31.7
-39.7
-47.6
(c)
(d)
S33
(MPa)
< 23.4
23.4
19.5
15.6
11.7
7.8
3.9
-0.0
-3.9
-7.8
-11.7
-15.6
-19.5
-23.4
(e)
(f)
(g)
Delamination
(h)
Delamination

Figure 7-16 FEA interlaminar tensile stress (σ_{33}) distribution at peak contact forces under 2 J impact energy: (a) unidirectional baseline at 1292 N; (b) unidirectional optimised at 1261 N; (c) fabric baseline at 1536 N; and (d) fabric 50% embedded at 1074 N. Photos of damage after 2 J impact loading: (e) unidirectional baseline; (f) unidirectional optimised; (g) fabric baseline; and (h) fabric 50% embedded T-joints

Figure 7-17 shows the elastic interlaminar shear stress distributions for the four T-joints. The stress contours are set to the interlaminar shear strength value (84.3 MPa) used in chapter five. The interlaminar shear strength is not exceeded in any of the T-joints. This indicates that failure is dominated by the interlaminar tensile stresses generated under impact loading.

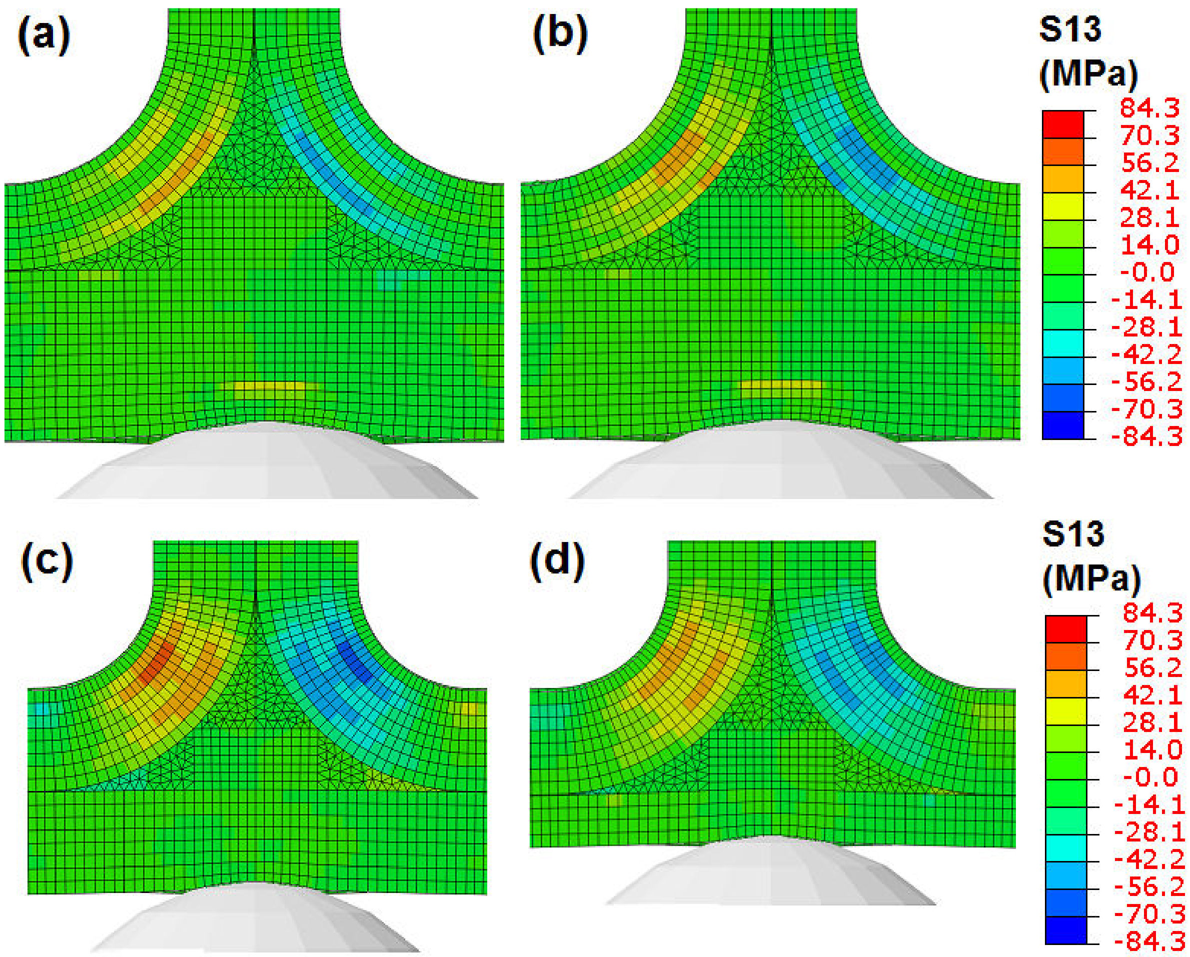

Figure 7-17 FEA interlaminar shear stress (τ_{13}) distribution at peak contact forces under 2 J impact energy: (a) unidirectional baseline at 1291 N; (b) unidirectional optimised at 1261 N; (c) fabric baseline at 1536 N; and (d) fabric embedded joints at 1074 N

Table 5-9 summarises the results of the FE impact analysis of the T-joints. The interlaminar tensile and shear failure stresses are not exceeded in the unidirectional baseline and optimised T-joints indicating they will not sustain delamination damage at 2 J incident impact energy. This prediction was confirmed by experimental observation (refer Figure 7-16c and Figure 7-16d). In the fabric samples, FEA predicts the peak interlaminar tensile stress is exceeded in the radius bend and delta-fillet regions and delaminations will occur. Again, this prediction was validated by experimental observation (refer Figure 7-16g and Figure 7-16h).

Table 7-3 Summary of the FEA results under 2J incident impact energy

T-joint	Impact Energy	FEA Peak Contact Force (N)	FEA Peak σ_{33} (MPa)	% of Z_t	FEA Peak τ_{13} (MPa)	% of S_{13}	Failure Mode (FEA)
UD baseline	2 J	1292	38.6***	81%*	51.7***	61%	Not failed
UD optimised	2 J	1261	38.9*** (0.8%)	82%*	46.0*** (-11%)	55%	Not failed
Fabric baseline	2 J	1536	52.0****	222%**	61.2***	73%	σ_{33} dominated
Fabric 50% embedded	2 J	1073	43.5**** (-16%)	186%**	55.7*** (-9%)	66%	σ_{33} dominated

* Z_t = 47.6 MPa, ** Z_t = 23.4 MPa, *** occurs in radius bend, **** occurs at delta-fillet interface

7.4 SUMMARY AND CONCLUSIONS

This preliminary study into the impact damage behaviour of bio-inspired T-joints resulted in similar conclusions to the quasi-static damage tolerance investigation presented in chapter five. The 50% embedded T-joint design improves the impact damage resistance whereas the optimised stiffener laminate stacking sequence does not affect the impact properties.

Experimental impact testing showed that the unidirectional optimised T-joint does not perform differently to the unidirectional baseline T-joint under impact loading because of the similarity in stiffness properties of the two designs. However it is postulated that if the stacking sequence of the skin laminate, which absorbs the majority of the impact energy, was optimised to resist impact loading the impact damage resistance of the skin could be improved. The fabric 50% embedded T-joint exhibited better impact damage resistance as measured by crack length along the stiffener flange/skin bond-line. Post-impact residual strength testing showed the length of the damage zone along the stiffener flange/skin bond-line could be used to assess the normalised residual strength of all four T-joints, indicating that all four designs had similar impact damage tolerance.

Dynamic explicit non-linear geometry FE analysis was used to determine the dynamic force-time curves and elastic interlaminar tensile and shear stress distributions in the four T-joint designs. The contact force, frequency and contact time were very similar in the unidirectional baseline and optimised T-joints because of the similarity to their stiffness properties. The elastic interlaminar tensile and shear stress distributions were also similar. Under a 2 J impact incident energy, the interlaminar tensile and shear stresses were not sufficient to initiate delamination damage within the T-joints, which was validated by experimental observation.

The bio-inspired optimisation did not alter the impact damage resistance because the stiffener laminate stacking sequence was optimised to minimise interlaminar stresses in the radius bend under bending loading and the impact damage loading induced tensile stresses in the T-joint stiffener. However it might be possible to optimise the ply-level properties in both the stiffener radius bend/delta-fillet region and the skin to minimise the interlaminar tensile stresses and thereby increase the damage resistance of the T-joint under low energy impact loading.

Considering the bio-inspired embedded design the peak contact force was reduced and the contact time was increased for the fabric 50% embedded T-joint compared to the fabric baseline joint due to the reduction in the skin bending stiffness. Despite this difference, the elastic interlaminar tensile and shear stress distributions were similar in the two T-joint designs. The experimental observations validated the FEA prediction that delamination damage would initiate in both the baseline and 50% embedded fabric T-joints under a 2 J impact incident energy.

The bio-inspired 50% embedded design alters the toughness of the T-joint so that damage that would normally propagate along the stiffener flange/skin bond-line is absorbed by crack branching/deflection in the radius bend region or is deflected towards the stiffener web where there are no embedded plies. It might be possible to strategically embed parts of primary structure in order to transfer impact energy towards less crucial secondary structure. The parameters influencing damage deflection in embedded T-joints under impact loading could be further investigated by a FE model that incorporates damage modelling.

CHAPTER 8:

8 MANUFACTURING AND CERTIFICATION OF BIO-INSPIRED COMPOSITE JOINTS

The purpose of this chapter is not to provide a comprehensive review of the processes of manufacturing and certifying bio-inspired composite T-joints, but to briefly discuss some important issues that may affect the implementation of bio-inspired composite joints by the aerospace industry.

The ultimate outcome of designing bio-inspired composite joints is to create a superior design that meets structural requirements with a reduction in weight. Weight savings are critical in reducing the operating costs of commercial aircraft, however production costs are also an important consideration. Bio-inspired composite joints will not be implemented on commercial aircraft unless it can be proven that the cost savings from weight reduction offsets any costs involved in redesign and production.

Another crucial consideration is certification. The aerospace industry has a very robust certification process that has led to a strong safety record for commercial aircraft. Conversely, the limits imposed by the rigorous certification requirements are sometimes a barrier to innovation and implementing new cost-saving technologies. The main certification documents for composite structures are FAR/CAR-23 and FAR/CAR-25 for civilian aircraft and MIL-HBK-17 for military aircraft.

Certification requirements differ depending on the part classification, which are classified according to the following:

- Principal Structural Element (PSE) - Primary structure which makes a significant contribution to carrying flight, ground and/or pressurisation loads and therefore there is a high chance that losing the part will mean losing the aircraft e.g. main wing spar or control surfaces.

- Secondary Structural Element (SSE) – Low chance that losing the part will mean losing the aircraft e.g. undercarriage doors.
- Tertiary Structural Element (TSE) – non-structural parts e.g. fillers, tips, fairings etc.

The bio-inspired design concepts in this PhD thesis have been applied to a carbon fibre composite T-joint representative of a stiffened skin structure. A stiffener-skin T-joint might be a principal structural element depending on its location and the consequence of losing the part. For example, if the stiffener is located on the flap and separating the stiffener from the skin means flap failure then that stiffener-skin joint is considered a PSE.

Principal structural elements have the most rigorous certification requirements. In industry there is no such thing as a 'pristine' structure. All structures are assumed to have Barely Visible Impact Damage (BVID) which equates to a dent 1/10,000th of an inch wide. Normally BVID is modelled as a ¼ x ∞ inch flaw or a ½ x ½ inch flaw. All structures are assumed to have BVID because it represents the limit of detection using conventional Non-Destructive Inspection (NDI) methods such as ultrasonics and thermography. It is assumed BVID exists in the worst location on a structure, which can be determined from finite element analysis (FEA) using the virtual crack closing technique (VCCT) or strain energy release criteria.

It is assumed that gross damage, such as the complete separation of a stiffener is an unlikely event (probability $<10^{-9}$). This is determined by the airworthiness requirements (AR) fail safe document. Any event that causes gross damage, such as the complete separation of a stiffener, is known as Visible Impact Damage (VID). Therefore, for certification purposes it must be shown that the structure can withstand design limit load with one stiffener completely disbonded and other structures sustaining BVID. Double failure with two stiffeners completely disbonded is not considered because it is an unlikely event.

In chapter five bio-inspired embedded T-joint designs were considered in which the stiffener and skin laminate plies are integrated to varying levels of embedment. However, a bonded joint is traditionally considered to consist of two distinct parts (e.g. stiffener and skin). In order to pass certification it must be proved that the bonded joint can withstand ultimate load (1.5 x design limit load) with BVID (refer Figure 8-1). Another requirement is to prove that the bonded joint can withstand operational loads, which are normal day-to-day loads e.g. cruise loads, without damage growth. This is normally proved via fatigue testing. It must also be proved that bonded joints can withstand design limit load (the highest load expected during the lifetime of the structure) with VID and that joints can withstand operational loads up to the time between two inspections (after which VID will be detected). If a bonded joint is deemed PSE it must also be shown that the joint can withstand design limit load with VID and with the bond-line completely failed (refer Figure 8-2).

These tough certification requirements means that PSE bonded joints are typically reinforced with fasteners, which adds to production costs and aircraft weight. However the example of bonded joints raises the issue of what is considered two distinct parts? For example, in chapters five and six the 50% embedded T-joint was constructed with the stiffener flange plies forming 50% of the skin. This type of design can only be formed into two distinct parts if the skin is severed. If the stiffener and skin of the 50% embedded T-joint are still considered two parts the bio-inspired bonded joint may actually perform worse under the certification requirements because it must be shown that design limit load can be sustained by only half of the skin (refer Figure 8-2a) compared to the conventional design where the stiffener separates cleanly, leaving the skin intact (refer Figure 8-2b). These certification requirements might dictate the level of integration (embedment) of parts possible within the existing certification framework.

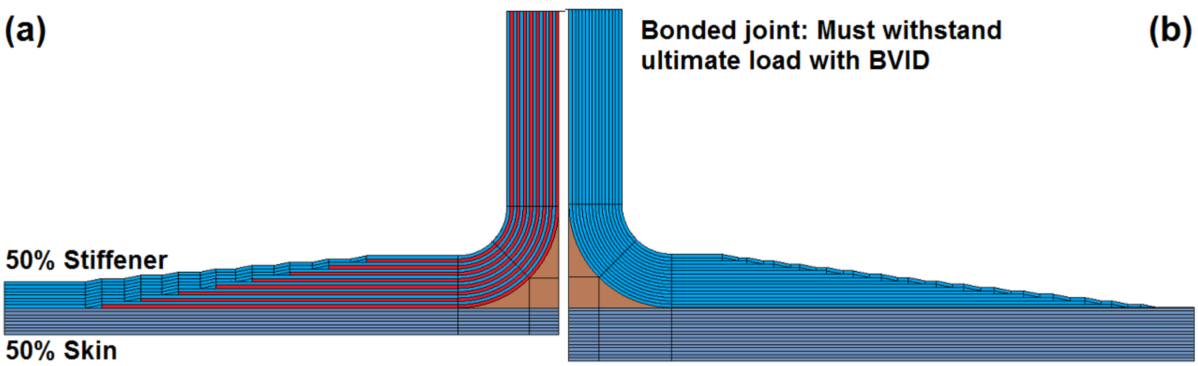

Figure 8-1 Certification requirements for bonded joints to withstand ultimate load with barely visible impact damage: (a) 50% embedded; and (b) conventional T-joint

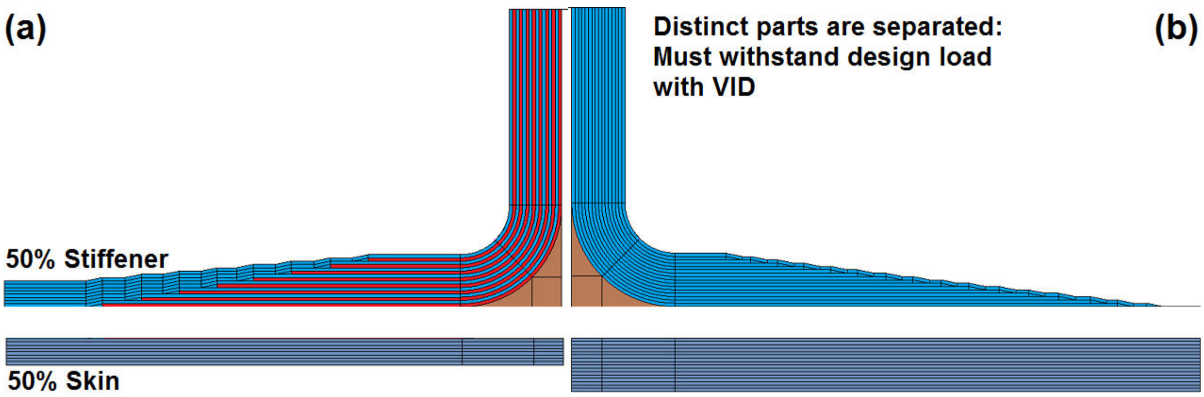

Figure 8-2 Certification requirements for PSE bonded joints to withstand design load with visible impact damage when distinct parts are separated: (a) 50% embedded; and (b) conventional T-joint

Manufacturing is trending towards more integrated structures, and this is blurring the line between what constitutes an assembled part and what constitutes distinct elements. For example, in the 787 fuselage the stiffeners and the skin are co-cured. Currently parts that are co-cured together in one shot manufacturing are still considered distinct elements for certification purposes. However implementing embedded design together with the co-cured one-shot manufacturing process may further blur this boundary.

Based on the research in chapter four, bio-inspired optimisation has proven an effective technique to improve the damage initiation strength of composite T-joints without incurring stiffness or weight penalties. Changing the stiffener laminate ply stacking pattern to tailor the internal stiffness and strength properties to suit the external loading conditions is more feasible using current manufacturing techniques than many other methods such as tailoring the internal material properties by altering the fibre volume fraction or through hybrid material selection.

Any additional cost penalties required for manufacturing non-standard ply orientations would be determined by the level of automation. Industry is trending towards increased levels of automation in composite manufacturing, e.g. using automated robots. Therefore the methodology and approach for creating parts using non-standard ply orientations could potentially be implemented without a significant cost penalty.

In the consideration of optimised stiffener laminate stacking sequences in chapter four and hierarchical design in chapter six the global in-plane and bending stiffness properties of the stiffener laminate were kept within a prescribed limit of ±10% of the baseline quasi-isotropic design. However the T-joint considered in chapter four is essentially a 2D structure and therefore the global properties were matched in the chord-wise direction only. When considering 3D stiffened panels it is important to ensure the design strain of the bio-inspired laminate is matched in both the chord-wise and span-wise directions compared to the baseline laminate. The design strain allowable is calculated using Equation 8-1.

$$\varepsilon = \frac{P_{\max}}{EA}$$ Equation 8-1

Where ε = design strain allowable, P_{max} = damage initiation or failure load (N), E = Young's modulus (MPa) and A = cross sectional area (mm^2).

The damage initiation or failure load P_{max} is determined by experimental testing. It is permissible to use the failure load instead of the damage initiation load provided the ratio of the damage initiation load to the failure load is not too low.

In the optimised T-joint the failure load P_{max}, Young's modulus E and cross sectional area A were approximately the same compared to the baseline T-joint. If P_{max} is defined as the damage initiation load, then the cross-sectional area could be reduced according to the increase in damage initiation load to equivalence the design strain between the baseline and the bio-inspired optimised designs, thus reducing the structural weight. In the embedded T-joints the cross-sectional area is smaller than the baseline. Experimental testing presented in chapter five showed that the normalised failure load $\frac{P_{\max}}{A}$ of the embedded and conventional T-joints is the same, therefore the allowable design strain should be equivalent. However if the damage initiation load is used to calculate the design strain then it is reduced for the embedded T-joint design. In this case it would be possible to use the hierarchical embedded/optimised T-joint design (refer chapter six) in order to equivalence the design strain to the baseline T-joint while preserving the damage tolerance benefits of an embedded design.

The issues of in-service impact damage resistance and repair of thin gauge composite parts has a major impact on the cost effectiveness of composite structures. To reduce these costs the allowable damage limit must be set at maximum size while still ensuring the safety of the aircraft [163]. Figure 8-3 illustrates the relationship between residual strength and impact damage size. The allowable damage limit (ADL) is set slightly above the barely visible impact damage (BVID), meaning the design ultimate load requirement is reduced. The critical damage threshold is equivalent to the visible impact damage (VID) threshold and indicates the damage size at which design limit load must be sustainable.

The experimental impact testing results discussed in chapter seven provided evidence that at very low impact energies (2 J) the 50% embedded design is more susceptible to crack branching and crack deflection in the radius bend area. However the damage initiated from low energy impact was equivalent to BVID of ¼ inch (6.35 mm) or ½ inch (12.7 mm) flaws, which for certification purposes are assumed to be present in every structure anyway. At higher impact energies (4 – 14 J), in which damage occurs along the stiffener flange/skin bond-line, the damage zone was reduced in the 50% embedded design due to a partial stabilisation of the dominant bond-line crack. Therefore, the embedded T-joint design is advantageous because it reduces the damage size under impact loading, which means the composite structure can sustain higher impact loads without requiring expensive repairs.

In summary, the manufacturing and certification issues of bio-inspired embedded, optimised and hierarchical composite T-joint designs require further research. However, after briefly considering the main issues the conclusion is that it would be possible to implement biomimetic design concepts within existing manufacturing and certification frameworks.

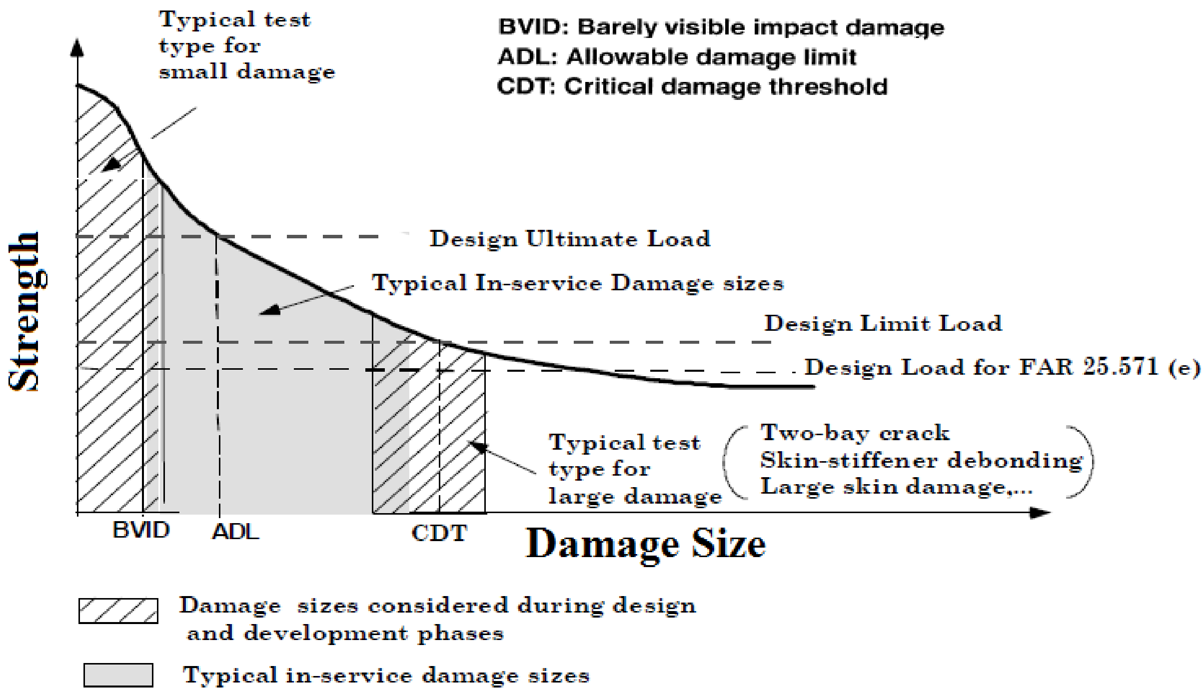

Figure 8-3 Residual strength versus damage size relationship as used for certification and maintenance planning. Reproduced from [163]

9 CONCLUDING REMARKS

Two key principles observed in natural load-bearing structures are hierarchical design and uniform strain. These two principles are linked. Experimental testing and imaging of tree branch-trunk joints from *Pinus radiata* complemented existing literature to confirm the first key principle - the structure of the tree branch-trunk joint is strongly hierarchical. This means that features at the material (nano- and micro-) and structural (meso- and macro-) length scales interact in synergy to enhance mechanical properties such as ductility and toughness. Tree branch-trunk joints are adapted to their loading environment through shape optimisation of the external radii, internal bond-line geometry, embedded design, and material optimisation including a density gradient, tailored microfibril angles and variable matrix chemical composition in the wood cell wall. Microscopic examination of the fracture surface of wood revealed multiple intrinsic toughening mechanisms including crack branching, crack deflection, fibril bridging and fibril pull-out. These micro-level mechanisms, together with the macro-level structural features are the primary toughening processes that provide high damage tolerance beyond damage initiation and peak load, despite the constituent materials of wood being inherently brittle.

The second key design principle synthesised from the literature is biological structures self-optimise to compensate for geometric stress concentrations to attain a uniform strain field. Uniform strain is a simple, effective principle to ensure that material is neither overloaded nor under-utilised. Uniform strain is linked to the first biological principle in that hierarchical modifications at the material-length scale compensate for structural-level stress concentrations such as changes in geometry to ensure that the structure is uniformly stressed. Uniform strain achieved through the mechanism of hierarchical design ensures natural structures are tailored to the external loading environment with maximum property-to-weight efficiency. Biological structures have metabolic processes that are able to respond to changes in the external loading conditions; for example, bone is being constantly remodelled to fit the dynamic external loading environment. Furthermore, biological structures are capable of repair through self-healing.

Two bio-inspired design concepts were extracted from the search of existing literature and the experimental work characterising the tree branch-trunk joint. The first concept of optimised ply orientation works at the material (ply) level. It involves optimising the stiffener laminate stacking sequence to minimise the peak interlaminar tensile stress concentration in the radius bend under an external bending load applied to the stiffener web. A bio-inspired optimisation program was designed to optimise the orientation of the fibres within the T-joint stiffener laminate to reduce the geometric stress concentration, producing a more uniform interlaminar stress distribution (as found within tree joints) within prescribed global stiffness constraints. The optimisation program was bio-inspired in three ways: (i) the optimisation algorithm in which the material properties were altered in order to fit the external loading conditions (analogous to evolutionary optimisation – survival of the best fit); (ii) the optimisation objective function to minimise the peak interlaminar tensile stress (analogous to strain under elastic loading conditions); and (iii) the technique of minimising the interlaminar tensile stress by altering the stiffener laminate ply stacking pattern, which was bio-inspired from the observed tailoring of the microfibril angle in the wood cell wall both in and around the branch-trunk joint. The optimisation program was simplified to a design of experiments (DoE) program considering quasi-isotropic and asymmetric hygrothermally stable stacking sequences for the stiffener laminate.

Finite element analysis (FEA) within the stiffener radius bend and delta-fillet regions revealed that bio-inspired optimised ply orientation lowers the interlaminar tensile and shear stress concentrations in the T-joint radius bend that initiate delamination damage under bending loading. This was experimentally validated with the optimised T-joint achieving significant improvement in the damage initiation load and absorbed elastic strain energy under bending loading. The increase in the damage initiation load could be approximated by the reduction in the peak interlaminar tensile stress in the T-joint radius bend. Under tensile loading the optimised stiffener laminate design also improved the damage initiation load and elastic energy compared to the baseline (quasi-isotropic) T-joint. The optimised ply orientation did not alter the failure (peak) load or toughness of the T-joint.

Bio-inspired optimisation was proven to be an effective technique to improve the delamination damage initiation strength and absorbed elastic strain energy of composite T-joints without incurring stiffness, weight or (most probably) cost penalties. It is believed that this bio-inspired optimisation methodology is flexible and can be applied to improve the damage initiation strength and elastic strain energy absorption of T-joints under other loading conditions (e.g. anti-symmetric bending), other joint designs (e.g. L-shaped joints and 90° angle brackets), and other objectives (e.g. optimise skin stacking sequence to minimise impact damage).

The second bio-inspired design concept was a structural modification inspired from the observation that tree branch-trunk joints are highly integrated structures with the branch embedded to the centre of the trunk. The carbon fibre laminate plies within the stiffener flange were integrated to form part of the skin to mimic this embedded design that occurs in tree joints. The embedded design was experimentally tested at 25, 50 and 75% integration of the stiffener flange into the skin under bending, tensile and compressive loading. The experimental results revealed that the embedded design increases the inelastic strain energy (ductility), strain energy to failure load (toughness), and damage tolerance of composite T-joints under both bending and tensile loading. More energy is required to fail a composite T-joint with higher levels of embedment.

Improvements in ductility, toughness and damage tolerance were attributed to increasing the number of stiffener flange/skin interfaces in the embedded design which induces crack deflection and crack branching (similar to the tree branch-trunk joint). This increases the strain energy release rate per volume of joint material as well as partially stabilising the dominant crack along the stiffener flange/skin bond-line. In comparison, a single dominant crack develops along the stiffener flange/skin bond-line of a conventional T-joint design, resulting in a more brittle failure mode.

The embedded T-joint design had the disadvantages of reducing the normalised damage initiation load (although the normalised peak load remained unchanged) under both tensile and bending loading and reducing the in-plane compressive strength of the skin. These disadvantages both resulted from increased skin flexibility caused by the reduction in the number of continuous skin plies in the embedded design with progressive integration of the flange into the skin. The reduction in the damage initiation load was investigated using non-linear FE analysis. The analysis revealed that the increased skin flexibility caused an increase in the interlaminar tensile and shear stresses in the critical radius bend/delta-fillet region which triggered early onset delamination damage.

These results showed that implementing only one biomimicked feature (i.e. optimised ply stacking or embedded plies) results in both advantages and disadvantages. The optimised stiffener ply stacking sequence concept improved the T-joint damage initiation strength, but did not improve damage tolerance and the T-joint still exhibited brittle failure. The embedded design concept improved the ductility, toughness and damage tolerance of the T-joint at the expense of reducing damage initiation strength. The biological principle of hierarchical design dictates that refinement of both material and structural properties is essential to create a T-joint that is both strong and tough.

The hierarchical approach to bio-inspired design was investigated by creating a composite T-joint with both optimised ply orientation and 50% flange/skin integration through embedded design. In combining these two biomimetic design strategies the disadvantage of the embedded design increasing the interlaminar stress concentration in the critical radius bend and delta-fillet regions was overcome by the advantage of the optimised laminate stacking sequence decreasing the geometric interlaminar stress concentrations in this critical zone. Similarly, the advantage of the improvement in damage tolerance in the embedded T-joint design overcame the disadvantage of the optimised joint exhibiting brittle failure. Hierarchical design enabled the production of a bio-inspired composite T-joint that is both strong and tough. Thus, the hierarchical T-joint was bio-inspired in three ways: at the material (ply) level through ply angle optimisation, at the structural level through embedded design, and in the interaction between the two levels compensating for each other's weaknesses via hierarchical design.

Finally, a preliminary investigation into the performance of the bio-inspired T-joint design concepts under dynamic impact loading was conducted due to the requirement for aerospace structures to resist in-service impact events such as hailstorms, tools dropped during maintenance or bird strike to avoid expensive repairs. Experimental impact testing showed that the optimised ply orientation does not alter the impact loading performance of the T-joint in comparison to the baseline quasi-isotropic design. The 50% embedded T-joint exhibited significantly better impact damage resistance as defined by crack length along the stiffener flange/skin bond-line. Post-impact residual tensile strength testing showed that the length of the damage zone along the stiffener flange/skin bond-line could be used to assess the normalised residual strength of all four T-joint designs, indicating that the bio-inspired optimised and embedded T-joints have the same impact damage tolerance as the baseline conventional quasi-isotropic T-joint designs.

Dynamic explicit non-linear geometry FE analysis was used to determine the force-time response and elastic interlaminar tensile and shear stress distributions in the bio-inspired T-joints under low energy impact loading. The contact force, frequency and contact time were very similar for the optimised T-joint design compared to the baseline T-joint because of the similarity in their stiffness properties. The elastic interlaminar tensile and shear stress distributions were also similar for the two unidirectional T-joint designs.

The peak contact force was significantly reduced and the contact time was increased for the fabric embedded T-joint due to the reduction in the skin bending stiffness. Despite this change the elastic interlaminar tensile and shear stresses were similar compared to the baseline T-joint. Similar to the quasi-static test results, the bio-inspired embedded design alters the toughness of the T-joint so that damage that would normally propagate along the stiffener flange/skin bond-line is absorbed through crack branching and crack deflection in the radius bend region or is deflected up towards the stiffener web (where there is no embedded design). It might be possible to use embedded design to strategically embed parts of the primary structure in order to deflect impact energy towards less crucial secondary structure.

Improvements in advanced manufacturing methods such as automated tape lay-up and stereolithography will better allow implementation of hierarchical design into aerospace structures, thereby enabling cost-effective production of innovative structures exhibiting uniform strain properties. As a final challenge, looking into the future the new frontier lies in the synthesis of bio-inspired materials through manufacturing processes that are characteristic of biological systems i.e. nano-scale self-assembly. Elucidating how nature extracts maximum efficiency by incorporating a number of toughening and strengthening architectures at each of the nano-, micro- and macro-length scales provides engineers with an enormous opportunity to apply these concepts to engineered materials. In conjunction with improved manufacturing methods, bio-inspired design provides an exciting opportunity to create new materials and structures with extraordinary properties.

In summary, the starting point of this PhD thesis was the hypothesis that natural structures can provide practical inspiration and a short-cut to innovation to improve the design of engineered structures such as carbon/epoxy composite T-joints. From these beginnings the research proceeded through a literature review of biological materials to focus on the natural fibre-based composite - wood. The macro- and micro-level architecture and failure modes of tree branch-trunk joints were evaluated and this information synthesized into bio-inspired design concepts to apply to aerospace carbon fibre composite T-joints. This thesis has presented experimental results and numerical finite element analyses to evaluate the structural properties of these novel bio-inspired design concepts under bending, tensile and compressive loading and impact loading. The results validate the hypothesis that biomimetic design is a useful approach capable of producing new design concepts for carbon fibre composite T-joints that exhibit improved strength and toughness.

9.1 RECOMMENDATIONS FOR FUTURE WORK

The research presented in this PhD thesis represents the beginning (and not the complete) assessment of biomimetic design applied to composite joints. More research and development is needed, including large scale demonstrations, fatigue testing and large-scale production solutions to mature the technology before the novel bio-inspired composite T-joint designs presented in this thesis could be implementation into real aircraft structures.

With this in mind the following research topics are recommended for future work:

- Use digital image correlation to perform direct strain measurements on the critical T-joint radius bend/delta-fillet region to experimentally validate changes in the strain field resulting from the bio-inspired optimised ply orientation design concept discussed in chapter four.
- Conduct a parametric study into the sensitivity of the optimised (for bending) ply stacking sequence to changes in the T-joint geometry such as varying radius and changes in the material properties including the orthotropic E_1/E_2 ratio.

- Conduct a study into the influence of the presence of flaws of various sizes and locations on the interlaminar tensile and shear stress distributions in the bio-inspired T-joint with an optimised stiffener laminate stacking sequence (refer chapter four).
- Apply the optimisation methodology developed in chapter four to other design objectives such as improved skin-side impact damage tolerance or fatigue resistance.
- Investigate the influence of process-induced residual thermal stresses on the performance of the optimised composite T-joint.
- Construct a damage model evaluating the strain energy release rate within the radius bend and at the stiffener flange/skin bond-line to better understand how the embedded design (discussed in chapter five) influences damage growth and alters the ductility and toughness of the T-joint under quasi-static loading conditions. This could be extended to a dynamic explicit analysis to investigate the influence of the embedded design under impact loading (as discussed in chapter seven).
- Investigate manufacturing issues in order to produce and test larger scale bio-inspired components such as a hierarchical multi-stringer stiffened skin panels with optimised ply orientation and embedded design to confirm that benefits in strength and toughness derived from the small scale element testing performed in this PhD study translate to larger structures.

REFERENCES

1. Mouritz, A and Cox, B. A mechanistic interpretation of the comparative in-plane mechanical properties of 3D woven, stitched, and pinned composites. Composites Part A 2010; 41, 709-728.
2. Mouritz, A. Review of z-pinned composite laminates. Composites Part A 2007; 38A(2383-2397).
3. Baker, A, Dutton, S and Kelly, D, *Composite Materials for Aircraft Structures*. 2nd ed: AIAA Education Series. 2004.
4. Meyers, MA, Chen, P-Y, Lin, AY-M and Seki, Y. Biological materials: Structure and mechanical properties. Progress in Materials Science 2008; 53, 1–206.
5. Darwin, C, *On the Origin of Species By Means of Natural Selection*, London: John Murray. 1859.
6. http://vip.manuterme.us/guanwang/come-and-visit/attraction-cornwall.html. 2011.
7. http://pascalepetit.blogspot.com/2011/02/ai-weiweis-sunflower-seeds-at-tate.html. 2011.
8. http://www.arup.com/Projects/30_St_Mary_Axe.aspx. 2011.
9. Fratzl, P and Weinkamer, R. Nature's hierarchical materials. Progress in Materials Science 2007; 52(8), 1263-1334.
10. http://www.arup.com/Projects/Chinese_National_Aquatics_Center.aspx. 2011.
11. Ball, P. Shark skin and other solutions. Nature 1999; 400, 507-509.
12. http://atoptics.wordpress.com/2011/05/27/interference-phenomena-on-soap-bubble-surface. 2011.
13. Metzger, K, *Mundener Forstliche Hefte*. Vol. 3, Berlin Heidelberg New York: Springer. 1893.
14. Wenthworth Thompson, D, *On Growth and Form*, Cambridge: University Press. 1917.
15. Munzinger, M, Kraft, O and Mattheck, C. Computer aided adhesive and assembly optimization method: Biomimetic optimization of adhesive joints. Journal of Materials Research 2006; 21(8), 2011-2017.
16. Reuschel, D and Mattheck, C. Three-dimensional fibre optimisation with computer aided internal optimisation. The Aeronautical Journal 1999; 103(1027), 415 - 420.
17. Goetz, K and Mattheck, C. Trees as a model for technical fibre composites. In: Proceedings of Proceedings of International Conference on Computer Aided Optimum Design of Structures, 2001.
18. Reuschel, D and Mattheck, C, *Optimization of fiber arrangement with CAIO (computer aided internal optimization) and application to tensile samples*, in *Computer aided optimum design of structures VI*. 1999, WIT Press: Southhampton.
19. Müller, U, Gindl, W and Jeronimidis, G. Biomechanics of a branch-stem junction in softwood. Trees 2006; 20, 643 – 648.
20. Chen, P-Y, Lin, A, Lin, Y-S, Seki, Y, Stokes, A, Peyras, J, Olevsky, E, Meyers, M and McKittrick, J. Structure and mechanical properties of selected biological materials. Journal of the Mechanical Behaviour of Biomedical Materials 2008; 1, 208-226.
21. McKittrick, J, Chen, P, Tombolato, L, Novitskaya, E, Trim, M, Hirata, G, Olevsky, E, Horstemeyer, M and Meyers, M. Energy absorbent natural materials and bioinspired design strategies: A review. Materials Science and Engineering C 2010; 30, 331-342.
22. Espinosa, H, Rim, J, Barthelat, F and Buehler, M. Merger of structure and material in nacre and bone: Perspectives on de novo biomimetic materials. Progress in Materials Science 2009; 54, 1059-1100.
23. Wegst, U and Ashby, M. The mechanical efficiency of natural materials. Philosophical Magazine 2004; 84(21), 2167-2181.
24. Weinkamer, R and Fratzl, P. Mechanical adaptation of biological materials - The examples of bone and wood. Materials Science and Engineering C 2011; 31, 1164-1173.
25. Gibson, L and Ashby, M, *Cellular Solids: Structure and Properties,*, Oxford, UK: Pergamon Press. 1988.
26. Kolednik, O, Predan, J, Fischer, F and Fratzl, P. Bioinspired design criteria for damage-resistant materials with periodically varying microstructure. Advanced Functional Materials 2011; 21, 3634-3641.
27. Launey, M and Ritchie, R. On the fracture toughness of advanced materials. Advanced Materials 2009; 21, 2103-2110.
28. Parsons, W, *Engineers and Engineering in the Renaissance*: Baltimore MD. 1939.

29. Ji, B and Gao, H. Mechanical properties of nanostructure of biological materials. Journal of the Mechanics and Physics of Solids 2004; 52, 1963-1990.
30. Ackbarow, T and Buehler, M. Alpha-helical protein domains unify strength and robustness through hierarchical nanostructures. Nanotechnology 2009; 20, 075103.
31. Tang, Z, Kotov, N, Magonov, S and Ozturk, B. Nanostructured artificial nacre. Nature 2003; 2, 413-419.
32. Jackson, A, Vincent, J and Turner, R. The mechanical design of nacre. Proceedings of the Royal Society B 1988; 234, 415–440.
33. Cunningham, A. Making the most of it - How nature turns weakness into strength. Science News 2006; 169(12), 184-185.
34. Lin, A and Meyers, MA. Growth and structure in abalone shell. Materials Science and Engineering A 2005; 390(1-2), 27-41.
35. Buehler, M. Molecular nanomechanics of nascent bone: fibrillar toughening by mineralization. Nanotechnology 2007; 18(29), 295102.
36. Munch, E, Launey, M, Alsem, D, Saiz, E, Tomsia, A and Ritchie, R. Tough, bio-inspired hybrid materials. Science 2008; 322, 1516-1520.
37. Fratzl, P, *Hierarchical structure and mechanical adaptation of biological materials*, in *Learning from Nature How to Design New Implantable Biomaterials*. 2004, Kluwer Academic Publishers: Netherlands. p. 15-34.
38. Norman, T, Vashishth, D and Burr, D. Fracture toughness of human bone under tension. Journal of Biomechanics 1995; 28, 309–320.
39. Jager, I and Fratzl, P. Mineralized collagen Mbrils: a mechanical model with a staggered arrangement of mineral particles. Biophysical Journal 2000; 79, 1737–1746.
40. Bacheva, D, Elsayed, M and Trask, R, *The skeleton of Euplectella Aspergillum as foundation for the development of novel composite aerospace structures*, in *International Conference on Composite Materials*. 2011: Jeju, South Korea.
41. Sarikaya, M, Fong, H, Sunderland, N, Flinn, B, Mayer, G, Mescher, A and Gaino, E. Biomimetic model of a sponge-spicular optical fiber – mechanical properties and structure. Journal of Materials Research 2001; 16(5), 1420-1428
42. Mayer, G and Sarikaya, M. Rigid biological composite materials: Structural examples for biomimetic design. Experimental Mechanics 2002; 42(4), 395-403.
43. Beismann, H, Wilhelmi, H, Bailleres, H, Spatz, H-C, Bogenrieder, A and Speck, T. Brittleness of twig bases in the genus Salix- fracture mechanics and ecological relevance. Journal of Experimental Botany 2000; 51, 617-633.
44. Reiterer, A, Stanzl-Tschegg, S and Tschegg, E. Mode I fracture and acoustic emission of softwood and hardwood. Wood Science and Technology 2000; 34, 417–430.
45. Wilson, B and Archer, R. Tree design - some biological solutions to mechanical problems. Bioscience 1979; 29, 293 – 298.
46. Jungnikl, K, Goebbels, J, Burgert, I and Fratz, P. The role of material properties for the mechanical adaptation at branch junctions. Trees 2009; 23, 605 - 610.
47. Burgert, I and Jungnikl, K. Adaptive growth of gymnosperm branches - Ultrastructural and micromechanical examinations. Journal of Plant Growth Regulations 2004; 23, 76 – 82.
48. Burns, LA, Mouritz, AP, Pook, D and Feih, S. Bio-inspired design of aerospace composite joints. In: Proceedings of Proceedings of Asia-Pacific International Symposium on Aerospace Technology (APISAT), . Melbourne, 2011.
49. Gordon, J and Jeronimidis, G. Composites with high work of fracture. Phil. Trans. R. Soc. London A 1980; 294, 545–550.
50. Bolza, E and Kloot, N, *The Mechanical Properties of 174 Australian Timbers* Melbourne: CSIRO. 1963.
51. Spatz, H, Koehler, L and Niklas, K. Mechanical behaviour of plant tissues: Composite materials or structures? Journal of Experimental Biology 1999; 202, 3269 - 3272.
52. Booker, R and Sel, l. The nanostructure of the cell wall of softwoods and its functions in a living tree. Holz als Roh- und Werkstoff 1998; 56, 1–8.
53. Eder, M, Jungnikl, K and Burgert, I. A close-up view of wood structure and properties across a growth ring of Norway spruce (Picea abies). Trees 2009; 23, 79–84.
54. Zhang, B, Fei, B, Yu, Y and Zhao, R. Microfibril angle variability in Masson Pine (Pinus massoniana Lamb.) using X-ray diffraction. Forestry Studies China 2007; 9(1), 33–38.

55. Phillips, G, Bodig, J and Goodman, J. Flow-grain analogy. Wood Science and Technology 1981; 14(2), 55–64.
56. Foley, C. A three-dimensional paradigm of fiber orientation in timber. Wood Science and Technology 2001; 35(5), 453-465.
57. Kramer, E. Wood grain pattern formation - A brief review. Journal of Plant Growth Regulation 2006; 25, 290-301.
58. Bonderer, L, Studart, A and Gauckler, L. Bioinspired design and assembly of platelet reinforced polymer films. Science 2008; 319, 1069-1073.
59. Burghard, Z, Zini, L, Srot, V, Bellina, P, Van Aken, P and Bill, J. Toughening through nature-adapted nanoscale design. Nano Letters 2009; 9(12), 4103-4108.
60. Podsiadlo, P, Kaushik, A, Arruda, E, Waas, A, Shim, B, Xu, J, Nandivada, H, Pumplin, B, Lahann, J, Ramamoorthy, A and Kotov, N. Ultrastrong and stiff layered polymer nanocomposites. Science 2007; 318, 80-83.
61. Mattheck, C. Teacher tree: The evolution of notch shape optimization from complex to simple. Engineering Fracture Mechanics 2006; 73, 1732-1742.
62. Mattheck, C, *Design in Nature: Learning from Trees*, New York: Springer Verlag. 1998.
63. Xu, L, Kuai, H and Sengupta, S. Dissimilar material joints with and without free-edge stress singularities: Part I. A biologically inspired design. Experimental Mechanics 2004; 44(6), 608-615
64. Mattheck, C, Kappel, R and Kraft, O, *Meaning of the 45 degree angle in mechanical design according to nature*, in *Design and Nature IV: Comparing Design in Nature with Science and Engineering*, C. Brebbia, Editor. 2008, WIT Press. p. 139-146.
65. Higgins, J and Pelham, L, *Application of Pi preform composite joints in fabrication of NASA composite crew module demonstration structure (abstract)*. 2004, AIAA.
66. Burns, L, Mouritz, A, Pook, D and Feih, S. Strength improvement to composite T-joints under bending through bio-inspired design. Composites: Part A 2012; 43, 1971–1980.
67. Tashiro, K and Kobayashi, M. Theoretical evaluation of three-dimensional elastic constants of native and regenerated celluloses: role of hydrogen bonds. Polymer 1992; 32, 1516-1526.
68. Cousins, W. Young's modulus of hemicellulose as related to moisture content. Wood Science and Technology 1978; 12(3), 161-167.
69. Cousins, W. Elastic modulus of lignin as related to moisture content. Wood Science and Technology 1976; 10(1), 9-17.
70. Cave, I. The longitudinal Young's modulus of Pinus radiata. Wood Science and Technology 1969; 3(1), 40-48.
71. Astley, R, Stol, K and Harrington, J. Modelling the elastic properties of softwood: Part II the cellular microstructure. Holz als Roh- und Werkstoff 1998; 56, 43–50.
72. Booker, R and Sell, J. The nanostructure of the cell wall of softwoods and its functions in a living tree Holz als Roh- und Werkstoff 1998; 56, 1-8.
73. Mishnaevsky, L and Qing, H. Micromechanical modelling of mechanical behaviour and strength of wood: State-of-the-art review. Computational Materials Science 2008; 44, 363–370.
74. Bergander, A and Salmen, L. Variations in transverse fibre wall properties: Relations between elastic properties and structure. Holaforschung 2000; 54, 654-660.
75. Jakob, H, Fratz, P and Tschegg, S. Size and arrangement of elementary cellulose fibrils in wood cells: A small-angle x-ray scattering study of Picea abies. Journal of Structural Biology 1994; 113, 13-22.
76. Peura, M, Mueller, M, Vainio, U, Saren, M, Saranpaa, P and Serimaa, R. X-ray microdiffraction reveals the orientation of cellulose microfibrils and the size of cellulose crystallites in single Norway spruce tracheids. Trees 2008; 22, 49–61.
77. Gindl, W. Comparing mechanical properties of normal and compression wood in Norway spruce: The role of Lignin in compression parallel to the grain. Holzforschung 2002; 56, 395–401.
78. Stanzl-Tschegg, S. Microstructure and fracture mechanical response of wood. International Journal of Fracture 2006; 139, 495–508.
79. Jeronimidis, G. The fracture behaviour of wood and the relations between toughness and morphology. Proceedings of the Royal Society London 1980; 208, 447–460.
80. Reiterer, A, Lichtenegger, H, Fratzl, P and Stanzl-Tschegg, S. Deformation and energy absorption of wood cell walls with different nanostructure under tensile loading. Journal of Materials Science 2001; 36, 4681–4686.
81. Feih, S, *Lecture slides*. 2008, RMIT University.

82. Lichtenegger, H, Reiterer, A, Stanzl-Tschegg, S and Fratzl, P. Variation of cellulose microfibril angles in softwoods and hardwoods - A possible strategy of mechanical optimization. Journal of Structural Biology 1999; 128, 257–269.
83. Faerber, J, Lichtenegger, H, Reiterer, A, Stanzl-Tschegg, S and Fratzl, P. Cellulose microfibril angles in a spruce branch and mechanical implications. Journal of Materials Science 2001; 36, 5087 – 5092.
84. Braendstroem, J. Microfibril angle of the S1 cell wall layer of Norway spruce compression wood tracheids. IAWA Journa 2004; 25(4), 415–423.
85. Bergander, A and Salmen, L. Cell wall properties and their effects on the mechanical properties of fibers. Journal of Materials Science 2002; 37, 151–156.
86. Carrington, H. The elastic properties of Spruce. Philosophical Magazine 1923; 45, 1055-1057.
87. Kramer, E and Borkowski, M. Wood grain patterns at branch junctions: modeling and implications. Trees 2004; 18, 493–500.
88. Eklund, L and Saell, H. The influence of wind on spiral grain formation in conifer trees. Trees 2000; 14, 324–328.
89. Lev-Yadun, S. Whirled grain in wood and topological defects. Journal of Theoretical Biology 2000; 205, 511-514.
90. Lev-Yadun, S and Aloni, R. Vascular differentiation in branch junctions of trees: Circular patterns and functional significance. Trees 1990; 4, 49-54.
91. Reiterer, A, Burgert, I, Sinn, G and Tschegg, S. The radial reinforcement of the wood structure and its implication on mechanical and fracture mechanical properties – A comparison between two tree species. Journal of Materials Science 2002; 37, 935–940.
92. Mattheck, C and Bethge, K. The structural optimisation of trees. Naturwissenschaften 1998; 85, 1 - 10.
93. Smith, I, Landis, E and Gong, M, *Fracture and Fatigue in Wood*, Sussex: John Wiley and Sons Ltd. 2003.
94. Gordon, J and Jeronimidis, G. Composites with high work of fracture. Philosophical Transactions of the Royal Society A 1980; 294, 545–550.
95. Koehler, L and Spatz, H. Micromechanics of plant tissues beyond the linear-elastic range. J Planta 2002; 215, 33-40.
96. Shigo, A. How tree branches are attached to trunks. Canadian Journal of Botany 1985; 63, 1391-1401.
97. Dean, T, Roberts, S, Gilmore, D, Maguire, D, Long, J, O'Hara, K and Seymour, R. An evaluation of the uniform stress hypothesis based on stem geometry in selected North American conifers. Trees 2002; 16, 559-568.
98. Dean, T and Long, J. Validity of constant-stress and elastic instability principles of stem formation in Pinus contorta and Trifolium pratense. Annals of Botany 1986; 58(6), 833–840.
99. West, P, Jackett, D and Sykes, S. Stresses in, and the shape of, tree stems in forest monoculture. Journal of Theoretical Biology 1989; 140, 327–343.
100. Timell, T, *Compression Wood in Gymnosperms*, Berlin: Springer. 1986.
101. Shigo, A, *A New Tree Biology*, Braunschweig: Thalacker. 1990.
102. Kwon, M, Bedgar, D, Piastuch, S, Davin, L and Lewis, N. Induced compression wood formation in Douglas fir (Pseudotsuga menziesii) in microgravity. Phytochemistry 2001; 57, 847-857.
103. Young, W, *Roark's Formulas for Stress and Strain*, New York: McGraw-Hill Book Company. 1989.
104. Shenoi, R and Hawkins, G. Influence of material and geometry variations on the behaviour of bonded tee connections in FRP ships. Composites 1992; 23(5), 335 – 345.
105. Gillespie, J and Byron Pipes, R. Behavior of integral composite joints - Finite element and experimental evaluation 1. Journal of Composite Materials 1978; 12, 408-421.
106. Avalon, SC and Donaldson, SL. Strength of composite angle brackets with multiple geometries and nanofiber-enhanced resins. Journal of Composite Materials 2010; 45(9), 1017-1030.
107. Orifici, A, Shah, S, Herszberg, I, Kotler, A and Weller, T. Failure analysis in postbuckled composite T-sections. Composite Structures 2008; 86, 146-153.
108. Shenoi, R, Read, P and Jackson, C. Influence of joint geometry and load regimes on sandwich tee joint behaviour. Journal of Reinforced Plastics and Composites 1998; 17, 725-740.
109. Dodkins, A, Shenoi, R and Hawkins, G. Design of joints and attachments in FRP ships' structures. Marine Structures 1994; 7, 365-398.
110. Dulieu-Barton, J, Earl, J and Shenoi, R. Determination of the stress distribution in foam-cored sandwich construction composite tee joints. Journal of Strain Analysis 2001; 36, 545-671.
111. Shenoi, R, Read, P and Hawkins, G. Fatigue failure mechanisms in fibre-reinforced plastic laminated tee joints. International Journal of Fatigue 1995; 17(6), 415-426.

112. Dulieu-Smith, J, Quinn, S, Shenoi, R, Read, P and Moy, S. Thermoelastic stress analysis of a GRP tee joint. Applied Composite Materials 1997; 4, 283-303.
113. Zimmermann, K, Zenkert, D and Siemetzki, M. Testing and analysis of ultra thick composites. Composites: Part B 2010; 41, 326-336.
114. Kumari, S and Sinha, P. Finite element analysis of composite wing T-joints. Journal of Reinforced Plastics and Composites 2002; 21(17), 1561-1585.
115. Davies, G and Ankersen, J. Virtual testing of realistic aerospace composite structures. Journal of Materials Science 2008; 43, 6586-6592.
116. Davies, G, Hitchings, D and Ankersen, J. Predicting delamination and debonding in modern aerospace composite structures. Composites Science and Technology 2006; 66, 846-854.
117. Linde, P, Pleitner, J and Rust, W, *Virtual testing of aircraft fuselage stiffened panels*, in *International Council of the Aeronautical Sciences (ICAS)*. 2004: Yokohama, Japan.
118. Orifici, A, Alberdi, I, Thomson, R and Bayandor, J. Compression and post-buckling damage growth and collapse analysis of flat composite stiffened panels. Composites Science and Technology 2008; 68, 3150–3160.
119. Orifici, A, Thomson, R, Degenhardt, R, Kling, A, Rohwer, K and Bayandor, J. Degradation investigation in a postbuckling composite stiffened fuselage panel. Composite Structures 2008; 82, 217-224.
120. Orifici, A, Thomson, R, Herszberg, I, Weller, T, Degenhardt, R and Bayandor, J. An analysis methodology for failure in postbuckling skin-stiffener interfaces. Composite Structures 2008; 86, 186-193.
121. Orifici, A, Abramovich, H, Herszberg, I, Kotler, A, Weller, T, Thomson, R and Bayandor, J, *Failure in skin-stiffener interfaces under postbuckling loads*, in *International Conference on Composite Structures (ICCS/14)*. 2007: Melbourne, Australia.
122. Kuhlmann, G and Rolfes, R. A hierarchic 3D finite element for laminated composites International Journal of Numerical Methods for Engineering 2004; 61(1), 96–116.
123. Dharmawan, F, Thomson, R, Li, H, Herszberg, I and Gellert, E. Geometry and damage effects in a composite marine T-joint. Composite Structures 2004; 66, 181–187.
124. Azzi, V and Tsai, S. Anisotropic strength of composites. Experimental Mechanics 1965; 5(9), 283–288.
125. Shivakumar, K, Allen, H and Avva, V. Interlaminar tension strength of graphite/epoxy composite laminates. AIAA Journal 1994; 32(7), 1478-1784.
126. Sun, C and Kelly, S. Failure in composite angle structures part I: Initial failure. Journal of Reinforced Plastics and Composites 1988; 7(3), 220-232.
127. Sun, C and Kelly, S. Failure in composite angle structures Part II: Onset of delamination. Journal of Reinforced Plastics and Composites 1988; 7, 233-243.
128. Hashin, Z. Failure criteria for unidirectional fiber composites. Journal of Applied Mechanics 1980; 47, 329-334.
129. Long, R. Static strength of adhesively bonded ARALL-1 Joints. Journal of Composite Materials 1991; 25, 391-415.
130. Feih, S and Shercliff, HR. Composite failure prediction of single-L joint structures under bending. Composites: Part A 2005; 36, 381-395.
131. Zhang, X. Impact damage in composite aircraft structures – experimental testing and numerical simulation. Proceedings of the Institution of Mechanical Engineers, Part G: Journal of Aerospace Engineering 1998; 212, 245-259.
132. Orifici, AC, Herszberg, I and Thomson, RS. Review of methodologies for composite material modelling incorporating failure. Composite Structures 2008; 86, 194–210.
133. Tong, L. An assessment of failure criteria to predict the strength of adhesively bonded composite double lap joints. Journal of Reinforced Plastics and Composites 1997; 16, 698-713.
134. Jackson, W and Martin, R, *An interlaminar tension strength specimen*, in *Symposium on Composite Materials: Testing and Design*, E. Camponeshi, Editor. 1993, American Society for Testing and Materials: Pittsburgh. p. 333-354.
135. Hiel, C, Sumich, M and Chappell, D. Curved beam test specimen for determining the interlaminar strength of a laminated composite. Journal of Composite Materials 1991; 25, 854-868.
136. O'Brien, T and Salpekar, S, *Scale effects on the transverse tensile strength of graphite epoxy composites*. 1991, NASA.
137. Lagace, P and Weems, D, *A through-the thickness strength specimen for composites*, in *Test Methods for Design Allowables for Fibrous Composites*, C. Chamis, Editor. 1989, American Society for Testing and Materials: Philadelphia. p. 197-207.

138. Li, H, Dharmawan, F, Herszberg, I and John, S. Fracture behaviour of composite maritime T-joints. Composite Structures 2006; 75, 339–350.
139. Greenhalgh, E, Lewis, A, Bowen, R and Grassi, M. Evaluation of toughening concepts at structural features in CFRP—Part I: Stiffener pull-off. Composites: Part A 2006; 37, 1521–1535.
140. Greenhalgh, E and Hiley, M. The assessment of novel materials and processes for the impact tolerant design of stiffened composite aerospace structures. Composites: Part A 2003; 34, 151-161.
141. Wiggenraad, J and Ubels, L, *Damage tolerance of a composite I-stiffened wing panel made of IM7/F3900-2 carbon-epoxy material*. 1998, NLR.
142. Soden, J, Weissenbach, G and Hill, B. The design and fabrication of 3D multi-layer woven T-section reinforcements. Composites: Part A 1999; 30, 213-220.
143. Ko, W, *Delamination stresses in semicircular laminated composite bars*. 1988, NASA.
144. Trask, R, Hallett, S, Helenon, F and Wisnom, M. Influence of process induced defects on the failure of composite T-joint specimens. Composites Part A 2012; 43(4), 748–757.
145. Tsai, S, *Weight and cost reduction by using unbalanced and unsymmetric laminates*, in *18th International Conference on Composite Materials*. 21 - 26 August 2011: Jeju, South Korea.
146. Radford, D and Diefendorf, R. Shape instabilities in composites resulting from laminate anisotropy. Journal of Reinforced Plastics and Composites 1993; 12, 58-75.
147. Cross, R, Haynes, R and Armanios, E. Families of hygrothermally stable asymmetric laminated composites. Journal of Composite Materials 2008; 42(7).
148. Haynes, R and Armanios, E, *Hygrothermally stable laminates with extension-twist and bend-twist couplings*, in *18th International Conference on Composite Materials*. 21 - 26 August 2011: Jeju, South Korea.
149. Haynes, R and Armanios, E. New families of hygrothermally stable composite laminates with optimal extension-twist coupling. AIAA Journal 2010; 48(12), 2954-2961.
150. Koh, T, Feih, S and Mouritz, A. Experimental determination of the structural properties and strengthening mechanisms of z-pinned T-joints. Composite Structures 2011; 93, 2222–2230.
151. Stickler, P, Ramula, M and Johnson, P. Experimental and numerical analysis of transverse stitched T-joints in bending. Composite Structures 2000; 50, 17-27.
152. Stickler, P and Ramula, M. Parametric analyses of stitched composite T-joints by the finite element method. Materials and Design 2002; 23, 751-758.
153. King, MJ, Sutherland, IJ and Le-Ngoc, L. Fracture toughness of wet and dry pinus radiata. Holz als Roh- und Werkstoff 1999; 57, 235 – 240.
154. Meyers, MA, Lin, A, Seki, Y, Chen, P-Y, Kad, B and Bodde, S. Structural biological composites: An overview. Journal of the Minerals, Metals and Materials Society 2006; 58(7), 35-41.
155. Lavender-CE. *VTM260 Series Prepreg Material Data Sheet*. [cited 2011 8 July]; Available from: http://www.lavender-ce.com/advanced-composite-material/technical-reference/.
156. Burns, LA, Mouritz, AP, Pook, D and Feih, S, *Bio-inspired design of aerospace composite joints*, in *Proceedings of Asia-Pacific International Symposium on Aerospace Technology (APISAT),* . 2011: Melbourne.
157. Long, RS. Static strength of adhesively bonded ARALL-1 joints. Journal of Composite Materials 1991; 25, 391-415.
158. Burns, LA, Mouritz, AP, Pook, D and Feih, S. Bio-inspired design of aerospace composite joints for improved damage tolerance. Composite Structures 2011; 94, 995-1004.
159. Fisher, R, *The Design of Experiments*. 1935.
160. Adams, R, *Optimum Structures - Design of Experiments*. 2010, RMIT University: Melbourne.
161. Sarikaya, M, Fong, H, Sunderland, N, Flinn, B, Mayer, G, Mescher, A and Gaino, E. Biomimetic model of a sponge-spicular optical fiber: Mechanical properties and structure. Journal of Materials Research 2001; 16(5), 1420-1428
162. Jackson, W and Martin, R. An interlaminar tensile strength specimen. In: Camponeschi Jr ET, (ed.) Composite materials: testing and design. American Society for Testing and Materials 1993; 11, 333-354.
163. Razi, H and Ward, S, *Principles for achieving damage tolerant primary composite aircraft structures*, in *11th DoD/FAA/NASA Conf. On Fibrous Composites in Structural Design*. 1996: Fort Worth, Texas.